APOPTOSIS AND AUTOPHAGY IN ACUTE CNS INJURIES: MECHANISM AND TREATMENT, 2nd Edition

EDITED BY: Gao Chen, Hua Feng, Gang Chen and Guohua Xi
PUBLISHED IN: Frontiers in Neuroscience

frontiers Research Topics

frontiers

ISSN 1664-8714
ISBN 978-2-8325-5247-6
DOI 10.3389/978-2-8325-5247-6

About Frontiers

Frontiers is more than just an open-access publisher of scholarly articles: it is a pioneering approach to the world of academia, radically improving the way scholarly research is managed. The grand vision of Frontiers is a world where all people have an equal opportunity to seek, share and generate knowledge. Frontiers provides immediate and permanent online open access to all its publications, but this alone is not enough to realize our grand goals.

Frontiers Journal Series

The Frontiers Journal Series is a multi-tier and interdisciplinary set of open-access, online journals, promising a paradigm shift from the current review, selection and dissemination processes in academic publishing. All Frontiers journals are driven by researchers for researchers; therefore, they constitute a service to the scholarly community. At the same time, the Frontiers Journal Series operates on a revolutionary invention, the tiered publishing system, initially addressing specific communities of scholars, and gradually climbing up to broader public understanding, thus serving the interests of the lay society, too.

Dedication to Quality

Each Frontiers article is a landmark of the highest quality, thanks to genuinely collaborative interactions between authors and review editors, who include some of the world's best academicians. Research must be certified by peers before entering a stream of knowledge that may eventually reach the public - and shape society; therefore, Frontiers only applies the most rigorous and unbiased reviews.
Frontiers revolutionizes research publishing by freely delivering the most outstanding research, evaluated with no bias from both the academic and social point of view. By applying the most advanced information technologies, Frontiers is catapulting scholarly publishing into a new generation.

What are Frontiers Research Topics?

Frontiers Research Topics are very popular trademarks of the Frontiers Journals Series: they are collections of at least ten articles, all centered on a particular subject. With their unique mix of varied contributions from Original Research to Review Articles, Frontiers Research Topics unify the most influential researchers, the latest key findings and historical advances in a hot research area! Find out more on how to host your own Frontiers Research Topic or contribute to one as an author by contacting the Frontiers Editorial Office: frontiersin.org/about/contact

APOPTOSIS AND AUTOPHAGY IN ACUTE CNS INJURIES: MECHANISM AND TREATMENT, 2nd Edition

Topic Editors:
Gao Chen, Zhejiang University, China
Hua Feng, Army Medical University, China
Gang Chen, First Affiliated Hospital of Soochow University, China
Guohua Xi, University of Michigan, United States

Publisher's note: This is a 2nd edition due to an article retraction.

Citation: Chen, G., Feng, H., Chen, G., Xi, G., eds. (2024). Apoptosis and Autophagy in Acute CNS Injuries: Mechanism and Treatment, 2nd Edition. Lausanne: Frontiers Media SA. doi: 10.3389/978-2-8325-5247-6

Table of Contents

05 ***Sirt3-Mediated Autophagy Contributes to Resveratrol-Induced Protection Against ER Stress in HT22 Cells***
Wen-Jun Yan, Ruo-Bin Liu, Ling-Kai Wang, Ya-Bing Ma, Shao-Li Ding, Fei Deng, Zhong-Yuan Hu and Da-Bin Wang

15 ***PERK Pathway Activation Promotes Intracerebral Hemorrhage Induced Secondary Brain Injury by Inducing Neuronal Apoptosis Both* in Vivo *and* in Vitro**
Chengjie Meng, Juyi Zhang, Baoqi Dang, Haiying Li, Haitao Shen, Xiang Li and Zhong Wang

26 ***Inhibition of Epac2 Attenuates Neural Cell Apoptosis and Improves Neurological Deficits in a Rat Model of Traumatic Brain Injury***
Ling Zhang, Li Zhang, Huixiang Liu, Feng Jiang, Huanjing Wang, Di Li and Rong Gao

36 ***Association of Brain CD163 Expression and Brain Injury/Hydrocephalus Development in a Rat Model of Subarachnoid Hemorrhage***
Chaohui Jing, Haining Zhang, Hajime Shishido, Richard F. Keep and Ya Hua

45 ***Annexin A7 Levels Increase in Rats With Traumatic Brain Injury and Promote Secondary Brain Injury***
Fan Gao, Di Li, Qin Rui, Haibo Ni, Huixiang Liu, Feng Jiang, Li Tao, Rong Gao and Baoqi Dang

53 ***The Role of Gaseous Molecules in Traumatic Brain Injury: An Updated Review***
Xiaoru Che, Yuanjian Fang, Xiaoli Si, Jianfeng Wang, Xiaoming Hu, Cesar Reis and Sheng Chen

62 ***Sirt3 Ameliorates Oxidative Stress and Mitochondrial Dysfunction After Intracerebral Hemorrhage in Diabetic Rats***
Jingwei Zheng, Ligen Shi, Feng Liang, Weilin Xu, Tao Li, Liansheng Gao, Zeyu Sun, Jun Yu and Jianmin Zhang

76 ***Asiatic Acid Prevents Oxidative Stress and Apoptosis by Inhibiting the Translocation of α-Synuclein Into Mitochondria***
Hongqun Ding, Yuyun Xiong, Jing Sun, Chen Chen, Jing Gao and Huaxi Xu

86 ***ErbB4 Preserves Blood-Brain Barrier Integrity via the YAP/PIK3CB Pathway After Subarachnoid Hemorrhage in Rats***
Huan Qian, Zhangqi Dou, Wu Ruan, Pingyou He, John H. Zhang and Feng Yan

95 ***Melatonin Protects Against Neuronal Apoptosis via Suppression of the ATF6/CHOP Pathway in a Rat Model of Intracerebral Hemorrhage***
Weilin Xu, Xiaoyang Lu, Jingwei Zheng, Tao Li, Liansheng Gao, Cameron Lenahan, Anwen Shao, Jianmin Zhang and Jun Yu

107 ***Andrographolide Alleviates Acute Brain Injury in a Rat Model of Traumatic Brain Injury: Possible Involvement of Inflammatory Signaling***
Li Tao, Li Zhang, Rong Gao, Feng Jiang, Jianbo Cao and Huixiang Liu

116 ***Electroacupuncture Improves Cerebral Vasospasm and Functional Outcome of Patients With Aneurysmal Subarachnoid Hemorrhage***
Jie Sun, Yuchun Liu, Junjun Zhang, Xiaosheng Chen, Zhiqing Lin, Sheng Nie, Manhua Shi, Xiang Gao and Yi Huang

124 ***METH-Induced Neurotoxicity is Alleviated by Lactulose Pretreatment Through Suppressing Oxidative Stress and Neuroinflammation in Rat Striatum***
Xiao-Li Xie, Wen-Tao Zhou, Kai-Kai Zhang, Li-Jian Chen and Qi Wang

131 ***G2019S LRRK2 Increases Stress Susceptibility Through Inhibition of DAF-16 Nuclear Translocation in a 14-3-3 Associated-Manner in* Caenorhabditis elegans**
Simei Long, Wenyuan Guo, Sophie Hu, Fengjuan Su, Yixuan Zeng, Jinsheng Zeng, Eng-King Tan, Christopher A. Ross and Zhong Pei

145 ***Exosomes Derived From miR-133b-Modified Mesenchymal Stem Cells Promote Recovery After Spinal Cord Injury***
Dong Li, Peng Zhang, Xiyang Yao, Haiying Li, Haitao Shen, Xiang Li, Jiang Wu and Xiaocheng Lu

154 ***Rapamycin Enhances Mitophagy and Attenuates Apoptosis After Spinal Ischemia-Reperfusion Injury***
Qiang Li, Shane Gao, Zhanrong Kang, Meiyan Zhang, Xin Zhao, Yu Zhai, Jianming Huang, Guo-Yuan Yang, Wanju Sun and Jian Wang

163 ***Crosstalk Between Autophagy and Cerebral Ischemia***
Yulin Sun, Yuanhan Zhu, Xiaojun Zhong, Xinle Chen, Jun Wang and Guozheng Ying

170 ***Carnosic Acid Mitigates Early Brain Injury After Subarachnoid Hemorrhage: Possible Involvement of the SIRT1/p66shc Signaling Pathway***
Lingfang Teng, Linfeng Fan, Yujiang Peng, Xijun He, Huihui Chen, Hongyu Duan, Fan Yang, Da Lin, Zheng Lin, Huiyong Li and Bo Shao

frontiers in Neuroscience

ORIGINAL RESEARCH
published: 27 February 2018
doi: 10.3389/fnins.2018.00116

Sir3-Mediated Autophagy Contributes to Resveratrol-Induced Protection against ER Stress in HT22 Cells

Wen-Jun Yan, Ruo-Bin Liu, Ling-Kai Wang, Ya-Bing Ma, Shao-Li Ding, Fei Deng, Zhong-Yuan Hu and Da-Bin Wang*

Department of Anesthesiology, Gansu Provincial Hospital, Lanzhou, China

Endoplasmic reticulum (ER) stress occurring in stringent conditions is critically involved in neuronal survival and death. Resveratrol is a non-flavonoid polyphenol that has neuroprotective effects against many neurological disorders. Here, we investigated the potential protective effects of resveratrol in an *in vitro* ER stress model mimicked by tunicamycin (TM) treatment in neuronal HT22 cells. We found that TM dose-dependently decreased cell viability and increased apoptosis, which were both significantly attenuated by resveratrol treatment. Resveratrol markedly reduced the expression or activation of ER stress-associated factors, including GRP78, CHOP, and caspase-12. The results of immunocytochemistry and western blot showed that resveratrol promoted autophagy in TM-treated cells, as evidenced by increased LC3II puncta number, bcelin1 expression and LC3II/LC3I ratio. Pretreatment with the autophagy inhibitor chloroquine could reduce the protective effects of resveratrol. In addition, the expression of Sirt3 protein and its downstream enzyme activities were significantly increased in resveratrol-treated HT22 cells. To confirm the involvement of Sirt3-mediated mechanisms, siRNA transfection was used to knockdown Sirt3 expression *in vitro*. The results showed that downregulation of Sirt3 could partially prevented the autophagy and protection induced by resveratrol after TM treatment. Our study demonstrates a pivotal role of Sirt3-mediated autophagy in mediating resveratrol-induced protection against ER stress *in vitro*, and suggests the therapeutic values of resveratrol in ER stress-associated neuronal injury conditions.

Keywords: resveratrol, autophagy, ER stress, Sirt3, HT22 cells

OPEN ACCESS

Edited by:
Gao Chen,
Zhejiang University, China

Reviewed by:
Maria Dolores Ledesma,
Centro de Biología Molecular Severo Ochoa (CSIC), Spain
Patricia Maciel,
Instituto de Pesquisa em Ciências da Vida e da Saúde (ICVS), Portugal

****Correspondence:***
Wen-Jun Yan
yanwenjun_gssyy@163.com

Specialty section:
This article was submitted to Neurodegeneration, a section of the journal Frontiers in Neuroscience

Received: *26 October 2017*
Accepted: *13 February 2018*
Published: *27 February 2018*

Citation:
Yan W-J, Liu R-B, Wang L-K, Ma Y-B, Ding S-L, Deng F, Hu Z-Y and Wang D-B (2018) Sirt3-Mediated Autophagy Contributes to Resveratrol-Induced Protection against ER Stress in HT22 Cells. Front. Neurosci. 12:116. doi: 10.3389/fnins.2018.00116

INTRODUCTION

The endoplasmic reticulum (ER) is the most important subcellular compartment that controls protein quality and calcium storage (Hawes et al., 2015). Under stress conditions, a cellular response named ER stress is triggered to preserve ER homeostasis through initiating the unfolded protein response (UPR), or to induce cell death via activating pro-apoptotic signaling cascades (Stefani et al., 2012). Accumulating evidence supports the concept that ER stress is involved in neuronal injury in various neurological disorders, ranging from acute insults (ischemic and traumatic brain injury) to chronic degenerative diseases (Alzheimer's disease and Parkinson's disease) (Valenzuela et al., 2016).

Autophagy, a Greek word meaning self-eating, represents a self-degradative process that balances energy sources via the bulk degradation and recycling of cytosolic proteins and organelles (Balduini et al., 2009). It is a highly conserved function among eukaryotes that plays a crucial role in maintaining cell survival under both physiological and pathological conditions. However, autophagy is a double-edged sword where under certain conditions, overactivation of autophagy could disrupt cellular homeostasis and result in cell death (Thorburn, 2014). It is now accepted that ER stress is a potent trigger for autophagy, and multiple ER stress associated signaling cascades also participates in autophagy process (Yin et al., 2017). Many previous studies have highlighted the need for developing autophagy-promoting strategies for diseases that are related to ER stress (Lee et al., 2015).

Resveratrol (3,4′,5-trihydroxyl-trans-stilbene, $C_{14}H_{12}O_3$) is a non-flavonoid polyphenolic phytoalexin discovered in the 1940s. This fat-soluble compound is present at high concentrations in grapes, peanuts, cassia and red wine (Ramprasath and Jones, 2010). Resveratrol has become a highly important natural active ingredient with many pharmacological properties, such as antioxidative, anti-inflammatory, anti-platelet, and anticancer effects (Carrizzo et al., 2013). Resveratrol is rapidly taken up after oral consumption of a low dose, and approximate 50–70% of the resveratrol could be absorbed by the body in human and rodents (Marier et al., 2002; Walle et al., 2004). In addition, resveratrol is able to cross the blood-brain barrier (BBB), and its neuroprotective activity has been demonstrated in stroke, brain trauma, seizure, and neurodegenerative diseases (Markus and Morris, 2008). However, the potential protective effects of resveratrol under ER stress conditions were not fully determined. Thus, this study was designed to investigate the effect of resveratrol in neuronal HT22 cells treated with the ER stress inducer tunicamycin (TM), and we also investigated the underlying mechanism with focus on Sirt3.

MATERIALS AND METHODS

Reagents and Antibodies

TM was purchased from Sigma (St. Louis, MO, USA). Resveratrol was obtained from Calbiochem (Darmstadt, Germany). Rapamycin, chloroquine and DAPI were obtained from Tocris (Bristol, UK). Antibody against GRP78 was purchased from Bioworld (St. Louis Park, MN, USA). Antibodies against CHOP, phospho-JNK, cleaved-caspase-12 and β-actin were obtained from Santa Cruz (Santa Cruz, CA, USA). Antibodies against Beclin1, LC3, LC3II, and Sirt3 were obtained from Cell Signaling (Danvers, MA, USA).

Cell Cultures

The hippocampal neuronal HT22 cells were cultured in Dulbecco's modified Eagle's medium (DMEM) supplemented with 10% fetal bovine serum at 37°C in a 5% CO_2 incubator.

Cell Viability Assay

Cell viability was assessed by the MTT assay as described previously with minor modifications (Chen et al., 2011). Cells (1×10^4 cells/well) were seeded in 96-well plates and subjected to various treatments. MTT solution at 5 mg/ml was added into each well, and incubated at 37°C in a 5% CO_2 incubator for 4 h. After the medium was carefully removed, DMSO was added to dissolve the blue formazan product. The absorbance was detected at 490 nm.

Lactate Dehydrogenase (LDH) Release Assay

Cellular toxicity was determined by measuring LDH release using a LDH kit as previously described (Dai et al., 2017).

Tunel Staining

Apoptosis was detected by TUNEL staining. HT22 cells were fixed by immersing slides in 4% methanol-free formaldehyde solution in PBS for 20 min and permeabilized with 0.2% Triton X-100 for 5 min. Cells were labeled with fluorescein TUNEL reagent mixture for 60 min at 37°C and the slides were examined by fluorescence microscopy and the number of TUNEL-positive cells was counted.

Immunocytochemistry

After being fixed with 4% paraformaldehyde for 15 min at room temperature, HT22 cells were washed with NaCl/Pi, permeabilized with 0.2% Triton X-100, and incubated with GRP78, LC3II or Sirt3 primary antibody overnight at 4°C. Cells were then incubated with Alexa 594-conjugated secondary antibody for 2 h at 37°C. Images were captured with an Olympus FV10i Confocal Microscope (Olympus, Tokyo, Japan).

RT-PCR Assays

Total RNA was prepared with the Trizol Reagent method, and 2 mg template RNA was used to synthesize the first strand of cDNA using a reverse transcription kit. The mRNA level of XBP1S was quantitated using a Bio-Rad iQ5 Gradient Real-Time PCR system (Bio-Rad Laboratories), and β-actin was used as an endogenous control.

Enzyme Activity Assays

The enzymatic activity of MnSOD and catalase was measured by use of a kit (Cayman Inc.) according to the manufacturer's protocol.

Short Interfering RNA (siRNA) and Transfection

The specific siRNA targeted Sirt3 (sc-61556), and control siRNA (sc-37007) were purchased from Santa Cruz. The above siRNA molecules were transfected with Lipofectamine 2000 in for 48 h before various treatments.

Western Blot Analysis

Proteins were loaded and separated by 10% SDS-PAGE gels, and transferred to polyvinylidene difluoride (PVDF) membranes. Membranes were blocked with 5% skimmed milk solution in TBST for 1 h, and then incubated overnight at 4°C with the primary antibodies. Immunoreactivity was detected with Super Signal West Pico Chemiluminescent Substrate (Thermo Scientific, Rockford, IL, USA).

Statistical Analysis

Statistical analysis was performed using SPSS 16.0. Statistical evaluation was performed by one-way analysis of variance (ANOVA). All samples were tested in triplicates and data from six independent experiments were used for analysis. A value of $p < 0.05$ was considered statistically significant.

RESULTS

Resveratrol Protects against TM-Induced Toxicity in HT22 Cells

HT22 cells were treated with TM at different concentrations, and the cell viability and LDH release were measured at 24 h. The results showed that TM at 50, 100, and 500 ng/ml significantly decreased cell viability (**Figure 1A**) and increased LDH release (**Figure 1B**), while 1 and 10 ng/ml TM had no such effects. Based on these results, 100 ng/ml TM was used in the following experiments. According to previous data and our pre-experimental results (Kim et al., 2012; Luyten et al., 2017), we used 50 μM resveratrol in this study. The results showed that 50 μM resveratrol partially prevented the decrease in cell viability (**Figure 1C**) and increase in LDH release (**Figure 1D**) after TM exposure. We also detected apoptosis using TUNEL staining, and reduced number of TUNEL-positive cells was observed in resveratrol treated cells compared to that in TM-treated alone group (**Figures 1E,F**).

Resveratrol Attenuates TM-Induced ER Stress in HT22 Cells

Immunocytochemistry was used to detect the expression of GRP78 in HT22 cells (**Figure 2A**), and the results showed that TM significantly increased the fluorescence of GRP78, which was partially reversed by resveratrol (**Figure 2B**). RT-PCR assay showed that resveratrol treatment preserved XBP1S mRNA levels after TM exposure (**Figure 2C**). We also detected the expression of ER stress associated pro-apoptotic factors using western blot (**Figure 2D**). The results showed that TM-induced CHOP induction (**Figure 2E**), JNK phosphorylation (**Figure 2**F), and caspase-12 cleavage (**Figure 2G**) were all significantly decreased by resveratrol, indicating the inhibition of ER stress.

Resveratrol Promotes Autophagy in HT22 Cells after TM Exposure

Western blot was performed to detect the expression of autophagy associated proteins (**Figure 3A**). The results showed that TM increased the expression of Beclin1 (**Figure 3B**) and the ratio of LC3II/LC3I (**Figure 3C**), which were both further increased by resveratrol treatment. In addition, we also detected the expression of LC3II by immunocytochemistry (**Figure 3D**). As shown in **Figure 3E**, TM increased the number of LC3II puncta, and resveratrol further increased LC3II puncta number.

Resveratrol Modulates TM-Induced Toxicity via Affecting Autophagy

To determine the role of autophagy in resveratrol-induced protection, HT22 cells were treated with the autophagy activator rapamycin (4 μM) or the autophagy inhibitor chloroquine (10 μM). The results of MTT assay showed that rapamycin could prevent TM-induced decrease in cell viability, whereas chloroquine partially reversed resveratrol-induced protection (**Figure 4A**). As shown in **Figure 4B**, TM-induced increase in

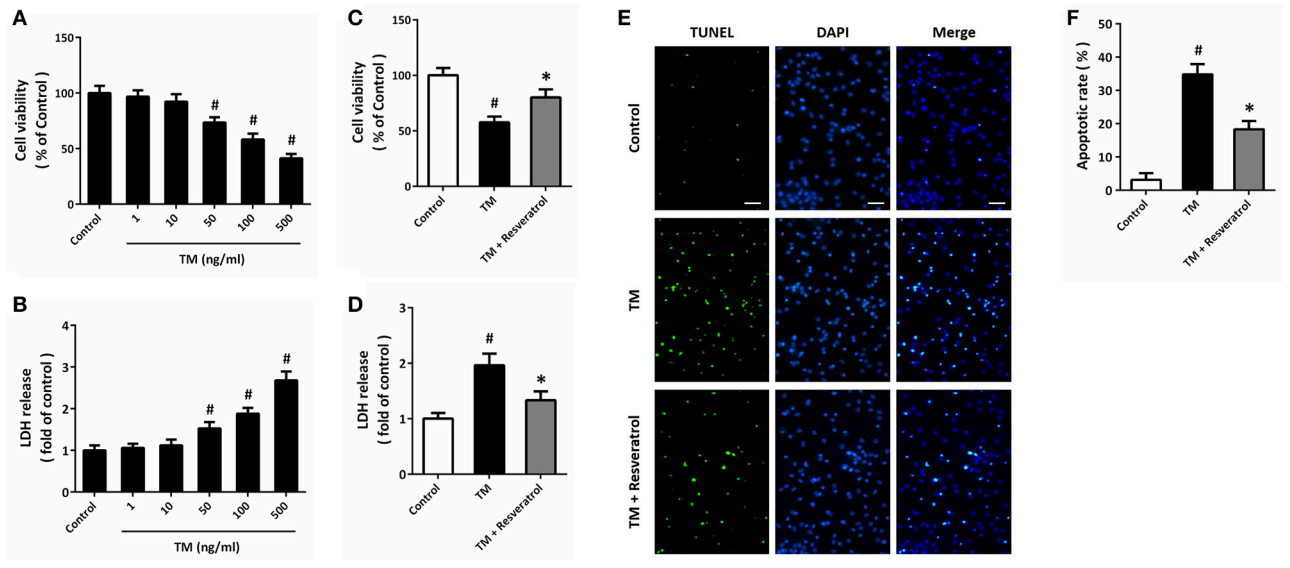

FIGURE 1 | Resveratrol protects against TM-induced toxicity in HT22 cells. HT22 cells were treated with TM at different concentrations for 24 h. Cell viability was measured by MTT assay **(A)**, and cytotoxicity was determined by LDH assay **(B)**. HT22 cells were treated with 100 ng/ml TM with or without 50 μM resveratrol for 24 h, and cell viability **(C)** and LDH release **(D)** were measured. TUNEL staining was performed to detect apoptosis, and the nuclei were stained by DAPI **(E)**. The apoptotic rate was assayed **(F)**. Data are shown as mean ± SEM. $^{\#}p < 0.05$ vs. Control. $^{*}p < 0.05$ vs. TM. Scale bar = 50 μm.

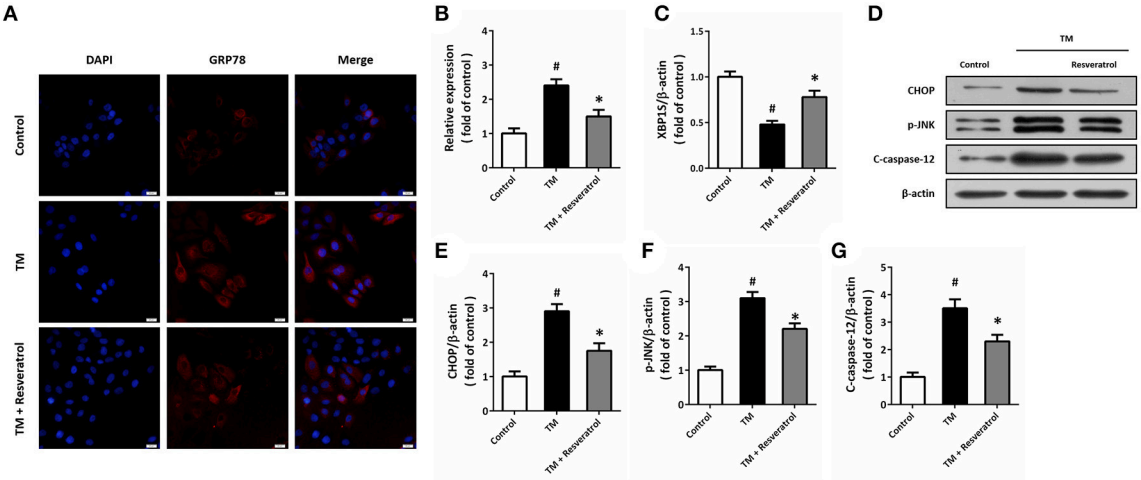

FIGURE 2 | Resveratrol attenuates TM-induced ER stress in HT22 cells. HT22 cells were treated with 100 ng/ml TM with or without 50 μM resveratrol for 24 h. The expression of GRP78 protein was detected by immunofluorescence staining **(A)** and calculated **(B)**. The mRNA levels of XBP1S was examined by RT-PCR **(C)**. The expression of CHOP, p-JNK and cleaved-caspase-12 was detected by western blot **(D–G)**. Data are shown as mean ± SEM. $^{\#}p < 0.05$ vs. Control. $^{*}p < 0.05$ vs. TM. Scale bar = 20 μm.

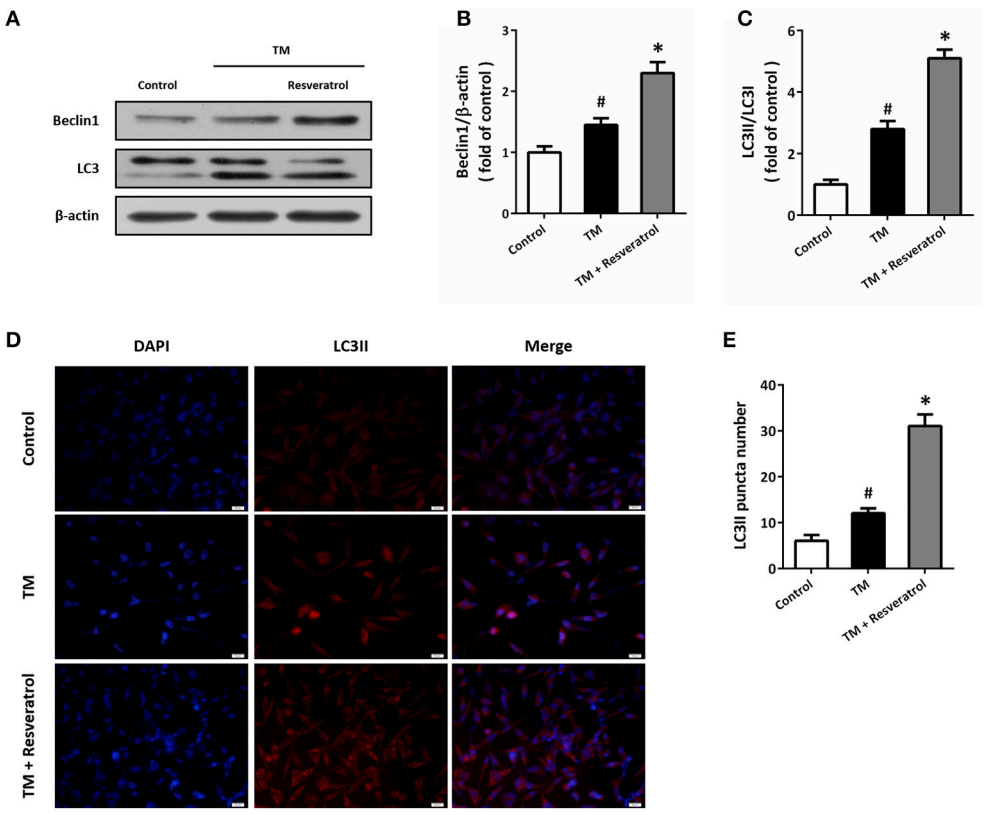

FIGURE 3 | Resveratrol promotes autophagy in HT22 cells after TM exposure. HT22 cells were treated with 100 ng/ml TM with or without 50 μM resveratrol for 24 h. The expression of Beclin1 and LC3 was detected by western blot **(A–C)**. Immunofluorescence staining of LC3II was performed to assess autophagy in HT22 cells **(D)**, and the number of LC3-positve puncta was counted **(E)**. Data are shown as mean ± SEM. $^{\#}p < 0.05$ vs. Control. $^{*}p < 0.05$ vs. TM. Scale bar = 20 μm.

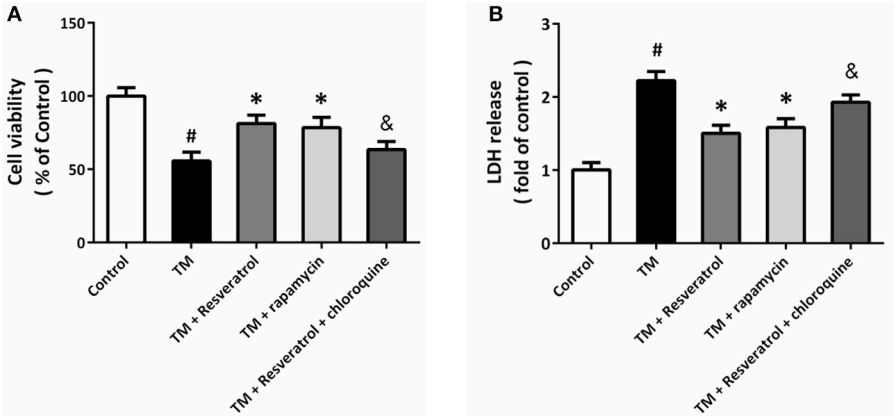

FIGURE 4 | Resveratrol modulates TM-induced toxicity via affecting autophagy. HT22 cells were treated with resveratrol, rapamycin or chloroquine, and exposed to TM for 24 h. Cell viability was measured by MTT assay **(A)**, and cytotoxicity was determined by LDH assay **(B)**. Data are shown as mean ± SEM. $^{\#}p < 0.05$ vs. Control. $^{*}p < 0.05$ vs. TM. $^{\&}p < 0.05$ vs. TM + Resveratrol.

LDH release was reduced by rapamycin, and the resveratrol-induced decrease in LDH release was attenuated by chloroquine.

Resveratrol Activates Sirt3 in TM-Treated HT22 Cells

Western blot was performed to detect the expression of Sirt3, and the results showed that TM significantly decreased Sirt3 expression, whereas resveratrol markedly increased Sirt3 expression both in the presence and absence of TM (**Figure 5A**). We also measured the enzymatic activities of MnSOD and CAT, two downstream targets of Sirt3, and the results showed that resveratrol significantly increased the activities of these enzymes (**Figures 5B,C**). To further determine the effect of resveratrol on acetylation state of MnSOD, we detected ac-MnSOD2 expression by western blot (**Figure 5D**). The results showed that resveratrol inhibited MnSOD acetylation both in the presence and absence of TM, and these effects were partially prevented by Sirt3 knockdown.

Sirt3 Activation Contributes to Resveratrol-Induced Autophagy Regulation

HT22 cells were transfected with Si-Sirt3 to knockdown Sirt3 expression, and the results of immunocytochemistry showed that Si-Sirt3 significantly reduced Sirt3 protein levels compared to Si-control (**Figures 6A,B**). Downregulation of Sirt3 partially prevented the induction of Beclin1 and the increase in LC3II/LC3I ratio induced by resveratrol (**Figures 6C–E**). In addition, Si-Sirt3 transfection also significantly diminished the LC3II puncta in resveratrol-treated HT22 cells (**Figures 6F,G**).

Knockdown of Sirt3 Partially Prevents Resveratrol-Induced Protection

To further demonstrate the involvement of Sirt3 in resveratrol-induced protection, HT22 cells was transfected with Si-Sirt3 or Si-control before TM and resveratrol treatment. The results of MTT assay showed that resveratrol-induced increase in cell viability after TM exposure was reduced by Sirt3 knockdown (**Figure 7A**). In addition, the reduced LDH release induced by resveratrol was partially prevented by Si-Sirt3 transfection (**Figure 7B**). As shown in **Figure 7C**, a similar result on caspase-12 cleavage was also observed. Moreover, resveratrol-induced effects on XBP1S mRNA (**Figure 7D**), CHOP and p-JNK levels (**Figures 7E–G**) were all partially prevented by Si-Sirt3 transfection compared to Si-control.

DISCUSSION

Accumulating evidence has suggested that resveratrol exerts neuroprotective effects against both acute and chronic neurological disorders. The results of our study provide evidence that resveratrol attenuates ER stress associated neuronal injury via regulating autophagy in HT22 cells. We found that (a) resveratrol reduces TM-induced cell damage and apoptosis; (b) resveratrol inhibits the expression of ER related proteins; (c) resveratrol-induced promotion of autophagy contributes to its protective effects; (d) resveratrol increases Sirt3 protein expression and activity; and (e) mechanistically, knockdown of Sirt3 partially prevents the resveratrol-induced autophagy and protection.

Compared with many other natural products with neuroprotective activities, resveratrol has unique advantages. First, as a natural product, resveratrol can be easily obtained from grapes, berries, peanuts, and wines in the daily diet. In humans, resveratrol is rapidly taken up and absorbed after oral consumption, and the plasma half-life of its metabolites is approximate 9 h (Walle et al., 2004). In addition, due to its lipophilic character, tissue levels of resveratrol is much higher than those found in plasma (Timmers et al., 2012). More importantly, resveratrol can cross the BBB and act on both neurons and glial cells, making it more suitable for neurological diseases. The effects of resveratrol on ER stress was originally

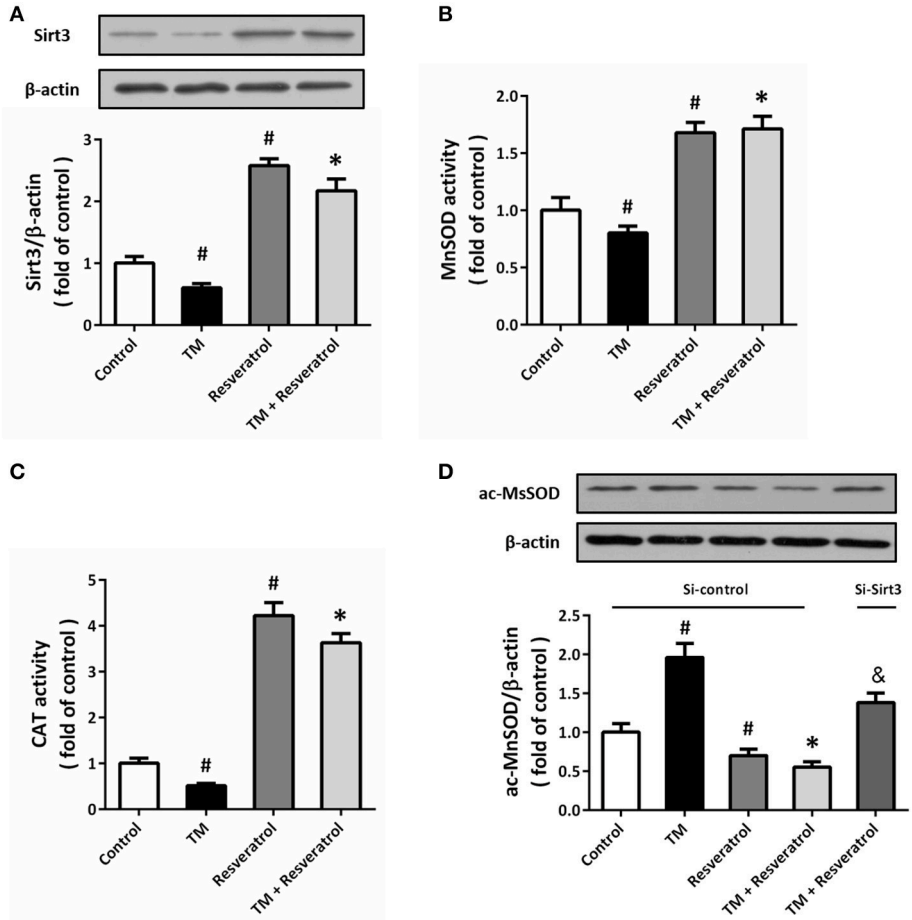

FIGURE 5 | Resveratrol activates Sirt3 in TM-treated HT22 cells. HT22 cells were treated with 100 ng/ml TM with or without 50 μM resveratrol for 24 h. The expression of Sirt3 protein was detected by western blot **(A)**, and the enzymatic activities of MnSOD **(B)**, and CAT **(C)** were determined. HT22 cells were transfected with Si-control or Si-Sirt3 for 48 h, and treated with 100 ng/ml TM with or without 50 μM resveratrol for 24 h. The expression of ac-MnSOD was detected by western blot **(D)**. Data are shown as mean ± SEM. $^{\#}p < 0.05$ vs. Control. $^{*}p < 0.05$ vs. TM. $^{\&}p < 0.05$ vs. Si-control.

investigated in cancers, and resveratrol-induced induction of ER stress was found in colon and lung cancer cells (Park et al., 2007; Gu et al., 2016). However, our results showed that resveratrol significantly decreased the TM-induced activation of ER related proteins. Actually, equivalent results have also been found in acute kidney injury and non-alcoholic fatty liver diseases (Ding et al., 2017; Wang et al., 2017), and more relevantly, in Abeta25-35 treated SH-SY5Y cells (Cheng et al., 2016b). Thus, resveratrol might exert both anti-ER stress and pro-ER stress effects in different disease conditions.

Resveratrol has been previously implicated in inducing autophagy in a variety of cell types. A previous study showed that resveratrol triggered autophagic cell death through AMPK activation and JNK-dependent p62/SQSTM1 expression in chronic myelogenous leukemia cells (Puissant and Auberger, 2010). Resveratrol was shown to engage a distinct subset of LC3II and promote noncanonical autophagic degradation downstream of the Ptdlns(3)P-WIPI-Atg7-Atg5 pathway (Mauthe et al., 2011). In addition, resveratrol was also shown to induce autophagy in both glioma cells and dopaminergic SH-SY5Y cells (Yamamoto et al., 2010; Lin et al., 2014). In our *in vitro* experiments, increased number of LC3II puncta, as well as the upregulated expression of Beclin1 and LC3II, were observed after resveratrol treatment, indicating the promotion of autophagy in TM-treated conditions. In cancer cells, resveratrol caused autophagy to promote cell death, whereas increased autophagy induced by resveratrol was shown to be beneficial in many other diseases, such as spinal cord injury, brain trauma and cerebral ischemia (He et al., 2017; Zhao et al., 2017). Our results using the autophagy activator and inhibitor showed that the protective effects of resveratrol could be partially prevented by autophagy inhibition, as evidenced by both cell viability and LDH release results. Previous studies have demonstrated that resveratrol-induced autophagy is a protective mechanism in inflammatory, mitochondrial dysfunction and oxidative stress conditions (Fu, 2015; Wu et al., 2016; Zhang et al., 2017). Thus, our results suggest that resveratrol could exert protective effects against ER stress associated neurological disorders through promoting autophagy.

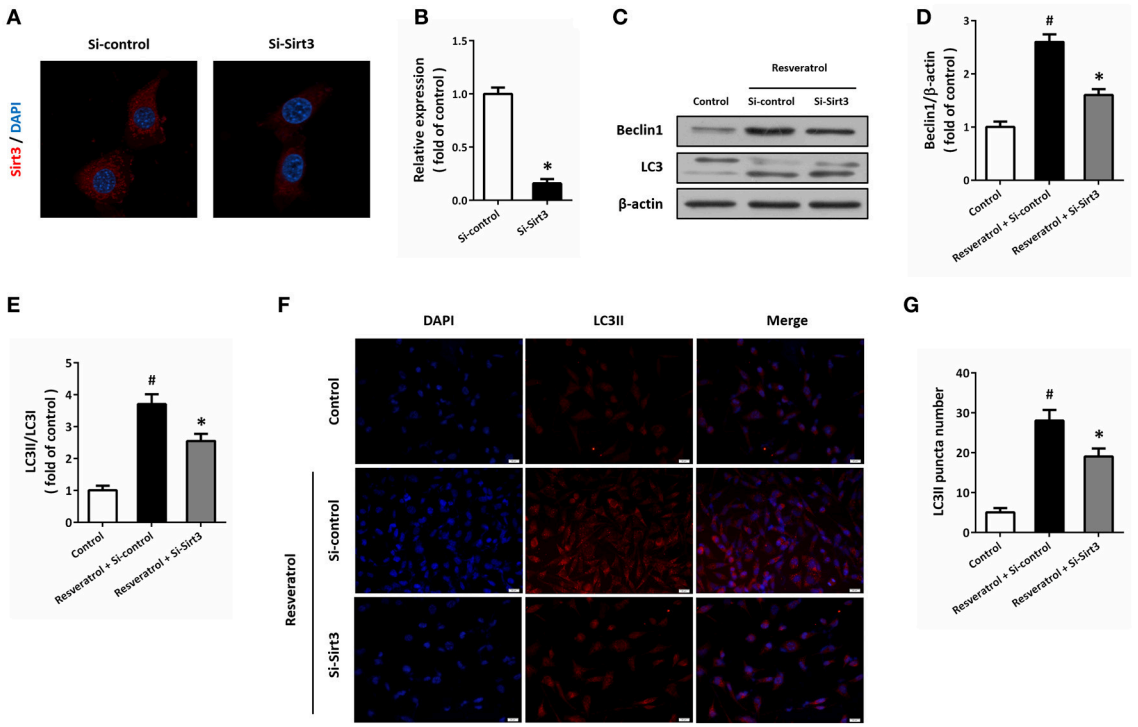

FIGURE 6 | Sirt3 activation contributes to resveratrol-induced autophagy regulation. HT22 cells were transfected with Si-control or Si-Sirt3 for 48 h, and the expression of Sirt3 protein was detected by immunofluorescence staining **(A)** and calculated **(B)**. After transfection, HT22 cells were treated with resveratrol for another 24 h, and the expression of Beclin1 and LC3 was detected by western blot **(C–E)**. Immunofluorescence staining of LC3II was performed to assess autophagy in HT22 cells **(F)**, and the number of LC3-positve puncta was counted **(G)**. Data are shown as mean ± SEM. $^{\#}p < 0.05$ vs. Control. $^{*}p < 0.05$ vs. Si-control. Scale bar = 20 μm.

The sirtuins are a conserved family of NAD^{+}-dependent protein deacetylases that have seven mammalian homologs (Sirtuin 1-7, aka Sirt1-7). Three sirtuin proteins, Sirt3, 4, and 5, are predominantly localized to the mitochondria, and Sirt3 has been shown to regulate almost every major aspect of mitochondrial biology in highly metabolic tissues, such as the brain (Bause and Haigis, 2013). Mitochondrial Sirt3 was demonstrated to act as a pro-survival factor playing an essential role to protect neurons under excitotoxicity (Kim et al., 2011). More recently, overexpression of Sirt3 was found to attenuate oxidative stress through regulating mitochondrial Ca^{2+} and mitochondrial biogenesis in neuronal cells (Dai et al., 2014a,b). In addition, Sirt3-mediated preservation of mitochondrial function and redox homeostasis are proved to contribute to the protective mechanism of multiple neuroprotective agents and strategies (Cheng et al., 2016a; Liu et al., 2017). Here, the results of western blot showed that resveratrol significantly increased Sirt3 protein expression both in the presence and absence of TM exposure, indicating the potential involvement of Sirt3 in its protective effects. Previous experiments have demonstrated that resveratrol could promote Sirt1 expression and activity. Resveratrol was shown to inhibit apoptosis via Sirt1 activation in hydrogen dioxide-treated osteoblast cells, and Sirt1-mediated Nrf2 activation contributed to the resistance to vascular calcification after resveratrol treatment (He et al., 2015; Zhang et al., 2016). More recently, resveratrol was shown to protect against mitochondrial Complex I deficiency via Sirt3-meidiated activation of mitochondrial SOD2 (Mathieu et al., 2016). In our study, increased activities of MnSOD and CAT were also observed in resveratrol-treated cells, and resveratrol-induced protection was partially prevented by Sirt3 knockdown using siRNA transfection. All these data indicated that the protective effects of resveratrol against TM was, at least partially, dependent on Sirt3 activation.

Acetylation and deacetylation are important posttranslational modifications employed in autophagy regulating (Bánréti et al., 2013). As class III histone deacetylases, Sirt1 and Sirt2 have been extensively implicated in modulating autophagy process (Ng and Tang, 2013). Recent studies have also identified multifaceted roles for Sirt3 in the regulation of autophagy. Sirt3 was shown to promote autophagy in AngII-induced myocardial hypertrophy through the deacetylation of FoxO1 in mice (Li et al., 2016). Sirt3 could directly bind and deacetylate SOD2, which in turn led to significant effects on mitochondrial ROS homeostasis and autophagic flux (Qiu et al., 2010; Liang et al., 2013). In our study, autophagy activation after resveratrol treatment was accompanied by increased expression of Sirt3 and elevated activity of MnSOD (also known as SOD2). More recently, Sirt3 was shown to activate autophagy and protect against ischemia in cortical neurons (Dai et al., 2017). Our results that knockdown of Sirt3 expression partially prevented the autophagy and protection induced by resveratrol, further supported the involvement of

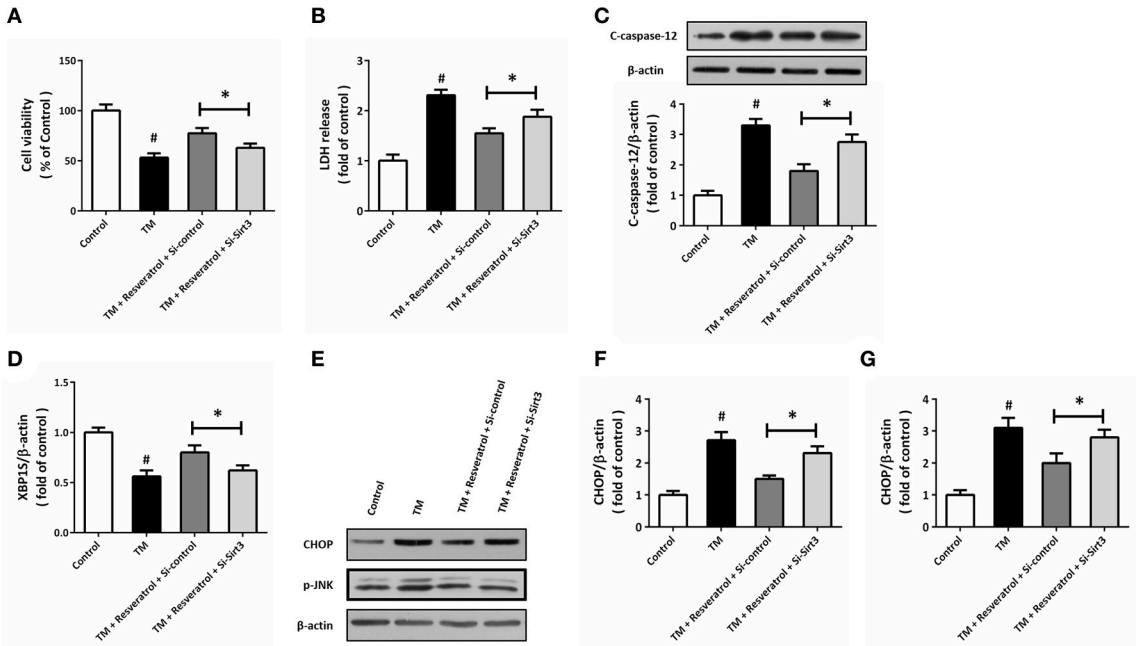

FIGURE 7 | Knockdown of Sirt3 partially prevents resveratrol-induced protection. HT22 cells were transfected with Si-control or Si-Sirt3 for 48 h, and treated with TM in the presence or absence of resveratrol for another 24 h. Cell viability was measured by MTT assay **(A)**, and cytotoxicity was determined by LDH assay **(B)**. The expression of cleaved-caspase-12 was detected by western blot **(C)**. The mRNA levels of XBP1S was examined by RT-PCR **(D)**. The expression of CHOP, p-JNK, and cleaved-caspase-12 was detected by western blot **(E–G)**. Data are shown as mean ± SEM. $^{\#}p < 0.05$ vs. Control. $^{*}p < 0.05$.

Sirt3 in autophagy regulation in neuronal cells, and indicated that resveratrol-induced protective effects were mediated by Sirt3 signaling. However, the role of Sirt3 in autophagy regulation has not been fully determined, especially some results was shown to be irreproducible (2017), and thus, some more experiments in gene knockout animals need to be performed in the future.

In summary, our results demonstrate that resveratrol exerts protective effects against TM-induced ER stress by regulating Sirt3-mediated autophagy in neuronal HT22 cells. These findings may reveal a new feature for the mechanism of resveratrol in neuroprotection, and provide further information regarding the role of Sirt3 in autophagy regulation.

AUTHOR CONTRIBUTIONS

W-JY: designed experiments. W-JY, Y-BM, FD, and S-LD: performed experiments; Z-YH, and D-BW: prepared the manuscript; R-BL and L-KW: edited the manuscript. The entire study was supervised by W-JY.

FUNDING

This work was financially supported by the National Natural Science Foundation of China (No. 81360193 and 81560214), and Natural Fund Project (1208RJZA110) and Health Industry Research Project (GSWSKY2015-01) of Gansu Province.

REFERENCES

(2017). Retracted: Sirt3 activation attenuated oxidized low-density lipoprotein-induced human umbilical vein endothelial cells' apoptosis by sustaining autophagy by Luo, X., Yang, Z., Zheng, S., Cao, Y., and Wu, Y. *Cell Biol. Int.* 41, 932. doi: 10.1002/cbin.10291

Balduini, W., Carloni, S., and Buonocore, G. (2009). Autophagy in hypoxia-ischemia induced brain injury: evidence and speculations. *Autophagy* 5, 221–223. doi: 10.4161/auto.5.2.7363

Bánréti, A., Sass, M., and Graba, Y. (2013). The emerging role of acetylation in the regulation of autophagy. *Autophagy* 9, 819–829. doi: 10.4161/auto.23908

Bause, A. S., and Haigis, M. C. (2013). SIRT3 regulation of mitochondrial oxidative stress. *Exp. Gerontol.* 48, 634–639. doi: 10.1016/j.exger.2012.08.007

Carrizzo, A., Forte, M., Damato, A., Trimarco, V., Salzano, F., Bartolo, M., et al. (2013). Antioxidant effects of resveratrol in cardiovascular, cerebral and metabolic diseases. *Food Chem. Toxicol.* 61, 215–226. doi: 10.1016/j.fct.2013.07.021

Chen, T., Liu, W., Chao, X., Qu, Y., Zhang, L., Luo, P., et al. (2011). Neuroprotective effect of osthole against oxygen and glucose deprivation in rat cortical neurons: involvement of mitogen-activated protein kinase pathway. *Neuroscience* 183, 203–211. doi: 10.1016/j.neuroscience.2011.03.038

Cheng, A., Yang, Y., Zhou, Y., Maharana, C., Lu, D., Peng, W., et al. (2016a). Mitochondrial SIRT3 mediates adaptive responses of neurons to exercise and metabolic and excitatory challenges. *Cell Metab.* 23, 128–142. doi: 10.1016/j.cmet.2015.10.013

Cheng, J., Xia, X., Rui, Y., Zhang, Z., Qin, L., Han, S., et al. (2016b). The combination of 1alpha,25dihydroxyvitaminD3 with resveratrol improves neuronal degeneration by regulating endoplasmic reticulum stress, insulin signaling and inhibiting tau hyperphosphorylation in SH-SY5Y cells. *Food Chem. Toxicol.* 93, 32–40. doi: 10.1016/j.fct.2016.04.021

Dai, S. H., Chen, T., Li, X., Yue, K. Y., Luo, P., Yang, L. K., et al. (2017). Sirt3 confers protection against neuronal ischemia by inducing autophagy: involvement of the AMPK-mTOR pathway. *Free Radic. Biol. Med.* 108, 345–353. doi: 10.1016/j.freeradbiomed.2017.04.005

Dai, S. H., Chen, T., Wang, Y. H., Zhu, J., Luo, P., Rao, W., et al. (2014a). Sirt3 attenuates hydrogen peroxide-induced oxidative stress through the preservation of mitochondrial function in HT22 cells. *Int. J. Mol. Med.* 34, 1159–1168. doi: 10.3892/ijmm.2014.1876

Dai, S. H., Chen, T., Wang, Y. H., Zhu, J., Luo, P., Rao, W., et al. (2014b). Sirt3 protects cortical neurons against oxidative stress via regulating mitochondrial Ca^{2+} and mitochondrial biogenesis. *Int. J. Mol. Sci.* 15, 14591–14609. doi: 10.3390/ijms150814591

Ding, S., Jiang, J., Zhang, G., Bu, Y., and Zhao, X. (2017). Resveratrol and caloric restriction prevent hepatic steatosis by regulating SIRT1-autophagy pathway and alleviating endoplasmic reticulum stress in high-fat diet-fed rats. *PLoS ONE* 12:e0183541. doi: 10.1371/journal.pone.0183541

Fu, D. G. (2015). Regulation of redox signalling and autophagy during cardiovascular diseases-role of resveratrol. *Eur. Rev. Med. Pharmacol. Sci.* 19, 1530–1536.

Gu, S., Chen, C., Jiang, X., and Zhang, Z. (2016). ROS-mediated endoplasmic reticulum stress and mitochondrial dysfunction underlie apoptosis induced by resveratrol and arsenic trioxide in A549 cells. *Chem. Biol. Interact.* 245, 100–109. doi: 10.1016/j.cbi.2016.01.005

Hawes, C., Kiviniemi, P., and Kriechbaumer, V. (2015). The endoplasmic reticulum: a dynamic and well-connected organelle. *J. Integr. Plant Biol.* 57, 50–62. doi: 10.1111/jipb.12297

He, N., Zhu, X., He, W., Zhao, S., Zhao, W., and Zhu, C. (2015). Resveratrol inhibits the hydrogen dioxide-induced apoptosis via Sirt 1 activation in osteoblast cells. *Biosci. Biotechnol. Biochem.* 79, 1779–1786. doi: 10.1080/09168451.2015.1062712

He, Q., Li, Z., Wang, Y., Hou, Y., Li, L., and Zhao, J. (2017). Resveratrol alleviates cerebral ischemia/reperfusion injury in rats by inhibiting NLRP3 inflammasome activation through Sirt1-dependent autophagy induction. *Int. Immunopharmacol.* 50, 208–215. doi: 10.1016/j.intimp.2017.06.029

Kim, D. W., Kim, Y. M., Kang, S. D., Han, Y. M., and Pae, H. O. (2012). Effects of resveratrol and trans-3,5,4′-Trimethoxystilbene on glutamate-induced cytotoxicity, heme Oxygenase-1, and Sirtuin 1 in HT22 neuronal cells. *Biomol. Ther.* 20, 306–312. doi: 10.4062/biomolther.2012.20.3.306

Kim, S. H., Lu, H. F., and Alano, C. C. (2011). Neuronal Sirt3 protects against excitotoxic injury in mouse cortical neuron culture. *PLoS ONE* 6:e14731. doi: 10.1371/journal.pone.0014731

Lee, W. S., Yoo, W. H., and Chae, H. J. (2015). ER stress and autophagy. *Curr. Mol. Med.* 15, 735–745. doi: 10.2174/1566524015666150921105453

Li, J., Chen, T., Xiao, M., Li, N., Wang, S., Su, H., et al. (2016). Mouse Sirt3 promotes autophagy in AngII-induced myocardial hypertrophy through the deacetylation of FoxO1. *Oncotarget* 7, 86648–86659. doi: 10.18632/oncotarget.13429

Liang, Q., Benavides, G. A., Vassilopoulos, A., Gius, D., Darley-Usmar, V., and Zhang, J. (2013). Bioenergetic and autophagic control by Sirt3 in response to nutrient deprivation in mouse embryonic fibroblasts. *Biochem. J.* 454, 249–257. doi: 10.1042/BJ20130414

Lin, T. K., Chen, S. D., Chuang, Y. C., Lin, H. Y., Huang, C. R., Chuang, J. H., et al. (2014). Resveratrol partially prevents rotenone-induced neurotoxicity in dopaminergic SH-SY5Y cells through induction of heme oxygenase-1 dependent autophagy. *Int. J. Mol. Sci.* 15, 1625–1646. doi: 10.3390/ijms15011625

Liu, S. G., Wang, Y. M., Zhang, Y. J., He, X. J., Ma, T., Song, W., et al. (2017). ZL006 protects spinal cord neurons against ischemia-induced oxidative stress through AMPK-PGC-1alpha-Sirt3 pathway. *Neurochem. Int.* 108, 230–237. doi: 10.1016/j.neuint.2017.04.005

Luyten, T., Welkenhuyzen, K., Roest, G., Kania, E., Wang, L., Bittremieux, M., et al. (2017). Resveratrol-induced autophagy is dependent on IP3Rs and on cytosolic $Ca^{(2)}$. *Biochim. Biophys. Acta* 1864, 947–956. doi: 10.1016/j.bbamcr.2017.02.013

Marier, J. F., Vachon, P., Gritsas, A., Zhang, J., Moreau, J. P., and Ducharme, M. P. (2002). Metabolism and disposition of resveratrol in rats: extent of absorption, glucuronidation, and enterohepatic recirculation evidenced by a linked-rat model. *J. Pharmacol. Exp. Ther.* 302, 369–373. doi: 10.1124/jpet.102.033340

Markus, M. A., and Morris, B. J. (2008). Resveratrol in prevention and treatment of common clinical conditions of aging. *Clin. Interv. Aging* 3, 331–339. doi: 10.2147/CIA.S3506

Mathieu, L., Costa, A. L., Le Bachelier, C., Slama, A., Lebre, A. S., Taylor, R. W., et al. (2016). Resveratrol attenuates oxidative stress in mitochondrial complex I deficiency: involvement of SIRT3. *Free Radic. Biol. Med.* 96, 190–198. doi: 10.1016/j.freeradbiomed.2016.04.027

Mauthe, M., Jacob, A., Freiberger, S., Hentschel, K., Stierhof, Y. D., Codogno, P., et al. (2011). Resveratrol-mediated autophagy requires WIPI-1-regulated LC3 lipidation in the absence of induced phagophore formation. *Autophagy* 7, 1448–1461. doi: 10.4161/auto.7.12.17802

Ng, F., and Tang, B. L. (2013). Sirtuins' modulation of autophagy. *J. Cell. Physiol.* 228, 2262–2270. doi: 10.1002/jcp.24399

Park, J. W., Woo, K. J., Lee, J. T., Lim, J. H., Lee, T. J., Kim, S. H., et al. (2007). Resveratrol induces pro-apoptotic endoplasmic reticulum stress in human colon cancer cells. *Oncol. Rep.* 18, 1269–1273. doi: 10.3892/or.18.5.1269

Puissant, A., and Auberger, P. (2010). AMPK- and p62/SQSTM1-dependent autophagy mediate resveratrol-induced cell death in chronic myelogenous leukemia. *Autophagy* 6, 655–657. doi: 10.4161/auto.6.5.12126

Qiu, X., Brown, K., Hirschey, M. D., Verdin, E., and Chen, D. (2010). Calorie restriction reduces oxidative stress by SIRT3-mediated SOD2 activation. *Cell Metab.* 12, 662–667. doi: 10.1016/j.cmet.2010.11.015

Ramprasath, V. R., and Jones, P. J. (2010). Anti-atherogenic effects of resveratrol. *Eur. J. Clin. Nutr.* 64, 660–668. doi: 10.1038/ejcn.2010.77

Stefani, I. C., Wright, D., Polizzi, K. M., and Kontoravdi, C. (2012). The role of ER stress-induced apoptosis in neurodegeneration. *Curr. Alzheimer Res.* 9, 373–387. doi: 10.2174/156720512800107618

Thorburn, A. (2014). Autophagy and its effects: making sense of double-edged swords. *PLoS Biol.* 12:e1001967. doi: 10.1371/journal.pbio.1001967

Timmers, S., Auwerx, J., and Schrauwen, P. (2012). The journey of resveratrol from yeast to human. *Aging* 4, 146–158. doi: 10.18632/aging.100445

Valenzuela, V., Martinez, G., Duran-Aniotz, C., and Hetz, C. (2016). Gene therapy to target ER stress in brain diseases. *Brain Res.* 1648, 561–570. doi: 10.1016/j.brainres.2016.04.064

Walle, T., Hsieh, F., DeLegge, M. H., Oatis, J. E. Jr., and Walle, U. K. (2004). High absorption but very low bioavailability of oral resveratrol in humans. *Drug Metab. Dispos.* 32, 1377–1382. doi: 10.1124/dmd.104.000885

Wang, N., Mao, L., Yang, L., Zou, J., Liu, K., Liu, M., et al. (2017). Resveratrol protects against early polymicrobial sepsis-induced acute kidney injury through inhibiting endoplasmic reticulum stress-activated NF-kappaB pathway. *Oncotarget* 8, 36449–36461. doi: 10.18632/oncotarget.16860

Wu, J., Li, X., Zhu, G., Zhang, Y., He, M., and Zhang, J. (2016). The role of resveratrol-induced mitophagy/autophagy in peritoneal mesothelial cells inflammatory injury via NLRP3 inflammasome activation triggered by mitochondrial ROS. *Exp. Cell Res.* 341, 42–53. doi: 10.1016/j.yexcr.2016.01.014

Yamamoto, M., Suzuki, S. O., and Himeno, M. (2010). Resveratrol-induced autophagy in human U373 glioma cells. *Oncol. Lett.* 1, 489–493. doi: 10.3892/ol_00000086

Yin, Y., Sun, G., Li, E., Kiselyov, K., and Sun, D. (2017). ER stress and impaired autophagy flux in neuronal degeneration and brain injury. *Ageing Res. Rev.* 34, 3–14. doi: 10.1016/j.arr.2016.08.008

Zhang, B., Xu, L., Zhuo, N., and Shen, J. (2017). Resveratrol protects against mitochondrial dysfunction through autophagy activation in human nucleus pulposus cells. *Biochem. Biophys. Res. Commun.* 493, 373–381. doi: 10.1016/j.bbrc.2017.09.015

Zhang, P., Li, Y., Du, Y., Li, G., Wang, L., and Zhou, F. (2016). Resveratrol ameliorated vascular calcification by regulating Sirt-1 and Nrf2. *Transplant. Proc.* 48, 3378–3386. doi: 10.1016/j.transproceed.2016.10.023

Zhao, H., Chen, S., Gao, K., Zhou, Z., Wang, C., Shen, Z., et al. (2017). Resveratrol protects against spinal cord injury by activating autophagy and inhibiting apoptosis mediated by the SIRT1/AMPK signaling pathway. *Neuroscience* 348, 241–251. doi: 10.1016/j.neuroscience.2017.02.027

Conflict of Interest Statement: The authors declare that the research was conducted in the absence of any commercial or financial relationships that could be construed as a potential conflict of interest.

frontiers in Neuroscience

ORIGINAL RESEARCH
published: 28 February 2018
doi: 10.3389/fnins.2018.00111

PERK Pathway Activation Promotes Intracerebral Hemorrhage Induced Secondary Brain Injury by Inducing Neuronal Apoptosis Both *in Vivo* and *in Vitro*

Chengjie Meng[1,2†], Juyi Zhang[1†], Baoqi Dang[3], Haiying Li[1], Haitao Shen[1], Xiang Li[1] and Zhong Wang[1*]*

[1] Department of Neurosurgery & Brain and Nerve Research Laboratory, The First Affiliated Hospital of Soochow University, Suzhou, China, [2] Department of Neurosurgery, Yancheng First Peoples' Hospital, Yancheng, China, [3] Department of Rehabilitation Medicine, Zhangjiagang Hospital of Traditional Chinese Medicine, Suzhou, China

OPEN ACCESS

Edited by:
Gao Chen,
Zhejiang University, China

Reviewed by:
Sheng Chen,
Second Affiliated Hospital of Zhejiang University School of Medicine, China
Yang Hu,
Stanford University, United States

***Correspondence:**
Xiang Li
xiangli2017@suda.edu.cn
Zhong Wang
15716201037@163.com

[†] These authors have contributed equally to this work.

Specialty section:
This article was submitted to Neurodegeneration, a section of the journal Frontiers in Neuroscience

Received: 20 December 2017
Accepted: 13 February 2018
Published: 28 February 2018

Citation:
Meng C, Zhang J, Dang B, Li H, Shen H, Li X and Wang Z (2018) PERK Pathway Activation Promotes Intracerebral Hemorrhage Induced Secondary Brain Injury by Inducing Neuronal Apoptosis Both in Vivo and in Vitro. Front. Neurosci. 12:111. doi: 10.3389/fnins.2018.00111

The protein kinase R (PKR)-like endoplasmic reticulum kinase (PERK) signaling pathway was reported to exert an important role in neuronal apoptosis. The present study was designed to investigate the roles of the PERK signaling pathway in the secondary brain injury (SBI) induced by intracerebral hemorrhage (ICH) and its potential mechanisms. Sprague–Dawley rats were used to establish ICH models by injecting autologous blood (100 μl), and cultured primary rat cortical neurons were exposed to oxyhemoglobin (10 μM) to mimic ICH *in vitro*. The PERK antagonist, GSK2606414, and inhibitor of eukaryotic translation initiation factor 2 subunit α (eIF2α) dephosphorylation, salubrinal, were used to study the roles of PERK signaling pathway in ICH-induced SBI. Our results showed that the protein levels of p-eIF2α and ATF4 were upregulated following ICH, peaking at 48 h. Application of GSK2606414 reversed this increase *in vivo* and *in vitro*, thereby preventing ICH-induced neuronal apoptosis. On the contrary, salubrinal inhibited the dephosphorylation of eIF2α, resulting in the elevation of p-eIF2α, which could activate downstream of PERK signaling and induce neuronal apoptosis and necrosis following ICH *in vitro* and *in vivo*. Thus, PERK signaling pathway plays an important role in ICH-induced apoptosis and blocking its activation has neuroprotective effects that alleviates SBI, suggesting that targeting this pathway could be a promising therapeutic strategy for improving patient outcome after ICH.

Keywords: PERK pathway, intracerebral hemorrhage, secondary brain injury, apoptosis, ER stress

INTRODUCTION

Intracerebral hemorrhage (ICH) is the most common subtype of hemorrhagic stroke, with an estimated annual incidence of 16/100,000 worldwide that is increasing with the aging population. Despite an increase in research and clinical trials for potential treatments for ICH, mortality remains high and no interventional therapy has been shown to improve patient outcome (Rodríguez-Yáñez et al., 2013; Wilkinson et al., 2017). It is generally accepted that ICH causes tissue displacement and destruction; this leads to secondary brain injury (SBI)

(Qureshi et al., 2001; Schlunk and Greenberg, 2015; Behrouz, 2016), which involves a series of pathophysiological processes including activation of apoptosis (Qureshi et al., 2001; Xiong and Yang, 2015), aggravation of ischemia and edema in brain tissue surrounding the hematoma (Gebel et al., 2002), and related toxic effects (Lee et al., 2006; Chen et al., 2015). SBI can cause metabolic disorders in cells and activate stress responses including endoplasmic reticulum (ER) stress and the unfolded protein response (UPR) that either reestablish cellular homeostasis or activate cell death programs (Niu et al., 2017).

ER stress is one of the primary mechanisms that lead to apoptosis. The accumulation of misfolded/unfolded proteins induce ER dysfunction induces ER stress. Subsequently, it is induced a signal transduction cascade which is the UPR, whereby the cell tries to restore homeostasis to prevent its death (Schröder and Kaufman, 2005). The UPR is facilitated by three types of ER stress sensor proteins, protein kinase R (PKR)-like endoplasmic reticulum kinase (PERK), activating transcription factor 6 (ATF6), and inositol requiring kinase 1 (IRE1). Activated PERK phosphorylation eukaryotic translation initiation factor 2 subunit α (eIF2α), which blocks most of protein translation and activates the transcription factor 4 (ATF4). PERK is a central ER stress sensor that enforces adaptive programs to recover homeostasis through a block of protein translation and the induction of the transcription factor ATF4. PERK pathway is turned off by protein phosphatase 1 (PP1) which dephosphorylates p-eIF2α (Godin et al., 2016).

The clearance of misfolded proteins by the UPR promotes neuronal survival. Thus, mild ER stress exerts neuroprotective effects by promoting autophagy (Fouillet et al., 2012), but can lead to cell death if it persists or is excessive (Tabas and Ron, 2011). The latter situation was shown to contribute to the pathophysiology of ischemia/reperfusion brain injury in rats (Nakka et al., 2010). In addition, in neurodegenerative diseases, inhibiting ER stress was found to suppress neuronal apoptosis (Moreno et al., 2013; Tsujii et al., 2015). CCAAT-enhancer-binding protein homologous protein (CHOP) is a downstream effector of the PERK pathway that functions as a pro-apoptotic factor (Jiang et al., 2012). Previous studies have shown that ER stress activates caspase-12 to induce cell apoptosis (Kim et al., 2010; Penke et al., 2016). However, and it is not known whether ER stress and apoptosis contribute to ICH-induced SBI.

The present study investigated the role of PERK signaling in SBI induced by ICH. The PERK inhibitor GSK2606414 and salubrinal, an inhibitor of eIF2α dephosphorylation, were used as experimental drugs both *in vitro* and *in vivo* (Boyce et al., 2005; Axten et al., 2012; Scheper and Hoozemans, 2013; Rubovitch et al., 2015).

MATERIALS AND METHODS

Ethical Approval

All experiments were approved by the Ethics Committee of the First Affiliated Hospital of Soochow University and were performed in accordance with the guidelines of the National Institutes of Health on the care and use of animals. Adult male Sprague–Dawley (SD) rats (250–300 g) were purchased from Animal Center of Chinese Academy of Sciences, Shanghai, China. The rats were housed in temperature- and humidity-controlled animal quarters with a 12hr light/dark cycle.

Experimental Design

In experiment 1, 48 rats (53 rats were used, but only 48 rats survived after the surgery) were randomly assigned to eight groups of 6 rats for each, a sham group and seven experimental groups arranged by time course: 4, 8, 12, 16, 24, 48, and 72 h after ICH. The rats were euthanized at the indicated time point after ICH, and the brain tissues were separated and taken for analysis (**Figure 1A**). *In vitro*, the primary hippocampal neurons were assigned to eight groups, a sham group, and seven experimental groups arranged by time: 4, 8, 12, 16, 24, 48, and 72 h after neurons treated by oxyhemoglobin (OxyHb) (**Figure 1B**).

In experiment 2, 36 rats (43 rats were used, but only 36 rats survived) were randomly divided into six groups: sham group, ICH group, ICH +vehicle (GSK2606414) group, ICH+GSK2606414 group, ICH +vehicle (salubrinal) group and ICH +salubrinal group ($n = 6$ for each group). The administrations of drugs in each group were shown in **Figure 1C**. First, GSK2606414 was dissolved in dimethylsulphoxide (DMSO) to 90 μg/μl and then diluted the store solution to 90 μg/5 μl by sterile saline, which was injected intracerebroventricularly (Yan et al., 2017). Salubrinal was dissolved in DMSO to 96 μg/μl and injected intraperitoneally (1 mg/kg body weight) as reported previously (Sokka et al., 2007). Then, rats were euthanized, and the brain tissues were separated and taken for analysis (**Figure 1C**). The cannulated right femoral artery was used to measure blood pressure and heart rate. The blood pressure and heart rate were no significant differences among sham group, ICH group, ICH + vehicle (GSK2606414) group, ICH+GSK2606414 group, ICH +vehicle (salubrinal) group and ICH +salubrinal group (Data not shown). *In vitro*, to mimic the effect of ICH, OxyHb (10 μM) was used to treat primary hippocampal neurons (**Figure 1D**).

Antibodies and Drugs

Anti-CHOP antibody (ab11419), anti-p-eIF2α antibody (ab32157), anti-eIF2α antibody (ab169528), anti-XBP1 anbibody (ab37152), anti-caspase-12 antibody (ab62484), Ms mAb to NeuN (ab104224), Rb mAb to NeuN (ab177487), and anti-β-Tubulin antibody (ab179513) were purchased from abcam (Cambridge, MA, USA). Anti-ATF-4 antibody (sc-200) was purchased from Santa Cruz (Santa Cruz, CA, USA). Anti-ATF6 antibody (70B1413.1) were purchased from Novus Biological (Littleton, Co, USA). Salubrinal and GSK2606414 were purchased from TargetMol (Boston, MA, USA).

Establishment of the ICH Model

Adult male SD rats (280–330 g) were anesthetized with intraperitoneal injection of 4% chloral hydrate (0.1 mL/kg body weight). After the rats were completely anesthetized, they were fixed in the stereotactic frame (ZH-Lanxing B type,

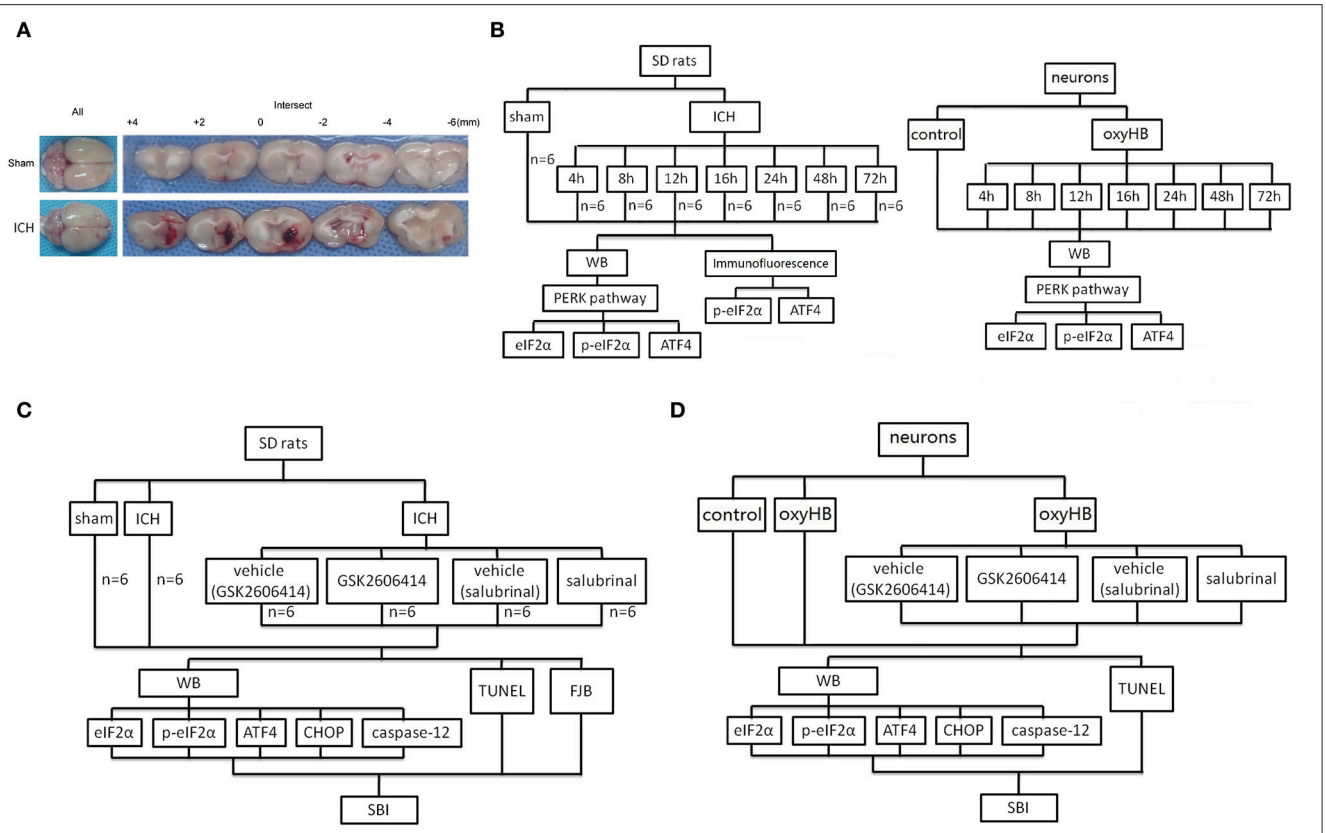

FIGURE 1 | ICH model and experimental design. **(A)** Representative whole brains and brain sections from ICH model rats. **(B)** Experiment 1 evaluated the expression of eIF2α, p-eIF2α, and ATF4 *in vitro* and *in vivo*. **(C)** Experiment 2 investigated the effects of PERK signaling on ICH-induced SBI and the underlying mechanisms *in vivo*. **(D)** Experiment 3 investigated the role of PERK signaling pathway *in vitro*.

Anhui Zhenghua Biological Equipment Co. Ltd. Anhui, China). Depending on the rat's response to the pain, additional chloral hydrate should be injected. The rat is then placed on the heating pad in a supine position and the pad is maintained at a temperature of about 27–35°C. Experimental ICH model was induced by using stereotaxic insertion of autologous blood using the modified methods described by Deinsberger et al. (1996). The position of basal ganglia was 0.2 mm posterior to bregma, 3.5 mm lateral to the midline, and 5.5 mm ventral to the cortical surface. Subsequently, 100 μl of autologous blood was collected from the heart using a 100 μl microinjector (Hamilton Company, Nevada, USA). After the microinjector was in position, 100 μl of autologous blood was injected over 5 min. Typical visual representation of the brain slices from each group were shown in **Figure 1A**. Bone wax was used to block the drilling, and medical suture line was used to stitch the scalp. Next, put the mouse back in the cage and gave enough food and water in the cage. The assessment of SBI occurred 48 h after the onset of ICH.

Western Blot Analysis

After collecting perihematomal tissues, we separately homogenized the perihematoma tissues from each experimental model. Brain homogenate was lysed in RIPA lysis buffer (Beyotime Institute of Biotechnology, Jiangsu, China). After at 16,000 g centrifuged for 5 min 4°C, the supernatant was collected. The supernatant was stored at −80°C for later use. A standard BCA (Beyotime Institute of Biotechnology) method was used to determine protein concentration. Then, a total of 50 μg protein each lane was subjected to SDS-PAGE (10%) and transferred to a membrane for ECL and imaging as reported previously (Zhai et al., 2016). The optical density was analyzed using Image J software (Rawak Software, Inc., Stuttgart, Germany).

Immunofluorescence Microscopy

The brain tissues were fixed in 4% paraformaldehyde, embedded in paraffin, cut into 4 μm sections, which was dewaxed immediately before immunofluorescence staining. Then, brain sections were stained with primary antibody, including NeuN antibody-neuronal cell marker (diluted 1:100) and antibodies for p-eIF2α (diluted 1:100), ATF-4 (diluted 1:100), at 4°C for 12 h. NEXT, brain sections were washed 3 times with PBS and stained with appropriate secondary antibodies. Normal rabbit IgG was used as negative controls for immunofluorescence assays (data not shown). Sections were observed with a fluorescence microscope (Olympus, BX50/BX-FLA/DP70, Olympus Co., Japan).

Terminal Deoxynucleotidyl Transferase–Mediated dUTP Nick End Labeling Staining

Terminal Deoxynucleotidyl Transferase–Mediated dUTP Nick End Labeling (TUNEL) staining was performed as described previously to detect cell apoptosis in brain (Zhai et al., 2016). The TUNEL-positive neurons were examined and were photographed in parallel by a fluorescence microscope (Olympus, BX50/BX-FLA/DP70, Olympus Co., Japan) (3 sections per rat).

Fluoro-Jade B (FJB) Staining

Fluoro-Jade B (FJB) is used to detect cell necrosis in brain tissue, which is a sensitive and highly specific fluorescent stain that reveals neuronal degradation (Zhu et al., 2014). FJB procedures were performed as previously described (Lin et al., 2012). Briefly, brain sections were deparaffinized. We used an oven to dehydrate brain sections. Then, we used xylenes and graded ethanol solutions to water for rehydrating brain sections. Brain sections were permeabilized in 0.04% Triton X-100. Next, we used FJB dye solution for incubating brain sections. Brain sections were examined and were photographed in parallel by a fluorescence microscope (Olympus, BX50/BX-FLA/DP70, Olympus Co., Japan). To evaluate the extent of cell necrosis, 6 microscopic fields in each tissue section were observed and photographed in parallel for FJB-positive cell counting. Microscopy was performed by an observer blind to the experimental condition.

Cell Culture and Treatment

Primary rat cortical neurons were obtained from 17-day-old SD rat embryos as described previously (Pacifici and Peruzzi, 2012). After a week of incubation, neurons were divided into 6 groups: control, OxyHb, OxyHb + vehicle (GSK2606414), OxyHb + GSK2606414, OxyHb + vehicle (salubrinal) and OxyHb + salubrinal. To mimic ICH, in OxyHb group, neurons were treated with OxyHb (10 μM) (Zhai et al., 2016); in OxyHb + vehicle (GSK2606414) group, cells were pretreated with DMSO (volume equal to GSK2606414) for 1 h and then exposed to 10 μM OxyHb; in OxyHb + GSK2606414 group, cells were pretreated with GSK2606414 (1 μM) for 1 h and then exposed to 10 μM OxyHb (Jiang et al., 2017); in OxyHb+vehicle (salubrinal) group, cells were pretreated with DMSO (volume equal to salubrinal) for 1 h and then exposed to 10 μM OxyHb; in OxyHb +salubrinal group, cells were pretreated with salubrinal (50 μM) for 1 h and then exposed to 10 μM OxyHb (Sokka et al., 2007) in fresh medium. After incubation for 48 h, cells were fixed with 4% paraformaldehyde. After these treatments, cellular morphology was observed by inverted phase contrast microscope, and the total protein of the cells was collected and stored at −80°C for western blot analysis.

Statistical Analysis

All data are presented as means ± SEM. Graph pad prism 7 was used for all statistical analysis. One-way ANOVA for multiple comparisons and Student–Newman–Keuls *post-hoc* test were used to determine the differences among all groups. $P < 0.05$ was considered to be significant difference.

RESULTS

ER Stress Pathways Activation Was Induced by ICH Both *in Vivo* and *in Vitro*

In experiment 1, the western blot analysis revealed that the levels of p-eIF2α and ATF-4 in the brain tissues were increased significantly from 4 h after ICH, reaching a peak at 48 h (**Figure 2A**). In addition, we also determined the other two ER stress pathways, and it was shown that ATF-6 and XBP-1 were elavated after ICH induction, exhibiting that ATF and IREα/XBP1 were also activated (**Figure 2B**). *In vitro*, to mimic ICH we used OxyHb to treat the neurons. And it was found that the level of p-eIF2α and ATF-4 were increased significantly from 4 h after OxyHb treatment and reached the peak at 48 h, as expected (**Figure 2C**). Furthermore, double immunofluorescence assay verified the ICH-induced increase in the protein level of p-eIF2α and ATF-4 in neurons at 48 h, which were also demonstrated that p-eIF2α and ATF-4 were mainly expressed in neurons (**Figures 2D,E**). So, we focused on PERK pathway in neurons in the following study at 48 h.

PERK Signaling Pathway Was Inhibited by GSK2606414 and Activated by Salubrinal *in Vivo*

The PERK inhibitor GSK2606414 was injected intracerebroventricularly at 1 h after ICH and the eIF2α dephosphorylation inhibitor salubrinal, as an agonist of PERK downstream signaling pathway, was injected intraperitoneally at 30 min before ICH, respectively. It was revealed that with the treatment of GSK2606414 and salubrinal, the protein levels of p-eIF2α and ATF-4 were decreased and increased compared with ICH + vehicle (GSK2606414) and ICH + vehicle (salubrinal) group respectively (**Figure 3A**).

PERK Pathway Promoted ICH-Induced Apoptosis *in Vivo*

Previous studies have shown that PERK signaling pathway was involved in ER stress-induced apoptosis. In the present study, we found that with the treatment of GSK2606414, the increase of CHOP and cleaved caspase-12 protein levels induced by ICH could be significantly reversed (**Figure 3B**). Meanwhile, as indicated in the histological evidence of neuronal apoptosis, the TUNEL was double labeled with ATF-4. The results showed that the number of TUNEL and ATF-4 double positive cells was increased following ICH relative to the sham group, but this effect was abrogated by GSK2606414 administration (**Figure 3C**). Similarly, the ICH-induced increase in the number of FJB-positive cells was reversed by GSK2606414 as compared to the ICH + vehicle (GSK2606414) group (**Figure 3D**). On the contrary, the salubrinal treatment could significantly promote the protein levels of CHOP and cleaved caspase-12 increase induced by

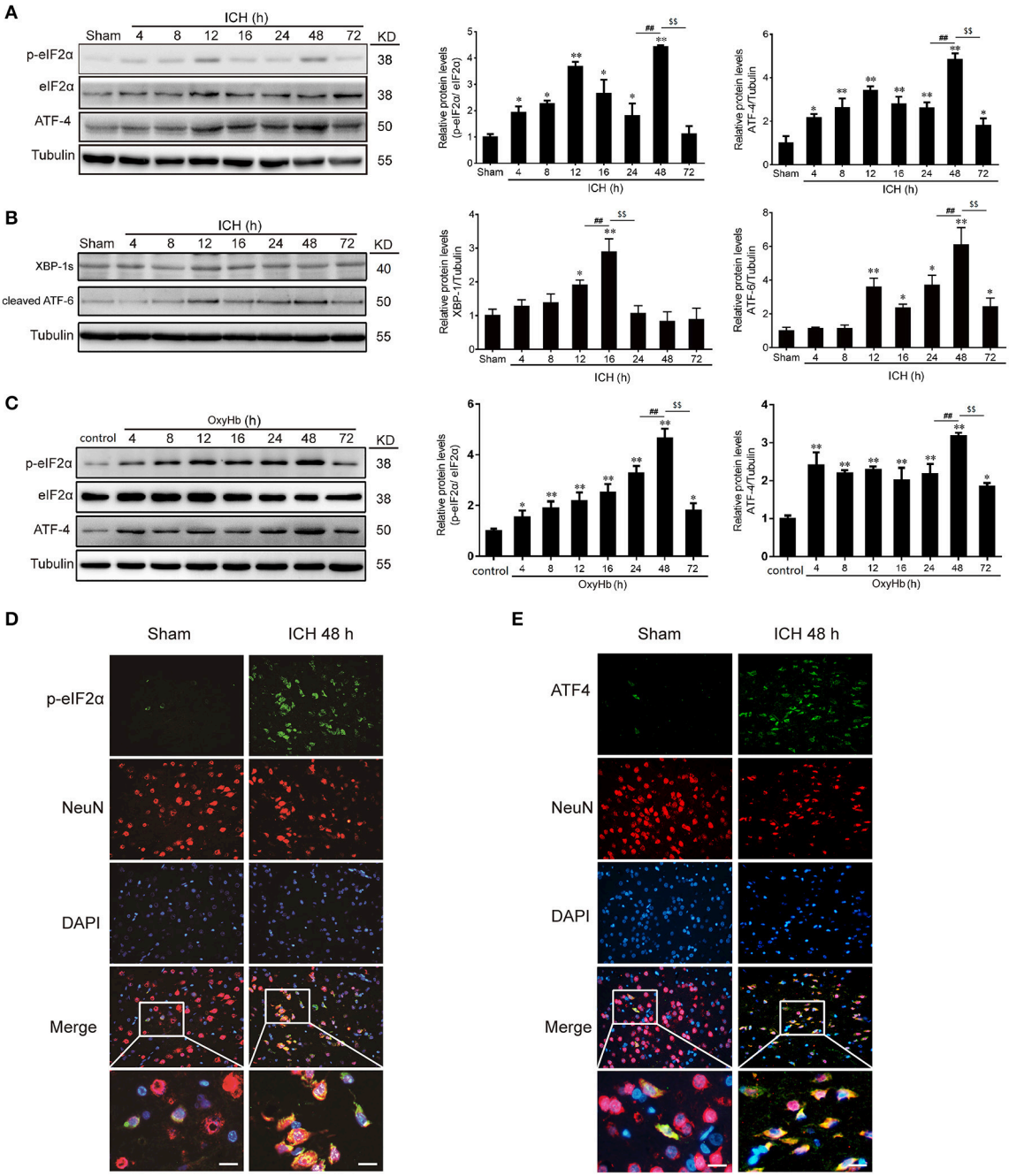

FIGURE 2 | p-eIF2α and ATF4 protein levels are increased after ICH *in vitro* and *in vivo*. **(A)** Brain tissue samples collected at different time points after ICH were analyzed for p-eIF2α, eIF2α, and ATF4 expression by western blot; tubulin served as a loading control. Protein levels were quantified with ImageJ software, and mean values for sham animals were normalized to 1.0. Data represent mean ± SEM ($n = 6$). $^{*}p < 0.05$, $^{**}p < 0.01$ vs. sham; $^{\#\#}p < 0.01$ 24 vs. 48 h; $^{\$\$}p < 0.01$ 48 vs. 72 h (one-way analysis of variance followed by the Student–Newman–Keuls *post-hoc* test). **(B)** The protein levels of ATF-6 and XBP-1 were detected by western blot, and tubulin served as a loading control. Protein levels were quantified with ImageJ software, and mean values for sham animals were normalized to 1.0. Data represent mean ± SEM ($n = 6$). $^{*}p < 0.05$, $^{**}p < 0.01$ vs. sham; $^{\#\#}p < 0.01$ 12 vs.16 h, 24 vs.48 h; $^{\$\$}p < 0.01$ 16 vs. 24 h, 48 vs. 72 h (one-way analysis of variance followed by the Student–Newman–Keuls *post-hoc* test). **(C)** Primary neurons were extracted and treated with 10 μM OxyHb for indicated times, and p-eIF2α, eIF2α, and ATF4 levels were detected by western blotting. Protein levels were quantified with ImageJ software, and mean values in the control group were normalized to 1.0. Data represent mean ± SEM ($n = 3$). $^{*}p < 0.05$, $^{**}p < 0.01$ vs. control; $^{\#\#}p < 0.01$ 24 vs. 48 h; $^{\$\$}p < 0.01$ 48 vs. 72 h (one-way analysis of variance followed by the Student–Newman–Keuls *post-hoc* test). **(D,E)** Double immunofluorescence analysis of brain tissue (between the cortex and the perihematoma) using antibodies against eIF2α (green) and NeuN (red) **(D)** or ATF4 (green) and NeuN (red) **(E)**; nuclei were labeled with DAPI (blue). Scale bar = 30 μm.

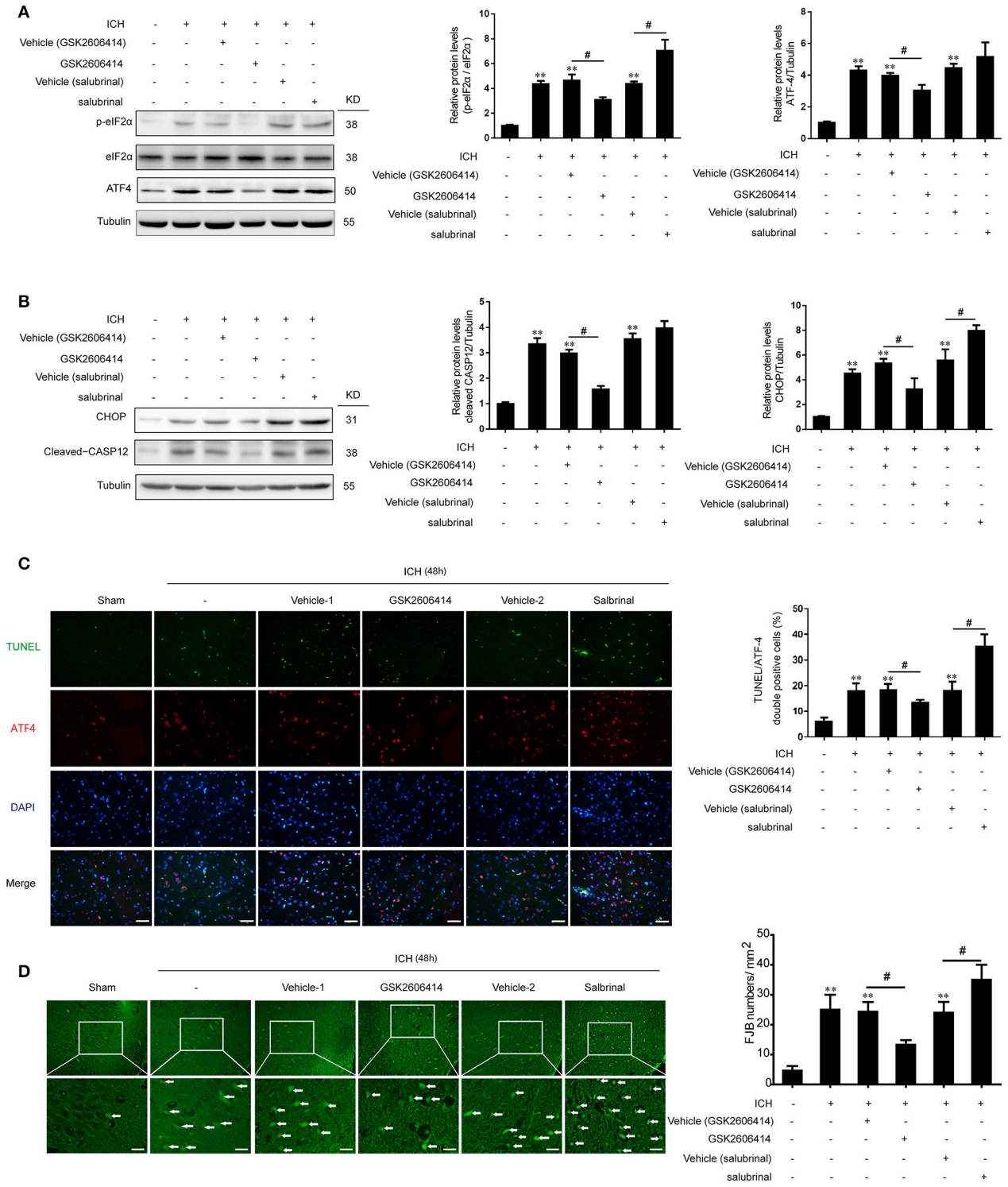

FIGURE 3 | Effect of PERK pathway inhibition and activation on SBI following ICH *in vivo*. **(A)** Brain tissue samples were collected and eIF2α phosphorylation and ATF4 expression were detected by western blotting. Tubulin served as a loading control. Protein levels were quantified with ImageJ software. Mean values for the sham group were normalized to 1.0. Data represent mean ± SEM ($n = 6$). $^{**}p < 0.01$ vs. sham; $^{\#}p < 0.05$ vs. indicated vehicle (one-way analysis of variance followed by the Student–Newman–Keuls *post-hoc* test). **(B)** Detection of CHOP and caspase-12 expression in sham, ICH, ICH + vehicle (GSK2606414), ICH + GSK2606414, ICH + vehicle (salubrinal), and ICH + salubrinal groups 48 h after ICH by western blotting. Data represent mean ± SEM ($n = 6$). $^{**}p < 0.01$ vs. sham; $^{\#}p < 0.05$ vs. indicated vehicle. **(C)** Induction of apoptosis 48 h after ICH, as detected with the TUNEL assay. Double immunofluorescence analysis was performed

(Continued)

FIGURE 3 | with TUNEL (green) and an antibody against ATF-4 (red); nuclei were labeled with DAPI (blue). Scale bar = 30 μm. Quantitative analysis of TUNEL and ATF-4 double positive neurons in each group. Data represent mean ± SEM ($n = 6$). $^{**}p < 0.01$ vs. sham; $^{\#}p < 0.05$ vs. indicated vehicle. **(D)** Detection of neuronal degradation in the cerebral cortex by FJB staining (green). Scale bar = 26 μm. Arrows indicate FJB-positive cells. FJB-positive cells/mm^2 was quantified at 48 h. Data represent mean ± SEM ($n = 6$). $^{**}p < 0.01$ vs. sham; $^{\#}p < 0.05$ vs. indicated vehicle.

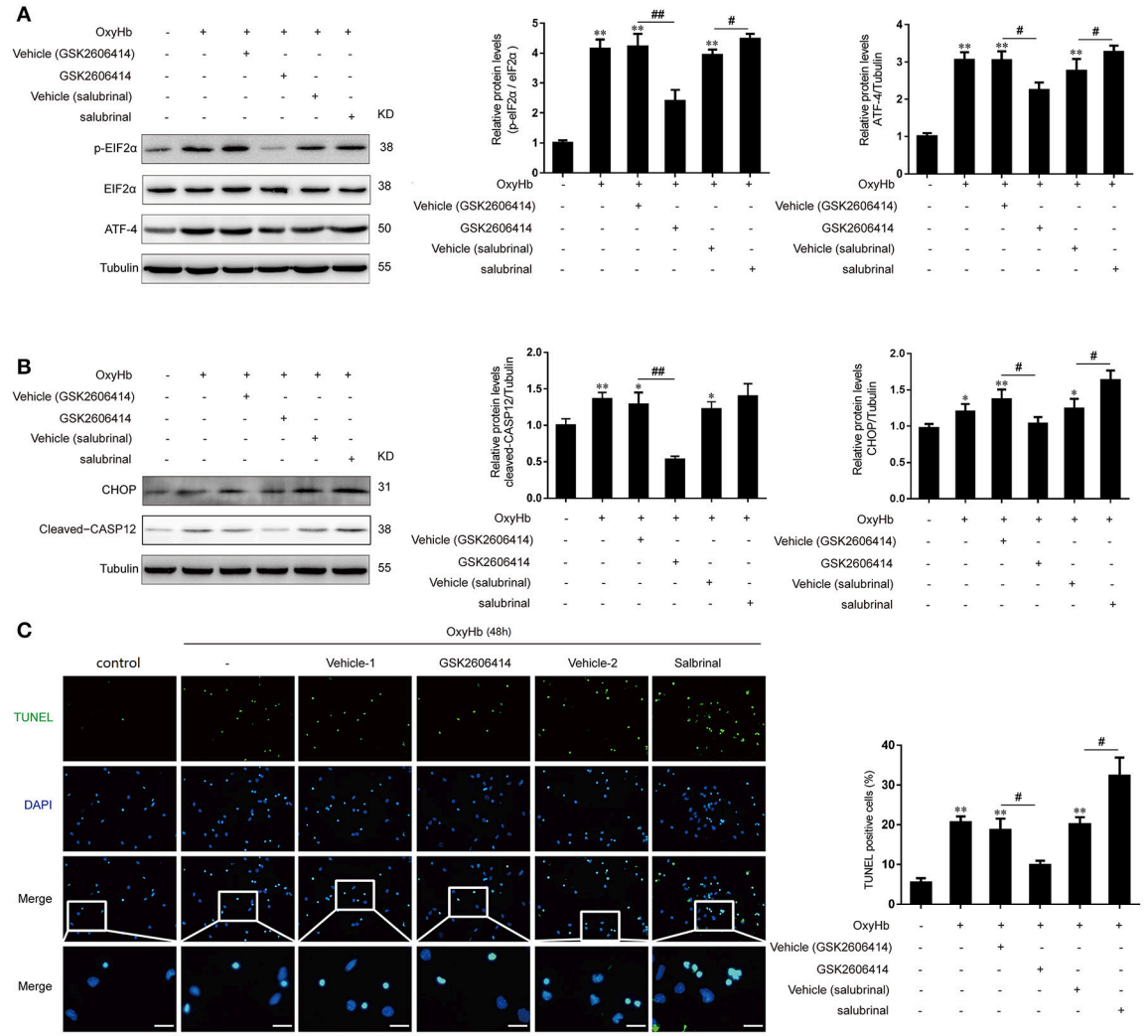

FIGURE 4 | Effect of PERK pathway inhibition and activation on OxyHb-induced neuronal apoptosis *in vitro*. Neurons were cultured with or without OxyHb for 48 h. Cells were exposed to GSK2606414 or salubrinal for 1 h before OxyHb treatment. **(A)** eIF2α phosphorylation and ATF4 expression in the control, OxyHb, OxyHb + vehicle (GSK2606414), OxyHb + GSK2606414, OxyHb + vehicle (salubrinal), and OxyHb + salubrinal groups were detected by western blotting. Data represent mean ± SEM ($n = 3$). $^{**}p < 0.01$ vs. control; $^{\#}p < 0.05$, $^{\#\#}p < 0.01$ vs. indicated vehicle. **(B)** CHOP and cleaved-caspase-12 expression in each group was detected by western blotting. Data represent mean ± SEM ($n = 3$). $^{*}p < 0.05$, $^{**}p < 0.01$ vs. control; $^{\#}p < 0.05$, $^{\#\#}p < 0.01$ vs. indicated vehicle. **(C)** Apoptosis in OxyHb-treated neurons at 48 h was detected with the TUNEL assay. Representative images from control, OxyHb, OxyHb + vehicle (GSK2606414), OxyHb + GSK2606414, OxyHb + vehicle (salubrinal), and OxyHb + salubrinal groups are shown. Scale bar = 20 μm. The percentage of TUNEL-positive cells was determined. Data represent mean ± SEM ($n = 3$). $^{**}p < 0.01$ vs. control; $^{\#}p < 0.05$ vs. indicated vehicle.

ICH (**Figure 3B**). Moreover, the TUNEL and ATF-4 double positive cells were significantly increased compared to the ICH+vehicle (salubrinal) group (**Figure 3C**), as well as the FJB-positive cells (**Figure 3D**). It was indicated that PERK pathway inhibition could rescue neuronal apoptosis and necrosis induced by ICH.

PERK Signaling Pathway Was Inhibited by GSK2606414 and Activated by Salubrinal *in Vitro*

In addition, we further investigated the role of PERK signaling pathway in primary neurons treated with OxyHb to mimic ICH. It was found that the protein levels of p-eIF2α and ATF-4 were

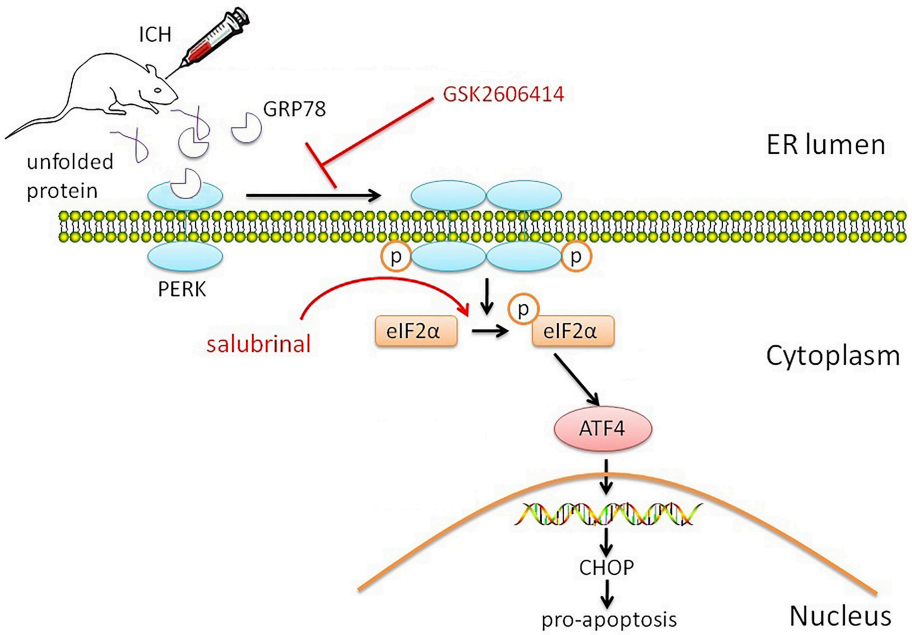

FIGURE 5 | Proposed role of PERK signaling pathway in SBI after ICH. The PERK signaling pathway is activated by ICH, resulting in increased p-eIF2α and ATF4 protein levels. The consequent activation of the ER stress response induces neuronal apoptosis, which is blocked by application of the PERK inhibitor GSK2606414. On the contrary, activation of PERK downstream signaling pathway by salubrinal promotes apoptosis and reduces neuronal survival by blocking eIF2α dephosphorylation.

significantly decreased after GSK2606414 treatment compared to the OxyHb + vehicle (GSK2606414) group, which showed the opposite effects with the treatment of salubrinal compared to the OxyHb +vehicle (salubrinal) group (**Figure 4A**).

PERK Signaling Pathway Promoted ICH-Induced Neuronal Apoptosis *in Vitro*

Similar to the results obtained in the *in vivo* experiments, with the treatment of OxyHb, the CHOP and cleaved-caspase-12 protein levels were significantly elevated, indicating that apoptosis induction (**Figure 4B**). Importantly, after the treatment of GSK2606414 and salubrinal, the protein levels of CHOP and cleaved-caspase-12 were significantly decreased and increased, respectively compared to the OxyHb + vehicle (GSK2606414) group and the OxyHb + vehicle (salubrinal) group respectively (**Figure 4B**). Accordingly, the number of TUNEL-positive primary neurons was decreased by GSK2606414 following OxyHb pretreatment relative to the OxyHb + vehicle (GSK2606414) group, while the opposite was observed in the OxyHb + salubrinal group as compared to the vehicle control (**Figure 4C**). These results demonstrate that the PERK pathway plays an important role in ICH-induced neuronal apoptosis.

DISCUSSION

ICH is followed by brain injury that can disrupt cell metabolism and activate cellular stress responses, including the UPR and ER stress (Niu et al., 2017). In this study, we investigated the role of PERK signaling in the pathophysiology of SBI following ICH and found that the PERK pathway was activated, as evidenced by increased protein levels of p-eIF2α and ATF4. The resultant ER stress induced neuronal apoptosis (**Figure 5**).

Disruption of ER function leads to ER stress (Roussel et al., 2013). Oxidative stress (Goswami et al., 2016), mitochondrial calcium overload (Zhou et al., 2015), perturbation of cellular ion balance (Varadarajan et al., 2013), and toxic glutamate release (Li et al., 2015) have been shown to induce ER stress in various diseases. The PERK pathway plays an important role in neuronal fate as an important mediator of ER stress. ER stress-associated PERK/eIF2α signaling is activated in response to elevated levels of misfolded proteins in the ER and temporarily halts protein translation, which can lead to neuronal death (Li et al., 2015; Radford et al., 2015). PERK/eIF2α signaling is increased in cerebral ischemia (Gharibani et al., 2015), and the constituent proteins have been shown to be upregulated in neurons upon central nervous system injury (Han et al., 2015; Rubovitch et al., 2015; Yan et al., 2017). Consistent with these observations, we found here that p-eIF2α and ATF4 levels were significantly elevated in neurons after ICH, with maximum levels observed after 48 h both *in vitro* and *in vivo*.

As a mediator of ER stress, PERK signaling is involved in neuronal apoptosis after subarachnoid hemorrhage; PERK is inhibited by Akt-associated anti-apoptotic pathways, which reduces early brain injury (Yan et al., 2017). PERK and eIF2α levels are elevated in traumatic brain injury (Rubovitch et al., 2015). Severe ER stress leads to apoptosis, while inhibition of

ER stress promotes neuronal survival and improves neurological function (Moreno et al., 2013; Rubovitch et al., 2015; Tsujii et al., 2015). In accordance with previous studies, we found that GSK2606414 suppressed p-eIF2α and ATF4 expression and promoted neuronal survival by suppressing apoptosis 48 h after ICH. Additionally, PERK inhibition decreased CHOP and cleaved caspase-12 levels. Thus, inhibiting PERK signaling has a neuroprotective effect following ICH. Indeed, GSK2606414 was shown to exert neuroprotective effects in tauopathies and Parkinson's and Alzheimer's diseases as a selective inhibitor of PERK (Halliday et al., 2015; Radford et al., 2015).

Some studies have suggested that increased PERK activation can reduce neuronal apoptosis in various diseases (Fouillet et al., 2012; Lin et al., 2013). There is no consensus on whether ER stress and UPR are beneficial or detrimental following central nervous system injury, and the role of PERK signaling in SBI after ICH remains unclear. Previous studies have shown that a mild stimulus can activate ER stress as a host defense mechanism, resulting in the degradation of damaged organelles and proteins by autophagy, which promotes neuronal survival (Fouillet et al., 2012; Yan et al., 2014). ER stress cannot counter stimuli that are severe and long-lived, resulting in apoptosis (Moreno et al., 2013; Tsujii et al., 2015). Perihematomal edema and the physiological response to hematoma after ICH can cause SBI (Aronowski and Zhao, 2011; Urday et al., 2015). Blood components, dysfunctional organelles, overproduced iron complexes, and cytokine levels continuously increase following ICH, resulting in disruption of normal protein folding and activation of ER stress and the UPR, which contribute to ICH-associated brain injury (Guo et al., 2012). In humans, intracerebral hematoma resolves gradually over a period of weeks, during which time the brain experiences continuous injury (Keep et al., 2012), leading to prolonged and severe ER stress and eventually neuronal apoptosis.

Also, there are a few limitations to this study. Firstly, in this study, we only focused exclusively on the role of PERK signaling pathway in adult male rats although ICH can affect females and is common in the elderly (Tsivgoulis et al., 2014). Secondly, a previous study has shown that PERK pathway via direct interaction to promote the enzymatic activity of calcineurin (Gao et al., 2016). Calcium overload in the cytoplasm is thought to be a potential mechanism of apoptosis induced by calcineurin; therefore, the precise relationship between PERK and calcineurin merits closer examination in future studies.

In conclusion, the results of this study demonstrate that PERK signaling pathway inhibition can reduce SBI after ICH by suppressing apoptosis. Based on these findings, we propose that PERK signaling pathway could be a key endogenous physiological regulatory signal pathway in neurons, suggesting that it might be a therapeutic target to alleviate SBI following ICH.

AUTHOR CONTRIBUTIONS

ZW and XL: Conceived and designed the study, including quality assurance and control; CM and JZ: Performed the experiments and wrote the paper; BD and HS: Designed the study's analytic strategy; XL and HL: Helped conduct the literature review and prepare the Materials and Methods section of the text. All authors read and approved the manuscript.

FUNDING

This work was supported by the Project of Jiangsu Provincial Medical Innovation Team (CXTDA2017003), Jiangsu Provincial Medical Youth Talent (QNRC2016728), Suzhou Key Medical Centre (Szzx201501), Scientific Department of Jiangsu Province (No. BE2017656), Suzhou Government (No. SYS201608 and LCZX201601), Jiangsu Province (No. 16KJB320008), Zhangjiagang Science & Technology Pillar Program (ZKS1712).

REFERENCES

Aronowski, J., and Zhao, X. (2011). Molecular pathophysiology of cerebral hemorrhage: secondary brain injury. *Stroke* 42, 1781–1786. doi: 10.1161/STROKEAHA.110.596718

Axten, J. M., Medina, J. R., Feng, Y., Shu, A., Romeril, S. P., Grant, S. W., et al. (2012). Discovery of 7-methyl-5-(1-{[3-(trifluoromethyl)phenyl]acetyl}-2,3-dihydro-1H-indol-5-yl)-7H-p yrrolo[2,3-d]pyrimidin-4-amine (GSK2606414), a potent and selective first-in-class inhibitor of protein kinase R (PKR)-like endoplasmic reticulum kinase (PERK). *J. Med. Chem.* 55, 7193–7207. doi: 10.1021/jm300713s

Behrouz, R. (2016). Re-exploring tumor necrosis factor alpha as a target for therapy in intracerebral hemorrhage. *Transl. Stroke Res.* 7, 93–96. doi: 10.1007/s12975-016-0446-x

Boyce, M., Bryant, K. F., Jousse, C., Long, K., Harding, H. P., Scheuner, D., et al. (2005). A selective inhibitor of eIF2alpha dephosphorylation protects cells from ER stress. *Science* 307, 935–939. doi: 10.1126/science.1101902

Chen, S., Yang, Q., Chen, G., and Zhang, J. H. (2015). An update on inflammation in the acute phase of intracerebral hemorrhage. *Transl. Stroke Res.* 6, 4–8. doi: 10.1007/s12975-014-0384-4

Deinsberger, W., Vogel, J., Kuschinsky, W., Auer, L. M., and Böker, D. K. (1996). Experimental intracerebral hemorrhage: description of a double injection model in rats. *Neurol. Res.* 18, 475–477. doi: 10.1080/01616412.1996.11740456

Fouillet, A., Levet, C., Virgone, A., Robin, M., Dourlen, P., Rieusset, J., et al. (2012). ER stress inhibits neuronal death by promoting autophagy. *Autophagy* 8, 915–926. doi: 10.4161/auto.19716

Gao, J., Jiang, Z., Wang, S., Zhou, Y., Shi, X., and Feng, M. (2016). Endoplasmic reticulum stress of Kupffer cells involved in the conversion of natural regulatory T cells to Th17 cells in liver ischemia-reperfusion injury. *J. Gastroenterol. Hepatol.* 31, 883–889. doi: 10.1111/jgh.13163

Gebel, J. M. Jr., Jauch, E. C., Brott, T. G., Khoury, J., Sauerbeck, L., Salisbury, S., et al. (2002). Natural history of perihematomal edema in patients with hyperacute spontaneous intracerebral hemorrhage. *Stroke* 33, 2631–2635. doi: 10.1161/01.STR.0000035284.12699.84

Gharibani, P., Modi, J., Menzie, J., Alexandrescu, A., Ma, Z., Tao, R., et al. (2015). Comparison between single and combined post-treatment with S-Methyl-N,N-diethylthiolcarbamate sulfoxide and taurine following transient focal cerebral ischemia in rat brain. *Neuroscience* 300, 460–473. doi: 10.1016/j.neuroscience.2015.05.042

Godin, J. D., Creppe, C., Laguesse, S., and Nguyen, L. (2016). Emerging roles for the unfolded protein response in the developing nervous system. *Trends Neurosci.* 39, 394–404. doi: 10.1016/j.tins.2016.04.002

Goswami, P., Gupta, S., Biswas, J., Sharma, S., and Singh, S. (2016). Endoplasmic reticulum stress instigates the rotenone induced oxidative

apoptotic neuronal death: a study in rat brain. *Mol. Neurobiol.* 53, 5384–5400. doi: 10.1007/s12035-015-9463-0

Guo, F., Hua, Y., Wang, J., Keep, R. F., and Xi, G. (2012). Inhibition of carbonic anhydrase reduces brain injury after intracerebral hemorrhage. *Transl. Stroke Res.* 3, 130–137. doi: 10.1007/s12975-011-0106-0

Halliday, M., Radford, H., Sekine, Y., Moreno, J., Verity, N., le Quesne, J., et al. (2015). Partial restoration of protein synthesis rates by the small molecule ISRIB prevents neurodegeneration without pancreatic toxicity. *Cell Death Dis.* 6:e1672. doi: 10.1038/cddis.2015.49

Han, Y., Yi, W., Qin, J., Zhao, Y., Zhang, J., and Chang, X. (2015). Carbon monoxide offers neuroprotection from hippocampal cell damage induced by recurrent febrile seizures through the PERK-activated ER stress pathway. *Neurosci. Lett.* 585, 126–131. doi: 10.1016/j.neulet.2014.11.040

Jiang, C., Zhang, S., Liu, H., Zeng, Q., Xia, T., Chen, Y., et al. (2012). The role of the IRE1 pathway in PBDE-47-induced toxicity in human neuroblastoma SH-SY5Y cells *in vitro*. *Toxicol. Lett.* 211, 325–333. doi: 10.1016/j.toxlet.2012.04.009

Jiang, X., Wei, Y., Zhang, T., Zhang, Z., Qiu, S., Zhou, X., et al. (2017). Effects of GSK2606414 on cell proliferation and endoplasmic reticulum stressassociated gene expression in retinal pigment epithelial cells. *Mol. Med. Rep.* 15, 3105–3110. doi: 10.3892/mmr.2017.6418

Keep, R. F., Hua, Y., and Xi, G. (2012). Intracerebral haemorrhage: mechanisms of injury and therapeutic targets. *Lancet Neurol.* 11, 720–731. doi: 10.1016/S1474-4422(12)70104-7

Kim, E. M., Shin, E. J., Choi, J. H., Son, H. J., Park, I. S., Joh, T. H., et al. (2010). Matrix metalloproteinase-3 is increased and participates in neuronal apoptotic signaling downstream of caspase-12 during endoplasmic reticulum stress. *J. Biol. Chem.* 285, 16444–16452. doi: 10.1074/jbc.M109.093799

Lee, S. T., Chu, K., Sinn, D. I., Jung, K. H., Kim, E. H., Kim, S. J., et al. (2006). Erythropoietin reduces perihematomal inflammation and cell death with eNOS and STAT3 activations in experimental intracerebral hemorrhage. *J. Neurochem.* 96, 1728–1739. doi: 10.1111/j.1471-4159.2006.03697.x

Li, Y., Li, J., Li, S., Li, Y., Wang, X., Liu, B., et al. (2015). Curcumin attenuates glutamate neurotoxicity in the hippocampus by suppression of ER stress-associated TXNIP/NLRP3 inflammasome activation in a manner dependent on AMPK. *Toxicol. Appl. Pharmacol.* 286, 53–63. doi: 10.1016/j.taap.2015.03.010

Lin, S., Yin, Q., Zhong, Q., Lv, F. L., Zhou, Y., Li, J. Q., et al. (2012). Heme activates TLR4-mediated inflammatory injury via MyD88/TRIF signaling pathway in intracerebral hemorrhage. *J. Neuroinflammation* 9:46. doi: 10.1186/1742-2094-9-46

Lin, W., Lin, Y., Li, J., Fenstermaker, A. G., Way, S. W., Clayton, B., et al. (2013). Oligodendrocyte-specific activation of PERK signaling protects mice against experimental autoimmune encephalomyelitis. *J. Neurosci.* 33, 5980–5991. doi: 10.1523/JNEUROSCI.1636-12.2013

Moreno, J. A., Halliday, M., Molloy, C., Radford, H., Verity, N., Axten, J. M., et al. (2013). Oral treatment targeting the unfolded protein response prevents neurodegeneration and clinical disease in prion-infected mice. *Sci. Transl. Med.* 5, 206ra138. doi: 10.1126/scitranslmed.3006767

Nakka, V. P., Gusain, A., and Raghubir, R. (2010). Endoplasmic reticulum stress plays critical role in brain damage after cerebral ischemia/reperfusion in rats. *Neurotox. Res.* 17, 189–202. doi: 10.1007/s12640-009-9110-5

Niu, M., Dai, X., Zou, W., Yu, X., Teng, W., Chen, Q., et al. (2017). Autophagy, endoplasmic reticulum stress and the unfolded protein response in intracerebral hemorrhage. *Transl. Neurosci.* 8, 37–48. doi: 10.1515/tnsci-2017-0008

Pacifici, M., and Peruzzi, F. (2012). Isolation and culture of rat embryonic neural cells: a quick protocol. *J. Vis. Exp.* e3965. doi: 10.3791/3965

Penke, B., Bogár, F., and Fülöp, L. (2016). Protein folding and misfolding, endoplasmic reticulum stress in neurodegenerative diseases: in trace of novel drug targets. *Curr. Protein Pept. Sci.* 17, 169–182. doi: 10.2174/1389203716666151102104653

Qureshi, A. I., Ling, G. S., Khan, J., Suri, M. F., Miskolczi, L., Guterman, L. R., et al. (2001). Quantitative analysis of injured, necrotic, and apoptotic cells in a new experimental model of intracerebral hemorrhage. *Crit. Care Med.* 29, 152–157. doi: 10.1097/00003246-200101000-00030

Radford, H., Moreno, J. A., Verity, N., Halliday, M., and Mallucci, G. R. (2015). PERK inhibition prevents tau-mediated neurodegeneration in a mouse model of frontotemporal dementia. *Acta Neuropathol.* 130, 633–642. doi: 10.1007/s00401-015-1487-z

Rodríguez-Yáñez, M., Castellanos, M., Freijo, M. M., Lopez Fernandez, J. C., Marti-Fabregas, J., Nombela, F., et al. (2013). Clinical practice guidelines in intracerebral haemorrhage. *Neurologia* 28, 236–249. doi: 10.1016/j.nrleng.2011.03.011

Roussel, B. D., Kruppa, A. J., Miranda, E., Crowther, D. C., Lomas, D. A., and Marciniak, S. J. (2013). Endoplasmic reticulum dysfunction in neurological disease. *Lancet Neurol.* 12, 105–118. doi: 10.1016/S1474-4422(12)70238-7

Rubovitch, V., Barak, S., Rachmany, L., Goldstein, R. B., Zilberstein, Y., and Pick, C. G. (2015). The neuroprotective effect of salubrinal in a mouse model of traumatic brain injury. *Neuromol. Med.* 17, 58–70. doi: 10.1007/s12017-015-8340-3

Scheper, W., and Hoozemans, J. J. (2013). A new PERKspective on neurodegeneration. *Sci. Transl. Med.* 5:206fs237. doi: 10.1126/scitranslmed.3007641

Schlunk, F., and Greenberg, S. M. (2015). The pathophysiology of intracerebral hemorrhage formation and expansion. *Transl. Stroke Res.* 6, 257–263. doi: 10.1007/s12975-015-0410-1

Schröder, M., and Kaufman, R. J. (2005). ER stress and the unfolded protein response. *Mutat. Res.* 569, 29–63. doi: 10.1016/j.mrfmmm.2004.06.056

Sokka, A. L., Putkonen, N., Mudo, G., Pryazhnikov, E., Reijonen, S., Khiroug, L., et al. (2007). Endoplasmic reticulum stress inhibition protects against excitotoxic neuronal injury in the rat brain. *J. Neurosci.* 27, 901–908. doi: 10.1523/JNEUROSCI.4289-06.2007

Tabas, I., and Ron, D. (2011). Integrating the mechanisms of apoptosis induced by endoplasmic reticulum stress. *Nat. Cell Biol.* 13, 184–190. doi: 10.1038/ncb0311-184

Tsivgoulis, G., Katsanos, A. H., Butcher, K. S., Boviatsis, E., Triantafyllou, N., Rizos, I., et al. (2014). Intensive blood pressure reduction in acute intracerebral hemorrhage: a meta-analysis. *Neurology* 83, 1523–1529. doi: 10.1212/WNL.0000000000000917

Tsujii, S., Ishisaka, M., Shimazawa, M., Hashizume, T., and Hara, H. (2015). Zonisamide suppresses endoplasmic reticulum stress-induced neuronal cell damage *in vitro* and *in vivo*. *Eur. J. Pharmacol.* 746, 301–307. doi: 10.1016/j.ejphar.2014.09.023

Urday, S., Beslow, L. A., Goldstein, D. W., Vashkevich, A., Ayres, A. M., Battey, T. W., et al. (2015). Measurement of perihematomal edema in intracerebral hemorrhage. *Stroke* 46, 1116–1119. doi: 10.1161/STROKEAHA.114.007565

Varadarajan, S., Tanaka, K., Smalley, J. L., Bampton, E. T., Pellecchia, M., Dinsdale, D., et al. (2013). Endoplasmic reticulum membrane reorganization is regulated by ionic homeostasis. *PLoS ONE* 8:e56603. doi: 10.1371/journal.pone.0056603

Wilkinson, D. A., Pandey, A. S., Thompson, B. G., Keep, R. F., Hua, Y., and Xi, G. (2017). Injury mechanisms in acute intracerebral hemorrhage. *Neuropharmacology*. doi: 10.1016/j.neuropharm.2017.09.033. [Epub ahead of print].

Xiong, X. Y., and Yang, Q. W. (2015). Rethinking the roles of inflammation in the intracerebral hemorrhage. *Transl. Stroke Res.* 6, 339–341. doi: 10.1007/s12975-015-0402-1

Yan, F., Cao, S., Li, J., Dixon, B., Yu, X., Chen, J., et al. (2017). Pharmacological inhibition of PERK attenuates early brain injury after subarachnoid hemorrhage in rats through the activation of Akt. *Mol. Neurobiol.* 54, 1808–1817. doi: 10.1007/s12035-016-9790-9

Yan, F., Li, J., Chen, J., Hu, Q., Gu, C., Lin, W., et al. (2014). Endoplasmic reticulum stress is associated with neuroprotection against apoptosis via autophagy activation in a rat model of subarachnoid hemorrhage. *Neurosci. Lett.* 563, 160–165. doi: 10.1016/j.neulet.2014.01.058

Zhai, W., Chen, D., Shen, H., Chen, Z., Li, H., Yu, Z., et al. (2016). A1 adenosine receptor attenuates intracerebral hemorrhage-induced secondary brain injury

in rats by activating the P38-MAPKAP2-Hsp27 pathway. *Mol. Brain* 9:66. doi: 10.1186/s13041-016-0247-x

Zhou, Y., Sun, P., Wang, T., Chen, K., Zhu, W., and Wang, H. (2015). Inhibition of calcium influx reduces dysfunction and apoptosis in lipotoxic pancreatic beta-cells via regulation of endoplasmic reticulum stress. *PLoS ONE* 10:e0132411. doi: 10.1371/journal.pone.0132411

Zhu, H. T., Bian, C., Yuan, J. C., Chu, W. H., Xiang, X., Chen, F., et al. (2014). Curcumin attenuates acute inflammatory injury by inhibiting the TLR4/MyD88/NF-kappaB signaling pathway in experimental traumatic brain injury. *J. Neuroinflammation* 11:59. doi: 10.1186/1742-2094-11-59

Conflict of Interest Statement: The authors declare that the research was conducted in the absence of any commercial or financial relationships that could be construed as a potential conflict of interest.

frontiers in Neuroscience

ORIGINAL RESEARCH
published: 23 April 2018
doi: 10.3389/fnins.2018.00263

Inhibition of Epac2 Attenuates Neural Cell Apoptosis and Improves Neurological Deficits in a Rat Model of Traumatic Brain Injury

Ling Zhang[1,2†], Li Zhang[2†], Huixiang Liu[2], Feng Jiang[2], Huanjing Wang[3], Di Li[1] and Rong Gao[2*]*

[1] Translational Medicine Center, The First People's Hospital of Zhangjiagang, Zhangjiagang, China, [2] Department of Neurosurgery, The First People's Hospital of Zhangjiagang, Zhangjiagang, China, [3] Department of Neurosurgery, Zhangjiagang Hospital of Traditional Chinese Medicine, Zhangjiagang, China

OPEN ACCESS

Edited by:
Gao Chen,
Zhejiang University, China

Reviewed by:
Wei Li,
Nanjing Drum Tower Hospital, China
Yang Wang,
Anhui Provincial Hospital, China

***Correspondence:**
Di Li
lidilab@sina.com
Rong Gao
lidi715@163.com

[†]These authors have contributed equally to this work.

Specialty section:
This article was submitted to Neurodegeneration, a section of the journal Frontiers in Neuroscience

Received: 13 February 2018
Accepted: 05 April 2018
Published: 23 April 2018

Citation:
Zhang L, Zhang L, Liu H, Jiang F, Wang H, Li D and Gao R (2018) Inhibition of Epac2 Attenuates Neural Cell Apoptosis and Improves Neurological Deficits in a Rat Model of Traumatic Brain Injury. Front. Neurosci. 12:263. doi: 10.3389/fnins.2018.00263

Traumatic brain injury (TBI) is a major cause of mortality and disability worldwide. TBI-induced neuronal apoptosis is one of the main contributors to the secondary injury process. The aim of this study is to investigate the involvement of Exchange protein directly activated by cAMP 2 (Epac2) on TBI. We found that the expression level of Epac2 surrounding the injured area of brain in rats of TBI model was significantly increased at 12 h after TBI. The role of Epac2 in TBI was further explored by using a selective Epac2 antagonist ESI-05 to decrease the Epac2 expression. We discovered that inhibition of Epac2 could improve the neurological impairment and attenuate brain edema following TBI. The Epac2 inhibition effectively reduced neuronal cell death and P38 MAPK signaling pathway may be involved in this process. Our results suggest that inhibition of Epac2 may be a potential therapy for TBI by reducing the neural cell death, alleviating brain edema and improving neurologic deficits.

Keywords: traumatic brain injury, Epac2, P38, apoptosis, neuroprotection

INTRODUCTION

Traumatic brain injury (TBI) is one of the leading causes of mortality and disability all over the world (Menon and Maas, 2015; Wang et al., 2018). TBI can result in physical, cognitive, social, emotional, and behavioral symptoms. TBI consists of a primary mechanical brain tissue injury that occur at the time of the initial trauma and a secondary insult with a series of pathological responses, including intracerebral hemorrhage, oxidative stress, neuroinflammation, blood-brain barrier (BBB) damage, autophage, and apoptosis (Cornelius et al., 2013; Li et al., 2017; Tang et al., 2017). The long-term consequence of TBI was dominated by the secondary injury, so the secondary brain injury has been the major focus to identify potential therapeutic targets in TBI management.

Epac (Exchange protein directly activated by cAMP) proteins have two isoforms, Epac1 and Epac2 (Gloerich and Bos, 2010). Epac1 is expressed throughout the body, while Epac2, the larger of the two isoforms, is highly enriched in brain and adrenals (Kawasaki et al., 1998). Epac2 is a guanine nucleotide exchange factor (GEF) to activate the small GTPase Rap (Kawasaki et al., 1998; Bos, 2003). Deletion of Epac2 causes brain dysfunction, such as impairments in memory and social

interaction (Fernandes et al., 2015; Lee et al., 2015). Epac2 activation was associated with astrocytic differentiation and inflammation (Oldenburger et al., 2014; Seo and Lee, 2016). Epac2 promotes neurotransmission in the hippocampus (Fernandes et al., 2015). Epac2 has been proposed as a promising target for treatment of diabetes, cancer and cardiovascular disease (Zhang et al., 2009; Parnell et al., 2015; Yang et al., 2017). However, the roles of Epac2 in traumatic brain injury are still unknown. In this study, we investigated the effects of Epac2 on neurological damage of TBI rat models, and demonstrated the possible signaling pathway involved in this process.

MATERIALS AND METHODS

Animals

Male Sprague-Dawley rats (280–300 g) were obtained from the Animal Center of Chinese Academy of Sciences, Shanghai, China. The animals were housed under controlled environmental conditions with a 12 h light/dark cycle place and were given unrestricted access to pellet food and water throughout the study. All experimental procedures were approved by the Institutional Animal Care and Use Committee of Soochow University and conformed to the National Institutes of Health Guide for the Care and Use of Laboratory Animals.

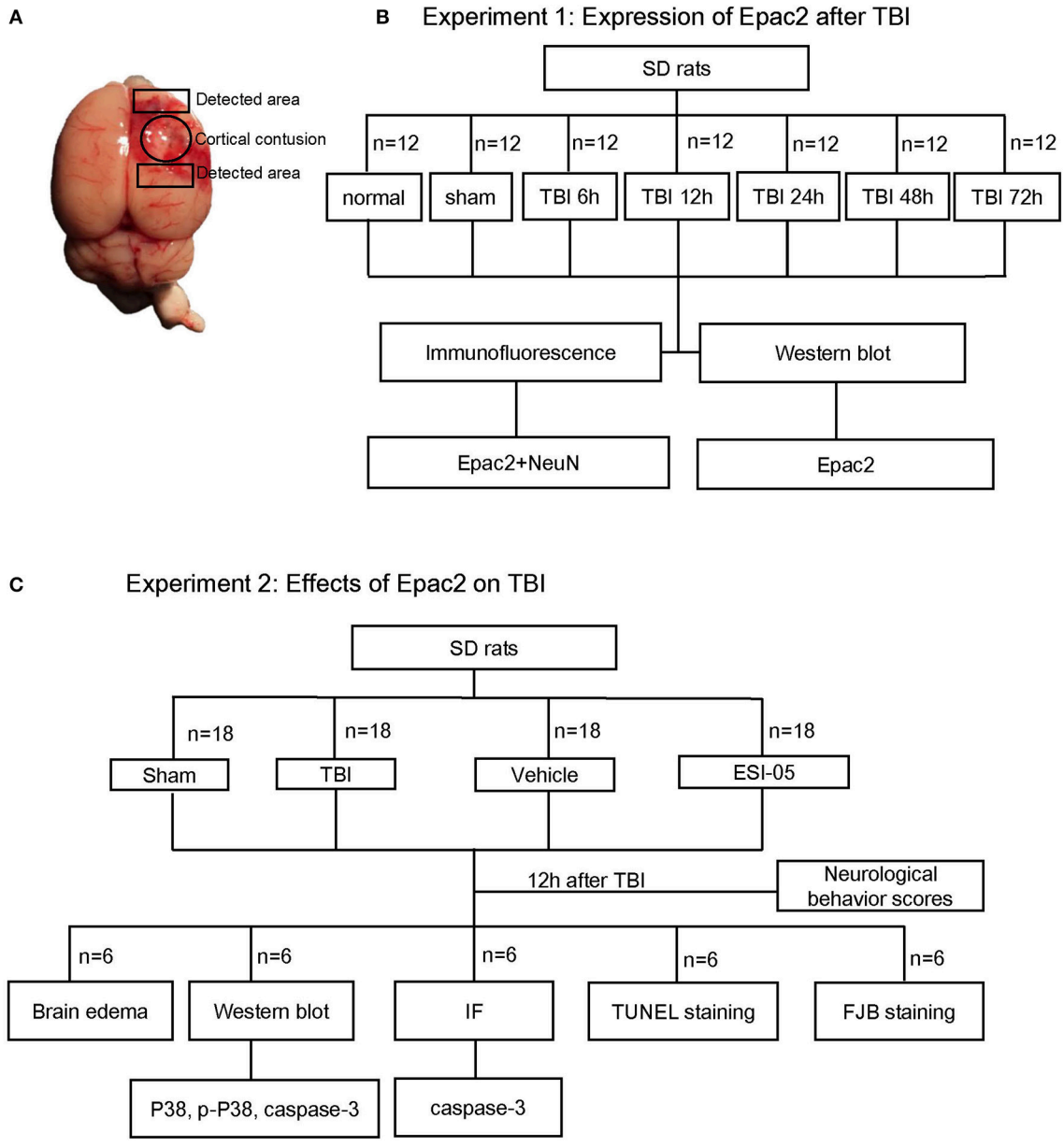

FIGURE 1 | Schematic representation of TBI model and experimental design. **(A)** Brains of TBI model, the studied region is surrounding the injured brain. **(B)** Experiment 1 was designed to detect the time course of Epac2 expression after TBI. **(C)** Experiment 2 was designed to detect the effects of Epac2 on TBI and investigate the possible mechanism.

TBI Model

Surgical procedures were performed as previously described (Li et al., 2017). The rats were anesthetized by an intraperitoneal injection of 4% chloral hydrate (10 ml/kg) (Dang et al., 2015). The head of them was fixed on a stereotaxic frame. After incision of the scalp, a craniotomy of 5 mm diameter was performed beside midline and behind the cranial coronal suture using a dental drill. Contusion was produced by letting a 40 g weight cylindrical steel rod (diameter 4 mm) drop onto the piston resting on the exposed dura from a height of 25 cm. The piston was allowed to compress the tissue a maximum of 5 mm (Hang et al., 2004). Then the scalp was sutured and the wound area was treated with lidocaine cream. In the sham group, animals underwent identical procedures, including craniotomy, but without brain injury. As shown in **Figure 1A**, the surrounding brain tissue of the injured cortex was dissected on ice, some of which were placed in 4% PFA, the others were stored in liquid nitrogen immediately until use.

Experimental Design

There was no significant difference in body temperature, weight, feed intake, and motor ability of all rats before the experiment.

1. Experiment 1. To explore the expression levels of Epac2 at each time point after TBI, SD rats were randomly assigned into three groups: the normal group ($n = 12$), the sham group ($n = 12$), and the TBI group ($n = 60$). The TBI group were divided into five subgroups ($n = 12$ for each time point) at 6, 12, 24, 48, and 72 h after TBI, respectively. All rats were sacrificed at the planned time point and the cortical tissue samples were collected for subsequent analysis such as western blot and immunofluorescence staining (**Figure 1B**). Mortality in the normal group and sham group is 0%, while in TBI group is 12% (8 of 68).
2. Experiment 2. To investigate the effects of Epac2 on TBI, we used the Epac2 selective antagonist ESI-05 (Sigma-Aldrich, SML1907) to reduce the expression level of Epac2 (Rehmann, 2013). Then we detect the changes of neuronal apoptosis, BBB damage, brain edema and other indicators after TBI. SD rats were randomly assigned into four groups: the sham group ($n = 18$), the TBI group ($n = 18$), the vehicle group ($n = 18$), and the ESI-05 group ($n = 18$). The vehicle group and the ESI-05 group were respectively injected into lateral ventricles with 1% DMSO (15 μl) and ESI-05 (10 μg/kg, dissolved in 1% DMSO) 30 min before TBI. At 12 h after TBI, all rats were sacrificed and samples were collected for subsequent analysis (**Figure 1C**). Mortality in the sham group is 0% (0 of 18), in TBI group is 14% (3 of 21), in vehicle group is 18% (4 of 22), and in ESI-05 group is 14% (3 of 21).

Western Blot

The cortical regions of the brains were collected and homogenized in the lysis buffer containing protease inhibitor. The proteins were extracted and the protein concentration was measured using a BCA protein assay kit (Thermo, 23227). Equal quantities of protein (40 μg) from each samples were loaded for SDS-PAGE. After electrophoresis, the protein was transferred onto polyvinylidene difluoride membranes (GE Healthcare, RPN303F). The membranes were blocked with 5% nonfat milk for 1 h at room temperature and subsequently incubated overnight at 4°C with the following primary antibodies: Epac2 (1:1,000, Cell Signaling, 43239), P38 (1:1,000, Abcam, ab17009), P-P38 (1:500, Abcam, ab38238), caspase-3 (1:1,000, Abcam, ab13847), GAPDH (1:10,000, Sigma, G9545). The membranes were incubated with appropriate secondary antibodies for 2 h at room temperature. The target band signals were detected by Enhanced chemiluminescence (ECL) method. The signals were quantified using Image J software.

Immunofluorescence Staining

The rats were sacrificed at 12 h after TBI. The brain tissue samples were immersed in the 4% paraformaldehyde for 36 h at 4°C and then gradient dehydrated with 15 and 30% sucrose solution until they sank to the bottom. Then frozen sections with a thickness of 15 μm were collected. The brain sections were rinsed in phosphate-buffered saline (PBS) with 0.3% Triton X-100 for 10 min, repeat 3 times. The sections were incubated with 10% normal horse serum for 1 h at room temperature to prevent nonspecific binding. Then the sections were incubated at 4°C overnight with the following primary antibodies: NeuN (Millipore, MAB377, 1:300), Epac2 (1:200, Cell Signaling, 43239), caspase-3 (1:200, Abcam, ab13847). After washing for 3 times with PBS, the sections were incubated with the fluorescent secondary antibodies for 1 h at room temperature in the dark. After washing for 3 times, the sections were covered with DAPI Fluoromount-G. Immunofluorescence staining was observed using a laser confocal microscopy (Leica, TCS SP8).

FJB Staining

Fluoro Jade B (FJB) (Histo-Chem, Jefferson) staining was used for detection of the damaged neurons. The sections were treated with 1% sodium hydroxide in 80% alcohol for 5 min, 70% alcohol for 2 min and rinsed with ddH2O for 2 min. The sections were then immersed in a solution of 0.06% potassium permanganate for 10 min and rinsed with ddH2O for 2 min. Subsequently, the sections were incubated in FJB staining solution (0.001% FJB in 0.1% acetic acid) for 20 min at room temperature and rinsed three times with ddH2O. The sections were dried at 50°C for about

TABLE 1 | Assessment of neurological behavior scores.

Category	Behavior	Score
Appetite	Finished meal	0
	Left meal unfinished	1
	Scarcely eat	2
Activity	Move freely in the cage	0
	Move under stimulus	1
	Barely moved	2
Deficits	No deficits	0
	Walk unsteadily	1
	Unable to walk	2

5–10 min. Then the slides were placed in xylene for 1 min before mounted with resinene.

Tunnel Staining

A TUNEL staining kit (Abcam, ab66110) was used to analyze apoptotic cell death. Frozen sections were fixed with fresh 4% paraformaldehyde for 15 min at room temperature. After washing with PBS for 2 times, the sections were covered with 20 μg/ml Proteinase K solution for each one and incubated for 5 min at room temperature. Then the sections were covered with 100 μl wash buffer and incubated at RT for 5 min. Then 50 μl DNA labeling solution was covered on the sections. Place the slides in a dark humidified incubator for 1 h at 37°C. After washing with ddH2O, the sections were incubated for 5 min at

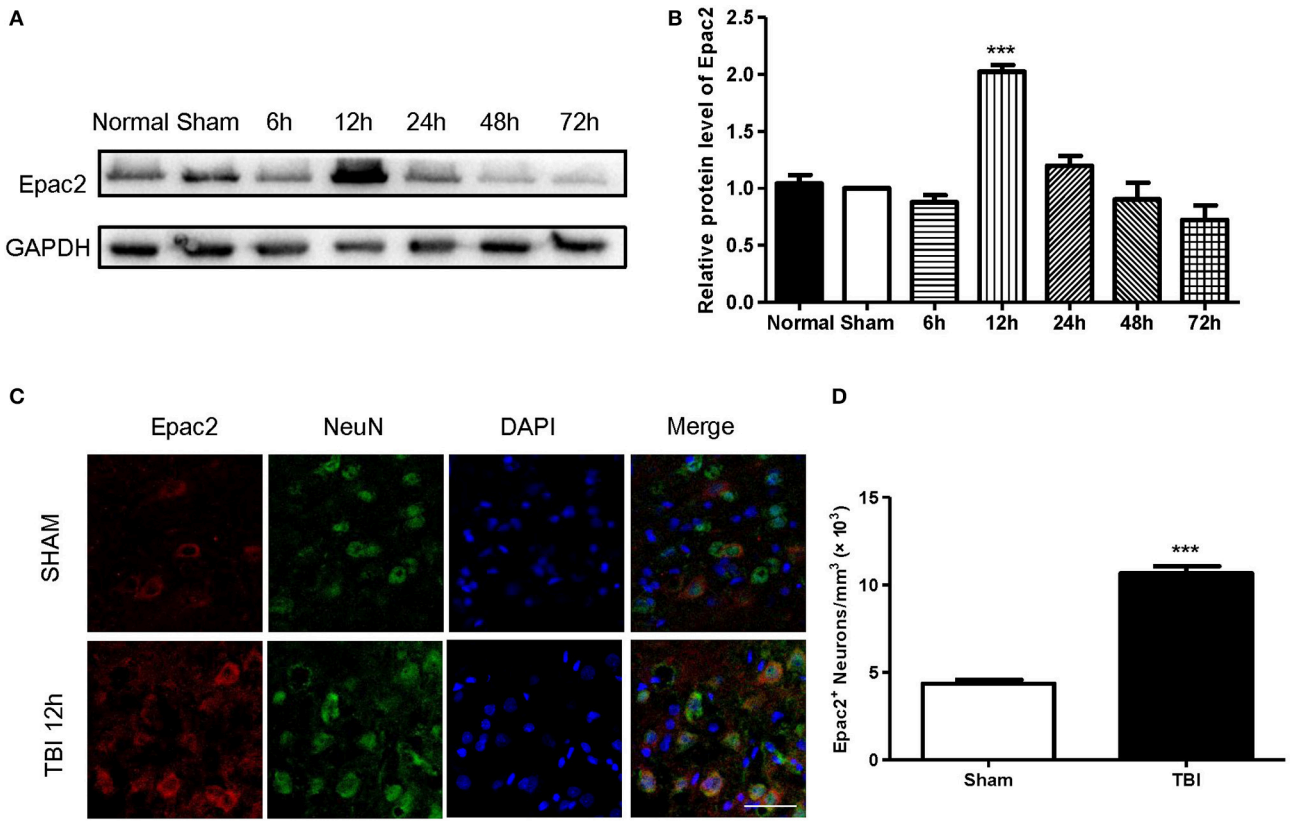

FIGURE 2 | Epac2 was co-located with neurons and dramatically increased at 12 h after TBI. **(A)** Western blot analysis showed the expression of Epac2 in normal and sham group and at 6, 12, 24, 48, and 72 h after TBI. GAPDH was used as a loading control. **(B)** Quantification of western blots for Epac2 as shown in **(A)**. **(C)** Immunofluorescence staining result showed that Epac2 (red) was expressed in neurons (green) and the expression level of Epac2 was increased at 12 h after TBI. **(D)** Quantitative analysis of Epac2-positive neurons. Scale bar = 50 μm. Data are presented as means ± SE. $n = 6$ in each group. $^{***}P < 0.001$ vs. sham group.

A

Group	Behavior Score
Sham	0.25 ± 0.11
TBI	2.88 ± 0.21 ***
Vehicle	2.81 ± 0.20***
ESI-05	1.88 ± 0.23 ##

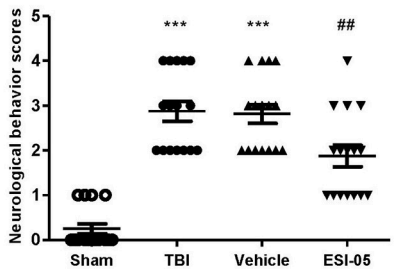

FIGURE 3 | Decrease of Epac2 improved neurological behavior impairment following TBI. **(A)** A table showed the neurological behavior scores in each group. **(B)** Scatter plot showed the neurological behavior scores of all rats in each group. Data are presented as means ± SE. $n = 18$ in each group. $^{***}P < 0.001$ vs. sham group, $^{\#\#}P < 0.01$ vs. vehicle group.

RT. Cover the sections with DAPI Fluoromount-G and observe under a laser confocal microscopy (Leica, TCS SP8).

Neurological Evaluation

Neurological function was evaluated in all rats of each group in Experiment 2 at 12 h after TBI. The appetite, activity, and neurological deficits of rats were assessed according to the previously published scoring system (**Table 1**). The highest score of 9 represents the most severe neurological deficit, while the lowest score of 0 indicates normal neurological function.

Brain Water Content Measurement

Six rats in each group of Experiment 2 were used for measurement of brain water content. Rats were sacrificed after 12 h of TBI. The brains were removed and the right hemispheres were collected. Immediately weigh the samples and the weight was recorded as wet weight. The samples were then dried at 100°C for 24 h and the weight at the moment was recorded as dry weight. The brain water content was calculated using the formula (wet weight-dry weight)/wet weight × 100%.

Statistical Analysis

To facilitate comparisons between groups, the western blot results were expressed as relative density of the band as compared GAPDH and then normalized to the mean value of the sham group. All data in this paper are presented as mean ± SE. SPSS Statistics was used for statistical analysis. The results were analyzed using one-way ANOVA test followed by Bonferroni's multiple comparison test. Statistical significance was accepted at $P < 0.05$.

RESULTS

The Expression of Epac2 Was Increased After TBI

To investigate the possible participation of Epac2 in the pathogenesis of TBI, we examined the expression and localization of Epac2 in brains subjected to TBI. Western blot was used to explore the expression level of Epac2 at different time point after TBI. The results showed that the expression level of Epac2 was dramatically increased at 12 h after TBI (**Figures 2A,B**). We used immunofluorescence staining to detect the expression and localization of Epac2 in brain. The results showed that Epac2 was colocalized with neuron and conformed that Epac2 expression level was significantly elevated in TBI model rats (**Figures 2C,D**).

The Decrease of Epac2 Alleviated Neurological Deficits Following TBI

Previous studies revealed that the neurological functions were impaired in TBI model. To assess whether Epac2 contributes to TBI, we used a loss-of-function strategy to evaluate the effect of Epac2 inhibition on behavioral recovery. The experimental results showed that the neurological behavior scores were significantly higher than the sham group, indicating that the rats of TBI group had a significant neurological function deficits compared with sham group. ESI-05 treatment could significantly decrease the neurological behavior scores (**Figures 3A,B**). These findings suggest that Epac2 inhibition improved neurological behavioral impairment following TBI. Decrease of Epac2 expression level contributed to alleviate neurological deficits after TBI.

The Reduction of Epac2 Decreased Brain Water Content After TBI

The expression of Epac2 was significantly increased at 12 h after TBI in Experiment 1. In order to explore the effects of Epac2 in pathological progress of TBI, in Experiment 2, we used ESI-05, the specific antagonist of Epac2, to decrease the Epac2 expression level. Brain water content represented the severity of brain edema. We compared the brain water content in the sham group, TBI group, vehicle group and ESI-05 group after TBI. We found that the brain water content was significantly increased in TBI model rats, and ESI-05 treatment could significantly reduce it while vehicle group couldn't **(Figure 4)**.

Inhibition of Epac2 Attenuated Neural Cell Apoptosis After TBI

The neuron apoptosis has always been the focus in studies of brain injury (Xu et al., 2016; Tang et al., 2017). We performed immunofluorescence staining and western blot of caspase-3, FJB staining and TUNEL staining to explore the role of Epac2 in neural cell death. Both of the western blot and immunofluorescence staining results showed that the expression of caspase-3 was significantly decreased in the ESI-05 treated group (**Figures 5A,D, 6A,B**). Few FJB-positive and TUNEL-positive apoptotic cells was found in the sham group. And the number of apoptotic cells was dramatically higher in TBI group. The FJB and TUNEL staining results also demonstrated that inhibition of Epac2 could significantly prevent the increase of cell death (**Figures 6C–F**). As shown in **Figure 5**, the expression of P38 has no significance between each experimental groups (**Figure 5B**). But the expression of p-P38 was markedly increased after TBI and treatment with ESI-05 could reverse this change (**Figure 5C**). These results indicated that inhibition of Epac2

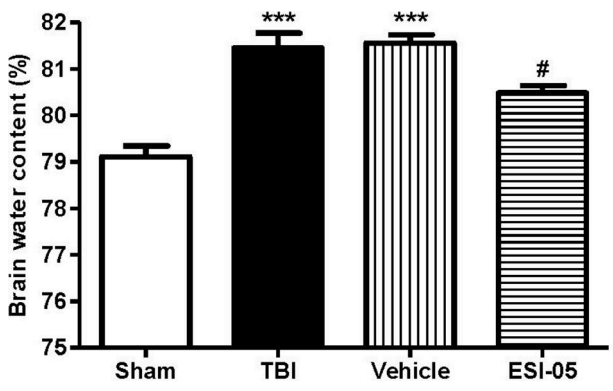

FIGURE 4 | Reduction of Epac2 alleviated brain edema after TBI. Brain water content of cerebrum in each group was measured by dry/wet method. Data are presented as means ± SE. $n = 6$ in each group. $^{***}P < 0.001$ vs. sham group, $^{\#}P < 0.05$ vs. vehicle group.

could reduce TBI-induce neural cell apoptosis and the inhibition of phosphorylation of P38 MAPK pathway may be involved.

DISCUSSION

The pathological changes including inflammation, oxidative damage, apoptosis and brain edema are the main causes of the secondary brain injury after TBI (Jennings et al., 2008; Onyszchuk et al., 2008). The key to treatment of TBI had to focus on how to alleviate the secondary damage after TBI. In this study, we explored the regulation of Epac2 in the secondary brain damage after TBI and studied the potential mechanisms. We found that the treatment of the selective Epac2 antagonist ESI-05 reduced neural cell death in the injured cerebral cortex and adjacent regions in rats of TBI models. Inhibition of Epac2 decreased TBI-induced P38 phosphorylation and caspase-3 activation in the cerebral cortex, attenuated neural cell death, alleviated brain edema and improved neurological functions after TBI.

Increased apoptosis takes an important part in the pathogenesis of brain damage. Caspases are a family of cysteine proteases which play an important role in apoptosis. Caspase-3, as a key molecule of apoptosis, plays a central role in the neural cell apoptosis after TBI (Clark et al., 2000). Our findings revealed a significant increase in cleaved caspase-3 after TBI, suggesting an increase of apoptosis in the brain following TBI. FJB, and TUNEL staining also confirmed increase of neural cell death after TBI. However, ESI-05 treatment ameliorated this TBI-induced neural cell apoptosis, indicating that the decrease of Epac2 could inhibit the TBI-induced neural cell death. This result was consistent with previous study showing that Epac2 was involved in apoptosis (Park and Juhnn, 2017).

Numerous studies have suggested the relationship between Epac2 and cell death. Previous studies showed that Urocortion-1 promoted cell survival and decreased cell necrosis through Epac2 and ERK1/2 (extracellular signal-regulated kinases 1/2) activation (Calderón-Sánchez et al., 2016). In H1299 lung cancer cells, Epac2 inhibition decreased cisplatin-induced apoptosis via Epac2-Rap1-Akt pathway (Park and Juhnn, 2017). Epac2 mediates cAMP-dependent growth arrest via activating Rap2A in neuroendocrine cells (Emery et al., 2017). Epac2-Rap1 signaling also attenuates mitochondrial ROS production and reduces myocardial arrhythmia susceptibility (Yang et al., 2017). In rat model of plantar incision, Epac2 mediates nociception priming through P38 pathway (Matsuda et al., 2017). In this study we explored the mechanisms of Epac2 mediates apoptosis in brain following TBI.

Mitogen-activated protein kinases (MAPKs) are serine/threonine protein kinases. They regulate cell functions including proliferation, differentiation, stress response, mitosis, cell survival and apoptosis (Pearson et al., 2001). P38 MAPK is

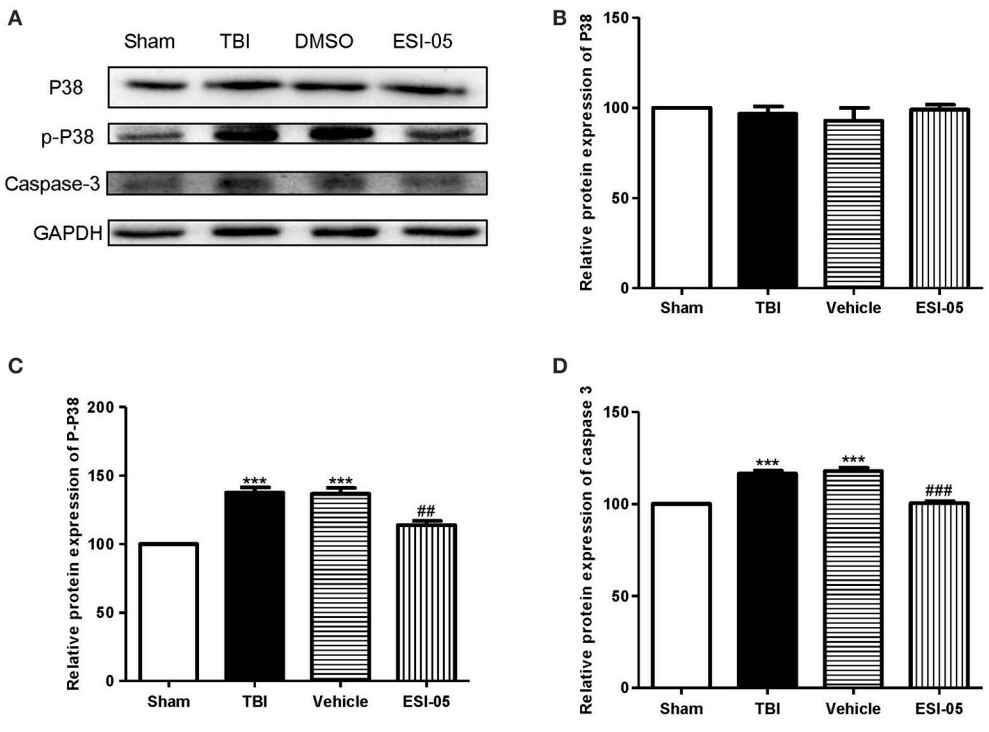

FIGURE 5 | Inhibition of Epac2 reduced apoptosis related protein caspase-3 in brain after TBI through inhibiting phosphorylation of P38. **(A)** Western blot analysis showed the expression of P38, p-P38, and caspase-3 in cerebral cortex in each group. GAPDH was used as a loading control. **(B–D)** Quantification of expression levels of P38, p-P38, and caspase-3 as shown in **(A)**. Data are presented as means ± SE. $n = 6$ in each group. $^{***}P < 0.001$ vs. sham group, $^{\#\#}P < 0.01$, $^{\#\#\#}P < 0.001$ vs. vehicle group.

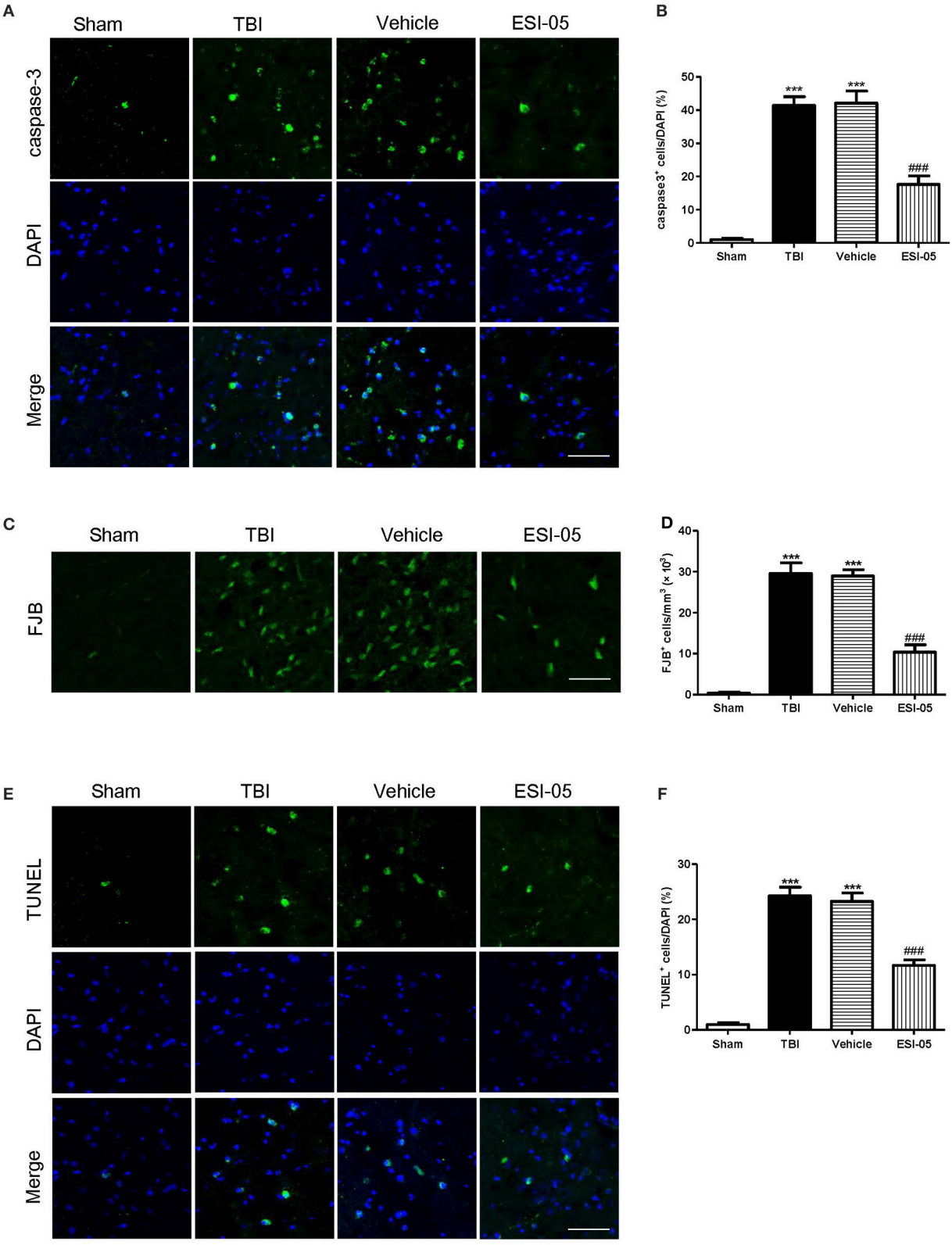

FIGURE 6 | Inhibition of Epac2 attenuated neural cell death in cerebral cortex after TBI. **(A,C,E)** Cortical cellular apoptosis was detected by immunofluorescence staining of caspase-3 (green), FJB staining (green), and TUNEL (green) staining in each group, respectively. **(B,D,F)** Quantitative analysis of caspase-3, FJB, and TUNEL-positive cells in cerebral cortex after TBI, respectively. Scale bar = 50 μm. Data are presented as means ± SE. $n = 6$ in each group. $^{***}P < 0.001$ vs. sham group, $^{\#\#\#}P < 0.001$ vs. vehicle group.

one of the well-characterized MAPK family members. Increasing data has shown that activated P38 MAPK subsequently regulates the inflammatory response, apoptosis, autophagy, cell survival, and cell death (Xia et al., 1995; Harada and Sugimoto, 1999; Nozaki et al., 2001; Irving and Bamford, 2002; Sridharan et al., 2011; Sui et al., 2014). Several studies showed that increased P38 MAPK activity plays a key role in neural cell death and inhibition of p38 MAPK plays a neuroprotective role (Takeda and Ichijo, 2002; Strassburger et al., 2008; Liu et al., 2014; Li et al., 2015; Wang et al., 2015). Epac proteins have been characterized as guanine nucleotide exchange factors for monomeric GTPases like Rap1 (Kawasaki et al., 1998) and Rab3a (Branham et al., 2009). The relationship between Rap1 and P38 has been shown in several studies (Gutiérrez-Uzquiza et al., 2010; Wu et al., 2015; Lu et al., 2016; Priego et al., 2016). In the present study, we also found that phosphorylation level of P38 protein was increased after TBI. Treatment with ESI-05 decreased this level. These results demonstrated that P38 MAPK pathway may involve in the regulation of neuronal apoptosis after TBI. Inhibition of Epac2 plays an anti-apoptotic role in TBI model rats and this process may be mediated through regulating P38 MAPK pathway (**Figure 7**). These results tallied with previous studies demonstrating that Epac2 could mediate growth arrest through P38 activation (Emery et al., 2017). To further conform the involvement of the P38 MAPK signaling pathway in Epac2's effect on TBI, SB203580, an inhibitor of P38 phosphorylation is needed to be used in the further investigation.

Cerebral edema is a dangerous secondary consequence of TBI and is associated with significant morbidity and mortality (Winkler et al., 2016). The development of cerebral edema plays a crucial role in the evolution of injury following TBI. Even a minor increase of brain water content can lead to a significant increase of intracranial pressure and the poor outcome (Marmarou et al., 2000). Thus alleviate brain edema is a promising treatment in TBI management. In the present study, we found that reduction of Epac2 could significantly alleviated brain water content of the injured hemisphere. This result might be due to the alleviation of blood brain barrier disruption. TBI increases the expression of inflammation factors, chemotactic factors and adhesion molecules in the neural system, which leads to encephaledema. Epac2 may be involve in the brain edema after TBI through affecting these factors. The mechanisms Epac2 involved in these processes need to be further investigated.

CONCLUSION

In summary, western blot and immunofluorescence staining results have shown that the expression of Epac2 was

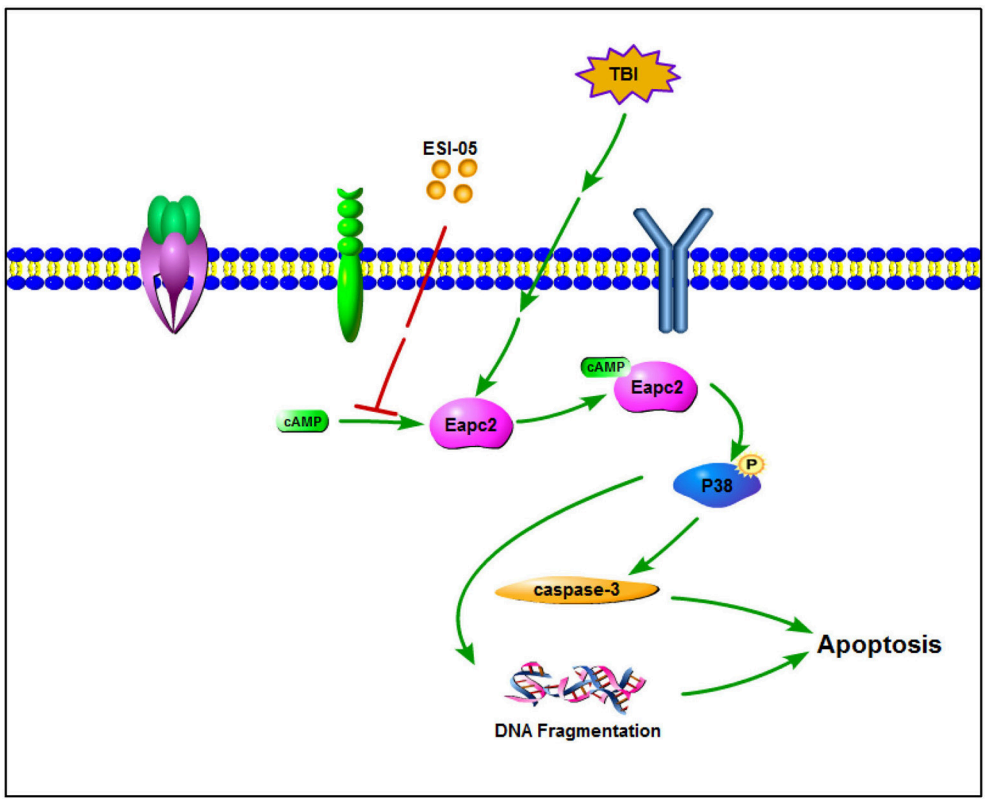

FIGURE 7 | A schematic model for Eapc2 regulation of neuronal cell death in TBI. Epac2 was increased after TBI and activating Epac2 subsequently promoted phosphorylation of P38-MAPK. Activation of P38-MAPK pathway consequently increased the expression of caspase-3, resulted in DNA fragmentation and neuron apoptosis, leading to neuronal cell death.

dramatically increased at 12 h after TBI. The brain water content measurement showed that reduction of Epac2 alleviated encephaledema in TBI model. The neurological behavioral test demonstrated that decrease of Epac2 improved neurobehavioral outcome after TBI. The immunohistochemistry, FJB, TUNEL, western blot were used to show that inhibition of Epac2 significantly attenuated the neuronal cell death after TBI. Phosphorylation of P38 was involved in this process. These data suggested that inhibition of Epac2 may play a neuroprotective role in TBI management through attenuating neural cell death, alleviating brain edema and improving neurological deficits, implying that Epac2 could be a new target for treatment of secondary neuronal injury after TBI.

AUTHOR CONTRIBUTIONS

DL and RG designed the experiments and edited the manuscript. LingZ and LiZ performed the experiments, analyzed the data and wrote the manuscript. HL and FJ interpreted the data and prepared the figures. HW performed the experiments and analyzed the data.

REFERENCES

Bos, J. L. (2003). Epac: a new cAMP target and new avenues in cAMP research. *Nat. Rev. Mol. Cell Biol.* 4, 733–738. doi: 10.1038/nrm1197

Branham, M. T., Bustos, M. A., De Blas, G. A., Rehmann, H., Zarelli, V. E., Trevi-o, C. L., et al. (2009). Epac activates the small G proteins Rap1 and Rab3A to achieve exocytosis. *J. Biol. Chem.* 284, 24825–24839. doi: 10.1074/jbc.M109.015362

Calderón-Sánchez, E., Díaz, I., Ordó-ez, A., and Smani, T. (2016). Urocortin-1 mediated cardioprotection involves XIAP and CD40-ligand recovery: role of EPAC2 and ERK1/2. *PLoS ONE* 11:e0147375. doi: 10.1371/journal.pone.0147375

Clark, R. S., Kochanek, P. M., Watkins, S. C., Chen, M., Dixon, C. E., Seidberg, N. A., et al. (2000). Caspase-3 mediated neuronal death after traumatic brain injury in rats. *J. Neurochem.* 74, 740–753. doi: 10.1046/j.1471-4159.2000.740740.x

Cornelius, C., Crupi, R., Calabrese, V., Graziano, A., Milone, P., Pennisi, G., et al. (2013). Traumatic brain injury: oxidative stress and neuroprotection. *Antioxid. Redox Signal.* 19, 836–853. doi: 10.1089/ars.2012.4981

Dang, B., Li, H., Xu, X., Shen, H., Wang, Y., Gao, A., et al. (2015). Cyclophilin A/cluster of differentiation 147 interactions participate in early brain injury after subarachnoid hemorrhage in rats. *Crit. Care Med.* 43, e369–e381. doi: 10.1097/CCM.0000000000001146

Emery, A. C., Xu, W., Eiden, M. V., and Eiden, L. E. (2017). Guanine nucleotide exchange factor Epac2-dependent activation of the GTP-binding protein Rap2A mediates cAMP-dependent growth arrest in neuroendocrine cells. *J. Biol. Chem.* 292, 12220–12231. doi: 10.1074/jbc.M117.790329

Fernandes, H. B., Riordan, S., Nomura, T., Remmers, C. L., Kraniotis, S., Marshall, J. J., et al. (2015). Epac2 mediates cAMP-dependent potentiation of neurotransmission in the hippocampus. *J. Neurosci.* 35, 6544–6553. doi: 10.1523/JNEUROSCI.0314-14.2015

Gloerich, M., and Bos, J. L. (2010). Epac: defining a new mechanism for cAMP action. *Annu. Rev. Pharmacol. Toxicol.* 50, 355–375. doi: 10.1146/annurev.pharmtox.010909.105714

Gutiérrez-Uzquiza, A., Arechederra, M., Molina, I., Ba-os, R., Maia, V., Benito, M., et al. (2010). C3G down-regulates p38 MAPK activity in response to stress by Rap-1 independent mechanisms: involvement in cell death. *Cell. Signal.* 22, 533–542. doi: 10.1016/j.cellsig.2009.11.008

Hang, C. H., Shi, J. X., Tian, J., Li, J. S., Wu, W., and Yin, H. X. (2004). Effect of systemic LPS injection on cortical NF-kappaB activity and inflammatory response following traumatic brain injury in rats. *Brain Res.* 1026, 23–32. doi: 10.1016/j.brainres.2004.07.090

Harada, J., and Sugimoto, M. (1999). An inhibitor of p38 and JNK MAP kinases prevents activation of caspase and apoptosis of cultured cerebellar granule neurons. *Jpn. J. Pharmacol.* 79, 369–378. doi: 10.1254/jjp.79.369

Irving, E. A., and Bamford, M. (2002). Role of mitogen- and stress-activated kinases in ischemic injury. *J. Cereb. Blood Flow Metab.* 22, 631–647. doi: 10.1097/00004647-200206000-00001

Jennings, J. S., Gerber, A. M., and Vallano, M. L. (2008). Pharmacological strategies for neuroprotection in traumatic brain injury. *Mini Rev. Med. Chem.* 8, 689–701. doi: 10.2174/138955708784567377

Kawasaki, H., Springett, G. M., Mochizuki, N., Toki, S., Nakaya, M., Matsuda, M., et al. (1998). A family of cAMP-binding proteins that directly activate Rap1. *Science.* 282, 2275–2279. doi: 10.1126/science.282.5397.2275

Lee, K., Kobayashi, Y., Seo, H., Kwak, J. H., Masuda, A., Lim, C. S., et al. (2015). Involvement of cAMP-guanine nucleotide exchange factor II in hippocampal long-term depression and behavioral flexibility. *Mol. Brain* 8:38. doi: 10.1186/s13041-015-0130-1

Li, D., Ni, H., Rui, Q., Gao, R., and Chen, G. (2017). Deletion of Mst1 attenuates neuronal loss and improves neurological impairment in a rat model of traumatic brain injury. *Brain Res.* 1688, 15–21. doi: 10.1016/j.brainres.2017.10.018

Li, H., Zhou, S., Wu, L., Liu, K., Zhang, Y., Ma, G., et al. (2015). The role of p38MAPK signal pathway in the neuroprotective mechanism of limb postconditioning against rat cerebral ischemia/reperfusion injury. *J. Neurol. Sci.* 357, 270–275. doi: 10.1016/j.jns.2015.08.004

Liu, X. W., Ji, E. F., He, P., Xing, R. X., Tian, B. X., and Li, X. D. (2014). Protective effects of the p38 MAPK inhibitor SB203580 on NMDA-induced injury in primary cerebral cortical neurons. *Mol. Med. Rep.* 10, 1942–1948. doi: 10.3892/mmr.2014.2402

Lu, L., Wang, J., Wu, Y., Wan, P., and Yang, G. (2016). Rap1A promotes ovarian cancer metastasis via activation of ERK/p38 and notch signaling. *Cancer Med.* 5, 3544–3554. doi: 10.1002/cam4.946

Marmarou, A., Fatouros, P. P., Barzó, P., Portella, G., Yoshihara, M., Tsuji, O., et al. (2000). Contribution of edema and cerebral blood volume to traumatic brain swelling in head-injured patients. *J. Neurosurg.* 93, 183–193. doi: 10.3171/jns.2000.93.2.0183

Matsuda, M., Oh-Hashi, K., Yokota, I., Sawa, T., and Amaya, F. (2017). Acquired exchange protein directly activated by cyclic adenosine monophosphate activity induced by p38 mitogen-activated protein kinase in primary afferent neurons contributes to sustaining postincisional nociception. *Anesthesiology* 126, 150–162. doi: 10.1097/ALN.0000000000001401

Menon, D. K., and Maas, A. I. (2015). Traumatic brain injury in 2014. Progress, failures and new approaches for TBI research. *Nat. Rev. Neurol.* 11, 71–72. doi: 10.1038/nrneurol.2014.261

Nozaki, K., Nishimura, M., and Hashimoto, N. (2001). Mitogen-activated protein kinases and cerebral ischemia. *Mol. Neurobiol.* 23, 1–19. doi: 10.1385/MN:23:1:01

Oldenburger, A., Timens, W., Bos, S., Smit, M., Smrcka, A. V., Laurent, A. C., et al. (2014). Epac1 and Epac2 are differentially involved in inflammatory and remodeling processes induced by cigarette smoke. *FASEB J.* 28, 4617–4628. doi: 10.1096/fj.13-248930

Onyszchuk, G., He, Y. Y., Berman, N. E., and Brooks, W. M. (2008). Detrimental effects of aging on outcome from traumatic brain injury: a behavioral, magnetic resonance imaging, and histological study in mice. *J. Neurotrauma* 25, 153–171. doi: 10.1089/neu.2007.0430

Park, J. Y., and Juhnn, Y. S. (2017). cAMP signaling increases histone deacetylase 8 expression via the Epac2-Rap1A-Akt pathway in H1299 lung cancer cells. *Exp. Mol. Med.* 49:e297. doi: 10.1038/emm.2016.152

Parnell, E., Palmer, T. M., and Yarwood, S. J. (2015). The future of EPAC-targeted therapies: agonism versus antagonism. *Trends Pharmacol. Sci.* 36, 203–214. doi: 10.1016/j.tips.2015.02.003

Pearson, G., Robinson, F., Beers, G. T., Xu, B. E., Karandikar, M., Berman, K., et al. (2001). Mitogen-activated protein (MAP) kinase pathways: regulation and physiological functions. *Endocr. Rev.* 22, 153–183. doi: 10.1210/er.22.2.153

Priego, N., Arechederra, M., Sequera, C., Bragado, P., Vázquez-Carballo, A., Gutiérrez-Uzquiza, Á., et al. (2016). C3G knock-down enhances migration and invasion by increasing Rap1-mediated p38α activation, while it impairs tumor growth through p38α-independent mechanisms. *Oncotarget* 7, 45060–45078. doi: 10.18632/oncotarget.9911

Rehmann, H. (2013). Epac-inhibitors: facts and artefacts. *Sci. Rep.* 3:3032. doi: 10.1038/srep03032

Seo, H., and Lee, K. (2016). Epac2 contributes to PACAP-induced astrocytic differentiation through calcium ion influx in neural precursor cells. *BMB Rep.* 49, 128–133. doi: 10.5483/BMBRep.2016.49.2.202

Sridharan, S., Jain, K., and Basu, A. (2011). Regulation of autophagy by kinases. *Cancers* 3, 2630–2654. doi: 10.3390/cancers3022630

Strassburger, M., Braun, H., and Reymann, K. G. (2008). Anti-inflammatory treatment with the p38 mitogen-activated protein kinase inhibitor SB239063 is neuroprotective, decreases the number of activated microglia and facilitates neurogenesis in oxygen-glucose-deprived hippocampal slice cultures. *Eur. J. Pharmacol.* 592, 55–61. doi: 10.1016/j.ejphar.2008.06.099

Sui, X., Kong, N., Ye, L., Han, W., Zhou, J., Zhang, Q., et al. (2014). p38 and JNK MAPK pathways control the balance of apoptosis and autophagy in response to chemotherapeutic agents. *Cancer Lett.* 344, 174–179. doi: 10.1016/j.canlet.2013.11.019

Takeda, K., and Ichijo, H. (2002). Neuronal p38 MAPK signalling: an emerging regulator of cell fate and function in the nervous system. *Genes Cells* 7, 1099–1111. doi: 10.1046/j.1365-2443.2002.00591.x

Tang, C., Shan, Y., Hu, Y., Fang, Z., Tong, Y., Chen, M., et al. (2017). FGF2 Attenuates neural cell death via suppressing autophagy after rat mild traumatic brain injury. *Stem Cells Int.* 2017:2923182. doi: 10.1155/2017/2923182

Wang, W., Tang, L., Li, Y., and Wang, Y. (2015). Biochanin A protects against focal cerebral ischemia/reperfusion in rats via inhibition of p38-mediated inflammatory responses. *J. Neurol. Sci.* 348, 121–125. doi: 10.1016/j.jns.2014.11.018

Wang, Y., Liu, Y., Lopez, D., Lee, M., Dayal, S., Hurtado, A., et al. (2018). Protection against TBI-induced neuronal death with post-treatment with a selective Calpain-2 inhibitor in mice. *J. Neurotrauma* 35, 105–117. doi: 10.1089/neu.2017.5024

Winkler, E. A., Minter, D., Yue, J. K., and Manley, G. T. (2016). Cerebral edema in traumatic brain injury: pathophysiology and prospective therapeutic targets. *Neurosurg. Clin. N. Am.* 27, 473–488. doi: 10.1016/j.nec.2016.05.008

Wu, Y., Zhou, J., Li, Y., Zhou, Y., Cui, Y., Yang, G., et al. (2015). Rap1A Regulates osteoblastic differentiation via the ERK and p38 mediated signaling. *PLoS ONE* 10:e0143777. doi: 10.1371/journal.pone.0143777

Xia, Z., Dickens, M., Raingeaud, J., Davis, R. J., and Greenberg, M. E. (1995). Opposing effects of ERK and JNK-p38 MAP kinases on apoptosis. *Science* 270, 1326–1331. doi: 10.1126/science.270.5240.1326

Xu, Z., Lv, X. A., Dai, Q., Ge, Y. Q., and Xu, J. (2016). Acute upregulation of neuronal mitochondrial type-1 cannabinoid receptor and it's role in metabolic defects and neuronal apoptosis after TBI. *Mol. Brain* 9:75. doi: 10.1186/s13041-016-0257-8

Yang, Z., Kirton, H. M., Al-Owais, M., Thireau, J., Richard, S., Peers, C., et al. (2017). Epac2-Rap1 signaling regulates reactive oxygen species production and susceptibility to Cardiac Arrhythmias. *Antioxid. Redox Signal.* 27, 117–132. doi: 10.1089/ars.2015.6485

Zhang, C. L., Katoh, M., Shibasaki, T., Minami, K., Sunaga, Y., Takahashi, H., et al. (2009). The cAMP sensor Epac2 is a direct target of antidiabetic sulfonylurea drugs. *Science* 325, 607–610. doi: 10.1126/science.1172256

Conflict of Interest Statement: The authors declare that the research was conducted in the absence of any commercial or financial relationships that could be construed as a potential conflict of interest.

frontiers in Neuroscience

ORIGINAL RESEARCH
published: 16 May 2018
doi: 10.3389/fnins.2018.00313

Association of Brain CD163 Expression and Brain Injury/Hydrocephalus Development in a Rat Model of Subarachnoid Hemorrhage

Chaohui Jing[1,2], *Haining Zhang*[1], *Hajime Shishido*[1], *Richard F. Keep*[1] *and Ya Hua*[1]*

[1] Department of Neurosurgery, University of Michigan, Ann Arbor, MI, United States, [2] Department of Neurosurgery, Xinhua Hospital, School of Medicine, Shanghai Jiaotong University, Shanghai, China

Hemoglobin contributes to brain cell damage and death following subarachnoid hemorrhage (SAH). While CD163, a hemoglobin scavenger receptor, can mediate the clearance of extracellular hemoglobin it has not been well-studied in SAH. In the current study, a filament perforation SAH model was performed in male rats. T2-weighted and T2*-weighted scans were carried out using a 7.0-Tesla MR scanner 24 h after perforation. T2 lesions and hydrocephalus were determined on T2-weighted images. A grading system based on MRI was used to assess SAH severity. The effects of SAH on CD163 were determined by immunohistochemistry staining and Western blots. SAH led to a marked increase in CD163 levels in cortex, white matter and periventricular regions from days 1 to 7. CD163 stained cells were co-localized with neurons, microglia/macrophages, oligodendrocytes and cleaved caspase-3-positive cells, but not astrocytes. Furthermore, CD163 protein levels were increased in rats with higher SAH grades, the presence of T2 lesions on MRI, or hydrocephalus. In conclusion, CD163 expression is markedly upregulated after SAH. It is associated with more severe hemorrhage, as well as MRI T2 lesion and hydrocephalus development.

Keywords: CD163, magnetic resonance imaging, T2 lesion, hydrocephalus, subarachnoid hemorrhage

OPEN ACCESS

Edited by:
Gang Chen,
First Affiliated Hospital of Soochow University, China

Reviewed by:
Sheng Chen,
Second Affiliated Hospital of Zhejiang University School of Medicine, China
Jieli Chen,
Henry Ford Hospital, United States

***Correspondence:**
Ya Hua
yahua@umich.edu

Specialty section:
This article was submitted to Neurodegeneration, a section of the journal Frontiers in Neuroscience

Received: *19 February 2018*
Accepted: *23 April 2018*
Published: *16 May 2018*

Citation:
Jing C, Zhang H, Shishido H, Keep RF and Hua Y (2018) Association of Brain CD163 Expression and Brain Injury/Hydrocephalus Development in a Rat Model of Subarachnoid Hemorrhage. Front. Neurosci. 12:313. doi: 10.3389/fnins.2018.00313

INTRODUCTION

Spontaneous subarachnoid hemorrhage (SAH) is usually caused by a ruptured intracranial aneurysm. It is a form of stroke with a high mortality rate and early brain injury after SAH is an important factor contributing to death and disability. However, the main mechanisms of the early brain injury are still unknown. A combination of elevated intracranial pressure, transient global ischemia injury, blood-brain barrier disruption, and brain edema may contribute to early brain injury after SAH (Sehba and Bederson, 2006; Lee et al., 2010; Jing et al., 2012).

Hemoglobin released from red blood cells induces cell death and brain injury in intracerebral hemorrhage (ICH) and SAH (Xi et al., 2006; Lee et al., 2010). Such damage may be limited by hemoglobin clearance and degradation. Hemoglobin tightly binds to haptoglobin and haptoglobin/hemoglobin complexes can be taken up by microglia/macrophages via the CD163 receptor (Madsen et al., 2001). Heme oxygenase-1 (HO-1) is a key enzyme of heme degradation

and the haptoglobin/hemoglobin-CD163-HO-1 system represents a basic line of defense against hemoglobin neurotoxicity by facilitating hemoglobin removal (Thomsen et al., 2013). We and others have demonstrated that CD163 is expressed and contributes to hematoma clearance following ICH (Cao et al., 2016; Liu et al., 2017; Leclerc et al., 2018), but the functions of CD163 have not been investigated after SAH.

The current study examined the impact of SAH on CD163 in an endovascular perforation model in rats due to similarities in the pathophysiological events observed in that model to those occurring in SAH patients suffering from aneurysmal rupture (Kooijman et al., 2014; Sehba, 2014). Nevertheless, the extent and volume of subarachnoid clot in that model is uncontrollable and varies between animals (Lee et al., 2009). Therefore, we used a new classification system based upon magnetic resonance image (MRI) to assess SAH severity (Shishido et al., 2015). Thus, T2*-weighted MRI was performed to measure blood accumulation in the brain after SAH. T2-weighted MRI was used for assessing hydrocephalus occurrence and lesion determination. Western blot and immunohistochemistry was used to assess CD163 expression following SAH.

EXPERIMENTAL PROCEDURES

Animals and SAH

All animal procedures used in this experiment were approved by the University of Michigan Committee on Use and Care of Animals. The animals were housed with *ad libitum* food and water. In total, 76 male Sprague-Dawley rats (250-350 g) purchased from Charles River Laboratories were used in this study. The filament perforation model was performed as previously described (Lee et al., 2010; Okubo et al., 2013). In brief, rats were anesthetized by 5% isoflurane and later isoflurane concentration was titrated at 2.5-3% after intubation. A feedback controlled heating pad was used to maintain rat rectal temperature at 36.5°C during surgical procedures. The left carotid artery and its branches were identified under a surgical microscope and the external carotid artery (ECA) was transected. A 3-0-nylon suture was entered through the stump of ECA into the internal carotid artery until it reached and perforated the bifurcation of intracranial internal carotid artery. The ECA was tightened to prevent blood loss after the nylon suture was withdrawn. Sham-operated rats underwent the same surgical procedure, but the nylon filament was not introduced far enough to perforate the internal carotid artery. The mortality rate was 24% (16/68) after SAH; no sham operated rats died ($n = 8$). Therefore, 40 SAH rats and 8 sham rats were euthanized at day 1, and 12 SAH rats were euthanized at day 7 for either immunohistochemistry or Western blots.

MRI Measurements and Grading

Twenty-four hours after SAH induction, MRI was performed in a 7.0 Tesla Varian MR scanner (Varian Inc., Palo Alto, California) including T2 fast spin-echo and T2* gradient-echo sequences. The chosen MRI parameters were: a field of view = 35 × 35 mm, matrix = 256 × 256 mm, and slice thickness = 0.5 mm. T2 lesions in the ipsilateral brain were identified when the pixel value was over 2 standard deviations (SD) from the mean in the contralateral brain. Measurements of ventricular volume were determined as described previously (Okubo et al., 2013). Hydrocephalus was identified when the ventricular volume following SAH was more than 3 SD above the mean in the control group.

SAH Grading in MRI

The rat perforation model produces different degrees of SAH and a bleeding scale, previously described by Shishido et al. (2015), was used to assess SAH severity. In brief, the MRI grades for perforation SAH model were as follows: grade 0: no SAH or intraventricular hemorrhage (IVH), grade 1: minimal or thin SAH without IVH, grade 2: minimal or thin SAH with IVH, grade 3: thick SAH without IVH, and grade 4 thick SAH with IVH. IVH was defined as at least one hypo-intensity clot recognized in any ventricle on T2* imaging. Thick SAH was defined as at least two slices with clots thicker than 0.5 mm on T2* MRI.

Immunohistochemistry

Immunohistochemistry was performed using the avidin-biotin-peroxidase complex techniques as previously reported (Jing et al., 2012; Liu et al., 2017). Rats were anesthetized with a lethal sodium dose of pentobarbital and underwent transcardiac perfusion with 4% paraformaldehyde. Subsequently, the brains were harvested, post-fixed in 4% paraformaldehyde overnight, and cryo-protected in 30% sucrose at 4°C. OCT compound embedded brains were sliced into 18 μm sections with a cryostat microtome, dried and preserved at −80°C. The primary antibody was mouse-anti-CD163 (AbD, MCA2311, 1:400). The secondary antibody was biotinylated horse-anti-mouse IgG (1:500, BA2001, Vector). Negative controls were executed by incubating with normal horse serum.

Immunofluorescence Labeling

For triple labeling, the primary antibodies were mouse-anti-CD163 (1:400, MCA2311, AbD), rabbit-anti-CD163 (1:300, ab87099, Abcam), mouse-anti-NeuN (Abcam, ab104225, 1:500), goat-anti-GFAP (1:2,000, ab53554, Abcam); goat-anti-IBA-1 (1:2,000, ab107159, Abcam); mouse-anti-CC1 (1:400, 2869730, Novus Biologicals) and rabbit-anti-cleaved caspase-3 (1:500, 9,661, CST). The secondary antibodies(Invitrogen) used in this study included Alexa Fluor 488-labeled (green channel) donkey-anti-mouse IgG, Alexa Fluor 488-labeled (green channel) donkey-anti-rabbit IgG, Alexa Fluor 594-labeled (red channel) donkey-anti-rabbit IgG, Alexa Fluor 594-labeled (red channel) donkey-anti-mouse IgG, and Alexa Fluor 594-labeled (red channel) donkey-anti-goat IgG. All the secondary antibodies used were diluted to 1:500. Cell nuclei were stained using Fluoroshield containing DAPI (blue channel, F6057, Sigma).

Western Blots

Western blots were undertaken as previously described for rats after SAH (Cao et al., 2016). Rats were anesthetized and underwent transcardiac perfusion with phosphate-buffered saline (PBS, 0.1 mmol/L, pH 7.4) for 5 min. Brain hemispheres were coronally cut into a section of 3-mm thickness through

the center of optic chiasm, and the ipsilateral and contralateral cortex separated. Tissue was homogenized in lysis buffer and the protein concentration measured. Fifty μg protein was separated and transferred to hybond-C pure nitrocellulose membrane (Amersham). After blocking with nonfat milk buffer, the membrane was incubated with rabbit-anti-CD163 (1:2,000, Ab182422, Abcam), and mouse-anti-β-actin (1:50,000, A3854, Sigma). The protein bands were visualized and exposed to Kodak X-OMAT film. The OD value of each band was analyzed with Image J software and CD163 protein levels presented as CD163 to β-actin ratio.

Statistical Analysis

All measurements were conducted by investigators blinded to treatment assignment and the values of each group were presented as means ± SD. Statistically differences among groups were analyzed by one-way ANOVA. Statistically differences were deemed significant if $p < 0.05$.

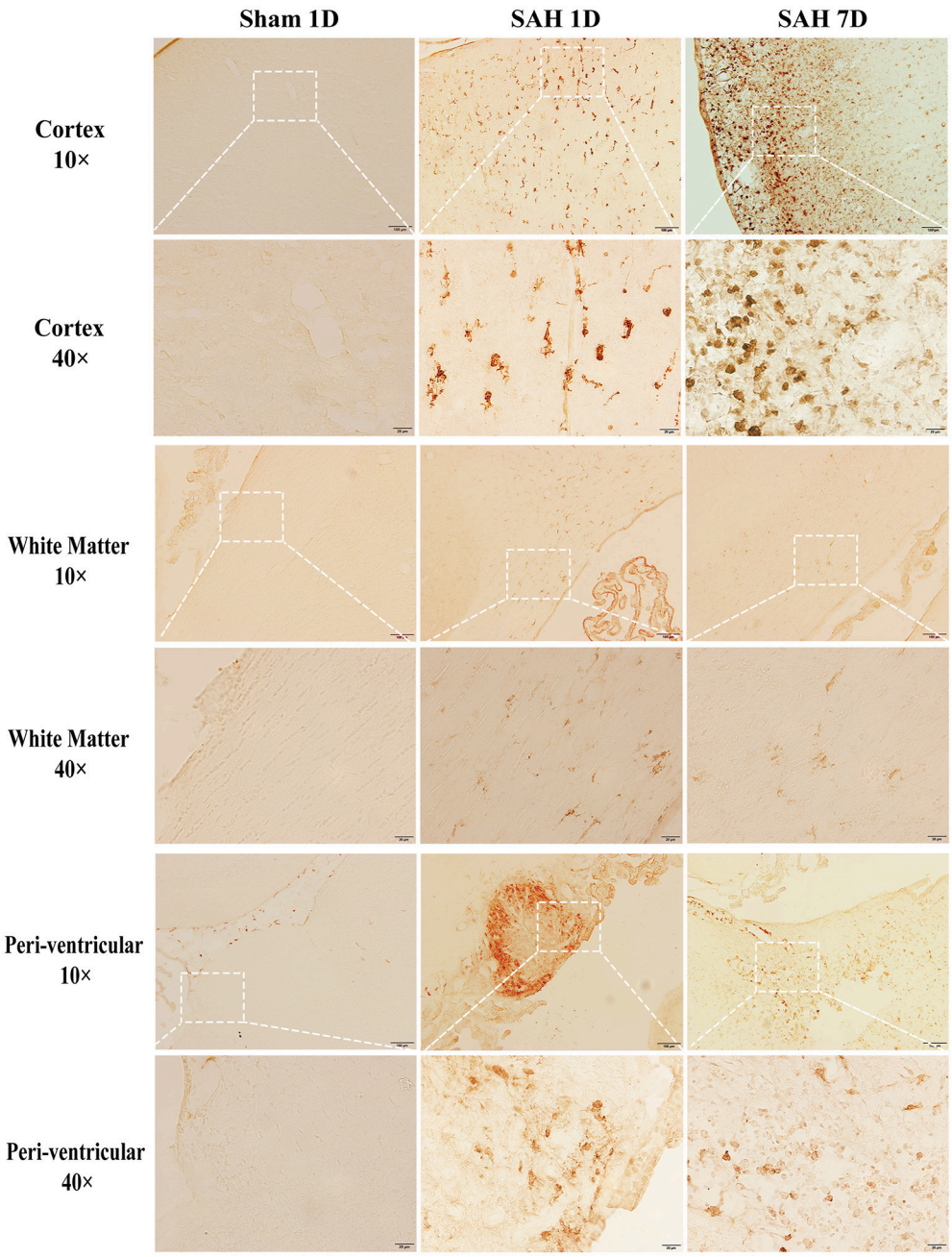

FIGURE 1 | CD163 immunoreactivity in cortex, white matter (WM) and periventricular area at days 1 and 7 after SAH or a sham operation. Low power (x10, scale bar = 100 μm) and high power (x40, scale bar = 20 μm) images are shown. The latter correspond to the box areas in the lower power images.

RESULTS

Brain injury and CD163 expression in the brain after SAH were diffuse. We used immunostaining to show the locations and cell types which express CD163. Brain CD163 levels were quantified by Western blots. One day after a sham operation, brain CD163 immunoreactivity was very low. In contrast, there were numerous CD163 positive cells in cortex, white matter and periventricular regions from days 1 to 7 after SAH (**Figure 1**). By Western blot, CD163 protein levels in ipsilateral cortex were upregulated after SAH, peaking at day 1(CD163/β-actin: 1.22 ± 0.31 vs. 0.09 ± 0.06 in sham, $p < 0.01$). However, high levels were still found 7 days after SAH (CD163/β-actin: 0.58 ± 0.10 vs. 0.09 ± 0.06 in sham, $p < 0.05$; **Figure 2**).

To examine CD163 expression in specific cell populations, triple immunofluorescence labeling was carried out 24 h following SAH. Cells that stained positively for CD163 co-localized with NeuN-(a neuronal nuclei label, **Figure 3A**), IBA-1-(a microglia/macrophage marker, **Figure 3C**), CC1-(an oligodendrocyte marker, **Figure 3D**) and cleaved caspase-3-(a marker of apoptosis, **Figure 3E**) positive cells. However, it did but not co-localize with GFAP-(an astrocyte label, **Figure 3B**) positive cells. Thus, CD163 protein was expressed by neurons, microglia/macrophages and oligodendrocytes after SAH, but not astrocytes. Cleaved caspase-3-positive cells were found mainly in superficial cortex and white matter, indicating apoptosis is occurred in those cells, some of which expressed CD163 protein.

All experimental rats were sorted on the basis of MRI grading. CD163-positive cells were found in SAH rats graded from 0 to 4 (**Figure 4A**). Compared with sham-operated and grades 0-2 (mild SAH) animals, the rats with grades 3-4 (severe SAH) had higher CD163 protein levels (CD163/β-actin: 1.29 ± 0.14 vs. 0.16 ± 0.05 in sham operated animals, $p < 0.01$; 0.76 ± 0.33 in grade 0-2 SAH, $p < 0.05$; **Figure 4B**).

T2 hyper-intensity areas in the ipsilateral cortex were found on T2 weighted images, and there were abundant CD163-positive cells in the T2 lesion (+) areas (**Figure 5A**). Accordingly, a marked increase of CD163 protein level was observed in T2 lesion (+) areas compared with sham-operated and T2 lesion (–) animals (CD163/β-actin: 1.60 ± 0.31 vs. 0.19 ± 0.05 in the control, $p < 0.01$; 0.30 ± 0.13 in T2 lesion (–) areas, $p < 0.01$; **Figure 5B**).

Hydrocephalus was also observed on T2 weighted images 24 h following SAH. Moreover, the SAH rats with hydrocephalus had higher CD163 immunoreactivity (**Figure 6A**). The CD163 expression assessed by Western blotting was higher in SAH rats with hydrocephalus compared with sham-operated and with no hydrocephalus animals (CD163/β-actin: 1.43 ± 0.49 vs. 0.18 ± 0.05 in the control, $p < 0.01$; 0.25 ± 0.09 in hydrocephalus (–) animals, $p < 0.01$; **Figure 6B**).

DISCUSSION

The main findings from our study are as listed below: (1) CD163 protein levels were elevated in rat brain following SAH; (2) CD163 protein was expressed by neurons, microglia/macrophages, and oligodendrocytes; (3) CD163-positive cells were also cleaved caspase-3-positive, indicating that CD163 positive cells could be apoptotic cells; and

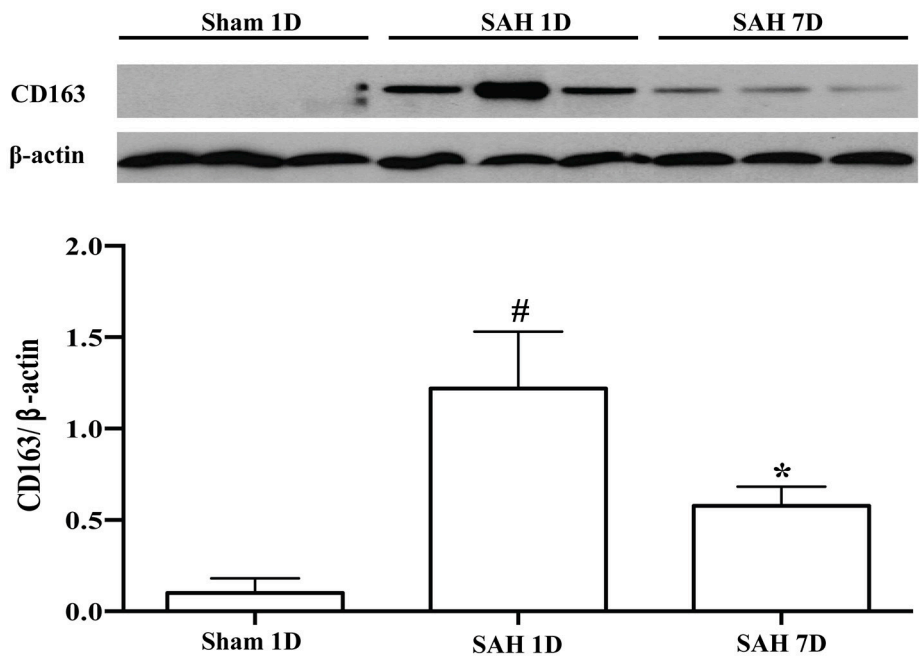

FIGURE 2 | CD163 expression in ipsilateral cortex after SAH (days 1 and 7) or a sham operation (day 1) as assessed by Western blot. Values are means ± SD, $^{*}p < 0.05$ vs. sham; $^{\#}p < 0.01$ vs. sham, $n = 3$, one-way ANOVA.

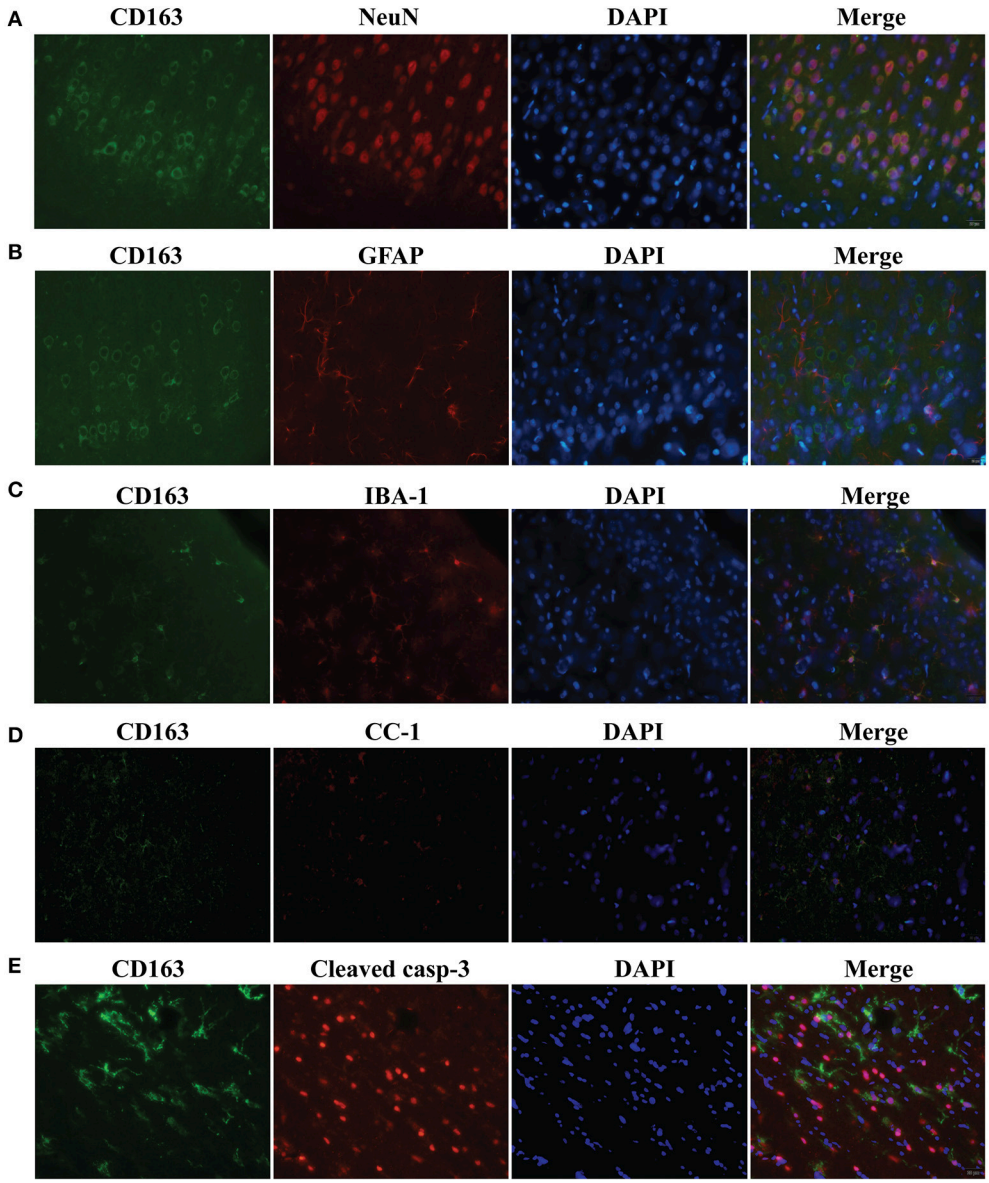

FIGURE 3 | Triple immunofluorescence staining with CD163, NeuN **(A)**, IBA-1 **(B)**, GFAP **(C)**, CC1 **(D)** and cleaved caspase-3 **(E)** at day 1 following SAH. Scale bar = 20 μm.

(4) CD163 overexpression was associated with severe hemorrhage, T2 lesion on MRI and hydrocephalus after SAH.

After SAH, hemoglobin is released through red cell lysis and it is important to understand how hemoglobin can be cleared. CD163 is a primary receptor for hemoglobin endocytosis and degradation. Our study found that CD163 expression rapidly increased in cortex, white matter and periventricular regions from days 1 to 7 following SAH. This response might be associated with penetration of hemoglobin into adjacent brain tissue from both the subarachnoid space and the ventricles (Turner et al., 1998). In microglia/macrophages, the CD163-mediated uptake is a high affinity pathway to eliminate extracellular hemoglobin and limit toxicity (Thomsen et al., 2013). However, our recent study also found that neurons could express CD163 after ICH (Liu et al., 2017) and there has been *in vitro* evidence that neuronal CD163 participates in hemoglobin-induced toxicity (Chen-Roetling and Regan, 2016). The difference in the effects of macrophage/microglia and neuronal CD163 may reflect the high ferritin expression in the former. The role of neuronal CD163 in SAH should be studied further.

Hemoglobin is degraded into heme which can then be metabolized by HO-1 into carbon monoxide, biliverdin, and

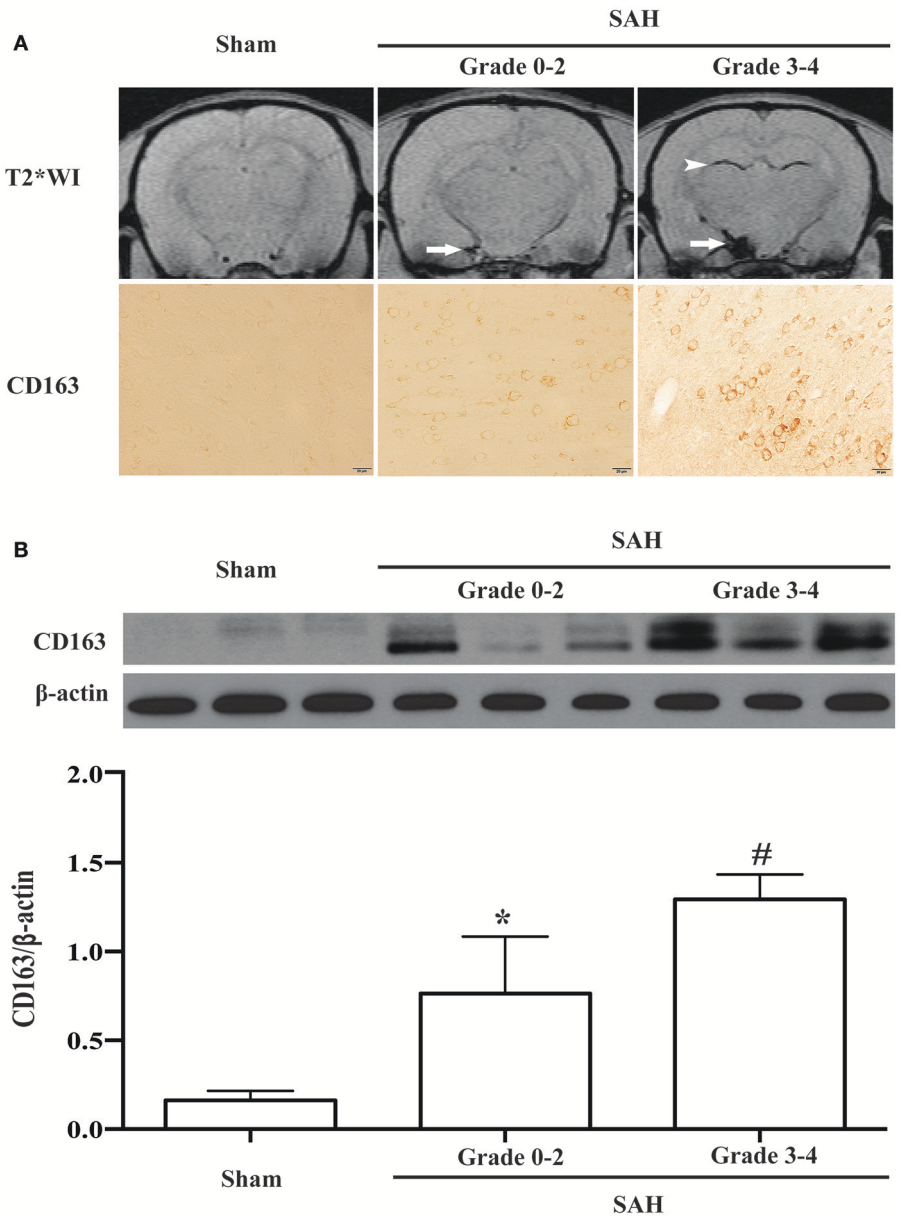

FIGURE 4 | (A) Representative T2* weighted MRI for SAH grading and corresponding CD163 immunoreactivity at day 1 following SAH or a sham operation. On the T2* weighted images (T2WI), arrows point to the subarachnoid blood masses and arrowheads point to intraventricular blood clots. Scale bar = 20 μm. **(B)** CD163 expression in the ipsilateral cortex at day 1 following SAH of different grades (0-2 or 3-4) or a sham operation as assessed by Western blot. Values are means±SD, $^{*}p < 0.05$ grade 0-2 vs. the other groups; $^{\#}p < 0.01$ grade 3-4 vs. sham, $n = 3$, one-way ANOVA.

free iron. Iron may then bind to ferritin, limiting iron-induced toxicity (Otterbein et al., 2003; Thomsen et al., 2013). Animal experimental studies have demonstrated that HO-1 protein expression is increased after SAH, followed by elevated free iron, transferrin, and ferritin levels, and that the iron chelator, deferoxamine, can reduce brain injury and neuronal death after SAH (Lee et al., 2010; LeBlanc et al., 2016; Guo et al., 2017). In view of above mentioned findings, it seems reasonable to speculate that the hemoglobin-CD163-HO-1 system is involved in acute brain damage following experimental SAH.

Cell apoptosis play an important role in early brain injury after SAH and is associated with poor outcomes (Lee et al., 2010; Sehba et al., 2012). Our data showed there was abundant co-localization of CD163 with cleaved caspase-3-positive cells. These findings suggest that CD163 may be associated with apoptotic cell death. Interestingly, CD163 expression is related with alternatively activated or anti-inflammatory microglia/macrophages that are found in the final resolution phase of inflammatory processes (Abraham and Drummond, 2006; Thomsen et al., 2013). Inflammation

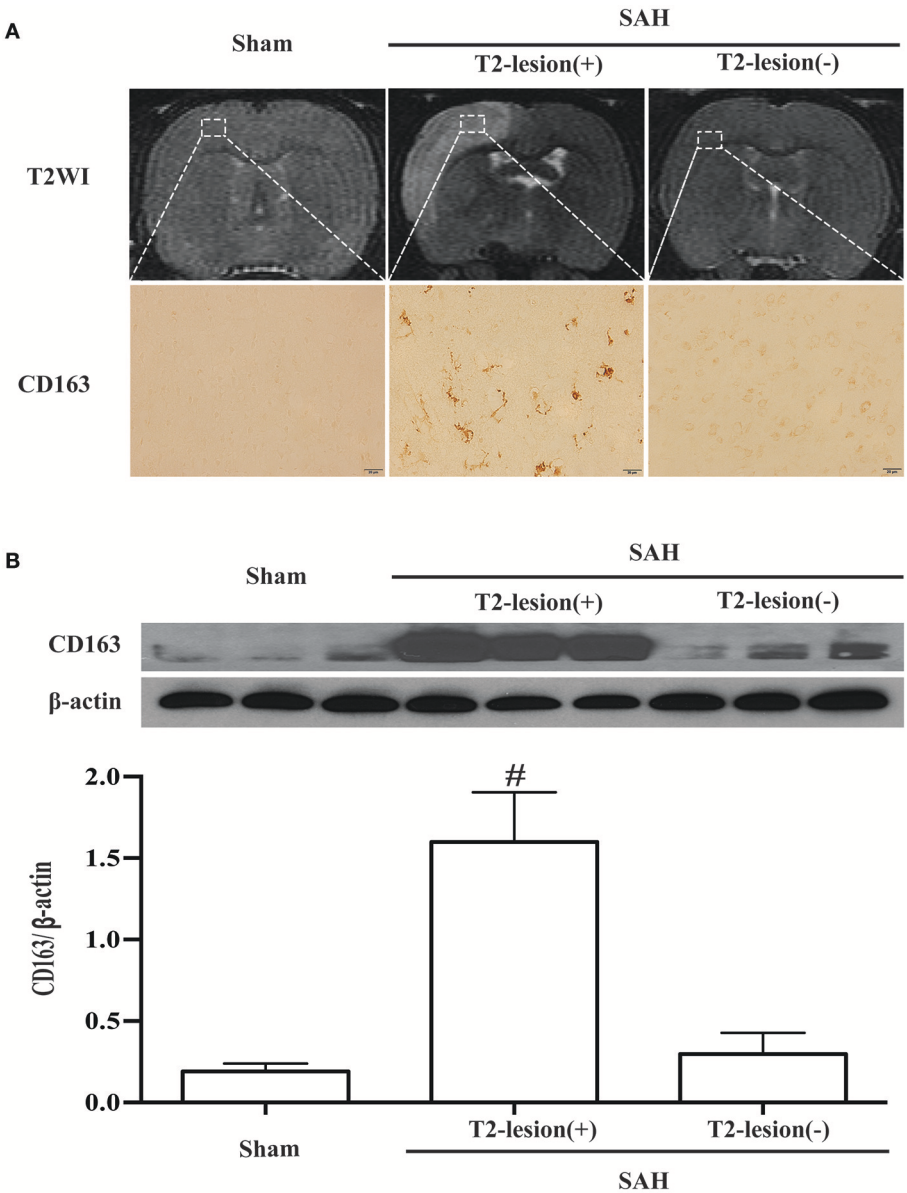

FIGURE 5 | SAH-induced lesions were identified on T2 weighted MRI (T2WI). **(A)** Representative example of a T2 lesion 1 day after SAH [T2-lesion (+)] compared to images from a sham-operated rat and an SAH rat with no lesion [T2-lesion (–)]. Corresponding CD163 immunoreactivity in ipsilateral cortex from the box area is shown below. Scale bar = 20 μm. **(B)** Western blots were used to quantify CD163 protein levels in the ipsilateral cortex at day 1 in sham operated and SAH rats with and without a T2 lesion. Values are mean±SD, $^{\#}p < 0.01$, T2-lesion (+) vs. the other groups, $n = 3$, one-way ANOVA.

is considered to be important in the mechanisms of cell death and brain injury following SAH (Li et al., 2017; Zhang et al., 2017). Thus, the role of CD163 in hemoglobin uptake, inflammation, early brain injury and iron overload, as well as long-term neurologic deficits deserves further study.

It is well-known that neurologic deficits are related to the amount of blood released following SAH. In addition, we have found that SAH-induced acute hydrocephalus and white matter injury are also associated with SAH severity (Okubo et al., 2013; Egashira et al., 2014). A MRI grading system has been developed to evaluate SAH severity without requiring euthanasia. We have found that SAH rats with grades 3-4 had large T2 lesions, worse neurological outcomes, a higher incidence of hydrocephalus and white matter injury compared to grades 0-2 (Guo et al., 2017). The present study found that the T2 lesion (+) areas matched with CD163 positively labeled areas at day 1 after SAH. Our previous study has demonstrated that HO-1 protein levels were also significantly increased in T2 lesion areas (Guo et al., 2017), indicating

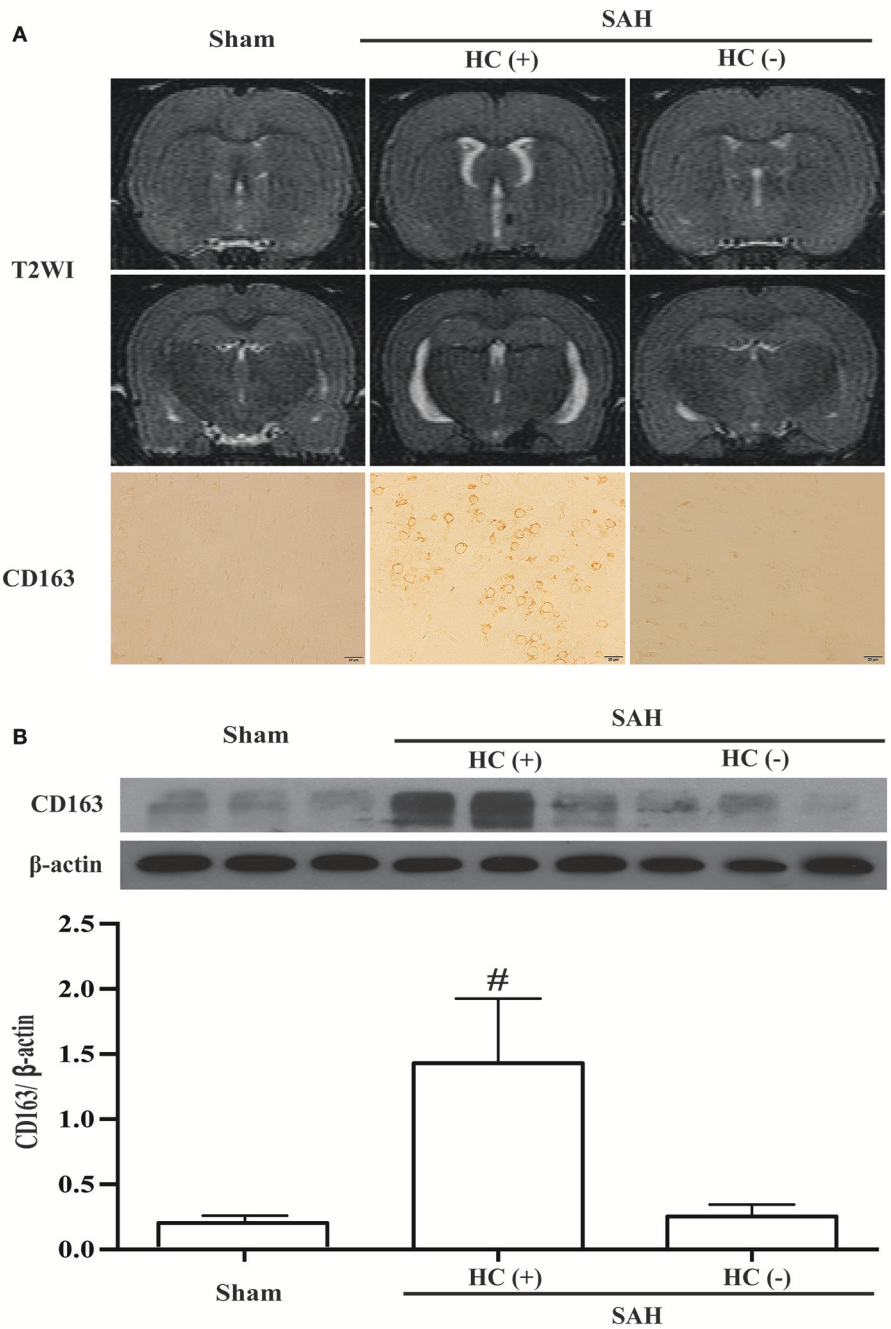

FIGURE 6 | SAH-induced hydrocephalus was identified on T2 weighted MRI (T2WI). **(A)** Representative image of hydrocephalus [HC (+)] 1 day after SAH, note the dilated lateral ventricles. For comparison, images are shown of an animal with no hydrocephalus after SAH [HC (–)] and a sham-operated rat at day 1. Corresponding CD163 immunoreactivity in the ipsilateral cortex is shown below; scale bar = 20 μm. **(B)** Western blots were used to quantify CD163 protein levels in the ipsilateral cortex at day 1 in sham operated and SAH rats with and without hydrocephalus. Values are means±SD, $^{\#}p < 0.01$, HC (+) vs. the other groups, $n = 3$, one-way ANOVA.

that iron overload may be a leading cause of T2 lesion formation.

There were limitations in this study: (1) A causal relationship between CD163 expression and SAH-induced brain injury was not determined in the current study; (2) CD163 expression after SAH only determined at days 1 and 7. CD163 might be involved in early brain injury and delayed brain recovery. In future studies, a full time-course of CD163 expression in the brain following SAH should be examined.

CONCLUSIONS

In summary, brain CD163 levels were increased in the acute phase of SAH, which was associated with hemorrhage severity, T2 lesion on MRI and hydrocephalus after SAH. The role of CD163 (beneficial or detrimental) in SAH remains to be determined.

AUTHOR CONTRIBUTIONS

Immunostaining, Western blotting, data analysis, drafted the manuscript: CJ. Designed the experiment and data analysis: YH, RK. Animal surgery: HS, HZ.

ACKNOWLEDGMENTS

This study was supported by grants NS-079157, NS-091545, NS-090925, NS-096917 and NS-106746 from the National Institutes of Health (NIH), by grant 81300994 from National Natural Science Foundation of China (NSFC). The content is solely the responsibility of the authors and does not necessarily represent the official views of the NIH and NSFC.

REFERENCES

Abraham, N. G., and Drummond, G. (2006). CD163-Mediated hemoglobin-heme uptake activates macrophage HO-1, providing an antiinflammatory function. *Circ. Res.* 99, 911–914. doi: 10.1161/01.RES.0000249616.10603.d6

Cao, S., Zheng, M., Hua, Y., Chen, G., Keep, R. F., and Xi, G. (2016). Hematoma changes during clot resolution after experimental intracerebral hemorrhage. *Stroke* 47, 1626–1631. doi: 10.1161/STROKEAHA.116.013146

Chen-Roetling, J., and Regan, R. F. (2016). Haptoglobin increases the vulnerability of CD163-expressing neurons to hemoglobin. *J. Neurochem.* 139, 586–595. doi: 10.1111/jnc.13720

Egashira, Y., Hua, Y., Keep, R. F., and Xi, G. (2014). Acute white matter injury after experimental subarachnoid hemorrhage: potential role of lipocalin 2. *Stroke* 45, 2141–2143. doi: 10.1161/STROKEAHA.114.005307

Guo, D., Wilkinson, D. A., Thompson, B. G., Pandey, A. S., Keep, R. F., Xi, G., et al. (2017). MRI Characterization in the Acute Phase of Experimental Subarachnoid Hemorrhage. *Transl. Stroke Res.* 8, 234–243. doi: 10.1007/s12975-016-0511-5

Jing, C. H., Wang, L., Liu, P. P., Wu, C., Ruan, D., and Chen, G. (2012). Autophagy activation is associated with neuroprotection against apoptosis via a mitochondrial pathway in a rat model of subarachnoid hemorrhage. *Neuroscience* 213, 144–153. doi: 10.1016/j.neuroscience.2012.03.055

Kooijman, E., Nijboer, C. H., van Velthoven, C. T., Kavelaars, A., Kesecioglu, J., and Heijnen, C. J. (2014). The rodent endovascular puncture model of subarachnoid hemorrhage: mechanisms of brain damage and therapeutic strategies. *J. Neuroinflammation* 11:2. doi: 10.1186/1742-2094-11-2

LeBlanc, R. H., Chen, R., Selim, M. H., and Hanafy, K. A. (2016). Heme oxygenase-1-mediated neuroprotection in subarachnoid hemorrhage via intracerebroventricular deferoxamine. *J. Neuroinflammation* 13:244. doi: 10.1186/s12974-016-0709-1

Leclerc, J. L., Lampert, A. S., Loyola Amador, C., Schlakman, B., Vasilopoulos, T., Svendsen, P., et al. (2018). The absence of the CD163 receptor has distinct temporal influences on intracerebral hemorrhage outcomes. *J. Cereb. Blood Flow Metab.* 38, 262-273. doi: 10.1177/0271678X17701459

Lee, J. Y., Keep, R. F., He, Y., Sagher, O., Hua, Y., and Xi, G. (2010). Hemoglobin and iron handling in brain after subarachnoid hemorrhage and the effect of deferoxamine on early brain injury. *J. Cereb. Blood Flow Metab.* 30, 1793–1803. doi: 10.1038/jcbfm.2010.137

Lee, J. Y., Sagher, O., Keep, R., Hua, Y., and Xi, G. (2009). Comparison of experimental rat models of early brain injury after subarachnoid hemorrhage. *Neurosurgery* 65, 331–343; discussion 343. doi: 10.1227/01.NEU.0000345649.78556.26

Li, J. R., Xu, H. Z., Nie, S., Peng, Y. C., Fan, L. F., Wang, Z. J., et al. (2017). Fluoxetine-enhanced autophagy ameliorates early brain injury via inhibition of NLRP3 inflammasome activation following subrachnoid hemorrhage in rats. *J. Neuroinflammation* 14:186. doi: 10.1186/s12974-017-0959-6

Liu, R., Cao, S., Hua, Y., Keep, R. F., Huang, Y., and Xi, G. (2017). CD163 Expression in neurons after experimental intracerebral hemorrhage. *Stroke* 48, 1369–1375. doi: 10.1161/STROKEAHA.117.016850

Madsen, M., Graversen, J. H., and Moestrup, S. K. (2001). Haptoglobin and CD163: captor and receptor gating hemoglobin to macrophage lysosomes. *Redox Rep.* 6, 386–388. doi: 10.1179/1351000011015 36490

Okubo, S., Strahle, J., Keep, R. F., Hua, Y., and Xi, G. (2013). Subarachnoid hemorrhage-induced hydrocephalus in rats. *Stroke* 44, 547–550. doi: 10.1161/STROKEAHA.112.662312

Otterbein, L. E., Soares, M. P., Yamashita, K., and Bach, F. H. (2003). Heme oxygenase-1: unleashing the protective properties of heme. *Trends Immunol.* 24, 449-455. doi: 10.1016/S1471-4906(03)00181-9

Sehba, F. A. (2014). Rat endovascular perforation model. *Transl. Stroke Res.* 5, 660–668. doi: 10.1007/s12975-014-0368-4

Sehba, F. A., and Bederson, J. B. (2006). Mechanisms of acute brain injury after subarachnoid hemorrhage. *Neurol. Res.* 28, 381–398. doi: 10.1179/016164106X114991

Sehba, F. A., Hou, J., Pluta, R. M., and Zhang, J. H. (2012). The importance of early brain injury after subarachnoid hemorrhage. *Prog. Neurobiol.* 97, 14–37. doi: 10.1016/j.pneurobio.2012.02.003

Shishido, H., Egashira, Y., Okubo, S., Zhang, H., Hua, Y., Keep, R. F., et al. (2015). A magnetic resonance imaging grading system for subarachnoid hemorrhage severity in a rat model. *J. Neurosci. Methods* 243, 115–119. doi: 10.1016/j.jneumeth.2015.01.035

Thomsen, J. H., Etzerodt, A., Svendsen, P., and Moestrup, S. K. (2013). The haptoglobin-CD163-heme oxygenase-1 pathway for hemoglobin scavenging. *Oxid. Med. Cell. Longev.* 2013:523652. doi: 10.1155/2013/5 23652

Turner, C. P., Bergeron, M., Matz, P., Zegna, A., Noble, L. J., Panter, S. S., et al. (1998). Heme oxygenase-1 is induced in glia throughout brain by subarachnoid hemoglobin. *J. Cereb. Blood Flow Metab.* 18, 257–273. doi: 10.1097/00004647-199803000-00004

Xi, G., Keep, R. F., and Hoff, J. T. (2006). Mechanisms of brain injury after intracerebral haemorrhage. *Lancet Neurol.* 5, 53–63. doi: 10.1016/S1474-4422(05)70283-0

Zhang, X., Wu, Q., Zhang, Q., Lu, Y., Liu, J., Li, W., et al. (2017). Resveratrol attenuates early brain injury after experimental subarachnoid hemorrhage via inhibition of NLRP3 inflammasome activation. *Front. Neurosci.* 11:611. doi: 10.3389/fnins.2017.00611

Conflict of Interest Statement: The authors declare that the research was conducted in the absence of any commercial or financial relationships that could be construed as a potential conflict of interest.

frontiers in Neuroscience

ORIGINAL RESEARCH
published: 29 May 2018
doi: 10.3389/fnins.2018.00357

Annexin A7 Levels Increase in Rats With Traumatic Brain Injury and Promote Secondary Brain Injury

Fan Gao[1†], Di Li[2†], Qin Rui[3], Haibo Ni[4], Huixiang Liu[4], Feng Jiang[4], Li Tao[5], Rong Gao[4] and Baoqi Dang[1*]*

[1] Department of Rehabilitation, Zhangjiagang Hospital of Traditional Chinese Medicine Affiliated to Nanjing University of Chinese Medicine, Suzhou, China, [2] Department of Neurosurgery and Translational Medicine Center, The First People's Hospital of Zhangjiagang, Suzhou, China, [3] Clinical Laboratory, The First People's Hospital of Zhangjiagang, Suzhou, China, [4] Department of Neurosurgery, The First People's Hospital of Zhangjiagang, Suzhou, China, [5] Department of Pharmacy, The First People's Hospital of Zhangjiagang, Suzhou, China

The incidence of traumatic brain injury (TBI) has been increasing annually. Annexin A7 is a calcium-dependent phospholipid binding protein. It can promote melting of the cell membrane. Recent studies have shown that it plays an important role in atherosclerosis, other cardiovascular diseases, and a variety of tumors. However, few studies of ANXA7 in TBI have been performed. We here observed how ANXA7 changes after TBI and discuss whether brain injury is associated with the use of ANXA7 antagonist intervention.

Experimental Results: 1. After TBI, ANXA7 levels were higher than in the sham group, peaking 24 h after TBI. 2. The use of siA7 was found to reduce the expression of A7 in the injured brain tissue, and also brain edema, BBB damage, cell death, and apoptosis relative to the sham group.

Conclusion: ANXA7 promotes the development of secondary brain injury (SBI) after TBI.

Keywords: AnnexinA7, traumatic brain injury, secondary brain injury, neuron apoptosis, rat models

OPEN ACCESS

Edited by:
Gang Chen,
First Affiliated Hospital of Soochow University, China

Reviewed by:
Yang Wang,
Anhui Provincial Hospital, China
Yuyun Xiong,
Affiliated Hospital of Jiangsu University, China

***Correspondence:**
Rong Gao
tsong@vip.sina.com
Baoqi Dang
zhenjiangdbq@163.com

[†]These authors have contributed equally to this work.

Specialty section:
This article was submitted to Neurodegeneration, a section of the journal Frontiers in Neuroscience

Received: *25 February 2018*
Accepted: *08 May 2018*
Published: *29 May 2018*

Citation:
Gao F, Li D, Rui Q, Ni H, Liu H, Jiang F, Tao L, Gao R and Dang B (2018) Annexin A7 Levels Increase in Rats With Traumatic Brain Injury and Promote Secondary Brain Injury. Front. Neurosci. 12:357. doi: 10.3389/fnins.2018.00357

INTRODUCTION

The incidence of traumatic brain injury (TBI) has been increasing annually due to an increased number of car accidents and falls by the elderly and has continued to increase year by year (Feigin et al., 2013). The death and disability caused by TBI have also increased accordingly. TBI can cause emotional and cognitive impairment, epilepsy, loss of limb function, and memory impairment, which seriously affects the health of the brain. The development of brain injury after initial injury can significantly aggravate the deterioration and death rate of TBI patients, here called secondary brain injury (SBI) (Hamasaki et al., 2017). At present, little is known about the complex cellular response to the SBI and no effective treatment options are available, especially during its acute phase. The mechanism and time-range study of SBI can provide direction for targeted treatment.

The mechanism of SBI after TBI is very complex. The most important pathological change is tissue edema. Ultrastructural studies have confirmed that the electrolyte and extracellular fluid enter the cerebral nerve cells after injury, resulting in cytotoxic edema. The hemangiogenic edema is caused by the disruption of the blood-brain barrier (BBB). The mechanical damage causes vasoconstriction and the capillary endothelial cells become significantly swollen (Viviani et al., 2014; Wang et al., 2014). Recent studies suggests excitatory neurotoxicity take primary responsibility for SBI.

Annexin is a phospholipid binding protein involved in assembly of the cell skeleton, which forms the basic structural units of the blood-brain barrier (BBB). It has a high affinity with Ca^{2+}. It also participates in the formation and opening of Na^{+} and Cl^{-} channels, works on vesicle transportation and the secretion of neurotransmitter (Raynal and Pollard, 1994; Hoque et al., 2014). Annexin A7 (ANXA7, A7) was the first member of the family to be found. It has two subtypes, which molecular weight is 47 and 51 kDa, respectively. When intracellular Ca^{2+} concentration is elevated, A7 protein conformation changes take place. The formation of polymer, with the combination of acidic phospholipid, eventually cause A7 protein to bind to a specific membrane and help some molecules to move through the lipid bilayer (Pollard and Rojas, 1988). There are reports showing that high levels of ANXA7 are expressed in brain tissue after cerebral hemorrhage in rats. This promotes the release of glutamate and N-methyl-D-aspartic acid receptor (NMDA) and mediated excitatory neurotoxicity, eventually promoting SBI.

In conclusion, many studies have demonstrated that ANXA7 promotes brain damage. However, the effect of A7 after TBI is not clear. This study established the rat TBI free fall model, studied in the expression and function of ANXA7 in the TBI secondary brain injury, and the mechanism of action provides a theoretical foundation for the development of new drugs and clinical treatments for TBI patients.

MATERIALS AND METHODS

Study Design and Experimental Groups

Two separate experiments (**Figure 1**).

Experiment 1: There was no obvious difference in weight, feed intake, and motor ability of all rats. To determine the time course of ANXA7 after TBI, 36 rats (36 surviving out of an initial cohort of 40) were randomly divided into six groups according to a computer-based randomization (EXCEL randbetween function), specifically sham, TBI 6 h, TBI 12 h, TBI 24 h, TBI 48 h, and TBI 72 h (Dash et al., 2016). Brain tissue surrounding the damaged area was sampled. Tissue in the front, close to the frontal lobe was used to perform Western blot analysis (WB). Tissue from the rear part close to the cerebellum was used for double immunofluorescence. Real-time PCR analysis was also performed with tissue from the sides to assess the expression and position of A7 in TBI rat brains (**Figure 1B**).

Experiment 2: To establish the role of A7 in TBI brain injury, 48 rats (48 surviving out of a group of 57) were randomly divided into four groups according to EXCEL randbetween function, specifically sham, TBI, TBI+ vector, and TBI+ siA7. At 24 h after TBI, which was based on the results of experiment 1, the rats were killed and damaged brain tissue was collected. Neurological testing was examined in all groups before decollation. We randomly selected 6 rats from each group for brain edema evaluation. Other rats were studied using Western blot analysis, terminal deoxynucleotidyl transferase–mediated dUTP nick-end labeling (TUNEL) staining and fluoro-jade B (FJB) staining to measure the expression of A7 and albumin, neuronal apoptosis, and necrosis. Brain tissue from the front area near the damage was used for WB, and tissue from the back was prepared into frozen sections (**Figure 1C**).

The experiment abides by the blind method strictly. All the samples were encoded by an independent investigator. The experimenters were blinded to all the sample types during the analysis.

Animals

Here, 97 male Sprague-Dawley rats weighing 280–300 g were purchased from the Animal Center of Soochow University (Suzhou, China), of which 84 were used for statistical analysis. Animals were housed in 12-h light/dark cycles at a controlled temperature and humidity with free access to food and water. All experimental protocols were approved by the Institutional Animal Care and Use Committee of Soochow University and were performed in accordance with guidelines of the National Institutes of Health Guide for the Care and Use of Laboratory Animals.

Traumatic Brain Injury Model

The TBI model was established using a freefall method (Liu et al., 2016). Rats were intraperitoneally anesthetized with 4% chloral hydrate (400 mg/kg) and fixed using a stereotactic instrument. A 5 mm parietal bone window was made behind the cranial coronal suture next to the midline using a bone drill, keeping the dura intact. A copper cylinder (4 mm in diameter, 5 mm in height) was placed in the bone window. A steel rod weighing 40 g with a flat-end was dropped into the copper cylinder from a height of 25 cm. The rats were allowed to recover until their heart rate and breathing returned to normal after a short pause. We carefully sterilized and stitched the wound. We placed the rats in a warm place and allowed them to recover completely. Sham group rats went through exact same procedure as the TBI group without the 40 g steel rod being dropped through the cylinder (**Figure 1A**).

Drug Injection

Twenty-four hours before TBI, rats were anesthetized and placed in a stereotaxic apparatus. We made a hole on the left side of the lateral ventricle, located exactly 1.5 mm posterior and 1.0 mm lateral to the bregma (Paul et al., 2015). SiA7 were configuration by 8 μl transfection reagent and 8 μl siA7 (0.52 μg/ul). Sixteen microliters siA7 and 16 μl vehicle (0.26 μg/ul) was injected by microinjection though the hole at a rate of 0.5 μL/min, 4.0 mm beneath the skull. Eventually, the incision was sutured and the rats were allowed to recover.

Real-Time PCR

Total RNA was isolated from brain tissue around the injured area using Trizol reagent (Invitrogen, US) in accordance with the manufacturer's instructions. According to the protocol provided by manufacturer (Thermo, US), complementary DNA (cDNA) was synthesized using 1 μg of the total RNA. Then, real-time PCR was performed using a QuantStudio™ Dx Real-time PCR Instrument (Life Technologies Corporation, US) with a PowerUp™ SYBR™ Green Master Mix Kit (ThermoFisher, US). The phases are briefly described as follows: the template was denatured at 95°C for 2 min, followed by 40 cycles of

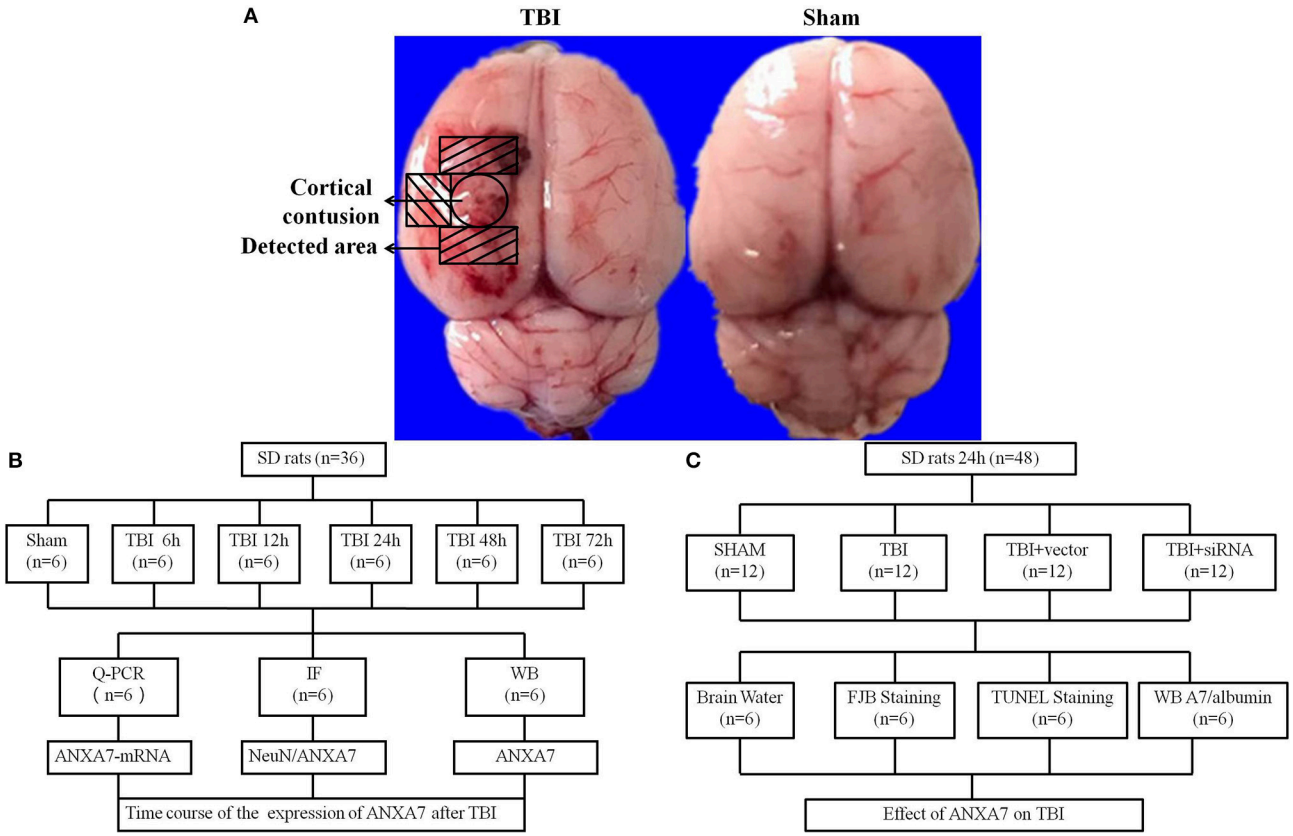

FIGURE 1 | Study design and experimental groups. **(A)** traumatic brain injury rat samples, the representative areas taken for assay; **(B)** experiment group 1 evaluated and located the expression of ANXA7 in TBI rats brain; **(C)** experiment group 2 established the function of ANXA7 in SBI.

amplification (95°C for 15 s, 60°C for 15 s, 72°C for 1 min). All samples were analyzed in triplicate. The expression of GAPDH messenger RNA (mRNA) served as an internal reference for each sample, and the relative mRNA expression levels of the target gene were calculated by relative quantification ($2^{-\Delta\Delta CT}$). The primers were as follows: Anxa7, 5′-CCC TGTTCATGCCTCCTACA-3′ and 5′-CACACGCTCTTGAGTT CCTG-3′, GAPDH, 5′-TGGCCTTCCGTGTTCCTACC-3′, 5′-TCTTCCACCACTTCGTCCGC-3′.

Western Blot Analysis

Protein extraction from whole-cell lysates of ipsilateral brain were obtained by gently homogenization in RIPA lysis buffer with phosphatase inhibitors (Beyotime, China) with further centrifugation at 13,000 g at 4°C for 20 min. The supernatant was collected and the protein concentration was assessed using the bicinchoninic acid (BCA) method with a Pierce™ BCA Protein Assay Kit (Thermo, US). Equal amounts of extracted proteins were loaded and subjected to electrophoresis on 12% SDS-polyacrylamide gels (Beyotime, China) and then transferred onto polyvinylidene difluoride (PVDF) membranes (Millipore, US). Blocking buffer with 5% defatted milk was used to block the membranes for 1 h at room temperature. These samples were then incubated with following antibodies overnight at 4°C: rabbit anti-A7 (1:1,000, Abcam, US), mouse anti-β-actin (1:10,000, Sigma, US), and chicken anti-albumin (1:1,000, Abcam, US). The membranes were then incubated with horseradish peroxidase-conjugated secondary antibodies for 2 h at 4°C, including goat anti-rabbit IgG-HRP (Invitrogen, US), goat anti-mouse IgG-HRP (Invitrogen, US) and goat anti-chicken IgG-HRP (Invitrogen, US). Immunoblots were finally probed with an Immobilon™ Western Chemiluminescent HRP Substrate (Millipore, US) and visualized with an imaging system (Bio-Rad, US). All data were analyzed using ImageJ software.

Immunofluorescence Staining

The rat brains were removed and fixed in 4% paraformaldehyde at 4°C for 24 h. Samples were dehydrated step by step with 15 and 30% sucrose in phosphate-buffered saline (PBS, pH 7.4) for 24 h, respectively, then embedded in OCT compound (Sakura, US) and frozen at −80°C until use. Frozen coronal slices (15 μm) were sectioned by using freezing microtome and Leica DMi8 (Leica Microsystems, Germany) and mounted on poly-L-lysine-coated glass slides. After three rounds of washing in 1% Triton-PBS buffer to rupture cell membranes, sections were blocked with 10% goat serum for at least 1 h at room temperature, and then incubated at 4°C overnight with primary antibodies: rabbit anti-A7 (1:100, Abcam), mouse anti-Neuron (1:200, Millipore, USA).

Secondary antibodies, including Alexa Fluor 488 donkey anti-rabbit IgG antibody (Invitrogen, US) and Alexa Fluor 555 donkey anti-mouse IgG antibody (Invitrogen, US) were incubated for 1 h at room temperature at a dilution of 1:1,000. The sections were observed with a laser confocal microscope Leica DMi8 (Leica Microsystems, Germany) and pictures were taken using LAS X software.

Brain Water Content

The brain water content was measured in the second experiment using the wet/dry method (Brockman et al., 2013). After surgery and separation of the brains from surrounding tissues, the brains were divided into ipsilateral and contralateral frontal and quickly weighed to get the wet weight. Then, the samples were placed in a 100°C oven for 24 h to obtain the dry weight. The percentage of brain water content (%) was calculated as [(wet weight – dry weight) / (wet weight)] × 100%.

Tunel Staining

Apoptosis was detected using terminal deoxynucleotidyltransferase-mediated dUTP nick end labeling (TUNEL) staining according to the manufacturer's protocol (Abcam, US). Frozen brain tissue sections were soaked in 4% polyformaldehyde/PBS for 15 min, then shifted into protease K working fluid incubating for 5 min. The samples were immersed in 4% polyformaldehyde/PBS for another 5 min and cleaned with wash buffer twice for 5 min each. We covered the brain slices in DNA labeling solution and stored them in a wet box away from light for 1 h. We washed the slices, added the antibody solution, and placed the samples in a dark, wet box for 30 min. We washed the samples in deionizing solution for 5 min. The samples were allowed to air dry and then sealed with DAPI. We observed the slides with a laser confocal microscope Leica DMi8 (Leica Microsystems, Germany) and took pictures using LASX software.

Fluoro-Jade B Staining

Fluoro-Jade B (FJB) staining was conducted as stipulated in the manufacturer's instructions (Millipore, US). After incubation with 1% sodium hydroxide in 80% alcohol for 5 min and 70% alcohol for 2 min, the frozen section were then transferred to a solution of 0.06% potassium permanganate for 10 min. Then, slides were immersed in 0.0004% fluoro-jade dye staining solution (0.1% acetic acid) for 20 min followed by rinsed in deionized water. The sections were washed and dried in an oven at 50°C for 5–8 min. The sections were then cleaned by immersion in xylene for at least 1 min and then coverslipped with Distyrene Plasticiser Xylene (DPX), a non-aqueous non-fluorescent plastic mounting medium. The sections were observed with a laser confocal microscope Leica DMi8 (Leica Microsystems, Germany) and pictures were taken using LAS X software.

Statistical Analyses

All data were analyzed using SPSS 18.0 software. Non-parametric testing was used in the brain water test. When other data were normally distributed, one-way ANOVA was used to compare different groups, *T*-test was used between two groups. The results were expressed as means ± standard deviations. $P < 0.05$ was considered indicative of statistically significant differences; $P < 0.01$ was considered indicative of highly statistically significantly differences.

RESULTS

The Expression of ANXA7 Protein Level in Brain After TBI

Western blot results are shown in **Figures 2A,B**: Group TBI 6 h, 12 h, 24 h, 48 h, and 72 h had significant differences from the sham group ($P < 0.01$); the TBI 12 h group showed no difference from the 24 h group ($P > 0.05$), the TBI 24 h group was different from the TBI 48 h group ($P < 0.05$). This indicates that undamaged brains have low levels of A7 protein. Six hours after TBI, the expression of A7 was significantly higher than baseline, peaking at 12–24 h. Forty-eight hours after TBI, A7 expression began to decline, and there is still a significant expression after 72 h.

The Expression of ANXA7 in mRNA Level in Brain After TBI

Q-PCR results are shown in **Figure 2C**: Groups TBI 6 h, 12 h, 24 h, 48 h, and 72 h all differed from the sham group ($P < 0.05$). Groups TBI 12 h and 48 h group showed no differences from the 24 h group ($P > 0.05$). This indicated that A7RNA was expressed in the sham group at a low level. This level had increased by 6 h after TBI, and significantly increased at 12 h. The high level expression continued to 48 h. There was still significant expression after 72 h.

The Expression of ANXA7 in Neurons Around the Damaged Area After TBI

If results are shown in **Figures 2D,E**: Group TBI 6 h, 12 h, 24 h, 48 h, 72 h has significantly differences with sham group ($P < 0.01$), TBI 12 h, 48 h group has no differences from the 24 h group ($P > 0.05$). This represented A7 expressed in neurons. The sham group showed a low level of expression, with a significant increase 6 h after TBI and a peak at 24 h. The high level of expression was sustained from 12 to 72 h.

The Effect of siA7 Intervention on A7 Protein Expression After TBI

Western blot siA7 results are shown in **Figures 3A,B**: The TBI group showed significant differences from the sham group ($P < 0.01$); TBI showed no differences from the TBI+vector group ($P > 0.05$); the TBI+siA7 group showed significant differences from the TBI group ($P < 0.01$). This indicates that A7 has a low level of protein expression in the sham group that significantly increases after TBI and is significantly reduced after siA7 intervention.

The Integrity of BBB in TBI Rats After siA7 Intervention

Western blot analysis with albumin are shown in **Figures 3C,D**: The TBI group showed significant differences from the sham

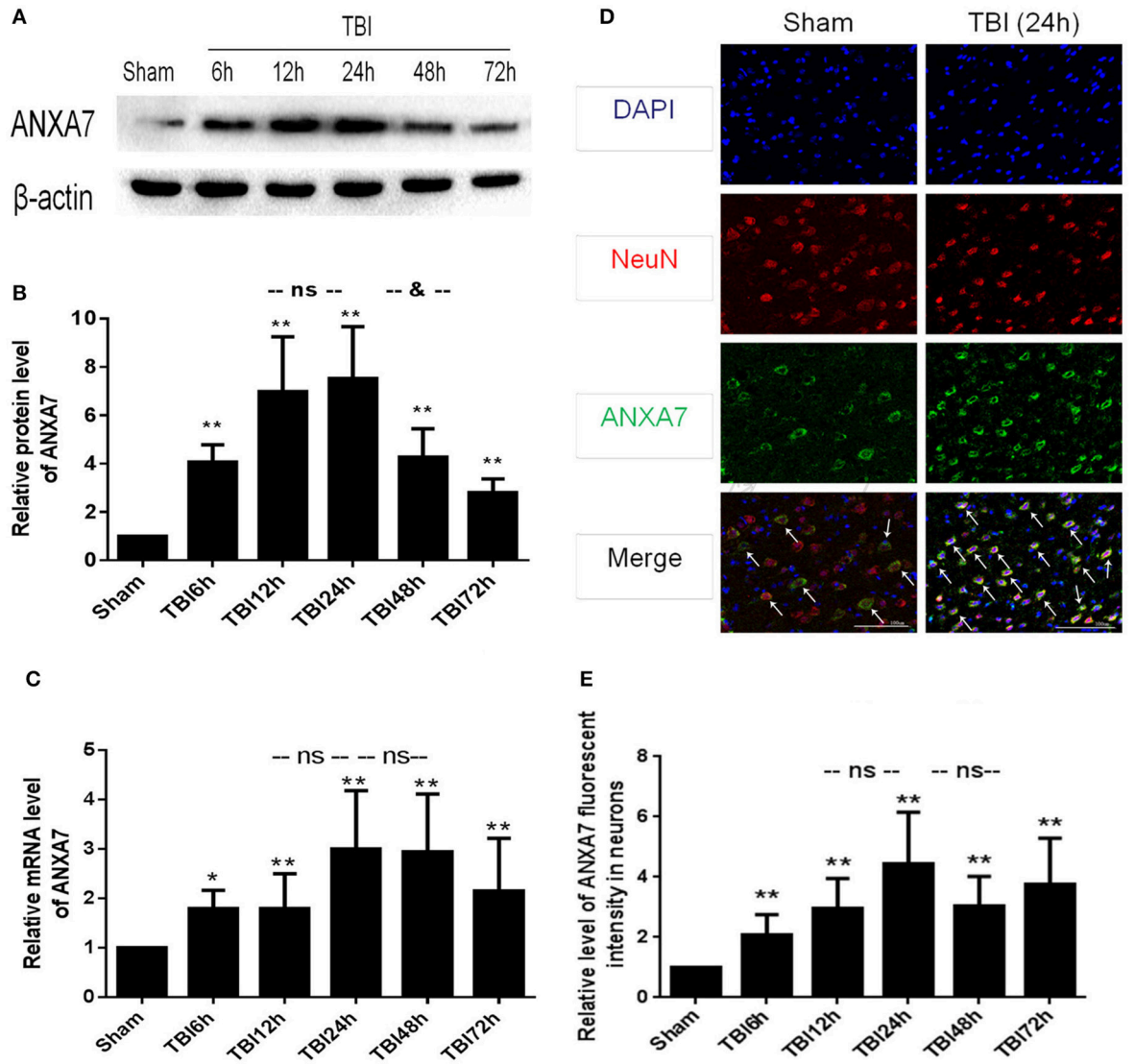

FIGURE 2 | ANXA7 protein level, mRNA level are increased after TBI in rats, and located in neurons. **(A,B)** ANXA7 protein level in brain after TBI. Sample of different time points were analyzed by western blot; β-actin served as a loading control. Protein levels were quantified with Image J software, and mean values for sham group were normalized to 1.0. Date = means ± SD. $^{**}P < 0.01$ vs. sham; $^{\&}P < 0.05$ vs. TBI 24 h; ns $P > 0.05$ vs. TBI 24 h. $n = 6$. **(C)** ANXA7 mRNA level in brain after TBI. Brain tissue collected at different time points were analyzed by Q-PCR. RQ were calculated and mean values for sham group were normalized to 1.0. Date = mean ± SD. $^{*}P < 0.05$ vs. sham; $^{**}P < 0.01$ vs. sham; ns $P > 0.05$ vs. TBI 24 h. $n = 6$. **(D,E)** ANXA7 in neurons near the damaged area after TBI. Double immunofluorescence analysis of brain tissue using antibodies against ANXA7 (green) and NeuN (red); nuclei were labeled with DAPI (blue). Quantitative analysis of NeuN and A7 double positive neurons. Date = mean ± SD. $^{**}P < 0.01$ vs. sham; ns $P > 0.05$ vs. TBI 24 h. Bar = 100 μm. $n = 6$.

group ($P < 0.01$); TBI has no differences with TBI+ vector group ($P > 0.05$); TBI+siA7 group has significant differences from the TBI group ($P < 0.01$). These results confirmed that the blood brain barrier had been significantly damaged after TBI injury, and the integrity of the BBB was significantly improved after the intervention of siA7.

Neuron Death in TBI Rats Treated With siA7 Injection

FIB staining results are shown in **Figures 3E,F**: The TBI group showed significant differences from the sham group ($P < 0.01$); TBI showed no differences from the TBI+ vector group ($P > 0.05$); the TBI+ siA7 group showed significant differences from the TBI group ($P < 0.01$). The degree of necrosis of neurons in rats after TBI was significantly greater than in the sham group, and significantly reduced after siA7 intervention.

Neuronal Apoptosis in TBI Rats Treated With siA7 Injection

TUNEL staining results are shown in **Figures 3G,H**: The TBI group has significantly differences with sham group ($P < 0.01$); TBI showed no differences from the TBI+ vector group

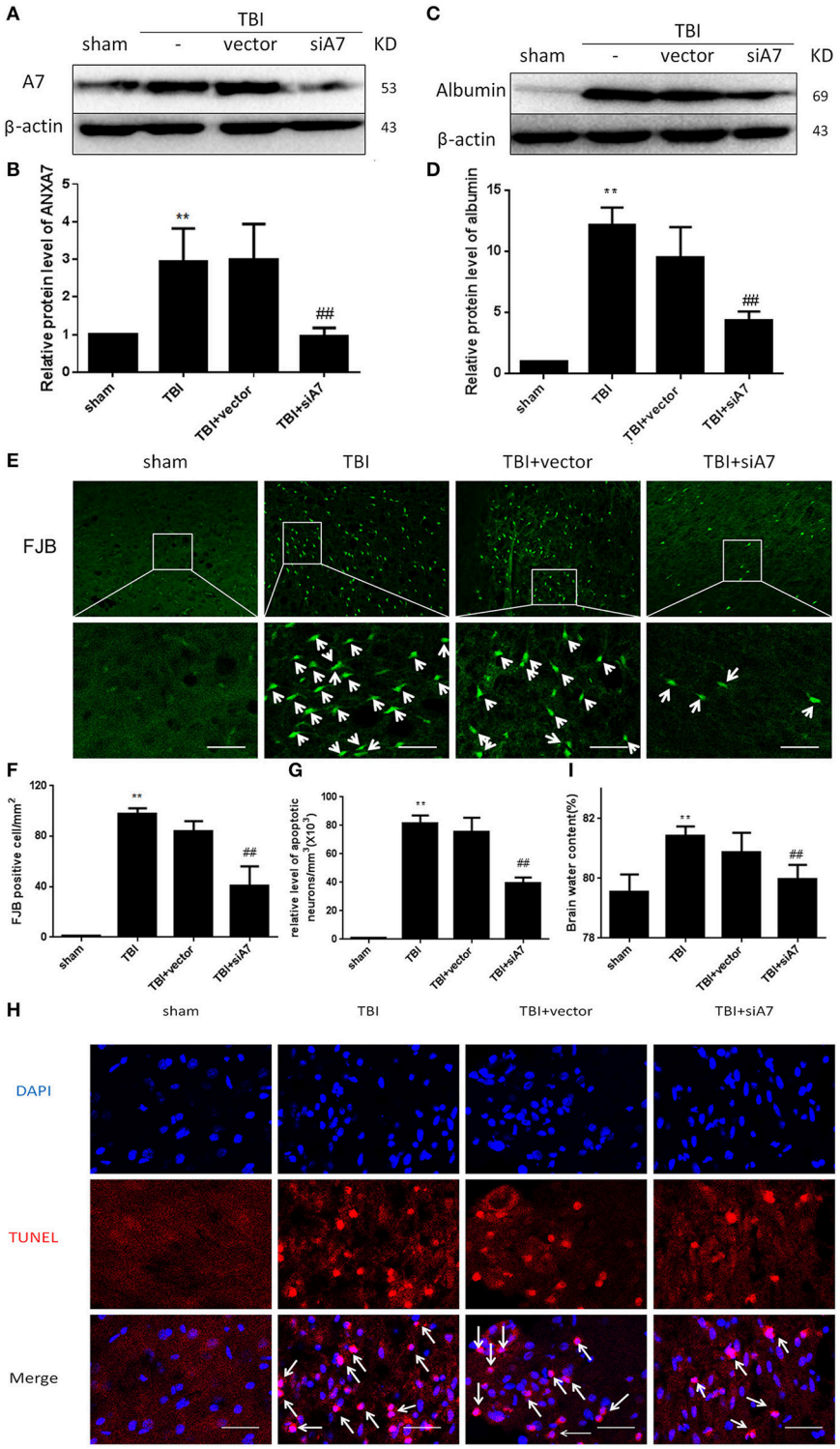

FIGURE 3 | SiA7 reduce ANXA7 in the injured brain tissue and reduce brain injury in rats after TBI. **(A,B)** Confirm the impact of siA7 on ANXA7 expression. A7 was detected in sham, TBI, TBI + vector, and TBI + siA7 groups 24 h after TBI by western blot. Date = means ± SD. $^{**}P < 0.01$ vs. sham, $^{\#\#}P < 0.01$ vs. TBI. $n = 6$. **(C,D)** The integrity of BBB in TBI rats was improved after siA7 intervention. Albumin was detected by western blot. Date = means ± SD. $^{**}P < 0.01$ vs. sham, $^{\#\#}P < 0.01$ vs. TBI. $n = 6$. **(E,F)** Neuron death was detected by FJB staining (green). FJB-positive cells/mm^2 was quantified. Data = mean ± SD. $^{**}P < 0.01$ vs. sham, $^{\#\#}P < 0.01$ vs. TBI. Bar = 50 μm. $n = 6$. **(G,H)** Neuronal apoptosis was detected with the TUNEL assay. Immunofluorescence analysis was performed with TUNEL (red), nuclei were labeled with DAPI (blue). TUNEL - nuclei positive neurons/mm^3 was quantified. Date = means ± SD. $^{**}P < 0.01$ vs. sham; $^{\#\#}P < 0.01$ vs. TBI. Bar = 50 μm. $n = 6$. **(I)** Brain water content was calculated as [(wet weight – dry weight)/(wet weight)] × 100%. Date = means ± SD. $^{**}P < 0.01$ vs. sham; $^{\#\#}P < 0.01$ vs. TBI. $n = 6$.

($P > 0.05$); the TBI+ siA7 group showed significant differences from the TBI group ($P < 0.01$). Results showed that the rate of apoptosis in rat neurons increased significantly after TBI and decreased significantly after siA7 intervention.

Cerebral Edema Index in TBI Rats Treated With siA7 Injection

Wet/dry method on brain edema are shown in **Figure 3I**: The TBI group showed significant differences from the sham group ($P < 0.01$); TBI showed no differences from the TBI+ vector group ($P > 0.05$); the TBI+ siA7 group showed significant differences from the TBI group ($P < 0.01$). The results indicated that the cerebral edema in TBI was significantly higher 24 h after TBI, which was significantly different from that of the sham operation group, and the cerebral edema index of the intervention group of the siA7 was significantly lower.

DISCUSSION

ANXA7 exists in many organs throughout the body, including the brain, heart, liver, parotid gland, spleen, lung, normal reticulocyte, and skeletal muscle (Herr et al., 2003; Guo et al., 2013). Recent studies have shown that ANXA7 plays a very important role in atherosclerosis, other cardiovascular diseases, and a variety of tumors (Tincani et al., 1998; Turnay et al., 2005). Results also showed ANXA7 to be widely expressed in brain tissue. During different periods of embryonic development, ANXA7 subcellular localization in brain cells changed from the cytoplasm to the nucleus (Rick et al., 2005). In the cortex of the adult brain, ANXA7 is located in the cytoplasm but not in the nucleus of vertebral body cells and in the top dendrites (Rick et al., 2005). There is a small amount of expression in the cytoplasm and nuclei of the astrocytes (Zhou et al., 2011). In the hippocampus of adrenal excision mice, ANXA7 was mainly located in glial cells, not in neurons or astrocytes (Moga et al., 2005).

When the concentration of cell calcium ions increases, the subcellular localization of ANXA7 shifts. These ions form a polymer to foster the combination with acidic phospholipids, eventually binding to specific parts of the molecule and moving through the lipid bilayer membrane, mediating the release of neurotransmitters and vesicle transport (Hoque et al., 2014). ANXA7 is expressed so widely and participates in basic physical and pathological activities. However, only a few studies of ANXA7 in brain disease have been reported.

In this experiment, we assessed the expression and function of A7 in TBI, ascertained the distribution of A7 in neurons in rats after TBI, and confirmed that A7 showed the most expression after TBI around the damaged brain tissue at both the mRNA and protein levels. The level of A7 was found to change over time, and the peak time of expression is consistent with clinical practice. By using siANXA7 to reduce the protein level of ANXA7 in brain tissue, the rates of brain edema, BBB damage, neuronal apoptosis, and death all declined. It was confirmed that ANXA7 promotes the development of SBI after TBI.

There are a few limitations to this study. The mechanism underlying the role of ANXA7 in TBI brain injury is unclear. ANXA7 mainly acts according to the Ca^{2+} concentration, and binding to the cell membrane. It can change the permeability of the cell membrane and promote protein release or transfer. In the case of Gerelsaikhan, the Snap-23 stabilized snare-complex plays an important role in neurotransmission (Gerelsaikhan et al., 2012). It is mainly distributed in the postsynaptic membrane in brain, and is the primary material engaged in the transportation of N-methyl-D-aspartic acid receptor (NMDA) receptors (Zhou et al., 2015). NMDA receptor is a subtype of glutamate receptor, which is the most important receptor to mediate Excitatory neurotoxicity (Lai et al., 2014; Newport et al., 2015). It can be speculated that A7 may participate in the process of excitatory neurotoxicity and promote nerve cell apoptosis in the SBI after TBI. The specific mechanism still needs further study. We expect this A7 study can help further understanding the mechanism of TBI, and the suppressive drugs of A7 may be helpful for clinical TBI treatment.

CONCLUSION

The results demonstrate that ANXA7 promotes the development of SBI after TBI. Based on this finding, we propose that ANXA7 might be a key physiological active substance after TBI brain damage, also we suggest that it could be a therapeutic target to SBI following TBI.

AUTHOR CONTRIBUTIONS

BD and RG designed the study. FG, DL, LT, QR, HN, FJ, and HL performed the research, collected and analyzed the data. FG wrote the paper. All authors discussed the results and revised the manuscript.

FUNDING

This work was supported by Youth Natural Science Foundation of Zhangjiagang Hospital of Traditional Chinese Medicine (zzyq1602), Zhangjiagang Science & Technology Pillar Program (ZKS1712).

ACKNOWLEDGMENTS

I would like to express my gratitude to all those who have helped me during the experiment and writing of this report. I gratefully acknowledge the help of BD and RG. I do appreciate their guidance, patience, and professional instruction as I completed my work. I would also like to thank DL, LT, QR, HN, FJ, and finally HL, who carefully taught me to perform experiments in laboratory settings.

REFERENCES

Brockman, E. C., Bayir, H., Blasiole, B., Shein, S. L., Fink, E. L., Dixon, C., et al. (2013). Polynitroxylated-pegylated hemoglobin attenuates fluid requirements and brain edema in combined traumatic brain injury plus hemorrhagic shock in mice. *J. Cereb. Blood Flow Metab*. 33, 1457–1464. doi: 10.1038/jcbfm.2013.104

Dash, P. K., Zhao, J., Kobori, N., Redell, J. B., Hylin, M. J., Hood, K. N., et al. (2016). Activation of alpha 7 cholinergic nicotinic receptors reduce blood-brain barrier permeability following experimental traumatic brain injury. *J. Neurosci.* 36, 2809–2818. doi: 10.1523/JNEUROSCI.3197-15.2016

Feigin, V. L., Theadom, A., Barker-Collo, S., Starkey, N. J., McPherson, K., Kahan, M., et al. (2013). Incidence of traumatic brain injury in New Zealand: a population-based study. *Lancet Neurol.* 12, 53–64. doi: 10.1016/S1474-4422(12)70262-4

Gerelsaikhan, T., Vasa, P. K., and Chander, A. (2012). Annexin A7 and SNAP23 interactions in alveolar type II cells and *in vitro*: a role for Ca(2+) and PKC. *Biochim. Biophys. Acta* 1823, 1796–1806. doi: 10.1016/j.bbamcr.2012.06.010

Guo, C., Liu, S., Greenaway, F., and Sun, M. Z. (2013). Potential role of annexin A7 in cancers. *Clin. Chim. Acta* 423, 83–89. doi: 10.1016/j.cca.2013.04.018

Hamasaki, M. Y., Machado, M. C. C., and Pinheiro Da Silva, F. (2017). Animal models of neuroinflammation secondary to acute insults originated outside the brain. *J. Neurosci. Res.* 96, 371–378. doi: 10.1002/jnr.24184

Herr, C., Clemen, C. S., Lehnert, G., Kutschkow, R., Picker, S. M., Gathof, B. S., et al. (2003). Function, expression and localization of annexin A7 in platelets and red blood cells: insights derived from an annexin A7 mutant mouse. *BMC Biochem.* 4:8. doi: 10.1186/1471-2091-4-8

Hoque, M., Rentero, C., Cairns, R., Tebar, F., Enrich, C., and Grewal, T. (2014). Annexins - scaffolds modulating PKC localization and signaling. *Cell. Signal.* 26, 1213–1225. doi: 10.1016/j.cellsig.2014.02.012

Lai, T. W., Zhang, S., and Wang, Y. T. (2014). Excitotoxicity and stroke: identifying novel targets for neuroprotection. *Prog. Neurobiol.* 115, 157–188. doi: 10.1016/j.pneurobio.2013.11.006

Liu, F., Chen, M. R., Liu, J., Zou, Y., Wang, T. Y., Zuo, Y. X., et al. (2016). Propofol administration improves neurological function associated with inhibition of pro-inflammatory cytokines in adult rats after traumatic brain injury. *Neuropeptides* 58, 1–6. doi: 10.1016/j.npep.2016.03.004

Moga, M. M., Dempah, D., and Zhou, D. (2005). Annexin 7-immunoreactive microglia in the hippocampus of control and adrenalectomized rats. *Neurosci. Lett.* 380, 42–47. doi: 10.1016/j.neulet.2005.01.022

Newport, D. J., Carpenter, L. L., McDonald, W. M., Potash, J. B., Tohen, M., Nemeroff, C. B., et al. (2015). Ketamine and other NMDA antagonists: early clinical trials and possible mechanisms in depression. *Am. J. Psychiatry* 172, 950–966. doi: 10.1176/appi.ajp.2015.15040465

Paul, G., Zachrisson, O., Varrone, A., Almqvist, P., Jerling, M., Lind, G., et al. (2015). Safety and tolerability of intracerebroventricular PDGF-BB in Parkinson's disease patients. *J. Clin. Invest.* 125, 1339–1346. doi: 10.1172/JCI79635

Pollard, H. B., and Rojas, E. (1988). Ca2+-activated synexin forms highly selective, voltage-gated Ca2+ channels in phosphatidylserine bilayer membranes. *Proc. Natl. Acad. Sci. U.S.A.* 85, 2974–2978. doi: 10.1073/pnas.85.9.2974

Raynal, P., and Pollard, H. B. (1994). Annexins: the problem of assessing the biological role for a gene family of multifunctional calcium- and phospholipid-binding proteins. *Biochim. Biophys. Acta* 1197, 63–93. doi: 10.1016/0304-4157(94)90019-1

Rick, M., Ramos Garrido, S. I., Herr, C., Thal, D. R., Noegel, A. A., and Clemen, C. S. (2005). Nuclear localization of Annexin A7 during murine brain development. *BMC Neurosci.* 6:25. doi: 10.1186/1471-2202-6-25

Tincani, A., Spatola, L., Cinquini, M., Meroni, P., Balestrieri, G., and Shoenfeld, Y. (1998). Animal models of antiphospholipid syndrome. *Rev. Rhum. Engl. Ed* 65, 614–618.

Turnay, J., Lecona, E., Fernandez-Lizarbe, S., Guzman-Aranguez, A., Fernandez, M. P., Olmo, N., et al. (2005). Structure-function relationship in annexin A13, the founder member of the vertebrate family of annexins. *Biochem. J.* 389, 899–911. doi: 10.1042/BJ20041918

Viviani, B., Boraso, M., Marchetti, N., and Marinovich, M. (2014). Perspectives on neuroinflammation and excitotoxicity: a neurotoxic conspiracy? *Neurotoxicology* 43, 10–20. doi: 10.1016/j.neuro.2014.03.004

Wang, Y., Chen, D., and Chen, G. (2014). Hyperbaric oxygen therapy applied research in traumatic brain injury: from mechanisms to clinical investigation. *Med. Gas Res.* 4:18. doi: 10.1186/2045-9912-4-18

Zhou, Q., Lai, Y., Bacaj, T., Zhao, M., Lyubimov, A. Y., Uervirojnangkoorn, M., et al. (2015). Architecture of the synaptotagmin-SNARE machinery for neuronal exocytosis. *Nature* 525, 62–67. doi: 10.1038/nature14975

Zhou, S. N., Li, C. S., Liu, L. Q., Li, Y., Wang, X. F., and Shen, L. (2011). Increased expression of annexin A7 in temporal lobe tissue of patients with refractory epilepsy. *Histol. Histopathol.* 26, 571–579. doi: 10.14670/HH-26.571

Conflict of Interest Statement: The authors declare that the research was conducted in the absence of any commercial or financial relationships that could be construed as a potential conflict of interest.

frontiers in Neuroscience

REVIEW
published: 08 June 2018
doi: 10.3389/fnins.2018.00392

The Role of Gaseous Molecules in Traumatic Brain Injury: An Updated Review

Xiaoru Che[1†], Yuanjian Fang[2†], Xiaoli Si[3], Jianfeng Wang[4], Xiaoming Hu[4], Cesar Reis[5,6] and Sheng Chen[2,4]*

[1] Department of Cardiology, Zhejiang Provincial People's Hospital, People's Hospital of Hangzhou Medical College, Hangzhou, China, [2] Department of Neurosurgery, The Second Affiliated Hospital, School of Medicine, Zhejiang University, Hangzhou, China, [3] Department of Neurology, The Second Affiliated Hospital, School of Medicine, Zhejiang University, Hangzhou, China, [4] Department of Neurosurgery, Taizhou Hospital, Wenzhou Medical University, Linhai, China, [5] Department of Physiology and Pharmacology, Loma Linda University, Loma Linda, CA, United States, [6] Department of Preventive Medicine, Loma Linda University Medical Center, Loma Linda, CA, United States

Traumatic brain injury (TBI) affects millions of people in China each year. TBI has a high mortality and often times a serious prognosis. The causative mechanisms of TBI during development and recovery from an injury remain vague, leaving challenges for the medical community to provide treatment options that improve prognosis and provide an optimal recovery. Biological gaseous molecules including nitric oxide (NO), carbon monoxide (CO), hydrogen sulfide (H_2S), and molecular hydrogen (H_2) have been found to play critical roles in physiological and pathological conditions in mammals. Accumulating evidence has found that these gaseous molecules can execute neuroprotection in many central nervous system (CNS) conditions due to their highly permeable properties allowing them to enter the brain. Considering the complicated mechanisms and the serious prognosis of TBI, effective and adequate therapeutic approaches are urgently needed. These four gaseous molecules can be potential attractive therapeutic intervention on TBI. In this review, we will present a comprehensive overview on the role of these four biological gasses in the development of TBI and their potential therapeutic applications.

Keywords: traumatic brain injury, gaseous molecules, neuroprotection, nitric oxide, carbon monoxide, hydrogen sulfide, molecular hydrogen, central nervous system

OPEN ACCESS

Edited by:
Gang Chen,
First Affiliated Hospital of Soochow University, China

Reviewed by:
Yujie Chen,
Army Medical University, China
Zhen-Ni Guo,
First Hospital, Jilin University, China

***Correspondence:**
Sheng Chen
saintchan@zju.edu.cn

† These authors have contributed equally to this work.

Specialty section:
This article was submitted to Neurodegeneration, a section of the journal Frontiers in Neuroscience

Received: *20 December 2017*
Accepted: *22 May 2018*
Published: *08 June 2018*

Citation:
Che X, Fang Y, Si X, Wang J, Hu X, Reis C and Chen S (2018) The Role of Gaseous Molecules in Traumatic Brain Injury: An Updated Review. Front. Neurosci. 12:392. doi: 10.3389/fnins.2018.00392

INTRODUCTION

Traumatic brain injury (TBI) affects 3–4 million people in China every year and accounts for 87% of deaths related to trauma. With its high mortality and serious prognosis, it is the fourth leading cause of death in young people (Liu, 2015). In addition, the incidence of TBI in the elderly appears to be increasing (Peeters et al., 2015). The causative mechanisms of TBI during development and recovery from an injury remain poorly understood. This poses great challenges for medical management following TBI, and leaves the medical community with challenges such as finding new treatment options to improve recovery following TBI (Seule et al., 2015; An et al., 2016).

Currently, various gaseous molecules (such as air content gasses, volatile anesthetics, non-volatile anesthetics, noble gasses) were thought to protect neural system in neurological diseases (Deng et al., 2014). Biological gaseous molecules, also referred as gasotransmitters, including

nitric oxide (NO), carbon monoxide (CO), hydrogen sulfide (H_2S), and molecular hydrogen (H_2), also serve critical roles in mammals' physiological and pathological conditions (Zhou et al., 2012). They can easily cross the blood–brain barrier (BBB) and spread through brain tissue due to their smaller molecular weights compared with chemically formulated drugs (Zhou et al., 2012; Deng et al., 2014). Accumulating evidence has demonstrated that these gaseous molecules provide neuroprotection in many diseases of the central nervous system (CNS) through different mechanisms and administration regimens (Ren et al., 2010; Charriaut-Marlangue et al., 2012; Zhan et al., 2012; Otterbein, 2013).

Considering the complicated mechanisms and the serious prognosis of TBI, effective and adequate therapeutic approaches are urgently needed. A better understanding of the physiological function and alterations of gaseous molecules in pathological conditions may provide a potentially attractive therapeutic intervention for TBI. In our review, we will present a comprehensive overview of the role of these four biological gasses in the development of TBI and their potential therapeutic applications.

NITRIC OXIDE

Nitric Oxide is the most recognized endogenous gasotransmitter in mammalian biology. It is mainly synthesized during L-arginine conversion with the assistance of three NO synthases (NOS): neuronal (n) NOS, inducible (i) NOS, and endothelial (e) NOS (Forstermann and Sessa, 2012). Despite nNOS being the predominant NO producer in CNS, iNOS, and eNOS can also be expressed in neurons and endothelial cells in the brain (Galea et al., 1992; Olivenza et al., 2000). NOS alteration leads to cerebral NO level changes and was found to be associated with TBI occurrence and secondary damage after TBI (Stover et al., 2014; Villalba et al., 2017). In addition, NO participates in the regulation of many biological process such as neurogenesis, cerebral blood flow (CBF) maintenance, oxidative stress reactions, and neuronal cell death (Uchiyama et al., 2002; Packer et al., 2003; Toda et al., 2009). Whether or not it has a protective or destructive role in the CNS remains controversial (Ockelford et al., 2016).

During pathophysiological processes in TBI, NO homeostasis is mainly mediated by NOS isoform activity (Cherian et al., 2004). eNOS and nNOS are constitutively expressed in the brain via induction of Ca^{++}, while iNOS becomes unregulated during brain damage or injury (Bredt and Snyder, 1990). Though the pathogenesis of TBI is driven by complex mechanisms, it was widely accepted that the inflammatory reaction is the main reason a response is elicited to brain injury (Corps et al., 2015). Inflammatory cascades promote expression of constitutive NOS isoforms and up-regulation of iNOS levels after TBI occurs (Olmos and Llado, 2014).

After TBI, the widespread brain injury may induce cell depolarization, such as rising extracellular potassium and intracellular Ca^{++} (Faden et al., 1989; Bezzi et al., 1998; Folkersma et al., 2011). Currently, studies suggest Ca^{++} accumulation can be mediated by the glutamate wave that follows TBI (Kawamata et al., 1992; Chamoun et al., 2010). Following inflammatory stimuli, extracellular glutamate concentrations in the brain tissue are markedly increased (Bezzi et al., 1998; Folkersma et al., 2011). These elevated glutamate levels were reported to be related to Ca^{++} influx and cytotoxicity during TBI (Chamoun et al., 2010). With the assistance of receptors such as NMDA receptors, the increased intracellular Ca^{++} consequently reacts with calmodulin and promotes the expression of constitutive NOS (Southam et al., 1991; Zur Nieden and Deitmer, 2006). This process appears in the early time period (30 min) of TBI sequela and contributes to the first NO peak (Marletta, 1994; Wada et al., 1998a). In addition, the NO produced by different constitutive NOS synthases may each contribute uniquely to the outcome. Activation of nNOS induces toxic effects that produce excitotoxicity and oxygen free radicals, such as Peroxynitrite ($ONOO^-$) to cause cell death (Wada et al., 1998a; Gahm et al., 2002). nNOS-derived NO is also involved in synaptic plasticity and neuronal signaling after TBI (Garthwaite, 1991). The function of eNOS-derived NO works against the toxic effect of nNOS-derived NO (Gahm et al., 2002). It participates in cerebrovascular responses by dilating blood vessels to maintain CBF (Goadsby et al., 1992; White et al., 2000). The expression of constitutive NOS isoforms also leads to transient hypertension surge through massive sympathetic discharge (Rosner et al., 1984).

In the later response phase, the inflammatory reaction following TBI induces the expression of iNOS (Minc-Golomb et al., 1994; Heneka and Feinstein, 2001). Normally, the response can be divided into two parts (Cherian et al., 2004). The first iNOS response starts 4 to 6 h after trauma, and peaks 8 to 23 h after TBI (Gahm et al., 2002; Ucal et al., 2017). iNOS expression may be associated with the increased amount of neutrophils and microglia during this response (Royo et al., 1999; Bayir et al., 2005). The second iNOS response starts 72 h after trauma and is related to the immunoreactivity of microglia and macrophages (Orihara et al., 2001). The waves of iNOS response peak 7 days following TBI (Wada et al., 1998b; Jin et al., 2012). The role of iNOS remains controversial, but many studies suggest that the NO released by iNOS can react with superoxide radicals and generate more deleterious reactive species, causing neuronal death and worsening neurological outcome (Sinz et al., 1999; Gorlach et al., 2000; Berka et al., 2014). In contrast to these detrimental effects, iNOS-derived NO also has the ability to attenuate oxidative stress reactions by preventing mitochondrial damage from reactive oxygen species (ROS) and decreasing redox iron activity (Bayir et al., 2005; Dungel et al., 2015).

Currently, the application of inhaled NO in TBI models is being investigated. Using closed head mild TBI mouse models, a study found that mild TBI induced a short-term memory loss and strong inflammatory reaction in the first 24 h after mild TBI. This injury only lasts for 2–3 days. Treatment with a low concentration and short duration (less than 8 h) of inhaled NO could prevent the adverse effects of mild TBI including acute and transient cognitive deficits and inflammation. Whereas, the group treated with a higher concentration of NO for 24 h showed no benefit in memory (Liu et al., 2013). Additionally, inhaled NO was shown

to significantly improve CBF and reduce intracranial pressure after TBI in mice. Long duration (24 h) inhalation reduced brain injury and improved neurological function (Terpolilli et al., 2013). Further investigation is warranted for the potential use of inhaled NO after TBI, particularly with regard to dosage and timing of administration (**Figure 1**).

CARBON MONOXIDE

Carbon Monoxide, traditionally thought of as a toxic gas, also acts as a gasotransmitter in both the extracellular and intracellular spaces. However, its biological function remains controversial (Coburn et al., 1963; Tenhunen et al., 1968). Heme oxygenase (HO) enzymes, including HO-1 and HO-2 are used in the process of heme degeneration and CO generation (Ewing and Maines, 1993; Li and Clark, 2000). HO-1, also named heat shock protein 32, is an inducible protein upregulated predominantly in numerous conditions of cellular stress. It was found to be up-regulated and play a cytoprotective role against oxidative stress after pediatric TBI (Cousar et al., 2006). In contrast, HO-2 is constitutively expressed in neural tissues (Geddes et al., 1996). While it was proved that HO-2 can prevent cellular injury after TBI via inhibition of oxidative stress (Chang et al., 2003). Despite this pathophysiological understanding, the role of CO remains poorly understood in the process of HO metabolism.

The measurement of CO fluctuation and cellular distribution after TBI has been recently studied. Accumulating evidence shows that HO can successfully increase CO production and response to cellular stress (Carratu et al., 2003; Chang et al., 2003; Kanu et al., 2006). CO production rapidly increases in the brain following induction of various pathophysiological conditions in the brain, including acute hypotension, hypoxia, glutamate metabolism, and glutamatergic seizures (Parfenova and Leffler, 2008). Additionally, CO was found to have different therapeutic functions in different brain pathologies.

As with NO, a very low concentration of CO can function as a vasodilator and a neurotransmitter in the brain (Zakhary et al., 1996; Leffler et al., 2006). Low concentrations of inhaled CO can prevent cerebral hypoxia and ischemia in occlusive cerebrovascular disease (Wang et al., 2011; Cai et al., 2017). Carbon monoxide-releasing molecules (CORMs)-A1 can reduce the inflammatory reaction in neuronal degenerative diseases (Chora et al., 2007). While in a mouse model of TBI, a recent study found that treatment with CORM-3 prevented the death of pericytes, thereby rescuing neural stem cells and ameliorating neurological impairment (Choi et al., 2016). The protective effect of CO appears to be related to the activation of sGC and NOS, namely cGMP and NO. However, a detailed mechanism was not described in these studies (Vieira et al., 2008; Queiroga et al., 2012; Schallner et al., 2013). In addition, CO inhibits oxidative apoptosis in the early phase following TBI by suppressing

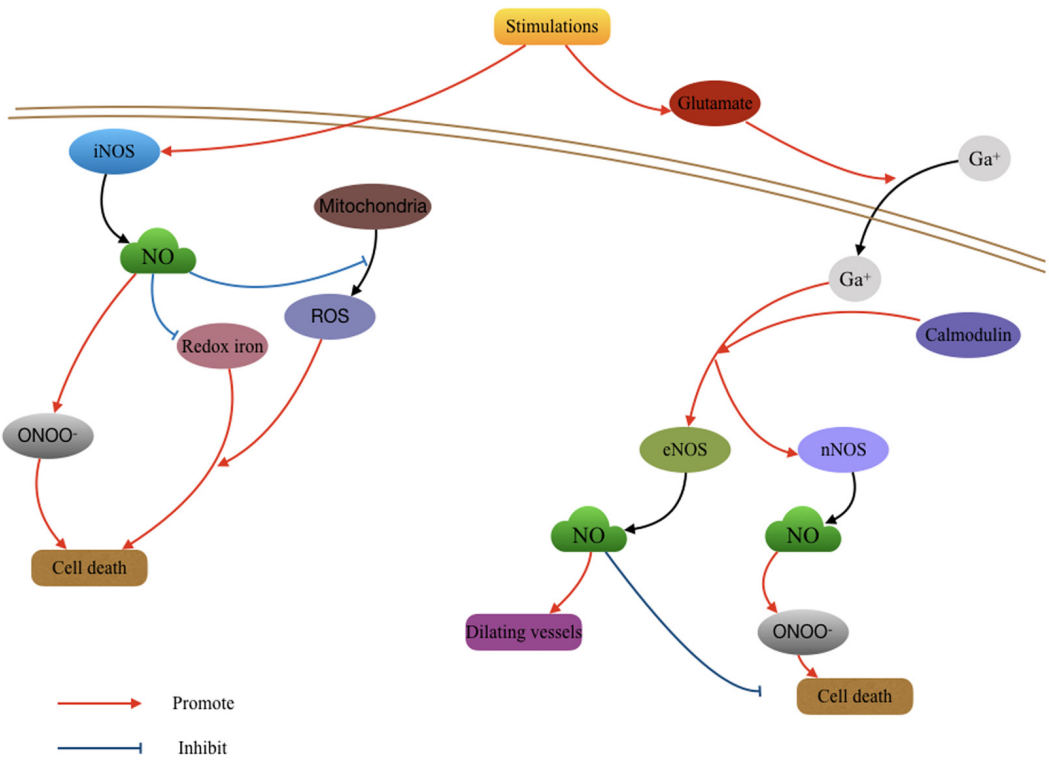

FIGURE 1 | Role of nitric oxide (NO) in the pathological changing after Traumatic brain injury (TBI). The activity of NO produced by different NO synthases (NOSs) function various effects in TBI. The deleterious effects of NO mainly resulted by the oxygen free radicals waves which subsequently caused cell death; the protective effects of NO may include vasodilatation and antioxidant effect.

potassium influx, caspases activation, and cytochrome c release (Dallas et al., 2011). CO can also increase the interaction between Nrf2 and HO-1, effectively promoting HO-1 expression and increased antioxidant responses (Wang et al., 2011; **Figure 2**).

In conclusion, the mechanisms of vasodilation, anti-inflammation, anti-apoptosis, anti-proliferation, and anti-oxidant effects of CO need to be further investigated in the TBI model as they are potential targets for therapeutic intervention in TBI. Inhaled CO was rarely applied in past studies since the inhaled form is not tissue specific and the unnecessary CO can bring partial systemic hypoxia and toxicity. These complications make CORMs potential donors of CO (Queiroga et al., 2015). Meanwhile, CO administration should be further investigated in the future pre-clinical or clinical studies.

HYDROGEN SULFIDE

Hydrogen Sulfide is another toxic gas that has important functions in physiological signal transduction (Liu H. et al., 2016). It can easily cross the cell membrane and enter intracellular compartments due to its high solubility in lipophilic solvents (Reiffenstein et al., 1992; Wang, 2002). H_2S is produced from the cysteine degradation process by two pyridoxal-5′-phosphate (PLP)-dependent enzymes, namely cystathionine β-synthase (CBS) and cystathionine γ-lyase (CSE). CBS is expressed primarily in the nervous system, liver and kidney. While CSE is expressed in the cardiovascular system and liver (Lowicka and Beltowski, 2007). In addition, brain H_2S was also found to be generated from cysteine with the assistance of 3-mercaptopyruvate sulfur transferase and cysteine amino transferase (Shibuya et al., 2009). It is involved in various biological functions after TBI including cerebrovascular regulation, oxidative stress reactions, inflammation, glutamate-mediated excitotoxicity, and apoptosis (Wang et al., 2014).

Recent studies demonstrated that the CBS and H_2S levels in the brain were decreased during the early phase (12–24 h) and increased in the late phase (3–7 days) after TBI (Jiang et al., 2013; Zhang et al., 2013). These changes were closely related to levels of oxidative stress and the pathogenesis of TBI (Scheff et al., 2013). CBS activity was found to be up-regulated via the Calcium/calmodulin pathway and enhanced H_2S production was found in response to glutamate (Eto and Kimura, 2002). However, CSE activity was less reported in the literature.

Using Sodium hydrosulfide (NaHS) as the H_2S source, a study found a significant difference between TBI and NaHS-treated TBI mice in measures of neuronal morphology and the density of the hippocampus (Zhang et al., 2013). 90 or 180 μmol/kg of NaHS treatment can significantly reduce loss of the brain tissue and protect against the neuron damage. It suggested that H_2S is also a neuroprotective gas for TBI treatment (Zhang et al., 2013). In addition, another study demonstrated that low dose NaHS (3 mg/kg) decreased the elevated BBB permeability, brain edema, and lesion volume in rats post-TBI. These effects were related to the activation of mitoK_{ATP} channels and reduction of oxidative stress. However, a higher dose of NaHS (10 mg/kg) gave a worse outcome in this study, which draws attention to the importance of dosage of H_2S supplement (Jiang et al., 2013). Furthermore, H_2S was proved able to exert neuroprotection via inhibiting microglia activation following inflammatory effects

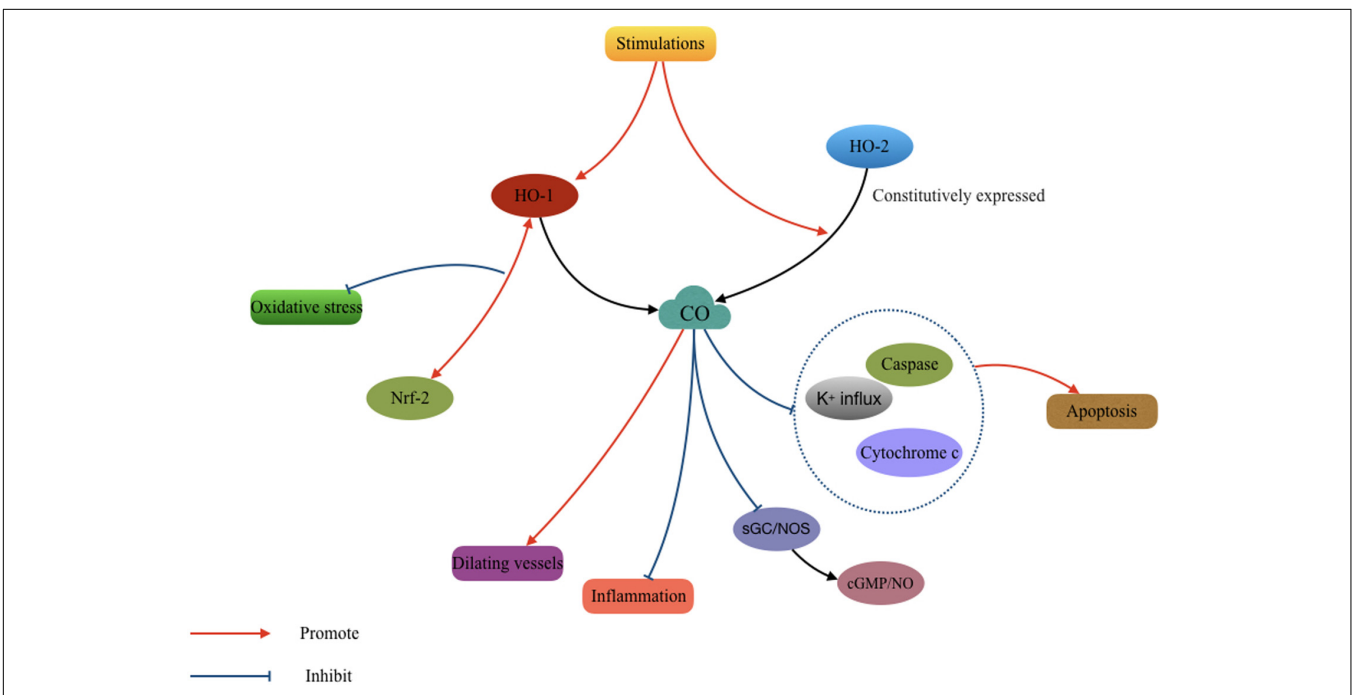

FIGURE 2 | Mechanisms involved in the cytoprotective effect of carbon monoxide (CO) after TBI. The CO produced by heme oxygenase (HO) isozymes participated in the process of antioxidantien, anti-inflammation, anti-apoptosis, and vasodilatation.

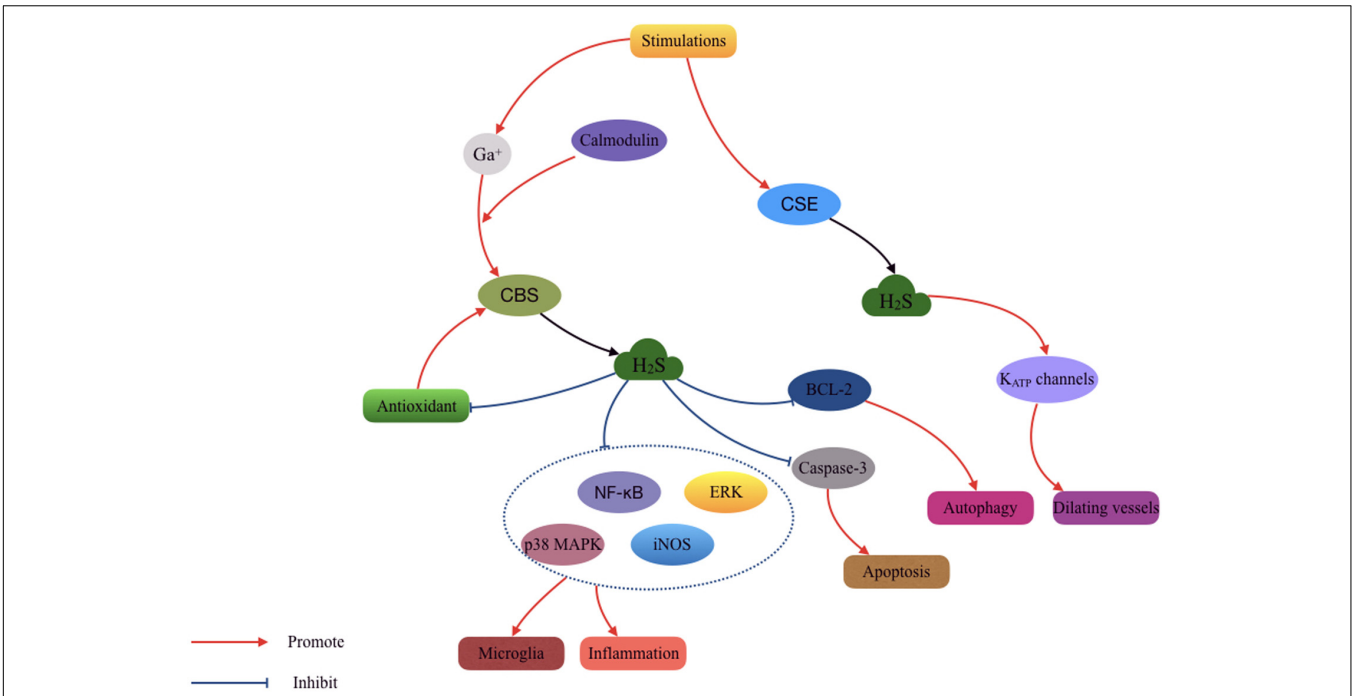

FIGURE 3 | Mechanisms involved in the cytoprotective effect of hydrogen sulfide (H_2S) after TBI. The H_2S produced by cystathionine γ-lyase (CSE) and cystathionine β-synthase (CBS) isozymes participated in the process of antioxidantien, anti-inflammation, anti-apoptosis, anti-autophagy, and vasodilatation.

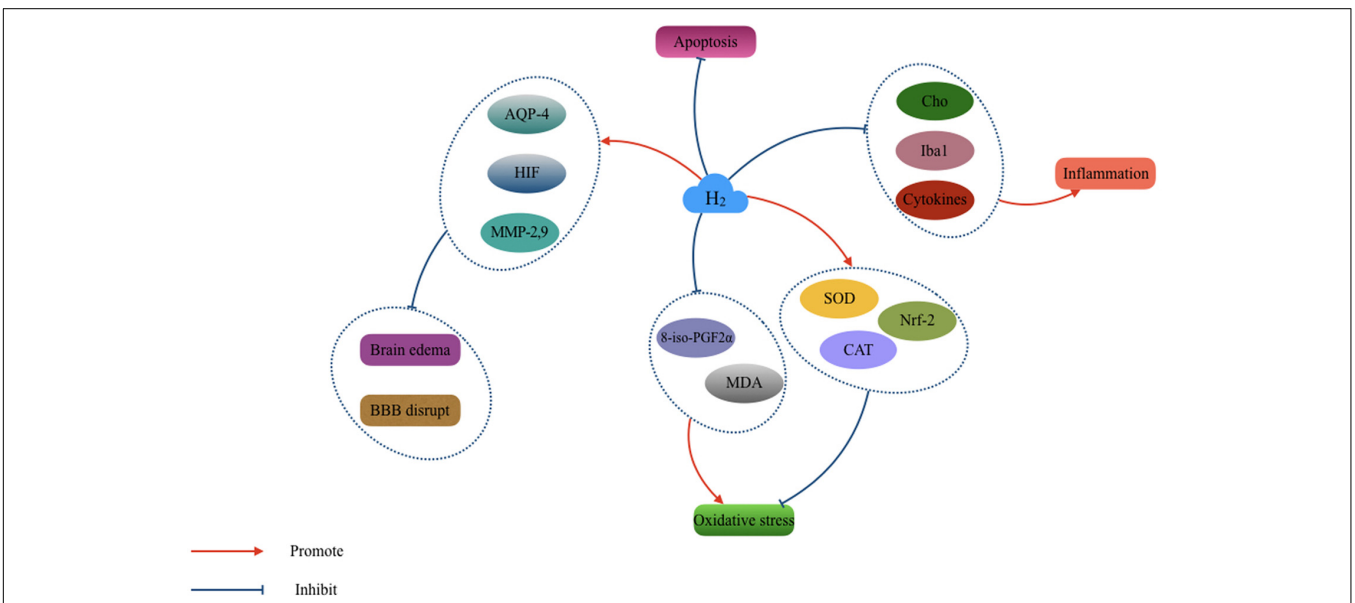

FIGURE 4 | The cytoprotective effect of H_2 in the pathological changing after TBI. hydrogen (H_2) acts essential role in the antioxidant, anti-inflammation, anti-apoptosis, and vasodilatation. It also can relieve the brain edema and blood–brain barrier (BBB) disruption after TBI.

and counteracts neurotoxicity. iNOS, NF-B, ERK, and p38 MAPK signaling pathways were inhibited in this process (Zhang Q. et al., 2014). Systemic administration of H_2S has also been shown to significantly reduce brain edema and behavioral symptoms by anti-apoptosis and anti-autophagy effects. H_2S reversed TBI-induced caspase-3 cleavage and Bcl-2 decline and prevented an increase in the Beclin-1/Bcl-2 ratio (Zhang M. et al., 2014; Fang et al., 2017).

In addition, low concentrations of H_2S may dilate cerebral vessels and protect against ischemia and hypoxia in the brain (Qu et al., 2006; Li et al., 2011). This effect is more likely led by CSE activation rather than CBS (Leffler et al., 2011). H_2S activates

K_{ATP} channels containing SUR2 subunits and acts on smooth muscle cells to promote vasodilation and subsequently maintain the CBF (Liang et al., 2011). However, fewer studies have investigated this effect in TBI models. The current understanding of the molecular mechanisms and biological roles of endogenous and exogenous H_2S remains poor. Also, the study investigating the role of H_2S-producing enzyme systems in TBI is unclear. This may be an area of focus in future H_2S studies after TBI. Additionally, the use of NaHS and H_2S in the clinical application requires optimal and safe concentration recommendations and strategy. Even a very low concentration (50 ppm) of inhaled H_2S could lead to intense damage due to its high solubility. Thus, direct inhalation of H_2S is not available (Qu et al., 2008; **Figure 3**).

HYDROGEN

Hydrogen (H_2) provides potential protective roles in neural diseases such as ischemic or hemorrhagic stroke (Cai et al., 2008; Zhan et al., 2012), TBI (Ji et al., 2010), CO poisoning (Sun et al., 2011), and neurodegenerative diseases (Fu et al., 2009). The underlying mechanisms may involve anti-oxygenation, anti-inflammation, anti-apoptosis effects, and BBB protection (Deng et al., 2014; Liu C.L. et al., 2016). The solubility of H_2 is low in the normal environment, and no/few endogenous cells produce H_2 in the mammalian CNS (Levitt, 1969; Sahakian et al., 2010). The therapeutic use of exogenous H_2 in neural diseases is under investigation. The main donor of exogenous H_2 in past research includes intravenous fluid of hydrogen-rich saline (Ono et al., 2011), potable H_2 water (Ishibashi et al., 2012), and inhaled H_2 gas (Nakao et al., 2010).

Inhalation of 2% H_2 from 5 min to 5 h after TBI was shown to attenuate BBB damage, brain edema, lesion volume, and improved neurological outcome. The potential mechanism might be associated with decreasing oxidative products (8-iso-PGF2α and MDA) and promotion of endogenous antioxidant enzymatic activity (SOD and CAT) (Ji et al., 2010). Similarly, another study found that 2.9% H_2 inhalation showed similar effects in brain tissues after surgery. However, this treatment failed to present the anti-oxidative or anti-inflammatory effects (Eckermann et al., 2011). In addition, hydrogen-rich saline facilitated synaptic plasticity and improved cognition after mild TBI. The hydrogen-rich saline protected TBI rat model through inhibition of oxidative damage and maintaining energy homeostasis (Hou et al., 2012). Recently, molecular hydrogen given in drinking water (mHW) was shown to relieve the acute alterations and neurodegenerative changes after TBI in a controlled cortical impact (CCI) model. The mHW alleviated brain edema, BBB disruption, and maintained normal brain interstitial fluid circulation. In addition, mHW increased ATP and nucleotide binding after TBI and inhibited pathological gene expressions that regulate oxidation/carbohydrate metabolism and suppressed cytokine activation (Dohi et al., 2014). In another study, pro-inflammatory cytokines (TNF-α, IL-1β, and HMGB1), inflammatory cell numbers (Iba1), and inflammatory metabolites (Cho) were attenuated, and anti-inflammatory cytokine (IL-10) was elevated after hydrogen-rich water therapy (Tian et al., 2016). In addition, H_2-rich water can also up-regulate the expression of Nrf2 which prevents oxidative damage in TBI-challenged rats (Yuan et al., 2015).

Based on the neuroprotective effects of H_2 published in the past, H_2 could be a promising therapy for clinical application (**Figure 4**). However, the adverse effects have not been well investigated. Researchers reported that some biological enzymes would decline upon ingestion of a certain concentration of H_2which may bring a potential toxicity. The intervention strategies and concentrations of H_2 used also differed among previous studies. Future studies should also focus on interactions between the anti-oxygenation, anti-inflammation, and anti-apoptosis effects induced by H_2 therapy.

CONCLUSION AND PROSPECTS

Biological gasses have smaller molecular weights compared to chemically formulated drugs. Thus, they can easily cross the BBB and diffuse to the brain tissues. Increasing evidence has demonstrated the potential clinical value of neuroprotective gasses in the treatment of neural diseases, including TBI. Endogenous gaseous are up-regulated during the pathological changes occurring after TBI, including redox reactions, inflammation, apoptosis, and excitotoxicity. Understanding the roles of endogenous gaseous molecules in different stages after TBI and determining an appropriate application strategy for exogenous gaseous molecules might provide us with more treatment options and significantly improve post TBI symptoms and outcome. However, the interaction between gasses and pathology is not well understood, and the application paradigms differ among published studies. The administration differences include in the gas source and gas ingestion methods, as well as the ideal concentrations needed for optimal results. In addition, safety and toxicity remain to be fully understood. Studies in this topic of TBI treatment could also focus on complicated aspects not studied or not elucidated in the current literature to help with the transition from current pre-clinical studies into future clinical studies.

AUTHOR CONTRIBUTIONS

SC was the principal investigator. XC and YF wrote the paper and made the original figures. XS and JW revised the figures. XH and CR handled the language and made some comments.

FUNDING

This study was supported by the National Natural Science Foundation of China (81500992), Natural Science Foundation of Zhejiang (LQ16H090002 and LY17H090012), Medical and Health Key Project of Zhejiang Province (2016RCA015), and Science & Research Program of Zhejiang Province (2015C33192).

REFERENCES

An, C., Jiang, X., Pu, H., Hong, D., Zhang, W., Hu, X., et al. (2016). Severity-dependent long-term spatial learning-memory impairment in a mouse model of traumatic brain injury. *Transl. Stroke Res.* 7, 512–520. doi: 10.1007/s12975-016-0483-5

Bayir, H., Kagan, V. E., Borisenko, G. G., Tyurina, Y. Y., Janesko, K. L., Vagni, V. A., et al. (2005). Enhanced oxidative stress in iNOS-deficient mice after traumatic brain injury: support for a neuroprotective role of iNOS. *J. Cereb. Blood Flow Metab.* 25, 673–684. doi: 10.1038/sj.jcbfm.9600068

Berka, V., Liu, W., Wu, G., and Tsai, A. L. (2014). Comparison of oxygen-induced radical intermediates in iNOS oxygenase domain with those from nNOS and eNOS. *J. Inorg. Biochem.* 139, 93–105. doi: 10.1016/j.jinorgbio.2014.06.011

Bezzi, P., Carmignoto, G., Pasti, L., Vesce, S., Rossi, D., Rizzini, B. L., et al. (1998). Prostaglandins stimulate calcium-dependent glutamate release in astrocytes. *Nature* 391, 281–285.

Bredt, D. S., and Snyder, S. H. (1990). Isolation of nitric oxide synthetase, a calmodulin-requiring enzyme. *Proc. Natl. Acad. Sci. U.S.A.* 87, 682–685. doi: 10.1073/pnas.87.2.682

Cai, J., Kang, Z., Liu, W. W., Luo, X., Qiang, S., Zhang, J. H., et al. (2008). Hydrogen therapy reduces apoptosis in neonatal hypoxia-ischemia rat model. *Neurosci. Lett.* 441, 167–172. doi: 10.1016/j.neulet.2008.05.077

Cai, W., Liu, H., Zhao, J., Chen, L. Y., Chen, J., Lu, Z., et al. (2017). Pericytes in brain injury and repair after ischemic stroke. *Transl. Stroke Res.* 8, 107–121. doi: 10.1007/s12975-016-0504-4

Carratu, P., Pourcyrous, M., Fedinec, A., Leffler, C. W., and Parfenova, H. (2003). Endogenous heme oxygenase prevents impairment of cerebral vascular functions caused by seizures. *Am. J. Physiol. Heart Circ. Physiol.* 285, H1148–H1157. doi: 10.1152/ajpheart.00091.2003

Chamoun, R., Suki, D., Gopinath, S. P., Goodman, J. C., and Robertson, C. (2010). Role of extracellular glutamate measured by cerebral microdialysis in severe traumatic brain injury. *J. Neurosurg.* 113, 564–570. doi: 10.3171/2009.12.JNS09689

Chang, E. F., Wong, R. J., Vreman, H. J., Igarashi, T., Galo, E., Sharp, F. R., et al. (2003). Heme oxygenase-2 protects against lipid peroxidation-mediated cell loss and impaired motor recovery after traumatic brain injury. *J. Neurosci.* 23, 3689–3696. doi: 10.1523/JNEUROSCI.23-09-03689.2003

Charriaut-Marlangue, C., Bonnin, P., Gharib, A., Leger, P. L., Villapol, S., Pocard, M., et al. (2012). Inhaled nitric oxide reduces brain damage by collateral recruitment in a neonatal stroke model. *Stroke* 43, 3078–3084. doi: 10.1161/STROKEAHA.112.664243

Cherian, L., Hlatky, R., and Robertson, C. S. (2004). Nitric oxide in traumatic brain injury. *Brain Pathol.* 14, 195–201. doi: 10.1111/j.1750-3639.2004.tb00053.x

Choi, Y. K., Maki, T., Mandeville, E. T., Koh, S. H., Hayakawa, K., Arai, K., et al. (2016). Dual effects of carbon monoxide on pericytes and neurogenesis in traumatic brain injury. *Nat. Med.* 22, 1335–1341. doi: 10.1038/nm.4188

Chora, A. A., Fontoura, P., Cunha, A., Pais, T. F., Cardoso, S., Ho, P. P., et al. (2007). Heme oxygenase-1 and carbon monoxide suppress autoimmune neuroinflammation. *J. Clin. Invest.* 117, 438–447. doi: 10.1172/JCI28844

Coburn, R. F., Blakemore, W. S., and Forster, R. E. (1963). Endogenous carbon monoxide production in man. *J. Clin. Invest.* 42, 1172–1178. doi: 10.1172/JCI104802

Corps, K. N., Roth, T. L., and Mcgavern, D. B. (2015). Inflammation and neuroprotection in traumatic brain injury. *JAMA Neurol.* 72, 355–362. doi: 10.1001/jamaneurol.2014.3558

Cousar, J. L., Lai, Y., Marco, C. D., Bayir, H., Adelson, P. D., Janesko-Feldman, K. L., et al. (2006). Heme oxygenase 1 in cerebrospinal fluid from infants and children after severe traumatic brain injury. *Dev. Neurosci.* 28, 342–347. doi: 10.1159/000094160

Dallas, M. L., Boyle, J. P., Milligan, C. J., Sayer, R., Kerrigan, T. L., Mckinstry, C., et al. (2011). Carbon monoxide protects against oxidant-induced apoptosis via inhibition of Kv2.1. *FASEB J.* 25, 1519–1530. doi: 10.1096/fj.10-173450

Deng, J., Lei, C., Chen, Y., Fang, Z., Yang, Q., Zhang, H., et al. (2014). Neuroprotective gases–fantasy or reality for clinical use? *Prog. Neurobiol.* 115, 210–245. doi: 10.1016/j.pneurobio.2014.01.001

Dohi, K., Kraemer, B. C., Erickson, M. A., Mcmillan, P. J., Kovac, A., Flachbartova, Z., et al. (2014). Molecular hydrogen in drinking water protects against neurodegenerative changes induced by traumatic brain injury. *PLoS One* 9:e108034. doi: 10.1371/journal.pone.0108034

Dungel, P., Perlinger, M., Weidinger, A., Redl, H., and Kozlov, A. V. (2015). The cytoprotective effect of nitrite is based on the formation of dinitrosyl iron complexes. *Free Radic. Biol. Med.* 89, 300–310. doi: 10.1016/j.freeradbiomed.2015.08.012

Eckermann, J. M., Chen, W., Jadhav, V., Hsu, F. P., Colohan, A. R., Tang, J., et al. (2011). Hydrogen is neuroprotective against surgically induced brain injury. *Med. Gas Res.* 1:7. doi: 10.1186/2045-9912-1-7

Eto, K., and Kimura, H. (2002). The production of hydrogen sulfide is regulated by testosterone and S-adenosyl-L-methionine in mouse brain. *J. Neurochem.* 83, 80–86. doi: 10.1046/j.1471-4159.2002.01097.x

Ewing, J. F., and Maines, M. D. (1993). Glutathione depletion induces heme oxygenase-1 (HSP32) mRNA and protein in rat brain. *J. Neurochem.* 60, 1512–1519. doi: 10.1111/j.1471-4159.1993.tb03315.x

Faden, A. I., Demediuk, P., Panter, S. S., and Vink, R. (1989). The role of excitatory amino acids and NMDA receptors in traumatic brain injury. *Science* 244, 798–800. doi: 10.1126/science.2567056

Fang, Y., Chen, S., Reis, C., and Zhang, J. (2017). The role of autophagy in subarachnoid hemorrhage: an update. *Curr. Neuropharmacol.* doi: 10.2174/1570159X15666170406142631 [Epub ahead of print].

Folkersma, H., Foster Dingley, J. C., Van Berckel, B. N., Rozemuller, A., Boellaard, R., Huisman, M. C., et al. (2011). Increased cerebral (R)-[(11)C]PK11195 uptake and glutamate release in a rat model of traumatic brain injury: a longitudinal pilot study. *J. Neuroinflammation* 8:67. doi: 10.1186/1742-2094-8-67

Forstermann, U., and Sessa, W. C. (2012). Nitric oxide synthases: regulation and function. *Eur. Heart J.* 33, 829–837, 837a–837d. doi: 10.1093/eurheartj/ehr304

Fu, Y., Ito, M., Fujita, Y., Ito, M., Ichihara, M., Masuda, A., et al. (2009). Molecular hydrogen is protective against 6-hydroxydopamine-induced nigrostriatal degeneration in a rat model of Parkinson's disease. *Neurosci. Lett.* 453, 81–85. doi: 10.1016/j.neulet.2009.02.016

Gahm, C., Holmin, S., and Mathiesen, T. (2002). Nitric oxide synthase expression after human brain contusion. *Neurosurgery* 50, 1319–1326.

Galea, E., Feinstein, D. L., and Reis, D. J. (1992). Induction of calcium-independent nitric oxide synthase activity in primary rat glial cultures. *Proc. Natl. Acad. Sci. U.S.A.* 89, 10945–10949. doi: 10.1073/pnas.89.22.10945

Garthwaite, J. (1991). Glutamate, nitric oxide and cell-cell signalling in the nervous system. *Trends Neurosci.* 14, 60–67. doi: 10.1016/0166-2236(91)90022-M

Geddes, J. W., Pettigrew, L. C., Holtz, M. L., Craddock, S. D., and Maines, M. D. (1996). Permanent focal and transient global cerebral ischemia increase glial and neuronal expression of heme oxygenase-1, but not heme oxygenase-2, protein in rat brain. *Neurosci. Lett.* 210, 205–208. doi: 10.1016/0304-3940(96)12703-8

Goadsby, P. J., Kaube, H., and Hoskin, K. L. (1992). Nitric oxide synthesis couples cerebral blood flow and metabolism. *Brain Res.* 595, 167–170. doi: 10.1016/0006-8993(92)91470-Y

Gorlach, C., Hortobagyi, T., Benyo, Z., and Wahl, M. (2000). Aminoguanidine reduces brain lesion volume after cold injury in the rat. *Pflugers Arch.* 440, 309–314. doi: 10.1007/s004240000293

Heneka, M. T., and Feinstein, D. L. (2001). Expression and function of inducible nitric oxide synthase in neurons. *J. Neuroimmunol.* 114, 8–18. doi: 10.1016/S0165-5728(01)00246-6

Hou, Z., Luo, W., Sun, X., Hao, S., Zhang, Y., Xu, F., et al. (2012). Hydrogen-rich saline protects against oxidative damage and cognitive deficits after mild traumatic brain injury. *Brain Res. Bull.* 88, 560–565. doi: 10.1016/j.brainresbull.2012.06.006

Ishibashi, T., Sato, B., Rikitake, M., Seo, T., Kurokawa, R., Hara, Y., et al. (2012). Consumption of water containing a high concentration of molecular hydrogen reduces oxidative stress and disease activity in patients with rheumatoid arthritis: an open-label pilot study. *Med. Gas Res.* 2:27. doi: 10.1186/2045-9912-2-27

Ji, X., Liu, W., Xie, K., Liu, W., Qu, Y., Chao, X., et al. (2010). Beneficial effects of hydrogen gas in a rat model of traumatic brain injury via reducing oxidative stress. *Brain Res.* 1354, 196–205. doi: 10.1016/j.brainres.2010.07.038

Jiang, X., Huang, Y., Lin, W., Gao, D., and Fei, Z. (2013). Protective effects of hydrogen sulfide in a rat model of traumatic brain injury via activation

of mitochondrial adenosine triphosphate-sensitive potassium channels and reduction of oxidative stress. *J. Surg. Res.* 184, e27–e35. doi: 10.1016/j.jss.2013.03.067

Jin, X., Ishii, H., Bai, Z., Itokazu, T., and Yamashita, T. (2012). Temporal changes in cell marker expression and cellular infiltration in a controlled cortical impact model in adult male C57BL/6 mice. *PLoS One* 7:e41892. doi: 10.1371/journal.pone.0041892

Kanu, A., Whitfield, J., and Leffler, C. W. (2006). Carbon monoxide contributes to hypotension-induced cerebrovascular vasodilation in piglets. *Am. J. Physiol. Heart Circ. Physiol.* 291, H2409–H2414. doi: 10.1152/ajpheart.01368.2005

Kawamata, T., Katayama, Y., Hovda, D. A., Yoshino, A., and Becker, D. P. (1992). Administration of excitatory amino acid antagonists via microdialysis attenuates the increase in glucose utilization seen following concussive brain injury. *J. Cereb. Blood Flow Metab.* 12, 12–24. doi: 10.1038/jcbfm.1992.3

Leffler, C. W., Parfenova, H., Basuroy, S., Jaggar, J. H., Umstot, E. S., and Fedinec, A. L. (2011). Hydrogen sulfide and cerebral microvascular tone in newborn pigs. *Am. J. Physiol. Heart Circ. Physiol.* 300, H440–H447. doi: 10.1152/ajpheart.00722.2010

Leffler, C. W., Parfenova, H., Jaggar, J. H., and Wang, R. (2006). Carbon monoxide and hydrogen sulfide: gaseous messengers in cerebrovascular circulation. *J. Appl. Physiol.* 100, 1065–1076. doi: 10.1152/japplphysiol.00793.2005

Levitt, M. D. (1969). Production and excretion of hydrogen gas in man. *N. Engl. J. Med.* 281, 122–127. doi: 10.1056/NEJM196907172810303

Li, X., and Clark, J. D. (2000). Heme oxygenase type 2 plays a role in formalin-induced nociception. *Pain* 86, 75–80. doi: 10.1016/S0304-3959(00)00238-4

Li, Z., Wang, Y., Xie, Y., Yang, Z., and Zhang, T. (2011). Protective effects of exogenous hydrogen sulfide on neurons of hippocampus in a rat model of brain ischemia. *Neurochem. Res.* 36, 1840–1849. doi: 10.1007/s11064-011-0502-6

Liang, G. H., Adebiyi, A., Leo, M. D., Mcnally, E. M., Leffler, C. W., and Jaggar, J. H. (2011). Hydrogen sulfide dilates cerebral arterioles by activating smooth muscle cell plasma membrane KATP channels. *Am. J. Physiol. Heart Circ. Physiol.* 300, H2088–H2095. doi: 10.1152/ajpheart.01290.2010

Liu, B. (2015). Current status and development of traumatic brain injury treatments in China. *Chin. J. Traumatol.* 18, 135–136. doi: 10.1016/j.cjtee.2015.04.002

Liu, C. L., Zhang, K., and Chen, G. (2016). Hydrogen therapy: from mechanism to cerebral diseases. *Med. Gas Res.* 6, 48–54. doi: 10.4103/2045-9912.179346

Liu, H., Wang, Y., Xiao, Y., Hua, Z., Cheng, J., and Jia, J. (2016). Hydrogen sulfide attenuates tissue plasminogen activator-induced cerebral hemorrhage following experimental stroke. *Transl. Stroke Res.* 7, 209–219. doi: 10.1007/s12975-016-0459-5

Liu, P., Li, Y. S., Quartermain, D., Boutajangout, A., and Ji, Y. (2013). Inhaled nitric oxide improves short term memory and reduces the inflammatory reaction in a mouse model of mild traumatic brain injury. *Brain Res.* 1522, 67–75. doi: 10.1016/j.brainres.2013.05.032

Lowicka, E., and Beltowski, J. (2007). Hydrogen sulfide (H2S) - the third gas of interest for pharmacologists. *Pharmacol. Rep.* 59, 4–24.

Marletta, M. A. (1994). Approaches toward selective inhibition of nitric oxide synthase. *J. Med. Chem.* 37, 1899–1907. doi: 10.1021/jm00039a001

Minc-Golomb, D., Tsarfaty, I., and Schwartz, J. P. (1994). Expression of inducible nitric oxide synthase by neurones following exposure to endotoxin and cytokine. *Br. J. Pharmacol.* 112, 720–722. doi: 10.1111/j.1476-5381.1994.tb13136.x

Nakao, A., Kaczorowski, D. J., Wang, Y., Cardinal, J. S., Buchholz, B. M., Sugimoto, R., et al. (2010). Amelioration of rat cardiac cold ischemia/reperfusion injury with inhaled hydrogen or carbon monoxide, or both. *J. Heart Lung Transplant.* 29, 544–553. doi: 10.1016/j.healun.2009.10.011

Ockelford, F., Saada, L., Gazit, E., and De Mel, A. (2016). Is nitric oxide assuming a Janus-face in the central nervous system? *Curr. Med. Chem.* 23, 1625–1637.

Olivenza, R., Moro, M. A., Lizasoain, I., Lorenzo, P., Fernandez, A. P., Rodrigo, J., et al. (2000). Chronic stress induces the expression of inducible nitric oxide synthase in rat brain cortex. *J. Neurochem.* 74, 785–791. doi: 10.1046/j.1471-4159.2000.740785.x

Olmos, G., and Llado, J. (2014). Tumor necrosis factor alpha: a link between neuroinflammation and excitotoxicity. *Mediators Inflamm.* 2014:861231. doi: 10.1155/2014/861231

Ono, H., Nishijima, Y., Adachi, N., Tachibana, S., Chitoku, S., Mukaihara, S., et al. (2011). Improved brain MRI indices in the acute brain stem infarct sites treated with hydroxyl radical scavengers, Edaravone and hydrogen, as compared to Edaravone alone. A non-controlled study. *Med. Gas Res.* 1:12. doi: 10.1186/2045-9912-1-12

Orihara, Y., Ikematsu, K., Tsuda, R., and Nakasono, I. (2001). Induction of nitric oxide synthase by traumatic brain injury. *Forensic Sci. Int.* 123, 142–149. doi: 10.1016/S0379-0738(01)00537-0

Otterbein, L. E. (2013). Quoth the Raven: carbon monoxide and nothing more. *Med. Gas Res.* 3:7. doi: 10.1186/2045-9912-3-7

Packer, M. A., Stasiv, Y., Benraiss, A., Chmielnicki, E., Grinberg, A., Westphal, H., et al. (2003). Nitric oxide negatively regulates mammalian adult neurogenesis. *Proc. Natl. Acad. Sci. U.S.A.* 100, 9566–9571. doi: 10.1073/pnas.1633579100

Parfenova, H., and Leffler, C. W. (2008). Cerebroprotective functions of HO-2. *Curr. Pharm. Des.* 14, 443–453. doi: 10.2174/138161208783597380

Peeters, W., Van Den Brande, R., Polinder, S., Brazinova, A., Steyerberg, E. W., Lingsma, H. F., et al. (2015). Epidemiology of traumatic brain injury in Europe. *Acta Neurochir.* 157, 1683–1696. doi: 10.1007/s00701-015-2512-7

Qu, K., Chen, C. P., Halliwell, B., Moore, P. K., and Wong, P. T. (2006). Hydrogen sulfide is a mediator of cerebral ischemic damage. *Stroke* 37, 889–893. doi: 10.1161/01.STR.0000204184.34946.41

Qu, K., Lee, S. W., Bian, J. S., Low, C. M., and Wong, P. T. (2008). Hydrogen sulfide: neurochemistry and neurobiology. *Neurochem. Int.* 52, 155–165. doi: 10.1016/j.neuint.2007.05.016

Queiroga, C. S., Tomasi, S., Wideroe, M., Alves, P. M., Vercelli, A., and Vieira, H. L. (2012). Preconditioning triggered by carbon monoxide (CO) provides neuronal protection following perinatal hypoxia-ischemia. *PLoS One* 7:e42632. doi: 10.1371/journal.pone.0042632

Queiroga, C. S., Vercelli, A., and Vieira, H. L. (2015). Carbon monoxide and the CNS: challenges and achievements. *Br. J. Pharmacol.* 172, 1533–1545. doi: 10.1111/bph.12729

Reiffenstein, R. J., Hulbert, W. C., and Roth, S. H. (1992). Toxicology of hydrogen sulfide. *Annu. Rev. Pharmacol. Toxicol.* 32, 109–134. doi: 10.1146/annurev.pa.32.040192.000545

Ren, C., Du, A., Li, D., Sui, J., Mayhan, W. G., and Zhao, H. (2010). Dynamic change of hydrogen sulfide during global cerebral ischemia-reperfusion and its effect in rats. *Brain Res.* 1345, 197–205. doi: 10.1016/j.brainres.2010.05.017

Rosner, M. J., Newsome, H. H., and Becker, D. P. (1984). Mechanical brain injury: the sympathoadrenal response. *J. Neurosurg.* 61, 76–86. doi: 10.3171/jns.1984.61.1.0076

Royo, N. C., Wahl, F., and Stutzmann, J. M. (1999). Kinetics of polymorphonuclear neutrophil infiltration after a traumatic brain injury in rat. *Neuroreport* 10, 1363–1367. doi: 10.1097/00001756-199904260-00038

Sahakian, A. B., Jee, S. R., and Pimentel, M. (2010). Methane and the gastrointestinal tract. *Dig. Dis. Sci.* 55, 2135–2143. doi: 10.1007/s10620-009-1012-0

Schallner, N., Romao, C. C., Biermann, J., Lagreze, W. A., Otterbein, L. E., Buerkle, H., et al. (2013). Carbon monoxide abrogates ischemic insult to neuronal cells via the soluble guanylate cyclase-cGMP pathway. *PLoS One* 8:e60672. doi: 10.1371/journal.pone.0060672

Scheff, S. W., Ansari, M. A., and Roberts, K. N. (2013). Neuroprotective effect of Pycnogenol(R) following traumatic brain injury. *Exp. Neurol.* 239, 183–191. doi: 10.1016/j.expneurol.2012.09.019

Seule, M., Brunner, T., Mack, A., Hildebrandt, G., and Fournier, J. Y. (2015). Neurosurgical and intensive care management of traumatic brain injury. *Facial Plast. Surg.* 31, 325–331. doi: 10.1055/s-0035-1562884

Shibuya, N., Tanaka, M., Yoshida, M., Ogasawara, Y., Togawa, T., Ishii, K., et al. (2009). 3-Mercaptopyruvate sulfurtransferase produces hydrogen sulfide and bound sulfane sulfur in the brain. *Antioxid. Redox Signal.* 11, 703–714. doi: 10.1089/ars.2008.2253

Sinz, E. H., Kochanek, P. M., Dixon, C. E., Clark, R. S., Carcillo, J. A., Schiding, J. K., et al. (1999). Inducible nitric oxide synthase is an endogenous neuroprotectant after traumatic brain injury in rats and mice. *J. Clin. Invest.* 104, 647–656. doi: 10.1172/JCI6670

Southam, E., East, S. J., and Garthwaite, J. (1991). Excitatory amino acid receptors coupled to the nitric oxide/cyclic GMP pathway in rat cerebellum during development. *J. Neurochem.* 56, 2072–2081. doi: 10.1111/j.1471-4159.1991.tb03468.x

Stover, J. F., Belli, A., Boret, H., Bulters, D., Sahuquillo, J., Schmutzhard, E., et al. (2014). Nitric oxide synthase inhibition with the antipterin VAS203 improves

outcome in moderate and severe traumatic brain injury: a placebo-controlled randomized Phase IIa trial (NOSTRA). *J. Neurotrauma* 31, 1599–1606. doi: 10.1089/neu.2014.3344

Sun, Q., Cai, J., Zhou, J., Tao, H., Zhang, J. H., Zhang, W., et al. (2011). Hydrogen-rich saline reduces delayed neurologic sequelae in experimental carbon monoxide toxicity. *Crit. Care Med.* 39, 765–769. doi: 10.1097/CCM.0b013e318206bf44

Tenhunen, R., Marver, H. S., and Schmid, R. (1968). The enzymatic conversion of heme to bilirubin by microsomal heme oxygenase. *Proc. Natl. Acad. Sci. U.S.A.* 61, 748–755. doi: 10.1073/pnas.61.2.748

Terpolilli, N. A., Kim, S. W., Thal, S. C., Kuebler, W. M., and Plesnila, N. (2013). Inhaled nitric oxide reduces secondary brain damage after traumatic brain injury in mice. *J. Cereb. Blood Flow Metab.* 33, 311–318. doi: 10.1038/jcbfm.2012.176

Tian, R., Hou, Z., Hao, S., Wu, W., Mao, X., Tao, X., et al. (2016). Hydrogen-rich water attenuates brain damage and inflammation after traumatic brain injury in rats. *Brain Res.* 1637, 1–13. doi: 10.1016/j.brainres.2016.01.029

Toda, N., Ayajiki, K., and Okamura, T. (2009). Cerebral blood flow regulation by nitric oxide: recent advances. *Pharmacol. Rev.* 61, 62–97. doi: 10.1124/pr.108.000547

Ucal, M., Kraitsy, K., Weidinger, A., Paier-Pourani, J., Patz, S., Fink, B., et al. (2017). Comprehensive profiling of modulation of nitric oxide levels and mitochondrial activity in the injured brain: an experimental study based on the fluid percussion injury model in rats. *J. Neurotrauma* 34, 475–486. doi: 10.1089/neu.2016.4411

Uchiyama, T., Otani, H., Okada, T., Ninomiya, H., Kido, M., Imamura, H., et al. (2002). Nitric oxide induces caspase-dependent apoptosis and necrosis in neonatal rat cardiomyocytes. *J. Mol. Cell Cardiol.* 34, 1049–1061. doi: 10.1006/jmcc.2002.2045

Vieira, H. L., Queiroga, C. S., and Alves, P. M. (2008). Pre-conditioning induced by carbon monoxide provides neuronal protection against apoptosis. *J. Neurochem.* 107, 375–384. doi: 10.1111/j.1471-4159.2008.05610.x

Villalba, N., Sackheim, A. M., Nunez, I. A., Hill-Eubanks, D. C., Nelson, M. T., Wellman, G. C., et al. (2017). Traumatic brain injury causes endothelial dysfunction in the systemic microcirculation through arginase-1-dependent uncoupling of endothelial nitric oxide synthase. *J. Neurotrauma* 34, 192–203. doi: 10.1089/neu.2015.4340

Wada, K., Chatzipanteli, K., Busto, R., and Dietrich, W. D. (1998a). Role of nitric oxide in traumatic brain injury in the rat. *J. Neurosurg.* 89, 807–818.

Wada, K., Chatzipanteli, K., Kraydieh, S., Busto, R., and Dietrich, W. D. (1998b). Inducible nitric oxide synthase expression after traumatic brain injury and neuroprotection with aminoguanidine treatment in rats. *Neurosurgery* 43, 1427–1436.

Wang, B., Cao, W., Biswal, S., and Dore, S. (2011). Carbon monoxide-activated Nrf2 pathway leads to protection against permanent focal cerebral ischemia. *Stroke* 42, 2605–2610. doi: 10.1161/STROKEAHA.110.607101

Wang, J. F., Li, Y., Song, J. N., and Pang, H. G. (2014). Role of hydrogen sulfide in secondary neuronal injury. *Neurochem. Int.* 64, 37–47. doi: 10.1016/j.neuint.2013.11.002

Wang, R. (2002). Two's company, three's a crowd: can H2S be the third endogenous gaseous transmitter? *FASEB J.* 16, 1792–1798. doi: 10.1096/fj.02-0211hyp

White, R. P., Vallance, P., and Markus, H. S. (2000). Effect of inhibition of nitric oxide synthase on dynamic cerebral autoregulation in humans. *Clin. Sci.* 99, 555–560. doi: 10.1042/cs0990555

Yuan, J., Wang, D., Liu, Y., Chen, X., and Zhang, H. (2015). Effects of hydrogen rich water on the expression of Nrf 2 and the oxidative stress in rats with traumatic brain injury. *Zhonghua Wei Zhong Bing Ji Jiu Yi Xue* 27, 911–915.

Zakhary, R., Gaine, S. P., Dinerman, J. L., Ruat, M., Flavahan, N. A., and Snyder, S. H. (1996). Heme oxygenase 2: endothelial and neuronal localization and role in endothelium-dependent relaxation. *Proc. Natl. Acad. Sci. U.S.A.* 93, 795–798. doi: 10.1073/pnas.93.2.795

Zhan, Y., Chen, C., Suzuki, H., Hu, Q., Zhi, X., and Zhang, J. H. (2012). Hydrogen gas ameliorates oxidative stress in early brain injury after subarachnoid hemorrhage in rats. *Crit. Care Med.* 40, 1291–1296. doi: 10.1097/CCM.0b013e31823da96d

Zhang, M., Shan, H., Chang, P., Wang, T., Dong, W., Chen, X., et al. (2014). Hydrogen sulfide offers neuroprotection on traumatic brain injury in parallel with reduced apoptosis and autophagy in mice. *PLoS One* 9:e87241. doi: 10.1371/journal.pone.0087241

Zhang, M., Shan, H., Wang, T., Liu, W., Wang, Y., Wang, L., et al. (2013). Dynamic change of hydrogen sulfide after traumatic brain injury and its effect in mice. *Neurochem. Res.* 38, 714–725. doi: 10.1007/s11064-013-0969-4

Zhang, Q., Yuan, L., Liu, D., Wang, J., Wang, S., Zhang, Q., et al. (2014). Hydrogen sulfide attenuates hypoxia-induced neurotoxicity through inhibiting microglial activation. *Pharmacol. Res.* 84, 32–44. doi: 10.1016/j.phrs.2014.04.009

Zhou, J., Wu, P. F., Wang, F., and Chen, J. G. (2012). Targeting gaseous molecules to protect against cerebral ischaemic injury: mechanisms and prospects. *Clin. Exp. Pharmacol. Physiol.* 39, 566–576. doi: 10.1111/j.1440-1681.2011.05654.x

Zur Nieden, R., and Deitmer, J. W. (2006). The role of metabotropic glutamate receptors for the generation of calcium oscillations in rat hippocampal astrocytes in situ. *Cereb. Cortex* 16, 676–687. doi: 10.1093/cercor/bhj013

Conflict of Interest Statement: The authors declare that the research was conducted in the absence of any commercial or financial relationships that could be construed as a potential conflict of interest.

frontiers in Neuroscience

ORIGINAL RESEARCH
published: 19 June 2018
doi: 10.3389/fnins.2018.00414

Sirt3 Ameliorates Oxidative Stress and Mitochondrial Dysfunction After Intracerebral Hemorrhage in Diabetic Rats

Jingwei Zheng[1†], Ligen Shi[1†], Feng Liang[1], Weilin Xu[1], Tao Li[1], Liansheng Gao[1], Zeyu Sun[1], Jun Yu[1] and Jianmin Zhang[1,2,3]**

[1] Department of Neurosurgery, The Second Affiliated Hospital, Zhejiang University School of Medicine, Hangzhou, China, [2] Brain Research Institute, Zhejiang University, Hangzhou, China, [3] Collaborative Innovation Center for Brain Science, Zhejiang University, Hangzhou, China

Aim: Sirtuin3 (sirt3) plays a pivotal role in improving oxidative stress and mitochondrial dysfunction which directly induced neuronal apoptosis after intracerebral hemorrhage (ICH). Reactive oxygen species (ROS) is also a critical activator in triggering NACHT, LRR, and PYD domains-containing protein 3 (NLRP3) inflammasomes activation which can regulate inflammatory responses in brain. Moreover, hyperglycemia can aggravate the ICH-induced damage. Hence, this study was designed to investigate the mechanisms of neuroprotection of sirt3 in hyperglycemic ICH.

Methods: ICH model was established by autologous blood injection. Hyperglycemia was induced by intraperitoneal injection with streptozotocin. Honokiol (HKL, a pharmacological agonist of sirt3) was injected intraperitoneally at doses of 2.5, 5, or 10 mg/kg. Sirt3 small interfering RNA transfection was implemented through intracerebroventricular injection. The expression of sirt3 and its downstream signaling molecules were detected using Western blotting or immunofluorescence staining. Morphological changes of mitochondria were detected by electron microscopy. SH-SY5Y cells were incubated with 10 μM oxyhemoglobin for 48 h to establish an *in vitro* ICH model, and then JC-1 staining was used to determine mitochondrial membrane potential ($\Delta\psi m$).

Results: Hyperglycemia could suppress sirt3 expression after ICH when compared with non-diabetic rats. Sirt3 protein expression was decreased to the minimum at 24 h in perihematoma tissues. Electron microscope analysis indicated that hyperglycemic ICH induced extensive mitochondrial vacuolization. HKL attenuated ROS accumulation, adenosine triphosphate reduction, and $\Delta\psi m$ through Sirt3–superoxide dismutase 2 (SOD2) and Sirt3–NRF1–TFAM pathway. Sirt3 knockdown could exacerbate the neuronal apoptosis and reverse the positive effects of HKL. Sirt3 activation could decrease NLRP3 and interleukin-1β levels through deacetylating SOD2 and scavenging ROS.

Conclusion: HKL protects against hyperglycemic ICH-induced neuronal injury via a sirt3-dependent manner.

Keywords: ICH, hyperglycemia, sirt3, mitochondrial dysfunction, oxidative stress

OPEN ACCESS

Edited by:
Hua Feng,
Army Medical University, China

Reviewed by:
Gang Chen,
The First Affiliated Hospital of Soochow University, China
Ye Xiong,
Henry Ford Hospital, United States
Zezong Gu,
University of Missouri, United States

****Correspondence:***
Jun Yu
2505020@zju.edu.cn
Jianmin Zhang
zjm135@zju.edu.cn

† These authors have contributed equally to this work.

Specialty section:
This article was submitted to Neurodegeneration, a section of the journal Frontiers in Neuroscience

Received: *07 April 2018*
Accepted: *30 May 2018*
Published: *19 June 2018*

Citation:
Zheng J, Shi L, Liang F, Xu W, Li T, Gao L, Sun Z, Yu J and Zhang J (2018) Sirt3 Ameliorates Oxidative Stress and Mitochondrial Dysfunction After Intracerebral Hemorrhage in Diabetic Rats. Front. Neurosci. 12:414. doi: 10.3389/fnins.2018.00414

INTRODUCTION

Intracerebral hemorrhage (ICH) is a serious public health problem with high rates of death and disability, and it accounts for 10–20% of stroke worldwide (Qureshi et al., 2009; van Asch et al., 2010). Perihematoma edema is the main manifestation of secondary brain injury (SBI) after ICH, and it may cause poor prognosis from increased intracranial pressure or hydrocephalus (Inaji et al., 2003; Murthy et al., 2015). Complicated mechanisms are involved in the formation of brain edema. The initial hematoma induces glutamate release and then leads to oxidative stress and mitochondrial dysfunction. Mitochondrial dysfunction may contribute to the deficiency of adenosine triphosphate (ATP) generation and then result in the failure of cellular pumps causing cytotoxic edema and neuronal apoptosis (Kim-Han et al., 2006; Brunswick et al., 2012; Prentice et al., 2015; Duan et al., 2016). Moreover, mitochondrial dysfunction caused the dysregulation of reactive oxygen species (ROS) homeostasis, ROS accumulation further caused damage in mitochondria, and persistence of vicious circles (Brunswick et al., 2012). NACHT, LRR, and PYD domains-containing protein 3 (NLRP3) inflammasomes are associated with inflammatory responses and cellular injury after ischemic stroke or ICH (Ma et al., 2014). Sufficient evidence demonstrated that ROS is a crucial activator in triggering NLRP3 activation (Chen et al., 2017; Gao et al., 2017). ROS scavenging may be an effective method in inhibiting neuroinflammation. Hence, oxidative stress and mitochondrial dysfunction may be the potential breakthrough in treatment of ICH injury.

Notably, factors such as diabetes mellitus, high blood pressure, and alcohol intake are thought to be predictors of poor outcomes after ICH (Kimura et al., 2007). Several studies also demonstrate that hyperglycemia is associated with severe brain edema and increased level of cell apoptosis in animal models of ICH (Song et al., 2003; Chiu et al., 2013). In addition, hyperglycemia can independently increase the risk of early death in patients with acute spontaneous ICH (Kimura et al., 2007). High blood glucose (HG) can also exacerbate stroke and reperfusion injury through oxidative stress and energy metabolism pathway (Robbins and Swanson, 2014). *In vitro*, hyperglycemia may also results in the activation of ROS and cause the dysregulation of mitochondrial membrane potential which precedes the neuronal apoptosis (Russell et al., 2002). Thus, it remains a great need to find a novel therapeutic target that may help dealing with SBI and hyperglycemia-induced damage in diabetic ICH patients.

Sirtuin3 (sirt3) is a NAD^+-dependent deacetylase predominately located in mitochondria. Simultaneously, sirt3 could maintain ROS homeostasis through the regulation of a variety of mitochondrial enzymes such as superoxide dismutase 2 (SOD2), which may transform harmful superoxide radicals into nontoxic oxygen or hydrogen peroxide (Qiu et al., 2010; Bause and Haigis, 2013). In addition, sirt3 was also involved in the mitochondrial basal ATP production through the respiratory chain and ATP synthase pathway (Ahn et al., 2008; Giralt and Villarroya, 2012). Moreover, it could react with peroxisome-proliferator-activated receptor-γ co-activator-1α (PGC-1α) which is the crucial controller of mitochondrial biogenesis, and then participated in the regulation of oxidative metabolism (Kong et al., 2010). Notably, a recent study demonstrated that hyperglycemia could inhibit sirt3 expression in retinal capillary endothelial cells and caused worse oxidative stress injury (Gao et al., 2016). A pervious study also indicated that cerebral AQP-4 expression was downregulated after hyperglycemic ICH in rats (Chiu et al., 2013). Gao et al. (2016) thought that hyperglycemia could result in the activation of poly ADP-ribose polymerase (PARP) which competitively utilized the same cofactor (NAD^+) with sirt3. However, the reason why hyperglycemia can suppress protein expression is still inconclusive. The above-mentioned observations inspired us that sirt3 may play a pivotal role in ICH-induced cerebral injury.

Honokiol (HKL) is a small molecular weight natural compound which can be extracted from *Magnolia grandiflora*. HKL is initially known for its anti-inflammatory, anti-cancerous, and antithrombotic properties (Woodbury et al., 2013). A recent study indicated that intraperitoneal administration of HKL could ameliorate cardiac hypertrophy by activating sirt3. Pharmaceutically, HKL could directly bind to sirt3 and increase sirt3 levels and its enzymatic activity (Pillai et al., 2015). Whether HKL administration can upregulate sirt3 levels and exert neuroprotection in hyperglycemic ICH rats has never been studied. Therefore, this study was designed to: (1) investigate whether hyperglycemia affects sirt3 expression after ICH and (2) explore whether HKL ameliorates oxidative stress and mitochondrial dysfunction via a sirt3-dependent manner.

MATERIALS AND METHODS

Animals

Adult male Sprague-Dawley rats (300–350 g) which were obtained from Slac Laboratory Co., Ltd. (Shanghai, China) were used for this study. A total of 288 rats were used for this study, and the details of grouping information were shown in **Supplementary Figure S1**. Sprague-Dawley rats were raised in triples in plastic cages with controlled temperature and humidity and a 12-h light/dark cycle. All animal experimental protocols were in compliance with the *Guide for the Care and Use of Laboratory Animals* of the National Institutes of Health and were approved by the Institutional Animal Care and Use Committee of Zhejiang University.

Hyperglycemia and ICH Model

Diabetic model was induced by intraperitoneal injection with streptozotocin (STZ; Sigma-S0130, Sigma–Aldrich Trading Co., Ltd., Shanghai, China) at 60 mg/kg for 3 days before operation (Chiu et al., 2013). Blood glucose was measured by OneTouch Select Test Strips (Johnson & Johnson) with the tail venous blood after overnight fasting, and hyperglycemia was defined as blood glucose $>$250mg/dl (Liu et al., 2011).

Sprague-Dawley rats were anesthetized with intraperitoneal pentobarbital (50 mg/kg) and experimental ICH surgery was induced in a stereotaxic frame (Stoelting Stereotaxic Instrument). A 1-mm-diameter burr hole was made in the skull (0.2 mm posterior to bregma and 3.5 mm right lateral to midline), then

100 μl fresh autologous blood (catheterization to femoral artery with PE10 tube) was injected into the right basal ganglia (5.5 mm depth below the skull) with a micro-injector within 5 min. In case of blood leakage, the needle would stay for another 10 min after complete injection, then the burr hole was blocked with bone wax (Yang et al., 1994; Song et al., 2003; Chiu et al., 2013). The rats in sham group received all the above-mentioned procedures but the 100 μl saline was injected instead of fresh autologous blood.

Small Interfering RNA and Intracerebroventricular Injection

In vivo: The sirt3 siRNA or scramble siRNA (Thermo Fisher Scientific) mixed with the transfection reagent (Engreen Biosystem Co., Ltd.; 500 pmol/10 μl) was injected into the right lateral ventricle at a rate of 2 μl/min 24 h before ICH (Zheng et al., 2015). The intracerebroventricular injection was performed as previously reported (Xu et al., 2017). After the rats were anesthetized with intraperitoneal pentobarbital (50 mg/kg), a 1-mm-diameter burr hole was made in the skull (1 mm posterior to bregma and 1.5 mm right lateral to midline). Then, 10 μl of the mixture of siRNA and transfection reagent was infused into the right lateral ventricle (3.5 mm depth below the skull). The needle stayed in the brain for another 10 min after injection and the burr hole was blocked with bone wax.

In vitro: SH-SY5Y cells were transfected with sirt3 siRNA or control siRNA (Thermo Fisher Scientific) mixed with the transfection reagent (Engreen Biosystem Co., Ltd.; final concentration: 100 nM).

Drug Administration

In vivo: HKL (Purity ≥ 98%, Sigma-H4914, Sigma–Aldrich Trading Co., Ltd., Shanghai, China) was dissolved in dimethyl sulfoxide (DMSO):phosphate-buffered saline (PBS) (1:1) and injected intraperitoneally at a dose of 2.5, 5, or 10 mg/kg immediately at 15 min before inducing ICH and 60 min after ICH (Harada et al., 2012; Sulakhiya et al., 2014). Vehicle rats (ICH + vehicle) received intraperitoneal injections of the same volumes of DMSO:PBS (1:1).

In vitro: SH-SY5Y cells were pre-incubated with 10 μM HKL (dissolved in DMSO:PBS = 1:1) for 6 h and then co-treatment with 10 μM oxyhemoglobin (OxyHb, Solarbio, H8020) for an additional 48 h. The control cells received the same volumes of DMSO:PBS (1:1).

Cell Culture

The human neuroblastoma SH-SY5Y cells were cultured (37°C, 5% CO_2) in DMEM/F12 (1:1) medium with 15% fetal bovine serum (FBS) and 100 U/ml penicillin. These cells were seeded in 5 * 5 cm^2 cell culture flask at a density range of 4×10^6/well − 5×10^6/well. Treatment of 10 μM OxyHb and 20 mM glucose for 48 h was used to induce an *in vitro* hyperglycemic ICH model (Meng et al., 2018).

Cell Viability: MTT Assay

Measurement of cell viability was determined using 3-(4,5-dimethylthiazol-2-yl)-2,5-diphenyltetrazolium bromide (MTT) assay kit (Beyotime, Shanghai, China). In brief, the SH-SY5Y cells grown in 96-well plates at a density range of 1×10^4/well − 3×10^4/well with a volume of culture medium measuring 100 μl/well were treated with 10 μl of MTT solution (5 mg MTT in 1 ml 0.01 M PBS, pH = 7.40); the mixture yield was then incubated at 37°C for 2 h. After incubation and discarding the medium, 100 μl of DMSO was added in each well to dissolve insoluble formazan. The cell viability was determined by measuring the absorbance at 570 nm using a microplate reader.

Measurement of Mitochondrial Membrane Potential ($\Delta\psi m$)

The SH-SY5Y cells planted in 96-well plates at a density range of 1×10^4/well − 3×10^4/well, then these cells were used for measuring $\Delta\psi m$. The $\Delta\psi m$ was measured by a JC-1 kit (Beyotime, Shanghai, China) following the manufacturer's instructions. SH-SY5Y cells were rinsed with PBS and incubated with JC-1 staining solution at 37°C for 20 min. Then, the inverted fluorescence microscope (Olympus, Tokyo, Japan) was used to capture the pictures and calculate the ratio of the red:green fluorescence.

Measurement of Brain Water Content

As described previously (Xu et al., 2017) to measure the brain water content after ICH, rats were sacrificed under deep pentobarbital anesthesia at 24 h after ICH. We swiftly removed the skull and take out brain tissues with removal of cerebellum and brain stem. Then the right hemispheres were immediately weighed (wet weight), and then dried at 100°C for 24 h in the Electro-Thermostatic Blast Oven. The dry weight of these brain tissues were acquired by reweighting. Ultimately, brain water content was calculated using the following formula: [(wet weight − dry weight)/wet weight] × 100.

Evaluation of Neurological Deficit

As described previously (Zhao et al., 2006) a combination score consisting of a battery of behavioral tests (foot fault, forelimb placing, postural reflex, and circling tests) was conducted as the comprehensive evaluation of the neurological functional deficits (NDSs). The NDS was performed before and at 1, 3, and 5 days after ICH. The final evaluation of neurological deficit (0–16) was the sum of the scores from the above-mentioned four tests. All the above-mentioned assessment was performed by an independent researcher who was blind to the experimental groups.

Immunofluorescence Staining and H&E Staining

Rats were sacrificed under deep pentobarbital anesthesia at 24 h after ICH, and then intracardially perfused with 0.1 mmol PBS and 4% paraformaldehyde (PFA). Coronal cryosections were preprocessed with 10% donkey serum and 0.3% triton X-100. Then the brain cryosections were incubated at 4°C with anti-sirt3 antibody (1:200, Abcam, ab86671), cleaved caspase-3 antibody (1:250, Cell Signaling Technology, CST#9661), Iba-1 (1:500, Abcam ab5076), NeuN (1:500, Abcam, ab177487). Twelve

hours later, cryosections were incubated with secondary antibody [Thermo Fisher Scientific, Donkey anti-Rabbit IgG (H+L) Alexa Fluor 488, Donkey anti-Mouse IgG (H+L) Alexa Fluor 594, Goat anti-Rabbit IgG (H+L) Alexa Fluor 488]. Then, the fluorescence microscope (Olympus, Tokyo, Japan) was used to capture the images.

As described previously (Xu et al., 2006) brain samples were dissected and embedded in paraffin. Five to eight micrometers of coronal sections were stained with 0.1% cresyl violet hematoxylin and eosin (H&E) and prepared for the subsequent microscope.

Terminal Deoxynucleotide Transferase dUTP Nick-End Labeling (TUNEL) Stain

A TUNEL staining kit (Roche, Switzerland) was used to assess neuronal apoptosis in basal ganglia (perihematoma) after ICH as previously described (Xu et al., 2017). Apoptosis was defined as TUNEL-positive cells, and counted by an independent individual. The number of TUNEL-positive cells was counted at 200× magnifications in each section.

Electron Microscopy

Rats were sacrificed under deep pentobarbital anesthesia at 24 h after ICH, and then perfused with 0.9% saline and 4% PFA. 1 mm^3 fragments of peri-hematoma tissues were obtained from right basal ganglia and then processed with glutaraldehyde (2.5%) at 4°C overnight. As described previously (Fan et al., 2017) the tissues were further handled through a succession of chemical treatment steps (1% osmium tetroxide, distilled water, etc.). Finally, the samples were imbedded in a mixture of propylene oxide and resin (1:1) overnight. After that, the samples were sliced into 100 nm sections and then stained with 4% uranyl acetate and 0.5% lead citrate. The ultrastructure of the basal ganglia was scanned using a transmission electron microscopy (Philips Tecnai 10).

Measurement of ATP Levels

The ATP level was examined by the luciferase-based ATP assay kit (Beyotime, Shanghai, China). As described in the instruction, the brain tissues were lysed in lysis buffer with centrifugation at 4°C and 12,000 × *g* for 5 min. Then, the supernatant was extracted for the ATP assay. Before the assay, the ATP working reagents [100 μl; ATP detection reagent:ATP detection reagent diluent (1:9)] were added into a micro-well for 5 min at 37°C. The samples (20 μl) were added and then (2 s later at least) measured by Varioskan Flash (Thermo Fisher Scientific). The ATP concentrations were calculated through the standard curve method. Then the protein levels of different samples were acquired using a detergent-compatible protein assay kit (Bio-Rad, Hercules, CA, United States). Ultimately, the ATP levels were displayed in the form of nanomoles per milligrams.

Measurement of ROS Level

Levels of ROS in brain tissues were examined using a ROS assay kit (JianCheng, China) according to the manufacturer's instructions. In brief, samples were lysed in 0.01 mol/l PBS with centrifugation at 4°C, 500 × *g* for 10 min. Then, the supernatant was extracted for the ROS assay. The supernatant (190 μl) and DCFH-DA (10 μl, 1 mol/l) were mixed in a micro-well at room temperature for 30 min. Afterward, the mixtures were measured by fluorophotometry. Then the protein levels of different samples were acquired using a detergent-compatible protein assay kit (Bio-Rad, Hercules, CA, United States). Ultimately, the ROS levels were displayed in the form of fluorescence/mg protein.

Western Blot

Six rats in each group at different time points had brain tissues harvested for western blot analysis. Western blot was performed as previously described (Xu et al., 2017). Briefly, frozen perihematoma tissues (basal ganglia) were homogenized in RIPA lysis buffer (Beyotime, Shanghai, China). Then the protein samples were separated by 10% or 12% SDS-PAGE, and transferred onto polyvinylidene fluoride (PVDF) membranes (Millipore). Then, the PVDF membranes were blocked with 5% bovine serum albumin for 1 h and incubated with the primary antibodies overnight, including: anti-sirt3 antibody (1:500, Abcam, ab86671), anti-NRF1 antibody (1:2000, Abcam, ab175932), anti-TFAM (1:1000, Abcam, ab131607), anti-SOD2 (1:5000, Abcam, ab13533), anti-Ac-SOD2 (1:1000, Abcam, ab137037), anti-cleaved caspase-3 (1:1000, CST, cst#9661), anti-Bax (1:1000, CST, cst#2772), anti-Bcl-2 (1:800, SantaCruz, sc-492), anti-NLRP3 (1:1000, ab210491, Abcam), anti-interleukin (IL)-1β (1:2000, Santa Cruz, sc-23459), and β-actin (1:5000, Abcam, ab8226). Then, the PVDF membranes were disposed with relevant secondary antibodies (1:5000) for 1 h at normal temperature. The signals of protein bands were detected with ChemiDoc detection system and quantified using Quantity One software (Bio-Rad, Hercules, CA, United States).

Statistical Analysis

All data are shown as means ± SD. Data from different groups were compared using one-way or two-way analysis of variance. The Kruskal–Wallis test was used to compare the difference of data in abnormal distribution. Then, Dunn–Bonferroni test was performed for *post hoc* comparison. Statistical Package for the Social Sciences (SPSS; version 22.0) and Prism (version 6.0) software were used for statistical analyses. The *P*-value <0.05 indicated statistical significance.

RESULTS

Physiological Data of Diabetic Rats

Diabetic model was induced by intraperitoneal injection with STZ at 60 mg/kg for 3 days before experimental ICH operation. Blood glucose was measured by glucometer (details were shown in the section "Materials and Methods") with the tail venous blood. Experimental ICH surgeries were performed in diabetic rats with stereotaxic frame and micro-injector. The representative brain sections from ICH model rats were shown in **Figure 1A**. The results of serial sections indicated that the sagittal length of hematoma in these groups were 0, 5.22 ± 0.62, and 5.52 ± 0.8 mm, respectively ($P < 0.05$,

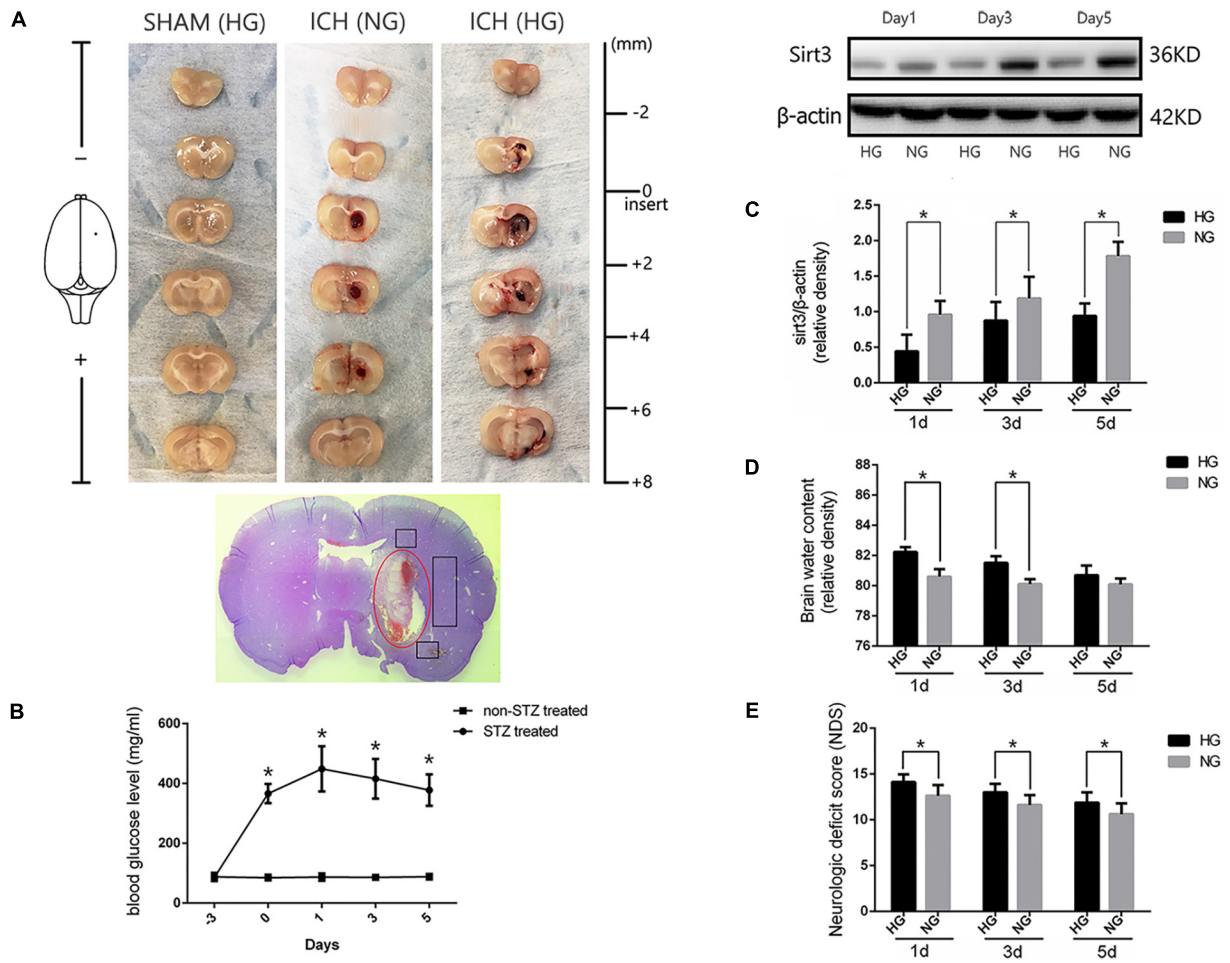

FIGURE 1 | Hyperglycemia suppressed sirt3 expression and aggravated cerebral injury after ICH. **(A)** Representative images of brain sections in each group. HE staining of ICH and the bleeding site (red circle). **(B)** Glucose levels of streptozotocin (STZ) treated and non-STZ-treated rats before and after experimental intracerebral hemorrhage (ICH), $^*P < 0.05$ versus non-STZ-treated group ($n = 6$ in each group). **(C)** Western blotting showed the sirt3 protein expression in HG and NG group on days 1, 3, and 5 after ICH, $^*P < 0.05$ ($n = 6$ in each group). HG, high blood glucose; NG, normal blood glucose. **(D)** The comparison of brain water content in HG and NG group on days 1, 3, and 5 after ICH, $^*P < 0.05$ ($n = 6$ in each group). **(E)** The comparison of neurologic deficit scores in HG and NG group on days 1, 3, and 5 after ICH, $^*P < 0.05$ ($n = 9$ in each group).

Supplementary Figure S2). Since the average sagittal length of rats was 6 mm (Paxinos and Watson, 1998) we calculated the percentages of damage (total lesion length and caudate nucleus distribution), and the results also showed no significant difference between ICH [normal blood glucose (NG)] and ICH [high blood glucose (HG)] group (86.9 ± 0.1% versus 0.92 ± 0.1%, $P < 0.05$). These results indicate that the ICH model is stability and reproducibility. As shown in the H&E staining picture, the perihematoma regions (black box) were used for examining the immunofluorescent staining. Significant differences were exhibited between STZ-treated and non-STZ-treated rats. The average blood glucose levels were 402.1 ± 64.2 and 86.7 ± 8.8 mg/dl, respectively, and this increase was maintained throughout 5 days in our research (**Figure 1B**). Other physiological parameters showed no significant differences between each group (**Supplementary Figure S3**).

Hyperglycemia Suppressed Sirt3 Expression and Aggravated Brain Injury After ICH

To investigate whether sirt3 expression is influenced by hyperglycemia. Western blotting was performed to explore the differences of sirt3 expression between non-diabetic and diabetic rats after ICH. The results showed that sirt3 expression was suppressed on days 1, 3, and 5 after ICH in HG group when compared with normal blood glucose (NG) group ($P < 0.05$, **Figure 1C**).

Intracerebral hemorrhage-induced brain injury was measured by neurological deficit scores and brain water content. Brain water content of lesioned hemisphere was 82.2 ± 0.32% in HG group and 80.4 ± 0.65% in NG group on day 1 after ICH ($P < 0.01$, **Figure 1D**). On day 3, the result was 81.5 ± 0.44% in HG group and 80.1 ± 0.33% in NG group ($P < 0.01$). However,

no significant difference was detected on day 5 after ICH between HG group: 80.1 ± 0.4% and NG group: 79.9 ± 0.4% ($P > 0.05$).

In addition, neurological deficit scores (**Figure 1E**) showed: 14.1 ± 0.8 in HG group and 12.6 ± 1.2 in NG group on day 1 after ICH ($P < 0.05$); 13.0 ± 0.9 in HG group and 11.6 ± 1.1 in NG group on day 3 ($P < 0.05$); 11.9 ± 1.1 in HG group and 10.6 ± 1.2 in NG group on day 5 ($P < 0.05$).

The above-mentioned findings indicated that hyperglycemia suppressed sirt3 expression after ICH may be one of the reasons why hyperglycemia could deteriorate ICH-induced cerebral injury.

Sirt3 Expression in Diabetic Rats After ICH

To investigate the time course of sirt3 expression in hyperglycemic ICH. We analyzed the sirt3 protein expression at 0 (sham group), 3, 6, 12, 24, 72, and 120 h after ICH. As shown in **Figure 2A**, the results of time course indicated that the protein expression of sirt3 was decreased to the minimum at 24 h after ICH ($P < 0.05$ versus the rest groups). Before that, sirt3 expression was increased at 6 h after ICH ($P < 0.05$ versus sham group).

Double immunofluorescence staining was performed to assess location of sirt3 expression. We found that sirt3 expression was decreased after ICH when compared with sham group (**Figure 2B**, $P < 0.05$).

Electron Microscopy Analysis

In the results of transmission electron microscopy, obvious changes were found in hyperglycemic ICH rats when compared with non-ICH diabetic rats. The magnifications were 4200 or 11,500 times. As shown in **Figure 2C**, (1) the asterisked mitochondria (the left one with damaged mitochondrial crest) showed serious vacuolization and swelling, the right one was a normal mitochondria with integrated mitochondrial crest; (2) the nuclear chromatin concentration and margination were also seen after hyperglycemic ICH; and (3) the ratio of mitochondria vacuolization (vacuolated/total mitochondria nearby the cell nuclear) was also calculated, the results indicated that hyperglycemic ICH induced extensive mitochondrial vacuolization and mitochondria swelling ($P < 0.05$).

HKL Increased the Expression of Sirt3 and Its Downstream Signaling Molecules After Hyperglycemic ICH

Three different doses of HKL were selected to identify the effective concentration for ICH. As shown in **Figure 3A**, Sirt3 levels were significantly enhanced by HKL in a dose-dependent manner ($P < 0.05$ versus ICH + vehicle group). Meanwhile, sirt3 levels were higher in high and medium dosage group (10, 5 mg/kg) than that in low dosage group (2.5 mg/kg).

Mitochondria played an important role in energy production and cell death, nuclear respiratory factor 1–mitochondrial transcription factor A (NRF1–TFAM) was a crucial signal pathway in mitochondrial biogenesis (Li et al., 2017). The present study indicated that NRF1 expression was significantly increased in medium and high dosage group ($P < 0.05$ versus ICH + vehicle group, **Figure 3B**), and its downstream protein-TFAM was also upregulated after HKL treatment ($P < 0.05$ versus ICH + vehicle group, **Figure 3C**). Sirt3 could directly bind and deacetylate SOD2, which plays a crucial role in scavenging ROS (Kawamura et al., 2010; Qiu et al., 2010; Tao et al., 2010). Consist with previous studies (Pillai et al., 2015; Yu et al., 2017; Zhai et al., 2017), the present study indicated that HKL could decrease ac-SOD2/SOD2 ratio ($P < 0.05$ versus ICH + vehicle group, **Figure 3D**).

As shown in **Figure 3E**, the results indicated that HKL (10 or 5 mg/kg) could protect against neuronal apoptosis via decreasing cleaved caspase3 expression ($P < 0.05$ versus ICH + vehicle group). Hence, we considered 10 mg/kg HKL as the optimal drug concentration.

Sirt3 Knockdown Reversed the Positive Effects of HKL in the Expression of Sirt3 and Its Downstream Molecules After Hyperglycemic ICH

Sirt3 siRNA was used to further investigate the effects of sirt3 in diabetic rats after hyperglycemic ICH. The double immunofluorescence staining results indicated that cleaved caspase3 levels were significantly decreased after HKL treatment ($P < 0.05$ versus ICH + vehicle group, **Figure 3F**). Sirt3 siRNA transfection could aggravate the upregulation of cleaved caspase3 and block the positive effects of HKL ($P < 0.05$ versus ICH + HKL group).

As shown in **Figure 4A**, sirt3 protein levels were significantly decreased in ICH + sirt3 siRNA group when compared with other groups ($P < 0.05$). Meanwhile, sirt3 siRNA transfection could block the activating effects of HKL in sirt3 expression ($P < 0.05$ versus ICH + HKL group). NRF1 and TFAM levels were also significantly decreased after sirt3 knockdown ($P < 0.05$ versus ICH + vehicle group, **Figures 4B,C**). HKL also failed to upregulate NRF1 and TFAM expression in ICH + HKL + siRNA group ($P < 0.05$ versus ICH + HKL group). In **Figure 4D**, Ac-SOD2/SOD2 ratio was significantly increased in ICH + sirt3 siRNA group when compared with ICH + HKL group and ICH + vehicle group ($P < 0.05$). Moreover, sirt3 siRNA could block the effects of HKL in Ac-SOD2/SOD2 ratio ($P < 0.05$ versus ICH + HKL group). Furthermore, in **Figure 4E**, the results indicated that cleaved caspase3 was distinctly increased in ICH + sirt3 siRNA group ($P < 0.05$ versus ICH + vehicle group). In ICH + HKL + sirt3 siRNA group, the anti-apoptosis effects of HKL were blunted after sirt3 silenced ($P < 0.05$ versus ICH + HKL group).

TUNEL Staining

Further TUNEL staining was used to confirm the effects of HKL on neuronal survival (**Figure 4F**). TUNEL-positive cells were significantly increased in ICH + vehicle group compared with sham group ($P < 0.05$). Greatly increase of TUNEL-positive cells were found in ICH + sirt3 siRNA group

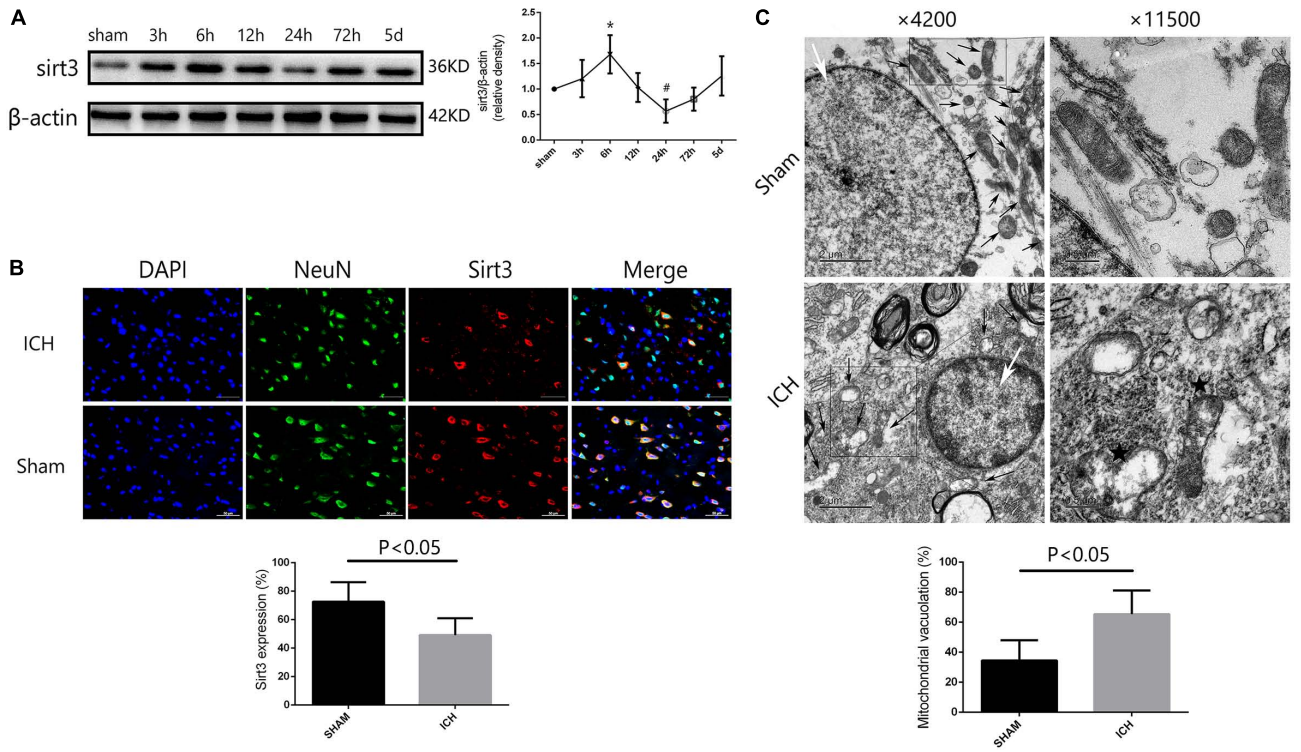

FIGURE 2 | Sirt3 protein expression and morphological changes of mitochondria after hyperglycemic ICH. **(A)** Western blotting showed that sirt3 protein expression was significantly decreased to the minimum at 24 h after ICH. Before that, sirt3 expression was reactively upregulated at 6 h after ICH, $^{*}P < 0.05$ versus sham group, $^{\#}P < 0.05$ versus the rest groups ($n = 6$ in each group at different time points). **(B)** Immunofluorescence staining showed the location of sirt3 protein in basal ganglia after hyperglycemic ICH at 24 h. Sirt3 expression was downregulated after ICH when compared with sham group ($P < 0.05$, 18 cryosections from 6 rats were calculated in each group, scale bars: 50 μm). **(C)** Transmission electron microscopy images of neuronal apoptosis and mitochondrial ultrastructure (white arrow: cell nucleus; black arrow: mitochondria). The ratio of mitochondrial vacuolization was increased after ICH when compared with sham group ($P < 0.05$, 18 TEM images from 6 rats were calculated in each group).

($P < 0.05$ versus ICH + vehicle group). Moreover, sirt3 agonist (HKL) could decrease ICH-induced neuronal apoptosis ($P < 0.05$ versus ICH + vehicle group), and such effects could be blocked by sirt3 siRNA ($P < 0.05$ versus ICH + HKL group).

Sirt3 Knockdown Aggravated Cerebral Injury via Exacerbating Oxidative Stress and Mitochondrial Dysfunction

Experimental ICH induction could distinctly increase brain water content in ipsilateral hemisphere 82.2 ± 0.33% at 24 h when compared with sham group 78.8 ± 0.6% ($P < 0.05$, **Figure 4G**). Brain water content was further elevated after sirt3 siRNA transfection 83.6 ± 0.7% ($P < 0.01$ versus the rest groups). HKL could alleviated brain edema 80.25 ± 0.33% after ICH ($P < 0.01$ versus the rest groups), and such effects were reversed after sirt3 knockdown 81.43 ± 0.48% ($P < 0.01$ versus ICH + HKL group).

In addition, neurological deficits were more severe in ICH + vehicle group (13.8 ± 1.3) than that of sham group ($P < 0.05$, **Figure 4H**), and sirt3 knockdown (15.0 ± 0.8) could aggravate neurological deficits after ICH ($P < 0.01$ versus ICH + vehicle group). HKL could decrease neurological deficit scores (11.56 ± 1.13, $P < 0.01$ versus ICH + vehicle group), and the positive effect of HKL was reversed after sirt3 knockdown (13.0 ± 1.0, $P < 0.01$ versus ICH + HKL group).

As shown in **Figure 4I**, ROS levels were significantly decreased in HKL-treated group ($P < 0.05$ versus ICH + vehicle group) which were consistent with the decrease of Ac-SOD2/SOD2 ratio. In addition, ROS accumulation was more severe in ICH + sirt3 siRNA group ($P < 0.05$ versus ICH + vehicle group) after sirt3 siRNA transfection. The positive effect of HKL in attenuating ROS accumulation was reversed after sirt3 knockdown ($P < 0.05$ versus ICH + HKL group).

Upregulation of sirt3 expression also enhanced ATP levels when compared with ICH group ($P < 0.05$, **Figure 4J**). Because, sirt3 activation upregulated NRF1 and TFAM expression that could promote mitochondrial biogenesis and then facilitate ATP generation. After sirt3 silenced, ATP reduction was more severe in ICH + sirt3 siRNA group than that of ICH group ($P < 0.05$). Meanwhile, in ICH + sirt3 siRNA + HKL group, sirt3 siRNA transfection could reverse the positive impact of sirt3 agonist in preserving against ATP reduction ($P < 0.05$ versus ICH + HKL group).

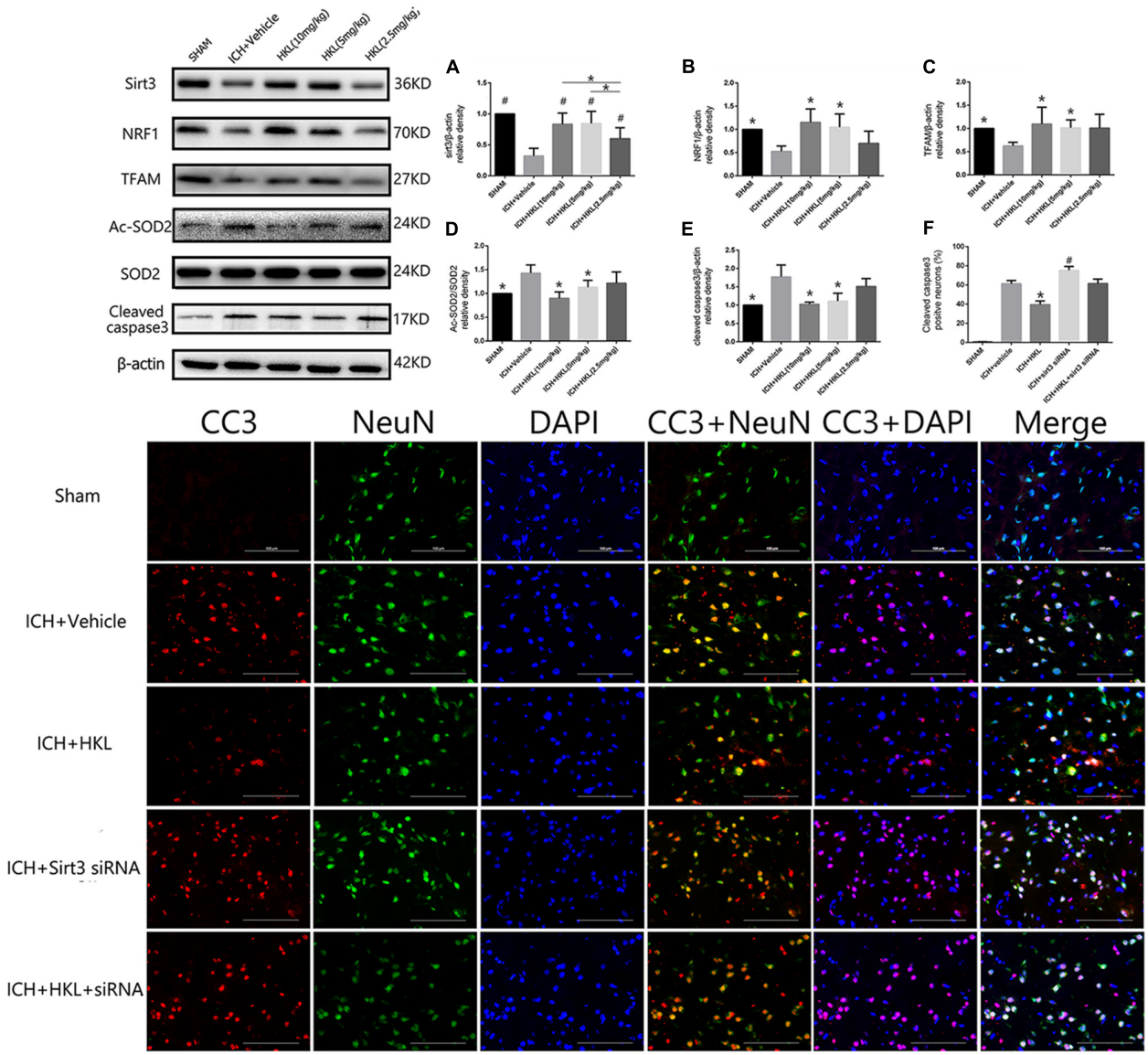

FIGURE 3 | HKL mediated the expression of sirt3 and its downstream signaling molecules after hyperglycemic ICH. **(A)** Sirt3 protein expression was significantly enhanced by HKL in a dose-dependent manner. $^{\#}P < 0.05$ versus ICH + vehicle group, $^{*}P < 0.05$ ($n = 6$ in each group). **(B)** NRF1 expression, $^{*}P < 0.05$ versus ICH + vehicle group ($n = 6$ in each group). **(C)** TFAM expression, $^{*}P < 0.05$ versus ICH + vehicle group ($n = 6$ in each group). **(D)** *Ac-SOD2/SOD2 ratio* (*Ac-SOD2*, acetylated SOD2), $^{*}P < 0.05$ versus ICH + vehicle group ($n = 6$ in each group). **(E)** Cleaved caspase3 expression, $^{*}P < 0.05$ versus ICH + vehicle group ($n = 6$ in each group). **(F)** Representative co-labeling cleaved-caspase3/NeuN images of ipsilateral basal ganglia. Quantification of cleaved caspase3-positive neurons (% = cleaved caspase3-positive neurons/total neurons), $^{*}P$ and $^{\#}P < 0.05$ versus the rest groups ($n = 6$ in each group). Scale bars: 100 μm.

Sirt3 Activation Improved Mitochondrial Permeability Potential and Cell Viability in SH-SY5Y Cells Exposed to OxyHb

Mitochondrial membrane potential ($\Delta\psi m$) was determined by JC-1 staining. As shown in **Figure 5A**, normal membrane potential indicated red fluorescence intensity in control group. Treatment of 10 μM OxyHb and 20 mM glucose increased green fluorescence intensity which represented the decline of $\Delta\psi m$ in SH-SY5Y cells. Pre-incubation with HKL attenuated OxyHb-induced collapse of $\Delta\psi m$, but sirt3 siRNA transfection reversed such effects. The results in scramble siRNA group indicated no significant difference between OxyHb group (data not shown). Quantification of JC-1 fluorescence intensity (red/green florescent area) was shown in **Figure 5B**.

Moreover, the effects of sirt3 activation in protecting SH-SY5Y cells from OxyHb-induced cell injury were evaluated by MTT assay (**Figure 5C**). The viability of SH-SY5Y cells was significantly increased after the treatment of HKL (81.76 ± 4.9%) when compared with OxyHb group (71.59 ± 3.01%). Sirt3 siRNA transfection could decrease the viability (62.9 ± 4.7%) and reverse the positive effect of HKL (72.22 ± 2.3%). The results in scramble

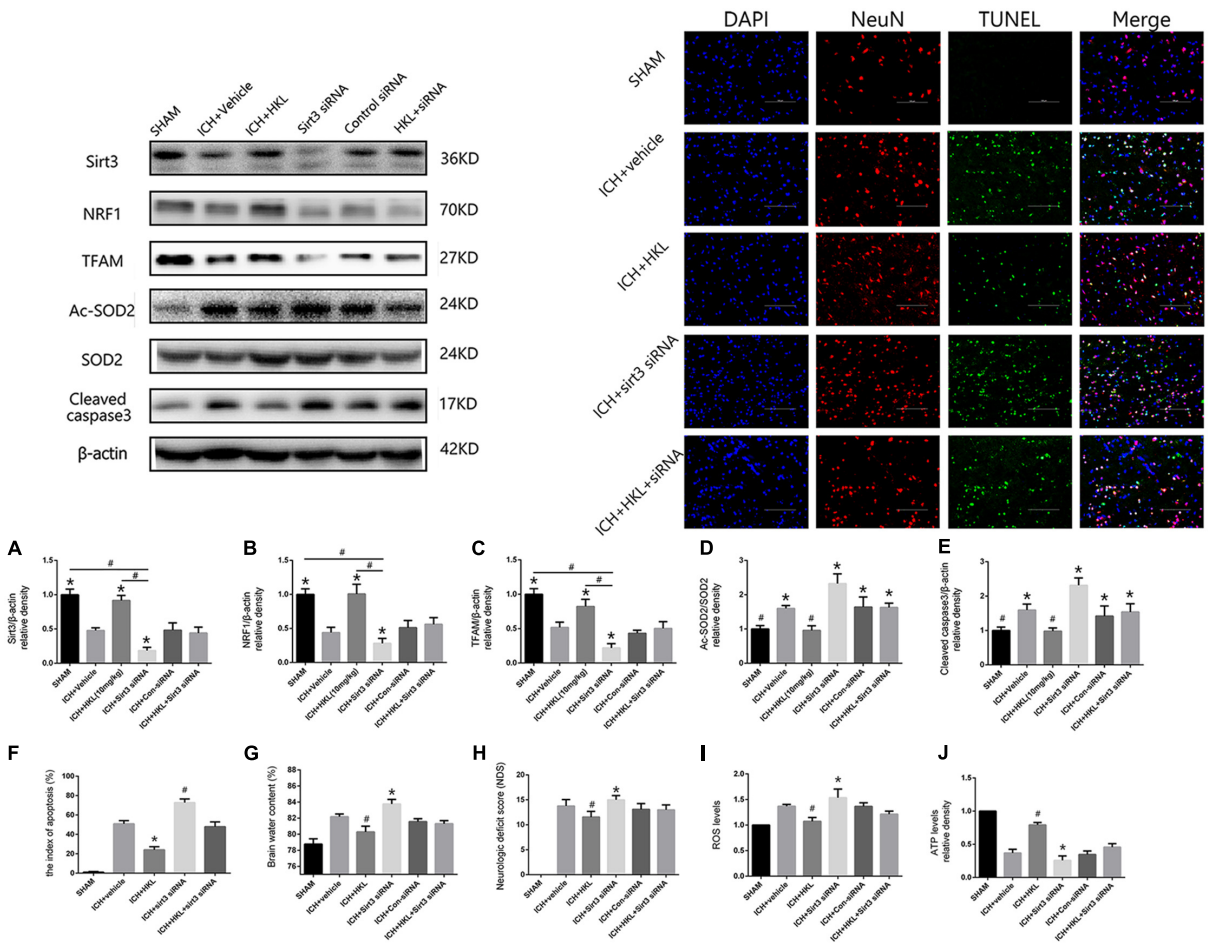

FIGURE 4 | Sirt3 knockdown abolished the positive effects of HKL and exacerbated cerebral injury. **(A)** Sirt3 expression. **(B)** NRF1 expression. **(C)** TFAM expression. $^{*}P < 0.05$ versus the rest three groups, $^{\#}P < 0.05$ ($n = 6$ in each group). **(D)** Ac-SOD2/SOD2 ratio. **(E)** Cleaved caspase3 expression. $^{*}P < 0.05$ versus the rest two groups, $^{\#}P < 0.05$ versus the rest four groups ($n = 6$ in each group). **(F)** Representative co-labeling TUNEL/NeuN pictures of ipsilateral basal ganglia. Quantification of TUNEL-positive neurons (the index of apoptosis = TUNEL-positive neurons/total neurons, $n = 6$ in each group), Scale bars: 100 μm. **(G)** Brain water content. **(H)** Neurologic deficit scores. **(I)** ROS levels. **(J)** ATP levels $^{*}P$ and $^{\#}P < 0.05$ versus the rest groups ($n = 6$ in each group).

siRNA group indicated no significant difference between OxyHb group (data not shown).

Sirt3 Attenuated Neuroinflammation Through Sirt3/ROS/NLRP3 Pathway

The present study indicated that Sirt3 expression was downregulated after hyperglycemic ICH, and then caused the increase of Ac-SOD2/SOD2 ratio which could aggravate ROS accumulation (**Figures 6A,B**). Since the mitochondrial ROS accumulation is one of the critical causes in triggering NLRP3 activation (Ma et al., 2014; Chen et al., 2017). The NLRP3 inflammasome plays a crucial role in neuro-inflammation after ICH, and NLRP3 activation can further lead to the release of pro-inflammatory cytokine IL-1β (Ma et al., 2014). NLRP3 and IL-1β levels were significantly increased after experimental ICH (**Figures 6C,D**). Sirt3 agonist (HKL) could significantly increase the sirt3 protein levels, and then deacetylated SOD2. Thereby, Ac-SOD2/SOD2 ratio and ROS levels were decreased after sirt3 upregulation, and then NLRP3 and IL-1β levels were suffered a corresponding decrease (**Figures 6E–H**). Inversely, sirt3 siRNA transfection could exacerbate neuroinflammation through upregulating sirt3 expression and consequently increasing NLRP3, IL-1β levels, and Ac-SOD2/SOD2 ratio.

In addition, the immunofluorescence staining results indicated that the amount of Iba-1-positive cells was significantly decreased when compared with ICH + Vehicle group ($P < 0.05$, **Figure 6I**). Sirt3 siRNA transfection could reverse such results and extremely increased the quantity of Iba-1-positive cells ($P < 0.05$ versus ICH + vehicle group, **Figure 6I**). It demonstrated that sirt3 attenuated neuroinflammation through sirt3/ROS/NLRP3 pathway.

DISCUSSION

In present study, we first demonstrated that: (1) hyperglycemia can aggravate the downregulation of sirt3 in animal models of

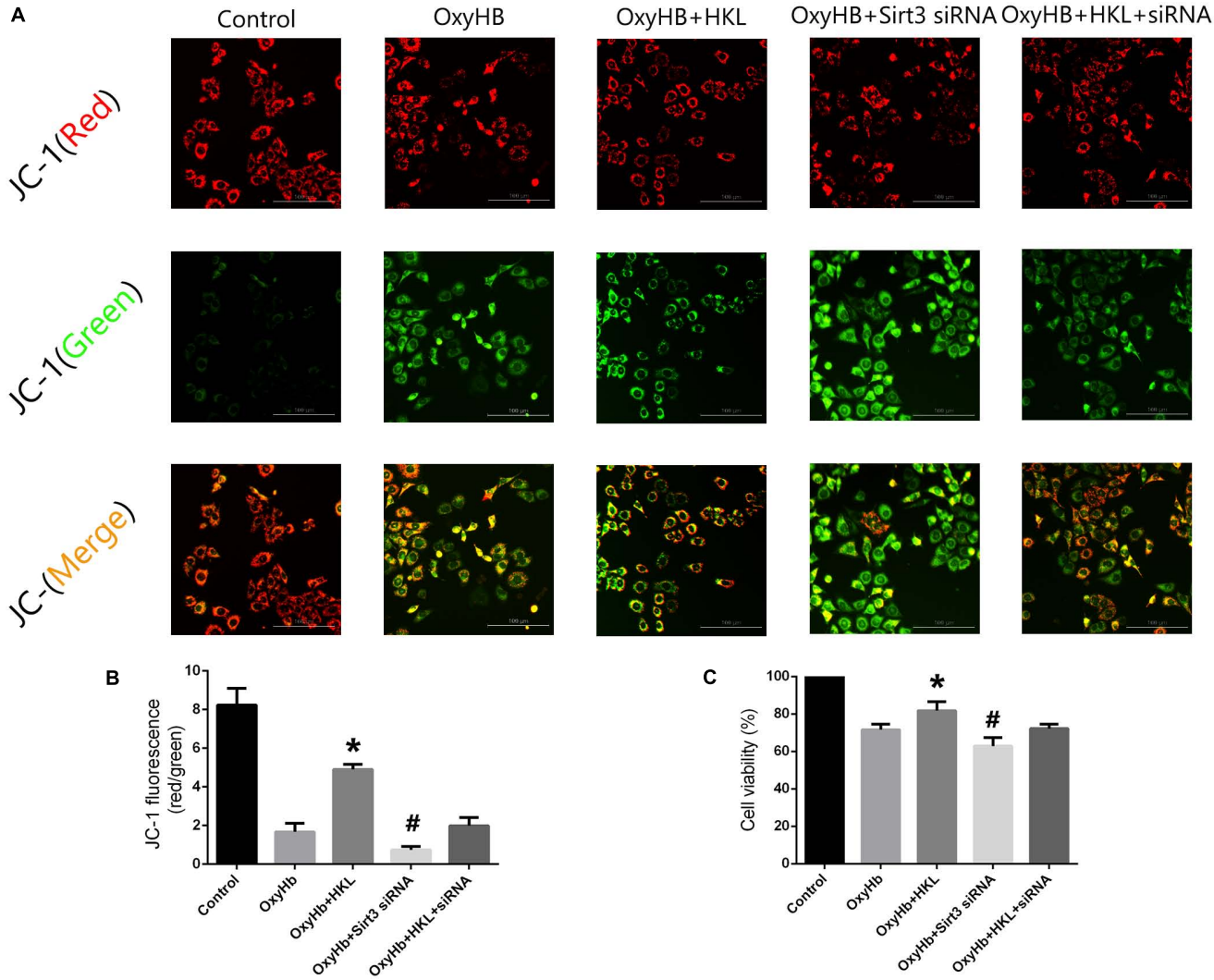

FIGURE 5 | Measurement of $\Delta\psi m$ and cell viability in SH-SY5Y cells. **(A)** Representative JC-1 staining pictures of SH-SY5Y cells. **(B)** Quantification of JC-1 fluorescence intensity (red/green florescent area), Scale bars: 100 μm. **(C)** Cell viability. $^{*}P$ and $^{\#}P < 0.05$ versus the rest groups ($n = 6$ in each group).

ICH; (2) HKL ameliorates oxidative stress and mitochondrial dysfunction via a sirt3-dependent manner after hyperglycemic ICH; and (3) Sirt3 activation could also decrease NLRP3 and IL-1β levels through deacetylating SOD2 and scavenging ROS.

Perihematomal edema is the main manifestation of SBI, and it is significantly associated with risk of poor functional outcomes (Murthy et al., 2015). The initial hematoma leads to mitochondrial dysfunction through the induction of glutamate release. Mitochondrial deficits cause ATP reduction and then result in the failure of cellular pumps causing cytotoxic edema and cell death (Kim-Han et al., 2006; Brunswick et al., 2012). Mitochondrial dysfunction may also lead to the overproduction of ROS which can induce inflammation and apoptosis (Prentice et al., 2015; Duan et al., 2016). The edema and ROS result in more cell apoptosis, further glutamate release, and persistence of vicious circles. In addition, hyperglycemia may also result in the activation of ROS and cause the dysregulation of mitochondrial membrane potential which precedes the neuronal apoptosis (Russell et al., 2002). Hence, oxidative stress and mitochondrial dysfunction are thought to play an important role in hyperglycemic ICH.

Interestingly, our research data indicated that hyperglycemia could suppress sirt3 expression in HG and NG group on days 1, 3 and 5, and then cause more serious cerebral damage after ICH. This finding was consistent with the previous study that hyperglycemia could inhibit sirt3 expression in retinal capillary endothelial cells (Gao et al., 2016). Moreover, the results of sirt3 expression showed no significant difference between ICH (NG) and ICH (HG) group at other time points. The details of the comparison were shown in **Supplementary Figure S4**. A pervious study also demonstrated that cerebral AQP-4 expression was downregulated in hyperglycemic ICH (Chiu et al., 2013). However, the reason

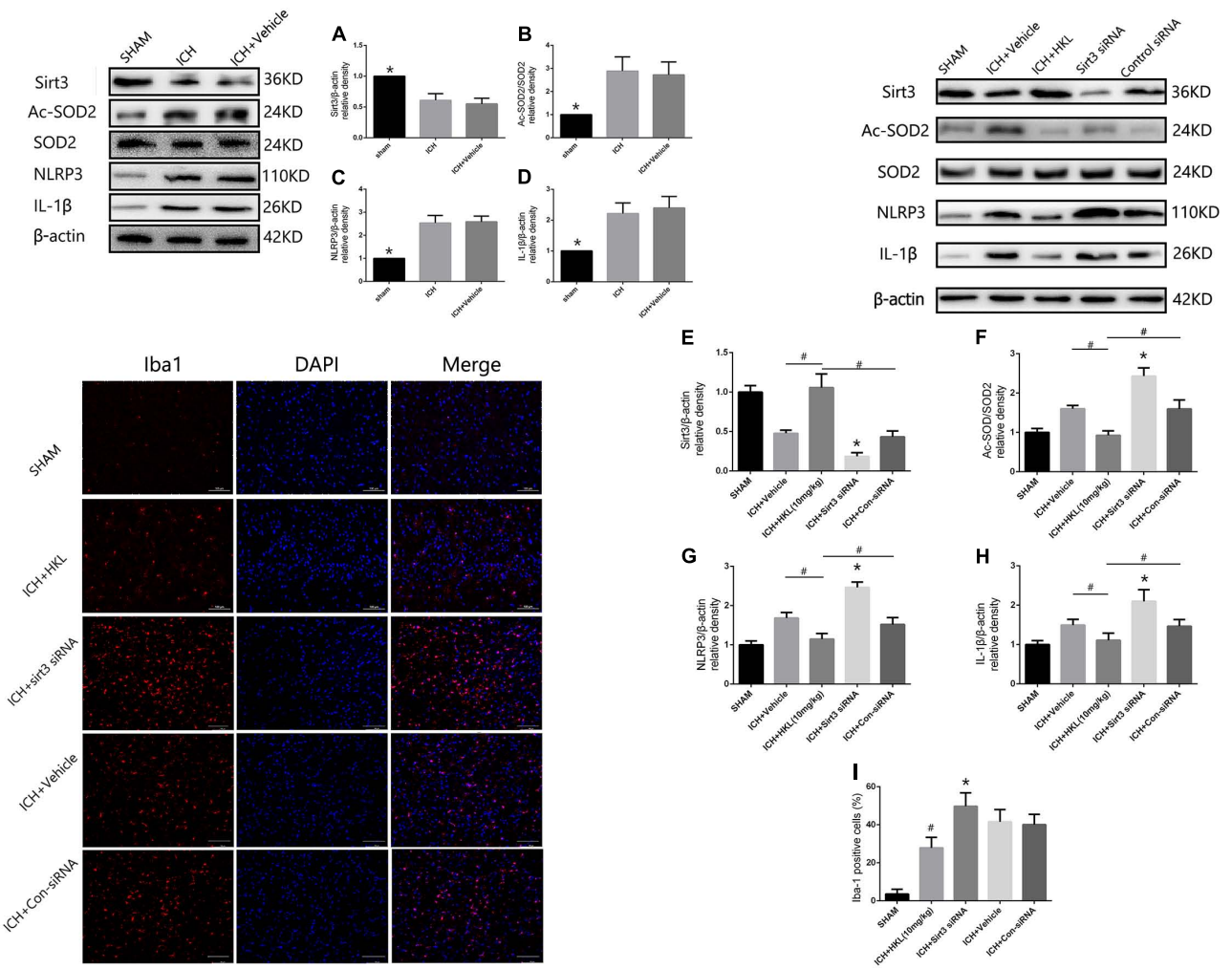

FIGURE 6 | Sirt3 attenuated neuroinflammation through Sirt3–ROS–NLRP3 signaling pathway. **(A)** Sirt3 expression. **(B)** Ac-SOD2/SOD2 ratio. **(C)** NLRP3 expression. **(D)** IL-1β expression. $^{*}P < 0.05$ versus the rest groups. **(E)** Sirt3 expression. **(F)** Ac-SOD2/SOD2 ratio. **(G)** NLRP3 expression. **(H)** IL-1β expression. $^{*}P < 0.05$ versus the rest groups, $^{\#}P < 0.05$ ($n = 6$ in each group). **(I)** Quantification of Iba-1 positive cells (% = Iba-1-positive cells/total cells, $^{*}P < 0.05$ versus the rest groups, $^{\#}P < 0.05$ versus the rest groups). Scale bars: 100 μm.

why hyperglycemia can suppress protein expression is still unknown. Gao et al. (2016) thought that hyperglycemia could result in the activation of PARP which competitively utilized the same cofactor (NAD^{+}) with sirt3. Hence, hyperglycemia-induced PARP activation was thought to be one of the reasons that caused the downregulation of sirt3 (Gao et al., 2016). Since the downregulation of sirt3, its neuroprotective effects were receded. Therefore, that may be one of the reasons why hyperglycemia can aggravate brain edema and neuronal apoptosis.

Mitochondrial dysfunction includes ATP reduction, damaged mitochondrial biogenesis, disordered membrane potential, and ROS accumulation (Pieczenik and Neustadt, 2007; Bhatti et al., 2017). Sirt3 is involved in the mitochondrial basal ATP production through the ETC and ATP synthase pathway (Ahn et al., 2008; Giralt and Villarroya, 2012). The electron transport chain (ETC) can create the mitochondrial membrane potential ($\Delta\psi m$) which is essential for ATP generation (Bause and Haigis, 2013). As we know, intracellular ATP level is essential for neuronal survival. ICH-induced mitochondrial deficits may contribute to ATP reduction and then result in the failure of cellular pumps causing neuronal apoptosis. The present study indicated that HKL improved $\Delta\psi m$ via activating sirt3. Moreover, ATP levels in perihematoma tissues were significantly decreased after hyperglycemic ICH injury. HKL could enhance ATP levels and sirt3 siRNA transfection could reverse such effects. In addition, we also found that NRF1 and TFAM expression were altered along with the alteration of sirt3 expression. Notably, NRF1 and TFAM are proven to play an important role in mitochondrial biogenesis (Li et al., 2017). As the upstream molecule of TFAM, NRF1 activation can increase TFAM expression and exert functions such as mitochondrial DNA transcription, maintenance, replication, and repair (Picca and Lezza, 2015).

A recent study also demonstrated that AMPK-PGC-1α-SIRT3 pathway is involved in the regulation of NRF1 and its downstream TFAM (Yu et al., 2017). Given the above-mentioned findings from previous and present studies, sirt3 may protect against neuronal apoptosis via improving ATP generation and mitochondrial biogenesis after hyperglycemic ICH.

Sirt3 has been shown to bind and deacetylate several metabolic and respiratory enzymes that participate in the regulation of ETC function (Giralt and Villarroya, 2012; Bause and Haigis, 2013). ETC plays a pivotal role in mitochondrial ROS production because of numerous O_2^- generated by complexes I and III. Sirt3 could maintain ROS homeostasis through SOD2, which may transform harmful superoxide radicals into nontoxic oxygen or hydrogen peroxide (Qiu et al., 2010; Bause and Haigis, 2013; Gao et al., 2016). The present study demonstrated that HKL decreased cellular Ac-SOD2/SOD2 ratio in a sirt3-dependent manner after hyperglycemic ICH. The deacetylation by sirt3 is essential for SOD2 activity and ROS elimination. Our research indicated that AcSOD2/SOD2 ratio was increased, and HKL could decrease AcSOD2/SOD2 ratio and increase SOD2 activity. Sirt3 siRNA transfection reversed such effects and aggravated oxidative stress injury after hyperglycemic ICH. In conclusion, sirt3 activation can also attenuate oxidative stress injury through deacetylating SOD2 after hyperglycemic ICH.

Furthermore, several studies have demonstrated that ROS is a critical activator which directly or indirectly induce NLRP3 activation (Zhou et al., 2010; Ma et al., 2014; Chen et al., 2017). A recent study has also shown that NLRP3-induced vascular inflammation can be inhibited through sirt3/SOD2/mtROS pathway (Chen et al., 2017). Notably, NLRP3 is associated with inflammatory responses which play a crucial role in SBI after ICH and ischemic stroke (Ma et al., 2014; Gao et al., 2017). Activation of innate inflammatory responses causes the release of inflammatory cytokines such as IL-1β and tumor necrosis factor-α (TNF-α) (Brunswick et al., 2012; Zhou et al., 2014). These factors further activate the downstream pathway which may cause BBB disruption and vasogenic edema, and ultimately lead to the extensive cell death (Xi et al., 2006; Wang and Dore, 2007). Hence, ROS scavenging may be an effective method in inhibiting NLRP3 activation and attenuating the relevant inflammation. Consistent with the above-mentioned studies, the present study indicated that sirt3 activation could deacetylate SOD2 and then scavenge excess ROS after hyperglycemic ICH. Ultimately, NLRP3 and IL-1β were decreased in a sirt3/SOD2/ROS-dependent pathway. These results implicated that sirt3 could mediate ICH-induced neuroinflammation through sirt3/ROS/NLRP3 signaling pathway.

CONCLUSION

In summary, all these findings reveal that sirt3 acts as a crucial factor in improving brain edema and neuronal apoptosis after hyperglycemic ICH. The neuroprotective mechanism of sirt3 mainly depends on the resistance to oxidative stress, mitochondrial dysfunction via SOD2 and NRF1–TFAM pathway. Meanwhile, the Sirt3/ROS/NLRP3 pathway also participates in mediating inflammatory reaction after hyperglycemic ICH. Such findings implicate a novel therapeutic target for hyperglycemic ICH.

AUTHOR CONTRIBUTIONS

JMZ is the principal investigator. JWZ and JY contributed to the study design, performance, and manuscript draft. FL, ZS, and LS analyzed the experimental data. WX, TL, and LG revised the manuscript and polished the language.

FUNDING

This study was supported by the Natural Science Foundation of Zhejiang Province (Y15H090022) and Basic Public Interests Research Plan of Zhejiang Province (GF18H090006) to JY; the Major Research and Development Project of Zhejiang Province (2017C03021) to JMZ.

SUPPLEMENTARY MATERIAL

The Supplementary Material for this article can be found online at: https://www.frontiersin.org/articles/10.3389/fnins.2018.00414/full#supplementary-material

FIGURE S1 | Grouping information.

FIGURE S2 | Stereological analysis.

FIGURE S3 | Physiological parameters.

FIGURE S4 | Sirt3 expression in HG and NG group at different time points after ICH.

REFERENCES

Ahn, B. H., Kim, H. S., Song, S., Lee, I. H., Liu, J., Vassilopoulos, A., et al. (2008). A role for the mitochondrial deacetylase Sirt3 in regulating energy homeostasis. *Proc. Natl. Acad. Sci. U.S.A.* 105, 14447–14452. doi: 10.1073/pnas.0803790105

Bause, A. S., and Haigis, M. C. (2013). SIRT3 regulation of mitochondrial oxidative stress. *Exp. Gerontol.* 48, 634–639. doi: 10.1016/j.exger.2012.08.007

Bhatti, J. S., Bhatti, G. K., and Reddy, P. H. (2017). Mitochondrial dysfunction and oxidative stress in metabolic disorders - A step towards mitochondria based therapeutic strategies. *Biochim. Biophys. Acta* 1863, 1066–1077. doi: 10.1016/j.bbadis.2016.11.010

Brunswick, A. S., Hwang, B. Y., Appelboom, G., Hwang, R. Y., Piazza, M. A., and Connolly, E. S. Jr. (2012). Serum biomarkers of spontaneous intracerebral hemorrhage induced secondary brain injury. *J. Neurol. Sci.* 321, 1–10. doi: 10.1016/j.jns.2012.06.008

Chen, M. L., Zhu, X. H., Ran, L., Lang, H. D., Yi, L., and Mi, M. T. (2017). Trimethylamine-N-oxide induces vascular inflammation by activating the NLRP3 inflammasome through the SIRT3-SOD2-mtROS signaling pathway. *J. Am. Heart Assoc.* 6:e006347. doi: 10.1161/JAHA.117.006347

Chiu, C. D., Chen, C. C., Shen, C. C., Chin, L. T., Ma, H. I., Chuang, H. Y., et al. (2013). Hyperglycemia exacerbates intracerebral hemorrhage via the

downregulation of aquaporin-4: temporal assessment with magnetic resonance imaging. *Stroke* 44, 1682–1689. doi: 10.1161/STROKEAHA.113.675983

Duan, X., Wen, Z., Shen, H., Shen, M., and Chen, G. (2016). Intracerebral hemorrhage, oxidative stress, and antioxidant therapy. *Oxid. Med. Cell. Longev.* 2016:1203285. doi: 10.1155/2016/1203285

Fan, L. F., He, P. Y., Peng, Y. C., Du, Q. H., Ma, Y. J., Jin, J. X., et al. (2017). Mdivi-1 ameliorates early brain injury after subarachnoid hemorrhage via the suppression of inflammation-related blood-brain barrier disruption and endoplasmic reticulum stress-based apoptosis. *Free Radic. Biol. Med.* 112, 336–349. doi: 10.1016/j.freeradbiomed.2017.08.003

Gao, J., Zheng, Z., Gu, Q., Chen, X., Liu, X., and Xu, X. (2016). Deacetylation of MnSOD by PARP-regulated SIRT3 protects retinal capillary endothelial cells from hyperglycemia-induced damage. *Biochem. Biophys. Res. Commun.* 472, 425–431. doi: 10.1016/j.bbrc.2015.12.037

Gao, L., Dong, Q., Song, Z., Shen, F., Shi, J., and Li, Y. (2017). NLRP3 inflammasome: a promising target in ischemic stroke. *Inflamm. Res.* 66, 17–24. doi: 10.1007/s00011-016-0981-7

Giralt, A., and Villarroya, F. (2012). SIRT3, a pivotal actor in mitochondrial functions: metabolism, cell death and aging. *Biochem. J.* 444, 1–10. doi: 10.1042/BJ20120030

Harada, S., Kishimoto, M., Kobayashi, M., Nakamoto, K., Fujita-Hamabe, W., Chen, H. H., et al. (2012). Honokiol suppresses the development of post-ischemic glucose intolerance and neuronal damage in mice. *J. Nat. Med.* 66, 591–599. doi: 10.1007/s11418-011-0623-x

Hebert, A. S., Dittenhafer-Reed, K. E., Yu, W., Bailey, D. J., Selen, E. S., Boersma, M. D., et al. (2013). Calorie restriction and SIRT3 trigger global reprogramming of the mitochondrial protein acetylome. *Mol. Cell* 49, 186–199. doi: 10.1016/j.molcel.2012.10.024

Inaji, M., Tomita, H., Tone, O., Tamaki, M., Suzuki, R., and Ohno, K. (2003). Chronological changes of perihematomal edema of human intracerebral hematoma. *Acta Neurochir. Suppl.* 86, 445–448. doi: 10.1007/978-3-7091-0651-8_91

Kawamura, Y., Uchijima, Y., Horike, N., Tonami, K., Nishiyama, K., Amano, T., et al. (2010). Sirt3 protects in vitro-fertilized mouse preimplantation embryos against oxidative stress-induced p53-mediated developmental arrest. *J. Clin. Invest.* 120, 2817–2828. doi: 10.1172/JCI42020

Kim-Han, J. S., Kopp, S. J., Dugan, L. L., and Diringer, M. N. (2006). Perihematomal mitochondrial dysfunction after intracerebral hemorrhage. *Stroke* 37, 2457–2462. doi: 10.1161/01.STR.0000240674.99945.4e

Kimura, K., Iguchi, Y., Inoue, T., Shibazaki, K., Matsumoto, N., Kobayashi, K., et al. (2007). Hyperglycemia independently increases the risk of early death in acute spontaneous intracerebral hemorrhage. *J. Neurol. Sci.* 255, 90–94. doi: 10.1016/j.jns.2007.02.005

Kong, X., Wang, R., Xue, Y., Liu, X., Zhang, H., Chen, Y., et al. (2010). Sirtuin 3, a new target of PGC-1alpha, plays an important role in the suppression of ROS and mitochondrial biogenesis. *PLoS One* 5:e11707. doi: 10.1371/journal.pone.0011707

Li, P. A., Hou, X., and Hao, S. (2017). Mitochondrial biogenesis in neurodegeneration. *J. Neurosci. Res.* 95, 2025–2029. doi: 10.1002/jnr.24042

Liu, J., Gao, B. B., Clermont, A. C., Blair, P., Chilcote, T. J., Sinha, S., et al. (2011). Hyperglycemia-induced cerebral hematoma expansion is mediated by plasma kallikrein. *Nat. Med.* 17, 206–210. doi: 10.1038/nm.2295

Ma, Q., Chen, S., Hu, Q., Feng, H., Zhang, J. H., and Tang, J. (2014). NLRP3 inflammasome contributes to inflammation after intracerebral hemorrhage. *Ann. Neurol.* 75, 209–219. doi: 10.1002/ana.24070

Meng, C., Zhang, J., Dang, B., Li, H., Shen, H., Li, X., et al. (2018). PERK pathway activation promotes intracerebral hemorrhage induced secondary brain injury by inducing neuronal apoptosis both in vivo and in vitro. *Front. Neurosci.* 12:111. doi: 10.3389/fnins.2018.00111

Murthy, S. B., Moradiya, Y., Dawson, J., Lees, K. R., Hanley, D. F., Ziai, W. C., et al. (2015). Perihematomal edema and functional outcomes in intracerebral hemorrhage: influence of hematoma volume and location. *Stroke* 46, 3088–3092. doi: 10.1161/STROKEAHA.115.010054

Paxinos, G., and Watson, C. (1998). *The Rat Brain in Stereotaxic Coordinates*. San Diego, CA: Academic Press.

Picca, A., and Lezza, A. M. (2015). Regulation of mitochondrial biogenesis through TFAM-mitochondrial DNA interactions: useful insights from aging and calorie restriction studies. *Mitochondrion* 25, 67–75. doi: 10.1016/j.mito.2015.10.001

Pieczenik, S. R., and Neustadt, J. (2007). Mitochondrial dysfunction and molecular pathways of disease. *Exp. Mol. Pathol.* 83, 84–92. doi: 10.1016/j.yexmp.2006.09.008

Pillai, V. B., Samant, S., Sundaresan, N. R., Raghuraman, H., Kim, G., Bonner, M. Y., et al. (2015). Honokiol blocks and reverses cardiac hypertrophy in mice by activating mitochondrial Sirt3. *Nat. Commun.* 6:6656. doi: 10.1038/ncomms7656

Prentice, H., Modi, J. P., and Wu, J.-Y. (2015). Mechanisms of neuronal protection against excitotoxicity, endoplasmic reticulum stress, and mitochondrial dysfunction in stroke and neurodegenerative diseases. *Oxid. Med. Cell. Long.* 2015, 1–7. doi: 10.1155/2015/964518

Qiu, X., Brown, K., Hirschey, M. D., Verdin, E., and Chen, D. (2010). Calorie restriction reduces oxidative stress by SIRT3-mediated SOD2 activation. *Cell Metab.* 12, 662–667. doi: 10.1016/j.cmet.2010.11.015

Qureshi, A. I., Mendelow, A. D., and Hanley, D. F. (2009). Intracerebral haemorrhage. *Lancet* 373, 1632–1644. doi: 10.1016/S0140-6736(09)60371-8

Robbins, N. M., and Swanson, R. A. (2014). Opposing effects of glucose on stroke and reperfusion injury: acidosis, oxidative stress, and energy metabolism. *Stroke* 45, 1881–1886. doi: 10.1161/STROKEAHA.114.004889

Russell, J. W., Golovoy, D., Vincent, A. M., Mahendru, P., Olzmann, J. A., Mentzer, A., et al. (2002). High glucose-induced oxidative stress and mitochondrial dysfunction in neurons. *FASEB J.* 16, 1738–1748. doi: 10.1096/fj.01-1027com

Song, E. C., Chu, K., Jeong, S. W., Jung, K. H., Kim, S. H., Kim, M., et al. (2003). Hyperglycemia exacerbates brain edema and perihematomal cell death after intracerebral hemorrhage. *Stroke* 34, 2215–2220. doi: 10.1161/01.STR.0000088060.83709.2C

Sulakhiya, K., Kumar, P., Jangra, A., Dwivedi, S., Hazarika, N. K., Baruah, C. C., et al. (2014). Honokiol abrogates lipopolysaccharide-induced depressive like behavior by impeding neuroinflammation and oxido-nitrosative stress in mice. *Eur. J. Pharmacol.* 744, 124–131. doi: 10.1016/j.ejphar.2014.09.049

Tao, R., Coleman, M. C., Pennington, J. D., Ozden, O., Park, S. H., Jiang, H., et al. (2010). Sirt3-mediated deacetylation of evolutionarily conserved lysine 122 regulates MnSOD activity in response to stress. *Mol. Cell* 40, 893–904. doi: 10.1016/j.molcel.2010.12.013

van Asch, C. J., Luitse, M. J., Rinkel, G. J., van der Tweel, I., Algra, A., and Klijn, C. J. (2010). Incidence, case fatality, and functional outcome of intracerebral haemorrhage over time, according to age, sex, and ethnic origin: a systematic review and meta-analysis. *Lancet Neurol.* 9, 167–176. doi: 10.1016/S1474-4422(09)70340-0

Wang, J., and Dore, S. (2007). Inflammation after intracerebral hemorrhage. *J. Cereb. Blood Flow Metab.* 27, 894–908. doi: 10.1038/sj.jcbfm.9600403

Woodbury, A., Yu, S. P., Wei, L., and Garcia, P. (2013). Neuro-modulating effects of honokiol: a review. *Front. Neurol.* 4:130. doi: 10.3389/fneur.2013.00130

Xi, G., Keep, R. F., and Hoff, J. T. (2006). Mechanisms of brain injury after intracerebral haemorrhage. *Lancet Neurol.* 5, 53–63. doi: 10.1016/S1474-4422(05)70283-0

Xu, H., Li, J., Wang, Z., Feng, M., Shen, Y., Cao, S., et al. (2017). Methylene blue attenuates neuroinflammation after subarachnoid hemorrhage in rats through the Akt/GSK-3beta/MEF2D signaling pathway. *Brain Behav. Immun.* 65, 125–139. doi: 10.1016/j.bbi.2017.04.020

Xu, X. S., Chua, C. C., Gao, J. P., Hamdy, R. C., and Chua, B. H. (2006). Humanin is a novel neuroprotective agent against stroke. *Stroke* 37, 2613–2619. doi: 10.1161/01.STR.0000242772.94277.1f

Yang, G. Y., Betz, A. L., Chenevert, T. L., Brunberg, J. A., and Hoff, J. T. (1994). Experimental intracerebral hemorrhage - relationship between brain edema, blood-flow, and blood-brain-barrier permeability in rats. *J. Neurosurg.* 81, 93–102. doi: 10.3171/jns.1994.81.1.0093

Yu, L., Gong, B., Duan, W., Fan, C., Zhang, J., Li, Z., et al. (2017). Melatonin ameliorates myocardial ischemia/reperfusion injury in type 1 diabetic rats by preserving mitochondrial function: role of AMPK-PGC-1alpha-SIRT3 signaling. *Sci. Rep.* 7:41337. doi: 10.1038/srep41337

Zhai, M. E., Li, B. Y., Duan, W. X., Jing, L., Zhang, B., Zhang, M., et al. (2017). Melatonin ameliorates myocardial ischemia reperfusion injury through SIRT3-dependent regulation of oxidative stress and apoptosis. *J. Pineal Res.* 63:e12419. doi: 10.1111/jpi.12419

Zhao, X. R., Zhang, Y. J., Strong, R., Grotta, J. C., and Aronowski, J. (2006). 15d-prostaglandin J(2) activates peroxisome proliferator-activated receptor-gamma, promotes expression of catalase, and reduces inflammation, behavioral dysfunction, and neuronal loss after intracerebral hemorrhage in rats. *J. Cereb. Blood Flow Metab.* 26, 811–820. doi: 10.1038/sj.jcbfm.9600233

Zheng, Y., Hu, Q., Manaenko, A., Zhang, Y., Peng, Y., Xu, L., et al. (2015). 17beta-Estradiol attenuates hematoma expansion through estrogen receptor alpha/silent information regulator 1/nuclear factor-kappa b pathway in hyperglycemic intracerebral hemorrhage mice. *Stroke* 46, 485–491. doi: 10.1161/STROKEAHA.114.006372

Zhou, R., Tardivel, A., Thorens, B., Choi, I., and Tschopp, J. (2010). Thioredoxin-interacting protein links oxidative stress to inflammasome activation. *Nat. Immunol.* 11, 136–140. doi: 10.1038/ni.1831

Zhou, Y., Wang, Y., Wang, J., Anne Stetler, R., and Yang, Q. W. (2014). Inflammation in intracerebral hemorrhage: from mechanisms to clinical translation. *Prog. Neurobiol.* 115, 25–44. doi: 10.1016/j.pneurobio.2013.11.003

Conflict of Interest Statement: The authors declare that the research was conducted in the absence of any commercial or financial relationships that could be construed as a potential conflict of interest.

frontiers in Neuroscience

ORIGINAL RESEARCH
published: 28 June 2018
doi: 10.3389/fnins.2018.00431

Asiatic Acid Prevents Oxidative Stress and Apoptosis by Inhibiting the Translocation of α-Synuclein Into Mitochondria

Hongqun Ding[1†], Yuyun Xiong[2†], Jing Sun[3], Chen Chen[3], Jing Gao[3] and Huaxi Xu[1*]*

[1] Department of Clinical Laboratory Diagnostics, School of Medicine, Jiangsu University, Zhenjiang, China, [2] Department of Clinical Laboratory, Affiliated Hospital of Jiangsu University, Zhenjiang, China, [3] Department of Medicinal Pharmacy, School of Pharmacy, Jiangsu University, Zhenjiang, China

OPEN ACCESS

Edited by:
Gang Chen,
First Affiliated Hospital of Soochow University, China

Reviewed by:
Chuang Wang,
Ningbo University, China
Xin Qi,
Case Western Reserve University, United States
Lan Luo,
Nanjing University, China
Hailiang Liu,
Harbin University, China

***Correspondence:**
Jing Gao
jinggao@ujs.edu.cn
Huaxi Xu
xuhx@ujs.edu.cn

[†] These authors have contributed equally to this work.

Specialty section:
This article was submitted to Neurodegeneration, a section of the journal Frontiers in Neuroscience

Received: 25 January 2018
Accepted: 07 June 2018
Published: 28 June 2018

Citation:
Ding H, Xiong Y, Sun J, Chen C, Gao J and Xu H (2018) Asiatic Acid Prevents Oxidative Stress and Apoptosis by Inhibiting the Translocation of α-Synuclein Into Mitochondria. Front. Neurosci. 12:431. doi: 10.3389/fnins.2018.00431

The association of α-synuclein (α-syn) with mitochondria occurs through interaction with mitochondrial complex I. Defects in this protein have been linked to the pathogenesis of Parkinson disease (PD). Overexpression of α-synuclein in cells has been suggested to cause elevations in mitochondrial oxidant radicals and structural and functional abnormalities in mitochondria. Asiatic acid (AA), a triterpenoid, is an antioxidant that is used for depression, and we have shown that pretreatment with AA can prevent PD-like damage, but its therapeutic effects in PD and mechanism remain unknown. In this study, we found that 0.5–2 mg AA/100 g diet significantly improves climbing ability in drosophila and extends their life-span—effects that we attributed to its antioxidant properties. AA also protected mitochondria against oxidative stress and apoptosis in a rotenone-induced cellular model. In an isolated mitochondria model, AA attenuated the decline in mitochondrial membrane potential that was induced by α-syn. Consequently, AA maintained membrane integrity and ATP production. Finally, we demonstrated that AA protects by blocking the translocation of α-syn into mitochondria. Our results suggest that mitochondria are crucial in PD and that AA is an excellent candidate for the prevention and therapy of this disease.

Keywords: α-synuclein, mitochondrion, apoptosis, asiatic acid, Parkinson disease

INTRODUCTION

Parkinson disease (PD) is a progressive neurodegenerative disorder that is characterized by the preferential loss of dopaminergic neurons in the substantia nigra pars compacta (SNpc)(Moore et al., 2005) and the formation of intracytoplasmic protein aggregates, termed Lewy bodies, a major component of which is α-synuclein (α-syn) (Spillantini et al., 1997). Increased expression of α-syn has been hypothesized to cause familial and sporadic PD, culminating in a loss of nigrostriatal dopaminergic neurons and motor deficits (Feany and Bender, 2000; Rochet et al., 2004; Lee and Trojanowski, 2006; Jellinger, 2012).

Mitochondrial dysfunction has been implicated in pathogenesis of PD, in which α-syn is central. In α-syn-expressing dopaminergic neuronal cultures, α-syn can translocate to the mitochondria, interact with respiratory complex I, and interfere with mitochondrial function (Devi et al., 2008). Moreover, recombinant human α-syn leads to a dose-dependent loss of mitochondrial transmembrane potential and phosphorylation capacity when incubated with isolated rat brain mitochondria (Banerjee et al., 2010). Hoogerheide et al. (2017) found that α-syn molecules could be captured by a voltage-dependent anion channel (VDAC) using free energy considerations that allow α-synuclein translocation and retraction.

Rotenone, a mitochondrial complex I inhibitor, causes the loss of ATP and increases α-syn levels and oxidative stress (Sherer et al., 2002). Most *in vitro* models of PD are "acute" models that might fail to mimic exactly the characteristics of PD, a chronic neurodegenerative disease. Therefore, we have used a "chronic" model with a low dose (5 nM) of rotenone for 4 weeks in human neuroblastoma SH-SY5Y cells (Sherer et al., 2002). Sherer et al. (2002) concluded that this model can be used efficiently to screen anti-PD drugs.

Asiatic acid (AA) is a triterpene that is extracted from *Centella asiatica* (L.) Urban (Umbelliferae), which has been used widely as an antioxidant and anti-inflammatory herb in Ayurvedic medicine and traditional Chinese medicine. AA has neuroprotective properties in cell culture and animal systems (Mook-Jung et al., 1999; Lee et al., 2000, 2012; Krishnamurthy et al., 2009), protecting neurons from C2 ceramide-induced cell death by antagonizing mitochondria-dependent apoptosis (Zhang et al., 2012). We have also reported that AA has neuroprotective effects through mitochondrial pathways (Xiong et al., 2009a; Xu et al., 2012).

In this study, we found that AA protects against Parkinson-like injury in drosophila, SH-SY5Y cells, and isolated mitochondria. Notably, the mechanism is related to direct prevention of mitochondrial permeability transition pores (MPTPs) opening and inhibition of the translation of α-syn to mitochondria. These results confirm that AA is a candidate molecule for the prevention or therapy of PD.

MATERIALS AND METHODS

Cells and Reagents

Human neuroblastoma SH-SY5Y cells were a gift from Dr. Zunji Ke, Institute for Nutritional Science, Chinese Academy of Sciences (Shanghai, China). Human recombinant wild-type α-syn from Escherichia coli was purchased from ProSpec-Tany TechnoGene Ltd. The purity was greater than 95% by RP-HPLC, according to the company. AA was obtained from Sigma (St. Louis, MO, United States); β-actin, α-syn, cytochrome C (Cyt C), peroxisome proliferator-activated re-ceptor gamma coactivator-1α (PGC-1α), BAX, and VDAC primary antibodies were obtained from Abcam (Cambridge, MA, United States); all secondary antibodies were obtained from Boster Biological Technology (Wuhan, China). All other reagents were acquired from commercial suppliers and were standard biochemical quality-grade.

Drosophila Culture

Transgenic Drosophila α-syn was a gift from Dr. Liu Jiankang, Xi'an Jiaotong University. According to previous methods (Long et al., 2009), non-PD flies (UAS wild-type alpha-synuclein/+) and PD flies (Ddc-GAL4/+; UAS wild-type alpha-synuclein/+) were housed in bottles, on the bottoms of which was medium that contained agar, cornmeal, sucrose, water, dried yeast, and propionic acid, at 25°C with a 12-h light-dark cycle. PD drosophila were divided into five groups: PD, 0.5 mg AA/100 g medium, 1 mg AA/100 g medium, 1 mg AA/100 g medium, and 2 mg alpha lipoic acid (LA)/100 g medium.

Climbing Assay and Life Span Observation

The climbing assay was performed as described (Feany and Bender, 2000; Pendleton et al., 2002). Briefly, every 230 flies were placed into one group, and every 10 flies were added to a 110 × 27 mm glass tube, around which a horizontal line was drawn 80 mm above the bottom of the vial. When the experiment was begun, the number of flies that climbed above the mark on the vial after 10 s was recorded, and every trial was repeated 10 times. All behavioral studies were performed in a quiet isolation room at 25°C in 60–70% humidity under a red light. The climbing tested commenced on Day 3 after eclosion. After the climbing assay, the flies were maintained until death to calculate their lifespan.

Spectrophotometric Determination of Intracellular Reduced Glutathione (GSH) and Malondialdehyde (MDA) Content

Drosophila were collected at DAY 36, ground on ice, and centrifuged at 12,000 × *g* for 6 min. The supernatant was taken, and the reaction was carried out according to the kit instructions. The intracellular GSH and MDA content was measured on a microplate reader.

SH-SY5Y Cell Culture

SH-SY5Y cells were cultured in medium with equal amounts of MEM and F-12, supplemented with 1% nonessential amino acids (Gibco), 10% heat-inactivated fetal calf serum (FCS), 100 U/ml penicillin, and 100 U/ml streptomycin in a humid atmosphere of 5% CO2 and 95% air at 37°C. For routine cultures, cells were grown in dishes and passaged approximately twice per week when they reached confluence. Then, 5 nM rotenone was added to the culture every 3 days when the medium was changed. After 4 weeks, cells were treated with AA for 24 h or detected immediately without rotenone treatment. Solvents were used as parallel controls. For the acute model, cells were plated in 6-well plates at a density of approximately 3 × 10 (Rochet et al., 2004) viable cells. Twenty-four hours later, the cells were treated with AA (0.01–100 nM containing 0.1% DMSO, which had no toxic effect on the cells) for 24 h and then exposed to a fresh batch of the same medium containing 100 nM rotenone for 24 h.

Preparation of Mouse Brain Mitochondria

Brain mitochondria were isolated from male ICR mice (weight 18–22 g) according to previous methods (Lai and Clark, 1979). Animal welfare and experimental procedures conformed to the Guide for the Care and Use of Laboratory Animals (Ministry of Science and Technology of China, 2006) and the related ethical regulations of our University. The experimental protocols were approved by ethics committee of Jiangsu University. Briefly, whole mouse brains, minus the cerebellum, were washed, minced, and homogenized in ice-cold isolation buffer (250 mmol/L sucrose, 10 mmol/L Tris–HCl, 0.5 mmol/L EDTA-K^+, 0.1% BSA, pH 7.4). After different centrifugation, the pellet was suspended in 3% Ficoll medium (3% Ficoll, 250 mmol/L sucrose, 0.5 mmol/L EDTA-K^+, and 10 mmol/L Tris–HCl, pH 7.4) and carefully layered onto 6% Ficoll medium. After being centrifuged at 11,500 × *g* for 30 min at 4°C, the mitochondrial pellet was suspended in isolation buffer (without BSA) and washed once. The final pellet was suspended in ice-cold storage buffer (250 mmol/L sucrose, 2.5 mmol/L KH_2PO4, and 10 mmol/L Tris–HCl, pH 7.4). The protein concentration was determined by Bradford assay (Nanjing Jiancheng Bioengineering Institute, Nanjing, China). Fresh mitochondria were prepared for each experiment and used within 4 h after isolation.

Fluorometric Analysis of Mitochondrial Membrane Potential (MMP)

Mitochondrial membrane potential reflects the functional state of the mitochondria within cells (Wadia et al., 1998). Changes in MMP were measured by the uptake of 5, 50, 6, 60-tetrachloro-1, 10, 3, 30-tetraethylbenzimidazolcarbocyanine iodide (JC-1) into the mitochondria. When excited at 488 nm, the monomeric form of JC-1 has an emission maximum at 525 nm, but the aggregated form (J-aggregates) has an emission maximum at 595 nm (Reers et al., 1991). Cells and isolated mitochondria were incubated with JC-1 at 37°C for 30 min in medium or reaction buffer (0.32 mmol/L sucrose, 10 mmol/L Tris, 20 mmol/L Mops, 50 μmol/L EGTA, 0.5 mmol/L $MgCl_2$, 0.1 mmol/L Pi (K^+), 5 mmol/L sodium succinate in the presence of 5 μg/mL JC-1). At the end of the incubation, the dye-loaded cells and mitochondria were collected by centrifugation, washed extensively with reaction buffer to remove excess dye, and then resuspended in the same buffer at the appropriate dilution. The cells were visualized under an inverted fluorescence microscope (Nikon, Ti-E Live Cell Imaging System Japan), and the fluorescence intensity was measured (488 nm excitation and 595 nm emission) on a Molecular Device spectrofluorometer (United States).

Mitochondrial Mass

To count the mitochondria, a suspension of cells in free serum medium was loaded with 200 nmol/L MitoTracker Red FM for 30 min at 37°C. Fluorescence intensity was measured at an excitation wavelength of 581 nm and emission wavelength of 644 nm using a fluorescence spectrometer (Molecular Devices Corporation, Sunnyvale, CA, United States). Amounts were determined by comparing the intensity of the fluorescence signal that was produced by 1 × 10 (Rochet et al., 2004) cells.

Measurement of ATP Synthesis by Mitochondria

ATP content was measured by luminometric assay, based on luciferin-luciferase reactions (Drew and Leeuwenburgh, 2003), using the Beyotime chemical luciferase ATP assay kit. Briefly, mitochondrial membranes were lysed in a buffer that contained 10 mmol/L Tris and 0.05% Triton X-100. Then, 50 μL of this lysate was added, and the luciferin-luciferase assay mixture was transferred to a white microplate. The results were measured on a multifunctional microplate reader (Perkinelmer, United States).

Quantification of ROS Levels

Reactive oxygen species (ROS) levels were measured using the ROS-specific probe 5′,6′-chloromethyl-2′,7′-dichlorodihydrofluorescein diacetate (H2DCFDA, Beyotime Institute of Biotechnology, Nantong, China). Cells and mitochondria were incubated with 10 μmol/L H2-DCFDA for 30 min at 37°C in medium or reaction buffer (0.32 mmol/L sucrose, 10 mmol/L Tris, 20 mmol/L Mops, 50 μmol/L EGTA, 0.5 mmol/L $MgCl_2$, 0.1 mmol/L Pi (K^+), 5 mmol/L sodium succinate) (Friberg et al., 2002). Next, the cells were visualized under an inverted fluorescence microscope (Nikon, Ti-E Live Cell Imaging System, Japan), and the mitochondria were monitored kinetically for 60 min at 37°C on a Molecular Device spectrofluorometer (United States) with 488 nm excitation and 525 nm emission filters.

Analysis of Mitochondrial Swelling

Mitochondrial swelling was assessed by measuring the absorbance of their suspension at 540 nm. Brain mitochondria were prepared in assay buffer (1 mg protein/mL) that contained 125 mmol/L sucrose, 50 mmol/L KCl, 2 mmol/L KH_2PO_4, 5 μmol/L rotenone, 10 mmol/L HEPES, and 5 mmol/L succinate. To induce mitochondrial swelling, 0.05 μg/μL α-syn was administered. Cyclosporine A (CsA) (50 nmol/L) was used as a positive reference (Elimadi et al., 2001). The extent of mitochondrial swelling was analyzed by measuring the decrease in absorbance (A) 0–60 min after the addition of α-syn at 37°C; a decrease in absorbance indicated an increase in mitochondrial swelling (Lee et al., 2002).

Western Blot

Equal amounts of cell protein and mitochondria sample were loaded onto a 12% SDS-polyacrylamide gel, separated, and transferred to a nitrocellulose membrane, which was then incubated overnight with anti-Cyt C, anti-α-syn, or anti-PGC1-α. The secondary antibody (1:1000 dilution) was HRP-conjugated anti-mouse or anti-rabbit IgG (Boster Biological Technology, Wuhan, China). The signals were detected using ECL according to the manufacturer's instructions and Kodak x-ray film.

Statistical Analysis

Differences were tested by one-way analysis of variance (ANOVA), followed Student–Newman–Keuls test as a *post hoc*

test. A value of $P < 0.05$ was considered significant. All experiments were done in triplicate and repeated three or four times.

RESULTS

AA Improves Climbing Ability and Prolongs the Life Span in PD Drosophila

As shown in **Figures 1A,C** the climbing ability of all drosophila decreased progressively with age. However, PD drosophila (male and female) climbed more slowly than non-PD drosophila from Days 3 to 42. Notably, 0.5–2 mg AA/100 g of culture medium significantly improved the climbing response in male and female PD drosophila from 18 to 42 days. As shown in **Figures 1B,D** male and female transgenic PD drosophila lived longer than control drosophila. AA significantly extended the lifespan of PD drosophila.

AA Has Antiapoptotic Effects in Rotenone-Induced SH-SY5Y Cell Damage

As shown in **Figure 2B**, the cell survival rate decreased after treatment with 100 nM rotenone. In contrast, 0.01–100 nM AA completely blocked the rotenone-induced decline in cell viability (**Figure 2B**). The pictures also show the same results compared with the rotenone group (**Figure 2A**), the treatment of AA (0.01–100 nM) prior to rotenone exposure clearly improved neuronal morphology, showing clear cell bodies and smooth processes. By flow cytometry, rotenone induced apoptosis in SH-SY5Y cells, which could be inhibited by AA (**Figure 2C**). The data on apoptotic protein–BAX also show the same results (**Figure 2D**).

AA Has Antioxidative Effects in Parkinson-Like Injuries

The amount of MDA often indicates the degree of lipid peroxidation in the body, indirectly reflecting the extent of cell damage. As shown in **Figure 3A**, MDA in PD flies increased by 2.8-fold compared with the normal control group, indicating a significant difference in the level of lipid peroxidation in drosophila. The MDA content in the AA group decreased from 64.5 to 76.7% compared with the PD group, showing a significant difference versus the control group ($P < 0.01$), indicating that AA antagonizes the overexpression of α-syn oxidative stress injury. However, 2 mg LA/100 g medium did not change the degree of lipid peroxidation in the fruit flies. The GSH content also showed the same results. It is indicated that AA could enhance the antioxidant capacity of PD fruit fly.

Asiatic acid also had antioxidative effects in SH-SY5Y cells and isolated brain mitochondria. As shown in **Figures 3B,C**, AA decreased the intensity of DCFH-DA fluorescence, which was elevated by rotenone. As seen in **Figure 3D**, untreated isolated mitochondria displayed substantial fluorescence, but mitochondria that were stressed with α-syn experienced an increase in ROS generation compared with untreated cells after 30 min. In contrast, 1–10 μmol AA/L attenuates the ROS

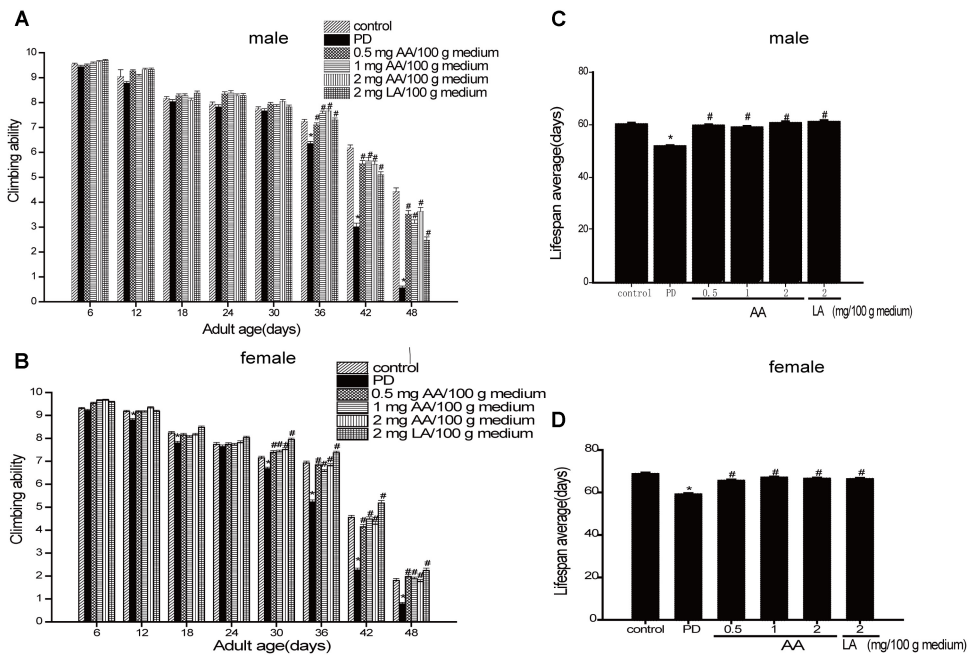

FIGURE 1 | Neuroprotective effects of AA against α-syn-induced injury in α-syn transgenic PD drosophila. Control and a-syn transgenic PD Drosophila were divided into indicated groups, and the climbing ability and the number of dead drosophila were assayed on indicated day. AA promotes climbing in α-syn transgenic PD drosophila ($N = 230$; $^{*}p < 0.05$ vs. non-PD group; $^{\#}p < 0.05$ vs. PD group) for **(A)** male and **(C)** female Drosophila melanogaster (average). AA prolongs the life-span of α-syn transgenic PD drosophila in **(B)** males and **(D)** females (mean ± SEM, $N = 230$; $^{*}p < 0.05$ vs. non-PD group; $^{\#}p < 0.05$ vs. PD group)).

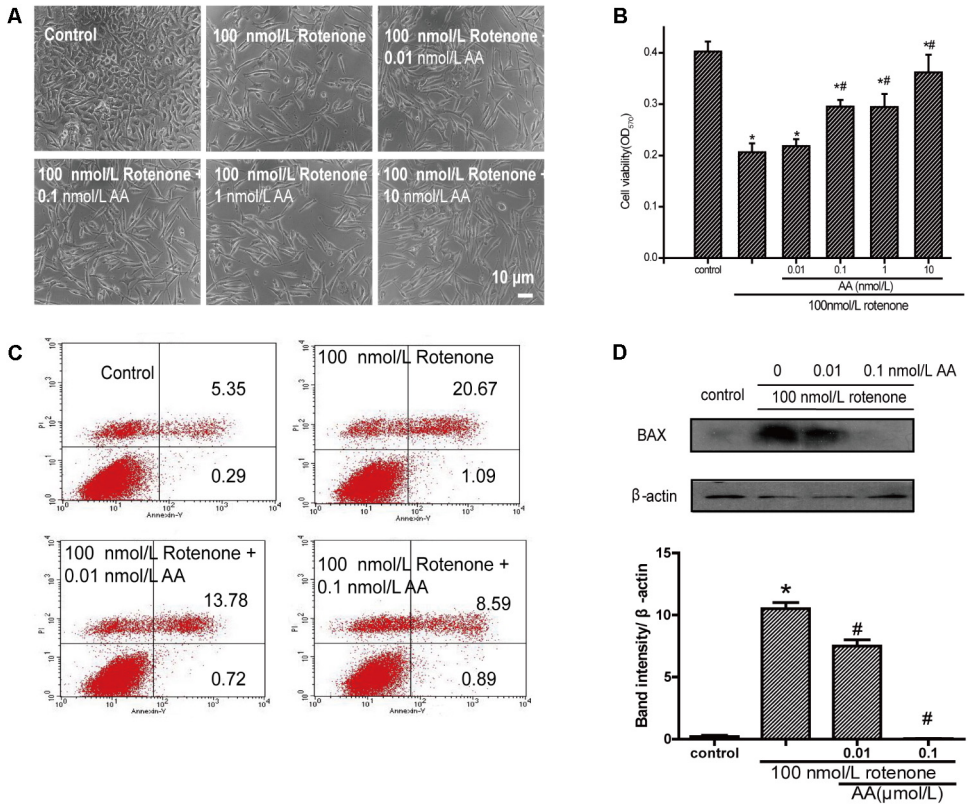

FIGURE 2 | Anti-apoptotic effects of AA in rotenone-induced SH-SY5Y cell damage. **(A)** Morphology of SH-SY5Y cells after 24 h of treatment with various concentrations of AA after 24 h 100 nM rotenone exposure. Bar: 10 μm. **(B)** Cell viability of SH-SY5Y cells treated with AA after rotenone-induced cell damage. The data represent means ± SD $n = 5$. $P < 0.05$ vs. control group. **(C)** SH-SY5H cells were treated with AA and rotenone, and apoptosis rates of SH-SY5Y cells were measured by Annexin V/PI. **(D)** Translation levels of BAX were measured by western blot. Data are expressed as means ± SD, $n = 3$. $^{*}p < 0.01$ vs. control group, $^{\#}p < 0.01$ vs. rotenone group.

generation that was induced by α-syn to normal levels. However, 100 μmol AA/L only partly attenuated the α-syn-induced ROS enhancement. CSA was a positive control and showed the same results as AA.

AA Protects Mitochondria Against Rotenone- and α-Syn-Induced Injury in SH-SY5Y Cells and Isolated Mitochondria

To determine whether AA can protect mitochondrial function, we first measured MMP in cultured SH-SY5Y cells. From the fluorescence microscopy images, we found that rotenone induced a significant decrease in MMP in cultured SH-SY5Y (**Figures 4A,B**). Nevertheless, pretreatment with AA (1 and 10 nM) blocked this decline, which indicated that AA protects mitochondria (**Figures 4A,B**).

Next, we investigated the effects of AA against rotenone induced the number of mitochondria reduced in SH-SY5Y cells. As shown in **Figures 4C,D**, AA enhanced the red fluorescence intensity, reflecting an increase in the number of mitochondria. AA also elevated the level of PGC1-α (**Figures 4E,F**), indicating the biogenesis of mitochondria.

When mitochondria were exposed to 0.05 μg α-syn/μL for 60 min, a loss of mitochondrial membrane potential of approximately 10% of J-aggregate fluorescence was observed (**Figure 4G**). Co-incubation with AA (1–10 μmol/L) significantly prevented the α-syn-induced decline in JC-1 fluorescence intensity dose-dependently (**Figure 4G**). MMP is the driver of ATP synthesis, and its loss is expected to result in decreased ATP levels in cells and isolated mitochondria. As shown in **Figure 3B**, 0.05 μg α-syn/μL decreased ATP levels from 100 to 50% compared with control. Treatment with 1–10 μmol AA/L for 1 h effected significant ATP production compared with the α-syn group (**Figure 4H**).

AA Lowers the Permeability of the Mitochondrial Membrane and Inhibits α-Syn Translocation to Mitochondria

The change in absorbance at 540 nm (A540) was measured to analyze mitochondrial swelling, which indirectly reflects the permeability of the mitochondrial membrane (Wills et al., 2010). The addition of 0.05 μg α-syn/μL to mitochondrial suspensions for 22.5 min resulted in a 6% decrease in A540, although the effect slightly lower than with 200 μmol/L Ca^{2+}, which caused

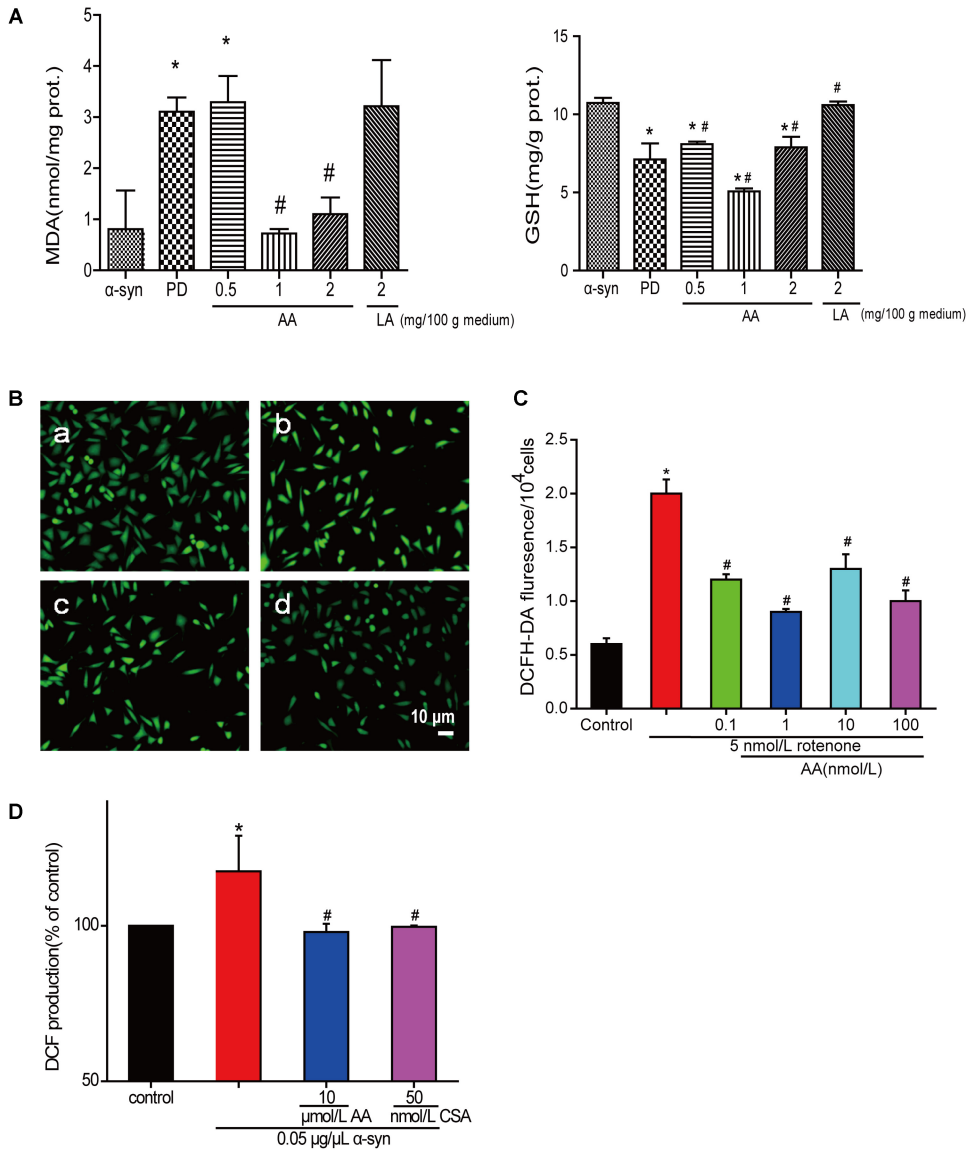

FIGURE 3 | AA reverses PD-like oxidative stress. **(A)** Effects of AA on the activities of MDA and GSH in α-syn transgenic PD drosophila. Control and a-syn transgenic PD Drosophila were divided into indicated groups, and they all collected at DAY 36. The level of MDA and GSH in supernatant of drosophila homogenate were detected by kits. (mean ± SD, $n = 3$, $^*p < 0.05$ vs. normal control group after treatment with different concentrations of AA or LA). **(B,C)** Intracellular ROS levels were determined based on DCF fluorescence under an inverted fluorescence microscope and on a spectrofluorometer. SH-SY5Y cells were treated with 5 nM rotenone exposure for 4 weeks and then various concentrations of AA after 24 h. a: control; b: 5 nmol/L chronic rotenone; c: 1 μM AA; d: 10 μM AA. Bar: 10 μm. Data are expressed as means ± SD, $n = 3$. $^*p < 0.01$ vs. control group, $\#p < 0.01$ vs. rotenone group. **(D)** Effects of AA on α-syn induced mitochondrial ROS formation (DCF production). Isolated mitochondria dyed with DCFH-DA were treated with vehicle or AA for 60 min at 37°C and exposed to 0 or 0.05 μg/μL α-syn at the same time. 60 min later fluorescence were detected on a spectrofluorometer. Data are expressed as means ± SD, $n = 3$. $^*p < 0.01$ vs. control group, $\#p < 0.01$ vs. α-syn group.

a 10% decrease compared with the control group. Mitochondrial swelling that was induced by α-syn was inhibited by pretreatment with 1–100 μmol AA/L for 3 min (**Figure 5A**)—an effect that was nearly the same as with CsA, a specific blocker of MPTPs, which lie in the sites where the mitochondrial inner and outer membranes meet. This result suggests that AA was.

The opening of MPTPs can stimulate the release of proapoptotic factors from the mitochondrial interspaces. Thus, we measured Cyt C in the mitochondria by immunoblotting. After mitochondria were incubated for 1 h with 0.05 μg α-syn/μL at 37°C, the level of Cyt C decreased markedly (**Figure 5B**), indicating its release into the extramitochondrial medium. Cotreatment with 10 μmol AA/L for 1 h partially inhibited α-syn-induced Cyt C release.

Next, we examined whether AA can block α-syn accumulation in the mitochondria. As shown in **Figure 5C**, after mitochondria

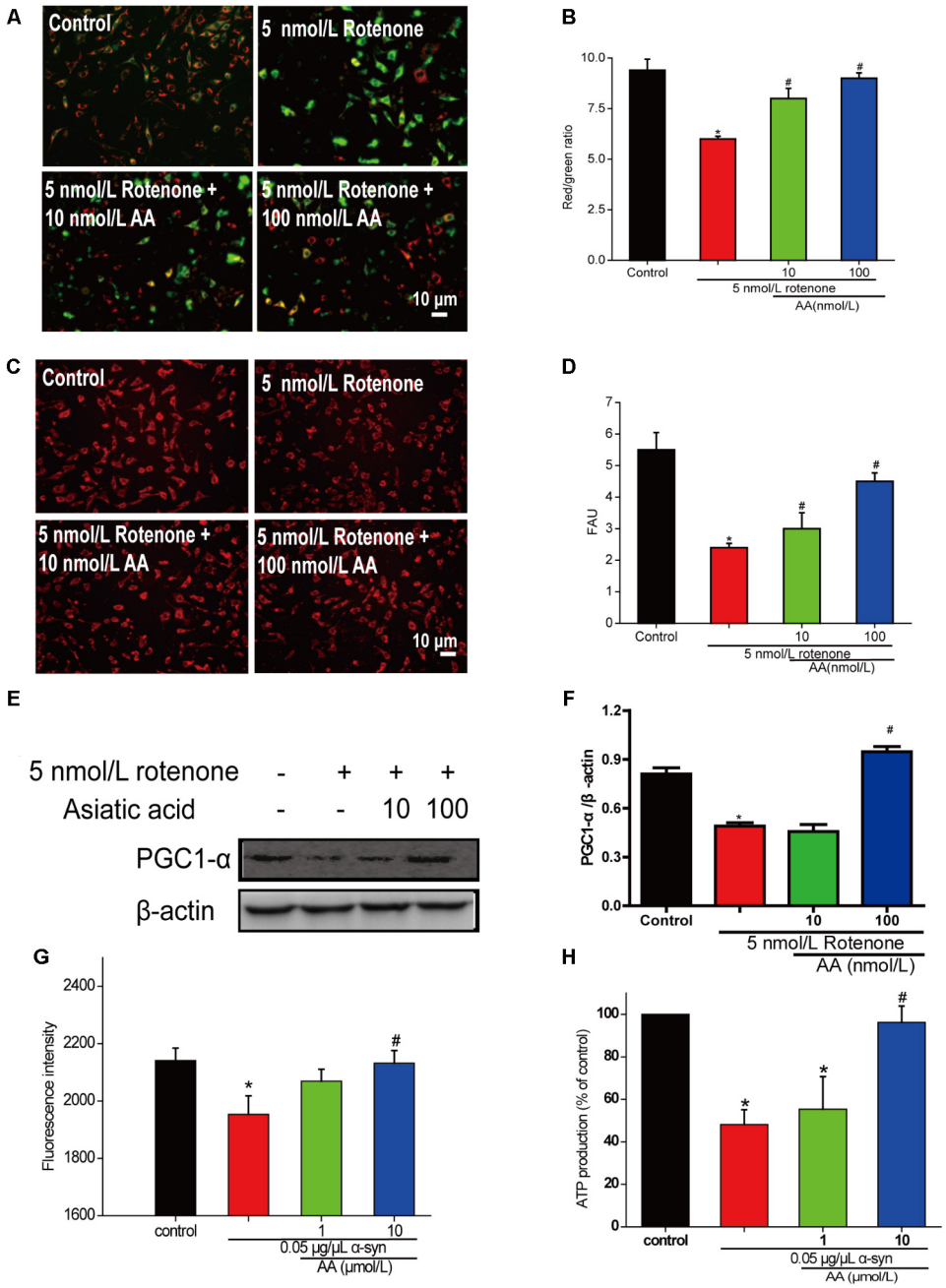

FIGURE 4 | AA protects against mitochondrial dysfunction induced by PD-like injury. **(A,B)** SH-SY5Y cells were treated with 5 nM rotenone exposure for 4 weeks and then various concentrations of AA after 24 h. Intracellular red and green fluorescence of JC-1 was determined under an inverted fluorescence microscope **(A)** and on a spectrofluorometer **(B)**. Mitochondria number was determined with an inverted fluorescence microscope **(C)** and spectrofluorometer **(D)** and based on expression of PGC1-α **(E,H)**. **(F)** Effects of AA on mitochondrial membrane potential (JC-1 fluorescence intensity). Isolated mitochondria were treated with vehicle or AA for 60 min at 37°C and exposed to 0 or 0.05 μg/μL α-syn at the same time. Data are expressed as means ± SD, n = 3. $^{*}p < 0.01$ vs. control group, $^{\#}p < 0.01$ vs. rotenone group. **(G)** Effects of AA on mitochondrial ATP synthesis. Isolated mitochondria were treated with vehicle or AA for 60 min at 37°C and exposed to 0 or 0.05 μg/μL α-syn at the same time. The values are expressed as percentage of control, which is set to 100%. Data are expressed as means ± SD, $n = 3$. $^{*}p < 0.01$ vs. control group, $^{\#}p < 0.01$ vs. α-syn group. Bar: 10 μm.

were incubated for 1 h with 0.05 μg α-syn/μL at 37°C, α-syn amassed in the mitochondria, which could be inhibited by 10 μmol AA/L. These results indicate that AA blocks mitochondrial translocation of α-syn.

DISCUSSION

Many observations suggest that α-syn causes neurodegeneration by interfering with multiple signaling pathways. α-syn

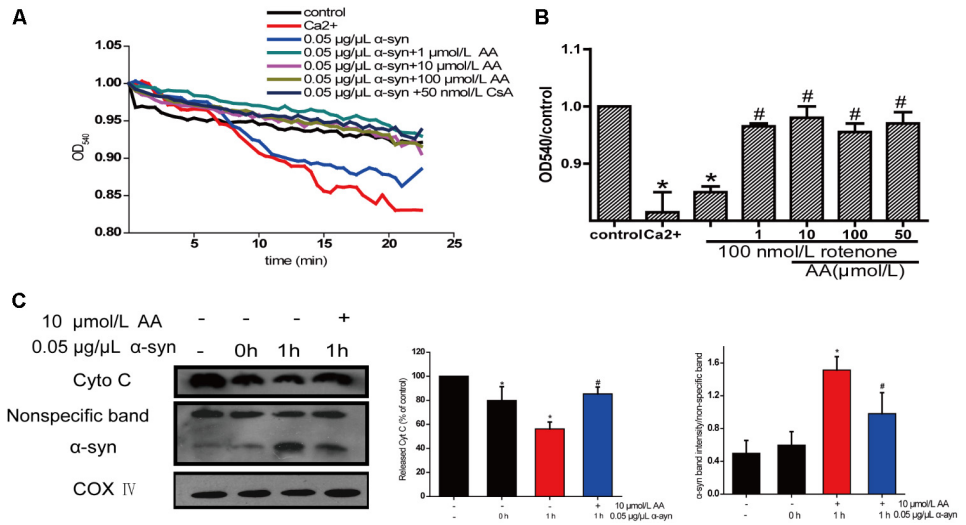

FIGURE 5 | Neuroprotective effects of AA against α-syn-induced injury in isolated mitochondria. Isolated mitochondria were treated with vehicle or AA for 60 min at 37°C and exposed to 0 or 0.05 μg/μL α-syn at the same time. **(A,B)** Inhibitory effects of AA on α-syn-induced mitochondrial swelling, which was reflected by the decrease in absorbance at 540 nm and the results were statistics at the endpoint of the experiment. **(C)** AA reverses α-syn-induced release of cyt C from mitochondria and mitochondrial translocation of α-syn. Data are expressed as means ± SD, $n = 3$. *$p < 0.01$ vs. control group, #$p < 0.01$ vs. α-syn group.

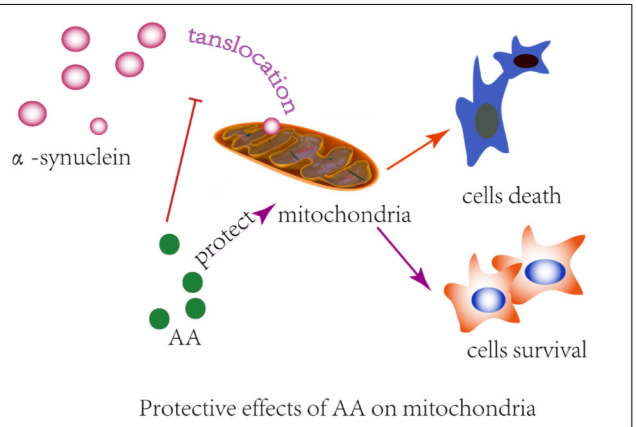

FIGURE 6 | Illustration of the protective effects of AA in α-syn- and rotenone-induced PD-like models. AA may maintain the integrity of the mitochondrial membrane and then block α-syn importation into mitochondria.

protein can form plasma membrane channels or modify their activity, thus altering membrane permeability to ions; abnormally associate with mitochondria and cause mitochondrial dysfunction (e.g., mitochondrial depolarization, Ca^{2+} dyshomeostasis, cytochrome c release); and interfere with autophagy regulation (Ottolini et al., 2017). Previously, we found that AA protects neuronal cells against rotenone-induced mitochondrial dysfunctional injury (Xiong et al., 2009b). In the present study, we found that AA protects against rotenone- and α-syn-induced damage *in vivo* and *in vitro* through a mechanism that is related to directly preventing MPTPs from opening and inhibiting α-syn translocation to mitochondria (**Figure 6**). Our results are consistent with previous reports that in PD, α-syn aggregates are associated with intact mitochondria but interact with and cause nuclear degradation, which might be a major cause of cell death (Power et al., 2017).

We observed a significant improvement in the climbing response of PD flies with 0.5–2 mg AA/100 g of culture medium. These results suggest that AA exerts its neuroprotective effects through the prevention of oxidative damage via potent ROS-scavenging ability. AA extended the average lifespan of female PD flies at 0.5 mg/100 grams of culture medium.

Mitochondrial dysfunction has been implicated in the pathogenesis of many neurodegenerative diseases (Lin and Beal, 2006). In recent years, isolated mitochondria from brain and liver have been used frequently to identify the direct mechanisms of mitochondria in pathology and pharmacology (Jia et al., 2008; Gao et al., 2009; Banerjee et al., 2010), demonstrating that it is a good model for studying neurodegenerative diseases and screening drugs for neurodegenerative diseases.

Recent neurochemical studies in the postmortem brains of patients with PD have revealed significant increases in α-syn, indicating a relationship between the accumulation of α-syn and PD (Wills et al., 2010). Although the physiological functions of α-syn are unknown, more and more researchers have identified an association between α-syn and mitochondria in cellular and mouse models (Devi et al., 2008; Shavali et al., 2008; Liu et al., 2009). There is also substantial evidence that implicates α-syn and its ability to aggregate and bind vesicle membranes in the development of PD (Giannakis et al., 2008). α-syn can accumulate in mitochondria, based on its N-terminal 32-amino-acid region, which targets dopaminergic neurons and isolated mitochondria (Devi et al., 2008). In parallel, we found that additional α-syn could be imported to mitochondria in only 1 h—an effect that could be blocked by 10 μmol/L AA.

Mitochondrial import of α-syn is dependent on the mitochondrial transmembrane potential (ΔΨm) and mitochondrial ATP. Under our experimental conditions, AA attenuated the α-syn-induced MMP decline and ATP synthesis. This result is consistent with our previous study, in which AA rescued SH-SY5Y cells from rotenone- and H_2O_2-induced damage by preventing mitochondrial dysfunction (Xiong et al., 2009a). Several lines of evidence suggest that α-syn regulates membrane stability, neuronal plasticity, and enzymatic activity (Perez et al., 2002; Recchia, 2004; Bennett, 2005; Cookson, 2005; Shults, 2006). Moreover, constitutive levels of α-syn may be important for maintaining the functional integrity of the mitochondrial membrane (Ellis et al., 2005; Devi et al., 2008).

Impaired integrity of the mitochondrial membrane destroys the transmembrane proton gradient and interrupts the synthesis of ATP but also indirectly induces an increase in ROS and the loss of enzyme activity and can even trigger apoptosis (Norenberg and Rao, 2007). Consistent with these data, we observed ROS overproduction and the release of mitochondrial Cyt C—which can initiate apoptosis—due to disruptions in the integrity of the mitochondrial membrane structure by α-syn. However, this damage was reversed by AA, which might maintain the functional integrity of mitochondrial membranes.

Further, AA blocked α-syn-induced mitochondrial swelling in our study. Generally, mitochondrial swelling has been considered to result from an increase in inner membrane permeability and opening of MPTPs, high-conductance channels with several macromolecular components, including VDAC. AA regulates VDAC expression, according to our previous study (Xiong et al., 2009a), implying that the maintenance of the mitochondrial membrane by AA is due to preventing the MPTPs from opening.

In summary, this study has demonstrated the protective effects of AA in α-syn- and rotenone-induced PD-like models. We found that this protection occurs mainly through the maintenance of membrane integrity and blockade α-syn importation into mitochondria (**Figure 4**). We also found that AA reverses the increase in MDA levels and the decline in GSH content that is induced by α-syn overexpression in PD flies. AA reduces oxidative stress, against the α-syn aggregation caused by cell death, to protect nerve cells and reduce or even revert the symptoms of PD.

AUTHOR CONTRIBUTIONS

HD and YX designed and conducted the research and wrote the paper. JS and CC performed the statistical analysis. JG supervised the study. HX reviewed the paper. All authors have read and approved the final manuscript.

FUNDING

This work was supported by the National Natural Science Foundation of China [31171143, 30971197, and 81503051], the National Key Projects of Fundamental R/D of China [973 Project: 2011CB510004], Natural Science Foundation of Jiangsu Province [BK20130476], and the Graduate Student Research and Innovation Program of Jiangsu Province [Grant No. CX10B_284Z].

ACKNOWLEDGMENTS

We thank Liwen Bianji, Edanz Editing China (www.liwenbianji.cn/ac), for editing the English text of a draft of this manuscript.

REFERENCES

Banerjee, K., Sinha, M., Pham Cle, L., Jana, S., Chanda, D., Cappai, R., et al. (2010). alpha-Synuclein induced membrane depolarization and loss of phosphorylation capacity of isolated rat brain mitochondria: implications in Parkinson's disease. *FEBS Lett.* 584, 1571–1576. doi: 10.1016/j.febslet.2010.03.012

Bennett, M. C. (2005). The role of alpha-synuclein in neurodegenerative diseases. *Pharmacol. Ther.* 105, 311–331. doi: 10.1016/j.pharmthera.2004.10.010

Cookson, M. R. (2005). The biochemistry of Parkinson's disease. *Annu. Rev. Biochem.* 74, 29–52. doi: 10.1146/annurev.biochem.74.082803.133400

Devi, L., Raghavendran, V., Prabhu, B. M., Avadhani, N. G., and Anandatheerthavarada, H. K. (2008). Mitochondrial import and accumulation of alpha-synuclein impair complex I in human dopaminergic neuronal cultures and Parkinson disease brain. *J. Biol. Chem.* 283, 9089–9100. doi: 10.1074/jbc.M710012200

Drew, B., and Leeuwenburgh, C. (2003). Method for measuring ATP production in isolated mitochondria: ATP production in brain and liver mitochondria of Fischer-344 rats with age and caloric restriction. *Am. J. Physiol. Regul. Integr. Comp. Physiol.* 285, R1259–R1267. doi: 10.1152/ajpregu.00264.2003

Elimadi, A., Sapena, R., Settaf, A., Le Louet, H., Tillement, J., and Morin, D. (2001). Attenuation of liver normothermic ischemia-reperfusion injury by preservation of mitochondrial functions with S-15176, a potent trimetazidine derivative1. *Biochem. Pharmacol.* 62, 509–516. doi: 10.1016/S0006-2952(01)00676-1

Ellis, C. E., Murphy, E. J., Mitchell, D. C., Golovko, M. Y., Scaglia, F., Barceló-Coblijn, G. C., et al. (2005). Mitochondrial lipid abnormality and electron transport chain impairment in mice lackingα-synuclein. *Mol. Cell. Biol.* 25, 10190–10201. doi: 10.1128/MCB.25.22.10190-10201.2005

Feany, M. B., and Bender, W. W. (2000). A *Drosophila* model of Parkinson's disease. *Nature* 404, 394–398. doi: 10.1038/35006074

Friberg, H., Wieloch, T., and Castilho, R. F. (2002). Mitochondrial oxidative stress after global brain ischemia in rats. *Neurosci. Lett.* 334, 111–114. doi: 10.1016/S0304-3940(02)01116-3

Gao, X., Zheng, C. Y., Yang, L., Tang, X. C., and Zhang, H. Y. (2009). Huperzine A protects isolated rat brain mitochondria against [beta]-amyloid peptide. *Free Radic. Biol. Med.* 46, 1454–1462. doi: 10.1016/j.freeradbiomed.2009.02.028

Giannakis, E., Pacífico, J., Smith, D. P., Hung, L. W., Masters, C. L., Cappai, R., et al. (2008). Dimeric structures of α-synuclein bind preferentially to lipid membranes. *Biochem. Biophys. Acta* 1778, 1112–1119. doi: 10.1016/j.bbamem.2008.01.012

Hoogerheide, D. P., Gurnev, P. A., Rostovtseva, T. K., and Bezrukov, S. M. (2017). Mechanism of alpha-synuclein translocation through a VDAC nanopore revealed by energy landscape modeling of escape time distributions. *Nanoscale* 9, 183–192. doi: 10.1039/c6nr08145b

Jellinger, K. (2012). The role of alpha-synuclein in neurodegeneration - An update. *Transl. Neurosci.* 3, 75–122. doi: 10.2478/s13380-012-0013-1

Jia, H., Li, X., Gao, H., Feng, Z., Li, X., Zhao, L., et al. (2008). High doses of nicotinamide prevent oxidative mitochondrial dysfunction in a cellular model and improve motor deficit in a Drosophila model of Parkinson's disease. *J. Neurosci. Res.* 86, 2083–2090. doi: 10.1002/jnr.21650

Krishnamurthy, R. G., Senut, M. C., Zemke, D., Min, J., Frenkel, M. B., and Greenberg, E. J. (2009). Asiatic acid, a pentacyclic triterpene from *Centella*

asiatica, is neuroprotective in a mouse model of focal cerebral ischemia. *J. Neurosci. Res.* 87, 2541–2550. doi: 10.1002/jnr.22071

Lai, J. C., and Clark, J. B. (1979). Preparation of synaptic and nonsynaptic mitochondria from mammalian brain. *Methods Enzymol.* 55, 51–60. doi: 10.1016/0076-6879(79)55008-3

Lee, C. S., Han, J. H., Jang, Y. Y., Song, J. H., and Han, E. S. (2002). Differential effect of catecholamines and MPP^+ on membrane permeability in brain mitochondria and cell viability in PC12 cells. *Neurochem. Int.* 40, 361–369. doi: 10.1016/S0197-0186(01)00069-9

Lee, K. Y., Bae, O. N., Serfozo, K., Hejabian, S., Moussa, A., Reeves, M., et al. (2012). Asiatic acid attenuates infarct volume, mitochondrial dysfunction, and matrix metalloproteinase-9 induction after focal cerebral ischemia. *Stroke* 43, 1632–1638. doi: 10.1161/STROKEAHA.111.639427

Lee, M. K., Kim, S. R., Sung, S. H., Lim, D., Kim, H., Choi, H., et al. (2000). Asiatic acid derivatives protect cultured cortical neurons from glutamate-induced excitotoxicity. *Res. Commun. Mol. Pathol. Pharmacol.* 108, 75–86.

Lee, V. M. Y., and Trojanowski, J. Q. (2006). Mechanisms of Parkinson's disease linked to pathological α-synuclein: new targets for drug discovery. *Neuron* 52, 33–38. doi: 10.1016/j.neuron.2006.09.026

Lin, M. T., and Beal, M. F. (2006). Mitochondrial dysfunction and oxidative stress in neurodegenerative diseases. *Nature* 443, 787–795. doi: 10.1038/nature05292

Liu, G., Zhang, C., Yin, J., Li, X., Cheng, F., Li, Y., et al. (2009). alpha-Synuclein is differentially expressed in mitochondria from different rat brain regions and dose-dependently down-regulates complex I activity. *Neurosci. Lett.* 454, 187–192. doi: 10.1016/j.neulet.2009.02.056

Long, J. G., Gao, H. X., Sun, L. J., Liu, J. K., and Zhao-Wilson, X. (2009). Grape extract protects mitochondria from oxidative damage and improves locomotor dysfunction and extends lifespan in a Drosophila Parkinson's disease model. *Rejuvenation Res.* 12, 321–331. doi: 10.1089/rej.2009.0877

Mook-Jung, I., Shin, J. E., Yun, S. H., Huh, K., Koh, J. Y., Park, H. K., et al. (1999). Protective effects of asiaticoside derivatives against beta-amyloid neurotoxicity. *J. Neurosci. Res.* 58, 417–425. doi: 10.1002/(SICI)1097-4547(19991101)58:3<417::AID-JNR7>3.0.CO;2-G

Moore, D. J., West, A. B., Dawson, V. L., and Dawson, T. M. (2005). Molecular pathophysiology of Parkinson's disease. *Annu. Rev. Neurosci.* 28, 57–87. doi: 10.1146/annurev.neuro.28.061604.135718

Norenberg, M. D., and Rao, K. V. (2007). The mitochondrial permeability transition in neurologic disease. *Neurochem. Int.* 50, 983–997. doi: 10.1016/j.neuint.2007.02.008

Ottolini, D., Cali, T., Szabo, I., and Brini, M. (2017). Alpha-synuclein at the intracellular and the extracellular side: functional and dysfunctional implications. *Biol. Chem.* 398, 77–100. doi: 10.1515/hsz-2016-0201

Pendleton, R. G., Parvez, F., Sayed, M., and Hillman, R. (2002). Effects of pharmacological agents upon a transgenic model of Parkinson's disease in *Drosophila melanogaster*. *J. Pharmacol. Exp. Ther.* 300, 91–96. doi: 10.1124/jpet.300.1.91

Perez, R. G., Waymire, J. C., Lin, E., Liu, J. J., Guo, F., and Zigmond, M. J. (2002). A role for alpha-synuclein in the regulation of dopamine biosynthesis. *J. Neurosci.* 22, 3090–3099. doi: 10.1523/JNEUROSCI.22-08-03090.2002

Power, J. H. T., Barnes, O. L., and Chegini, F. (2017). Lewy bodies and the mechanisms of neuronal cell death in Parkinson's disease and dementia with lewy bodies. *Brain Pathol.* 27, 3–12. doi: 10.1111/bpa.12344

Recchia, A. (2004). Alpha-Synuclein and Parkinson's disease. *FASEB J.* 18, 617–626. doi: 10.1096/fj.03-0338rev

Reers, M., Smith, T. W., and Chen, L. B. (1991). J-aggregate formation of a carbocyanine as a quantitative fluorescent indicator of membrane potential. *Biochemistry* 30, 4480–4486. doi: 10.1021/bi00232a015

Rochet, J. C., Outeiro, T. F., Conway, K. A., Ding, T. T., Volles, M. J., Lashuel, H. A., et al. (2004). Interactions among alpha-synuclein, dopamine, and biomembranes: some clues for understanding neurodegeneration in Parkinson's disease. *J. Mol. Neurosci.* 23, 23–34. doi: 10.1385/JMN:23:1-2:023

Shavali, S., Brown-Borg, H. M., Ebadi, M., and Porter, J. (2008). Mitochondrial localization of alpha-synuclein protein in alpha-synuclein overexpressing cells. *Neurosci. Lett.* 439, 125–128. doi: 10.1016/j.neulet.2008.05.005

Sherer, T. B., Betarbet, R., Stout, A. K., Lund, S., Baptista, M., Panov, A. V., et al. (2002). An in vitro model of Parkinson's disease: linking mitochondrial impairment to altered alpha-synuclein metabolism and oxidative damage. *J. Neurosci.* 22, 7006–7015. doi: 10.1523/JNEUROSCI.22-16-07006.2002

Shults, C. W. (2006). Lewy bodies. *Proc. Natl. Acad. Sci. U.S.A.* 103, 1661–1668. doi: 10.1073/pnas.0509567103

Spillantini, M. G., Schmidt, M. L., Virginia, M.-Y., Lee, J. Q., Trojanowski, R. J., Michel, G., et al. (1997). α-Synuclein in Lewy bodies. *Nature* 388, 839–840. doi: 10.1038/42166

Wadia, J. S., Chalmers-Redman, R. M., Ju, W. J., Carlile, G. W., Phillips, J. L., Fraser, A. D., et al. (1998). Mitochondrial membrane potential and nuclear changes in apoptosis caused by serum and nerve growth factor withdrawal: time course and modification by (-)-deprenyl. *J. Neurosci.* 18, 932–947. doi: 10.1523/JNEUROSCI.18-03-00932.1998

Wills, J., Jones, J., Haggerty, T., Duka, V., Joyce, J. N., Sidhu, A., et al. (2010). Elevated tauopathy and alpha-synuclein pathology in postmortem Parkinson's disease brains with and without dementia. *Exp. Neurol.* 225, 210–218. doi: 10.1016/j.expneurol.2010.06.017

Xiong, Y., Ding, H., Xu, M., and Gao, J. (2009a). Protective effects of asiatic acid on rotenone-or H_2O_2-induced injury in SH-SY5Y cells. *Neurochem. Res.* 34, 746–754. doi: 10.1007/s11064-008-9844-0

Xiong, Y. Y., Ding, H. Q., Xu, M. F., and Gao, J. (2009b). Protective effects of asiatic acid on rotenone- or H_2O_2-induced injury in SH-SY5Y cells. *Neurochem. Res.* 34, 746–754. doi: 10.1007/s11064-008-9844-0

Xu, M. F., Xiong, Y. Y., Liu, J. K., Qian, J. J., Zhu, L., and Gao, J. (2012). Asiatic acid, a pentacyclic triterpene from *Centella asiatica*, is neuroprotective in a mouse model of focal cerebral ischemia. *Acta Pharmacol. Sin.* 87, 578–587. doi: 10.1038/aps.2012.3

Zhang, X., Wu, J., Dou, Y., Xia, B., Rong, W., Rimbach, G., et al. (2012). Asiatic acid protects primary neurons against C2-ceramide-induced apoptosis. *Eur. J. Pharmacol.* 679, 51–59. doi: 10.1016/j.ejphar.2012.01.006

Conflict of Interest Statement: The authors declare that the research was conducted in the absence of any commercial or financial relationships that could be construed as a potential conflict of interest.

frontiers in Neuroscience

ORIGINAL RESEARCH
published: 24 July 2018
doi: 10.3389/fnins.2018.00492

ErbB4 Preserves Blood-Brain Barrier Integrity via the YAP/PIK3CB Pathway After Subarachnoid Hemorrhage in Rats

*Huan Qian[1], Zhangqi Dou[2], Wu Ruan[2], Pingyou He[2], John H. Zhang[3] and Feng Yan[2]**

[1] Department of Plastic Surgery, The Second Affiliated Hospital, School of Medicine, Zhejiang University, Hangzhou, China, [2] Department of Neurosurgery, The Second Affiliated Hospital, School of Medicine, Zhejiang University, Hangzhou, China, [3] Division of Physiology, Department of Basic Sciences, Loma Linda University School of Medicine, Loma Linda, CA, United States

Studies have suggested that blood-brain barrier (BBB) disruption contributes to the pathogenesis of early brain injury after subarachnoid haemorrhage (SAH). Activation of the receptor tyrosine kinase ErbB4 can cause intramembrane proteolysis and release a soluble intracellular domain (ICD) that modulates transcription in the nucleus. This study was carried out to investigate the potential roles of ErbB4 in preserving BBB integrity after experimental SAH, as well as the underlying mechanisms of its protective effects. Endovascular perforation was used to prepare a rat SAH model. The SAH grade, neurological score, brain edema and BBB permeability were evaluated after surgery. Immunohistochemistry was used to determine the localization of ErbB4 and yes-associated protein (YAP). ErbB4 activator Nrg1 isoform β1 (Nrg1β1), Specific ErbB4 siRNA, YAP siRNA and PIK3CB specific inhibitor TGX 221 were used to manipulate the proposed pathway. The expression levels of ErbB4 ICD and YAP were markly increased after SAH. Double immunohistochemistry labeling showed that ErbB4 and YAP were expressed in endothelial cells and neurons. Activation of ErbB4 by Nrg1β1 (dosage 150 ng/kg) treatment promoted the neurobehavioral deficit, alleviated the brain water content and reduced albumin leakage 24 and 72 h after SAH. ErbB4 activation significantly promoted YAP and PIK3CB activity and increased the expression of tight junction proteins Occludin and Claudin-5. Depletion of ErbB4 aggravated neurological impairment and BBB disruption after SAH. The beneficial effects of ErbB4 activation were abolished by YAP small-interfering RNA and specific PIK3CB inhibitor. Activation of ErbB4 improved neurological performance after SAH through the YAP/PIK3CB signaling pathway, this neuroprotective effects may associated with BBB maintenance.

Keywords: ErbB4, YAP, PIK3CB, blood-brain barrier, early brain injury, subarachnoid hemorrhage

OPEN ACCESS

Edited by:
Gang Chen,
School of Medicine, Loma Linda University, China

Reviewed by:
Zongyi Xie,
Chongqing Medical University, China
Xihui Liu,
University of Texas Southwestern Medical Center, United States

****Correspondence:***
Feng Yan
fengyanzju@zju.edu.cn

Specialty section:
This article was submitted to Neurodegeneration, a section of the journal Frontiers in Neuroscience

Received: *02 May 2018*
Accepted: *02 July 2018*
Published: *24 July 2018*

Citation:
Qian H, Dou Z, Ruan W, He P, Zhang JH and Yan F (2018) ErbB4 Preserves Blood-Brain Barrier Integrity via the YAP/PIK3CB Pathway After Subarachnoid Hemorrhage in Rats. Front. Neurosci. 12:492. doi: 10.3389/fnins.2018.00492

INTRODUCTION

Aneurysmal subarachnoid hemorrhage (SAH) is one of the most life-threatening diseases, with high mortality and disability rates (Connolly et al., 2012). Recent studies have shifted the research focus from SAH-induced vasospasm to early brain injury. Defined as the pathophysiological event that occurs within 72 h after SAH, early brain injury (EBI) has been proposed as the primary

determinant of poor outcome in SAH patients (Sehba et al., 2012). Nevertheless, the definitive mechanisms of EBI after SAH have remained unclear, and blood-brain barrier (BBB) disruption plays an important role (Chen et al., 2014; Li et al., 2015). Strategies against BBB disruption after SAH may be helpful in attenuating EBI and lead to a better prognosis.

ErbB4 (EGFR family member v-erb-b2 avian erythroblastic leukemia viral oncogene homolog 4) is a kind of epidermal growth factor receptor kinases, which has been proven to play a key role in the regulation of neurite outgrowth, axonal guidance and synaptic signaling (Huang et al., 2000; Shamir et al., 2012). ErbB4 can undergo intramembrane proteolysis to release a soluble intracellular domain (ICD) (Ni et al., 2001). The ErbB4 ICD relocalizes to the nucleus, where it regulates transcription through its association with transcriptional co-regulators (Vidal et al., 2005; Gilmore-Hebert et al., 2010). Mice lacking ErbB4 receptor have shown defects in axon guidance in the central nervous system (Tidcombe et al., 2003). In an oxidative stress injury study, ErbB4 promoted the survival of endothelial cells and preserved BBB integrity (Lok et al., 2009). However, the precise role of ErbB4 during the pathological process after subarachnoid hemorrhage (SAH) and its acting pathway remain largely unknown.

ErbB4 was found to be a major receptor that could activate Yes-associated protein (YAP), which has emerged as a critical signaling hub that regulates cellular growth and organ size maintenance (Dong et al., 2007). Activation of YAP stimulated the expression of genes that contribute to cellular development (Zhao et al., 2010). PIK3CB is a catalytic component of phosphoinositol-3-kinase (PI3K), which was reported to be activated downstream of YAP (Lin et al., 2015). This study investigated potential effects of ErbB4 with its downstreams on BBB integrity in EBI after SAH.

MATERIALS AND METHODS

Study Design

All procedures were conducted following the institutional Animal Care and Use Committee at Zhejiang University and in accordance with NIH guidelines for the Care and Use of Laboratory Animals. Two hundred and eight three Male Sprague-Dawley (SD) rats (290–330 g; Harlan, Indianapolis, IN, United States) were housed in a humidity-controlled room (25 ± 1°C, 12-h light/dark cycle) and were raised with free access to water and food.

Experiment 1

To detect the time course expressions of ErbB4 and YAP in the sham group and at 3, 6, 12, 24, and 72 h after SAH (n = 6 in each group). Double immunohistochemistry staining of ErbB4/YAP with CD31 was performed at 24 h after SAH (n = 2) for morphological study.

Experiment 2

Extracellular domain of Neuregulin 1 isoformβ1 (Nrg1β1, R&D systems, Minneapolis, MN, United States) was used for activation of ErbB4, and administered intraperitoneally at 1 h after SAH induction. Besides the sham and vehicle groups, two groups of rats received a different dosage of Nrg1β1 (50 ng/kg and 150 ng/kg, n = 6). The dose of Nrg1β1was set according to a previous study (Depboylu et al., 2015). For outcome evaluation, neurobehavioral scores, brain edema and albumin extravasation were measured at 24 and 72 h after SAH in all groups (n = 6). The expression levels of ErbB4, ErbB4 ICD, YAP, PIK3CB, Occludin and Claudin-5 were analyzed via Western blotting.

Experiment 3

ErbB4 small-interfering RNA (siRNA) was injected via intracerebroventricular (ICV) administration at 24 h before SAH induction. The neurobehavior, brain edema, albumin extravasation and expression of ErbB4, YAP, PIK3CB, Occludin and Claudin-5 were measured at 24 h after SAH in all groups. The rats were randomly assigned into the following groups: SAH + Vehicle, SAH + Nrg1β1, SAH + Nrg1β1 + scrambled siRNA (in 5 μl sterile saline), and SAH + Nrg1β1 + ErbB4 siRNA (in 5 μl of sterile saline).

Experiment 4

Yes-associated protein siRNA was administered by ICV injection at 24 h before SAH. Neurobehavior, brain edema, albumin extravasation and the expression levels of ErbB4, YAP, PIK3CB, Occludin, and Claudin-5 were measured at 24 h after SAH in all groups. Rats were randomly assigned into the following groups: SAH + Vehicle, SAH + Nrg1β1, SAH + Nrg1β1 + scrambled siRNA (in 5 μl of sterile saline), and SAH + Nrg1β1 + YAP siRNA (in 5 μl of sterile saline).

Experiment 5

The PIK3CB specific inhibitor TGX 221 (2.5 mg/kg, I.V., Cayman Chemical Corp., Ann Arbor, MI, United States) dissolved in PBS was administered at 1 h before SAH induction (Sturgeon et al., 2008). Control animals were injected with the same volume of PBS. Neurobehavior, brain edema, BBB permeability and western blots were measured at 24 h after SAH in all groups.

SAH Model

The SAH rat model was induced by endovascular perforation as previously described (Yan et al., 2017a). The rats underwent tracheal intubation with 3% isoflurane anesthesia. Next, we dissected the left external carotid artery, and a sharpened, 4-0 monofilament nylon suture was inserted vertically into the left internal carotid artery through the bifurcation of the external carotid artery until we felt slight resistance. The suture was then further advanced to impale the vessel. Sham-operated rats underwent nearly the same procedure, and we withdrew the suture once resistance was felt without any puncture.

Intracerebroventricular Drug Injection

Intracerebroventricular drug injection was performed as reported previously (Yan et al., 2017b). The rats were placed in a stereotaxic apparatus under 2.5% isoflurane anesthesia. The needle of a 10-μl Hamilton syringe (Microliter701; Hamilton Company, Reno, NV, United States) was stereotactically inserted

through a burr hole into the left lateral ventricle, which is coordinated relative to the bregma as follows: 1.5 mm posterior, 1.0 mm lateral and 3.5 mm below the horizontal plane of the skull. Next, 500 pmol/5 μl of ErbB4 siRNA (Thermo Fisher Scientific, Waltham, MA, United States), YAP siRNA (Thermo Fisher Scientific, Waltham, MA, United States), or scrambled siRNA (Thermo Fisher Scientific, Waltham, MA, United States) was injected at 1 day before SAH induction with Lipofectamine 2000 (Thermo Fisher Scientific, Waltham, MA, United States) at the rate of 0.5 μl/min. To enhance the gene silencing efficiency, two different ErbB4 siRNAs were mixed (5′ CCCACUAGUCAUGACUGCAUUUACU3′ and 5′AGUAAAUGCAGU-CAUGACUAGUGGG3′) and two different YAP siRNAs were mixed (5′GGCUGC-GAUUGAAA CAGCAGGAGUU3′ and 5′AACUCCUGCUGUUUCAAUCGC AGC-C3′).

SAH Grade

The severity of SAH was quantified using a previously published grading scale at the time of euthanasia (Sugawara et al., 2008). The basal cistern was divided into 6 segments, and the amount of the subarachnoid blood clot on each segment was scored from 0 to 3. Each rat received a total SAH score ranging from 0 to 18, and rats with mild SAH (score < 8) were excluded from this study.

Neurological Score

Neurological deficits were evaluated at 24 and 72 h after SAH according to the modified Garcia's scoring system (Garcia et al., 1995): spontaneous activity, symmetry in movement of four limbs, forepaw outstretching, climbing, body proprioception, and response to vibrissae touch. The total scores of the modified Garcia's test ranged from 3 to 18. Additionally, beam balance test (4-point scoring system) was performed (Tang et al., 2015). The rats were placed on a beam, and the walking distance within 1 min was measured (0–4).

Brain Water Content

The brains were collected 24 and 72 h after SAH induction and were separated into the left hemisphere, right hemisphere, cerebellum and brain stem. Each part was weighed immediately after removal (wet weight) and then was dried in an oven at 105°C for 72 h before another weighing (dry weight). The percentage of water content was calculated following the equation: [(wet weight- dry weight)/wet weight] × 100% (Chen et al., 2015).

Immunofluorescence Staining

Double-immunofluorescence staining of cerebral cortex was performed at 24 h after SAH as described previously (Xie et al., 2017). Sections were incubated overnight at 4°C with rabbit anti-ErbB4 (Abcam, Cambridge, MA, United States), rabbit anti-YAP (Cell Signaling Technology, Beverly, MA, United States), and mouse anti-CD31 (Abcam, Cambridge, MA, United States), followed by fluorescence dye-conjugated secondary antibodies (Jackson Immunoresearch, West Grove, PA, United States) for 3 h at 20°C. The sections were then visualized with a fluorescence microscope. Photomicrographs were analyzed using Image-Pro Plus software (Olympus, Melville, NY, United States).

Western Blotting

Western blot analysis was performed as previously described (Yan et al., 2014). The left brain hemisphere (perforation side) was collected according to scheduled time point. Equivalent amounts of protein (50 μg) were loaded onto sodium dodecyl sulfate (SDS) polyacrylamide gels and were separated by electrophoresis. The proteins were transferred onto nitrocellulose membranes, which were blocked by a blocking buffer. Primary antibodies were diluted to incubate with the membrane under gentle agitation at 4°C overnight: anti-ErbB4 (Abcam, Cambridge, MA, United States), anti-YAP (Cell Signaling Technology, Beverly, MA, United States), anti-PIK3CB (Abcam, Cambridge, MA, United States), anti-Occludin (Abcam, Cambridge, MA, United States), anti-Claudin-5 (Thermo Fisher Scientific, Waltham, MA, United States) and anti-β-actin (Santa Cruz Biotechnology, Dallas, TX, United States). Appropriate secondary antibodies were incubated with the membrane for 2 h at room temperature. Chemiluminescent detection was performed to identify the immune bands using the ECL Plus kit (Amersham Bioscience, Arlington Heights, IL, United States). Data was analyzed by densitometry with Image J software.

Statistical Analysis

One-way ANOVA followed by Turkey's multiple comparisons test was used for comparison between groups. The data were expressed as means ± SEM. $P < 0.05$ was considered statistically significant. All statistical analyses were performed using GraphPad Prism for Windows (LaJolla, CA, United States).

RESULTS

Mortality and Exclusion

There was no significant difference in the SAH grading score in all SAH groups (**Supplementary Figures S1A,B**). No rats died in the sham group. The mortality rate for each group is listed as follows: SAH group 18.18% (8/44), SAH + Vehicle group 21.43% (9/42), SAH + Nrg1β1 (50 ng/kg) group 17.07% (7/41), SAH + Nrg1β1 (150 ng/kg) group 13.51% (5/37), SAH + Nrg1β1 + Scr siRNA group 13.33% (2/15), SAH + Nrg1β1 + ErbB4 siRNA group 22.22% (4/18), SAH + Nrg1β1 + Scr siRNA group 14.29% (2/14), SAH + Nrg1β1 + YAP siRNA group 23.53% (4/17), SAH + Nrg1β1 + TGX 221 group 26.32% (5/19) (**Supplementary Figure S1C**). According to the SAH grading score, 19 rats with mild SAH were excluded from this study (**Supplementary Table S1**).

Time Course of Endogenous ErbB4, ErbB4 ICD and YAP Expression After SAH

Western blot analysis was applied on the rats of all groups at different time points after SAH induction (**Figure 1A**). The results demonstrated a significant increasing in the expression of ErbB4 ICD as early as 3 h after SAH. This trend continued and reached a peak at 72 h after SAH, while the total ErbB4 level remained stable ($p < 0.05$, **Figure 1B**).

A similar tendency was observed in the expression of YAP, which started to increase at 3 h after SAH ($p < 0.05$, **Figure 1C**). Morphological study with double immunohistochemistry staining showed that ErbB4 expression was colocalized with CD31 (Marker for endothelial cell), YAP was also proved to be intensely expressed in CD31-positive cells (**Figure 1D**). Double immunostaining showed that both ErbB4 and YAP were colocalized with Neuron at 24 h after SAH (**Supplementary Figure S2**).

Nrg1β1 Treatment Improves Neurobehavioral Functions and Reduces BBB Permeability After SAH

Remarkable neurobehavioral impairment was observed in the vehicle and Nrg1β1 (50 ng/kg)-treated group compared with that in the sham group at 24 and 72 h after SAH. Post-SAH administration of high-dosage Nrg1β1 (150 ng/kg) significantly improved the neurobehavioral performance ($p < 0.05$, **Figures 2A,B**). Brain water content in both hemispheres significantly increased in rats from the vehicle and Nrg1β1 (50 ng/kg)-treated group at 24 and 72 h after SAH ($p < 0.05$, **Figures 2C,E**). Nrg1β1 (150 ng/kg) treatment significantly decreased brain water content and attenuated brain swelling compared with the vehicle and Nrg1β1 (50 ng/kg) -treated group ($p < 0.05$, **Figures 2C,E**). BBB permeability was assessed by albumin extravasation in the ipsilateral hemisphere. Western blot analysis demonstrated a remarkable increased expression of albumin in vehicle and Nrg1β1 (50 ng/kg)-treated rats at 24 and 72 h after SAH that was significantly reversed by Nrg1β1 (150 ng/kg) treatment ($p < 0.05$, **Figures 2D,F**).

ErbB4 Activation by Nrg1β1 Administration Stabilizes Tight Junction Proteins After SAH

The expression of ErbB4 and its downstream signals was measured by western blot analysis (**Figure 3A**). The ratio of ErbB4 ICD/ErbB4 expression significantly increased after Nrg1β1 (50 ng/kg) administration and was further increased by high-dose Nrg1β1 (150 ng/kg) treatment compared with that in the sham and vehicle group ($p < 0.05$, **Figure 3B**). The expression level of YAP and PIK3CB was also significantly upregulated after Nrg1β1 administration, and there was a significant dose-dependent effect ($p < 0.05$, **Figures 3C,D**). The expression levels of tight junction proteins Occludin and Claudin-5 were significantly reduced at 24 h after SAH in the vehicle and low-dose Nrg1β1 (50 ng/kg)-treatment group. Treatment of Nrg1β1 (150 ng/kg) significantly reversed this tendency ($p < 0.05$, **Figures 3E,F**).

Silencing ErbB4 Aggravates Neurological Deficits and BBB Disruption After SAH

ErbB4 knockdown by siRNA significantly aggravated neurological deficits and increased albumin extravasation at 24 h after SAH ($p < 0.05$, **Figures 4A,B**) compared with that in the Nrg1β1-treatment group. The silencing efficacy of ErbB4 with its downstream signals and their effects on tight junction protein expression was measured by western blotting analysis (**Figure 4C**). Injection of scrambled siRNA had no effect on the expression of ErbB4 after Nrg1β1 administration ($p > 0.05$, **Figure 4D**), while specific ErbB4 siRNA significantly decreased the ratio of ErbB4 ICD/ErbB4 ($p < 0.05$, **Figure 4D**). ErbB4 activation

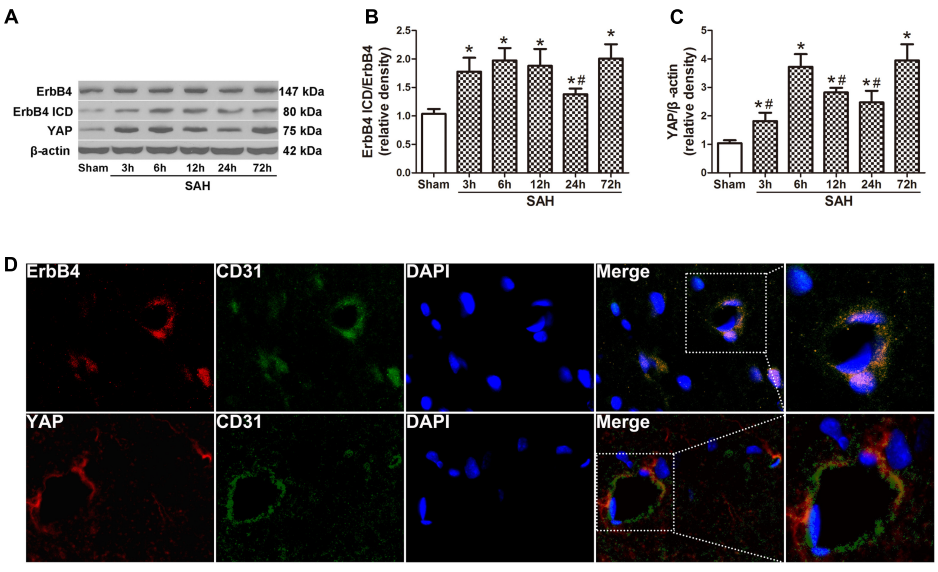

FIGURE 1 | Expression of endogenous ErbB4, ErbB4 ICD and YAP after subarachnoid haemorrhage (SAH) induction. Representative Western blot bands of ErbB4, ErbB4 ICD and YAP from the ipsilateral hemisphere after SAH **(A)**, quantitative analyses of ErbB4 ICD/ErbB4 **(B)** and YAP **(C)** expression. $n = 6$. Double immunostaining showed that both ErbB4 and YAP were colocalized with CD31-positive endothelial cells at 24 h after SAH **(D)**. $n = 2$, $^*p < 0.05$ versus sham; $\#p < 0.05$ versus 72 h.

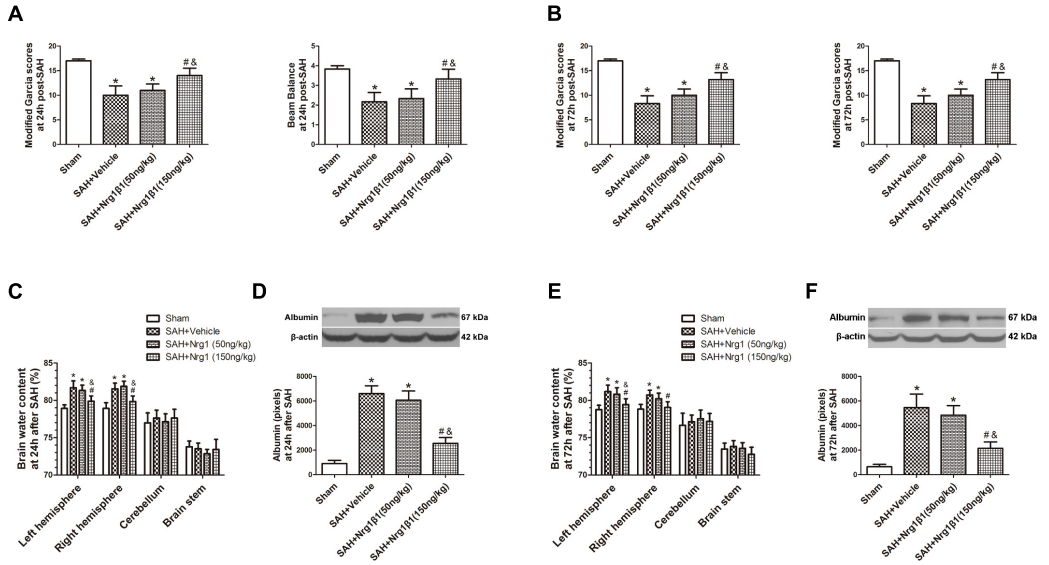

FIGURE 2 | Neuregulin1 isoformβ1 (Nrg1β1) treatment improved neurological functions, reduced brain water content and deceased albumin leakage at 24 and 72 h after SAH. Neurological impairment **(A,B)**, increased brain water content **(C,E)** and albumin extravasation **(D,F)** were found in the SAH + Vehicle groups. Nrg1β1 (150 ng/kg) treatment significantly alleviated neurological deficit **(A,B)**, reduced brain water content **(C,E)** and deceased albumin extravasation **(D,F)**. $n = 6$ for each group. $^*p < 0.05$ versus sham; $\#p < 0.05$ versus SAH + vehicle; $\&p < 0.05$ versus SAH + Nrg1β1 (50 ng/kg).

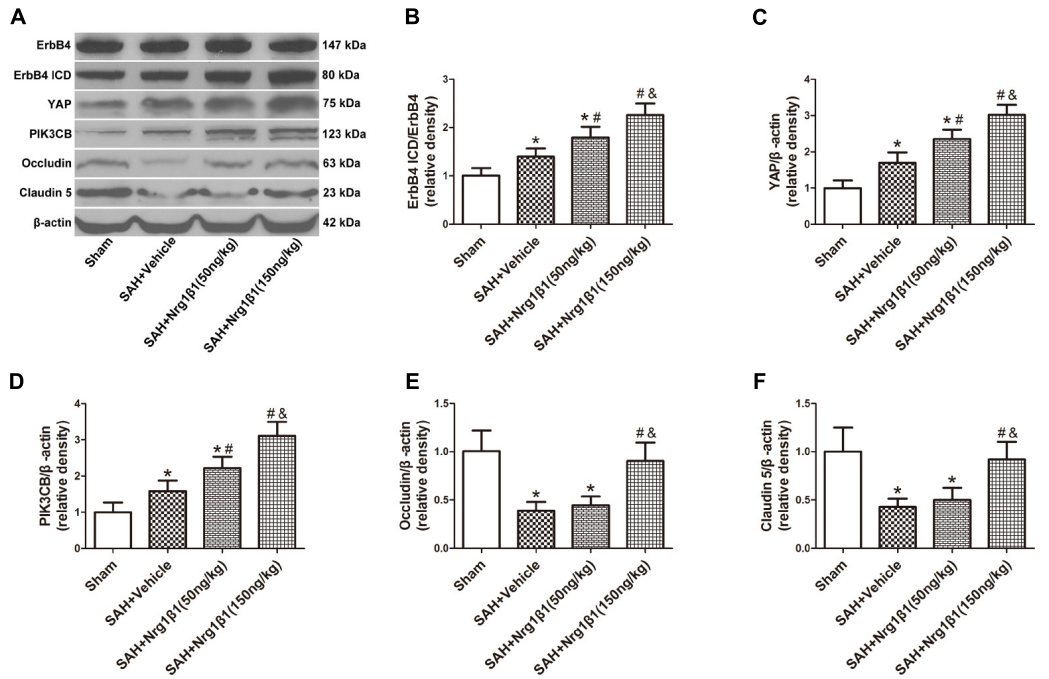

FIGURE 3 | ErbB4 activation by Nrg1β1 administration stabilizes tight junction proteins. Representative western blot bands of ErbB4, YAP, PIK3CB, Occludin and Claudin 5 **(A)**, the expression of ErbB4 ICD/ErbB4 **(B)**, YAP **(C)**, and PIK3CB **(D)** were increased at 24 h after SAH induction and were further up-regulated by high-dose Nrg1β1 (150 ng/kg) administration. SAH induction significantly reduced the expression of Occludin **(E)** and Claudin-5 **(F)**. Nrg1β1 (150 ng/kg) administration significantly reversed this effect. $n = 6$, $^*p < 0.05$ versus sham; $\#p < 0.05$ versus SAH + vehicle; $\&p < 0.05$ versus SAH + Nrg1β1 (50 ng/kg).

promoted YAP expression with its downstream protein PIK3CB, which were both remarkably decreased by ErbB4 siRNA administration ($p < 0.05$, **Figures 4E,F**). The increased expression of Occludin and Claudin-5 after Nrg1β1 treatment was significantly reversed by ErbB4 siRNA injection ($p < 0.05$, **Figures 4G,H**).

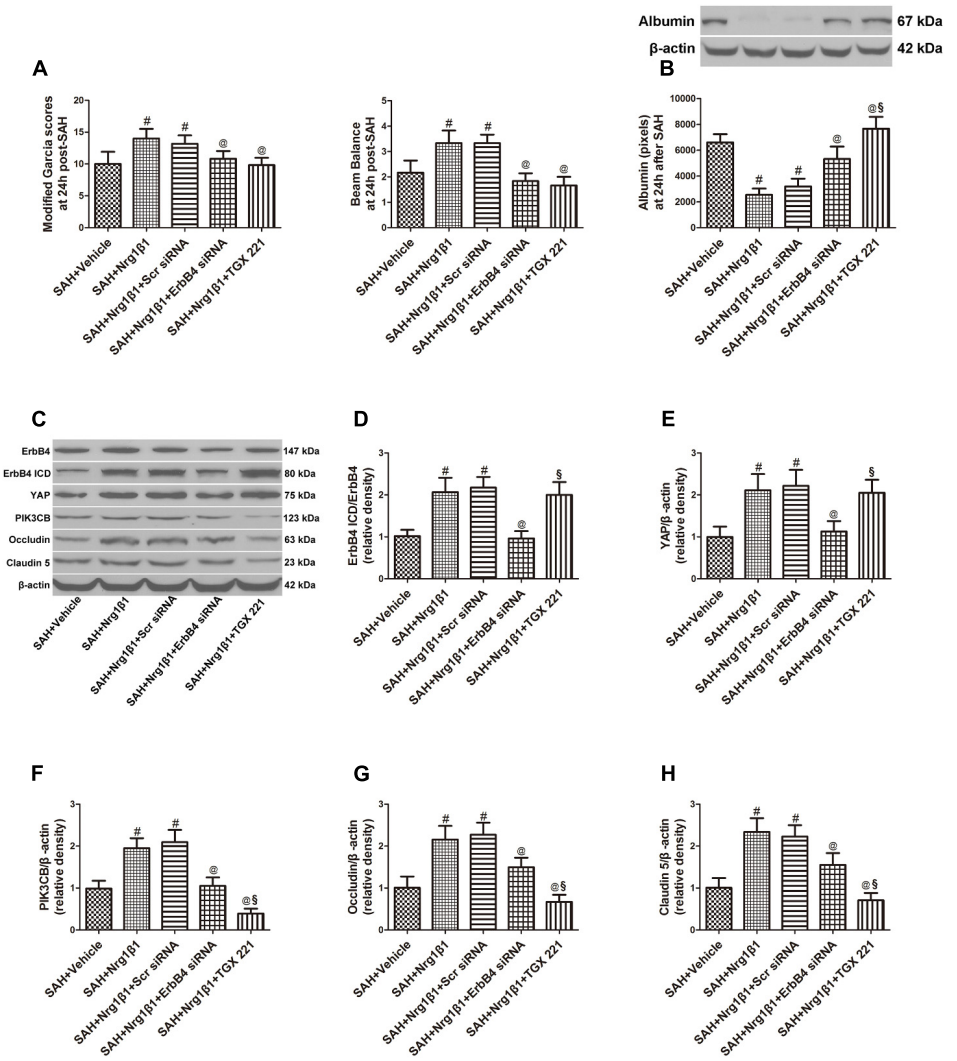

FIGURE 4 | Effects of ErbB4 siRNA pre-treatment on blood-brain barrier integrity at 24 h after SAH. ErbB4 siRNA aggravated neurological deficits **(A)** and increased albumin extravasation **(B)**. Representative western blot bands of ErbB4, YAP, PIK3CB, Occludin and Claudin 5 **(C)**. ErbB4 knockdown decreased the expression of ErbB4 ICD/ErbB4 **(D)**, YAP **(E)**, and PIK3CB **(F)**. The increased expression levels of Occludin and Claudin-5 after Nrg1β1 treatment were significantly reduced by ErbB4 depletion **(G,H)**. The PIK3CB specific inhibitor TGX 221 did not affect the expression of ErbB4 ICD/ErbB4 **(D)**, YAP **(E)** and significantly reduced the expression of PIK3CB **(F)**, Occludin **(G)** and Claudin-5 **(H)**. $n = 6$, #$p < 0.05$ versus SAH + vehicle; @$p < 0.05$ versus SAH + Nrg1β1; §$p < 0.05$ versus SAH + Nrg1β1 + ErbB4siRNA.

YAP Knockdown Reversed the Protective Effects of ErbB4 Activation on BBB Integrity After SAH

Subarachnoid haemorrhage rats were administered scrambled or YAP-specific siRNA before Nrg1β1 treatment to further explore the downstream signaling pathway participating in ErbB4 activation. YAP depletion significantly aggravated neurological deficits and increased albumin extravasation at 24 h after SAH ($p < 0.05$, **Figures 5A,B**). Western blot analysis was used to measure the effects of YAP knockdown and PIK3CB inhibition on tight junction protein expression (**Figure 5C**). Both scrambled and YAP siRNA injection had no effect on the increased ratio of ErbB4 ICD/ErbB4 expression after Nrg1β1 administration ($p > 0.05$, **Figure 5D**). YAP knockdown by specific siRNA significantly reduced the expression of YAP and its downstream PIK3CB ($p < 0.05$, **Figures 5E,F**). The expression level of tight junction protein Occludin and Claudin-5 were highly preserved by Nrg1β1 treatment at 24 h after SAH, but this tendency was significantly abolished by YAP siRNA pre-administration ($p < 0.05$, **Figures 5G,H**).

Inhibition of PIK3CB Reverses the Beneficial Effects of erbB4 Activation on BBB Integrity After SAH

The potent PIK3CB inhibitor TGX 221 significantly aggravated neurological deficits and increased albumin extravasation

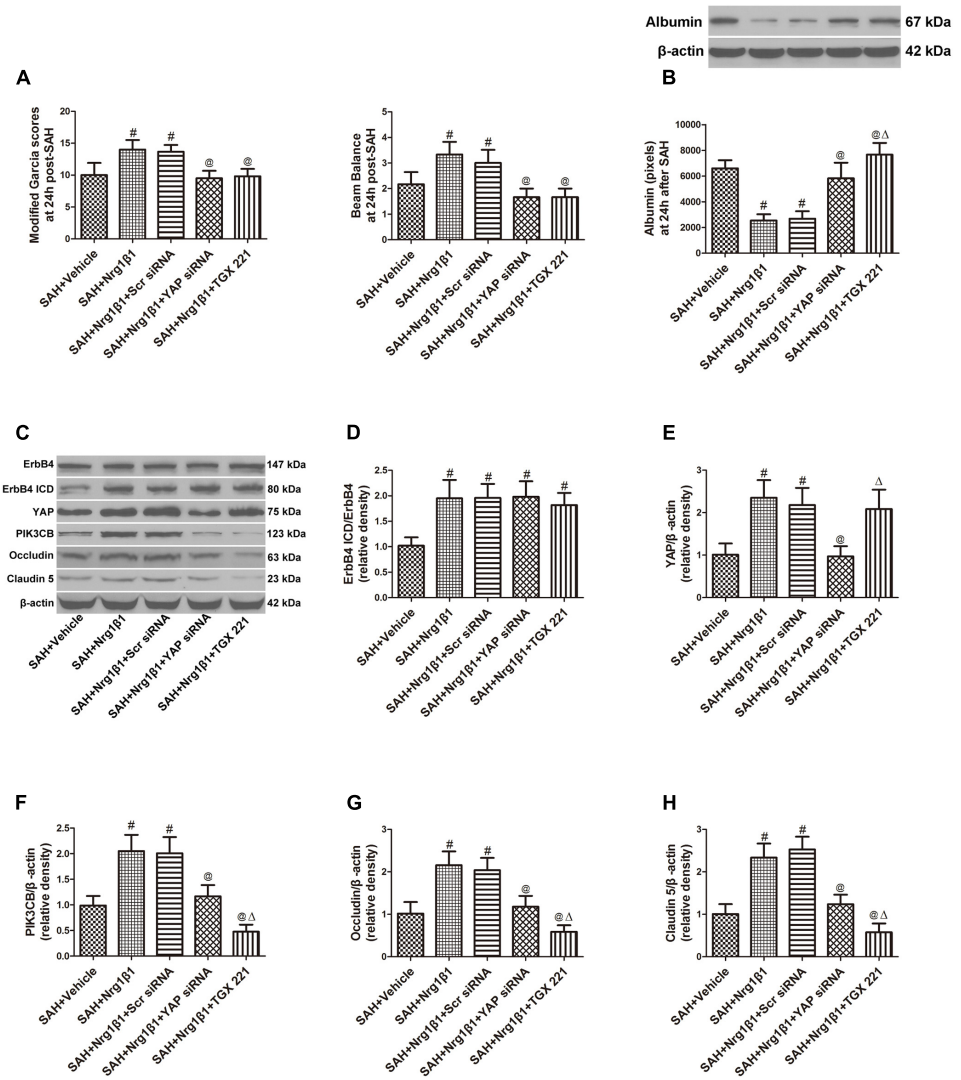

FIGURE 5 | Effects of YAP siRNA pre-treatment on blood-brain barrier integrity at 24 h after SAH. YAP siRNA aggravated neurological deficits **(A)** and increased albumin extravasation **(B)**. Representative western blot bands of ErbB4, YAP, PIK3CB, Occludin and Claudin 5 **(C)**. YAP knockdown did not affect the ratio of ErbB4 ICD/ErbB4 **(D)**, and reduced the expression of YAP **(E)**, PIK3CB **(F)**, Occludin **(G)**, and Claudin-5 **(H)**. PIK3CB inhibition by TGX 221 had no effect on the expression of ErbB4 ICD/ErbB4 **(D)** and YAP **(E)**, and significantly reduced the expression of PIK3CB **(F)**, Occludin **(G)** and Claudin-5 **(H)**. $n = 6$, #$p < 0.05$ versus SAH + Vehicle; @$p < 0.05$ versus SAH + Nrg1β1; $p < 0.05$ versus SAH + Nrg1β1 + YAP siRNA.

at 24 h after SAH ($p < 0.05$, **Figures 4A,B**). Western blotting indicated that TGX 221 injection did not affect the ratio of ErbB4 ICD/ErbB4 and YAP expression ($p > 0.05$, **Figures 4D,E**) but remarkly reduced PIK3CB expression ($p < 0.05$, **Figures 4F**, **5F**). The increased expression of tight junction protein Occludin and Claudin-5 by Nrg1β1 treatment was significantly reversed by TGX 221 administration ($p < 0.05$, **Figures 4G,H**, **5G,H**).

DISCUSSION

In the present study, we elucidated the ErbB4-mediated signaling pathway in BBB protection following SAH in rats. This study demonstrated a significant increase in the expression of ErbB4 ICD and YAP in the rat brain within 72 h after SAH. Double-immunofluorescence staining indicated that both ErbB4 and YAP were expressed in endothelial cells. Activation of ErbB4 by recombinant Nrg1β1 treatment improved the neurological deficit, reduced brain edema and alleviated BBB disruption after SAH, which were associated with increased expression of tight junction protein Occludin and Claudin 5. Specific siRNA injection eliminated the protective effects of ErbB4 activation after SAH induction, accompanied by the reduction of YAP and PIK3CB expression. YAP siRNA administration reversed the protective effects of ErbB4 activation with reduced downstream signal expression. The neuroprotective effects of ErbB4/YAP/PIK3CB signaling

activation was significantly abolished by PIK3CB inhibition, with degraded tight junction proteins and increased BBB disruption. These data indicated that ErbB4 has great effects on maintaining BBB integrity and ameliorating EBI after SAH in rats, possibly through the YAP/PIK3CB signaling pathway.

ErbB4 is one of the epidermal growth factor receptor tyrosine kinase (RTKs) family, which has great effects on neural development and differentiation. ErbB4 is unusual among RTKs in its ability to undergo regulated intramembrane proteolysis to release a soluble ICD (Ni et al., 2001). The ErbB4 ICD relocalizes to the nucleus, where it regulates transcription through its association with transcriptional co-regulators (Vidal et al., 2005; Gilmore-Hebert et al., 2010). Recent studies have suggested that ErbB4 plays an essential role in the regulation of neurite outgrowth, axonal guidance and synaptic signaling (Huang et al., 2000; Shamir et al., 2012). Previous studies have proven that mice lacking ErbB4 receptor could show defects in axon guidance in the central nerves system (Tidcombe et al., 2003). Upregulated ErbB4 expression helps to protect against neuronal cell apoptosis after brain ischaemia (Lu et al., 2016). ErbB4 was found to promote the survival of endothelial cells and preserve BBB integrity (Lok et al., 2009) in a study about oxidative stress injury. In this study, we found that ErbB4 activation significantly alleviated neurological deficits, reduced brain edema and alleviated BBB disruption after SAH. Increased expression of tight junction proteins Occludin and Claudin-5 were observed after ErbB4 activation, which was accompanied by improved BBB integrity after SAH. ErbB4 blockage by specific siRNA could significantly reverse these beneficial effects and aggravate BBB disruption. These findings suggested the protective effects of ErbB4 on maintaining BBB integrity after SAH.

The transcriptional co-activator YAP was found to be essential for cell proliferation as a nuclear effecter of the Hippo-kinase cascade, which is a critical signaling hub that regulates organ growth and size maintenance. Studies have showed that YAP regulates the expression of target genes manipulate DNA transcription (Zhao et al., 2010). Once activated, YAP stimulated fetal and adult cardiomyocyte proliferation (Lin et al., 2015). In the past decade, many components of the Hippo pathway were discovered by Drosophila mosaic genetic screens and proved to be highly conserved in mammals (Low et al., 2014). Among them, YAP was confirmed to be functional in organ size regulation and tumourigenesis in mammals as a directly phosphorylated transcription co-activator. A study by Haskins et al. provided compelling evidence that ErbB4 and its activator Nrg1β1 robustly regulate the Hippo-YAP pathway. Elevation of ErbB4 in cultured mammary epithelial cells promoted the expression of genes regulated by YAP, implying ErbB4-YAP signaling might exist in mammals (Haskins et al., 2014). In this study, activation of ErbB4 significantly increased YAP expression. Knockdown of ErbB4 by specific siRNA significantly down-regulated the expression level of YAP and its downstream signals. Meanwhile, YAP blockage by specific siRNA abolished protective effects of ErbB4 activation, aggravated neurological deficits and BBB disruption, and degraded tight junction expression without affecting ErbB4 expression. These results suggested that the protective role of ErbB4 in maintaining BBB integrity after SAH may be mediated by YAP.

PIK3CB is an p110 catalytic component of Class IA PI3Kwhich has been found to be directly regulated by YAP (Ilic and Roberts, 2010; Lin et al., 2015). YAP has been reported to increase the expression of PIK3CB, and promote cardiomyocyte survival (Lin et al., 2015). The present study demonstrated that the activation of ErbB4 significantly enhanced the expression of YAP and PIK3CB and improved BBB integrity after SAH. Knockdown of ErbB4 or YAP by specific siRNA significantly reduced PIK3CB expression and aggravated BBB disruption. PIK3CB inhibition by TGX 221 significantly reversed the beneficial effects of ErbB4 activation, aggravated neurological deficits and BBB disruption, and degraded tight junction expression without affecting the expression of ErbB4 and YAP.

There are some limitations in this study. Double-immunofluorescence staining indicated that ErbB4 and YAP both expressed in neuron and endothelial cells, which implied that ErbB4 signaling activation could protect against SAH in multiple ways besides BBB maintenance. Previous study have demonstrated the anti-apoptotic effects of ErbB4 in endothelial cells (Lok et al., 2009). Our study showed strong expression of ErbB4 and YAP in neurons, which implied that ErbB4 activation may effects neuron survival after SAH. This hypnosis needs further exploration. In conclusion, this study demonstrated that activation of ErbB4 could improve neurological impairment and reduce brain edema after SAH via the YAP/PIK3CB signaling pathway, this effects may associated with and preserved BBB integrity.

AUTHOR CONTRIBUTIONS

HQ and FY conceived and designed the study, including quality assurance and control. ZD and WR performed the experiments and wrote the paper. PH designed the study's analytic strategy. JZ helped conduct the literature review. All the authors read and approved the manuscript.

FUNDING

This research was supported by the Zhejiang Provincial Natural Science Foundation of China under grant no. LY18H090005.

SUPPLEMENTARY MATERIAL

The Supplementary Material for this article can be found online at: https://www.frontiersin.org/articles/10.3389/fnins.2018.00492/full#supplementary-material

FIGURE S1 | Representative Photograph of SAH model, SAH grading and mortality among each group. **(A)** Representative photographs of sham and SAH

model. **(B)** There was no significant difference of SAH grading among all the experimental groups. **(C)** The mortality for each group are listed as follow: The mortality rate for each group is listed as follows: SAH group 18.18% (8/44), SAH + Vehicle group 21.43% (9/42), SAH + Nrg1β1 (50 ng/kg) group 17.07% (7/41), SAH + Nrg1β1 (150 ng/kg) group 13.51% (5/37), SAH + Nrg1β1 + Scr siRNA group 13.33% (2/15), SAH + Nrg1β1 + ErbB4 siRNA group 22.22% (4/18), SAH + Nrg1β1 + Scr siRNA group 14.29% (2/14), SAH + Nrg1β1 + YAP siRNA group 23.53% (4/17), SAH + Nrg1β1 + TGX 221 group 26.32% (5/19). No statistically significant difference was observed among all the operated groups.

FIGURE S2 | Immunofluorescence double staining of ErbB4 (red), YAP (red), and neuronal marker (NeuN, green) showed that the expression of ErbB4 and YAP were localized in neurons at 24 h after SAH. n = 2, bars = 100 μm.

TABLE S1 | Numbers of animals used in each group.

REFERENCES

Chen, S., Feng, H., Sherchan, P., Klebe, D., Zhao, G., Sun, X., et al. (2014). Controversies and evolving new mechanisms in subarachnoid hemorrhage. *Prog. Neurobiol.* 115, 64–91. doi: 10.1016/j.pneurobio.2013.09.002

Chen, Y., Zhang, Y., Tang, J., Liu, F., Hu, Q., Luo, C., et al. (2015). Norrin protected blood-brain barrier via frizzled-4/beta-catenin pathway after subarachnoid hemorrhage in rats. *Stroke* 46, 529–536. doi: 10.1161/STROKEAHA.114.007265

Connolly, E. S. Jr., Rabinstein, A. A., Carhuapoma, J. R., Derdeyn, C. P., Dion, J., Higashida, R. T., et al. (2012). Guidelines for the management of aneurysmal subarachnoid hemorrhage: a guideline for healthcare professionals from the American Heart Association/American Stroke Association. *Stroke* 43, 1711–1737. doi: 10.1161/STR.0b013e3182587839

Depboylu, C., Rösler, T. W., de Andrade, A., Oertel, W. H., and Höglinger, G. U. (2015). Systemically administered neuregulin-1beta1 rescues nigral dopaminergic neurons via the ErbB4 receptor tyrosine kinase in MPTP mouse models of Parkinson's disease. *J. Neurochem.* 133, 590–597. doi: 10.1111/jnc.13026

Dong, J., Feldmann, G., Huang, J., Wu, S., Zhang, N., Comerford, S. A., et al. (2007). Elucidation of a universal size-control mechanism in *Drosophila* and mammals. *Cell* 130, 1120–1133. doi: 10.1016/j.cell.2007.07.019

Garcia, J. H., Wagner, S., Liu, K. F., and Hu, X. J. (1995). Neurological deficit and extent of neuronal necrosis attributable to middle cerebral artery occlusion in rats. Statistical validation. *Stroke* 26, 627–634; discussion 635. doi: 10.1161/01.STR.26.4.627

Gilmore-Hebert, M., Ramabhadran, R., and Stern, D. F. (2010). Interactions of ErbB4 and Kap1 connect the growth factor and DNA damage response pathways. *Mol. Cancer Res.* 8, 1388–1398. doi: 10.1158/1541-7786.MCR-10-0042

Haskins, J. W., Nguyen, D. X., and Stern, D. F. (2014). Neuregulin 1-activated ERBB4 interacts with YAP to induce Hippo pathway target genes and promote cell migration. *Sci. Signal.* 7:ra116. doi: 10.1126/scisignal.2005770

Huang, Y. Z., Won, S., Ali, D. W., Wang, Q., Tanowitz, M., Du, Q. S., et al. (2000). Regulation of neuregulin signaling by PSD-95 interacting with ErbB4 at CNS synapses. *Neuron* 26, 443–455. doi: 10.1016/S0896-6273(00)81176-9

Ilic, N., and Roberts, T. M. (2010). Comparing the roles of the p110alpha and p110beta isoforms of PI3K in signaling and cancer. *Curr. Top. Microbiol. Immunol.* 347, 55–77. doi: 10.1007/82_2010_63

Li, Z., Liang, G., Ma, T., Li, J., Wang, P., Liu, L., et al. (2015). Blood-brain barrier permeability change and regulation mechanism after subarachnoid hemorrhage. *Metab. Brain Dis.* 30, 597–603. doi: 10.1007/s11011-014-9609-1

Lin, Z., Zhou, P., von Gise, A., Gu, F., Ma, Q., Chen, J., et al. (2015). Pi3kcb links Hippo-YAP and PI3K-AKT signaling pathways to promote cardiomyocyte proliferation and survival. *Circ. Res.* 116, 35–45. doi: 10.1161/CIRCRESAHA.115.304457

Lok, J., Sardi, S. P., Guo, S., Besancon, E., Ha, D. M., Rosell, A., et al. (2009). Neuregulin-1 signaling in brain endothelial cells. *J. Cereb. Blood Flow Metab.* 29, 39–43. doi: 10.1038/jcbfm.2008.94

Low, B. C., Pan, C. Q., Shivashankar, G. V., Bershadsky, A., Sudol, M., and Sheetz, M. (2014). YAP/TAZ as mechanosensors and mechanotransducers in regulating organ size and tumor growth. *FEBS Lett.* 588, 2663–2670. doi: 10.1016/j.febslet.2014.04.012

Lu, Y. M., Gao, Y. P., Tao, R. R., Liao, M. H., Huang, J. Y., Wu, G., et al. (2016). Calpain-dependent ErbB4 cleavage is involved in brain ischemia-induced neuronal death. *Mol. Neurobiol.* 53, 2600–2609. doi: 10.1007/s12035-015-9275-2

Ni, C. Y., Murphy, M. P., Golde, T. E., and Carpenter, G. (2001). gamma -Secretase cleavage and nuclear localization of ErbB-4 receptor tyrosine kinase. *Science* 294, 2179–2181. doi: 10.1126/science.1065412

Sehba, F. A., Hou, J., Pluta, R. M., and Zhang, J. H. (2012). The importance of early brain injury after subarachnoid hemorrhage. *Prog. Neurobiol.* 97, 14–37. doi: 10.1016/j.pneurobio.2012.02.003

Shamir, A., Kwon, O. B., Karavanova, I., Vullhorst, D., Leiva-Salcedo, E., Janssen, M. J., et al. (2012). The importance of the NRG-1/ErbB4 pathway for synaptic plasticity and behaviors associated with psychiatric disorders. *J. Neurosci.* 32, 2988–2997. doi: 10.1523/JNEUROSCI.1899-11.2012

Sturgeon, S. A., Jones, C., Angus, J. A., and Wright, C. E. (2008). Advantages of a selective beta-isoform phosphoinositide 3-kinase antagonist, an anti-thrombotic agent devoid of other cardiovascular actions in the rat. *Eur. J. Pharmacol.* 587, 209–215. doi: 10.1016/j.ejphar.2008.03.017

Sugawara, T., Ayer, R., Jadhav, V., and Zhang, J. H. (2008). A new grading system evaluating bleeding scale in filament perforation subarachnoid hemorrhage rat model. *J. Neurosci. Methods* 167, 327–334. doi: 10.1016/j.jneumeth.2007.08.004

Tang, J., Hu, Q., Chen, Y., Liu, F., Zheng, Y., Tang, J., et al. (2015). Neuroprotective role of an N-acetyl serotonin derivative via activation of tropomyosin-related kinase receptor B after subarachnoid hemorrhage in a rat model. *Neurobiol. Dis.* 78, 126–133. doi: 10.1016/j.nbd.2015.01.009

Tidcombe, H., Jackson-Fisher, A., Mathers, K., Stern, D. F., Gassmann, M., and Golding, J. P. (2003). Neural and mammary gland defects in ErbB4 knockout mice genetically rescued from embryonic lethality. *Proc. Natl. Acad. Sci. U.S.A.* 100, 8281–8286. doi: 10.1073/pnas.1436402100

Vidal, G. A., Naresh, A., Marrero, L., and Jones, F. E. (2005). Presenilin-dependent gamma-secretase processing regulates multiple ERBB4/HER4 activities. *J. Biol. Chem.* 280, 19777–19783. doi: 10.1074/jbc.M412457200

Xie, Z., Enkhjargal, B., Reis, C., Huang, L., Wan, W., Tang, J., et al. (2017). Netrin-1 preserves blood-brain barrier integrity through deleted in colorectal cancer/focal adhesion kinase/RhoA signaling pathway following subarachnoid hemorrhage in rats. *J. Am. Heart Assoc.* 6:e005198. doi: 10.1161/JAHA.116.005198

Yan, F., Cao, S., Li, J., Dixon, B., Yu, X., Chen, J., et al. (2017a). Pharmacological inhibition of PERK attenuates early brain injury after subarachnoid hemorrhage in rats through the activation of Akt. *Mol. Neurobiol.* 54, 1808–1817. doi: 10.1007/s12035-016-9790-9

Yan, F., Tan, X., Wan, W., Dixon, B. J., Fan, R., Enkhjargal, B., et al. (2017b). ErbB4 protects against neuronal apoptosis via activation of YAP/PIK3CB signaling pathway in a rat model of subarachnoid hemorrhage. *Exp. Neurol.* 297, 92–100. doi: 10.1016/j.expneurol.2017.07.014

Yan, F., Li, J., Chen, J., Hu, Q., Gu, C., Lin, W., et al. (2014). Endoplasmic reticulum stress is associated with neuroprotection against apoptosis via autophagy activation in a rat model of subarachnoid hemorrhage. *Neurosci. Lett.* 563, 160–165. doi: 10.1016/j.neulet.2014.01.058

Zhao, B., Li, L., Lei, Q., and Guan, K. L. (2010). The Hippo-YAP pathway in organ size control and tumorigenesis: an updated version. *Genes Dev.* 24, 862–874. doi: 10.1101/gad.1909210

Conflict of Interest Statement: The authors declare that the research was conducted in the absence of any commercial or financial relationships that could be construed as a potential conflict of interest.

frontiers in Neuroscience

ORIGINAL RESEARCH
published: 19 September 2018
doi: 10.3389/fnins.2018.00638

Melatonin Protects Against Neuronal Apoptosis via Suppression of the ATF6/CHOP Pathway in a Rat Model of Intracerebral Hemorrhage

Weilin Xu[1†], Xiaoyang Lu[1†], Jingwei Zheng[1†], Tao Li[1], Liansheng Gao[1], Cameron Lenahan[2], Anwen Shao[1], Jianmin Zhang[1,3,4] and Jun Yu[1]**

[1] Department of Neurosurgery, Second Affiliated Hospital, School of Medicine, Zhejiang University, Hangzhou, China, [2] Burrell College of Osteopathic Medicine, New Mexico State University, Las Cruces, NM, United States, [3] Brain Research Institute, Zhejiang University, Hangzhou, China, [4] Collaborative Innovation Center for Brain Science, Zhejiang University, Hangzhou, China

OPEN ACCESS

Edited by:
Gang Chen,
The First Affiliated Hospital of Soochow University, China

Reviewed by:
Federico Herrera,
Instituto de Tecnologia Química e Biológica (ITQB-NOVA), Portugal
Xuemin Xu,
University of Texas of the Permian Basin, United States

***Correspondence:**
Jun Yu
2505020@zju.edu.cn
Jianmin Zhang
zjm135@zju.edu.cn

† These authors have contributed equally to this work as co-first authors

Specialty section:
This article was submitted to Neurodegeneration, a section of the journal Frontiers in Neuroscience

Received: 14 May 2018
Accepted: 27 August 2018
Published: 19 September 2018

Citation:
Xu W, Lu X, Zheng J, Li T, Gao L, Lenahan C, Shao A, Zhang J and Yu J (2018) Melatonin Protects Against Neuronal Apoptosis via Suppression of the ATF6/CHOP Pathway in a Rat Model of Intracerebral Hemorrhage. Front. Neurosci. 12:638. doi: 10.3389/fnins.2018.00638

Neuronal apoptosis is an important factor accounting for the poor outcomes of intracerebral hemorrhage (ICH). This study first showed that inhibition of activating transcription factor 6 (ATF6) could alleviate secondary brain injury through anti-apoptosis after ICH in rats. Melatonin, ATF6 and CCAAT/enhancer-binding protein homologous protein (CHOP) siRNAs were applied in this study. Brain edema, neurological functions, blood-brain barrier (BBB) integrity were evaluated at 24 h after ICH. Western blot analysis was used to evaluate the protein level of target proteins (ATF6, CHOP, Bip, Bcl-2, Bax, and cleaved caspase-3). Reverse transcription-polymerase chain reaction (RT-PCR) was used to assess the mRNA level of ATF6, CHOP and cleaved caspase-3. Terminal deoxynucleotidyl transferase-mediated dUTP nick end labeling (TUNEL) and caspase-3 immunofluorescence staining were applied to evaluate the neuronal cell death. The results suggested that the levels of ATF6 and its downstream protein, CHOP, were upregulated and reached the peak at 24 h after ICH. ATF6 was highly expressed in neurons. The administration of melatonin significantly decreased the mRNA and protein levels of ATF6, and its downstream targets, CHOP and cleaved caspase-3, but increased the Bcl-2/Bax ratio, which ameliorated the neurological functions. The CHOP siRNA significantly reversed the pro-apoptotic effect induced by the increased ATF6 level after ICH. Melatonin could protect against neuronal apoptosis via suppression of ATF6/CHOP arm of ER-stress-response pathway.

Keywords: intracerebral hemorrhage, mesencephalic astrocyte-derived neurotrophic factor (ATF6), CCAAT/enhancer-binding protein homologous protein (CHOP), apoptosis, secondary brain injury

Abbreviations: ATF6, activating transcription factor 6; BBB, blood brain barrier; CHOP, CCAAT/enhancer-binding protein (C/EBP) homologous protein; EB, Evans blue; ER, endoplasmic reticulum; ICH, intracerebral hemorrhage; IRE1, inositol requiring kinase 1; NSS, Neurological Severity Score; PERK, protein kinase-like ER kinase; RT-PCR, reverse transcription-polymerase chain reaction; SD, Sprague–Dawley; TUNEL, Terminal deoxynucleotidyl transferase (TdT)-mediated dUTP nick end labeling; UPR, unfolded protein response.

INTRODUCTION

Intracerebral hemorrhage is one of the most common types of stroke (Feigin et al., 2009; Steiner et al., 2014), which is featured by a high rate of death and disability (van Asch et al., 2010; Krishnamurthi et al., 2014). The underlying mechanisms accounting for the poor prognosis after ICH include neural apoptosis, neuroinflammation, oxidative stress, et al (Shen et al., 2017; Zeng et al., 2017). Among them, apoptosis plays a pivotal role in the secondary brain injuries. Surgical procedures are restricted and can only relieve a small number of patients (Pías-Peleteiro et al., 2017). Many studies focus on the pharmacological treatment of ICH, but no target has been launched with specific efficacy.

The ER is an organelle which mainly provides a topologically distinct membranous network for protein modification, proper protein folding and assembly (Senkal et al., 2010). Insults that perturb ER function result in ER stress (Roussel et al., 2013). The pathophysiological process of inflammation, oxidative stress, mitochondrial calcium overloading (Zhou et al., 2015), and toxic glutamate release induced by ICH could greatly activate the ER stress response. Finally, the overloaded proteins could further trigger UPR (Schroder and Kaufman, 2005). The UPR is mainly conducted via three types of ER stress sensor proteins, IRE1, RNA-activated PERK, and ATF6. Among the three, ATF6 was reported to display the key roles in the UPR (DuRose et al., 2006; Wu et al., 2007; Doroudgar and Glembotski, 2012).

Long-lasting and serious ER stress was reported to cause cell death (Tabas and Ron, 2011; Fouillet et al., 2012). Once the ER stress is over activated, protein synthesis outpaces protein-folding capacity, then ATF6 moves to the Golgi, and is cleaved by the Golgi-localized proteases, SP1 and SP2 (Ye et al., 2000). The resulting 50 kD cytosolic fragment translocates to the nucleus, binds to elements in ATF6-responsive genes, and up-regulates its downstream target, CHOP. CHOP is a transcriptional factor and is involved in the commitment phase of ER stress-mediated apoptosis (Li et al., 2014). Suppression of ATF6 was also reported to provide neuroprotection in a cerebral ischemic model (Menzie-Suderam et al., 2018), but the role of ATF6 has not yet been explored in ICH.

Furthermore, as ATF6 is one of the main proteins in the UPR, we hypothesized that melatonin conducted its neuroprotective effects via suppressing the activation of ATF6/CHOP pathway. The neuroprotective effects of melatonin have been widely verified. In recent years, many studies put the focus on the effects of melatonin on ER stress (Fernández et al., 2015; Lin et al., 2018). Their results suggested that melatonin could exert its neuroprotective effects via suppression of ER stress.

In this study, we verified the following hypotheses: (1) ICH resulted in an increase of ATF6 expression; (2) the suppression of ATF6 by melatonin reduced brain edema, alleviated BBB disruption, and improved neurological functions; (3) selective inhibition of ATF6 expression with siRNA protected neuronal cells from apoptosis via suppressing the expression of CHOP and other pro-apoptotic factors, Bax and cleaved caspase-3.

MATERIALS AND METHODS

Animals

We did all the operations according to the Institutional Animal Care and Use Committee of Zhejiang University. The procedures were conducted according to the National Institutes of Health's Guide for the Care and the Use of Laboratory Animals and the ARRIVE (Animal Research: Reporting *in vivo* Experiments) guidelines. We only chose Sprague–Dawley (SD, Male) rats (291 rats, 280–330 g) (SLAC Laboratory Animal Co., Ltd. Shanghai, China) in this study (**Supplementary Table I**). We kept the rats in a 12 h day/night cycle (22 ± 1°C; 60 ± 5% humidity). The rats were free to water and food.

ICH Rat Model

The ICH model was performed as previously described (Zhou et al., 2014). We used pentobarbital (40 mg/kg, intraperitoneal injection) to anesthetize the rat and then immobilized it in a stereotaxic frame (Stoelting Co., United States). Briefly, the right femoral artery was exposed and we obtained blood (100 μl) for the following injection. Then, we used cranial drill to make a burr hole 3.5 mm lateral right of the bregma. Afterward, the blood was manually injected in the right striatum (5.5 mm depth). We withdraw the needle 10 min after injection. Finally, we used medical bone wax to seal the burr hole and closed the incision with sutures. For the rats in sham group, we did all the procedures except for the injection.

Experimental Design (Figure 1)

In the first step, we explored the effects of melatonin. Sixty rats were distributed into five groups: sham (n = 12), ICH (n = 12), ICH + vehicle (n = 12), ICH + melatonin (100 mg/kg, n = 12), ICH + melatonin (150 mg/kg, n = 12). We assessed neurobehavior conditions, brain edema (n = 6), and EB extravasation (n = 6) at 24 h after ICH in each group.

In the second step, the time course of ATF6 and CHOP was evaluated in sham group and ICH groups with different time points. Forty-six rats were randomized distributed into seven groups: sham (n = 8), 3 h (n = 6), 6 h (n = 6), 12 h (n = 6), 24 h (n = 8), 48 h (n = 6), and 72 h (n = 6). Western blot analysis was performed in each group (n = 6). Two rats in the sham and ICH(24 h) were used for colocalized immunofluorescence staining of ATF6 with neuronal nuclei (NeuN).

In the third step, in order to further explore the underlying mechanisms of neuroprotective effects of melatonin, ninety-six rats were distributed into five groups: sham (n = 20), ICH + vehicle (n = 20), ICH + melatonin (best dosage, n = 20), ICH + scramble siRNA (500 pmol in 5 μl in sterile saline, n = 18), or ICH + CHOP siRNA (500 pmol in 5 μl in sterile saline, n = 18). The siRNA was injected intracerebroventricularly at 48 h before induction of ICH. Six rats per group were used for Western blot analysis and RT-PCR, respectively. Furthermore, five rats in each group were used for TUNEL and caspase-3 staining.

In the fourth step, we adopted ATF6 siRNA to further verify the mechanisms mentioned above, as melatonin is not a selective

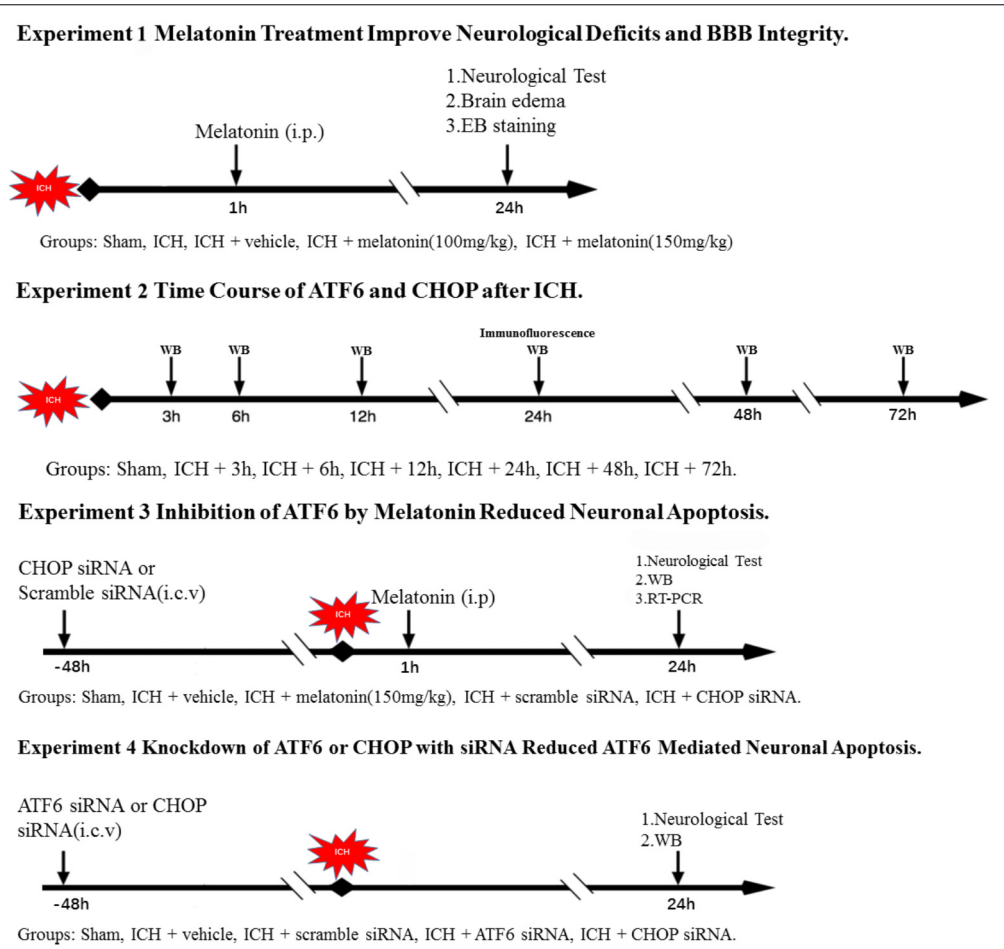

FIGURE 1 | Experimental design and animal groups.

inhibitor of ATF6. Sixty rats were distributed into five groups: sham (n = 12), ICH + vehicle (n = 12), ICH + scramble siRNA (500 pmol in 5 μl in sterile saline, n = 12), ICH + ATF6 siRNA (500 pmol in 5 μl in sterile saline, n = 12), and ICH + CHOP siRNA (500 pmol in 5 μl in sterile saline, n = 12). The siRNA was injected intracerebroventricularly at 48 h before induction of ICH. Six rats per group were used for Western blot analysis and RT-PCR, respectively.

Behavioral Assessment

Neurobehavior conditions were assessed at 24 h after ICH based on a system named the NSS (Cui et al., 2017). Detailed information about the marking system is displayed in **Supplementary Table II**.

Brain Water Content

We used wet–dry method to evaluated the brain water content at 24 h after ICH. Briefly, after euthanasia, we collected the brain hemisphere and weighed it (wet weight). Then, right hemisphere of the brain was put in an oven for 72 h (105°C, dry weight). Finally, we calculate the brain water content as follows: [(wet weight - dry weight)/(wet weight)] × 100% (Chen et al., 2015).

Evans Blue (EB) Staining

Evans blue staining was applied to evaluate the blood–brain barrier integrity. 2% EB solution (8 mL/kg, Sigma–Aldrich) was intra-peritoneally injected after anesthetization. After 24 h, the rats received trans-cardiac perfusion with 0.1M PBS. Next, the brain was removed and homogenized in 50% trichloroacetic acid. The sample was incubated in a water bath (50°C) for 48 h and centrifuged at 15,000 × g for 30 min. Afterward, the supernatant was detected through spectro-fluorophotometry at 620 nm (Zhao et al., 2016).

Immunofluorescence and Calculation of Apoptotic Cells

After anesthetization, transcardial perfusion with 0.1M PBS was performed, followed by another perfusion with 4% paraformaldehyde (pH = 7.4). Then, the cerebral hemispheres were removed and put into 4% PFA for post-fixation (4°C, 24 h). Afterward, the brains were transferred to sucrose solution (30%, 2 days). Next, the brains were coronally sliced into 10 μm sections, which were then fixed on slides and used for immunofluorescence staining, and then

blocked with 10% normal donkey serum for 2 h at room temperature and incubated at 4°C overnight with primary antibodies: ATF6 (1:200, abcam ab203119), caspase-3 (1:200, abcam ab49822), NeuN (1:500, abcam ab104224). Additionally, secondary antibodies were applied for 2 h at room temperature. Finally, the sections were assessed with a fluorescence microscope (Olympus, Tokyo, Japan) and pictures were further processed by Photoshop 13.0(Adobe Systems Inc., Seattle, WA, United States). Additionally, TUNEL (Roche Inc., Basel, Switzerland) staining was applied to assessed cellular apoptosis of brain tissues.

Western Blot Analysis

First, the rats received trans-cardiac perfusion with 0.1M PBS after being anesthetized, then we collected the brain tissues around hematoma (**Figure 2A**), which were further processed as previously reported (Nakka et al., 2010), and 40 μg of protein from each sample was used for electrophoresis (100 V, 1 h) and then transferred to the polyvinylidene fluoride membranes at 250 V for 1 h. Afterward, the protein was incubated with primary antibodies overnight (4°C): ATF6 (1:500, abcam ab203119), CHOP (1:1000, abcam ab11419), Bip/GRP78 (1:2000, abcam ab21685), MMP-9 (1:800, SCBT, sc-12759), β-actin (1:5000, abcam ab8226), Bax (1:1000, abcam ab32503), Bcl-2 (1:500, abcam ab59348), and caspase-3 (1:500, abcam ab49822). After that, the proteins were incubated with secondary antibodies (1:10000, Zhongshan Gold Bridge) for 1 h. Finally, the ECL Plus chemiluminescence reagent kit (Amersham Bioscience, Arlington Heights, IL, United States) was used to detected the proteins. We displayed the results as the relative density which is the ratio of the grayscale value of the target proteins to that of β-actin.

Small Interfering RNA and Intracerebroventricular Injection

The intracerebroventricular injection was conducted as previously reported (Zhou et al., 2018). After the rats were anesthetized, we used cranial drill to make a burr hole at 1 mm posterior to bregma and 1.5 mm right lateral to midline. Afterward, following the manufacturer's instructions, a total volume of 5 μl (500 pmol) of rat ATF6 siRNA or CHOP siRNA (Thermo Fisher Scientific, United States) dissolved in nuclease-free water was injected into the right ventricle (3.5 mm depth below the skull) with a pump at the rate of 0.5 μl/min at

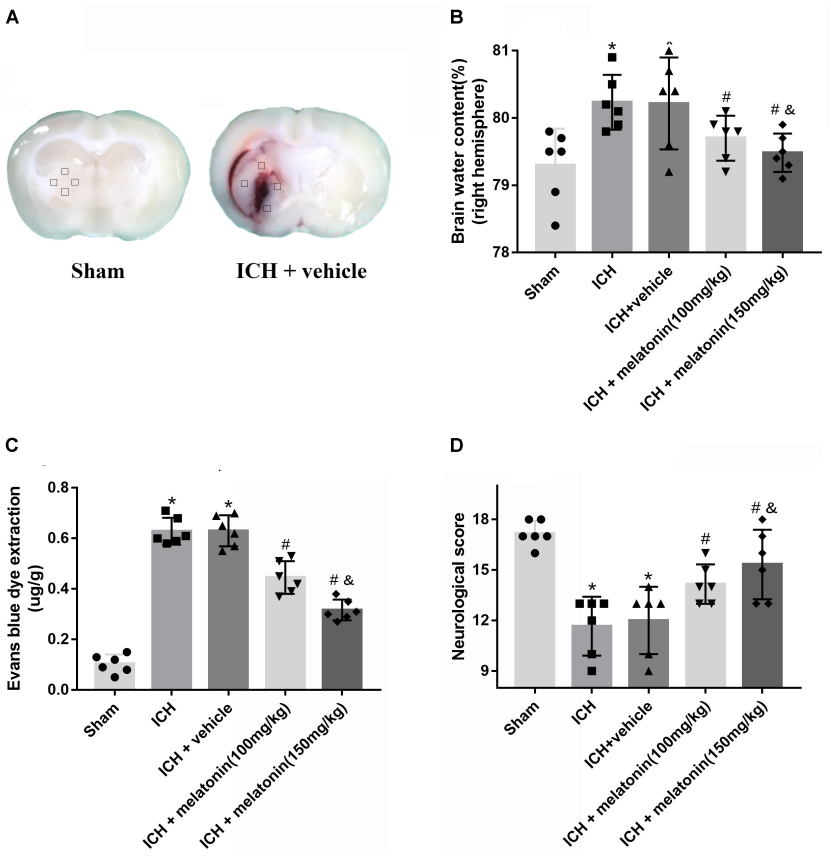

FIGURE 2 | Effects of melatonin on neurological functions, brain edema and BBB leakage. **(A)** Representative pictures of brain slices in sham and ICH group (24 h); **(B)** the quantification of brain water content at 24 h after ICH; **(C)** the quantification of Evans blue dye extravasation at 24 h after ICH ($n = 6$ for each group); **(D)**. The quantification of neurological functions; The bars represent the mean ± SD. $^{*}p < 0.05$ vs. sham, $^{\#}p < 0.05$ vs. ICH at 24 h, $^{\&}p < 0.05$ vs. ICH + melatonin (100 mg/kg).

48 h before ICH. The same volume of scramble siRNA (Thermo Fisher Scientific, United States) was used as a negative control. Finally, the needle was kept in place for 5 min. Finally, we used medical bone wax to sealed the burr hole and the incision was closed with sutures.

Real-Time Polymerase Chain Reaction (RT-PCR)

TRIzol reagent (Sigma–Aldrich, St. Louis, MO, United States) was applied to extract total RNA. Then, RNA (1 μg) from each sample was reverse-transcribed to cDNA by PrimeScript™ RT reagent kit (Takara Bio Inc, Shiga, Japan). Afterward, qRT-PCR was conducted with SYBR® Premix Ex Taq™ (Takara Bio Inc, Shiga, Japan) on a 7300 Plus Read-Time PCR System (Thermo Fisher Scientific, Waltham, MA, United States). The cDNA was used as a template in a 20 ml reaction volume (10 μl of PCR mix, 5 pmol of forward and reverse primers, 1 μl cDNA template and proper volume of water), including a blank control (without template) in all experiments. The PCR reaction was performed as follows: initial denaturation at 94°C for 3 min; 45 cycles of denaturation at 94°C for 20 s, annealing at 60°C for 60 s, and elongation at 72°C for 45 s; and final elongation at 72°C for 3 min. Each sample was examined in triplicate. The primer sequences are as follows:

(1) ATF6: 5′-AAGTGAAGAACCATTACTTTATATC-3′ (forward) and 5′-TTTCTGCTGGCTATTTGT-3′ (reverse); (GenBank ID: 2138640)
(2) CHOP: 5′-GGAAGTGCATCTTCATACACCACC-3′ (forward) and 5′-TGACTGGAATCTGGAGAGAGCGAGGGC-3′ (reverse); (GenBank ID: 2138665)
(3) caspase-3: 5′-CGGACCTGTGGACCTGAAAA-3′ (forward) and 5′-TAGTAACCGGGTGCGTAGA-3′ (reverse); (GenBank ID: 2138666)
(4) β-actin: 5′-CACTGCCGCATCCTCTTCCT-3′ (forward) and 5′-AACCGCTCATTGCCGATAGTG-3′ (reverse); (GenBank ID: 2138668)

Statistical Analysis

Results were displayed as mean ± SD. We performed the analysis with SPSS 22.0 software (IBM, United States). One-way ANOVA analysis of variance was applied for the comparison between different groups, with a $p < 0.05$ deeming to be statistically significant. However, we used non-parametric statistics to analyze data regarding the time-course of ATF6 as it did not pass the normality test.

RESULTS

Physiological Data, BBB Integrity and Neurological Functions Assessment

During the surgery, we collected the physiological parameters, including body temperature, heart rate, blood pressure, blood glucose, PO2 and PCO2. No significant differences of physiological parameters were observed across each group (**Supplementary Tables III**, **IV**).

In order to assess the BBB permeability, brain water content and neurological functions at 24 h after ICH, two dosages of melatonin (100 mg/kg, 150 mg/kg) were administered intraperitoneally at 1 h after ICH. The induction of ICH significantly increased the brain water volume ($p < 0.05$ vs. sham). However, the administration of a high dose of melatonin was more significant in reducing brain water content at 24 h after ICH ($p < 0.05$ vs. ICH + vehicle, **Figure 2B**). The EB extravasation was increased in ipsilateral hemisphere of ICH compared with the rats in sham group ($p < 0.05$ vs. sham), while the rats receiving the higher dose of melatonin displayed a lower level of EB leakage ($p < 0.05$ vs. ICH + vehicle, **Figure 2C**). In addition, remarkable neurobehavioral function impairment was observed in ICH group while administration of the higher dose of melatonin significantly improved the neurological functions ($p < 0.05$, **Figure 2D**).

Changes of the Expression of ATF6 and Its Role in Melatonin-Mediated Neuroprotection at 24 h After ICH

The results of time-course study showed that the level of ATF6 started to rise at 3 h and reached peak at 24 h after ICH ($p < 0.05$, **Figure 3A**). The expression of CHOP significantly increased at 12 h, and peaked at 24 h after ICH ($p < 0.05$, **Figure 3B**). Furthermore, the double immunostaining of ATF6 with NeuN in sham and ICH + vehicle groups showed that ATF6 was highly expressed in neurons (**Figure 3C**).

Based on the neuroprotective effects of melatonin, which has been proved above, we chose high dose of melatonin for mechanism study. The results showed that administration of the high dose of melatonin significantly reduced the expression of ATF6 compared with ICH + vehicle group in both protein and mRNA levels ($p < 0.05$, **Figures 4A–C**). Additionally, the ratio of Bcl-2/Bax was significantly reduced, while the mRNA and protein level of cleaved caspase-3 was increased in ICH + vehicle group ($p < 0.05$, vs. sham). The administration of the higher dose of melatonin could significantly reverse these results ($p < 0.05$, vs. ICH + vehicle, **Figures 4A–C**). Furthermore, the administration of melatonin significantly reduced the expression level of MMP-9, which was increased after the introduction of ICH ($p < 0.05$, vs. ICH + vehicle, **Figures 4A,B**). The increase of MMP-9 further indicated the disruption of BBB except for the results from EB testing. The results of TUNEL staining suggested that the number of TUNEL positive cells and caspase-3 significantly increased at 24 h after ICH ($p < 0.05$, ICH vs. sham), whereas the number of TUNEL-positive and caspase-3 positive cells was obviously decreased after the administration of the higher dose of melatonin ($p < 0.05$, vs. ICH + vehicle, **Figures 5A,B**, **6A,B**).

Role of Downstream CHOP in the ATF6-Mediated Pro-apoptotic Effects 24 h After ICH

In order to explore the role of CHOP in the ATF6 signaling pathway, ATF6 siRNA and CHOP siRNA were injected intracerebroventricularly at 48h before ICH. The results showed that the administration of ATF6 siRNA could significantly reduce

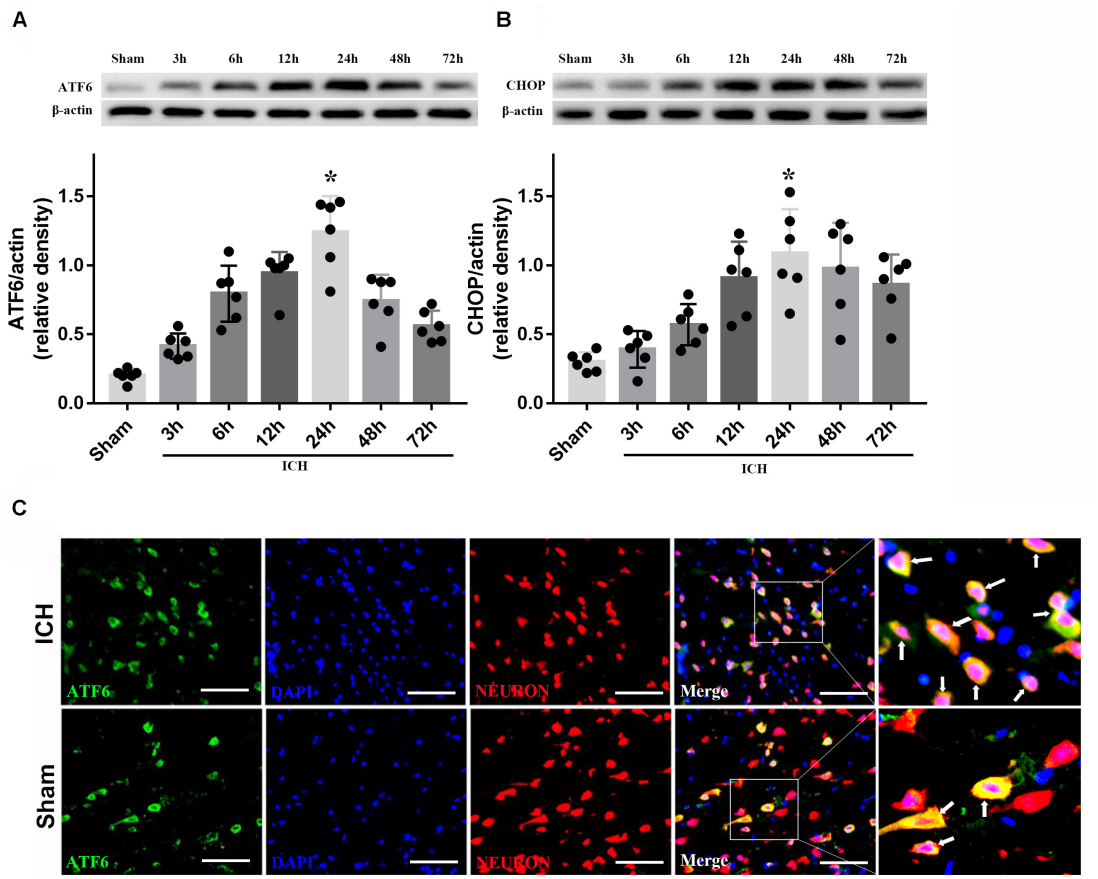

FIGURE 3 | Expression of ATF6 and CHOP. **(A)** Time course of ATF6 in injured hemisphere after ICH; **(B)** time course of CHOP; $n = 6$ for each group. The bars represent the mean ± SD. *$p < 0.05$ vs. sham; **(C)** Representative microphotographs of immunofluorescence staining showing localization of ATF6 (green) and NeuN (red) in the perihematomal region after ICH ($N = 2$ for each group). Scale bar = 50 μm.

the level of CHOP expression in both protein and mRNA levels, while CHOP siRNA had no effects on the expression of ATF6, which was elevated at 24 h after ICH ($p < 0.05$, vs. sham). However, the increased expression of CHOP induced by ATF6 at 24 h after ICH was significantly suppressed by CHOP siRNA ($p < 0.05$ vs. ICH + vehicle, **Figures 7A,B**). Meanwhile, the induction of ICH could increase the cell apoptosis by decreasing Bcl-2/Bax ratio and increasing cleaved caspase-3 expression ($p < 0.05$, sham vs. ICH + vehicle); However, these pro-apoptotic effects could be significantly reversed by CHOP siRNA ($p < 0.05$, vs. ICH + vehicle, **Figures 7A,B**).

DISCUSSION

In this study, we explored the neuroprotective effects of melatonin in a new mechanism mediated by suppression of ATF6/CHOP pathway in the experimental ICH of rats. The induction of ICH could significantly enhance the expression of ATF6, and its downstream effector, CHOP, both of which peaked at 24 h after ICH. ATF6 was expressed primarily in neurons. Up-regulation of ATF6 and CHOP expression increased neuronal apoptosis, which would be partially offset by administration of the higher dose of melatonin. Melatonin significantly improved the neurological functions, reduced brain edema, BBB disruption and neuronal apoptosis by suppressing the expression of ATF6 and CHOP in both protein and mRNA levels, increasing Bcl-2 expression, and reducing the levels of Bax and cleaved caspase-3. In addition, the inhibition of CHOP signaling with siRNA markedly decreased the pro-apoptotic effects of ATF6 induced by ICH.

Intracerebral hemorrhage is usually caused by ruptured vessels that are degenerated due to long-standing hypertension (Boulouis et al., 2017). The underlying mechanisms include the disturbance of ion hemostasis, the induction of oxidative stress, and apoptosis. The ER is an organelle which mainly manipulates protein synthesis and processing (Qiu et al., 2017). Insults that perturb ER function result in ER stress (Gong et al., 2017). It could be induced by inflammation, oxidative stress, mitochondrial calcium overloading (Louessard et al., 2017), and toxic glutamate release. Overactivation of ER stress leads to an accumulation of misfolded proteins in the ER. ATF6, a single-pass transmembrane protein, is the key response factor in the regulation of misfolded proteins.

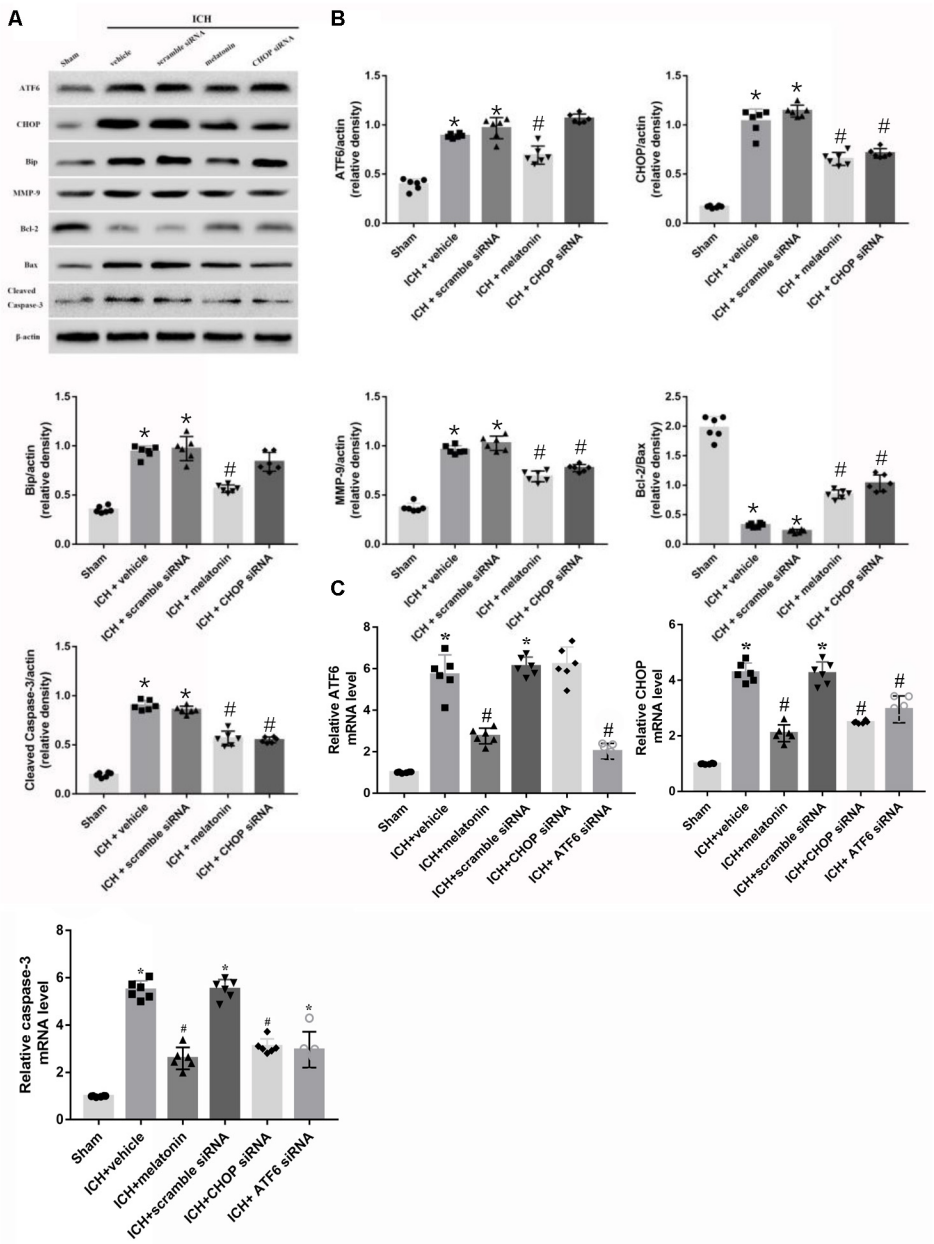

FIGURE 4 | Intraperitoneal administration of melatonin Promotes Neuronal Survival at 24 h after ICH. **(A)** Representative Western blot images. **(B)** Quantitative analyses of ATF6, CHOP, Bip, MMP-9, Bcl-2, Bax, cleaved caspase-3; **(C)** Relative level of mRNAs of ATF6, CHOP and caspase-3. $n = 6$ for each group. The bars represent the mean ± SD. *$p < 0.05$ vs. sham, #$p < 0.05$ vs. ICH + vehicle.

ER stress could significantly increase the activation of ATF6, which then translocates to the Golgi, where it is cleaved by the Golgi-localized proteases, SP1 and SP2 (Glembotski, 2014). The resulting 50 kD cytosolic fragment translocates to the nucleus, binds to elements in ATF6-responsive genes, resulting in the sustained reduction of global protein synthesis, thereby determining the fate of the cells (Stephens and Nicchitta, 2008; Xiong et al., 2017). In an *in vitro* study of hypoxic-ischemic encephalopathy (HIE), the cells suffering from hypoxia could have significantly increased levels of cleaved ATF6, which would promote apoptosis. The results demonstrated that ATF6 is an important factor in triggering HIE brain injury (Liu et al., 2015). In the present study, we determined the time course of the expression level of ATF6 and its downstream signal, CHOP, after ICH. The results were consistent with the abovementioned observations that protein levels of ATF6 and CHOP were significantly increased and peaked at 24 h after ICH. Based upon these results, the activity of ATF6 was strongly associated with increased pro-apoptotic markers in the experimental ICH model.

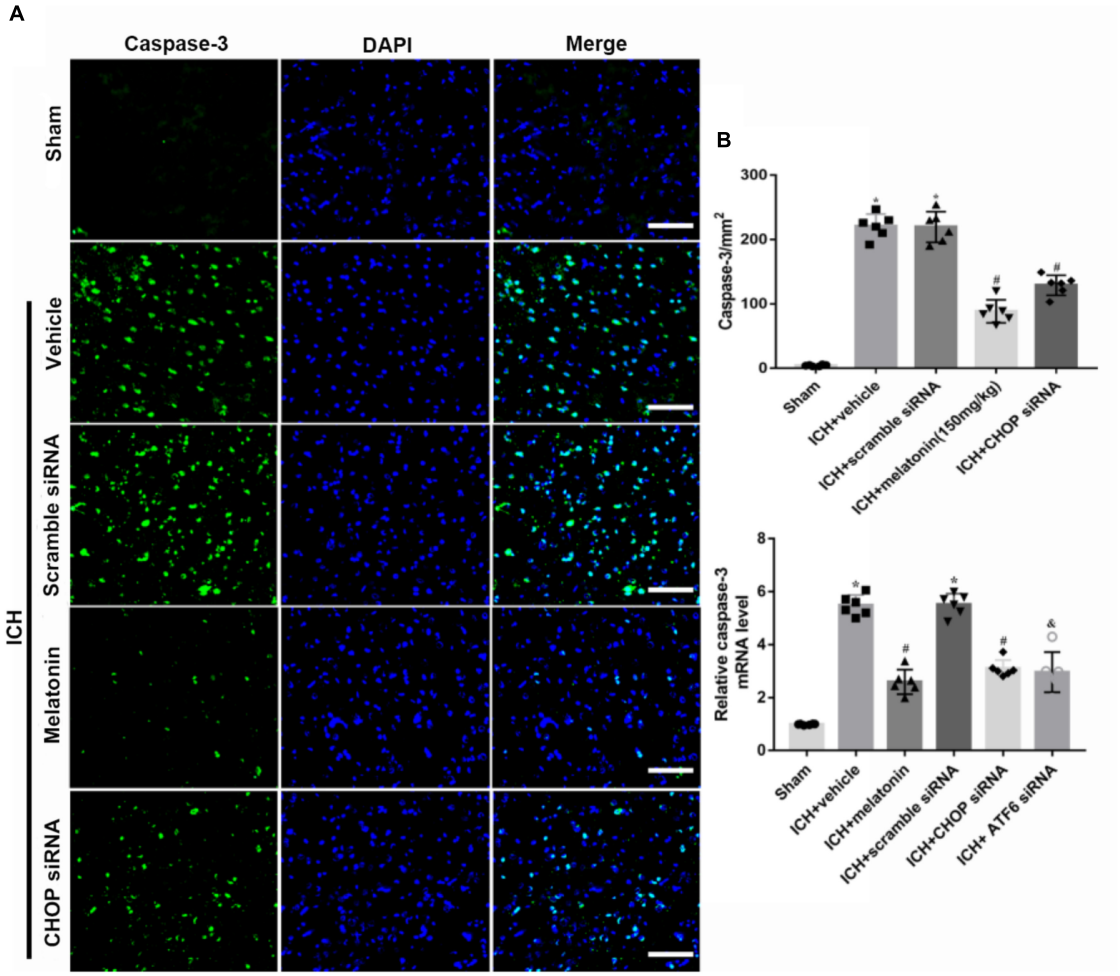

FIGURE 5 | The administration of melatonin significantly decreased the number of caspase-3 and DAPI double-stained cells in the perihematomal region 24 h after ICH. **(A)** Representative microphotographs showed the co-localization of DAPI (blue) with caspase-3 (green)-positive cells in injured brain hemisphere at 24 h after ICH; **(B)** quantitative analysis of caspase-3 positive cells showed that melatonin decreased the number of apoptotic cells after ICH.

We further investigated the role of ATF6 in experimental ICH and its relationship with melatonin by intraperitoneal injection of it 1 h after ICH. The administration of melatonin could significantly reduce the protein and mRNA levels of ATF6 expression. In addition, the expression of Bcl-2 was up-regulated while Bax and cleaved caspase-3 levels were down-regulated. Colocalized immunofluorescence staining showed that neuronal apoptosis was significantly increased after ICH, while the administration of melatonin reversed the results. Furthermore, the induction of ICH significantly increased the level of EB and MMP-9, which was offset by the administration of melatonin. MMP-9, also known as type IV collagenase, belongs to the family of zinc-dependent metalloendo-peptidases. It could degrade the structures of cell junctions, like Claudin-5, ZO-1, et al., and destroy the BBB (Vafadari et al., 2016). The levels of EB and MMP-9 were increased, which indicated that the BBB was destroyed after ICH. However, the administration of melatonin restored the integrity of BBB. Additionally, melatonin could improve neurobehavioral deficits and reduce brain edema at 24 h after ICH. These results were consistent with what has been reported in the literature. The neuroprotective effects of melatonin have been verified in many studies. The mechanisms involved anti-inflammation, anti-oxidative stress, BBB protection and anti-apoptosis (Ramos et al., 2017; Wu et al., 2017). Recently, an increasing amount of studies have demonstrated roles of melatonin in the regulation of ER stress. Melatonin reduced cellular apoptosis and autophagy via suppression of ER stress in both *in vivo* and *in vitro* studies (Hosseinzadeh et al., 2016; Tungkum et al., 2017).

However, the role of ATF6 currently remains controversial. Contrary to our study, the activation of ATF6 was also reported to act as a cellular protective factor in many disease models. For example, in cultured cardiac myocytes, Peter J. and his colleagues demonstrated that adenovirus over-expressing ATF6 could protect cardiac myocytes from apoptosis by down-regulation of miR-455 and *calr* expression (Belmont et al., 2012). In addition, the activation of ATF6 branch of the UPR was also reported to improve the outcomes after cerebral ischemia

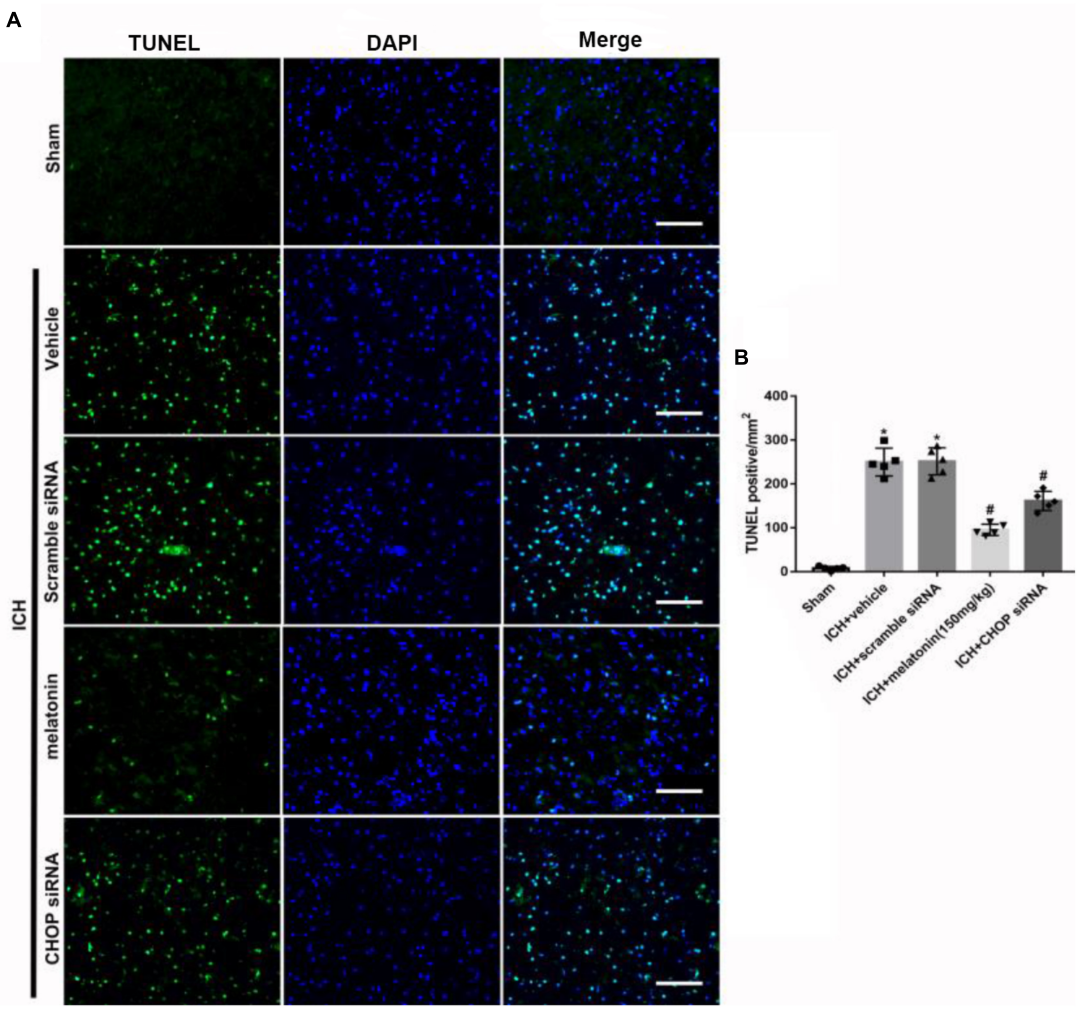

FIGURE 6 | The administration of melatonin significantly decreased the number of TUNEL and DAPI double-stained cells in the perihematomal region 24 h after ICH. **(A)** Representative microphotographs showed the co-localization of DAPI (blue) with TUNEL (green)-positive cells in injured brain hemisphere at 24 h after ICH; **(B)** Quantitative analysis of TUNEL-positive cells showed that melatonin decreased the number of apoptotic cells after ICH. Scale bar = 100 μm. *$p < 0.05$ vs. sham, #$p < 0.05$ vs. ICH + vehicle.

(Yu et al., 2018). On the contrary, it has been demonstrated in a rat model of spinal cord injury, that knockout of ATF6 could protect against ER stress and promote oligodendrocyte precursor cell survival (Saraswat et al., 2018). Actually, the activation of ATF6 branch of UPR has dual roles in the regulation of cell survival. If the injury is mild and short, the activation of ATF6 could help to fold the proteins in a right way and decrease the ER stress, otherwise, the ATF6 would initiate the pro-apoptotic pathway. In response to the ER stress, ATF6 regulates the expression of several genes, the products of which can either relieve ER stress or trigger cell death if the stress cannot be relieved (DuRose et al., 2006). ICH is a subtype of stroke and characterized by high mortality and morbidity. The devastating outcome after ICH was mainly caused by direct damages to the brain parenchyma from blood accumulation and secondary injuries such as brain edema, BBB disruption, and inflammation, which leads to neuronal apoptosis or necrosis. The resulting accumulations of blood components, overproduced iron complexes, dysfunctional organelles, and other cytokines can disrupt normal protein folding, leading to activation of UPR/ER stress, which eventually leads to the irreversible disruption of brain parenchyma and massive cell death (Niu et al., 2017). The results of this study suggested that overactivated ER stress occurred at 24 h after ICH and suppression of ATF6 reduced neuronal apoptosis. In addition, Quan et al. (2015) found that melatonin could bind to its receptor and further suppress the activation of ER stress markers, including (Bip)/(GRP78), which is essential for the activation of ATF6. In the present study, the use of melatonin could significantly decrease the level of Bip and ATF6, suggesting that melatonin could suppress the activation of ATF6 via reducing the level of Bip (Quan et al., 2015).

We further explored the role of CHOP in melatonin-mediated neuroprotection. CHOP remains in low levels

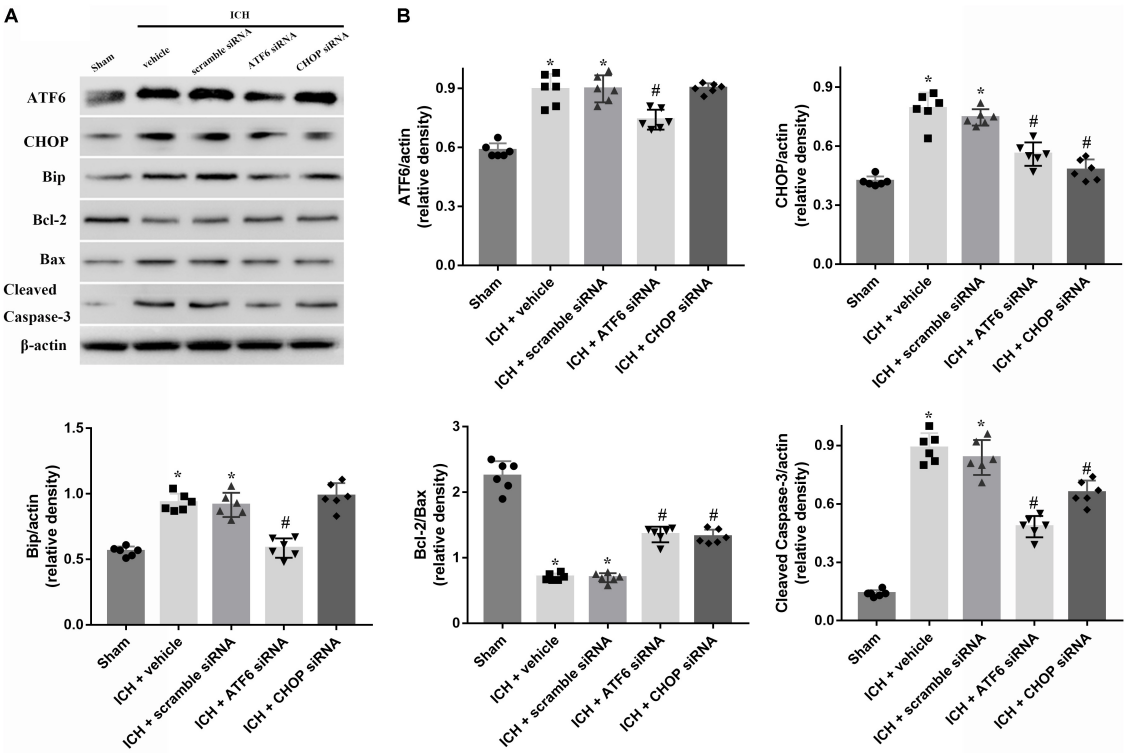

FIGURE 7 | Application of ATF6 siRNA promotes neuronal survival at 24 h after ICH. **(A)** Representative Western blot images. **(B)** Quantitative analyses of ATF6, CHOP, Bip, Bcl-2, Bax, cleaved caspase-3. $n = 6$ for each group. The bars represent the mean ± SD. *$p < 0.05$ vs. sham, #$p < 0.05$ vs. ICH + vehicle.

under normal conditions, but is greatly up-regulated in response to ER stress (Tabas and Ron, 2011). The active role of CHOP has been reported in many diseases. Miyazaki et al. (2011) demonstrated that CHOP deficiency could attenuate myocardial reperfusion injury by inhibiting cellular apoptosis and inflammation. In the rat model of ischemic stroke, suppression of CHOP expression could prevent ER stress overactivation and finally promote neuroprotection. Furthermore, Gotoh et al. (2002) explored the role of ATF6/CHOP pathway in the NO-mediated apoptosis in macrophages. They demonstrated that cell apoptosis induced by p50ATF6 could be inhibited by either a CHOP or ATF6 form (Gotoh et al., 2002). The mechanisms of CHOP-mediated apoptosis are reported to be the suppression of Bcl-2 expression and promotion of Bax expression both *in vivo* and *in vitro* (Wang et al., 1998; Sok et al., 1999; Fu et al., 2010). Based on the results aforementioned, CHOP acted as a pro-apoptotic factor mediated by ATF6 in the ER stress. In the present study, the results suggested that the level of CHOP significantly increased at 12 h and peaked at 24 h after ICH. However, the application of ATF6 siRNA or melatonin distinctly reduced both the protein and mRNA levels of CHOP expression, as well as the expression of Bax and cleaved caspase-3. Additionally, the pro-apoptotic characteristics of ATF6 induced by ICH could be partially reversed by the use of CHOP siRNA, which suggested that the CHOP also acts as a pro-apoptotic factor in the ATF6/CHOP pathway. All of the results suggested that melatonin exerts its neuroprotective role in ICH via suppression of ATF6 and CHOP expression.

Although this study verified the value of melatonin in a novel mechanism mediated via ATF6/CHOP signaling, some limitations could not be ignored. Firstly, melatonin could exert its neuroprotective effects in many pathways by the regulation of ER stress. This study only explored its role in the ATF6/CHOP pathway. Secondly, only the pro-apoptotic characteristic of ATF6 was evaluated in this study, without further investigation of its role in inflammation or autophagy. Therefore, studies focusing on further exploration of melatonin in ER stress and other characteristics of ATF6 in the experimental ICH model are needed.

ETHICS STATEMENT

All experimental protocols were warranted by the ethics committee of Zhejiang University. The procedures were conducted according to NIH guidelines.

AUTHOR CONTRIBUTIONS

WX and TL designed the study. WX, JinZ, and XL completed the experiments. AS and LG performed the statistical analysis.

WX and JinZ finished writing the manuscript. CL and XL revised the manuscript. JY and JiaZ participated in discussion development and provided expert guidance.

FUNDING

This work was funded by China Postdoctoral Science Foundation (2017M612010), National Natural Science Foundation of China (81701144, 81371433), National Key Research and Development Program of China (2017YFC1308500), and Key Program of Science and Technology Development of Zhejiang (2017C03021).

SUPPLEMENTARY MATERIAL

The Supplementary Material for this article can be found online at: https://www.frontiersin.org/articles/10.3389/fnins.2018.00638/full#supplementary-material

REFERENCES

Belmont, P. J., Chen, W. J., Thuerauf, D. J., and Glembotski, C. C. (2012). Regulation of microRNA expression in the heart by the ATF6 branch of the ER stress response. *J. Mol. Cell. Cardiol.* 52, 1176–1182. doi: 10.1016/j.yjmcc.2012.01.017

Boulouis, G., Morotti, A., Goldstein, J. N., and Charidimou, A. (2017). Intensive blood pressure lowering in patients with acute intracerebral haemorrhage: clinical outcomes and haemorrhage expansion. systematic review and meta-analysis of randomised trials. *J. Neurol. Neurosurg. Psychiatry* 88, 339–345. doi: 10.1136/jnnp-2016-315346

Chen, M., Li, X., Zhang, X., He, X., Lai, L., Liu, Y., et al. (2015). The inhibitory effect of mesenchymal stem cell on blood-brain barrier disruption following intracerebral hemorrhage in rats: contribution of TSG-6. *J. Neuroinflammation* 12:61. doi: 10.1186/s12974-015-0284-x

Cui, J., Cui, C., Cui, Y., Li, R., Sheng, H., Jiang, X., et al. (2017). Bone marrow mesenchymal stem cell transplantation increases GAP-43 expression via ERK1/2 and PI3K/Akt pathways in intracerebral hemorrhage. *Cell. Physiol. Biochem.* 2, 137–144. doi: 10.1159/000477122

Doroudgar, S., and Glembotski, C. C. (2012). New concepts of endoplasmic reticulum function in the heart: programmed to conserve. *J. Mol. Cell. Cardiol.* 55, 85–91. doi: 10.1016/j.yjmcc.2012.10.006

DuRose, J. B., Tam, A. B., and Niwa, M. (2006). Intrinsic capacities of molecular sensors of the unfolded protein response to sense alternate forms of endoplasmic reticulum stress. *Mol. Biol. Cell* 17, 3095–3107. doi: 10.1091/mbc.e06-01-0055

Feigin, V. L., Lawes, C. M., Bennett, D. A., Barker-Collo, S. L., and Parag, V. (2009). Worldwide stroke incidence and early case fatality reported in 56 population-based studies: a systematic review. *Lancet Neurol.* 8, 355–369. doi: 10.1016/S1474-4422(09)70025-0

Fernández, A., Ordóñez, R., Reiter, R. J., González-Gallego, J., and Mauriz, J. L. (2015). Melatonin and endoplasmic reticulum stress: relation to autophagy and apoptosis. *J. Pineal Res.* 59, 292–307. doi: 10.1111/jpi.12264

Fouillet, A., Levet, C., Virgone, A., Robin, M., Dourlen, P., Rieusset, J., et al. (2012). ER stress inhibits neuronal death by promoting autophagy. *Autophagy* 8, 915–926. doi: 10.4161/auto.19716

Fu, H. Y., Okada, K., Liao, Y., Tsukamoto, O., Isomura, T., Asai, M., et al. (2010). Ablation of C/EBP homologous protein attenuates endoplasmic reticulum-mediated apoptosis and cardiac dysfunction induced by pressure overload. *Circulation* 122, 361–369. doi: 10.1161/CIRCULATIONAHA.109.917914

Glembotski, C. C. (2014). Roles for ATF6 and the sarco/endoplasmic reticulum protein quality control system in the heart. *J. Mol. Cell. Cardiol.* 71, 11–15. doi: 10.1016/j.yjmcc.2013.09.018

Gong, L., Tang, Y., An, R., Lin, M., Chen, L., and Du, J. (2017). RTN1-C mediates cerebral ischemia/reperfusion injury via ER stress and mitochondria-associated apoptosis pathways. *Cell Death Dis.* 8:e3080. doi: 10.1038/cddis.2017.465

Gotoh, T., Oyadomari, S., Mori, K., and Mori, M. (2002). Nitric oxide-induced apoptosis in RAW 264.7 macrophages is mediated by endoplasmic reticulum stress pathway involving ATF6 and CHOP. *J. Biol. Chem.* 277, 12343–12350. doi: 10.1074/jbc.M107988200

Hosseinzadeh, A., Kamrava, S. K., Joghataei, M. T., Darabi, R., Shakeri-Zadeh, A., Shahriari, M., et al. (2016). Apoptosis signaling pathways in osteoarthritis and possible protective role of melatonin. *J. Pineal Res.* 61, 411–425. doi: 10.1111/jpi.12362

Krishnamurthi, R. V., Moran, A. E., Forouzanfar, M. H., Bennett, D. A., Mensah, G. A., Lawes, C. M., et al. (2014). The global burden of hemorrhagic stroke: a summary of findings from the GBD 2010 study. *Glob. Heart* 9, 101–106. doi: 10.1016/j.gheart.2014.01.003

Li, Y., Guo, Y., Tang, J., Jiang, J., and Chen, Z. (2014). New insights into the roles of CHOP-induced apoptosis in ER stress. *Acta Biochim. Biophys. Sin.* 46, 629–640. doi: 10.1093/abbs/gmu048

Lin, Y. W., Chen, T. Y., Hung, C. Y., Tai, S. H., Huang, S. Y., Chang, C. C., et al. (2018). Melatonin protects brain against ischemia/reperfusion injury by attenuating endoplasmic reticulum stress. *Int. J. Mol. Med.* 42, 182–192. doi: 10.3892/ijmm.2018.3607

Liu, L., Liu, C., Lu, Y., Liu, L., and Jiang, Y. (2015). ER stress related factor ATF6 and caspase-12 trigger apoptosis in neonatal hypoxic-ischemic encephalopathy. *Int. J. Clin. Exp. Pathol.* 8, 6960–6966.

Louessard, M., Bardou, I., Lemarchand, E., Thiebaut, A. M., Parcq, J., Leprince, J., et al. (2017). Activation of cell surface GRP78 decreases endoplasmic reticulum stress and neuronal death. *Cell Death Differ.* 24, 1518–1529. doi: 10.1038/cdd.2017.35

Menzie-Suderam, J. M., Mohammad-Gharibani, P., Modi, J., Ma, Z., Tao, R., Prentice, H., et al. (2018). Granulocyte-colony stimulating factor protects against endoplasmic reticulum stress in an experimental model of stroke. *Brain Res.* 1682, 1–13. doi: 10.1016/j.brainres.2017.12.022

Miyazaki, Y., Kaikita, K., Endo, M., Horio, E., Miura, M., Tsujita, K., et al. (2011). C/EBP homologous protein deficiency attenuates myocardial reperfusion injury by inhibiting myocardial apoptosis and inflammation. *Arterioscler. Thromb. Vasc. Biol.* 31, 1124–1132. doi: 10.1161/ATVBAHA.111.224519

Nakka, V. P., Gusain, A., and Raghubir, R. (2010). Endoplasmic reticulum stress plays critical role in brain damage after cerebral ischemia/reperfusion in rats. *Neurotox. Res.* 17, 189–202. doi: 10.1007/s12640-009-9110-5

Niu, M., Dai, X., Zou, W., Yu, X., Teng, W., Chen, Q., et al. (2017). Autophagy, endoplasmic reticulum stress and the unfolded protein response in intracerebral hemorrhage. *Transl. Neurosci.* 8, 37–48. doi: 10.1515/tnsci-2017-0008

Pías-Peleteiro, J., Campos, F., Castillo, J., and Sobrino, T. (2017). Endothelial progenitor cells as a therapeutic option in intracerebral hemorrhage. *Neural Regen. Res.* 12, 558–561. doi: 10.4103/1673-5374.205085

Qiu, J., Wang, X., Wu, F., Wan, L., Cheng, B., Wu, Y., et al. (2017). Low dose of apelin-36 attenuates ER stress-associated apoptosis in rats with ischemic stroke. *Front. Neurol.* 8:556. doi: 10.3389/fneur.2017.00556

Quan, X., Wang, J., Liang, C., Zheng, H., and Zhang, L. (2015). Melatonin inhibits tunicamycin-induced endoplasmic reticulum stress and insulin resistance in skeletal muscle cells. *Biochem. Biophys. Res. Commun.* 463, 1102–1107. doi: 10.1016/j.bbrc.2015.06.065

Ramos, E., Patiño, P., Reiter, R. J., Gil-Martín, E., Marco-Contelles, J., Parada, E., et al. (2017). Ischemic brain injury: new insights on the protective role of melatonin. *Free Radic. Biol. Med.* 104, 32–53. doi: 10.1016/j.freeradbiomed.2017.01.005

Roussel, B. D., Kruppa, A. J., Miranda, E., Crowther, D. C., Lomas, D. A., and Marciniak, S. J. (2013). Endoplasmic reticulum dysfunction in neurological disease. *Lancet Neurol.* 12, 105–118. doi: 10.1016/S1474-4422(12)70238-7

Saraswat, O. S., Hetman, M., and Whittemore, S. R. (2018). ATF6α deletion modulates the ER stress response after spinal cord injury but does not affect locomotor recovery. *J. Neurotrauma* 35, 486–491. doi: 10.1089/neu.2015.3993

Schroder, M., and Kaufman, R. J. (2005). ER stress and the unfolded protein response. *Mutat. Res.* 569, 29–63. doi: 10.1016/j.mrfmmm.2004.06.056

Senkal, C. E., Ponnusamy, S., Bielawski, J., Hannun, Y. A., and Ogretmen, B. (2010). Antiapoptotic roles of ceramide-synthase-6-generated C_{16}-ceramide *via* selective regulation of the ATF6/CHOP arm of ER-stress-response pathways. *FASEB J.* 24, 296–308. doi: 10.1096/fj.09-135087

Shen, H., Liu, C., Zhang, D., Yao, X., Zhang, K., Li, H., et al. (2017). Role for RIP1 in mediating necroptosis in experimental intracerebral hemorrhage model both *in vivo* and *in vitro*. *Cell Death Dis.* 8:e2641. doi: 10.1038/cddis.2017.58

Sok, J., Wangm X. Z., Batchvarova, N., Kuroda, M., Harding, H., and Ron, D. (1999). CHOP-Dependent stress-inducible expression of a novel form of carbonic anhydrase VI. *Mol. Cell. Biol.* 19, 495–504. doi: 10.1128/MCB.19.1.495

Steiner, T., Al-Shahi Salman, R., Beer, R., Christensen, H., Cordonnier, C., Csiba, L., et al. (2014). European Stroke Organisation (ESO) guidelines for the management of spontaneous intracerebral hemorrhage. *Int. J. Stroke* 9, 840–855. doi: 10.1111/ijs.12309

Stephens, S. B., and Nicchitta, C. V. (2008). Divergent regulation of protein synthesis in the cytosol and endoplasmic reticulum compartments of mammalian cells. *Mol. Biol. Cell* 19, 623–632. doi: 10.1091/mbc.e07-07-0677

Tabas, I., and Ron, D. (2011). Integrating the mechanisms of apoptosis induced by endoplasmic reticulum stress. *Nat. Cell Biol.* 13, 184–190. doi: 10.1038/ncb0311-184

Tungkum, W., Jumnongprakhon, P., Tocharus, C., Govitrapong, P., and Tocharus, J. (2017). Melatonin suppresses methamphetamine-triggered endoplasmic reticulum stress in C6 cells glioma cell lines. *J. Toxicol. Sci.* 42, 63–71. doi: 10.2131/jts.42.63

Vafadari, B., Salamian, A., and Kaczmarek, L. (2016). MMP-9 in translation: from molecule to brain physiology, pathology, and therapy. *J. Neurochem.* 139, 91–114. doi: 10.1111/jnc.13415

van Asch, C. J., Luitse, M. J., Rinkel, G. J., van der Tweel, I., Algra, A., and Klijn, C. J. (2010). Incidence, case fatality, and functional outcome of intracerebral haemorrhage over time, according to age, sex, and ethnic origin: a systematic review and meta-analysis. *Lancet Neurol.* 9, 167–176. doi: 10.1016/S1474-4422(09)70340-0

Wang, X. Z., Kuroda, M., Sok, J., Batchvarova, N., Kimmel, R., Chung, P., et al. (1998). Identification of novel stress-induced genes downstream of chop. *EMBO J.* 17, 3619–3630. doi: 10.1093/emboj/17.13.3619

Wu, H. J., Wu, C., Niu, H. J., Wang, K., Mo, L. J., Shao, A. W., et al. (2017). Neuroprotective Mechanisms of Melatonin in Hemorrhagic Stroke. *Cell. Mol. Neurobiol.* 37, 1173–1185. doi: 10.1007/s10571-017-0461-9

Wu, J., Rutkowski, D. T., Dubois, M., Swathirajan, J., Saunders, T., Wang, J., et al. (2007). ATF6alpha optimizes long-term endoplasmic reticulum function to protect cells from chronic stress. *Dev. Cell* 13, 351–364. doi: 10.1016/j.devcel.2007.07.005

Xiong, Y., Chen, H., Lin, P., Wang, A., Wang, L., and Jin, Y. (2017). ATF6 knockdown decreases apoptosis, arrests the S phase of the cell cycle, and increases steroid hormone production in mouse granulosa cells. *Am. J. Physiol. Cell Physiol.* 312, C341–C353. doi: 10.1152/ajpcell.00222.2016

Ye, J., Rawson, R. B., Komuro, R., Chen, X., Dave, U. P., Prywes, R., et al. (2000). ER stress induces cleavage of membrane-bound ATF6 by the same proteases that process SREBPs. *Mol. Cell* 6, 1355–1364. doi: 10.1016/S1097-2765(00)00133-7

Yu, Z., Sheng, H., Liu, S., Zhao, S., Glembotski, C. C., Warner, D. S., et al. (2018). Activation of the ATF6 branch of the unfolded protein response in neurons improves stroke outcome. *J. Cereb. Blood Flow Metab.* 37, 1069–1079. doi: 10.1177/0271678X16650218

Zeng, J., Chen, Y., Ding, R., Feng, L., Fu, Z., Yang, S., et al. (2017). Isoliquiritigenin alleviates early brain injury after experimental intracerebral hemorrhage via suppressing ROS- and/or NF-κB-mediated NLRP3 inflammasome activation by promoting Nrf2 antioxidant pathway. *J Neuroinflammation* 14:119. doi: 10.1186/s12974-017-0895-5

Zhao, H., Zhang, X., Dai, Z., Feng, Y., Li, Q., Zhang, J. H., et al. (2016). P2X7 receptor suppression preserves blood-brain barrier through inhibiting RhoA activation after experimental intracerebral hemorrhage in rats. *Sci Rep.* 6:23286. doi: 10.1038/srep23286

Zhou, K., Enkhjargal, B., Xie, Z., Sun, C., Wu, L., Malaguit, J., et al. (2018). Dihydrolipoic acid inhibits lysosomal rupture and NLRP3 through lysosome-associated membrane protein-1/calcium/calmodulin-dependent protein kinase II/TAK1 pathways after subarachnoid hemorrhage in rat. *Stroke* 49, 175–183. doi: 10.1161/STROKEAHA.117.018593

Zhou, X., Xie, Q., Xi, G., Keep, R. F., and Hua, Y. (2014). Brain cd47 expression in a swine model of intracerebral hemorrhage. *Brain Res.* 1574, 70–76. doi: 10.1016/j.brainres.2014.06.003

Zhou, Y., Sun, P., Wang, T., Chen, K., Zhu, W., and Wang, H. (2015). Inhibition of calcium influx reduces dysfunction and apoptosis in lipotoxic pancreatic β-cells via regulation of endoplasmic reticulum stress. *PLOS One* 10:e0132411. doi: 10.1371/journal.pone.0132411

Conflict of Interest Statement: The authors declare that the research was conducted in the absence of any commercial or financial relationships that could be construed as a potential conflict of interest.

frontiers in Neuroscience

ORIGINAL RESEARCH
published: 20 September 2018
doi: 10.3389/fnins.2018.00657

Andrographolide Alleviates Acute Brain Injury in a Rat Model of Traumatic Brain Injury: Possible Involvement of Inflammatory Signaling

Li Tao[1†], Li Zhang[2†], Rong Gao[2], Feng Jiang[2], Jianbo Cao[1] and Huixiang Liu[2*]*

[1] Department of Pharmacy and Translational Medicine Center, Zhangjiagang First People's Hospital, Suzhou, China,
[2] Department of Neurosurgery, Zhangjiagang First People's Hospital, Suzhou, China

OPEN ACCESS

Edited by:
Gang Chen,
The First Affiliated Hospital of Soochow University, China

Reviewed by:
Yang Wang,
Anhui Provincial Hospital, China
Sheng Chen,
Zhejiang University School of Medicine, China

***Correspondence:**
Jianbo Cao
Caojianbo65@126.com
Huixiang Liu
liuhuixianglab@sina.com

[†]These authors have contributed equally to this work

Specialty section:
This article was submitted to Neurodegeneration, a section of the journal Frontiers in Neuroscience

Received: 14 May 2018
Accepted: 03 September 2018
Published: 20 September 2018

Citation:
Tao L, Zhang L, Gao R, Jiang F, Cao J and Liu H (2018) Andrographolide Alleviates Acute Brain Injury in a Rat Model of Traumatic Brain Injury: Possible Involvement of Inflammatory Signaling. Front. Neurosci. 12:657. doi: 10.3389/fnins.2018.00657

Neuroinflammation plays an important role in secondary injury after traumatic brain injury (TBI). Andrographolide (Andro), a diterpenoid lactone isolated from *Andrographis paniculata*, has been demonstrated to exhibit anti-inflammatory activity in neurodegenerative disorders. This study therefore aimed to investigate the potential neuroprotective effects of Andro after TBI and explore the underlying mechanisms. In our study, we used a weight-dropped model to induce TBI in Sprague–Dawley rats, the neurological deficits were assessed using modified neurological severity scores, Fluoro-Jade B (FJB) and terminal deoxynucleotidyl transferase (TdT) dUTP Nick-End Labeling (TUNEL) staining were employed to examine neuronal degeneration and apoptosis after TBI, immunofluorescence was designed to investigate microglial activation. Quantitative Real-time PCR and ELISA were conducted to detect the expression levels of pro-inflammatory cytokines, Western blot was used to examine the expression level of proteins of relative signaling pathway. Our results showed that after Andro administration, the neurological deficit was attenuated, and the cerebral edema and apoptosis in brain tissues were also decreased following TBI. Both microglial activation and the expression of pro-inflammatory cytokines were significantly inhibited by Andro after TBI. Moreover, Andro inhibited NF-κB p65 subunit translocation and decreased the expression levels of phosphorylated extracellular signal regulated kinase (ERK) and p38 MAPK after TBI. Altogether, this study suggests that Andro could improve neurobehavioral function by inhibiting NF-κB and MAPK signaling pathway in TBI, which might provide a new approach for treating brain injury.

Keywords: andrographolide, inflammation, apoptosis, traumatic brain injury, neuroprotection

INTRODUCTION

Traumatic brain injury (TBI) is a prevalent healthcare concern with more than 10 million people suffering annually worldwide. It has been a major cause of mortality and disability resulting from traffic accidents, falls, and external mechanical concussion etc, especially in children and young adults (Hyder et al., 2007; Gardner and Zafonte, 2016). TBI can lead to temporary or permanent

motor deficit and cognition deficits which negatively affects the quality of life of patients. Despite the progress in diagnosis, neuroradiology, neurosurgical care and treatment in recent years, effective treatment strategies for improving functional outcome of TBI patients remain limited. Therefore, it is important to develop novel therapeutic interventions that could be helpful for TBI patients.

The pathophysiology of TBI can be divided with two parts: primary and secondary injury. Primary brain injury involve brain contusion, skull fractures, diffused axonal injury and intracranial hemorrhage, usually causes immediate neuronal death (Laplaca et al., 2007; Cheng et al., 2012). Secondary brain injury is a complicated cellular processes and biochemical cascades which occur in minutes and last for days following the traumatic events, resulting in exacerbated damage, progressive neurodegeneration and cell death (Kabadi and Faden, 2014). The mechanism of TBI-induced secondary injury includes glutamate excitotoxicity (Hyder et al., 2007), oxidative stress (Zhang et al., 2018), blood-brain barrier (BBB) disruption (Lutton et al., 2017), neuroinflammation and mitochondrial dysfunction (Lozano et al., 2015). It is well known that neuroinflammation occurs in both primary and secondary injury following TBI, as well as in other neurodegenerative diseases (Eikelenboom et al., 2010; Perry et al., 2010). As the resident immune cells in brain, microglia plays important roles in response to neuronal pathology. Activated microglia release a complex series of pro-inflammatory factors such as nitric oxide (NO), tumor necrosis factor (TNF), prostaglandin E2 (PGE2) and, interleukin (IL), leading to detrimental effects and neuronal dysfunction (Chiu et al., 2016). Therefore, inhibiting microglial activation might be a beneficial therapeutic target for treating TBI patients.

Andrographolide (Andro) is a natural diterpenoid from Chinese traditional herb *Andrographis paniculata*, which is widely used for treating fever, upper respiratory tract infections, laryngitis, diarrhea and rheumatoid arthritis (Batkhuu et al., 2002; Shen et al., 2002; Xia et al., 2004). Recently, several studies have reported that Andro exerts neuroprotective effects via inhibiting neuroinflammation and oxidative stress in neurodegenerative disorders. It has been reported that Andro could reduce the expression of NADPH oxidase 2 (NOX2), as well as inducible-nitric oxide synthase (iNOS), and it protect against cerebral ischemia via attenuating nuclear factor kappa B (NF-κB) and inhibiting the expression of hypoxia-inducible factor 1-α (HIF-1α) (Lu et al., 2006; Chern et al., 2011). Moreover, it has been reported that Andro reduced inflammation-mediated dopaminergic neurodegeneration by inhibiting microglial activation, indicating that Andro may be a new finding in clinical use in treating Parkinson's disease (PD) (Wang et al., 2004, 2007). However, it remains unknown that whether Andro has impact on microglia-mediated inflammatory response in a model of TBI. Therefore, our main purpose of this work was to investigate neuroprotective effect of Andro after TBI and explore its underlying mechanism.

MATERIALS AND METHODS

Animals and Treatment

Male adult Sprague–Dawley (SD) rats (300–350 g) were purchased from Animal Center of Chinese Academy of Sciences, Shanghai, China. The animals were housed in a temperature- and humidity-controlled room with a 12 h light/dark cycle and they were supplied with food and water *ad libitum*. All procedures of animal experiments were approved by the Institutional Animal Care Committee of the Soochow University and were according to the guidelines of the National Institutes of Health on the care and use of animals.

A total 96 rats (118 rats were used, 96 rats were survived) were randomly divided into four groups: [(1) sham group (n = 24) (2) TBI group (n = 24) (3) TBI + saline (NS) group (n = 24) (4) TBI + Andro group (n = 24)]. [Mortality in the sham group is 0% (0 of 24), in TBI group is 25% (8 of 32), in TBI + NS group is 23% (7 of 31), and in TBI + Andro group is 23% (7 of 31)]. As described in previous study (Chern et al., 2011), Andro (Sigma-Aldrich) was first dissolved in ethanol, then it was diluted with 0.9% normal saline (NS). Rats were injected intraperitoneally with Andro (1 mg/kg) at 1 h after TBI model was conducted. The dose and administration method were chosen according to the previous study (Chan et al., 2010). Rats of TBI + NS group received an equal volume of saline, intraperitoneally. The brain areas around the injured cortex as shown in **Figures 1A,B** were collected for subsequent analysis.

Experimental Model of Traumatic Brain Injury

Rat experimental model of TBI was established according to modified Feeney's method (Feeney et al., 1981). Briefly, after shaving and sterilization, rats were fixed in a stereotactic frame, then a midline incision was made over the skull to expose the right parietal bone. A right 5 mm parietal craniotomy was drilled 2 mm caudal to the oronal suture and 3 mm from the midline. We modified the method of Feeney's weight-drop model, an object weighing 40 g was dropped along a steel rod onto the dura from a height of 25 cm to cause severe brain injury (Feeney et al., 1981).

Evaluation of Neurological Behavior Function

The modified neurological severity scores (mNSS) method was performed at 24 h to evaluate neurological function after TBI, a series of composite tests including motor, sensory, reflex and balance tests were measured and scaled from 0 to 18 score (Jin et al., 2014). The score of 0 means normal while 18 means severe brain injury.

Brain Water Content

The brain edema of rats in each group was examined using a wet/dry method at 24 h post-injury. Briefly, bilateral brains were weighed separately as wet weight after quickly removed from the skull. The brains were dryed at 100 C in an oven for 72 h and weighed again as dry weight. The brain water content

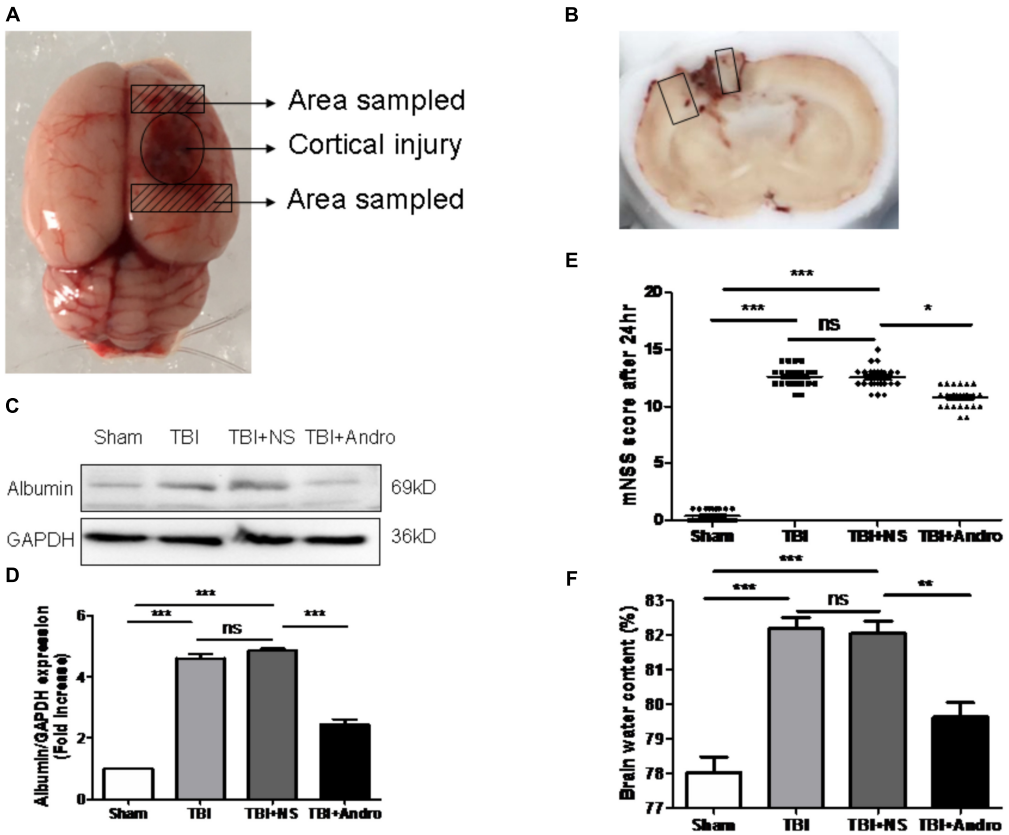

FIGURE 1 | Andro treatment improved neurological function, reduced blood-brain barrier (BBB) disruption and cerebral edema after TBI. **(A)** A schematic image of the cortical contusion area induced by weight-dropping model of traumatic injury and the sampled area around the injured brain. **(B)** A schematic of a coronal section and the microphotographed areas used in immunofluorescence staining are marked with a box. **(C)** The expression level of albumin in peri-contusive cortex was examined by Western blot analysis at 24 h after TBI. **(D)** Relative expression levels of albumin were calculated based on densitometry analysis. The mean values of albumin in the sham group were normalized to 1.0. **(E)** Neurological function was measured by mNSS tests at 24 h after TBI. **(F)** Brain water content of each group was measured at 24 h after TBI. Data are presented as the mean ± SD. $^{*}p < 0.05$, $^{**}p < 0.01$ $^{***}p < 0.001$, ns $p > 0.05$; $n = 6$ in each group.

was calculated using the formula as follows: [(wet weight-dry weight)/wet weight] × 100% (Chen et al., 2017).

Brain Tissue Preparation

For immunofluorescence staining, the rats in each group were sacrificed and perfused intracardially with NS and then fixed with 500 mL 4% paraformaldehyde at 24 h after TBI. The brains were quickly removed from skull and fixed with 4% paraformaldehyde. Then, the brains were dehydrated in 15%, 30% sucrose until infiltration was complete. For quantitative real-time PCR and Western Blot analysis, the rats were only infused with NS, then the brain tissues were quickly removed and the peri-contusive cortex were collected and stored at -80 C until use.

Immunofluorescence Staining

The brains tissues were quickly removed from the rats, after embedded in paraffin and dehydration, brains tissues were sectioned at 15 μm. The staining for Iba1 (Wako Pure Chemical Industries, Osaka, Japan) was performed. Sections were first blocked with 5% bovine serum for 1 h and then incubated with primary antibodies at 4 C overnight. Sections were incubated with secondary antibodies (Life Technologies, United States) for 1 h after washing 3 times with PBST, After final washing, the sections were stained with DAPI (Southern Biotech, United States) for 30 min and observed in a fluorescent microscope (Leica, TCS SP8). Fluoro-Jade B (FJB) and terminal deoxynucleotidyl transferase (TdT) dUTP Nick-End Labeling (TUNEL) staining were performed to detect neuronal degeneration and apoptosis after TBI according to the manufacturer's instructions. The relative fluorescence intensity was analyzed using Image J program.

Quantitative Real-Time PCR

Quantitative real-time PCR analysis was performed to examine the gene expression levels of pro-inflammatory cytokines. Total RNA was extracted from peri-contusive cortex with the Trizol Reagents (Invitrogen Life Technologies, United States). cDNA was synthesized using a cDNA synthesis kit (Thermo Scientific) according to the manufacturer's protocol. cDNA was amplified with SYBR Green (Thermo Fisher, United States) using specific

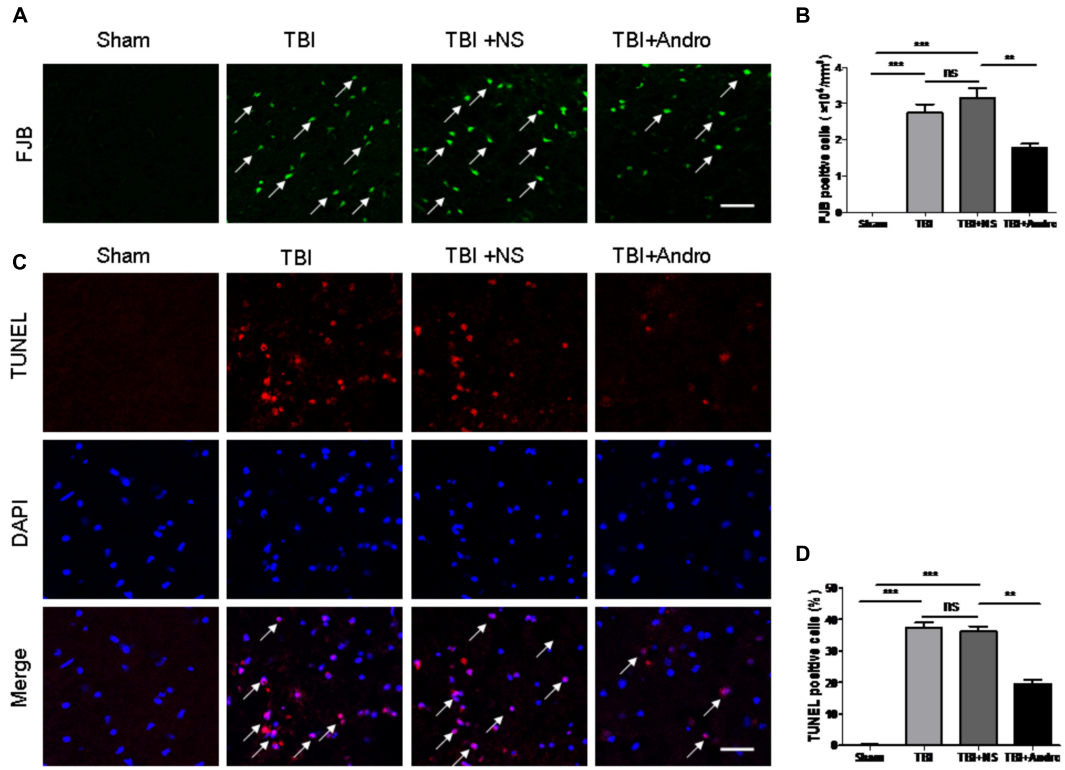

FIGURE 2 | Andro treatment decreased the number of neuronal degeneration and apoptosis after TBI. **(A)** Degenerating neurons were detected with Fluoro-Jade B staining at 24 h after TBI. Arrows indicated the FJB-positive cells. **(B)** Percentage of FJB-positive cells around the injured brain tissues. **(C)** Apoptotic cells were labeled with TUNEL staining at 24 h after TBI. Arrows indicated the TUNEL-positive cells. **(D)** Percentage of TUNEL-positive cells around the injured brain tissues. Data are presented as the mean ± SD. $^{*}p < 0.05$, $^{**}p < 0.01$ $^{***}p < 0.001$, ns $p > 0.05$; $n = 6$ in each group. Scale Bars = 50 μm.

primers of TNF-α, IL-6, IL-1β or GAPDH. The primer sequences were referred to our previous study (Tao et al., 2018). $2^{-(\Delta\Delta CT)}$ method was choosed to calculate the quantification of relative gene expression and the values were normalized to GAPDH.

Enzyme-Linked Immunosorbent Assay (ELISA)

The peri-contusive cortex were collected and homogenized. Then the supernatants were collected and centrifuged at 12,000 × *g* for 20 min. The expression of TNF-α, IL-1β and IL-6 were measured with ELISA kits (Boster Biosciences Co., Wuhan, China).

Western Blot Analysis

The peri-contusive cortex were collected and lysed in RIPA buffer with protease inhibitors and the lysates were centrifuged at 12,000 × *g* for 15 min at 4 C. Protein concentration was determined using a BCA assay kit (Thermo Scientific). A total 80 μg protein was loaded on SDS–PAGE gel and transferred to polyvinylidene difluoride membranes (Millipore, MA, united States). Then the membranes were blocked with 5% fresh skimmed milk for 2 h, incubated with primary antibodies against albumin (Abcam Cambridge, United Kingdom), p38 MAPK (Abcam Cambridge, United Kingdom), ERK (Cell Signaling Technology, United States), NF-κB p65 (Cell Signaling Technology, United States) at 4 C overnight. After overnight incubation, the membranes were washed and incubated with secondary antibodies conjugated to horseradish peroxidase (Invitrogen Life Technologies, United States) for 1 h. Finally, protein bands were detected with enhanced chemiluminescence (ECL) reagents (Millipore, United States) in a Western Blotting Detection System. The relative protein quantity was analyzed by ImageJ software (National Institutes of Health, United States).

Statistical Analysis

SPSS 19.0 software and GraphPad Prism were used in the experiment for data analysis. The data were presented as mean ± SD. Statistical significance was subjected to one-way ANOVA followed by Tukey's test. $p < 0.05$ was considered statistically significant.

RESULTS

Andro Attenuated Neurological Deficit, Cerebral Edema and BBB Breakdown in Rats Following TBI

Neurological function was confirmed using mNSS test at 24 h after injury in all groups of rats. Rat in TBI and TBI + NS

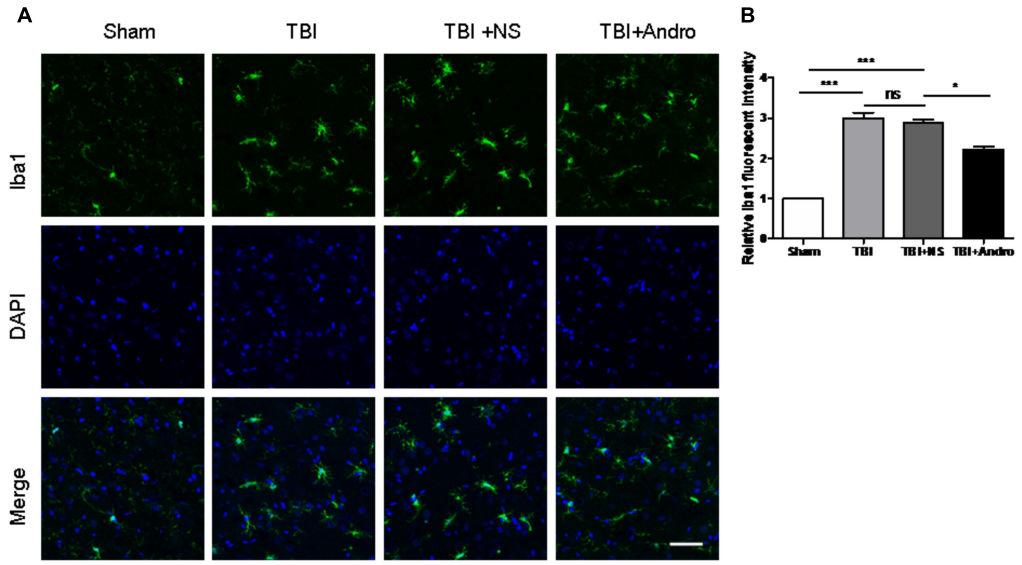

FIGURE 3 | Andro treatment inhibited microglia activation after TBI. **(A)** Double staining for Iba1 (green) and 4, 6-diamino-2-phenylindole (DAPI, blue) in peri-contusive cortex at 24 h after TBI. Microglia cells were highly ramified, exhibited long branching processes and a small cellular body in the sham group. In response to brain injury, the branches of microglia become short, retracted and thick. In Andro treatment group, microglia showed a smaller cellular body. Scale Bars = 50 μm. **(B)** The relative fluorescent intensity of Iba1. Data are presented as the mean ± SD. $*p < 0.05$, $**p < 0.01$ $***p < 0.001$, ns $p > 0.05$; $n = 6$ in each group.

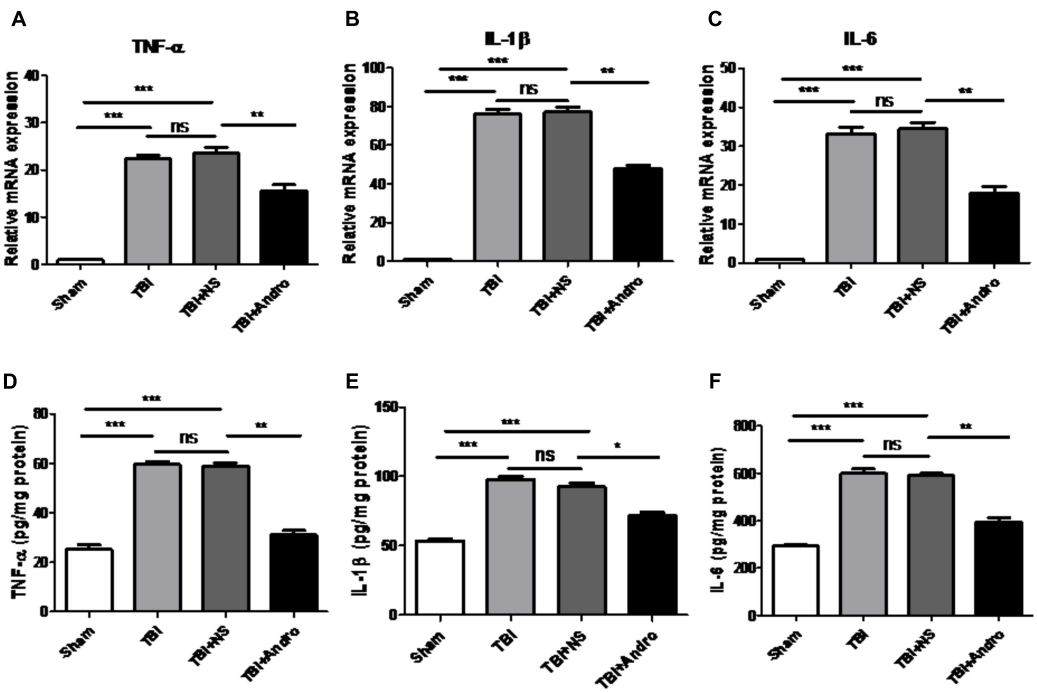

FIGURE 4 | Andro treatment decreased the expression levels of pro-inflammatory cytokines after TBI. The mRNA levels of TNF-α **(A)**, IL-1β **(B)** and IL-6 **(C)** in peri-contusive cortex were determined by QPCR at 6 h after TBI. The protein levels of TNF-α **(D)**, IL-1β **(E)** and IL-6 **(F)** in peri-contusive cortex were measured by ELISA at 24 h after TBI. All data are presented as the mean ± SD. $*p < 0.05$, $**p < 0.01$ $***p < 0.001$, ns $p > 0.05$; $n = 6$ in each group.

group showed higher scores than sham group. As shown in **Figure 1E**, the scores of rats treated with Andro were decreased than that of TBI + NS group. Next, we detected the expression of albumin in each group to examine BBB breakdown after TBI. The results suggested that Andro treatment decreased the albumin expression induced by TBI (**Figures 1C,D**). Brain water content

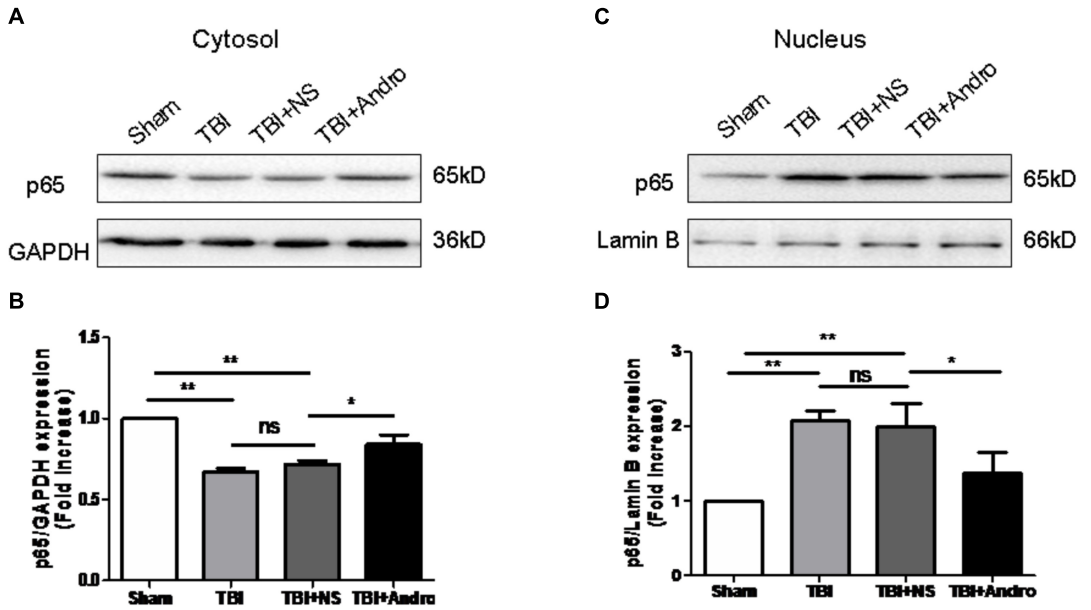

FIGURE 5 | Andro treatment suppressed NF-κB translocation from the cytosol to the nucleus after TBI. Both cytoplasmic **(A)** and nuclear **(C)** protein were extracted in peri-contusive cortex at 24 h after TBI. The expression levels of NF-κB p65 were examined by Western blot analysis. Relative expression levels of NF-κB p65 in cytoplasmic **(B)** and nuclear **(D)** protein were calculated based on densitometry analysis. The mean values of NF-κB p65 in the sham group were normalized to 1.0. All data are presented as the mean ± SD. $^{*}p < 0.05$, $^{**}p < 0.01$ $^{***}p < 0.001$, ns $p > 0.05$; $n = 6$ in each group.

is an important indicator to in the prognosis after TBI. Our data showed that brain water content was markedly increased in the TBI and TBI + NS group compared with sham group. Andro treatment decreased brain water content 24 h after TBI (**Figure 1F**).

Andro Inhibited Neuronal Apoptosis in Rats Following TBI

Fluoro-Jade B staining, widely used as a marker of damaged neuronal cells, was performed to determine neuronal degeneration at 24 h after TBI. FJB staining is widely used as a maker of damaged neuronal cells (Ullah et al., 2011). The number of FJB-positive cells was significantly increased after injury, while Andro treatment decreased the number of FJB-positive cells (**Figures 2A,B**). Additionally, TUNEL staining was performed to detect neuronal apoptosis at 24 h after injury. As our results indicated that the number of TUNEL-positive cells was markedly increased after TBI and it was also decreased by Andro administration (**Figures 2C,D**). Both FJB and TUNEL staining revealed that Andro inhibited neuronal degeneration and apoptosis after TBI.

Andro Inhibited Microglial Activation Following TBI

To investigate the effect of Andro on microglial activation, immunofluorescence staining of Iba1 was performed at 24 h after TBI. In the sham group, microglia cells were ramified with small cellular body, while microglia cells became thickened with larger bodies after injury. In Andro treatment group, cells showed a smaller cell body compared with TBI and TBI + NS group (**Figures 3A,B**).

Andro Decreased the Production of Pro-Inflammatory Cytokines Following TBI

The expression of TNF-α, IL-1β and IL-6 in the peri-contusive tissues were detected by qPCR and ELISA at 6 h and 24 h after TBI, separately. As shown in **Figure 4**, the expression of TNF-α, IL-1β and IL-6 were expressed at a low level in sham group. The expression of TNF-α, IL-1β and IL-6 was increased in TBI and TBI + NS group, while in the group of Andro treatment, the expression of pro-inflammatory cytokines were decreased.

Andro Inhibited NF-κB Translocation and MAPK Activation Following TBI

Both NF-κB and MAPK signaling pathway were involved in the modulation of pro-inflammatory cytokines (Tao et al., 2014). To investigate the underlying mechanism of the anti-inflammatory effect of Andro, we detected the expression of NF-κB and MAPK by Western blot analysis at 24 h after injury. As shown in **Figure 5**, Andro treatment inhibited p65 translocation from cytoplasm to nucleus after injury. Moreover, we determined the expression of p-ERK and p-p38 MAPK at 24 h after injury. The results of Western blot analysis suggested that Andro decreased the expression level of both p-ERK and p-p38 MAPK induced by TBI (**Figure 6**).

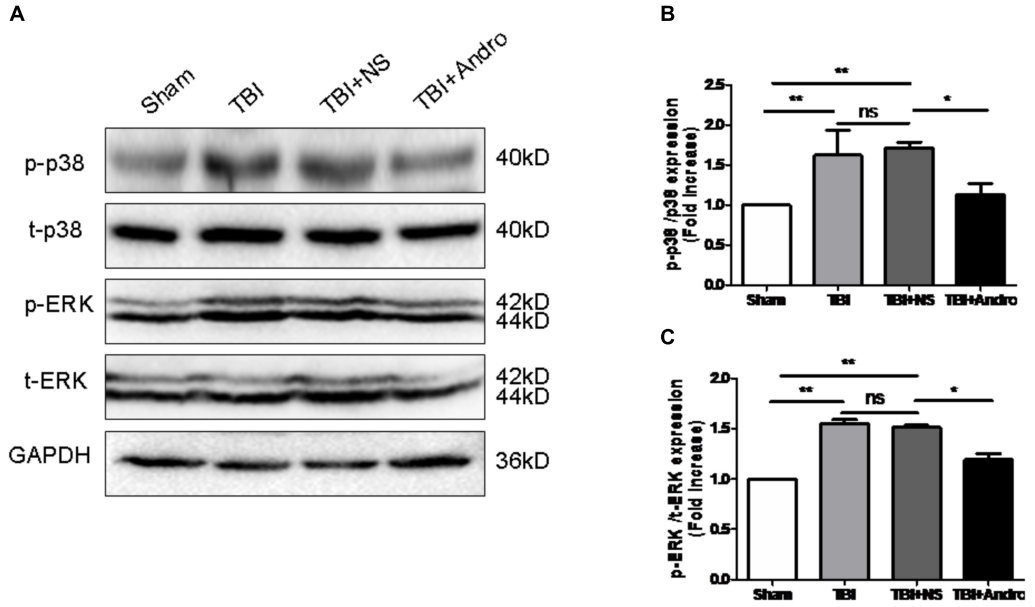

FIGURE 6 | Andro treatment inhibited the phosphorylation of p38 MAPK and ERK after TBI. **(A)** The expression levels of p-p38 MAPK and p-ERK in peri-contusive cortex were examined by Western blot analysis at 24 h after TBI. Relative expression levels of p-p38 MAPK **(B)** and p-ERK **(C)** were calculated based on densitometry analysis. The mean values of *p*-p38 MAPK and *p*-ERK in the sham group were normalized to 1.0. All data are presented as the mean ± SD. $^{*}p < 0.05$, $^{**}p < 0.01$ $^{***}p < 0.001$, ns $p > 0.05$; $n = 6$ in each group.

DISCUSSION

In this study, we demonstrated that Andro, a natural diterpenoid from Chinese traditional herb, conferred neuroprotective effect in rat model of TBI. Our data showed that Andro reduced brain edema, neuronal apoptosis and neurological deficit. In addition, Andro inhibited the expression of pro-inflammatory cytokines including TNF-α, IL-6 and IL-1β by QPCR and ELISA analysis. Moreover, Andro inhibited NF-κB p65 translocation from cytoplasm into the nucleus, the expression of p-ERK, p-p38 MAPK induced by TBI was also decreased after Andro treatment. To our knowledge, it is the first time we reported that Andro may attenuate acute neuroinflammation mediated by NF-κB and MAPK activation in acute phase of TBI.

It is well known that edema formation, increased oxidative stress, calcium influx, excitotoxicity, inflammation and cell death or apoptosis contribute to the process of secondary injury (Werner and Engelhard, 2007; Lutton et al., 2017). Brain edema exacerbation is a major and severe pathophysiological change induced by TBI (Lutton et al., 2017). In our study, we found that Andro reduced TBI-induced brain edema, moreover, Andro decreased the expression of albumin after injury, indicating that Andro rehabilitate the BBB integrity. Apoptosis plays a critical role in secondary brain injury following TBI. Neuronal apoptosis occurs as early as 4 h around the lesion site after injury and may last for weeks (Liu et al., 1997; He et al., 2018). Our results showed that Andro significantly reduced neuronal apoptosis and degeneration at 24 h after TBI.

Persistent neuroinflammation, characterized by glial cell activation, is associated with neurodegeneration and is an important mediator of progressive secondary injury (Chiu et al., 2016). Microglia cells exist in resting state in normal conditions, which is characterized by ramified morphology. When activated with stimuli, microglia cells became amoeboid and protected the damaged CNS (Morganti-Kossmann et al., 2007; Kadhim et al., 2008; Skaper et al., 2017, 2018). Activated microglia can produce and release a large number of pro-inflammatory cytokines and mediators, which can further exacerbate the inflammatory response and contribute to secondary brain injuries (Ding et al., 2014; Chen et al., 2017). Previous studies have been revealed that Andro inhibited microglia activation and decreased the production of pro-inflammatory chemicals in a rat model of stroke (Chan et al., 2010). However, the effects of Andro on TBI-induced microglial activation and the mechanism of Andro on neuroinflammation remain unknown. Our results indicated that in a rat model of TBI, microglia were activated at the acute phase of brain injury (24 h) and the expression of TNF-α, IL-1β and IL-6 were up regulated. After Andro administration, both microglia activation and the release of pro-inflammatory cytokines were inhibited, suggesting that Andro treatment could attenuate the microglial activation, reduce brain edema, ameliorate neuronal death and improve neurological function.

In order to further understand the mechanism by which Andro treatment inhibits TBI-induced inflammation, we detected the expression of relative factors involved in the NF-κB and MAPK signaling pathways. NF-κB activation is the first step in regulating inflammatory responses (Viatour et al., 2005; Zhang et al., 2018). Growing evidence has revealed that NF-κB signaling pathway also plays important role in TBI-induced inflammatory responses (Zhu et al., 2014; Chen et al., 2017; Zhao et al., 2017).

Previous studies have demonstrated that Andro could decrease the production of cytokines including TNF-α and IL-1β, and pro-inflammatory factors such as PGE2 through inhibiting NF-κB activation to protect against cerebral ischemia (Chan et al., 2010; Chern et al., 2011). Moreover, it has been reported that Andro reduced inflammation-mediated dopaminergic neurodegeneration by inhibiting microglial activation, indicating that Andro may be a new finding in clinical use in treating Parkinson's disease (PD). However, the mechanism of its anti-inflammatory effects in TBI model remains unknown. In our present study, Andro treatment suppressed not only production of pro-inflammatory cytokines but also NF-κB translocation from the cytosol to the nucleus. Mitogen-activated protein kinases (MAPKs), a family of serine/threonine protein kinases, are composed of three members: ERK, JNK and p38 MAPK. The MAPK signaling pathway is one of the major pathways involved in regulating inflammatory responses (Luo et al., 2013). Here, we found that Andro inhibited NF-κB p65 translocation and suppressed the expression of p-p38 MAPK and p-ERK. These results revealed that Andro could inhibit inflammatory responses after TBI via NF-κB and MAPK pathway.

It is our first time to demonstrate that Andro had neuroprotective effects in TBI. However, there exist some limitations about this study. We demonstrated the neuroprotective effects of Andro in early time point (24 h) after TBI, further investigations are needed to illuminate the effect of Andro in long-term recovery processes. Taken together, it is likely that Andro exhibited neuroprotective effects through inhibiting inflammation by blocking the NF-κB and MAPK activation in TBI.

AUTHOR CONTRIBUTIONS

HL and JC conceived and designed the study. LT and LZ acquired the data and drafted the manuscript. RG and FJ contributed to data analysis and interpretation.

REFERENCES

Batkhuu, J., Hattori, K., Takano, F., Fushiya, S., Oshiman, K., and Fujimiya, Y. (2002). Suppression of NO production in activated macrophages in vitro and ex vivo by neoandrographolide isolated from *Andrographis paniculata*. *Biol. Pharm. Bull.* 25, 1169–1174. doi: 10.1248/bpb.25.1169

Chan, S. J., Wong, W. S., Wong, P. T., and Bian, J. S. (2010). Neuroprotective effects of andrographolide in a rat model of permanent cerebral ischaemia. *Br. J. Pharmacol.* 161, 668–679. doi: 10.1111/j.1476-5381.2010.00906.x

Chen, X., Wu, S., Chen, C., Xie, B., Fang, Z., Hu, W., et al. (2017). Omega-3 polyunsaturated fatty acid supplementation attenuates microglial-induced inflammation by inhibiting the HMGB1/TLR4/NF-κB pathway following experimental traumatic brain injury. *J. Neuroinflamm.* 14:143. doi: 10.1186/s12974-017-0917-3

Cheng, G., Kong, R. H., Zhang, L. M., and Zhang, J. N. (2012). Mitochondria in traumatic brain injury and mitochondrial-targeted multipotential therapeutic strategies. *Br. J. Pharmacol.* 167, 699–719. doi: 10.1111/j.1476-5381.2012.02025.x

Chern, C. M., Liou, K. T., Wang, Y. H., Liao, J. F., Yen, J. C., and Shen, Y. C. (2011). Andrographolide inhibits PI3K/AKT-dependent NOX2 and iNOS expression protecting mice against hypoxia/ischemia-induced oxidative brain injury. *Planta Med.* 77, 1669–1679. doi: 10.1055/s-0030-1271019

Chiu, C. C., Liao, Y. E., Yang, L. Y., Wang, J. Y., Tweedie, D., Karnati, H. K., et al. (2016). Neuroinflammation in animal models of traumatic brain injury. *J. Neurosci. Methods* 272, 38–49. doi: 10.1016/j.jneumeth.2016.06.018

Ding, K., Wang, H., Xu, J., Lu, X., Zhang, L., and Zhu, L. (2014). Melatonin reduced microglial activation and alleviated neuroinflammation induced neuron degeneration in experimental traumatic brain injury: possible involvement of mTOR pathway. *Neurochem. Int.* 76, 23–31. doi: 10.1016/j.neuint.2014.06.015

Eikelenboom, P., Van, E. E., Hoozemans, J. J., Veerhuis, R., Rozemuller, A. J., and van Gool, W. A. (2010). Neuroinflammation - an early event in both the history and pathogenesis of Alzheimer's disease. *Neuro Degenerat. Dis.* 7, 38–41. doi: 10.1159/000283480

Feeney, D. M., Boyeson, M. G., Linn, R. T., Murray, H. M., and Dail, W. G. (1981). Responses to cortical injury: I. Methodology and local effects of contusions in the rat. *Brain Res.* 211, 67–77. doi: 10.1016/0006-8993(81)90067-6

Gardner, A. J., and Zafonte, R. (2016). Neuroepidemiology of traumatic brain injury. *Handb. Clin. Neurol.* 138, 207–223. doi: 10.1016/B978-0-12-802973-2.00012-4

He, H., Liu, W., Zhou, Y., Liu, Y., Weng, P., Li, Y., et al. (2018). Sevoflurane post-conditioning attenuates traumatic brain injury-induced neuronal apoptosis by promoting autophagy via the PI3K/AKT signaling pathway. *Drug Des. Devel. Ther.* 12, 629–638. doi: 10.2147/DDDT.S158313

Hyder, A. A., Wunderlich, C. A., Puvanachandra, P., Gururaj, G., and Kobusingye, O. C. (2007). The impact of traumatic brain injuries: a global perspective. *Neurorehabilitation* 22, 341–353.

Jin, Q., Cheng, J., Liu, Y., Wu, J., Wang, X., Wei, S., et al. (2014). Improvement of functional recovery by chronic metformin treatment is associated with enhanced alternative activation of microglia/macrophages and increased angiogenesis and neurogenesis following experimental stroke. *Brain Behav. Immun.* 40, 131–142. doi: 10.1016/j.bbi.2014.03.003

Kabadi, S. V., and Faden, A. I. (2014). Neuroprotective strategies for traumatic brain injury: improving clinical translation. *Int. J. Mol. Sci.* 15, 1216–1236. doi: 10.3390/ijms15011216

Kadhim, H. J., Duchateau, J., and Sébire, G. (2008). Cytokines and brain injury: invited review. *J. Intens. Care Med.* 23, 236–249. doi: 10.1177/0885066608318458

Laplaca, M. C., Simon, C. M., Prado, G. R., and Cullen, D. K. (2007). CNS injury biomechanics and experimental models. *Prog. Brain Res.* 161, 13–26. doi: 10.1016/S0079-6123(06)61002-9

Liu, X. Z., Xu, X. M., Hu, R., Du, C., Zhang, S. X., McDonald, J. W., et al. (1997). Neuronal and glial apoptosis after traumatic spinal cord injury. *J. Neurosci.* 17, 5395–5406. doi: 10.1523/JNEUROSCI.17-14-05395.1997

Lozano, D., Gonzales-Portillo, G. S., Acosta, S., de la Pena, I., Tajiri, N., Kaneko, Y., et al. (2015). Neuroinflammatory responses to traumatic brain injury: etiology, clinical consequences, and therapeutic opportunities. *Neuropsychiatr. Dis. Treat.* 11, 97–106. doi: 10.2147/NDT.S65815

Lu, D. Y., Liou, H. C., Tang, C. H., and Fu, W. M. (2006). Hypoxia-induced iNOS expression in microglia is regulated by the PI3-kinase/Akt/mTOR signaling pathway and activation of hypoxia inducible factor-1alpha. *Biochem. Pharmacol.* 72, 992–1000. doi: 10.1016/j.bcp.2006.06.038

Luo, C. L., Li, Q. Q., Chen, X. P., Zhang, X. M., Li, L. L., Li, B. X., et al. (2013). Lipoxin A4 attenuates brain damage and downregulates the production of pro-inflammatory cytokines and phosphorylated mitogen-activated protein kinases in a mouse model of traumatic brain injury. *Brain Res.* 1502, 1–10. doi: 10.1016/j.brainres.2013.01.037

Lutton, E. M., Razmpour, R., Andrews, A. M., Cannella, L. A., Son, Y. J., Shuvaev, V. V., et al. (2017). Acute administration of catalase targeted to ICAM-1 attenuates neuropathology in experimental traumatic brain injury. *Sci. Rep.* 7:3846. doi: 10.1038/s41598-017-03309-4

Morganti-Kossmann, M. C., Satgunaseelan, L., Bye, N., and Kossmann, T. (2007). Modulation of immune response by head injury. *Injury* 38, 1392–1400. doi: 10.1016/j.injury.2007.10.005

Perry, V. H., Nicoll, J. A., and Holmes, C. (2010). Microglia in neurodegenerative disease. *Nat. Rev. Neurol.* 6, 193–201. doi: 10.1038/nrneurol.2010.17

Shen, Y. C., Chen, C. F., and Chiou, W. F. (2002). Andrographolide prevents oxygen radical production by human neutrophils: possible mechanism(s) involved in its anti-inflammatory effect. *Br. J. Pharmacol.* 135, 399–406. doi: 10.1038/sj.bjp.0704493

Skaper, S. D., Facci, L., Zusso, M., and Giusti, P. (2017). Neuroinflammation, mast cells, and Glia: dangerous liaisons. *Neuroscientist* 23, 478–498. doi: 10.1177/1073858416687249

Skaper, S. S., Facci, L., Zusso, M., and Giusti, P. (2018). An inflammation-centric view of neurological disease: beyond the neuron. *Front. Cell Neurosci.* 12:72. doi: 10.3389/fncel.2018.00072

Tao, L., Li, D., Liu, H., Jiang, F., Xu, Y., Chen, G., et al. (2018). Neuroprotective effects of metformin on traumatic brain injury in rats associated with NF-κB and MAPK signaling pathway. *Brain Res. Bull.* 140, 154–161. doi: 10.1016/j.brainresbull.2018.04.008

Tao, L., Zhang, F., Hao, L., Wu, J., Jia, J., Liu, J.-Y., et al. (2014). 1-O-Tigloyl-1-O-deacetyl-nimbolinin B Inhibits LPS-Stimulated inflammatory responses by suppressing NF-κB and JNK activation in microglia cells. *J. Pharmacol. Sci.* 125, 364–374. doi: 10.1254/jphs.14025FP

Ullah, N., Naseer, M. I., Ullah, I., Lee, H. Y., Koh, P. O., and Kim, M. O. (2011). Protective effect of pyruvate against ethanol-induced apoptotic neurodegeneration in the developing rat brain. *Neuropharmacology* 61, 1248–1255. doi: 10.1016/j.neuropharm.2011.06.031

Viatour, P., Merville, M. P., Bours, V., and Chariot, A. (2005). Phosphorylation of NF-kappaB and IkappaB proteins: implications in cancer and inflammation. *Trends Biochem. Sci.* 30, 43–52. doi: 10.1016/j.tibs.2004.11.009

Wang, T., Liu, B., Zhang, W., Wilson, B., and Hong, J. S. (2004). Andrographolide reduces inflammation-mediated dopaminergic neurodegeneration in mesencephalic neuron-glia cultures by inhibiting microglial activation. *J. Pharmacol. Exp. Ther.* 308, 975–983. doi: 10.1124/jpet.103.059683

Wang, Y. J., Wang, J. T., Fan, Q. X., and Geng, J. G. (2007). Andrographolide inhibits NF-kappaBeta activation and attenuates neointimal hyperplasia in arterial restenosis. *Cell Res.* 17, 933–941. doi: 10.1038/cr.2007.89

Werner, C., and Engelhard, K. (2007). Pathophysiology of traumatic brain injury. *BJA* 99, 4–9. doi: 10.1093/bja/aem131

Xia, Y. F., Ye, B. Q., Li, Y. D., Wang, J. G., He, X. J., Lin, X., et al. (2004). Andrographolide attenuates inflammation by inhibition of NF-kappa B activation through covalent modification of reduced cysteine 62 of p50. *J. Immunol.* 173, 4207–4217. doi: 10.4049/jimmunol.173.6.4207

Zhang, H., Zhang, D., Li, H., Yan, H., Zhang, Z., Zhou, C., et al. (2018). Biphasic activation of nuclear factor-κB and expression of p65 and c-Rel following traumatic neuronal injury. *Inflamm. Res.* 63, 109–115. doi: 10.3892/ijmm.2018.3567

Zhao, Y., Lee, J. H., Chen, D., Gu, X., Caslin, A., Li, J., et al. (2017). DL-3-n-butylphthalide induced neuroprotection, regenerative repair, functional recovery and psychological benefits following traumatic brain injury in mice. *Neurochem. Int.* 11, 82–92. doi: 10.1016/j.neuint.2017.03.017

Zhu, H., Bian, C., Yuan, J., Chu, W., Xiang, X., Chen, F., et al. (2014). Curcumin attenuates acute inflammatory injury by inhibiting the TLR4/MyD88/NF-κB signaling pathway in experimental traumatic brain injury. *J. Neuroinflammation* 11:59. doi: 10.1186/1742-2094-11-59

Conflict of Interest Statement: The authors declare that the research was conducted in the absence of any commercial or financial relationships that could be construed as a potential conflict of interest.

frontiers in Neuroscience

ORIGINAL RESEARCH
published: 09 October 2018
doi: 10.3389/fnins.2018.00724

Electroacupuncture Improves Cerebral Vasospasm and Functional Outcome of Patients With Aneurysmal Subarachnoid Hemorrhage

Jie Sun[1†], Yuchun Liu[1†], Junjun Zhang[1], Xiaosheng Chen[1], Zhiqing Lin[1], Sheng Nie[1], Manhua Shi[2], Xiang Gao[1] and Yi Huang[1*]*

[1] Department of Neurosurgery, Ningbo First Hospital, Ningbo Hospital, Zhejiang University School of Medicine, Ningbo, China, [2] Department of Acupuncture, Ningbo First Hospital, Ningbo Hospital, Zhejiang University School of Medicine, Ningbo, China

OPEN ACCESS

Edited by:
Gao Chen,
Zhejiang University, China

Reviewed by:
Daniel Pirici,
University of Medicine and Pharmacy of Craiova, Romania
Qiang Liu,
Barrow Neurological Institute (BNI), United States

***Correspondence:**
Xiang Gao
qinyuecui@163.com
Yi Huang
huangy102@gmail.com

[†] These authors are co-first authors of this work

Specialty section:
This article was submitted to Neurodegeneration, a section of the journal Frontiers in Neuroscience

Received: 29 May 2018
Accepted: 20 September 2018
Published: 09 October 2018

Citation:
Sun J, Liu Y, Zhang J, Chen X, Lin Z, Nie S, Shi M, Gao X and Huang Y (2018) Electroacupuncture Improves Cerebral Vasospasm and Functional Outcome of Patients With Aneurysmal Subarachnoid Hemorrhage. Front. Neurosci. 12:724. doi: 10.3389/fnins.2018.00724

Cerebral vasospasm is the major cause of a poor outcome after aneurysmal subarachnoid hemorrhage (aSAH), and effective treatments for vasospasm are limited. The purpose of this study was to research the impact of electroacupuncture (EA) on cerebral vasospasm and the outcomes of patients with aSAH. A total of 60 age- and sex-matched aSAH patients were collected from Ningbo First Hospital between December 2015 and June 2017. All patients were given a basic treatment of nimodipine and randomized into two groups. The study group was treated with EA therapy on the Baihui (GV20) acupoint, and the control group was given mock transcutaneous electrical nerve stimulation. Cerebral vasospasm was measured by computed tomographic perfusion (CTP) and transcranial doppler (TCD). The mean flow velocity (MFV) in the middle cerebral artery (MCA), cerebral blood flow (CBF), cerebral blood volume (CBV), and mean transit time (MTT) of the patients were analyzed. The CBV and MTT exhibited significant differences between the study and control groups on the 1st ($p = 0.026$ and $p = 0.001$), 7th ($p = 0.020$ and $p < 0.001$), and 14th ($p = 0.001$ and $p < 0.001$) day after surgery, whereas CBF exhibited statistical significance only on the 14th day after surgery ($p = 0.002$). The MFV in MCA were significantly reduced after EA treatment in all patients (all $p < 0.001$). Additionally, the MFV in the MCA in patients treated with EA were considerably reduced compared with those of the control group (3rd day $p = 0.046$; 5th day, $p = 0.010$; 7th day, $p < 0.001$). Moreover, better outcomes were noted in the EA-treated group for the 1st month ($p < 0.001$) and 3rd month ($p = 0.001$) after surgery than in the control group. In conclusion, EA represents a potential method to treat cerebral vasospasm after aSAH and can improve the outcomes of patients with aSAH.

Keywords: aneurysmal subarachnoid hemorrhage, electroacupuncture, cerebral vasospasm, Baihui (GV20), computed tomographic perfusion, transcranial doppler

Abbreviations: AQP, aquaporin; aSAH, aneurysmal subarachnoid hemorrhage; CBF, cerebral blood flow; CBV, cerebral blood volume; CTP, computed tomographic perfusion; EA, electroacupuncture; EDV, end-diastolic velocity; GOS, glasgow outcome scale; MCA, middle cerebral artery; MFV, mean flow velocity; MMP, matrix metalloproteinase; MTT, mean transit time; PSV, peak systolic velocity; TCD, transcranial doppler.

INTRODUCTION

Aneurysmal subarachnoid hemorrhage (aSAH) is a devastating event accounted for 5% of all stroke cases (Sehba et al., 2012; Garg and Bar, 2017). The incidence of aSAH is approximately 9 per 100,000, and the mortality is approximately 60% within 6 months (Steiner et al., 2013). The surgical treatment of aSAH includes endovascular coiling and surgical clipping. However, there are a lot of complications frequently occur after successful surgery (Connolly et al., 2012; Steiner et al., 2013), such as cerebral vasospasm, rebleeding, or hydrocephalus. Cerebral vasospasm typically appears on the third day after aSAH, is maximal at 6–8 days, and subsequently lasts 2–3 weeks (Wilkins, 1990). There are approximately 23% of deaths or disabilities in patients with aSAH due to cerebral vasospasm (Keyrouz and Diringer, 2007). Delayed cerebral vasospasm is considered as the major cause of poor outcomes in aSAH patients in subsequent decades (Dusick and Gonzalez, 2013).

According to the past research, cerebral vasospasm after aSAH was regarded as an outcome of many factors, such as inflammatory changes, abnormal endothelial hypertrophy, prolonged contraction of the smooth muscle cells, and gene expression in the brain arteries (Rothoerl and Ringel, 2007). In addition, it seems possible that disruptions in either or both nitric oxide and endothelin-1 metabolism may play key roles in the pathogenesis of cerebral vasospasm (Findlay et al., 2016). Consequently, various methods are used to prevent cerebral vasospasm on the basis of its pathogenesis, such as the endothelin antagonist clazosentan, the cholesterol-lowering agent simvastatin, and the vasodilator magnesium sulfate, calcium channel blocker nicardipine (van Gijn and Rinkel, 2001; Wilson et al., 2005; van Gijn et al., 2007). However, some researchers find that the prevention of cerebral vasospasm does not improve the outcomes of aSAH patients (Macdonald et al., 2008; Vergouwen, 2009; Macdonald et al., 2011).

Acupuncture has been used to treat aSAH effectively and safely for centuries (Hu et al., 1993). In recent years, numerous studies have demonstrated that acupuncture can increase the content of nitric oxide in vascular endothelial cell, activate the activity, and improve the function of injured vascular endothelial cells (Chen and Ma, 2003; Kim et al., 2006). In addition, acupuncture or EA at the Baihui (GV20) and left Zusanli (ST36) acupoints in rat model significantly reduces the expression of the proinflammatory enzyme MMP2 and the water channel proteins AQP4, to relieve inflammation related brain edema (Xu et al., 2014). Therefore, we hypothesized that EA might be used to improve cerebral vasospasm and the outcomes of patients with aSAH. In this study, we recruited 60 age- and sex-matched volunteers and performed a case–control study to investigate and validate the impact of EA treatment on patients with aSAH from a Chinese Han population.

MATERIALS AND METHODS

Participants

This double-blinded, randomized controlled study was approved by the Ethics Committee of Ningbo First Hospital. A total of 60 age- and sex-matched aSAH patients from Department of Neurosurgery, who were randomly allocated by computer algorithm to the study group (n = 30) or the control group (n = 30). Inclusion criteria were as follows: (1) the individuals were aged older than 18 years and had the ability to begin acupuncture treatment within 24 h after aSAH; (2) aSAH were independently diagnosed by at least two neurosurgeons using computed tomography and cerebral angiography; (3) the patients with aneurysm who had been treated by the operative treatment such as endovascular coiling or surgical clipping; (4) written informed consent was obtained before the study. Exclusion criteria were as follows: (1) the patients with traumatic or infectious aSAH; (2) the patients without ability to undergo TCD; (3) the patients with severe heart, hepatic and renal dysfunctions; (4) the patients with cardiac pacemaker; or (5) the patients with a previous EA experience.

Intervention

EA treatment started within 24 h of aSAH, after intracranial aneurysm surgery including endovascular coiling or surgical clipping. EA was applied four times in 2 weeks, and it was performed by the same acupuncturist with over 10 years acupuncture treatment experience. At the same time, standard medicine treatments, such as hemodilution (triple-H) therapy, nimodipine, hypertension control, and hypervolemic, were appropriated for all patients.

Study and Control Group

The patients in the study group were administered EA therapy using HANS100A analgesic apparatus (Nanjing Jisheng Medical Technology Co., Nanjing, China) with a dilatational wave of 2 Hz in the GV20 position. The electric current was gradually increased (0 up to 5 mA), and the speed depended on the patient's pain threshold. Each treatment session based on the electric current intensity of 5 mA and lasted 30 min. EA treatment was performed on the 1st, 3rd, 5th, and 7th days after the operation. The MFV in the MCA was measured by TCD (Prosound α10, Aloka Co, Ltd, Tokyo, Japan) before and after EA therapy (**Figure 1**). The MFV was calculated according to the primary study (Lysakowski et al., 2001). The control group received standard medicine treatments as same as the study group, but without EA treatment. In addition, cerebral vasospasm was measured by CTP on the 1st, 7th, and 14th day after surgery, and the dates of CBF, CBV, and MTT were collected.

Statistics

The sample size was calculated based on the primary study. The incidence rate of delayed ischemic neurological deficit in the acupuncture group was 10%, and the control group was 38.9% (Cho et al., 2015). To detect a significance level of 0.05 between the groups with 80% power at the assumption of a drop-out rate of 20% and a 1-tailed $\alpha = 0.05$, 54 patients (27 participants in each group) were required for this study (Shuster, 2014). Data were represented as mean ± standard deviation (SD) or number (%) and analyzed using SPSS version 23.0 (IBM Corp. Armonk, NY, United States) software. Categorical variables were analyzed with the chi-square test or Fisher's exact test, and the means

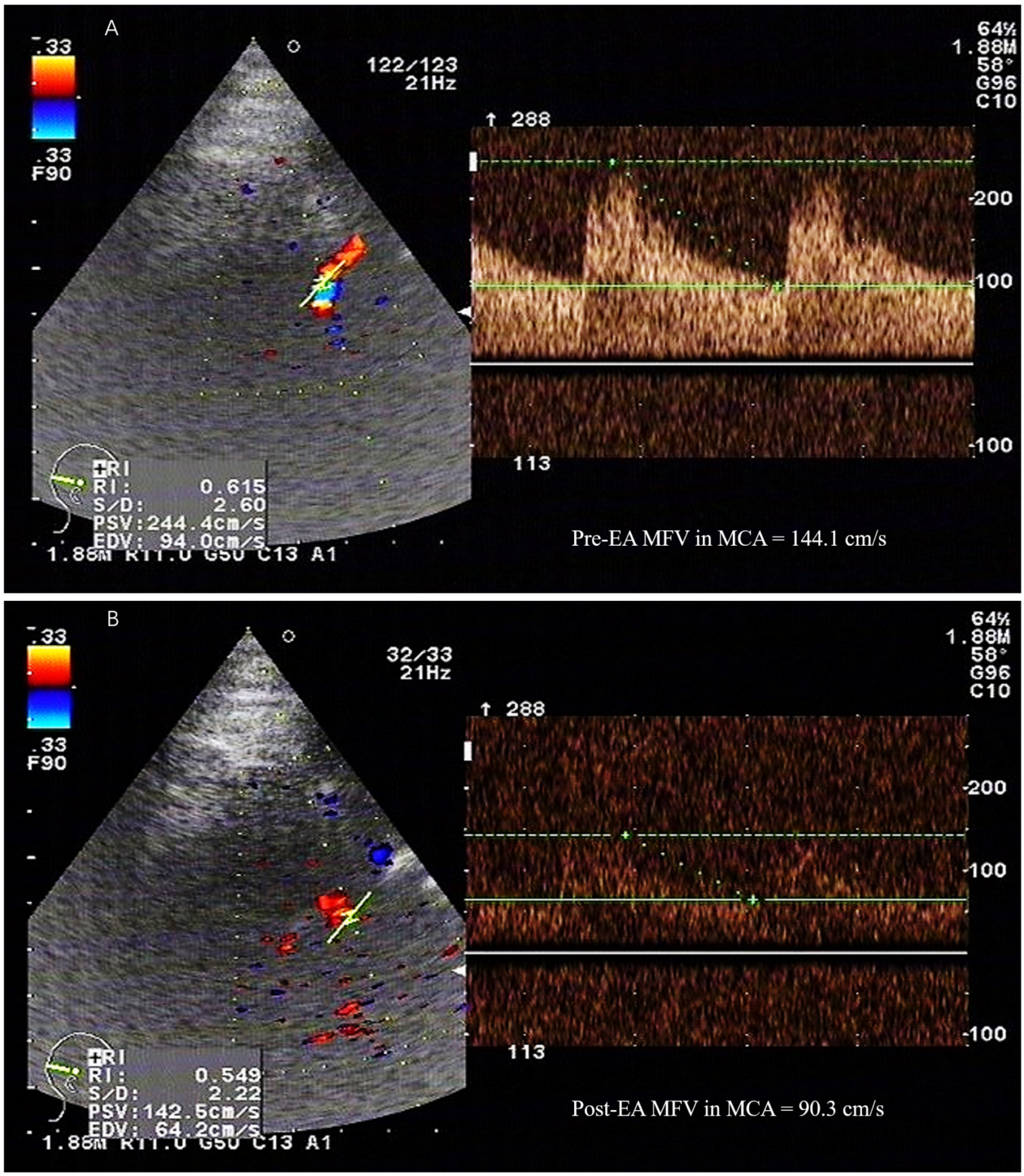

FIGURE 1 | The MFV in the MCA was measured by TCD. PSV, peak systolic velocity; EDV, end-diastolic velocity; MFV, mean flow velocity; MCA, middle cerebral artery; TCD, transcranial doppler; EA, electroacupuncture. A 52-year-old female patient with subarachnoid hemorrhage caused by rupture of right anterior communicating artery aneurysm, developed vasospasm on the 5th day after surgery. The maximum value of flow velocity in systole was calculated at the apex of the waveform, which defined as PSV. EDV was measured at end diastole, and indicated the lowest point of waveform. MFV was calculated as EDV plus a third of the difference between PSV and EDV (MFV [cm/s] = [PSV + 2EDV]/3). TCD detection showed that the MFV in MCA in the range of 120∼140 cm/s was indicative of mild cerebral vasospasm, 140∼200cm/s was accord with moderate cerebral vasospasm, and above 200 cm/s was consistent with severe cerebral vasospasm. **(A)** TCD showed a high MFV in MCA (144.1cm/s) before EA. **(B)** The MFV in MCA (90.3cm/s) was decreased after EA.

of continuous variables were analyzed using the Student's *t*-test. Statistical significance was defined as a *p*-value of <0.05.

RESULTS

Clinical Characteristics of the Subjects

The clinical characteristics of the patients are presented in **Table 1**. The control group consisted of 30 aSAH patients (13 males and 17 females) with a mean age of 51.9 ± 9.51 years. The study group underwent EA therapy and consisted of 30 aSAH patients (13 males and 17 females) with a mean age of 52.67 ± 11.27 years. No significant differences in the aneurysm location ($p = 0.612$), aneurysms therapies ($p = 0.121$), Hunt-Hess grade ($p = 0.793$), and Fisher grade ($p = 0.279$) were noted between the two groups.

Cerebral Vasospasm Was Measured by CTP

Significant differences in CBF, CBV, and MTT variations were noted in both groups on the 1st, 7th, and 14th days after surgery (all $p < 0.001$, **Table 2**, **Figures 2A–C**). The CBF was considerably increased in the study group on the 14th day after surgery (study group vs. control group: 47.10 ± 7.79 vs. 41.52 ± 5.65, $p = 0.002$, **Table 3**, **Figure 2D**). The CBV was markedly increased in the study group compared with the control group on the 1st (study group vs. control group: 3.84 ± 0.68 vs. 4.20 ± 0.53, $p = 0.026$), 7th (study group vs. control group: 3.57 ± 0.67 vs. 3.19 ± 0.54, $p = 0.020$), and 14th days (study group vs. control group: 4.33 ± 0.66 vs. 3.79 ± 0.59, $p = 0.001$, **Table 3**, **Figure 2E**) after surgery. Besides, the MTT was considerably reduced in the study group compared with the control group on the 1st (study group vs. control group: 6.89 ± 0.92 vs. 7.82 ± 1.16, $p = 0.001$), 7th (study group vs. control group: 7.43 ± 0.98 vs. 8.48 ± 1.15, $p < 0.001$), and 14th (study group vs. control group: 6.81 ± 0.97 vs. 9.50 ± 1.17, $p < 0.001$, **Table 3**, **Figure 2F**) days after surgery.

TABLE 1 | Patient characteristics of the two groups.

Characteristics	Study group (*n* = 30)	Control group (*n* = 30)	*p*-value
Age(years)	52.67 ± 11.27	51.9 ± 9.51	0.777
Male/female	13/17	13/17	1.000
Aneurysm location			0.612
Anterior communicating Artery	13	13	
Posterior communicating Artery	7	10	
Middle cerebral artery	2	3	
Posterior inferior cerebellar artery	3	0	
Basilar artery	0	1	
Vertebral artery	2	1	
Supraclinoid internal carotid artery	2	1	
Multiple intracranial aneurysms	1	1	
Aneurysms therapies			0.121
Coiling	4	26	
Clipping	0	30	
Hunt–Hess grade			0.793
I–II	17	18	
III–V	13	12	
Fisher grade			0.279
I	7	12	
II-III	19	13	
IV	4	5	

Age was analyzed using student's t-test and other data were analyzed using chi-square test.

TABLE 2 | The changes in CBF, CBV, and MTT in the two groups over time.

	Variable	1st day	7th day	14th day	*p*-value
Study group	CBF (mL/100 g/min)	37.40 ± 7.44	33.26 ± 6.20	47.10 ± 7.79	<0.001
	CBV (mL/100 g)	3.84 ± 0.68	3.57 ± 0.67	4.33 ± 0.66	<0.001
	MTT (s)	6.89 ± 0.92	7.43 ± 0.98	6.81 ± 0.97	<0.001
Control group	CBF (mL/100 g/min)	38.05 ± 6.94	33.15 ± 6.76	41.52 ± 5.65	<0.001
	CBV (mL/100 g)	4.20 ± 0.53	3.19 ± 0.54	3.79 ± 0.59	<0.001
	MTT (s)	7.82 ± 1.16	8.48 ± 1.15	9.50 ± 1.17	<0.001

CBF, cerebral blood flow; CBV, cerebral blood volume; MTT, mean transit time. All the data were analyzed using student's t-test.

Cerebral Vasospasm Was Relieved After EA Therapy and Measured by TCD

As presented in **Table 4**, statistically significant variations in the MFV levels of MCA were noted between the two groups based on the length of time after surgery. Significant differences in the MFV of MCA were noted between the two groups on the 3rd (study group vs. control group: 115.32 ± 19.22 vs. 124.60 ± 15.80, $p = 0.046$), 5th (study group vs. control group: 117.34 ± 18.49 vs. 128.68 ± 14.37, $p = 0.010$), and 7th (study group vs. control group: 108.19 ± 16.16 vs. 124.94 ± 14.85, $p < 0.001$, **Table 4**, **Figure 3A**) day after surgery. In the study group, all patients accepted EA therapy at the same time point after surgery (1st, 3rd, 5th, and 7th day), and the MFV in MCA was significantly reduced compared with that measured post-EA on the 1st (Pre-EA vs. Post-EA: 118.49 ± 20.38 vs. 109.12 ± 18.40, $p < 0.001$), 3rd (Pre-EA vs. Post-EA: 125.29 ± 22.51 vs. 115.32 ± 19.22, $p < 0.001$), 5th (Pre-EA vs. Post-EA: 128.37 ± 22.15 vs. 117.34 ± 18.49, $p < 0.001$), and 7th (Pre-EA vs. Post-EA: 118.94 ± 18.61 vs. 108.19 ± 16.16, $p < 0.001$, **Table 5**, **Figure 3B**) day.

Patients With aSAH Exhibited a Better Outcome After EA Treatment

The GOS score was used 1 or 3 months after surgery to assess the clinical outcome of patient survival. Significant differences were noted in the outcomes of the two groups at 1 ($p < 0.001$, **Table 6**, **Figure 3C**) and 3 months ($p = 0.001$, **Table 6**, **Figure 3D**) after surgery, and more patients exhibited a good outcome in the study group.

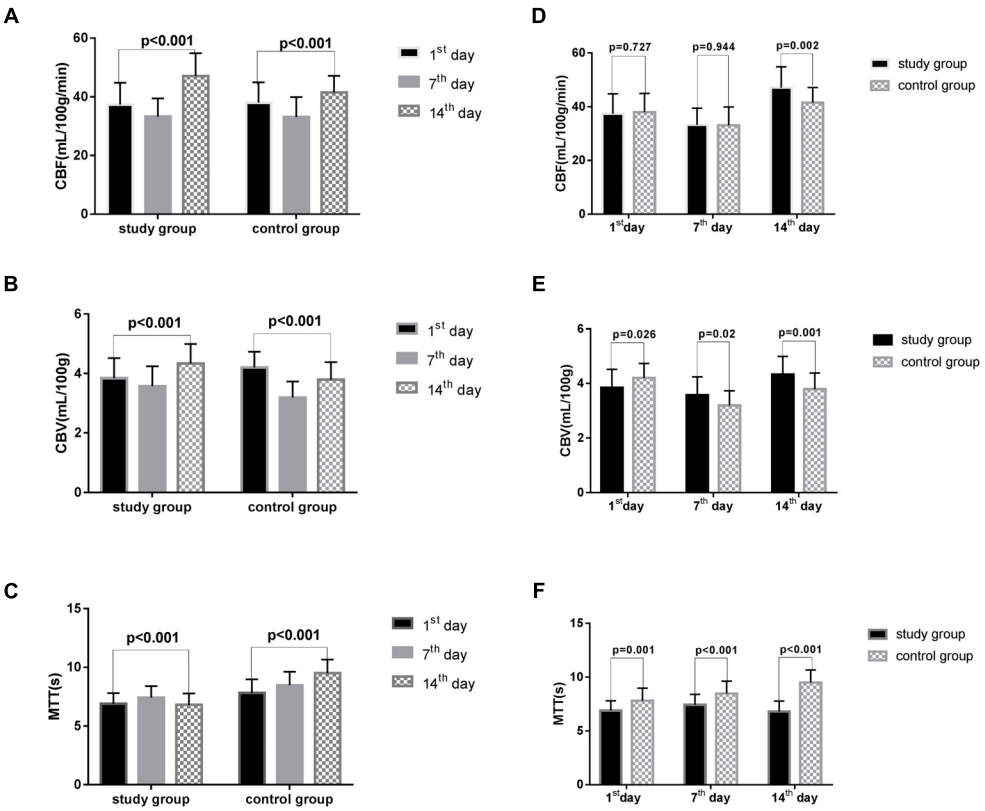

FIGURE 2 | The CBF, CBV, MTT in two groups. CBF, cerebral blood flow; CBV, cerebral blood volume; MTT, mean transit time. All the data were analyzed using student's *t*-test. **(A)** CBF variations in the two groups based on time after surgery. **(B)** The variation in CBV in the two groups based on time after surgery. **(C)** The variation in the MTT of the two groups based on time after surgery. **(D)** The difference in CBF in two groups on the 1st, 7th, and 14th day after surgery. **(E)** The difference in CBV in the two groups on the 1st, 7th, and 14th day after surgery. **(F)** The difference in MTT in the two groups on the 1st, 7th, and 14th day after surgery.

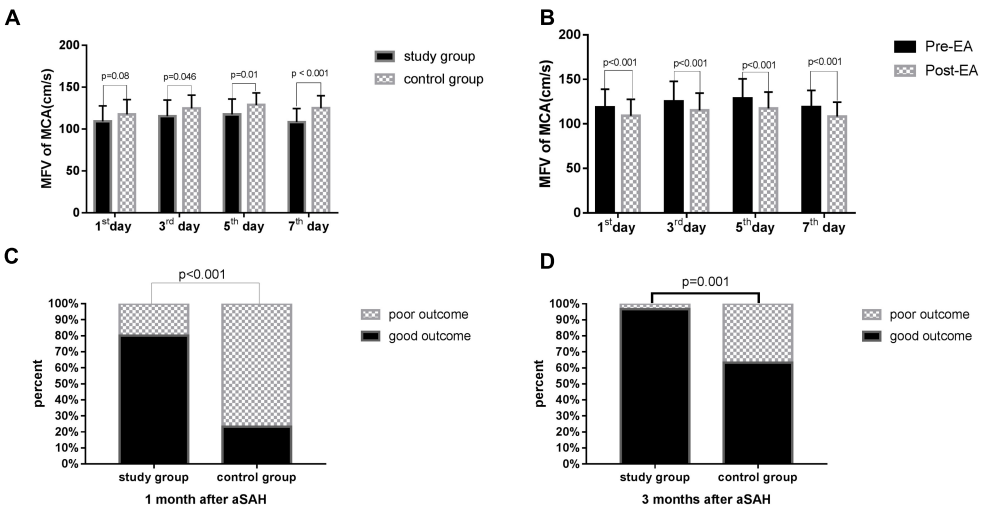

FIGURE 3 | The MFV in MCA and the outcome in the two groups. MFV, mean flow velocity; MCA, middle cerebral artery. The GOS score was used 1 or 3 months after surgery to assess the clinical outcome of patient survival. **(A)** Comparison of MFV in MCA in the study group versus control group on the 1st, 3rd, 5th, and 7th day after surgery. The data were analyzed using student's *t*-test. **(B)** Comparison of MFV in MCA in the study group pre-EA versus post-EA on the 1st, 3rd, 5th, and 7th day after surgery. The data were analyzed using student's *t*-test. **(C)** Comparison of outcome in the study group versus control group 1 month after surgery The data were analyzed using chi-square test. **(D)** Comparison of outcome in the study group versus control group 3 months after surgery. The data were analyzed using chi-square test.

TABLE 3 | Comparisons of CBF, CBV, and MTT in the two groups over time.

Variable	Study group	Control group	*p*-value
CBF1st (mL/100 g/min)	37.40 ± 7.44	38.05 ± 6.94	0.727
CBF7th (mL/100 g/min)	33.26 ± 6.20	33.15 ± 6.76	0.944
CBF14th (mL/100 g/min)	47.10 ± 7.79	41.52 ± 5.65	0.002
CBV1st (mL/100 g)	3.84 ± 0.68	4.20 ± 0.53	0.026
CBV7th (mL/100 g)	3.57 ± 0.67	3.19 ± 0.54	0.020
CBV14th (mL/100 g)	4.33 ± 0.66	3.79 ± 0.59	0.001
MTT1st (s)	6.89 ± 0.92	7.82 ± 1.16	0.001
MTT7th (s)	7.43 ± 0.98	8.48 ± 1.15	<0.001
MTT14th (s)	6.81 ± 0.97	9.50 ± 1.17	<0.001

CBF1st/7th/14th, cerebral blood flow on the 1st, 7th, and 14th day after surgery, respectively; CBV1st/7th/14th, cerebral blood volume on the 1st, 7th, and 14th day after surgery, respectively; MTT1st/7th/14th, mean transit time on the 1st, 7th, and 14th day after surgery, respectively. All the data were analyzed using student's t-test.

TABLE 4 | The MFV level in MCA in the two groups.

Time day	Study group	Control group	*p*-value
1st (cm/s)	109.12 ± 18.40	117.42 ± 17.67	0.080
3rd (cm/s)	115.32 ± 19.22	124.60 ± 15.80	0.046
5th (cm/s)	117.34 ± 18.49	128.68 ± 14.37	0.010
7th (cm/s)	108.19 ± 16.16	124.94 ± 14.85	<0.001
p-value	<0.001	<0.001	

MFV, mean flow velocity; MCA, middle cerebral artery. All the data were analyzed using student's t-test.

TABLE 5 | The MFV level in MCA in the study group.

	MFV1st	MFV3rd	MFV5th	MFV7th
Pre-EA (cm/s)	118.49 ± 20.38	125.29 ± 22.51	128.37 ± 22.15	118.94 ± 18.61
Post- EA (cm/s)	109.12 ± 18.40	115.32 ± 19.22	117.34 ± 18.49	108.19 ± 16.16
p-value	<0.001	<0.001	<0.001	<0.001

EA, electroacupuncture; MFV, mean flow velocity; MCA, middle cerebral artery; MFV1st/3rd/5th/7th, mean flow velocity in the study group on the 1st, 3rd, 5th, and 7th day after the operation.
All the data were analyzed using student's t-test.

TABLE 6 | The outcome of aSAH patients in the two groups.

	1 Month after aSAH		3 Months after aSAH	
	Good outcome (GOS > 3)	Poor outcome (GOS≦3)	Good outcome (GOS > 3)	Poor outcome (GOS≦3)
Study group	24	6	29	1
Control group	7	23	19	11
p-value	<0.001		0.001	

aSAH, Aneurysmal subarachnoid hemorrhage; GOS, Glasgow Outcome Scale. All the data were analyzed using chi-square test.

DISCUSSION

Cerebral ischemia after aSAH is a complex complication involving delayed cerebral vasospasm that may cause clinical deterioration, cerebral infarctionand death. Cerebral vasospasm after aSAH may related with multifactorial etiology, and this hypothesis was confirmed by the massive available treatment modalities. Currently, strong evidence supports that nimodipine and the triple-H therapy are benefits for cerebral vasospasm patients (Adamczyk et al., 2013). Many treatments have improved the prognosis, but the neurological outcomes remain poor in the patients with delayed cerebral vasospasm. Therefore, it is urgent to identify safer and more efficacious methods to manage cerebral vasospasm and improve the outcomes of aSAH patients. EA is a advanced therapy on the basis of combination of traditional acupuncture and modern electrotherapy and is recommended as a treatment for stroke (Li et al., 2014). Here, our results demonstrate that EA at GV20 significantly reduces cerebral vasospasm after aSAH and improves the outcomes of aSAH patients.

Acupuncture at the Baihui (GV20) acupoint had been used to treat stroke for hundreds of years (Wang et al., 2014). Currently, scientists revealed that acupuncture Baihui (GV20) could protect the neuro in ischemic stroke animal models. Dong et al.'s (2009) study suggested that EA preconditioning of the Baihui (GV20) acupoint could ease the brain edema and attenuate blood–brain barrier disruption via effecting the related protein activity. Kim et al. (2013) found that EA at the Baihui (GV20) and Dazhui (GV14) acupoints could increase CBF and improve the functional recovery in acute moderate focal cerebral ischemia. Wang et al. (2012) reported that EA pretreatment at the Baihui (GV20) acupoint could protect the brain against transient ischemic injury through activating the anti-inflammatory proteins. Given that cerebral vasospasm begins 24–72 h after aSAH, early intervention of EA is urgent and necessary. In our study, in all patients who accepted EA therapy after coiling or clipping, the occurrence of rebleeding during EA treatment was avoided. In addition, to ensure the safety of all patients, treatment with nimodipine and other supporting agents was also administered. There are various advantages of EA compared with manual acupuncture. EA can be performed standardly, measured objectively, and controlled fully. Besides, EA has also been recommended for clinical trials and mechanistic research on acupuncture (Tsuchiya et al., 2007).

In our study, cerebral vasospasm was monitored by CTP and TCD. CTP has been used in patients with aSAH (Sviri et al., 2006; van der Schaaf et al., 2006) and has rapidly gained popularity given its simplicity, speed, and veracity (Washington et al., 2011). CTP can detect the reduction of CBF, prolongation of MTT, and the status of CBV (Dankbaar et al., 2010). Moreover, threshold values of 35 mL/100 g/min for CBF and 5.5 s for MTT are suggested for the diagnosis of cerebral vasospasm (Sanelli et al., 2011), and CBV exhibited the lowest diagnostic accuracy among all variables (Othman et al., 2016). The results of this study demonstrated that the CBV and MTT were significantly

different between the study and control groups at 1, 7, and 14 days after surgery, whereas CBF exhibited statistical significance only 14 days after surgery. In addition, TCD works on that blood-flow velocity within an artery increases as the artery narrows, result in doppler frequency shift (Purkayastha and Sorond, 2012). The maximum value of flow velocity in systole was calculated at the apex of the waveform, which defined as PSV (Fotakopoulos et al., 2018). EDV was measured at end diastole, and indicated the lowest point of waveform (Fotakopoulos et al., 2018). MFV was calculated as EDV plus a third of the difference between PSV and EDV (MFV [cm/s] = [PSV + 2EDV]/3) (Lysakowski et al., 2001). TCD detection showed that the MFV in MCA in the range of 120 ∼ 140 cm/s was indicative of mild cerebral vasospasm, 140 ∼ 200 cm/s was accord with moderate cerebral vasospasm, and above 200 cm/s was consistent with severe cerebral vasospasm (Sebastian et al., 2013). A skilled researcher operated TCD monitoring at a specific time every other day. In our study, the MFV levels of MCA were significantly reduced after EA treatment in the same patients. Additionally, the MFV levels of MCA in patients with EA treatment were markedly reduced than the control group. These findings suggest that EA is a potential method to relieve cerebral vasospasm after aSAH. Recent study suggested that EA Baihui (GV20) and Dazhui (GV14) could significantly increase cerebral cortex acetylcholine release, and repair nerve damage (Kim et al., 2013). Several studies have demonstrated that acupuncture enhances the nitric oxide production and increases local circulation (Tsuchiya et al., 2007). Dong et al. (2009) found that EA at GV20 could reduce MMP2 and the water channel proteins, AQP4 and AQP9, which repair brain injury and improve functional outcomes depending on the mitigation of inflammation-related brain edema in model rats. We believe that these effects may explain the main mechanism through which EA treatment improves patient outcomes, and the outcome of the study group was significantly improved than the control group. Therefore, we think that the effect of EA treatment appears after it is continuously applied to aSAH patients over a 2-week period.

Study Limitations

Apparently, our research has several limitations. First, only one center was included in this study, multicenter with a more homogeneous samples were needed to certificate the specific treatment effect in the future. Second, only a limited number of measurement timepoints were included in the study, so more frequent timepoints in the assessment of cerebral vasospasm should be included in future studies. Third, protein signaling pathways were not investigated in the current study, but should be a focus of future research. Fourth, the craniotomy procedure might affect cerebral vasospasm and the curative effect of EA therapy. Thus, a comparison between the clipping and coiling group is required in the future.

CONCLUSION

In summary, our study confirmed that cerebral vasospasm was presented in patients with aSAH. EA therapy at the Baihui (GV20) position could increase the MFV of cerebral circulation and improve the outcome of aSAH patients. It is a safe and convenient treatment to improve cerebral vasospasm and the outcomes of aSAH patients.

AUTHOR CONTRIBUTIONS

XG, JS, and YH designed the study and edited the manuscript. ZL, YL, JZ, SN, and MS were responsible for data acquisition and experiments. YL and XC conducted data analysis and drafted the manuscript.

FUNDING

This study was supported by the grants from the Zhejiang Provincial Natural Science Foundation of China (Grant No. LQ17H090002), Chinese Medicine Science and Technology projects of Zhejiang province (Grant No. 2015ZB100), Medicine and Health Science and Technology projects of Zhejiang province (Grant No. 2018KY665), Ningbo Natural Science Foundation (Grant No. 2017A610223), and Ningbo Health Branding Subject Fund (Grant No. PPXK2018-04).

REFERENCES

Adamczyk, P., He, S., Amar, A. P., and Mack, W. J. (2013). Medical management of cerebral vasospasm following aneurysmal subarachnoid hemorrhage: a review of current and emerging therapeutic interventions. *Neurol. Res. Int.* 2013:462491. doi: 10.1155/2013/462491

Chen, S., and Ma, S. X. (2003). Nitric oxide in the gracile nucleus mediates depressor response to acupuncture (ST36). *J. Neurophysiol.* 90, 780–785. doi: 10.1152/jn.00170.2003

Cho, S. Y., Lee, D. H., Shin, H. S., Lee, S. H., Koh, J. S., Jung, W. S., et al. (2015). The efficacy and safety of acupuncture for cerebral vasospasm after subarachnoid hemorrhage: study protocol for a randomized controlled trial. *Trials* 16:68. doi: 10.1186/s13063-015-0591-7

Connolly, E. S. Jr., Rabinstein, A. A., Carhuapoma, J. R., Derdeyn, C. P., Dion, J., Higashida, R. T., et al. (2012). Guidelines for the management of aneurysmal subarachnoid hemorrhage: a guideline for healthcare professionals from the American Heart Association/american Stroke Association. *Stroke* 43, 1711–1737. doi: 10.1161/STR.0b013e3182587839

Dankbaar, J. W., de Rooij, N. K., Rijsdijk, M., Velthuis, B. K., Frijns, C. J., Rinkel, G. J., et al. (2010). Diagnostic threshold values of cerebral perfusion measured with computed tomography for delayed cerebral ischemia after aneurysmal subarachnoid hemorrhage. *Stroke* 41, 1927–1932. doi: 10.1161/STROKEAHA.109.574392

Dong, H., Fan, Y. H., Zhang, W., Wang, Q., Yang, Q. Z., and Xiong, L. Z. (2009). Repeated electroacupuncture preconditioning attenuates matrix metalloproteinase-9 expression and activity after focal cerebral ischemia in rats. *Neurol. Res.* 31, 853–858. doi: 10.1179/174313209x393960

Dusick, J. R., and Gonzalez, N. R. (2013). Management of arterial vasospasm following aneurysmal subarachnoid hemorrhage. *Semin. Neurol.* 33, 488–497. doi: 10.1055/s-0033-1364216

Findlay, J. M., Nisar, J., and Darsaut, T. (2016). Cerebral vasospasm: a review. *Can. J. Neurol. Sci.* 43, 15–32. doi: 10.1017/cjn.2015.288

Fotakopoulos, G., Makris, D., Kotlia, P., Kapsalaki, E., Papanikolaou, J., Georgiadis, I., et al. (2018). The value of computed tomography perfusion & transcranial doppler in early diagnosis of cerebral vasospasm in aneurysmal & traumatic subarachnoid hemorrhage. *Future Sci. OA* 4:FSO313. doi: 10.4155/fsoa-2018-0015

Garg, R., and Bar, B. (2017). Systemic complications following aneurysmal subarachnoid hemorrhage. *Curr. Neurol. Neurosci. Rep.* 17:7. doi: 10.1007/s11910-017-0716-3

Hu, H. H., Chung, C., Liu, T. J., Chen, R. C., Chen, C. H., Chou, P., et al. (1993). A randomized controlled trial on the treatment for acute partial ischemic stroke with acupuncture. *Neuroepidemiology* 12, 106–113. doi: 10.1159/000110308

Keyrouz, S. G., and Diringer, M. N. (2007). Clinical review: prevention and therapy of vasospasm in subarachnoid hemorrhage. *Crit. Care* 11:220. doi: 10.1186/cc5958

Kim, D. D., Pica, A. M., Duran, R. G., and Duran, W. N. (2006). Acupuncture reduces experimental renovascular hypertension through mechanisms involving nitric oxide synthases. *Microcirculation* 13, 577–585. doi: 10.1080/10739680600885210

Kim, J. H., Choi, K. H., Jang, Y. J., Bae, S. S., Shin, B. C., Choi, B. T., et al. (2013). Electroacupuncture acutely improves cerebral blood flow and attenuates moderate ischemic injury via an endothelial mechanism in mice. *PLoS One* 8:9. doi: 10.1371/journal.pone.0056736

Li, J., He, J. J., Du, Y. H., Cui, J. J., Ma, Y., and Zhang, X. Z. (2014). Electroacupuncture improves cerebral blood flow and attenuates moderate ischemic injury via Angiotensin II its receptors-mediated mechanism in rats. *BMC Complement. Altern. Med.* 14:12. doi: 10.1186/1472-6882-14-441

Lysakowski, C., Walder, B., Costanza, M. C., and Tramer, M. R. (2001). Transcranial doppler versus angiography in patients with vasospasm due to a ruptured cerebral aneurysm: a systematic review. *Stroke* 32, 2292–2298. doi: 10.1161/hs1001.097108

Macdonald, R. L., Higashida, R. T., Keller, E., Mayer, S. A., Molyneux, A., Raabe, A., et al. (2011). Clazosentan, an endothelin receptor antagonist, in patients with aneurysmal subarachnoid haemorrhage undergoing surgical clipping: a randomised, double-blind, placebo-controlled phase 3 trial (CONSCIOUS-2). *Lancet Neurol.* 10, 618–625. doi: 10.1016/S1474-4422(11)70108-9

Macdonald, R. L., Kassell, N. F., Mayer, S., Ruefenacht, D., Schmiedek, P., Weidauer, S., et al. (2008). Clazosentan to overcome neurological ischemia and infarction occurring after subarachnoid hemorrhage (CONSCIOUS-1): randomized, double-blind, placebo-controlled phase 2 dose-finding trial. *Stroke* 39, 3015–3021. doi: 10.1161/STROKEAHA.108.519942

Othman, A. E., Afat, S., Nikoubashman, O., Muller, M., Schubert, G. A., Bier, G., et al. (2016). Volume perfusion CT imaging of cerebral vasospasm: diagnostic performance of different perfusion maps. *Neuroradiology* 58, 787–792. doi: 10.1007/s00234-016-1695-9

Purkayastha, S., and Sorond, F. (2012). Transcranial doppler ultrasound: technique and application. *Semin. Neurol.* 32, 411–420. doi: 10.1055/s-0032-1331812

Rothoerl, R. D., and Ringel, F. (2007). Molecular mechanisms of cerebral vasospasm following aneurysmal SAH. *Neurol. Res.* 29, 636–642. doi: 10.1179/016164107X240224

Sanelli, P. C., Ugorec, I., Johnson, C. E., Tan, J., Segal, A. Z., Fink, M., et al. (2011). Using quantitative CT perfusion for evaluation of delayed cerebral ischemia following aneurysmal subarachnoid hemorrhage. *AJNR Am. J. Neuroradiol.* 32, 2047–2053. doi: 10.3174/ajnr.A2693

Sebastian, J., Derksen, C., Khan, K., Ibrahim, M., Hameed, B., Siddiqui, M., et al. (2013). Derivation of transcranial Doppler criteria for angiographically proven middle cerebral artery vasospasm after aneurysmal subarachnoid hemorrhage. *J. Neuroimaging* 23, 489–494. doi: 10.1111/j.1552-6569.2012.00771.x

Sehba, F. A., Hou, J., Pluta, R. M., and Zhang, J. H. (2012). The importance of early brain injury after subarachnoid hemorrhage. *Prog. Neurobiol.* 97, 14–37. doi: 10.1016/j.pneurobio.2012.02.003

Shuster, J. J. (2014). Sample size verification for clinical trials. *Clin. Transl. Sci.* 7, 60–62. doi: 10.1111/cts.12115

Steiner, T., Juvela, S., Unterberg, A., Jung, C., Forsting, M., Rinkel, G., et al. (2013). European stroke organization guidelines for the management of intracranial aneurysms and subarachnoid haemorrhage. *Cerebrovasc. Dis.* 35, 93–112. doi: 10.1159/000346087

Sviri, G. E., Britz, G. W., Lewis, D. H., Newell, D. W., Zaaroor, M., and Cohen, W. (2006). Dynamic perfusion computed tomography in the diagnosis of cerebral vasospasm. *Neurosurgery* 59, 319–325; discussion 319–325. doi: 10.1227/01.NEU.0000222819.18834.33

Tsuchiya, M., Sato, E. F., Inoue, M., and Asada, A. (2007). Acupuncture enhances generation of nitric oxide and increases local circulation. *Anesth. Analg.* 104, 301–307. doi: 10.1213/01.ane.0000230622.16367.fb

van der Schaaf, I., Wermer, M. J., van der Graaf, Y., Velthuis, B. K., van de Kraats, C. I., and Rinkel, G. J. (2006). Prognostic value of cerebral perfusion-computed tomography in the acute stage after subarachnoid hemorrhage for the development of delayed cerebral ischemia. *Stroke* 37, 409–413. doi: 10.1161/01.STR.0000198831.69035.43

van Gijn, J., Kerr, R. S., and Rinkel, G. J. (2007). Subarachnoid haemorrhage. *Lancet* 369, 306–318. doi: 10.1016/S0140-6736(07)60153-6

van Gijn, J., and Rinkel, G. J. (2001). Subarachnoid haemorrhage: diagnosis, causes and management. *Brain* 124(Pt 2), 249–278. doi: 10.1093/brain/124.2.249

Vergouwen, M. D. (2009). Effect of endothelin-receptor antagonists on delayed cerebral ischemia after aneurysmal subarachnoid hemorrhage remains unclear. *Stroke* 40, e715–e716. doi: 10.1161/STROKEAHA.109.565887

Wang, Q., Wang, F., Li, X., Yang, Q., Li, X., Xu, N., et al. (2012). Electroacupuncture pretreatment attenuates cerebral ischemic injury through alpha7 nicotinic acetylcholine receptor-mediated inhibition of high-mobility group box 1 release in rats. *J. Neuroinflammation* 9:24. doi: 10.1186/1742-2094-9-24

Wang, W. W., Xie, C. L., Lu, L., and Zheng, G. Q. (2014). A systematic review and meta-analysis of Baihui (GV20)-based scalp acupuncture in experimental ischemic stroke. *Sci. Rep.* 4:3981. doi: 10.1038/srep03981

Washington, C. W., Zipfel, G. J., and Participants in the International Multi-disciplinary Consensus Conference on the Critical Care Management of Subarachnoid Hemorrhage (2011). Detection and monitoring of vasospasm and delayed cerebral ischemia: a review and assessment of the literature. *Neurocrit. Care* 15, 312–317. doi: 10.1007/s12028-011-9594-8

Wilkins, R. H. (1990). Cerebral vasospasm. *Crit. Rev. Neurobiol.* 6, 51–77.

Wilson, S. R., Hirsch, N. P., and Appleby, I. (2005). Management of subarachnoid haemorrhage in a non-neurosurgical centre. *Anaesthesia* 60, 470–485. doi: 10.1111/j.1365-2044.2005.04152.x

Xu, H., Zhang, Y., Sun, H., Chen, S., and Wang, F. (2014). Effects of acupuncture at GV20 and ST36 on the expression of matrix metalloproteinase 2, aquaporin 4, and aquaporin 9 in rats subjected to cerebral ischemia/reperfusion injury. *PLoS One* 9:e97488. doi: 10.1371/journal.pone.0097488

Conflict of Interest Statement: The authors declare that the research was conducted in the absence of any commercial or financial relationships that could be construed as a potential conflict of interest.

frontiers in Neuroscience

ORIGINAL RESEARCH
published: 02 November 2018
doi: 10.3389/fnins.2018.00802

METH-Induced Neurotoxicity Is Alleviated by Lactulose Pretreatment Through Suppressing Oxidative Stress and Neuroinflammation in Rat Striatum

Xiao-Li Xie[1], *Wen-Tao Zhou*[1], *Kai-Kai Zhang*[2], *Li-Jian Chen*[2] *and Qi Wang*[2]*

[1] *Department of Toxicology, School of Public Health, Southern Medical University (Guangdong Provincial Key Laboratory of Tropical Disease Research), Guangzhou, China,* [2] *Department of Forensic Pathology, School of Forensic Medicine, Southern Medical University, Guangzhou, China*

Abuse of methamphetamine (METH) results in neurological and psychiatric abnormalities. Lactulose is a poorly absorbed derivative of lactose and can effectively alleviate METH-induced neurotoxicity in rats. The present study was designed to investigate the effects of lactulose on METH-induced neurotoxicity. Rats received METH (15 mg/kg, 8 intraperitoneal injections, 12-h interval) or saline and received lactulose (5.3 g/kg, oral gavage, 12-h interval) or vehicle 2 days prior to the METH administration. Reactive oxygen species (ROS) and malondialdehyde (MDA) were measured. Protein levels of toll-like receptor 4 (TLR4), myeloid differentiation factor 88 (MyD88), tumor necrosis factor receptor associated factor 6 (TRAF6), nuclear factor κB (NFκB), interleukin (IL)-1β, IL-6, TNF-α, cleaved caspase 3, and poly(ADP-ribose) polymerase-1 (PARP-1) were determined by western blotting. mRNA expressions of nuclear factor erythroid 2-relatted factor-2 (Nrf2), p62, and heme oxygenase-1 (HO-1) were assessed by RT-qPCR. The lactulose pretreatment decreased METH-induced cytoplasmic damage in rat livers according to histopathological observation. Compared to the control group, overproduction of ROS and MDA were observed in rat striatums in the METH alone-treated group, while the lactulose pretreatment significantly attenuated the METH-induced up-regulation of oxidative stress. The lactulose pretreatment significantly repressed over-expressions of proteins of TLR4, MyD88, TRAF6, NFκB, IL-1β, IL-6, TNF-α, cleaved caspase 3, PARP-1. The lactulose pretreatment increased mRNA expressions of Nrf2, p62, and HO-1. These findings suggest that lactulose pretreatment can alleviate METH-induced neurotoxicity through suppressing neuroinflammation and oxidative stress, which might be attributed to the activation of the Nrf2/HO-1 axis.

Keywords: METH, neuroinflammation, oxidative stress, lactulose, Nrf2/HO-1 axis

OPEN ACCESS

Edited by:
Gang Chen,
First Affiliated Hospital of Soochow University, China

Reviewed by:
Lezi E,
Duke University, United States
Xiangping Chu,
University of Missouri–Kansas City, United States

***Correspondence:**
Qi Wang
wangqi_legmed@126.com

Specialty section:
This article was submitted to Neurodegeneration, a section of the journal Frontiers in Neuroscience

Received: *05 August 2018*
Accepted: *15 October 2018*
Published: *02 November 2018*

Citation:
Xie X-L, Zhou W-T, Zhang K-K, Chen L-J and Wang Q (2018) METH-Induced Neurotoxicity Is Alleviated by Lactulose Pretreatment Through Suppressing Oxidative Stress and Neuroinflammation in Rat Striatum. Front. Neurosci. 12:802. doi: 10.3389/fnins.2018.00802

INTRODUCTION

Methamphetamine (METH) is a popular new-type psychostimulant drug that may result in neurotoxicity. METH-induced neurotoxicity may be related to apoptosis (Jumnongprakhon et al., 2014), oxidative stress (Nguyen et al., 2015; Wen et al., 2016) and inflammatory changes (Gonçalves et al., 2010; Park et al., 2017). Overproduction of reactive oxygen species (ROS) induced by

METH may play a key role in oxidative damage (Gluck et al., 2001). METH can also trigger a neuroinflammatory process by releasing pro-inflammatory molecules, acting as processors (Coelho-Santos et al., 2012; Park et al., 2017). The pro-inflammatory molecules may indirectly result in neurotoxicity and the activation of glial cells, which could exacerbate neuroinflammation (Park et al., 2017).

Nuclear factor erythroid 2-relatted factor-2 (Nrf2) is a fundamental regulator of antioxidant response element-dependent transcription. It plays a significant role in the cellular adaptive response to oxidative stress (Yang et al., 2018). Besides its antioxidant function, Nrf2 activation also plays a central role in the regulation of inflammation (Kuhn et al., 2011). Under unstressed conditions, a low level of Nrf2 is maintained by Kelch-like ECH-associated protein 1, while under oxidative stress conditions, Nrf2 is released to activate antioxidant response elements (e.g., heme oxygenase-1, HO-1) in the nucleus (Suzuki et al., 2013). Sequestosome-1 (SQSTM1, p62) expression can prevent Nrf2 degradation and enhance its nuclear accumulation (Sun et al., 2016). In addition, p62 is a target gene of Nrf2 (Jain et al., 2010) and they can form a positive feedback loop by inducing an antioxidant response element and an anti-inflammatory effect.

Lactulose is a non-digestible galactose-fructose disaccharide. Lactulose is metabolized in the colon by bacterial flora to short-chain fatty acids, which increases H^+ concentration and promotes the formation of NH_4^+ from NH_3 (ammonia) in the colon. Accumulation of ammonia in the colon effectively reduces serum ammonia concentration and subsequently alleviates adverse effects of hyperammonemia (Moratalla et al., 2017), such as neurotoxicity, neurocognitive defects. Therefore, lactulose can be used as prevention and treatment of hepatic encephalopathy with cirrhosis, as it can effectively improve patients' neurocognitive impairment and reverse low-grade cerebral edema by preventing hyperammonemia and inflammation (Rai et al., 2015; Moratalla et al., 2017). In this study, rats were pretreated with lactulose/vehicle and administered with METH/saline. Focusing on oxidative stress, inflammatory responses and the Nrf2/HO-1 axis, the effects of lactulose on METH-induced neurotoxicity in rat striatum were clarified.

MATERIALS AND METHODS

Chemicals

METH (purity of 99.1%, identified by the National Institute for Food and Drug Control, Guangzhou, China) was purchased from the National Institute for the Control of Pharmaceutical and Biological Products (Beijing, China). Lactulose was obtained from Pharmaceutical Associates Inc., Greenville, SC. DCFH-DA was purchased from Sigma Chemical Co (St. Louis, MO, USA).

Animals and Treatments

A total of eighteen male Sprague Dawley rats (5-weeks-old) were purchased from the Laboratory Animal Center of Southern Medical University (Guangzhou, China). The rats were singly housed in plastic cages in an animal facility maintained under standard conditions (room temperature, 23 ± 1°C; relative humidity, 44 ± 5%; and a light/dark cycle of 12 h) and given free access to a basal diet and water. The animals were acclimatized for 1 week prior to the beginning of the experiment. This study was reviewed and approved by the National Institutes of Health Guide for the Care and Use of Laboratory Animals of the Southern Medical University.

Briefly, the rats were randomly divided into 3 groups (6 rats in each group). The rats received 8 intraperitoneal (i.p.) injections of METH (15 mg/ml/kg body weight/injection) or saline (1 ml/kg) at 12 h (h) intervals. When exposed to this dose, rats have a similar concentration of METH in the blood at 1 h after the last injection to the median value of METH in the blood of METH abusers (Melega et al., 2007; Huang et al., 2015). Therefore, the single dose of METH was chosen based on previous studies (Huang et al., 2015; Wang et al., 2017). Two days prior to the METH treatment, the rats were pretreated with lactulose (5.3 g/kg body weight, oral gavage, every 12 h) or vehicle (100 mg/mL galactose and 80 mg/mL lactose) until the day before sacrifice. The dose of lactulose, which was chosen in this study, could effectively enhance ammonia excretion and has been used as an treatment for the cirrhosis patients with hepatic encephalopathy and neurocognitive defects (Jia and Zhang, 2005; Nicaise et al., 2008; Al Sibae and McGuire, 2009; Northrop et al., 2016). All rats were killed by rapid decapitation 24 h after the last injection of METH/saline. The livers as well as the striatums were quickly excised. The livers were fixed in 10% phosphate-buffered formalin for histopathological observation and the striatums were stored at −80°C for subsequent analyses.

Histopathological Observation

Liver tissues were embedded in paraffin, sectioned at 3-μm thickness, and stained with hematoxylin and eosin (H&E) for histopathological examination.

Detections of ROS Production in Rat Striatum

Striatum tissues were washed with ice-cold PBS. Then they were made into single-cell suspension by homogenizer and centrifuged at 500 g for 10 min at 4°C. After being washed twice with ice-cold PBS, the cells were re-suspended. The re-suspension solution was divided into two parts: One part was used to determine the protein content after ultrasonic disruption using the Bradford protein assay kit (Bio-Rad, Hercules, CA), and the other part was incubated with 10 μM DCFH-DA (Sigma), kept out of light for 30 min at 37°C and washed twice with ice-cold PBS. DCFH-DA fluorescence was determined by flow cytometry (BD LSRFortessa™, BD, CA, USA). The results of ROS generation were calculated as DCFH-DA fluorescence per microgram and expressed as fold changes compared with the mean value of the control group.

Measurement of Malondialdehyde (MDA) Content in Rat Striatum

Striatums of rats were homogenized in RIPA lysis buffer on ice and centrifuged at 12,000 g for 10 min at 4°C to collect the supernatant. The total protein content was tested with

the Bradford protein assay kit (Bio-Rad, Hercules, CA). MDA content was determined using a Lipid Peroxidation MDA Assay Kit (Nanjing Jiancheng Bioengineering Institute, China) following the manufacturer's instructions. MDA content was calculated and expressed as nanomole per microgram (nmol/mg) protein.

Real-Time Quantitative RT-PCR (RT-qPCR) Analysis for Nrf2/HO-1 Axis in Rat Striatum

Briefly, cDNA copies of total RNA were obtained using a PrimeScript™ RT Master Mix (RR036A, Takara Biotechnology Co., LTD.). RT-qPCR was conducted using Premix Ex TaqTM GC (RR820A, Takara) on the StrataGene MX 3005P Multiplex Quantitative PCR System (Agilent Technologies, USA), with primers for Nrf2, HO-1, and p62. The PCR program cycles were set as follows: initial denaturing at 95°C for 30 s, followed by 40 cycles at 95°C for 15 s, and 60°C for 30 s. β-actin was used as an internal standard, and the mRNA levels of the target genes were normalized to β-actin. mRNA expressions in the METH alone and the METH plus lactulose groups were displayed as fold changes compared to the mean value of the control group. All the RT-qPCR experiments were performed in triplicate. Detailed information of the primers is listed in **Supplementary Table 1**.

Western Blotting Analysis for Inflammatory-Related Factors and Apoptosis in Rat Striatum

Proteins were extracted from the rat striatum as described previously (Wang et al., 2017). The proteins were separated by SDS-polyacrylamide gel electrophoresis (PAGE). After electrophoresis, the proteins were transferred to polyvinylidine difluoride membranes. The membranes were then blocked with 5% milk-Tris-buffered solution-Tween solution for 2 h and subsequently incubated overnight at 4°C followed by appropriate secondary antibodies for 2 h at room temperature. Bands were visualized using the ECL system (BIO-RAD Laboratories, Inc., California, USA). Primary antibodies against toll-like receptor 4 (TLR4, sc-293072, Santa Cruz Biotechnology), myeloid differentiation factor 88 (MyD88, sc-74532, Santa Cruz), tumor necrosis factor (TNF) receptor associated factor 6 (TRAF6, sc-8409, Santa Cruz), nuclear factor (NF) κB (sc-8008, Santa Cruz), interleukin (IL)-1β (sc-12742, Santa Cruz), IL-6 (sc-57315, Santa Cruz), TNF-α (sc-12744, Santa Cruz), caspase 3 (9665, Cell Signaling Technology), poly(ADP-ribose) polymerase-1 (PARP-1, sc-8007, Santa Cruz), and GAPDH (sc-32233, Santa Cruz) were used.

Densitometric analysis was conducted using Tanon Gel Image System (version 4.2). Data of relative integrated optical density values of bands are presented as bar charts.

Statistical Analysis

All values were expressed as means ± SEM. Statistical analyses were conducted using the scientific statistics software SPSS (version 16). One-way analysis of variance (ANOVA) with repeated measures, followed by *post-hoc* Tukey tests, was used for comparisons of multiple groups. Values of $p < 0.05$ were considered as statistically significant.

RESULTS

Lactulose Decreased METH-Induced Hepatotoxicity in Rats

Extensive cytoplasmic damage was observed in the livers of the METH alone-treated rats (**Figure 1b**), while no obvious changes of hepatocellular morphology were observed in the control group (**Figure 1a**) by histopathological observation. METH-induced changes in hepatocellular morphology were attenuated under pretreatment with lactulose (**Figure 1c**).

Lactulose Suppressed Overproductions of ROS and MDA Induced by METH in Rat Striatum

As shown in **Figure 2A**, the ROS level was more significantly augmented in the METH alone-treated rats than that in control rats, which indicates the pro-oxidative effect of METH. However, the pretreatment with lactulose markedly decreased METH-induced increasing of ROS compared with the METH alone-treated group. Consistently, **Figure 2B** shows that the MDA content significantly increased in the METH alone-treated group compared with the control group, while the pretreatment with lactulose effectively suppressed the increase.

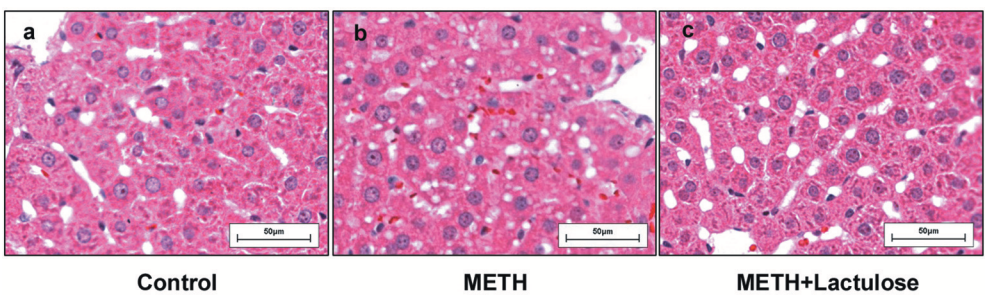

FIGURE 1 | Histopathological observation of rat livers. **(a)** No pathological change was observed in the control group. **(b)** Vacuolar degeneration in the cytoplasmic was observed in the METH alone-treated rats. **(c)** The cytoplasmic damage was obviously attenuated by the pretreatment with lactulose.

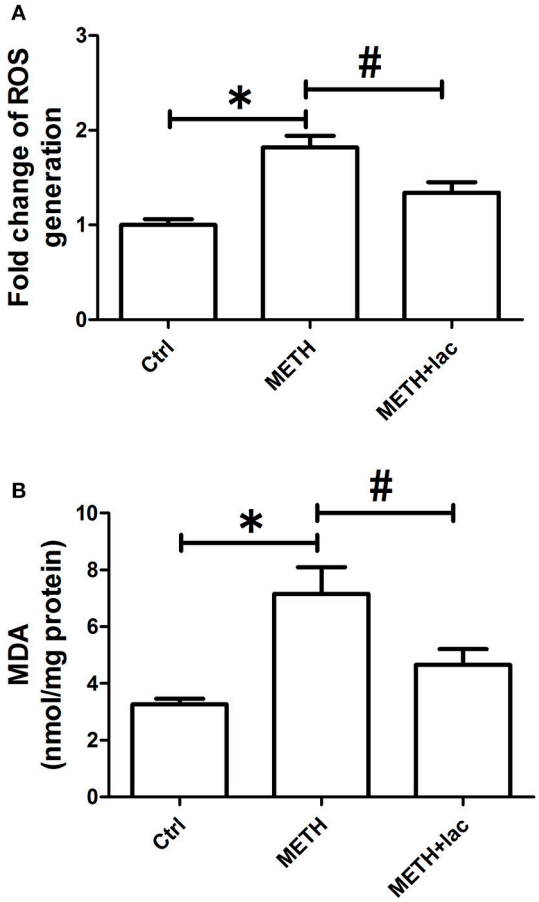

FIGURE 2 | Detection of ROS generation **(A)** and MDA production **(B)** in rat striatum. **(A)** Compared to the control group, over-generation of ROS was detected in the METH alone-treated rats, while the pretreatment with lactulose significantly decreased the ROS generation induced by METH. Significant compared to the control group (*$p < 0.05$); Significant compared to the METH alone-treated group (#$p < 0.05$). Lact, Lactulose. **(B)** Overproduction of MDA was observed in the METH alone-treated rats compared to the control group. The pretreatment with lactulose significantly suppressed the production of MDA resulting from the METH treatment. Significant compared to the control group (*$p < 0.05$); Significant compared to the METH alone-treated group (#$p < 0.05$). Lact, Lactulose.

Lactulose Up-Regulated mRNA Expressions of Nrf2/Ho-1 Axis, Decreased Protein Expressions of Inflammatory-Related Factors and Suppressed Apoptosis in Rat Striatum

The lactulose pretreatment markedly up-regulated mRNA expressions of Nrf2, HO-1, and p62, compared with the METH alone-treated group (**Figure 3**). The lactulose pretreatment significantly repressed over-expressions of proteins of TLR4, MyD88, TRAF6, NFκB, IL-1β, IL-6, and TNF-α induced by METH. Expressions of cleaved caspase 3 and PARP1 were substantially decreased by the lactulose pretreatment compared to the METH-alone group (**Figure 4**).

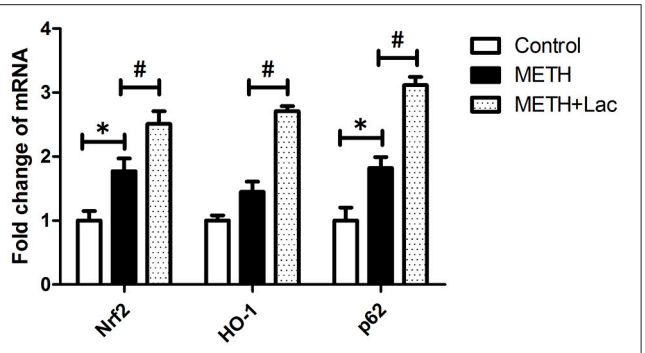

FIGURE 3 | RT-qPCR analysis for genes of *Nrf2*, *HO-1,* and *p62* in rat striatum. Compared to the control group, mRNA expressions of Nrf2 and p62 were significantly up-regulated in the METH alone-treated rats, while no change of HO-1 was observed. The pretreatment with lactulose significantly increased mRNA expressions of Nrf2, HO-1 and p62 compared to the METH alone-treated rats. Significant compared to the control group (*$p < 0.05$); Significant compared to the METH alone-treated group (#$p < 0.05$). Lact, Lactulose.

DISCUSSION

In this study, obvious hepatic injury can be detected after METH alone treatment, showing as cytoplasmic vacuolar degeneration. However, the lactulose pretreatment effectively reduced the cytoplasmic damage. These findings indicate that the model was successfully established (Halpin and Yamamoto, 2012).

Overproduction of ROS was observed in striatums of the METH alone-treated group, indicating the pro-oxidative effects of METH. Overproduction of MDA, a final product of lipid peroxidation, was found in striatums of the METH alone-treated group, suggesting the induction of oxidative stress. However, when compared with the METH alone-treated rats, the lactulose pretreatment significantly attenuated productions of ROS and MDA. These findings indicated that pretreatment with lactulose can suppress METH-induced up-regulation of oxidative stress.

Toll-like receptors (TLRs) are a class of immunological pattern recognition receptors that play a fundamental role in pathogen recognition as well as in inflammatory responses. TLR4, also called CD284, can recruit the adaptor proteins (for example MyD88) bind to TRAF6, and then trigger NFκB activation to induce the transcription of pro-inflammatory cytokines, such as IL-6, IL-1β, TNF-α (Moscat et al., 2006; Zhang et al., 2013; Wang et al., 2018). Previous studies have reported that TLR4 plays an important part in METH-induced neuroinflammation (Du et al., 2017). In this study, over-expressions of proteins of TLR4, MyD88, and TRAF6 were observed in the METH alone-treated rats when compared with the control group. Consistently, protein expressions of NFκB as well as the pro-inflammatory cytokines, IL-6, IL-1β, and TNF-α, were also significantly up-regulated after METH treatment. These results confirmed that METH treatment induced neuroinflammation by activating the TLR4/NFκB pathway, whereas decreased

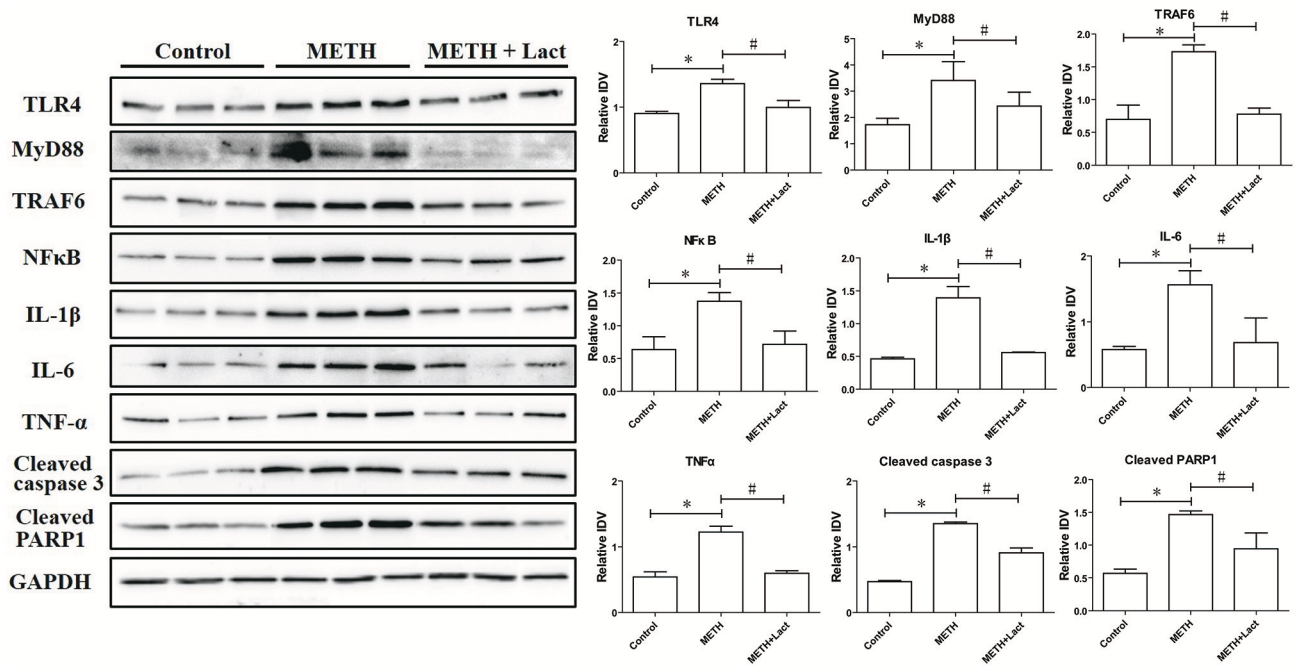

FIGURE 4 | Western blotting analysis for protein expressions of TLR4, MyD88, TRAF6, NFκB, IL-1β, IL-6, TNF-α, cleaved caspase 3 and PARP1 in rat striatum. Compared to the control group, expressions of TLR4, MyD88, TRAF6, NFκB, IL-1β, IL-6, TNF-α, cleaved caspase 3 and PARP1 significantly increased in the METH alone-treated group, while the lactulose pretreatment effectively alleviated these over-expressions, suggesting suppressions of neuroinflammation and apoptosis induced by METH. Significant compared to the control group (*$p < 0.05$); Significant compared to the METH alone-treated group (#$p < 0.05$). Lact, Lactulose.

protein expressions of TLR4, MyD88, TRAF6, NFκB, IL-6, IL-1β, and TNF-α were observed in the lactulose-pretreated group, suggesting the alleviation of neuroinflammation by lactulose.

The Nrf2/HO-1 axis is commonly referred to as an antioxidant system, which can be activated by ROS overproduction (Suzuki and Yamamoto, 2017). Besides its anti-oxidative function, Nrf2/HO-1 axis is an important part of the regulation of inflammation (Kuhn et al., 2011). In our previous study, in the whole-cell lysates of rat striatum, METH-induced over-expression of Nrf2 and p62 protein leves were significantly attenuated by the lactulose pretreatment. However, in cell nucleus, protein expressions of Nrf2 and HO-1 obviously decreased in METH alone-treated rats, but increased by the pretreatment with lactulose compared to the METH alone-treated rats, suggesting excessive accumulation of Nrf2 in cytoplasm paradoxically repressed Nrf2 nuclear transformation and induction of HO-1 from the level of protein (Xie et al., 2018). In this study, mRNA expressions of Nrf2, HO-1 and p62 in the whole-cell lysates of rat striatum were examined. Compared with the control group, the mRNA expression of Nrf2 was markedly up-regulated by METH treatment, whereas no significant change of HO-1 in the mRNA level was observed. These findings might suggest that as one of the downstream response elements of Nrf2, HO-1 was not effectively activated in rat striatums at transcription level. Furthermore, mRNA expression of p62 was significantly up-regulated in the striatums of METH alone-treated rats, while the lactulose pretreatment further increased mRNA expressions of Nrf2 and its targets, HO-1 and p62, suggesting activation of Nrf2/HO-1 axis by lactulose. The lactulose pretreatment can induce nucleus translocation of Nrf2. Therefore, to maintain the activation of Nrf2/HO-1 axis, mRNA expression of Nrf2 were further up-regulated by the lactulose pretreatment. Moreover, p62 is a target gene for Nrf2 and can create a positive feedback loop by inducing a downstream response element (Jain et al., 2010). In addition, p62 can be selective turnover by autophagy. Lactulose pretreatment increased turnover of p62 by alleviating impaired autophagy flux and decreased p62 protein expression (Xie et al., 2018). Thus, in the lactulose pretreatment group, the increased mRNA levels and decreased protein expressions of Nrf2 and p62 were observed in the whole-cell lysates of rat striatum when compared with METH-alone group, which may be caused by differences in translation efficiency or RNA/protein kinetics, though further investigations are needed to clarify the underlying mechanism.

Compared with the control group, increased expressions of proteins of cleaved caspase 3 and PARP1 were found in the METH alone-treated rats, implying its neurotoxicity. Previous studies have reported that METH-induced increase of oxidative stress and pro-inflammatory cytokines may activate downstream apoptosis (Allagnat et al., 2012; Park et al., 2017), which may play an important role in METH-induced neurotoxicity. However, in this study, decreased protein

expressions of cleaved caspase 3 and PARP1 were observed in lactulose-pretreated rats, suggesting alleviation of METH-induced neurotoxicity.

METH abuse could also induce obvious neurocognitive defects (Cuzen et al., 2015), which is correlated with high serum ammonia levels. Lactulose could improve neurocognitive scores by reducing serum ammonia in cirrhotic patients with minimal hepatic encephalophthy (Moratalla et al., 2017). Therefore, we speculated that the treatment with lactulose might attenuate METH-induced neurotoxicity as well as neurocognitive defects and be favorable to improving the therapeutic effects of METH intoxication/addiction, at least at certain exert, which should be confirmed in further clinical practices.

In summary, oxidative stress and neuroinflammation induced by METH may play an important role in its neurotoxicity, while pretreatment with lactulose can alleviate the neurotoxicity through repressing oxidative stress and decreasing neuroinflammation, which might attribute to the activation of Nrf2/HO-1 axis.

AUTHOR CONTRIBUTIONS

X-LX drafted the manuscript and carried out WB/RT-qPCR experiments. W-TZ carried out animal experiment. K-KZ and L-JC carried out WB/ RT-qPCR experiments. QW designed the study. All authors read and approved the final manuscript.

FUNDING

This work was supported by the National Natural Science Foundation of China (Grant No. 81401556, 81601641, and 81871526), the Scientific Research Foundation for the Returned Overseas Chinese Scholars, the National Education Ministry (Grant No. 2015-311).

SUPPLEMENTARY MATERIAL

The Supplementary Material for this article can be found online at: https://www.frontiersin.org/articles/10.3389/fnins.2018.00802/full#supplementary-material

REFERENCES

Al Sibae, M. R., and McGuire, B. M. (2009). Current trends in the treatment of hepatic encephalopathy. *Ther. Clin. Risk Manage.* 5, 617–626. doi: 10.2147/TCRM.S4443

Allagnat, F., Fukaya, M., Nogueira, T. C., Delaroche, D., Welsh, N., Marselli, L., et al. (2012). C/EBP homologous protein contributes to cytokine-induced pro-inflammatory responses and apoptosis in beta-cells. *Cell Death Diff.* 19, 1836–1846. doi: 10.1038/cdd.2012.67

Coelho-Santos, V., Gonçalves, J., Fontes-Ribeiro, C., Silva, A. P., (2012). Prevention of methamphetamine-induced microglial cell death by TNF-alpha and IL-6 through activation of the JAK-STAT pathway. *J. Neuroinflammation* 9:103. doi: 10.1186/1742-2094-9-103

Cuzen, N. L., Koopowitz, S. M., Ferrett, H. L., Stein, D. J., and Yurgelun-Todd, D. (2015). Methamphetamine and cannabis abuse in adolescence: a quasi-experimental study on specific and long-term neurocognitive effects. *BMJ Open* 5:e005833. doi: 10.1136/bmjopen-2014-005833

Du, S. H., Qiao, D. F., Chen, C. X., Chen, S., Liu, C., Lin, Z., et al. (2017). Toll-like receptor 4 mediates methamphetamine-induced neuroinflammation through caspase-11 signaling pathway in astrocytes. *Front. Mol. Neurosci.* 10:409. doi: 10.3389/fnmol.2017.00409

Gluck, M. R., Moy, L. Y., Jayatilleke, E., Hogan, K. A., Manzino, L., and Sonsalla, P. K. (2001). Parallel increases in lipid and protein oxidative markers in several mouse brain regions after methamphetamine treatment. *J. Neurochem.* 79, 152–160. doi: 10.1046/j.1471-4159.2001.00549.x

Gonçalves, J., Baptista, S., Martins, T., Milhazes, N., Borges, F., Ribeiro, C. F., et al. (2010). Methamphetamine-induced neuroinflammation and neuronal dysfunction in the mice hippocampus: preventive effect of indomethacin. *Eur. J. Neurosci.* 31, 315–326. doi: 10.1111/j.1460-9568.2009.07059.x

Halpin, L. E., and Yamamoto, B. K. (2012). Peripheral ammonia as a mediator of methamphetamine neurotoxicity. *J. Neurosci.* 32, 13155–13163. doi: 10.1523/JNEUROSCI.2530-12.2012

Huang, W., Xie, W. B., Qiao, D., Qiu, P., Huang, E., Li, B., et al. (2015). Caspase-11 plays an essential role in methamphetamine-induced dopaminergic neuron apoptosis. *Toxicol. Sci.* 145, 68–79. doi: 10.1093/toxsci/kfv014

Jain, A., Lamark, T., Sjøttem, E., Larsen, K. B., Awuh, J. A., Øvervatn, A., et al. (2010). p62/SQSTM1 is a target gene for transcription factor NRF2 and creates a positive feedback loop by inducing antioxidant response element-driven gene transcription. *J. Biol. Chem.* 285, 22576–22591. doi: 10.1074/jbc.M110.118976

Jia, L., and Zhang, M. H. (2005). Comparison of probiotics and lactulose in the treatment of minimal hepatic encephalopathy in rats. *World J. Gastroenterol.* 11, 908–911. doi: 10.3748/wjg.v11.i6.908

Jumnongprakhon, P., Govitrapong, P., Tocharus, C., Tungkum, W., and Tocharus, J. (2014). Protective effect of melatonin on methamphetamine-induced apoptosis in glioma cell line. *Neurotox. Res.* 25, 286–294. doi: 10.1007/s12640-013-9419-y

Kuhn, A. M., Tzieply, N., Schmidt, M. V., von Knethen, A., Namgaladze, D., Yamamoto, M., et al. (2011). Antioxidant signaling via Nrf2 counteracts lipopolysaccharide-mediated inflammatory responses in foam cell macrophages. *Free Radic. Biol. Med.* 50, 1382–1391. doi: 10.1016/j.freeradbiomed.2011.02.036

Melega, W. P., Cho, A. K., Harvey, D., and Laćan, G. (2007). Methamphetamine blood concentrations in human abusers: application to pharmacokinetic modeling. *Synapse* 61, 216–220. doi: 10.1002/syn.20365

Moratalla, A., Ampuero, J., Bellot, P., Gallego-Durán, R., Zapater, P., Roger, M., et al. (2017). Lactulose reduces bacterial DNA translocation, which worsens neurocognitive shape in cirrhotic patients with minimal hepatic encephalopathy. *Liver Int.* 37, 212–223. doi: 10.1111/liv.13200

Moscat, J., Diaz-Meco, M. T., Albert, A., and Campuzano, S. (2006). Cell signaling and function organized by PB1 domain interactions. *Mol. Cell* 23, 631–640. doi: 10.1016/j.molcel.2006.08.002

Nguyen, X. K., Lee, J., Shin, E. J., Dang, D. K., Jeong, J. H., Nguyen, T. T., et al. (2015). Liposomal melatonin rescues methamphetamine-elicited mitochondrial burdens, pro-apoptosis, and dopaminergic degeneration through the inhibition PKCdelta gene. *J. Pineal Res.* 58, 86–106. doi: 10.1111/jpi.12195

Nicaise, C., Prozzi, D., Viaene, E., Moreno, C., Gustot, T., Quertinmont, E., et al. (2008). Control of acute, chronic, and constitutive hyperammonemia by wild-type and genetically engineered Lactobacillus plantarum in rodents. *Hepatology* 48, 1184–1192. doi: 10.1002/hep.22445

Northrop, N. A., Halpin, L. E., and Yamamoto, B. K. (2016). Peripheral ammonia and blood brain barrier structure and function after methamphetamine. *Neuropharmacology* 107, 18–26. doi: 10.1016/j.neuropharm.2016.03.018

Park, J. H., Seo, Y. H., Jang, J. H., Jeong, C. H., Lee, S., and Park, B. (2017). Asiatic acid attenuates methamphetamine-induced neuroinflammation and neurotoxicity through blocking of NF-kB/STAT3/ERK and mitochondria-mediated apoptosis pathway. *J. Neuroinflammation* 14:240. doi: 10.1186/s12974-017-1009-0

Rai, R., Ahuja, C. K., Agrawal, S., Kalra, N., Duseja, A., Khandelwal, N., et al. (2015). Reversal of low-grade cerebral edema after lactulose/rifaximin therapy in patients with cirrhosis and minimal hepatic encephalopathy. *Clin. Transl. Gastroenterol.* 6:e111. doi: 10.1038/ctg.2015.38

Sun, X., Ou, Z., Chen, R., Niu, X., Chen, D., Kang, R., et al. (2016). Activation of the p62-Keap1-NRF2 pathway protects against ferroptosis in hepatocellular carcinoma cells. *Hepatology* 63, 173–184. doi: 10.1002/hep.28251

Suzuki, T., Motohashi, H., and Yamamoto, M. (2013). Toward clinical application of the Keap1-Nrf2 pathway. *Trends Pharmacol. Sci.* 34, 340–346. doi: 10.1016/j.tips.2013.04.005

Suzuki, T., and Yamamoto, M. (2017). Stress-sensing mechanisms and the physiological roles of the Keap1-Nrf2 system during cellular stress. *J. Biol. Chem.* 292, 16817–16824. doi: 10.1074/jbc.R117.800169

Wang, Q., Wei, L. W., Xiao, H. Q., Xue, Y., Du, S. H., Liu, Y. G., et al. (2017). Methamphetamine induces hepatotoxicity via inhibiting cell division, arresting cell cycle and activating apoptosis: *in vivo* and *in vitro* studies. *Food Chem. Toxicol.* 105, 61–72. doi: 10.1016/j.fct.2017.03.030

Wang, Z., Zhang, Y. H., Guo, C., Gao, H. L., Zhong, M. L., Huang, T. T., et al. (2018). Tetrathiomolybdate treatment leads to the suppression of inflammatory responses through the TRAF6/NFkappaB pathway in LPS-stimulated BV-2 Microglia. *Front. Aging Neurosci.* 10:9. doi: 10.3389/fnagi.2018.00009

Wen, D., An, M., Gou, H., Liu, X., Liu, L., Ma, C., et al. (2016). Cholecystokinin-8 inhibits methamphetamine-induced neurotoxicity via an anti-oxidative stress pathway. *Neurotoxicology* 57, 31–38. doi: 10.1016/j.neuro.2016.08.008

Xie, X. L., He, J. T., Wang, Z. T., Xiao, H. Q., Zhou, W. T., Du, S. H., et al. (2018). Lactulose attenuates METH-induced neurotoxicity by alleviating the impaired autophagy, stabilizing the perturbed antioxidant system and suppressing apoptosis in rat striatum. *Toxicol. Lett.* 289, 107–113. doi: 10.1016/j.toxlet.2018.03.015

Yang, B., Cheng, H., Wang, L., Fu, J., Zhang, G., Guan, D., et al. (2018). Protective roles of NRF2 signaling pathway in cobalt chloride-induced hypoxic cytotoxicity in human HaCaT keratinocytes. *Toxicol. Appl. Pharmacol.* 355, 189–197. doi: 10.1016/j.taap.2018.06.030

Zhang, L., Zhang, J., Yang, L., Dong, Y., Zhang, Y., and Xie, Z. (2013). Isoflurane and sevoflurane increase interleukin-6 levels through the nuclear factor-kappa B pathway in neuroglioma cells. *Br. J. Anaesth* 110 (Suppl. 1), i82–i91. doi: 10.1093/bja/aet115

Conflict of Interest Statement: The authors declare that the research was conducted in the absence of any commercial or financial relationships that could be construed as a potential conflict of interest.

frontiers in Neuroscience

ORIGINAL RESEARCH
published: 07 November 2018
doi: 10.3389/fnins.2018.00782

G2019S LRRK2 Increases Stress Susceptibility Through Inhibition of DAF-16 Nuclear Translocation in a 14-3-3 Associated-Manner in *Caenorhabditis elegans*

*Simei Long[1†], Wenyuan Guo[2†], Sophie Hu[3], Fengjuan Su[1], Yixuan Zeng[4], Jinsheng Zeng[1], Eng-King Tan[5,6,7], Christopher A. Ross[8] and Zhong Pei[1]**

[1] Department of Neurology, National Key Clinical Department and Key Discipline of Neurology, Guangdong Provincial Key Laboratory of Diagnosis and Treatment of Major Neurological Diseases, The First Affiliated Hospital, Sun Yat-sen University, Guangzhou, China, [2] Department of Neurology, The First Affiliated Hospital, Guangzhou Medical University, Guangzhou, China, [3] Cumming School of Medicine, University of Calgary, Calgary, AB, Canada, [4] Shenzhen Second People's Hospital, The First Affiliated Hospital of Shenzhen University, Shenzhen, China, [5] Department of Neurology, Singapore General Hospital, Singapore, Singapore, [6] National Neuroscience Institute, Singapore, Singapore, [7] Duke-NUS Graduate Medical School, Singapore, Singapore, [8] Division of Neurobiology, Department of Psychiatry–Departments of Neuroscience, Neurology, and Pharmacology, Johns Hopkins University School of Medicine, Baltimore, MD, United States

OPEN ACCESS

Edited by:
Guohua Xi,
University of Michigan Health System, United States

Reviewed by:
Gang Chen,
First Affiliated Hospital of Soochow University, China
Xinchun Jin,
Soochow University, China
Qiang Liu,
Barrow Neurological Institute (BNI), United States

***Correspondence:**
Zhong Pei
peizhong@mail.sysu.edu.cn

† These authors have contributed equally to this work

Specialty section:
This article was submitted to Neurodegeneration, a section of the journal Frontiers in Neuroscience

Received: *21 June 2018*
Accepted: *09 October 2018*
Published: *07 November 2018*

Citation:
Long S, Guo W, Hu S, Su F, Zeng Y, Zeng J, Tan E-K, Ross CA and Pei Z (2018) G2019S LRRK2 Increases Stress Susceptibility Through Inhibition of DAF-16 Nuclear Translocation in a 14-3-3 Associated-Manner in Caenorhabditis elegans. Front. Neurosci. 12:782. doi: 10.3389/fnins.2018.00782

Mutations in *leucine-rich repeat kinase 2* (*LRRK2*) are common causes of familial Parkinson's disease (PD). Oxidative stress plays a key role in the pathogenesis of PD. Mutations in LRRK2 have been shown to increase susceptibility to oxidative stress. To explore mechanisms underlying susceptibility to oxidative stress in LRRK2 mutants, we generated stable *Caenorhabditis elegans* (*C. elegans*) strains in which human LRRK2 proteins including wild type LRRK2 (WT), G2019S LRRK2 (G2019S), and G2019S-D1994A kinase-dead LRRK2 (KD) were expressed in all neurons. Human 14-3-3 β was injected into LRRK2 transgenic worms to allow co-expression of 14-3-3 β and LRRK2 proteins. We found that G2019S transgenic worms had increased sensitivity to stress (heat and juglone treatment) and impaired stress-induced nuclear translocation of DAF-16. In addition, G2019S inhibited *ftt2* (a *14-3-3* gene homolog in *C. elegans*) knockdown-associated nuclear translocation of DAF-16. Comparably, overexpression of human 14-3-3 β could attenuate G2019S-associated toxicity in response to stress and rescued G2019S-mediated inhibition of *sod-3* and *dod-3* expression. Taken together, our study provides evidence suggesting that 14-3-3-associated inhibition of DAF-16 nuclear translocation could be a mechanism for G2019S LRRK2-induced oxidative stress and cellular toxicity. Our findings may give a hint that the potential of 14-3-3 proteins as neuroprotective targets in PD patients carrying LRRK2 mutations.

Keywords: Parkinson's disease, G2019S LRRK2, stress, 14-3-3, daf-16, *Caenorhabditis elegans*

INTRODUCTION

Parkinson's disease (PD, [MIM: 168600]) is a neurodegenerative disorder caused by genetic and environmental factors. A substitution of serine for glycine at position 2019 (G2019S) in the kinase domain of leucine-rich repeat kinase 2 (LRRK2, [MIM: 609007]) represents the most prevalent genetic mutation in PD (Zimprich et al., 2004; Di Fonzo et al., 2005; Gilks et al., 2005;

Nichols et al., 2005). Furthermore, oxidative stress is also believed to play an important role in the pathogenesis of PD (Halliwell, 2006; Gandhi and Abramov, 2012), as elevated levels of reactive oxygen species (ROS) have been implicated as a pathological feature of PD. For example, G2019S LRRK2 causes uncoupling of mitochondrial oxidative phosphorylation (Mortiboys et al., 2010; Papkovskaia et al., 2012) which consequently promotes ROS accumulation and neurodegeneration (Lu et al., 2004; Angeles et al., 2011; Lebel et al., 2012). While G2019S LRRK2 and stress are involved in the pathogenesis of PD, the underlying pathway linking these processes is unknown.

DAF-16, a homolog of mammalian FoxO (forkhead box O subclass of transcription factors), is an important transcriptional regulator of genes that rapidly respond to and neutralize the effects of oxidative stress, such as superoxide dismutase (McElwee et al., 2003). Translocation of DAF-16 from cytoplasm into the nucleus is a key step for its transcription factor activity. Moreover, 14-3-3 is a key regulator of DAF-16 nuclear translocation. 14-3-3 proteins can bind to phosphorylated FoxO in mammalian cells (Brunet et al., 1999; Durocher et al., 2000; Obsil et al., 2003) and phosphorylated DAF-16 in *C. elegans* (Cahill et al., 2001), and this binding leads to retention of forkhead proteins in the cytoplasm, thereby rendering them inactive. In parallel, 14-3-3 proteins are also required for SIR-2.1-induced transcriptional activation of DAF-16 and stress resistance (Berdichevsky et al., 2006).

The family of 14-3-3 proteins comprises evolutionarily conserved modulator proteins that regulate multiple signaling pathways through binding to specific Ser/Thr-phosphorylated motifs on target proteins (Tzivion and Avruch, 2002; Tzivion et al., 2006; Morrison, 2009). This protein family includes seven isoforms in mammals (Ichimura et al., 1988; Martin et al., 1993) and two (PAR-5 and FTT-2) in *C. elegans* (Wang and Shakes, 1996). 14-3-3s have been implicated in the pathogenesis of several neurodegenerative diseases including PD, Alzheimer's disease, Huntington's disease and amyotrophic lateral sclerosis. In PD, markedly low levels of 14-3-3 were detected in human PD brain. Disruption of 14-3-3 has been shown to mediate toxicity while overexpression of 14-3-3 is protective via multiple mechanisms such as inhibition of apoptosis and attenuation of protein aggregation in both genetic and toxic models of PD.

14-3-3 proteins have been shown to interact with wild type LRRK2 and several PD-associated LRRK2 mutants including R1441C, R1441G, R1441H, Y1699C, and I2020T, but not G2019S, which has been shown to disrupt the interaction with 14-3-3 proteins (Dzamko et al., 2010; Nichols et al., 2010; Li et al., 2011). Disruption of 14-3-3 protein expression and function has been recently implicated in PD pathogenesis (Slone et al., 2015). Furthermore, a strong neuroprotective effect of enhanced 14-3-3 expression has been shown in multiple cellular and animal models of PD (Yacoubian et al., 2010). Collectively, 14-3-3 proteins play an important role in LRRK2 mutant-linked Parkinsonism.

We hypothesized that G2019S LRRK2 reduces stress resistance by inhibiting DAF-16 nuclear translocation, which may be mediated by *ftt-2*. G2019S disrupts and indirectly decreases the stress response system by increasing sensitivity to stress through DAF-16. 14-3-3 β is a potential target that can rescue the loss of stress resistance ability. To investigate whether 14-3-3 protein can regulate G2019S LRRK2-induced toxicity in the current study, we generated *C. elegans* strains expressing human wild type LRRK2, G2019S LRRK2 and G2019S D1994A kinase-dead (KD) LRRK2, and injected 14-3-3 β into these LRRK2 transgenic worms. We discovered that pan-neuronal expression of G2019S LRRK2 caused defects in stress resistance and impaired stress-induced or 14-3-3 protein-associated DAF-16 nuclear translocation in *C. elegans*. We also investigated G2019S LRRK2-induced defects in *sod-3* and *dod-3* mRNA expression by modulating DAF-16 localization. Our data suggest that human 14-3-3 β [MIM: 601289] protein could rescue G2019S LRRK2-associated toxicity in response to stress.

RESULTS

G2019S LRRK2 Enhanced Toxicity in Response to Environmental Stress and Impaired Stress-Induced DAF-16 Nuclear Translocation

We generated *C. elegans* strains expressing human wild type LRRK2, G2019S LRRK2 and G2019S D1994A KD LRRK2 in all neurons to investigate the responses of different LRRK2 strains to two different kinds of stress conditions: thermal and oxidative (**Supplementary Figures S1**, **S2** and **Supplementary Table S1**). A strain expressing red fluorescent protein (RFP) alone served as a control. Analysis of sensitivity in response to stress was conducted in age-synchronized populations of nematodes. In the present study, all strains remained alive during the first 3 h of heat stress. However, control worms exhibited 50.0% ± 7.1% survival in response to heat stress for 7 h, while survival rates of WT, G2019S and KD transgenic worms were 42.0% ± 7.0%, 18.0% ± 5.4%, and 46.0% ± 7.0%, respectively. Compared with the control strain, WT showed a similar result, but G2019S significantly decreased the survival rate (**Figure 1A**, $p < 0.01$); whereas, KD could rescue G2019S-mediated loss of heat resistance (**Figure 1A**, $p < 0.05$). Meanwhile, similar results were achieved in oxidative stress experiments. RFP control worms exhibited 15.9% ± 3.0% survival after exposure to juglone for 7 h, while survival rates of WT, G2019S and KD transgenic worms were 10.4% ± 2.6%, 6.4% ± 2.0%, and 18.3% ± 3.2%, respectively. Compared with the control strain, WT showed similar results, but G2019S significantly decreased the survival rate (**Figure 1B**, $p < 0.01$); whereas, KD could rescue G2019S-mediated loss of juglone resistance (**Figure 1B**, $p < 0.01$).

DAF-16, a FoxO transcription factor, is a key player in stress resistance in *C. elegans*. Translocation of DAF-16 from the cytoplasm into the nucleus is necessary for its transcriptional activity (Henderson and Johnson, 2001; Lin et al., 2001). A *C. elegans* strain expressing DAF-16::GFP (TJ356) was used to investigate the role of DAF-16 in G2019S-mediated loss of stress resistance. This strain has been shown to respond to environmental stress by displaying DAF-16 nuclear translocation. Three different status of DAF-16 were show in **Figure 1C**. To examine nuclear translocation of DAF-16 in different LRRK2

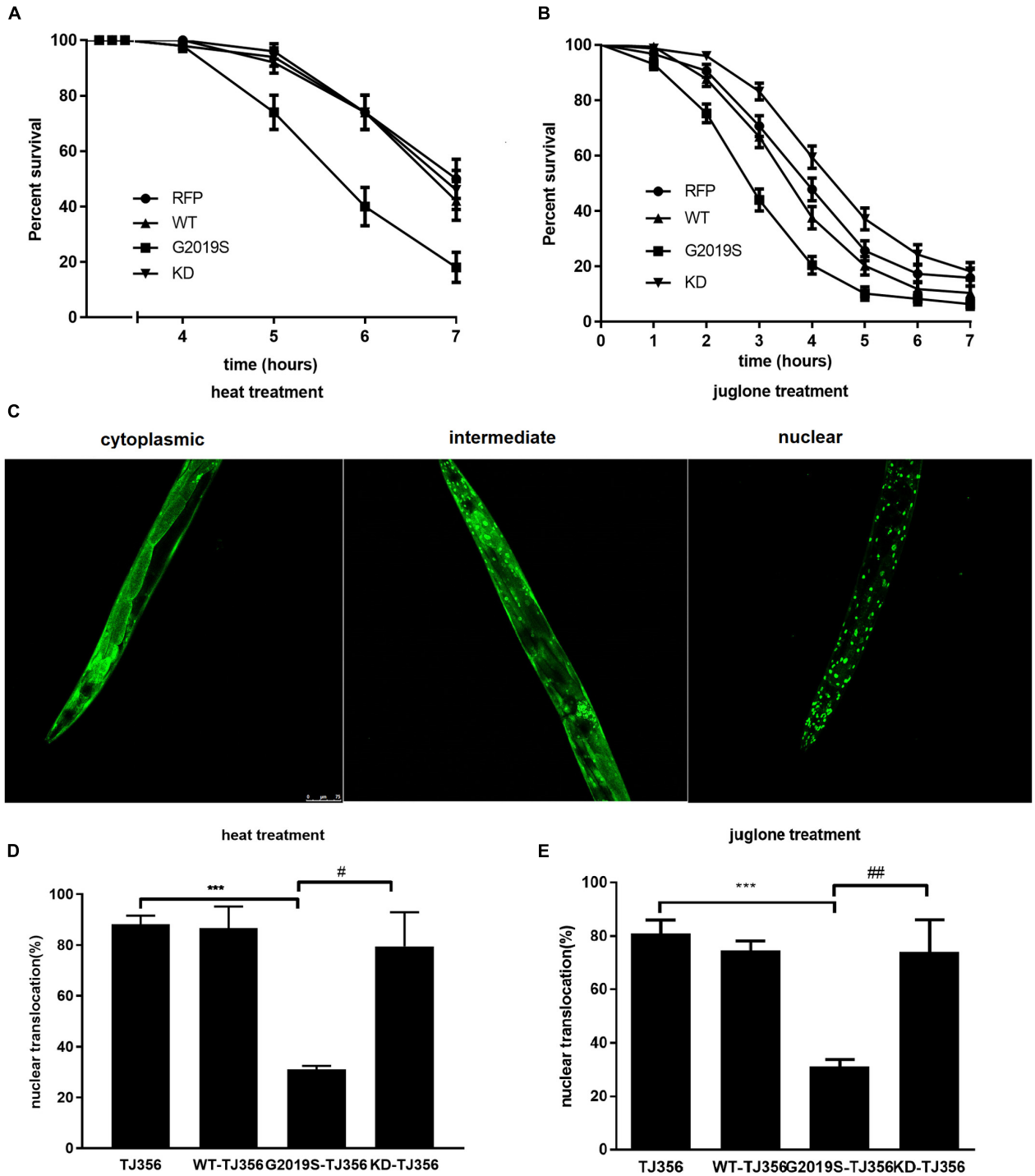

FIGURE 1 | G2019S LRRK2 increased sensitivity to stress and impaired stress-induced DAF-16 nuclear translocation. **(A)** Nematode expressing G2019S LRRK2 increased sensitivity to heat stress. The RFP strain served as a control. **(B)** Nematode expressing G2019S LRRK2 increased sensitivity to oxidative stress (juglone treatment). The RFP strain served as a control. **(C)** Three different status of DAF-16 localization (cytoplasm and nucleus and both). The worm is the TJ356 strain. Scale bar = 75 μm. **(D)** Quantification of stress-induced DAF-16 nuclear translocation in adult synchronized worms. After reaching adulthood, the worms were exposed to heat stress (35°C) or juglone treatment (400 μM) for 1 h and counted for the presence of nuclear or cytoplasmic DAF16::GFP. Intermediate status and nuclear status of DAF-16 were counted as nuclear DAF-16. Error bars indicate SEM. $^{***}P < 0.001$, represent TJ356 vs. G2019S-TJ356. $^{\#}P < 0.05$, represent G2019S-TJ356 vs. KD-TJ356. **(E)** Quantification of stress-induced DAF-16 nuclear translocation in adult synchronized worms. After they reached adulthood, the worms were exposed to juglone (400 μM) for 1 h and counted for the presence of nuclear or cytoplasmic DAF16::GFP. Intermediate status and nuclear status of DAF-16 were counted as the nuclear DAF-16. Error bars indicate SEM. $^{***}P < 0.001$, represent TJ356 vs. G2019S-TJ356. $^{\#\#}P < 0.01$, represent G2019S-TJ356 vs. KD-TJ356.

strains, LRRK2 strains were crossed with the TJ356 strain to generate WT-TJ356, G2019S-TJ356 and KD-TJ356 strains. Numbers of worms exhibiting DAF-16 nuclear translocation was calculated 60 min after heat stress or juglone treatment. DAF-16 was predominantly localized in the cytoplasm in both WT-TJ356 and G2019S-TJ356 strains under normal conditions (data not shown). However, in response to stress, DAF-16 was translocated from the cytoplasm into the nucleus in most of the TJ356 control strain. In contrast, nuclear translocation of DAF-16 was moderate in the G2019S-TJ356 strain (**Figure 1D**, $p < 0.01$ for heat treatment; **Figure 1E**, $p < 0.01$ for juglone treatment). However, KD could rescue G2019S-mediated inhibition of DAF-16 nuclear translocation in response to heat stress (**Figure 1D**, $p < 0.01$) or juglone (**Figure 1E**, $p < 0.01$).

Under stress, percentages of worms exhibiting nuclear translocation of DAF-16 were similar among WT-TJ356, KD-TJ356 and TJ356 strains (heat treatment: TJ356, 88.2% ± 1.4%; G2019S-TJ356, 31.0% ± 1.0%; WT-TJ356, 86.7% ± 4.9%; KD-TJ356, 79.5% ± 9.5%; juglone treatment: TJ356, 81.0% ± 4.9%; G2019S-TJ356, 31.0% ± 2.7%; WT-TJ356, 74.0% ± 3.5%; KD-TJ356, 74.0% ± 12.0%). Thus, our data suggest that G2019S blocks DAF-16 nuclear translocation under stress conditions.

G2019S LRRK2 Inhibited mRNA Expression of Stress-Resistance Genes

DAF-16 controls redox metabolism by regulating the expression of anti-oxidative stress molecules and lifespan-associated genes, such as *sod-3* and *dod-3*. In response to heat stress, we found reduced expression levels of *sod-3* and *dod-3* in the G2019S transgenic *C. elegans* strain compared with controls; notably, both genes are under the regulation of DAF-16. As shown in **Figures 2A,B**, in response to heat stress, the G2019S transgenic strain inhibited mRNA expression of *sod-3* (0.28 ± 0.04-fold, $p < 0.01$ vs. control) and *dod-3* (0.36 ± 0.02-fold, $p < 0.05$ vs. control), while other LRRK2 transgenic strains showed no significant difference from the control strain [*sod-3* expression (WT: 0.83 ± 0.17, KD: 0.90 ± 0.09); *dod-3* expression (WT: 0.80 ± 0.10, KD: 1.07 ± 0.23)].

Similarly, we examined the mRNA expression levels of *sod-3* and *dod-3* of all strains in response to juglone. Compared with the control strain, the G2019S transgenic strain significantly reduced expression levels of *sod-3* and *dod-3*. As shown in **Figures 2C,D**, in response to juglone, the G2019S transgenic strain inhibited mRNA expression of *sod-3* (0.24 ± 0.04-fold, $p < 0.01$ vs. control) and *dod-3* (0.24 ± 0.04-fold, $p < 0.001$ vs. control), while other LRRK2 transgenic strains showed no significant difference from the control strain [*sod-3* expression (WT: 1.15 ± 0.16, KD: 1.08 ± 0.09); *dod-3* expression (WT: 1.06 ± 0.05, KD: 0.99 ± 0.05)]. Thus, our data suggest that G2019S modulates the regulation of stress-resistance genes.

G2019S LRRK2 Impaired DAF-16 Nuclear Translocation in a 14-3-3 Protein-Dependent Manner

The *C. elegans* 14-3-3 protein ortholog FTT-2 acts as a key regulator of DAF-16 by binding to DAF-16 and regulating its sub-cellular localization via sequestration in the cytoplasm (Li et al., 2006). Given that 14-3-3 interacts with LRRK2, we investigated the role of 14-3-3 in G2019S LRRK2-associated inhibition of DAF-16 nuclear localization using RNA-mediated gene interference (RNAi) against *ftt-2*. Western blotting was performed to detect protein expression levels of strains N2 (**Figures 3A,B**) and TJ356, WT-TJ356, G2019S-TJ356, KD-TJ356 (**Figures 3E,F**) fed RNAi control OP50 or *ftt-2* OP50. DAF-16::GFP was diffusely and predominantly localized in the cytoplasm in the progeny of TJ356 receiving control RNAi (L4440), whereas DAF-16::GFP was predominantly localized in the nuclei of the TJ356 strain receiving *ftt-2* RNAi (**Figure 3C**). Furthermore, when worms were fed with control RNAi (L4440), all strains exhibited cytoplasmic localization of DAF-16. After being fed with *ftt-2* RNAi, worms from WT-TJ356 and KD-TJ356 strains exhibited DAF-16 nuclear localization. However, DAF-16 was still localized in the cytoplasm of the G2019S-TJ356 strain. The percentage of worms with nuclear translocation of DAF-16 was approximately the same among WT-TJ356, KD-TJ356 and TJ356 strains (L4440: TJ356, 6.4% ± 1.9%; G2019S-TJ356, 4.3% ± 1.2%; WT-TJ356, 13.4% ± 3.4%; KD-TJ356, 8.0% ± 2.0%; *ftt2* RNAi: TJ356, 88.0% ± 2.0%; G2019S-TJ356, 13.3% ± 1.9%; WT-TJ356, 77.5% ± 2.5%; KD-TJ356, 82.2% ± 11.2%). Compared with the TJ356 control strain, G2019S-TJ356 exhibited a significantly decreased number of nuclear DAF16::GFP (**Figure 3D**, $p < 0.001$); whereas, KD could rescue G2019S-mediated inhibition of DAF-16 nuclear translocation (**Figure 3D**, $p < 0.001$). Thus, our data suggest that G2019S inhibits *ftt-2* -induced DAF-16 nuclear localization.

Human 14-3-3 β Protein Rescued G2019S LRRK2-Associated Toxicity in Response to Stress

To examine whether 14-3-3 can rescue G2019S LRRK2-associated toxicity, we generated *C. elegans* strains co-expressing human 14-3-3 β and LRRK2 by injecting a plasmid containing 14-3-3 β fused with a green fluorescent protein (GFP) marker into WT, G2019S and KD transgenic worms. Subsequently, WT-14-3-3 β, G2019S-14-3-3 β and KD-14-3-3 β were selected using the GFP marker (**Figure 4A**). After exposure to heat stress at 35°C for 7 h, all G2019S worms died, while survival rates were 48.3% ± 6.6% for WT, 62.0% ± 6.9% for WT-14-3-3 β, 47.1% ± 7.0% for G2019S-14-3-3 β, 55.8% ± 4.0% for KD, and 46.8% ± 4.0% for KD-14-3-3 β. The survival rate of G2019S was significantly different from that of G2019S-14-3-3 β (**Figure 4D**, $p < 0.001$), while the survival rate of WT (or KD) was similar to WT-14-3-3 β (or KD-14-3-3 β) (**Figures 4B,F**). In comparison, when worms were exposed to juglone for 7 h, survival rates were 53.1% ± 4.2% for WT, 55% ± 5.0% for WT-14-3-3 β, 22.0% ± 3.4% for G2019S, 52.5% ± 0.0% for G2019S-14-3-3 β, 61.0% ± 4.1% for KD, and 69.3% ± 4.6% for KD-14-3-3 β. The survival rate of G2019S was significantly different from that of G2019S-14-3-3 β (**Figure 4E**, $p < 0.001$), while the survival rate of

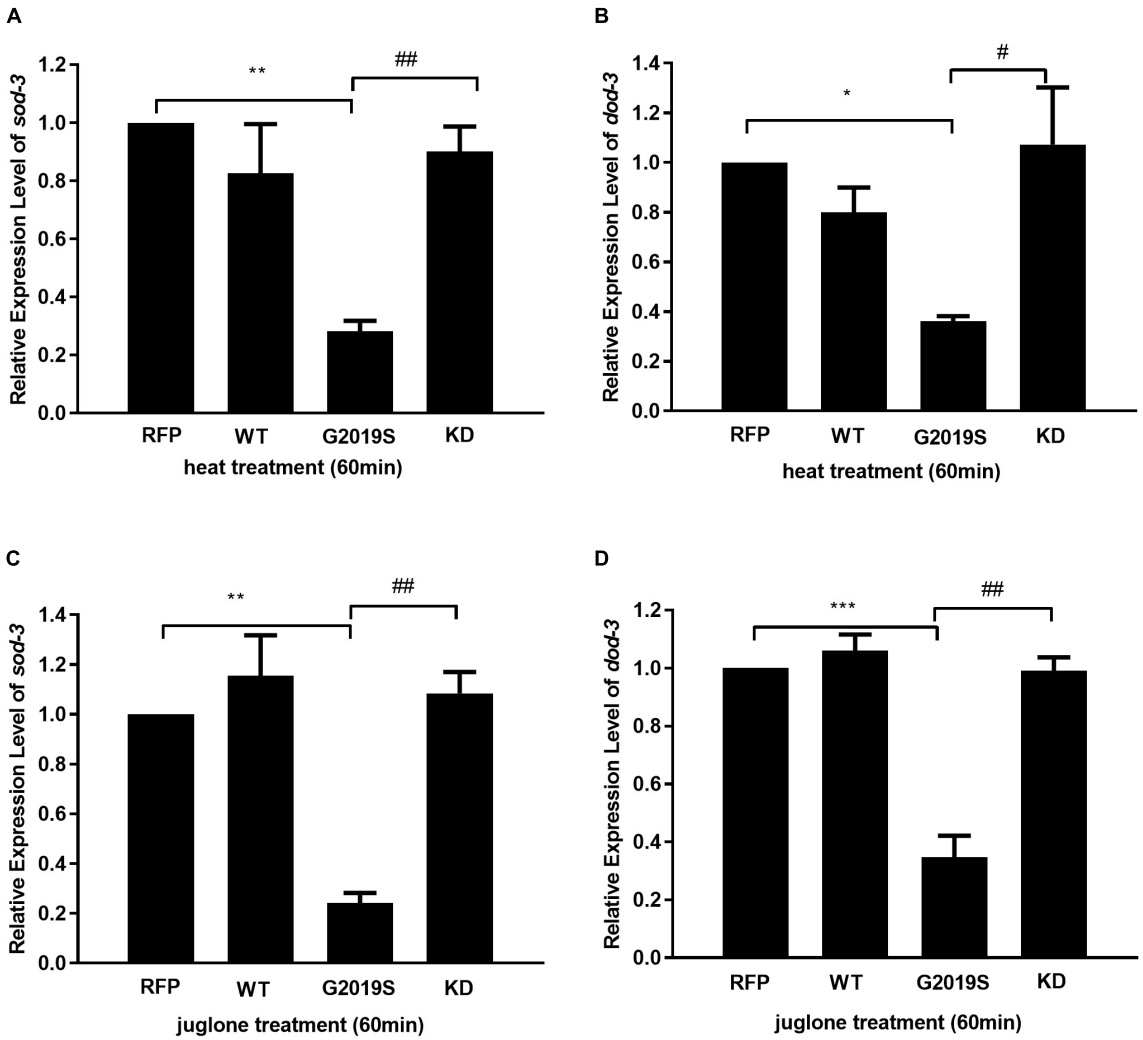

FIGURE 2 | G2019S LRRK2 induced defect in mRNA expression of stress-resistance genes. **(A)** Expression of *sod-3* in transgenic strains after heat treatment for 60 min. Nematodes expressing G2019S showed reduced expression of *sod-3* (**$p < 0.01$ versus RFP strain) whereas KD could rescue G2019S-mediated deficit in expression of *sod-3* ($^{\#\#}p < 0.01$ versus G2019S strain). **(B)** Expression of *dod-3* in transgenic strains after heat treatment for 60 min. Nematodes expressing G2019S showed reduced expression of *dod-3* (*$p < 0.05$ versus RFP strain) whereas KD could rescue G2019S-mediated deficit in expression of *dod-3* ($^{\#}p < 0.05$ versus G2019S strain). **(C)** Expression of *sod-3* in transgenic strains after juglone treatment for 60 min. Nematodes expressing G2019S LRRK2 showed reduced expression of *sod-3* (**$p < 0.01$ versus RFP strain) whereas KD could rescue G2019S LRRK2-associated defect in mRNA expression of *sod-3* ($^{\#\#}p < 0.01$ versus G2019S strain). **(D)** Expression of *dod-3* in transgenic strains after juglone treatment for 60 min. Nematodes expressing G2019S LRRK2 showed reduced expression of *dod-3* (***$p < 0.001$ versus RFP strain) whereas KD could rescue G2019S LRRK2-associated defect in mRNA expression of *dod-3* ($^{\#\#}p < 0.01$ vs. G2019S strain).

WT (or KD) was similar to WT-14-3-3 β (or KD-14-3-3 β) (**Figures 4C,G**).

Human 14-3-3 β Protein Rescued G2019S LRRK2-Mediated Inhibition of Stress-Resistance Gene mRNA Expression

Our data show that co-expression of human *14-3-3* β can rescue the expression of stress-resistant genes *sod-3* and *dod-3* in the G2019S transgenic strain in response to heat stress. When worms were exposed to heat stress at 35°C for 1 h, mRNA expression of *sod-3* and *dod-3* in the G2019S strain was significantly different from that of G2019S-14-3-3 β (**Figures 5C,D**, $p < 0.001$); whereas, the survival rate of WT (or KD) was similar to WT-14-3-3 β (or KD-14-3-3 β) (**Figures 5A,B,E,F**). Expression of *sod-3* in WT-14-3-3 β, G2019S-14-3-3 β, and KD-14-3-3 β was 0.88 ± 0.03, 0.92 ± 0.15, and 0.88 ± 0.12, respectively; whereas, *dod-3* expression was 1.41 ± 0.13, 1.16 ± 0.08, and 1.25 ± 0.13, respectively.

As shown in **Figure 5**, human 14-3-3β can rescue expression of stress-resistant genes *sod-3* and *dod-3* in the G2019S transgenic strain in response to juglone. When worms were exposed to juglone for 1 h, mRNA expression of *sod-3* and *dod-3* in the

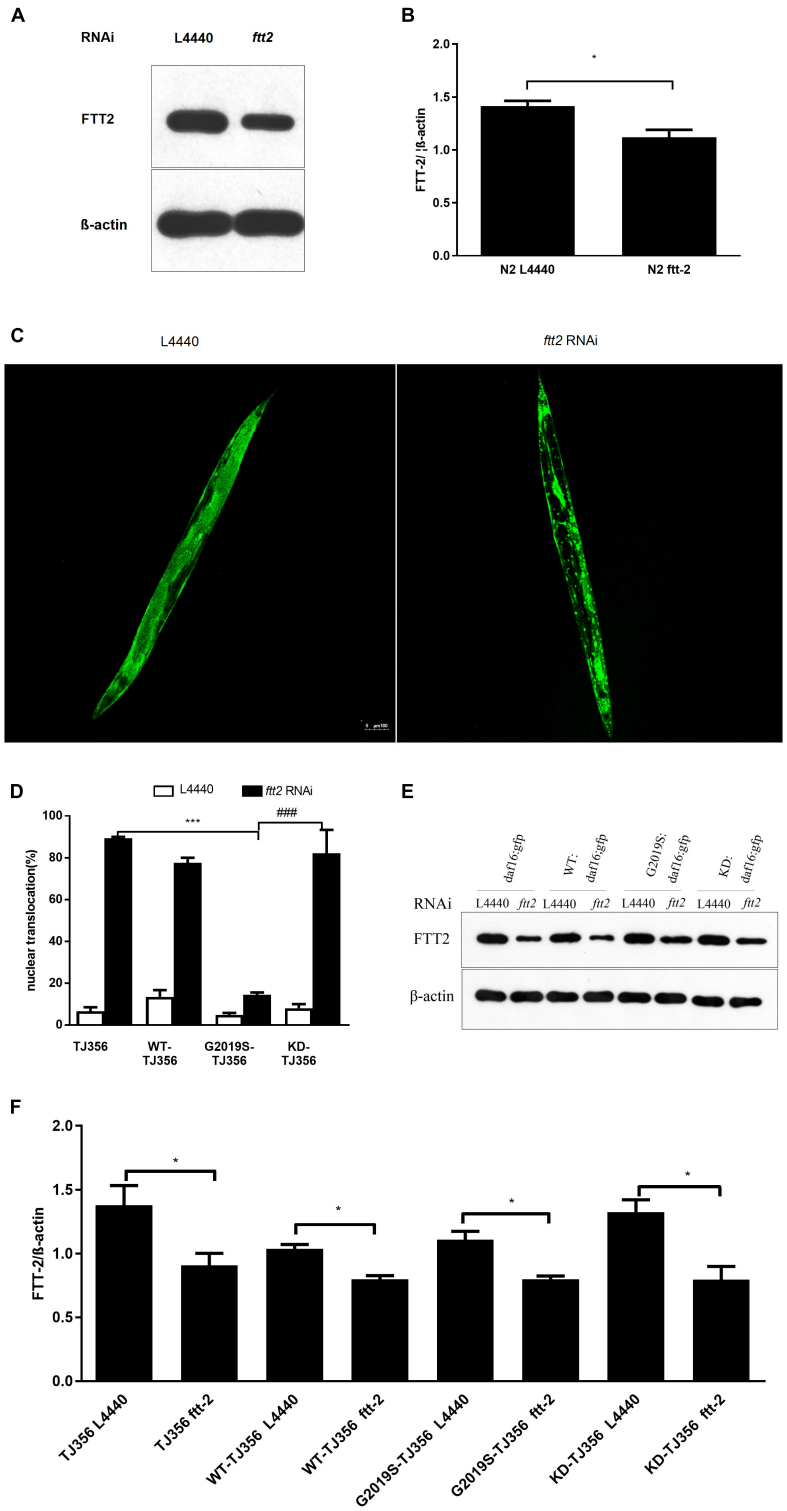

FIGURE 3 | *C. elegansftt-2* is important in G2019S LRRK2-associated defect in DAF-16 nuclear translocation. Worms were synchronized and fed with control (L4440) RNAi or *ftt-2* RNAi. Worm lysate was followed by Western blotting with an antibody against pan 14-3-3 to detect FTT-2 protein (28 kDa). **(A)** Detection on Western blots of FTT-2 proteins (28 kDa) in N2 strain fed with control (L4440) RNAi or *ftt-2* RNAi. **(B)** Quantification to show the effect of *ftt2* RNAi. $*p < 0.05$. **(C)** Representative images show cytoplasmic localization (treated with control L4440 RNAi) and DAF-16 nuclear localization (treated with *ftt-2* RNAi). Scale bar = 100 μm. **(D)** Quantification of DAF-16 nuclear localization. Error bars indicate SEM. **(E)** Detection on Western blots of FTT-2 proteins (28 kDa) in *C. elegans* fed with control (L4440) RNAi or *ftt-2* RNAi. Worm lysate was followed by Western blotting with an antibody against pan-14-3-3. **(F)** Quantification to show the effect of *ftt2* RNAi. $*p < 0.05$, $***p < 0.001$ for TJ356 vs.G2019S TJ356; $###p < 0.001$ for G2019S TJ356 vs. KD TJ356.

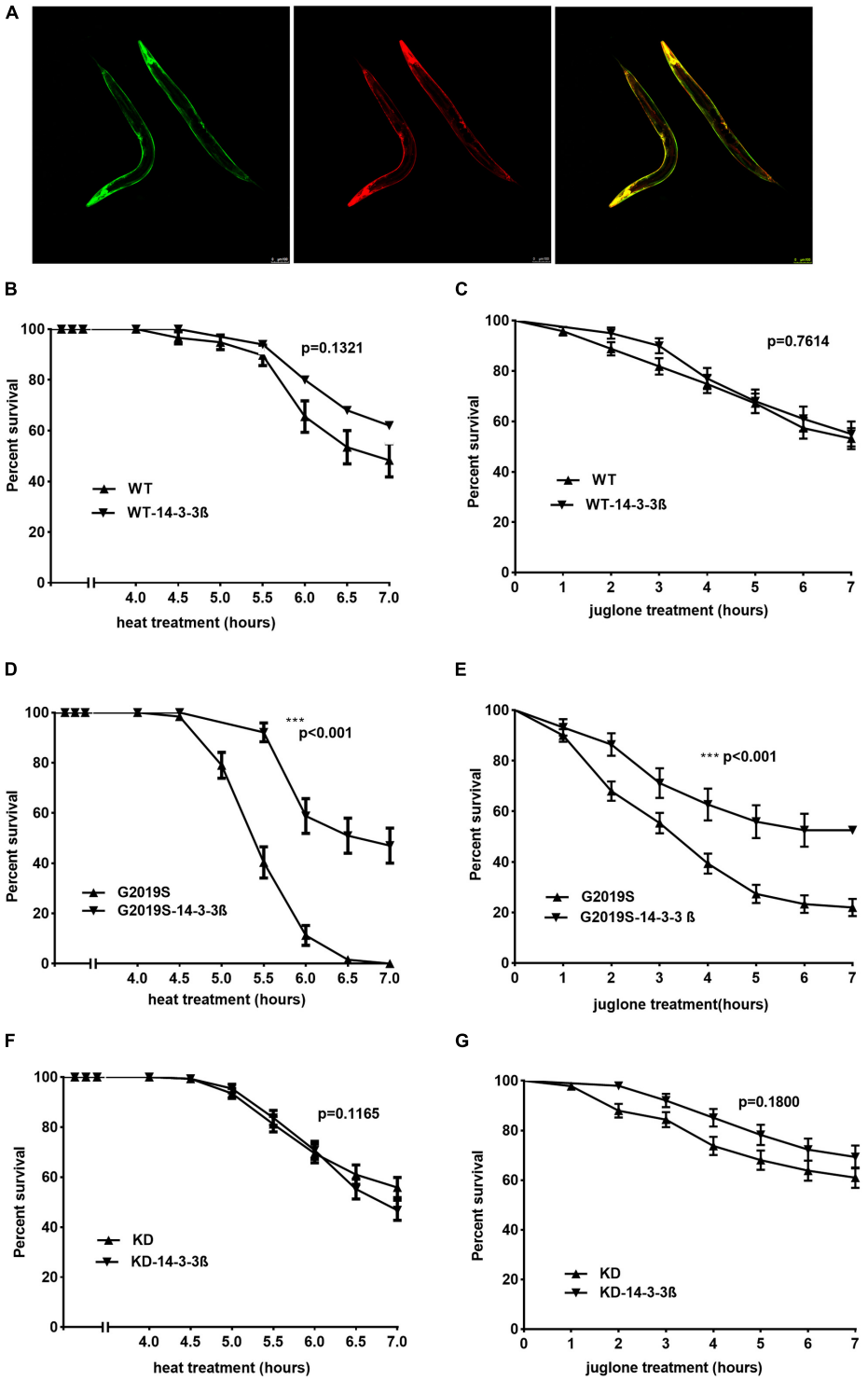

FIGURE 4 | 14-3-3 β protein can rescue G2019S LRRK2-associated toxicity in response to stress. **(A)** Representative images of adult worms pan-neuronal expressing human 14-3-3 β in LRRK2 transgenic worms visualized by epifluorescence microscopy (GFP fused with 14-3-3; RFP co-injection with LRRK2). Scale bar = 100 μm. **(B)** Human 14-3-3 β showed no effect on WT LRRK2 in response to heat stress. Error bars indicate SEM. $P = 0.1321$. **(C)** Human 14-3-3 β showed no effect on WT LRRK2 in response to juglone. Error bars indicate SEM. $P = 0.7614$. **(D)** Human 14-3-3 β can rescue G2019S LRRK2-associated toxicity in response to heat stress. Error bars indicate SEM. $^{***}p < 0.001$. **(E)** Human 14-3-3 β can rescue G2019S LRRK2-associated toxicity in response to juglone. Error bars indicate SEM. $^{***}p < 0.001$. **(F)** Human 14-3-3 β showed no effect on KD LRRK2 in response to heat stress. Error bars indicate SEM. $P = 0.1165$. **(G)** Human 14-3-3 β showed no effect on KD LRRK2 in response to juglone. Error bars indicate SEM. $P = 0.1800$.

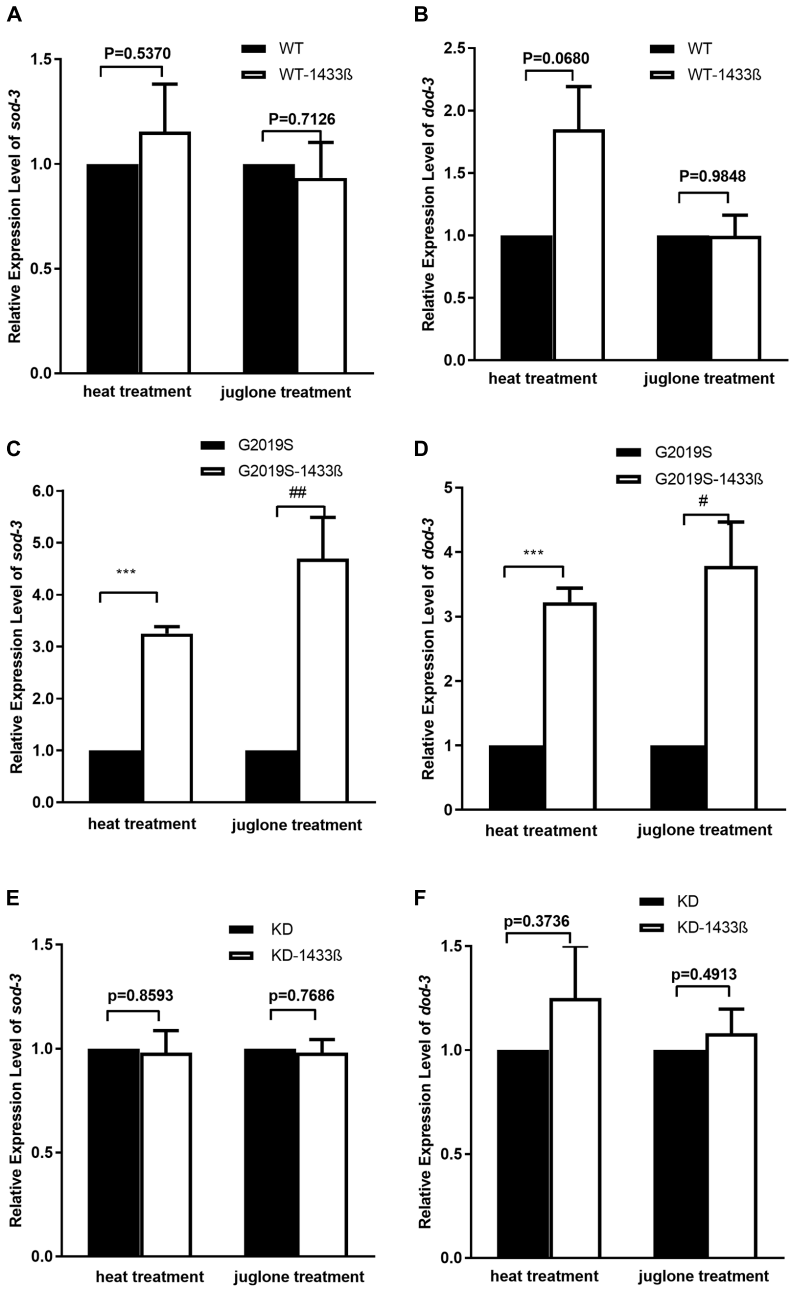

FIGURE 5 | 14-3-3 β protein can rescue G2019S LRRK2-associated defect in mRNA expression of stress-resistance genes. **(A)** Expression of *sod-3* in transgenic strains after heat treatment for 60 min. Human 14-3-3 β showed no effect on WT LRRK2 in mRNA expression of *sod-3* ($p = 0.5370$). Expression of *sod-3* in transgenic strains after juglone treatment for 60 min. Human 14-3-3 β showed no effect on WT LRRK2 in mRNA expression of *sod-3* ($p = 0.7126$). **(B)** Expression of *dod-3* in transgenic strains after heat treatment for 60 min. Human 14-3-3 β showed no effect on WT LRRK2 in mRNA expression of *dod-3* ($p = 0.0680$). Expression of *dod-3* in transgenic strains after juglone treatment for 60 min. Human 14-3-3 β showed no effect on WT LRRK2 in mRNA expression of *dod-3* ($p = 0.9849$). **(C)** Expression of *sod-3* in transgenic strains after heat treatment for 60 min. Human 14-3-3 β could rescue G2019S LRRK2-associated deficit in mRNA expression of *sod-3* ($^{***}p < 0.001$ versus G2019S strain). Expression of *sod-3* in transgenic strains after juglone treatment for 60 min. Nematodes expressing G2019S LRRK2 showed reduced expression of *sod-3* ($^{\#\#}p < 0.01$ versus RFP strain). **(D)** Expression of *dod-3* in transgenic strains after heat treatment for 60 min. Human 14-3-3 β could rescue G2019S LRRK2-associated deficit in mRNA expression of *dod-3* ($^{***}p < 0.001$ versus G2019S strain). Expression of *dod-3* in transgenic strains after juglone treatment for 60 min. Nematodes expressing G2019S LRRK2 showed reduced expression of *dod-3* ($^{\#}p < 0.05$ versus G2019S strain). **(E)** Expression of *sod-3* in transgenic strains after heat treatment for 60 min. Human 14-3-3 β showed no effect on KD LRRK2 in mRNA expression of *sod-3* ($p = 0.8593$). Expression of *sod-3* in transgenic strains after juglone treatment for 60 min. Human 14-3-3 β showed no effect on KD LRRK2 in mRNA expression of *sod-3* ($p = 0.7686$). **(F)** Expression of *dod-3* in transgenic strains after heat treatment for 60 min. Human 14-3-3 β showed no effect on KD LRRK2 in mRNA expression of *dod-3* ($p = 0.3736$). Expression of *dod-3* in transgenic strains after juglone treatment for 60 min. Human 14-3-3 β showed no effect on KD LRRK2 in mRNA expression of *dod-3* ($p = 0.4913$).

G2019S strain was significantly different from that of G2019S-14-3-3 β (**Figures 5C,D**, $p < 0.01$ for *sod-3* and $p < 0.05$ for *dod-3*); whereas, the survival rate of WT (or KD) was similar to WT-14-3-3 β (or KD-14-3-3 β) (**Figures 5A,B,E,F**). Expression of *sod-3* in WT-1433 β, G2019S-1433 β, and KD-1433 β was 1.02 ± 0.04, 1.07 ± 0.01, and 1.05 ± 0.02, respectively; whereas, *dod-3* expression was 1.05 ± 0.16, $1.21 \pm 0.09$and 1.07 ± 0.11, respectively.

DISCUSSION

In the present study, we examined the role of 14-3-3 and DAF-16 proteins in LRRK2 pathophysiology in *C. elegans*. Our data is consistent with our hypothesis that G2019S LRRK2 increased sensitivity to stress and impaired stress-induced DAF-16 nuclear translocation. Furthermore, G2019S LRRK2 inhibited 14-3-3 protein-associated DAF-16 nuclear translocation. In contrast, overexpression of human 14-3-3 β could rescue G2019S LRRK2-associated toxicity in response to stress and ameliorate G2019S LRRK2-associated down-regulation of *sod-3* and *dod-3* expression (two DAF-16 pathway genes). Collectively, the present data suggest that increased stress susceptibility of G2019S LRRK2 is associated with inhibition of DAF-16 nuclear translocation in a 14-3-3-associated manner. Given the critical role of DAF-16 in stress resistance, our findings imply that DAF-16 may play an important role in 14-3-3-mediated attenuation of G2019S LRRK2 toxicity.

G2019S Increases Sensitivity to Stress by Impairing Nuclear Localization of DAF-16

We generated transgenic *C. elegans* expressing human WT LRRK2 and PD-linked mutant G2019S LRRK2 or G2019S kinase dead LRRK2 in all neurons. Consistent with previous studies, sensitivity to stress was significantly increased in G2019S worms.

DAF-16, the only FoxO transcription factor in *C. elegans*, plays an important role in stress resistance. DAF-16 is activated by nuclear translocation in response to environmental stress. Once DAF-16 is activated, it activates expression of downstream genes such as *sod-3* and *dod-3* to increase stress resistance. Consistently, under heat and juglone stress, nuclear translocation of DAF-16 was evident in most *C. elegans* of both control and WT strains; whereas, DAF-16 was only detected in a relatively small population of G2019S *C. elegans*. Furthermore, G2019S-induced impairment of DAF-16 nuclear translocation resulted in loss of stress resistance, suggesting that blockage of DAF-16 nuclear translocation may be one mechanism by which G2019S elicits toxicity.

G2019S Impairs 14-3-3 Knockdown-Induced DAF-16 Nuclear Translocation

Previously, LRRK2 has been shown to directly phosphorylate FoxO, an analog of DAF-16, initiating an apoptotic pathway (Kanao et al., 2010). Phosphorylation of DAF-16 is a key upstream event of DAF-16 signaling. Following phosphorylation, DAF-16 can translocate to the nucleus to activate downstream gene expression. The 14-3-3 family of proteins is a major player in the regulation of DAF-16 translocation between the nucleus and cytoplasm. For example, the 14-3-3 protein FTT-2 has been reported to bind to Akt-phosphorylated DAF-16 and consequently confine it to the cytoplasm. However, inhibition of 14-3-3 protein by either genetics or stress (oxidative or heat stress) (Oh et al., 2005; Sunayama et al., 2005; Landis and Murphy, 2010) promotes nuclear translocation of DAF-16. Consistently, in the present study, 14-3-3 knockdown by siRNA induced DAF-16 nuclear translocation. Furthermore, G2019S blocked, whereas G2019S kinase dead completely restored, 14-3-3 knockdown-induced nuclear translocation of DAF-16. Collectively, our data suggest that G2019S blocked 14-3-3 knockdown-induced nuclear translocation of DAF-16 in a kinase-dependent manner.

14-3-3 β Ameliorates G2019S LRRK2-Induced Toxicity by Restoring *sod-3* and *dod-3*

14-3-3 proteins are a key hub for dysregulated proteins in transcriptional analysis of PD patients (Ulitsky et al., 2010). All 14-3-3 isoforms except 14-3-3 σ can interact with the PD-related protein LRRK2 (Nichols et al., 2010). Our results showed that overexpression of human 14-3-3 β could rescue G2019S LRRK2-associated deficiency in response to stress. Additionally, this rescue effect was associated with restored expression of *sod-3* and *dod-3* in G2019S worms. Given that *sod-3* and *dod-3* are direct downstream genes of DAF-16, our results suggest that 14-3-3 may rescue G2019S-mediated loss of stress resistance via modulation of DAF-16 activity.

Potential Interplay Among LRRK2, 14-3-3, and DAF-16

Phosphorylation of DAF-16 is a key event in DAF-16 signaling pathways. Phosphorylation can promote or inhibit DAF-16 nuclear translocation depending on the function of kinases. For example, phosphorylation by Akt restricts DAF-16 to the cytoplasm, while JNK promotes nuclear translocation (Oh et al., 2005).

We found that G2019S LRRK2 could block stress/14-3-3 knockdown-associated nuclear translocation. This event is kinase-dependent, as the kinase dead strain of G2019S completely rescued this event. Given that LRRK2 can directly interact with 14-3-3 and DAF-16, both interactions may have a role in nuclear translocation of DAF-16. Interestingly, pathogenic mutations such as R1441C, R1441G, R1441H, Y1699C, and I2020T, but not G2019S, disrupt the interaction with 14-3-3 (Nichols et al., 2010). Furthermore, oxidative stress reportedly reduces the binding of 14-3-3 to WT, kinase-dead LRRK2 and G2019S to the same degree (Mamais et al., 2014). Thus, the interaction of G2019S with 14-3-3 is less likely to play a critical role in DAF-16 nuclear translocation.

LRRK2 has been reported to phosphorylate FoxO1 at S319 (Kanao et al., 2010). We also identified S314 to be a conserved phosphorylated site in DAF-16 (**Figure 6A**). In the present

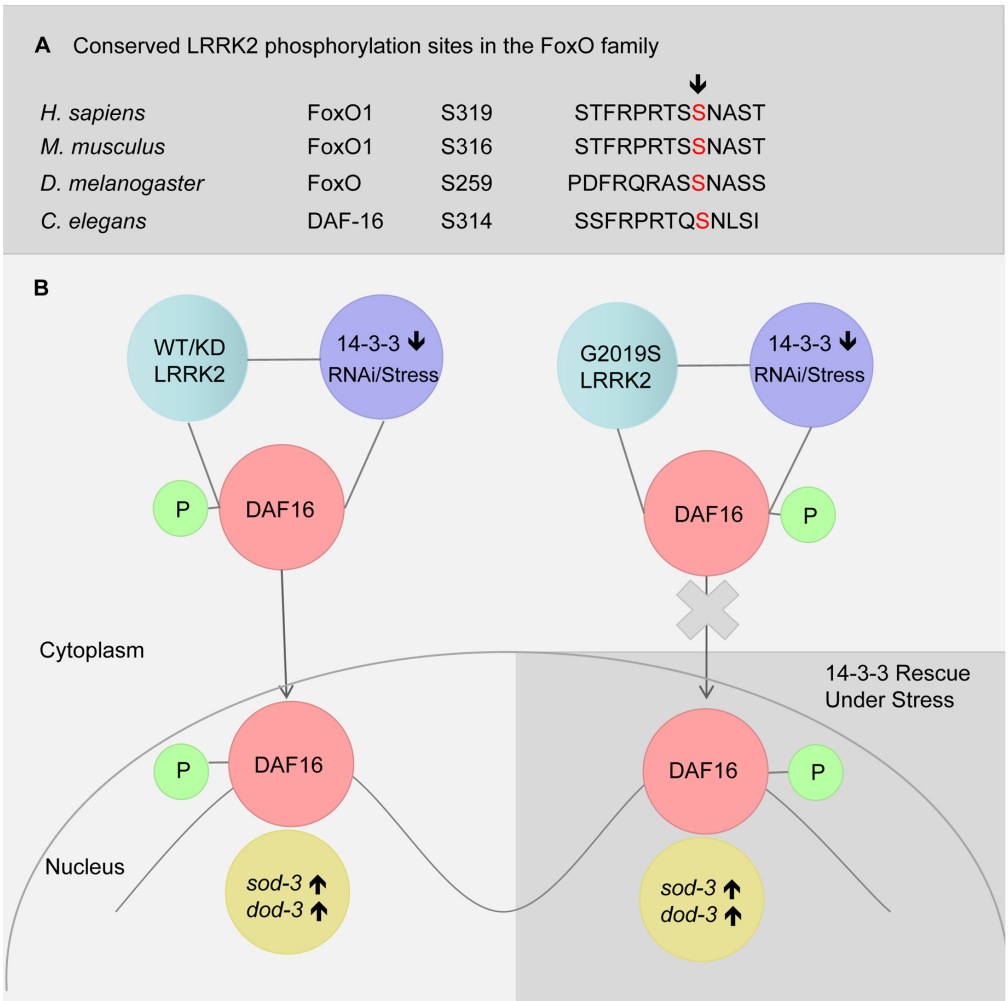

FIGURE 6 | A model of LRRK2 and 14-3-3 associated DAF-16 nuclear translocation in response to stress. **(A)** Alignment of putative LRRK2 phosphorylation sites in FoxO family. **(B)** RNAi knockdown of 14-3-3 or stress (heat or juglone treatment) induced DAF-16 nuclear translocation in *C. elegans* expressing WT-LRRK2 or G2019S-KD LRRK2. Meanwhile, G2019S LRRK2 inhibited DAF-16 nuclear translocation, resulting in stress response deficiency which was rescued by 14-3-3.

study, G2019S did not affect sub-cellular localization of DAF-16 under normal conditions (data not shown). We propose that G2019S LRRK2 phosphorylation of DAF-16 inhibits nuclear translocation under normal conditions. There may be two possible explanations for this observation. First, phosphorylation of DAF-16 by G2019S alone may not be sufficient to induce the translocation of DAF-16. Alternatively, G2019S-mediated phosphorylation of DAF-16 may restrict DAF-16 to the cytoplasm. In the current study, we found that G2019S impaired 14-3-3 knockdown-induced DAF-16 translocation, suggesting that the second possibility is the most likely scenario. Normally in WT and G2019S-KD LRRK2, LRRK2 binds with DAF-16 following its phosphorylation to restrict DAF-16 to the cytoplasm. Under stress and 14-3-3 knockdown, 14-3-3 may interact with additional kinases such as JNK to further promote DAF-16 nuclear translocation (**Figure 6B**). In the case of G2019S LRRK2, G2019S possesses increased kinase activity in relation to LRRK2; thus, under stress or 14-3-3 knockdown, G2019S negatively regulates DAF-16 to prevent nuclear translocation. Further study is needed to examine whether G2019S can indeed phosphorylate specific sites of DAF-16 to directly restrict DAF-16 nuclear translocation or indirectly via reduce the interaction between DAF-16 and 14-3-3. Finally, given the complex regulatory mechanisms of DAF-16 translocation, other possibilities such as varying phosphorylation levels, roles for additional kinases including Akt and JNK, potential involvement of Sir2, and post-translational modifications also need further investigation.

MATERIALS AND METHODS

Strains

Several *C. elegans* strains were obtained from the Caenorhabditis Genetics Center or elsewhere, as indicated, including Bristol N2, TJ356, and BZ555 strains. All strains used were maintained

and handled as previously described (Brenner, 1974). Strains were maintained at 20°C on NGM plates with OP50 as food, unless otherwise noted. Bristol N2 was used as a reference strain. NGM was made with Agar (MBCHEN) and Tryptone (OXOID, Ltd.) and other chemicals from Guangzhou Chemical Reagent Factory. Mixed-stage animals were maintained as bulk culture on NGM agar at room temperature (20°C). For most experiments, *C. elegans* strains were age synchronized using a bleaching method, and underwent development from larval stage L1 to L4, which was considered as the beginning of adulthood and counted as adult day 0. L4-stage worms were then picked and transferred to new NGM plates for growth into adults.

Plasmids

Human cDNA encoding full-length FLAG-tagged human WT LRRK2 and mutants (LRRK2 G2019S and G2019S KD) generated by site-directed mutagenesis were previously constructed in pcDNA3.1 vectors, as described (Smith et al., 2005). The *C. elegans* promoter for the pan-neuronal transporter UNC51 was used to drive transgene expression in all neurons. The pu51p vector including unc51 promoter was obtained from Kuwahara et al. (2008). The pu51p vector was used as a *C. elegans* expression vector. We constructed transgenic plasmids expressing human WT LRRK2 and mutants (G2019S and G2019S KD) with the pu51p vector. WT LRRK2 and mutant (G2019S and G2019S KD) LRRK2 cDNA fragments were obtained by cutting between *NheI* and *BamHI* sites of modified pcDNA3.1 and inserting fragments into pu51p between *NheI* and *KpnI* sites of pu51p. Additionally, we constructed transgenic a pu51p-14-3-3 β-GFP plasmid expressing 14-3-3 β protein fused with eGFP. First, the enhanced GFP sequence was inserted into *XhoI* and *SacI* sites of pu51p. Second, the PCR product of 14-3-3 β was inserted into *NheI* and *XhoI* sites immediately upstream of GFP in the modified pu51p to create pu51p-14-3-3-GFP. All RNAi vectors were purchased from Open Biosystems (Boston, MA, United States).

Generating Transgenic *C. elegans* Strains

LRRK2 transgenic nematodes were created by co-injecting a cocktail of DNA containing 50 ng/μL of pu51p-WT LRRK2, pu51p-G2019S LRRK2, or pu51p-G2019S KD LRRK2 plasmid along with the co-marker pu51p-RFP (100 ng/μL). Human *14-3-3* β transgenic nematodes were created by injecting 100 ng/μL of pu51p-14-3-3β-GFP plasmid. This cocktail of DNA was injected into the gonad of young adult hermaphrodites of the N2 strain using a previously described method (Mello et al., 1991). Injected nematodes were grown at 20°C. Nematodes with stable arrays (over 50% transmittance) were analyzed by PCR for the presence LRRK2 cDNA and chosen for chromosomal integrations. L4 nematodes carrying arrays were subjected to UV-irradiation (30,000 μJ/cm^2) and grown further to generate F1 progenies. Two hundred F1 nematodes were individually grown in a single plate and selected for 75% transmittance. Four nematodes were picked from every F2 population with 75% transmittance, and then individually grown in single plate and selected for 100% transmittance. With a yield of 1–2% stable integrants, transgenic nematodes were out-crossed with Bristol N2 nematodes at least five times and PCR analyzed for the presence of transgenic cDNA. LRRK2/DAF-16::GFP strains (carrying GFP) were created by conventional crossing of WT LRRK2 or mutant LRRK2 strains with TJ356 (DAF-16::GFP), and verified by checking both RFP and GFP markers. Representative integrated strains from each strain were used in repeated experiments throughout this study, and their detailed genotypes and strain designations are listed in **Table 1**.

Nematodes were synchronized either by a bleaching method or letting nematodes lay eggs for 2–3 h.

Stress Assay

Assays were performed using two dishes of 25 adult nematodes for each condition and strain. Nematodes were exposed to NGM agar containing 400 μM juglone or heated to 35°C. Treatment with juglone was begun on adult day 3, while treatment at 35°C was begun on adult day 2. Nematode viability was checked every hour with a soft touch at the tip of pharynx of the nematode. Nematodes that crawled up the side of the plate were excluded from all analyses.

RNAi Knockdown

RNAi knockdown assay was performed according to Kamath et al. (2001). HT115 bacteria was grown overnight in LB media containing 50 μg/mL ampicillin. Bacteria was then plated on NGM plates containing 1 mM IPTG and allowed to grow overnight at room temperature. Nematodes were synchronized by a bleaching method and exposed at L4 stage to HT115 bacteria containing either the pL4440 expression vector with the *ftt2* open reading frame (ORF) (Open Biosystems) or empty vector. On

TABLE 1 | Transgenic *C. elegans* strains used in this study.

Designation	Genotype
1. RFP	*Punc51p::RFP*
2. WT	*Punc51p::LRRK2(WT)*
3. G2019S	*Punc51p::LRRK2(G2019S)*
4. KD	*Punc51p::LRRK2(G2019S D1994A)*
5. TJ356	*zls356 IV [DAF-16p::DAF-16a/b::GFP + rol-6]*
6. WT-TJ356	*Punc51p::LRRK2(WT);zls356 IV*
7. G2019S-TJ356	*Punc51p::LRRK2(G2019S);zls356 IV*
8. KD-TJ356	*Punc51p::LRRK2(G2019S D1994A);zls356 IV*
9. WT-14-3-3β	*Punc51p::LRRK2(WT);Punc51p::14-3-3β::GFP*
10. G2019S-14-3-3β	*Punc51p::LRRK2(G2019S);Punc51p::14-3-3β::GFP*
11. KD-14-3-3β	*Punc51p::LRRK2(G2019S D1994A);Punc51p::14-3-3β::GFP*

TABLE 2 | Amplimer sets used for PCR.

Name	Forward sequence	Reverse sequence
act-1	5′-CACGGTATCGTCACCAACTG-3′	5′-GCTTCAGTGAGGAGGACTGG-3′
sod-3	5′-TCGGTTCCCTGGATAACTTG-3′	5′-TTCCAAAGGATCCTGGTTTG-3′
dod-3	5′-GCCATGTGCATATTGTGGAG-3′	5′-AGGAGGACGTATCCGATGAA-3′

adult day 2 of the next generation, nematodes were used in several experiments.

DAF-16 Nuclear Localization Assay

For quantification of DAF-16::GFP localization, synchronized eggs from TJ356 animals (i.e., transgenic animals expressing DAF-16::GFP) or other strains (as indicated) were seeded onto either control or appropriate RNAi plates. For stress response experiments, adult day 1 worms were transferred to new plates and subjected to heat shock (35°C) or plates containing 400 μM juglone. GFP localization was then analyzed using a Nikon AZ100 fluorescent microscope at 5× magnification. An animal was scored as having nuclear GFP if more than one head hypodermic nuclei contained DAF-16::GFP. For single time point experiments, worms were blindly scored for the presence or absence of GFP accumulation within the nuclei of indicated cells ($n \geq 120$ or greater).

Western Blotting

Protein extracts were prepared from mixed-stage worms grown to near confluence on five 60-mm NGM plates. Worms were washed with M9 buffer and collected by brief centrifugation at 3,000 × *g* for 1 min. The worm pellet was homogenized in ice-cold lysed buffer (1% Triton X-100 in PBS) supplemented with a cocktail of protease inhibitors (Roche), and then sonicated five times for 5 s each. The mixture was then incubated on ice for 30 min. Homogenates were clarified after centrifugation at 14,000 × *g* for 20 min. The supernatant was collected for sodium dodecyl sulfate polyacrylamide gel electrophoresis (SDS-PAGE) and Western blotting using anti-14-3-3 (1:8000, Abcam) for FTT-2 detection. An anti-actin antibody (1:4000, PTG) was used for protein control.

Quantitative RT Real-Time PCR Assay

Total RNA from *C. elegans* was extracted using an E.Z.N.A. total RNA extraction kit (OMEGA Biotek). Intact RNA was checked by running a 1.0% agarose/formaldehyde gel and quantified spectrometrically (Beckman Coulter DU 800) before proceeding to subsequent steps. Five-hundred nanograms of total RNA were reverse-transcribed using PrimeScript™ RT Master Mix (Perfect Real Time) Kit (Takara) according to the manufacturer's instructions. Real-Time PCR was performed on an Opticon MONITORTM Software (MJ Research) using SYBR® Premix Ex Taq™ II (TliRNaseH Plus) (Takara). Expression levels for each target gene were calculated by the $2^{-\Delta\Delta CT}$ method (Livak and Schmittgen, 2001). All analyses were performed in triplicate. Primers used for RT real-time PCR are listed in **Table 2**.

Statistical Analysis

Survival analysis was done using logrank test. According to reference and previous study, we need 50 animals per group. Statistical analysis was done using SPSS Statistics software. Survival curves were analyzed by the Kaplan–Meier method. Chi-square was conducted in the daf16 translocation assay. We take Convenience Sampling. At least 50 animals were randomly selected in stress assay and 30 animals were randomly selected in daf16 translocation assay. Descriptive statistics of the results are using mean and SD. Results of Western and qRT-PCR were evaluated by using a *t*-test. All the curves and column diagrams were performed using Graphpad Prism 7 software.

AUTHOR CONTRIBUTIONS

SL and ZP conceived and coordinated the study and wrote the paper. SL, FS, and WG designed, performed, and analyzed the experiments shown in **Figures 1**, **2**, **4**, **5**. SL, YZ, and SH designed, performed, and analyzed the experiments shown in **Figures 3**, **6**. JZ, CR, and E-KT provided technical assistance and contributed to the preparation of the figures. All authors reviewed the results and approved the final version of the manuscript.

FUNDING

The study was supported by the grants from: the National Natural Science Foundation of China (Grant Nos. 81671102 and 81371255); The National Key Research and Development Program of China, Stem Cell and Translational Research (Grant No. 2017YFA0105104); Guangdong provincial science and technology plan project (Grant Nos. 2016B030230002 and 2017A040406007); Guangdong Provincial Key Laboratory for Diagnosis and Treatment of Major Neurological Diseases (Grant No. 2017B030314103); The Southern China International Cooperation Base for Early Intervention and Functional Rehabilitation of Neurological Diseases (2015B050501003); and Guangdong Provincial Engineering Center for Major Neurological Disease Treatment.

ACKNOWLEDGMENTS

We are grateful to Dr. King L. Chow, Hong Kong University of Science and Technology for assistance in helping us learn techniques in developing stable *C. elegans* lines. We are also thankful to Dr. Bin Hu for providing input on the models, our results, and final editing. This study was supported by the grants from Some nematode strains used in this work were provided by the Caenorhabditis Genetics Center, which is funded by the NIH National Center for Research Resources (NCRR). We also thank LiwenBianji, Edanz Group China (www.liwenbianji.cn/ac), for editing the English text of a draft of this manuscript.

SUPPLEMENTARY MATERIAL

The Supplementary Material for this article can be found online at: https://www.frontiersin.org/articles/10.3389/fnins.2018.00782/full#supplementary-material

FIGURE S1 | Generation of *C. elegans* lines over expressing WT or G2019S or G2019S kinase dead (KD) LRRK2. **(A)** Representative images of adult worms from

LRRK2 transgenic lines visualized by epifluorescence microscopy (RFP) of the whole body. Scale bar = 50 μm. **(B)** Detection of transgene LRRK2. Single worm PCR is detected for a ∼617 bp fragment of LRRK2 cDNA. Plasmid WT LRRK2 used for transformation served as a positive control. M: DNA size marker in kb. **(C)** Detection on Western blots of LRRK2 proteins (280 kDa) in *C. elegans* over expressing WT, G2019S, and KD LRRK2, but not in the RFP strain. Worm lysate was followed by Western blotting with an antibody against FLAG.

FIGURE S2 | DA neurodegeneration in *C. elegans* lines over expressing WT or G2019S or G2019S kinase dead (KD) LRRK2. **(A)** G2019S LRRK2 expression leads to DA neurodegeneration. Control and *C. elegans* expressing WT or KD LRRK2 contained intact DA neurons (CEP neurons) and smooth neuritis, whereas the G2019S LRRK2 over expression line displayed prominent loss of DA neurons (white arrows) during adult day 2. Scale bar = 75 μm. **(B)** The DA neuron degeneration was quantified by the loss of CEP neurons in transgenic animals during adult day 2. BZ555 (Pdat-1::GFP) worm was a control. Error bars indicate SEM. G2019S LRRK2 strain and control were significantly different ($p < 0.01$) whereas KD could rescue G2019S-mediated loss of DA neurons. **(C)** Numbers of bends every 30 s for control and transgenic lines in adult day 2. G2019S LRRK2 strain and control were significantly different ($p < 0.001$) whereas KD could rescue G2019S-mediated loss of motor ability. WT LRRK2 strain was similar with control strain.

TABLE S1 | Transgenic *C. elegans* strains used in DA neuron degeneration assay.

REFERENCES

Angeles, D. C., Gan, B. H., Onstead, L., Zhao, Y., Lim, K. L., and Dachsel, J. (2011). Mutations in LRRK2 increase phosphorylation of peroxiredoxin 3 exacerbating oxidative stress-induced neuronal death. *Humanmutation* 32, 1390–1397. doi: 10.1002/humu.21582

Berdichevsky, A., Viswanathan, M., Horvitz, H. R., and Guarente, L. C. (2006). *C. elegans* SIR-2.1 interacts with 14-3-3 proteins to activate DAF-16 and extend life span. *Cell* 125, 1165–1177. doi: 10.1016/j.cell.2006.04.036

Brenner, S. (1974). The genetics of *Caenorhabditis elegans*. *Genetics* 77, 71–94.

Brunet, A., Bonni, A., Zigmond, M. J., Lin, M. Z., Juo, P., Hum, L. S., et al. (1999). Akt promotes cell survival by phosphorylating and inhibiting a Forkhead transcription factor. *Cell* 96, 857–868. doi: 10.1016/S0092-8674(00)80595-4

Cahill, C. M., Tzivion, G., Nasrin, N., Ogg, S., Dore, J., Ruvkun, G., et al. (2001). Phosphatidylinositol 3-kinase signaling inhibits DAF-16 DNA binding and function via 14-3-3-dependent and 14-3-3-independent pathways. *J. Biol. Chem.* 276, 13402–13410. doi: 10.1074/jbc.M010042200

Di Fonzo, A., Rohe, C. F., Ferreira, J., Chien, H. F., Vacca, L., and Stocchi, F. (2005). A frequent LRRK2 gene mutation associated with autosomal dominant Parkinson's disease. *Lancet* 365, 412–415. doi: 10.1016/S0140-6736(05)17829-5

Durocher, D., Taylor, I. A., Sarbassova, D., Haire, L. F., Westcott, S. L., Jackson, S. P., et al. (2000). The molecular basis of FHA domain:phosphopeptide binding specificity and implications for phospho-dependent signaling mechanisms. *Mol. Cell.* 6, 1169–1182. doi: 10.1016/S1097-2765(00)00114-3

Dzamko, N., Deak, M., Hentati, F., Reith, A. D., Prescott, A. R., Alessi, D. R., et al. (2010). Inhibition of LRRK2 kinase activity leads to dephosphorylation of Ser(910)/Ser(935), disruption of 14-3-3 binding and altered cytoplasmic localization. *Biochem. J.* 430, 405–413. doi: 10.1042/BJ20100784

Gandhi, S., and Abramov, A. Y. (2012). Mechanism of oxidative stress in neurodegeneration. *Oxid. Med. Cell. Longev.* 2012:428010. doi: 10.1155/2012/428010

Gilks, W. P., Abou-Sleiman, P. M., Gandhi, S., Jain, S., Singleton, A., Lees, A. J., et al. (2005). A common LRRK2 mutation in idiopathic Parkinson's disease. *Lancet* 365, 415–416. doi: 10.1016/S0140-6736(05)17830-1

Halliwell, B. (2006). Oxidative stress and neurodegeneration: where are we now? *J. Neurochem.* 97, 1634–1658. doi: 10.1111/j.1471-4159.2006.03907.x

Henderson, S. T., and Johnson, T. E. (2001). DAF-16 integrates developmental and environmental inputs to mediate aging in the nematode *Caenorhabditis elegans*. *Curr. Biol.* 11, 1975–1980. doi: 10.1016/S0960-9822(01)00594-2

Ichimura, T., Isobe, T., Okuyama, T., Takahashi, N., Araki, K., Kuwano, R., et al. (1988). Molecular cloning of cDNA coding for brain-specific 14-3-3 protein, a protein kinase-dependent activator of tyrosine and tryptophan hydroxylases. *Proc. Natl. Acad. Sci. U.S.A.* 85, 7084–7088. doi: 10.1073/pnas.85.19.7084

Kamath, R. S., Martinez-Campos, M., Zipperlen, P., Fraser, A. G., and Ahringer, J. (2001). Effectiveness of specific RNA-mediated interference through ingested double-stranded RNA in *Caenorhabditis elegans*. *Genome Biol.* 2:RESEARCH0002. doi: 10.1186/gb-2000-2-1-research0002

Kanao, T., Venderova, K., Park, D. S., Unterman, T., Lu, B., and Imai, Y. (2010). Activation of FoxO by LRRK2 induces expression of proapoptotic proteins and alters survival of postmitotic dopaminergic neuron in Drosophila. *Hum. Mol. Genet.* 19, 3747–3758. doi: 10.1093/hmg/ddq289

Kuwahara, T., Koyama, A., Koyama, S., Yoshina, S., Ren, C. H., Kato, T., et al. (2008). A systematic RNAi screen reveals involvement of endocytic pathway in neuronal dysfunction in alpha-synuclein transgenic *C. elegans*. *Hum. Mol. Genet.* 17, 2997–3009. doi: 10.1093/hmg/ddn198

Landis, J. N., and Murphy, C. T. (2010). Integration of diverse inputs in the regulation of *Caenorhabditis elegans* DAF-16/FOXO. *Dev. Dynam.* 239, 1405–1412. doi: 10.1002/dvdy.22244

Lebel, M., Picard, F., Ferland, G., and Gaudreau, P. (2012). Drugs, nutrients, and phytoactive principles improving the health span of rodent models of human age-related diseases. *J. Gerontol. Ser. A Biol. Sci. Med. Sci.* 67, 140–151. doi: 10.1093/gerona/glr038

Li, J., Tewari, M., Vidal, M., and Lee, S. S. (2006). The 14-3-3 protein FTT-2 regulates DAF-16 in *Caenorhabditis elegans*. *Dev. Biol.* 301, 82–91. doi: 10.1016/j.ydbio.2006.10.013

Li, X., Wang, Q. J., Pan, N., Lee, S., Zhao, Y., Chait, B. T., et al. (2011). Phosphorylation-dependent 14-3-3 binding to LRRK2 is impaired by common mutations of familial Parkinson's disease. *PLoS One* 6:e17153. doi: 10.1371/journal.pone.0017153

Lin, K., Hsin, H., Libina, N., and Kenyon, C. (2001). Regulation of the *Caenorhabditis elegans* longevity protein DAF-16 by insulin/IGF-1 and germstrain signaling. *Nat. Genet.* 28, 139–145. doi: 10.1038/88850

Livak, K. J., and Schmittgen, T. D. (2001). Analysis of relative gene expression data using real-time quantitative PCR and the 2(-Delta Delta C(T)) Method. *Methods* 25, 402–408. doi: 10.1006/meth.2001.1262

Lu, T., Pan, Y., Kao, S. Y., Li, C., Kohane, I., Chan, J., et al. (2004). Gene regulation and DNA damage in the ageing human brain. *Nature.* 429, 883–891. doi: 10.1038/nature02661

Mamais, A., Chia, R., Beilina, A., Hauser, D. N., Hall, C., Lewis, P. A., et al. (2014). Arsenite stress down-regulates phosphorylation and 14-3-3 binding of leucine-rich repeat kinase 2 (LRRK2), promoting self-association and cellular redistribution. *J. Biol. Chem.* 289, 21386–21400. doi: 10.1074/jbc.M113.528463

Martin, H., Patel, Y., Jones, D., Howell, S., Robinson, K., and Aitken, A. (1993). Antibodies against the major brain isoforms of 14-3-3 protein. An antibody specific for the N-acetylated amino-terminus of a protein. *FEBS Lett.* 331, 296–303. doi: 10.1016/0014-5793(93)80356-Y

McElwee, J., Bubb, K., and Thomas, J. H. (2003). Transcriptional outputs of the *Caenorhabditis elegans* forkhead protein DAF-16. *Aging Cell* 2, 111–121. doi: 10.1046/j.1474-9728.2003.00043.x

Mello, C. C., Kramer, J. M., Stinchcomb, D., and Ambros, V. (1991). Efficient gene transfer in *C. elegans:* extrachromosomal maintenance and integration of transforming sequences. *EMBO J.* 10, 3959–3970. doi: 10.1002/j.1460-2075.1991.tb04966.x

Morrison, D. K. (2009). The 14-3-3 proteins: integrators of diverse signaling cues that impact cell fate and cancer development. *Trends Cell Biol.* 19, 16–23. doi: 10.1016/j.tcb.2008.10.003

Mortiboys, H., Johansen, K. K., Aasly, J. O., and Bandmann, O. (2010). Mitochondrial impairment in patients with Parkinson disease with the G2019S mutation in LRRK2. *Neurology* 75, 2017–2020. doi: 10.1212/WNL.0b013e3181ff9685

Nichols, R. J., Dzamko, N., Morrice, N. A., Campbell, D. G., Deak, M., Ordureau, A., et al. (2010). 14-3-3 binding to LRRK2 is disrupted by multiple Parkinson's disease-associated mutations and regulates cytoplasmic localization. *Biochem. J.* 430, 393–404. doi: 10.1042/BJ20100483

Nichols, W. C., Pankratz, N., Hernandez, D., Paisan-Ruiz, C., Jain, S., Halter, C. A., et al. (2005). Genetic screening for a single common LRRK2 mutation in familial Parkinson's disease. *Lancet* 365, 410–412. doi: 10.1016/S0140-6736(05)17828-3

Obsil, T., Ghirlando, R., Anderson, D. E., Hickman, A. B., and Dyda, F. (2003). Two 14-3-3 binding motifs are required for stable association of Forkhead transcription factor FOXO4 with 14-3-3 proteins and inhibition of DNA binding. *Biochemistry* 42, 15264–15272. doi: 10.1021/bi035 2724

Oh, S. W., Mukhopadhyay, A., Svrzikapa, N., Jiang, F., Davis, R. J., and Tissenbaum, H. A. (2005). JNK regulates lifespan in *Caenorhabditis elegans* by modulating nuclear translocation of forkhead transcription factor/DAF-16. *Proc. Natl. Acad. Sci. U.S.A.* 102, 4494–4499. doi: 10.1073/pnas.050074 9102

Papkovskaia, T. D., Chau, K. Y., Inesta-Vaquera, F., Papkovsky, D. B., Healy, D. G., and Nishio, K. (2012). G2019S leucine-rich repeat kinase 2 causes uncoupling protein-mediated mitochondrial depolarization. *Hum. Mol. Genet.* 21, 4201–4213. doi: 10.1093/hmg/dds244

Slone, S. R., Lavalley, N., McFerrin, M., Wang, B., and Yacoubian, T. A. (2015). Increased 14-3-3 phosphorylation observed in Parkinson's disease reduces neuroprotective potential of 14-3-3 proteins. *Neurobiol. Dis.* 79, 1–13. doi: 10.1016/j.nbd.2015.02.032

Smith, W. W., Pei, Z., Jiang, H., Moore, D. J., Liang, Y., West, A. B., et al. (2005). Leucine-rich repeat kinase 2 (LRRK2) interacts with parkin, and mutant LRRK2 induces neuronal degeneration. *Proc. Natl. Acad. Sci. U.S.A.* 102, 18676–18681. doi: 10.1073/pnas.0508052102

Sunayama, J., Tsuruta, F., Masuyama, N., and Gotoh, Y. (2005). JNK antagonizes Akt-mediated survival signals by phosphorylating 14-3-3. *J. Cell Biol.* 170, 295–304. doi: 10.1083/jcb.200409117

Tzivion, G., and Avruch, J. (2002). 14-3-3 proteins: active cofactors in cellular regulation by serine/threonine phosphorylation. *J. Biol. Chem.* 277, 3061–3064. doi: 10.1074/jbc.R100059200

Tzivion, G., Gupta, V. S., Kaplun, L., and Balan, V. (2006). 14-3-3 proteins as potential oncogenes. *Semin. Cancer Biol.* 16, 203–213. doi: 10.1016/j.semcancer. 2006.03.004

Ulitsky, I., Krishnamurthy, A., Karp, R. M., and Shamir, R. (2010). DEGAS: de novo discovery of dysregulated pathways in human diseases. *PLoS One* 5:e13367. doi: 10.1371/journal.pone.0013367

Wang, W., and Shakes, D. C. (1996). Molecular evolution of the 14-3-3 protein family. *J. Mol. Evol.* 43, 384–398. doi: 10.1007/BF02339012

Yacoubian, T. A., Slone, S. R., Harrington, A. J., Hamamichi, S., Schieltz, J. M., Caldwell, K. A., et al. (2010). Differential neuroprotective effects of 14-3-3 proteins in models of Parkinson's disease. *Cell Death Dis.* 1:e2. doi: 10.1038/ cddis.2009.4

Zimprich, A., Biskup, S., Leitner, P., Lichtner, P., Farrer, M., Lincoln, S., et al. (2004). Mutations in LRRK2 cause autosomal-dominant parkinsonism with pleomorphic pathology. *Neuron* 44, 601–607. doi: 10.1016/j.neuron.2004. 11.005

Conflict of Interest Statement: The authors declare that the research was conducted in the absence of any commercial or financial relationships that could be construed as a potential conflict of interest.

frontiers in Neuroscience

ORIGINAL RESEARCH
published: 22 November 2018
doi: 10.3389/fnins.2018.00845

Exosomes Derived From miR-133b-Modified Mesenchymal Stem Cells Promote Recovery After Spinal Cord Injury

Dong Li[1†], Peng Zhang[2†], Xiyang Yao[2], Haiying Li[2], Haitao Shen[2], Xiang Li[2], Jiang Wu[2] and Xiaocheng Lu[2*]*

[1] Department of Neurosurgery, Lianyungang Hospital of Traditional Chinese Medicine, Lianyungang, China, [2] Department of Neurosurgery, Brain and Nerve Research Laboratory, The First Affiliated Hospital of Soochow University, Suzhou, China

OPEN ACCESS

Edited by:
Gao Chen,
Zhejiang University, China

Reviewed by:
Ye Xiong,
Henry Ford Health System, United States
Varun Kesherwani,
University of Nebraska Medical Center, United States

***Correspondence:**
Jiang Wu
szjiangwu@163.com
Xiaocheng Lu
xclu_suda@126.com;
xiaochenglu@suda.edu.cn

[†] These authors have contributed equally to this work

Specialty section:
This article was submitted to Neurodegeneration, a section of the journal Frontiers in Neuroscience

Received: 23 August 2018
Accepted: 29 October 2018
Published: 22 November 2018

Citation:
Li D, Zhang P, Yao X, Li H, Shen H, Li X, Wu J and Lu X (2018) Exosomes Derived From miR-133b-Modified Mesenchymal Stem Cells Promote Recovery After Spinal Cord Injury. Front. Neurosci. 12:845. doi: 10.3389/fnins.2018.00845

Dysregulation of microRNAs (miRNAs) has been found in injured spinal cords after spinal cord injury (SCI). Previous studies have shown that miR-133b plays an important role in the differentiation of neurons and the outgrowth of neurites. Recently, exosomes have been used as novel biological vehicles to transfer miRNAs locally or systemically, but little is known about the effect of the delivery of exosome-mediated miRNAs on the treatment of SCI. In the present study, we observed that mesenchymal stem cells, the most common cell types known to produce exosomes, could package miR-133b into secreted exosomes. After SCI, tail vein injection of miR-133b exosomes into rats significantly improved the recovery of hindlimb function when compared to control groups. Additionally, treatment with miR-133b exosomes reduced the volume of the lesion, preserved neuronal cells, and promoted the regeneration of axons after SCI. We next observed that the expression of RhoA, a direct target of miR-133b, was decreased in the miR-133b exosome group. Moreover, we showed that miR-133b exosomes activated ERK1/2, STAT3, and CREB, which are signaling pathway proteins involved in the survival of neurons and the regeneration of axons. In summary, these findings demonstrated that systemically injecting miR-133b exosomes preserved neurons, promoted the regeneration of axons, and improved the recovery of hindlimb locomotor function following SCI, suggesting that the transfer of exosome-mediated miRNAs represents a novel therapeutic approach for the treatment of SCI.

Keywords: exosome, miR-133b, spinal cord injury, axon regeneration, MSCs

INTRODUCTION

Traumatic spinal cord injury (SCI) often results in irreversible neurological deficits, with an annual incidence of 15–40 cases per million throughout the world (Sekhon and Fehlings, 2001). Increasing evidence has shown that the spinal cord suffers from primary mechanical injury followed by secondary injury, including inflammation, ischemia, lipid peroxidation, and apoptosis, although the exact pathophysiological mechanisms are still unknown (Popovich, 2014; Stenudd et al., 2015). To date, major progress has been made on neuroprotection and regeneration in preclinical studies;

however, finding effective treatments for SCI remains a challenge for basic science and clinical investigators (Dietz and Fouad, 2014).

MicroRNAs (miRNAs) are endogenous ∼22 nucleotide non-coding RNAs that can regulate the expression of protein-coding genes by binding to complementary sites in the 3′-untranslated regions (UTRs) of their target mRNAs (Bartel and Chen, 2004). Recent studies have shown that miRNAs play important roles in synaptic activity, regeneration, and neurogenesis in the central nervous system (CNS). Moreover, several miRNAs have been reported as potentially novel targets for the treatment of SCI, including miR-486, miR-21, and miR-126 (Jee et al., 2012; Hu et al., 2013, 2015). Recently, Yu et al. demonstrated that miR-133b is essential for functional recovery after SCI in zebrafish (Yu et al., 2011). In addition, our previous study indicated that miR-133b promotes the outgrowth of neurites by targeting Ras homolog gene family member A (RhoA) *in vitro* (Lu et al., 2015).

Exosomes are small-membrane vesicles (30–100 nm) derived from the luminal membranes of multivesicular bodies and are secreted from several types of cells (Thery et al., 2002). These extracellular vesicles mediate intercellular communication by transferring miRNAs, mRNAs, DNA, and proteins between cells without direct cell-to-cell contact (Umezu et al., 2014; Lou et al., 2015). Growing evidence suggests that, as intercellular communicators, exosomes act not only locally but also systemically (Katakowski et al., 2013; Lou et al., 2015). Moreover, accumulating studies have demonstrated that exosomes can be manufactured in culture by transferring therapeutic miRNAs to exosome-producing cells; among the cell types known to produce exosomes, mesenchymal stem cells (MSCs) are the most common (Roccaro et al., 2013; Phinney et al., 2015; Long et al., 2017). Therefore, we hypothesized that systemic injection of exosomes derived from miR-133b-modified MSCs could transfer miR-133b into the injured spinal cord and improve functional recovery after SCI.

MATERIALS AND METHODS

Animals

Adult male Sprague–Dawley rats weighing 250–300 g were purchased from the Animal Center of the Chinese Academy of Sciences, Shanghai, China. The animal experimental protocols, including care, breeding, and operative procedures, were approved by the Animal Care and Use Committee of Soochow University and complied with the Guide for the Care and Use of Laboratory Animals approved by the National Institutes of Health.

Preparation of MSC-Derived miR-133b Exosomes

Primary rat MSCs were isolated from male rats weighing 80–100 g. Briefly, the bone marrow of the femurs and tibias was flushed out with PBS followed by centrifugation. The pellet was suspended in Dulbecco's modified Eagle medium (DMEM; Life Technologies, United States) with 10% heat-inactivated fetal bovine serum (FBS; Life Technologies) and 1% penicillin–streptomycin, and was then incubated under a humidified atmosphere with 5% CO_2 at 37°C. The medium was replaced every 3 days, and the MSCs were passaged when the cultures reached 90% confluence.

MSCs were transfected with miR-133b mimic and negative control using Lipofectamine 3000 (Invitrogen, United States) in serum-free medium according to the manufacturer's instructions. At 72 h after transfection, exosomes were obtained from MSC supernatants using the ExoQuick-TC Kit (System Biosciences, United States). Subsequently, exosome pellets were resuspended in PBS at a total protein concentration of 10 μg/μl. Moreover, the exosomes were characterized by western blotting of exosome surface markers, including CD81, CD63, and CD9. The sequence of the miR-133b mimic was 5'-UUUGGUCCCCUUCAACCAGCUA-3′.

Compression Spinal Cord Injury Model

Male rats were anesthetized by chloral hydrate (400 mg/kg body weight). Following dissection of the paraspinal muscles, a laminectomy from T9–T11 was performed. Subsequently, SCI was inflicted with an aneurysm clip of 35 g closing force for 60 s at the T10 level as previously described (Figley et al., 2014; Soubeyrand et al., 2014). Finally, the incision was closed in layers with silk sutures. The sham-operated rats only received laminectomy. After surgery, all animals received penicillin and an analgesic for 3 days, and the bladders were manually voided thrice daily. At 24 h following trauma, the animals received treatments by tail intravenous injection of miR-133b exosomes (100 μg exosomes in 0.5 mL of PBS), miR-con exosomes (100 μg exosomes in 0.5 mL PBS), or PBS (0.5 ml) as previously described (Zhang et al., 2015).

Experimental Groups

The rats were randomly divided into four groups, and testing was performed by blinded observers: (1) sham group (the rats were subjected to sham operation), (2) control group (the rats received SCI and were treated with PBS), (3) miR-con group (the rats were subjected to SCI and treated with miR-con exosomes), and (4) miR-133b group (the rats were subjected to SCI and treated with miR-133b exosomes).

Western Blot Analysis

Total protein was extracted with RIPA lysis buffer (Beyotime Institute of Biotechnology, China). We used the BCA protein assay kit to assess protein concentrations (Beyotime Institute of Biotechnology). For *in vivo* studies, a 10-mm long segment of the spinal cord containing the injury site was harvested at 4 days following SCI (four animals per group). For western blot analysis, 30 μg of protein was separated by 12% SDS–PAGE and transferred to PVDF membranes (Merck Millipore, Germany). Following blocking with 5% non-fat milk, the membranes were incubated with primary antibodies overnight at 4°C: mouse anti-CD63 (Abcam, Cambridge, United Kingdom), rabbit anti-CD81 (Abcam), rabbit anti-CD9 (Abcam), mouse anti- neurofilament (NF) (Abcam), rabbit anti-growth-associated protein 43 (GAP43) (Abcam), rabbit anti-p-signal transducer and

activator of transcription 3 (STAT3) (Cell Signaling Technology, United States), mouse anti-STAT3 (Cell Signaling Technology), rabbit anti-p-cAMP response element-binding protein (CREB) (Abcam), rabbit anti-CREB (Abcam), rabbit anti-RhoA (Cell Signaling Technology), or rabbit anti-β-actin (Cell Signaling Technology). Horseradish peroxidase (HRP)-conjugated goat anti-rabbit or mouse was used as secondary antibody (Cell Signaling Technology). Finally, bands were visualized by enhanced chemiluminescence (ECL) Plus (Thermo Scientific, United States), and the relative band densities were determined by Image Lab (Version 2.0.1).

Real-Time PCR

Total RNAs from MSCs, exosomes, or spinal cords (four animals per group) were extracted by TRIzol reagent (Invitrogen) according to the manufacturer's instructions. For *in vivo* studies, a 10-mm long spinal cord segment containing the injury epicenter was harvested. Total RNA was reverse-transcribed to cDNA using the PrimeScript RT reagent kit (TaKaRa, Japan). Quantitative real-time PCR was performed using the miScript SYBR Green PCR kit (QIAGEN, Germany). The relative expression of miRNA normalized to U6 was calculated using the $2^{-\Delta\Delta CT}$ method.

Behavioral Assessment

The recovery of hindlimb locomotor function was evaluated by using the Basso–Beattie–Bresnahan (BBB) locomotor rating scale of 0 (no motor activity) to 21 (normal locomotion) (Basso et al., 1995). Two independent investigators blinded to the treatment observed the movement and scored the locomotor function preinjury and at days 1, 3, 5, 9, and 14 post-injury as previously described (Hu et al., 2013; Datto et al., 2015).

Tissue Processing, Hematoxylin–Eosin (HE) Staining, and Immunohistochemistry

Animals were anesthetized terminally with an overdose of inhalation isoflurane at day 4 after injury. The spinal cords were embedded in an optimal cutting temperature compound. The T9–T11 spinal cord segments near the epicenter of the lesion were collected for histological evaluation. HE staining was performed in accordance with the manufacturer's instructions to quantify the area of lesion cavity using Imagepro-Plus software. The T9–T11 spinal cord segments in transverse sections were dissected in six rats per group, and every eighth section derived from each animal was used to determine the area of cystic cavity in each group as previously described (Chen et al., 2014; Wang et al., 2014).

For immunohistochemistry, briefly, longitudinal sections containing the lesion site were deparaffinized with xylene and hydrated in graded alcohol, followed by boiling in citrate buffer (pH 6.0) twice for 5 min. Subsequently, to inactivate the endogenous peroxidase, the sections were cooled off and incubated in 3% H_2O_2 for 15 min at room temperature. The slides were then blocked with 10% FBS for 10 min and incubated with primary antibodies overnight at 4°C, including rabbit anti-GAP43, rabbit anti-NF, rabbit anti-MBP (Abcam), and mouse anti-NeuN (Abcam). Following washing with TBS, the sections were incubated with fluorescence-labeled secondary antibodies (Abcam). Finally, the sections were stained with DAPI and visualized under a confocal laser-scanning microscope (Olympus LSM-GB200, Tokyo, Japan).

Statistical Analyses

Data were analyzed with SPSS 19.0 (SPSS Inc., Chicago, IL, United States). All data represent at least three independent experiments and are expressed as means ± standard deviations (SD). One-way analysis of variance (ANOVA) with Tukey's *post hoc* test was used to compare the levels of different groups. BBB scores were analyzed by repeated measures ANOVA followed by Bonferroni *post hoc* corrections. Statistical significance was set at $p < 0.05$.

RESULTS

Reduced Expression of miR-133b in Injured Spinal Cords

The expression levels of miR-133b in injured spinal cords were measured by qRT-PCR at 12 h, 24 h, 2, 3, 4, 5, and 7 days after acute SCI. The results revealed that the expression of miR-133b was significantly downregulated at 24 h or later following SCI (**Figure 1A**).

MSCs Packaged miR-133b Into Secreted Exosomes

MSCs were cultured as described above and characterized as being positive for CD73, CD90, and CD105, but negative for CD34 and CD45 (data not shown). MSCs were then transfected with miR-133b mimic and negative control (the transfection efficiency was approximately 90%). Exosomes were isolated from MSC supernatants at 72 h after transfection. To characterize the exosomes, we carried out western blot analysis, which showed that exosomes expressed common exosomal marker proteins, including CD9, CD63, and CD81 (**Figure 1B**), as previously described (Roccaro et al., 2013). As shown in **Figure 1C**, qRT-PCR revealed that the expression levels of miR-133b were approximately 2.5-fold higher in exosomes derived from miR-133b-transfected MSCs than in those from MSCs transfected with miR-con. These results demonstrated that MSCs efficiently packaged miR-133b into secreted exosomes.

miR-133b Exosomes Improved Functional Recovery, Reduced the Lesion Volume, and Preserved Neurons After SCI

We first explored using qRT-PCR whether the tail vein injection of exosomes would change the miR-133b expression in spinal cords. As shown in **Figure 2A**, compared with the control groups, the expression of miR-133b was significantly increased in the miR-133b exosome-injected group at day 4 following SCI.

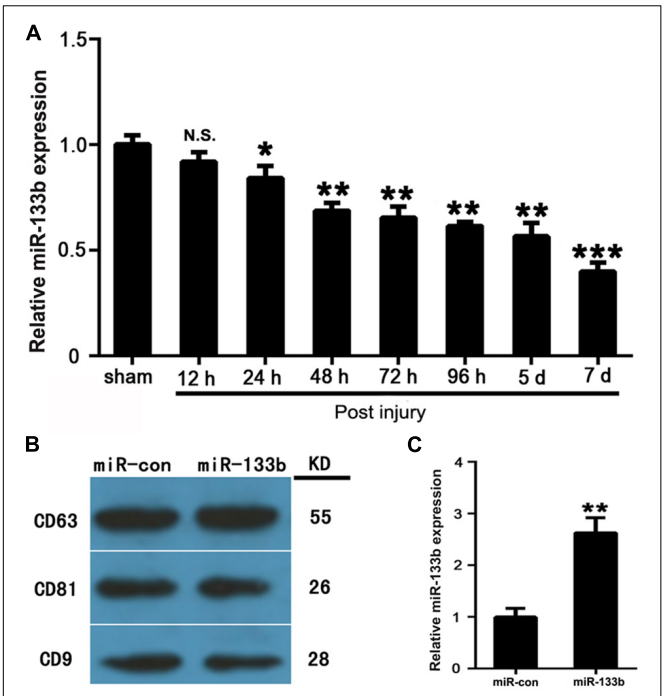

FIGURE 1 | MSCs package miR-133b into secreted exosomes. **(A)** Expression levels of miR-133b in injured spinal cords were measured by qRT-PCR at 12 h, 24 h, and at 2, 3, 4, 5, and 7 days after acute SCI. **(B)** Expressions of CD63, CD81, and CD9 in exosomes derived from miR-133b- or miR-con-transfected MSCs were evaluated by western blot. **(C)** Expression of miR-133b in exosomes derived from miR-133b- or miR-con-transfected MSCs was assessed by qRT-PCR. Values are presented as means ± SD. NS: $p > 0.05$, $^{*}p < 0.05$, $^{**}p < 0.01$, $^{***}p < 0.001$, $n = 4$ per group.

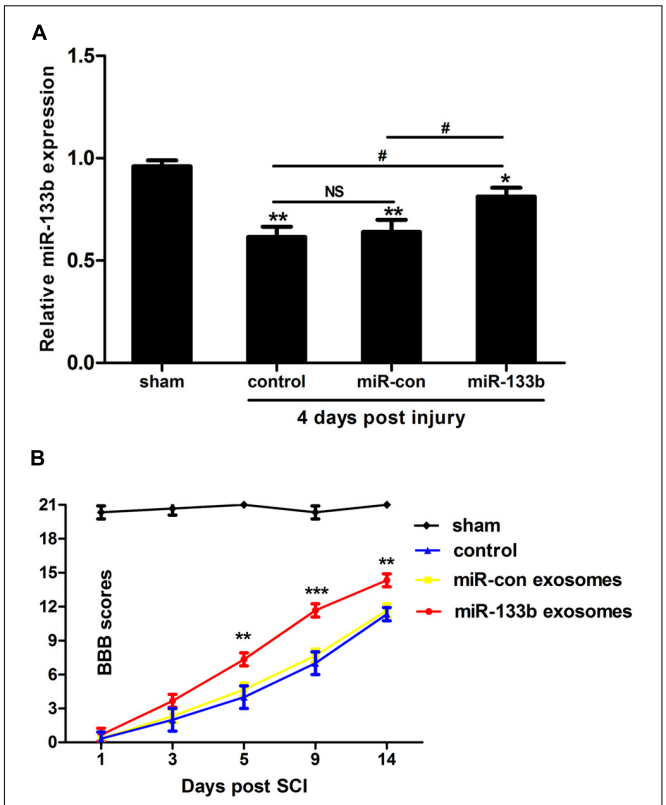

FIGURE 2 | Injection of miR-133b exosomes improved recovery after SCI. **(A)** Relative expression of miR-133b at the lesion site was evaluated by qRT-PCR following various treatments after SCI. Tail vein injection of miR-133b exosomes significantly increased miR-133b expression in the injured spinal cord when compared with control groups. **(B)** Hindlimb functional recovery was monitored at 1, 3, 5, 9, and 14 days after SCI using BBB scoring. Values are means ± SD. NS: $p > 0.05$, $^{*}p < 0.05$, $^{**}p < 0.01$, $^{***}p < 0.001$, $^{\#}p < 0.05$, $n = 4$ per group for miR-133b expression and $n = 6$ per group for hindlimb functional recovery.

To investigate whether miR-133b exosomes had a beneficial effect on the recovery of hindlimb locomotor function after acute SCI, the BBB locomotor grading scale was used at different time points after SCI. Immediately after SCI, the BBB score was approximately 0–1, indicating that the SCI model was successful. Spontaneous functional recovery was observed in all groups after SCI, as described previously (Pinzon et al., 2008). After 5 days, improved recovery with significant differences between miR-133b and miR-con exosome-injected rats was observed (day 5, $p < 0.01$; day 9, $p < 0.001$; and day 14, $p < 0.01$), indicating that the tail vein injection of miR-133b exosomes improved the recovery of hindlimb locomotor function after SCI (**Figure 2B**).

We next evaluated the effect of miR-133b exosomes on the volume of the lesion and the preservation of NeuN+ neurons after SCI by immunohistochemistry. HE staining showed that miR-133b exosomes significantly decreased the area of lesion cavity when compared to miR-con or the control group (**Figures 3A,C**). At day 4 after SCI, neurons in the injured spinal cord were stained with antibodies directed against NeuN, a specific marker of mature neurons. As shown in **Figures 3B,D**, the results showed significantly increased mature neuron numbers in injured rats receiving miR-133b exosomes compared to rats receiving miR-con exosomes ($p < 0.01$).

miR-133b Exosomes Promoted Axonal Outgrowth After SCI

To investigate the potential effect of miR-133b exosomes on the outgrowth of axons, an immunohistochemistry study of GAP43 and NF was carried out (Van der Zee et al., 1989). The results showed that the expression of GAP43 was increased in the miR-133b exosomes group compared to the miR-con or control group (**Figure 4**). Moreover, we observed that treatment with miR-133b exosomes enhanced NF expression at day 4 after SCI (**Figure 5**). Finally, western blot results confirmed significant increases in the protein levels of GAP43 and NF in the miR-133b exosomes group compared with those in the miR-con group (**Figures 6A,B**).

Effect of miR-133b Exosomes on Neuroprotection-Related Pathways and Phosphorylation of CREB and STAT3

Our previous study indicated that RhoA is a direct target of miR-133b (Lu et al., 2015). Moreover, RhoA has been shown to be involved in the death of neuronal cells in the spinal

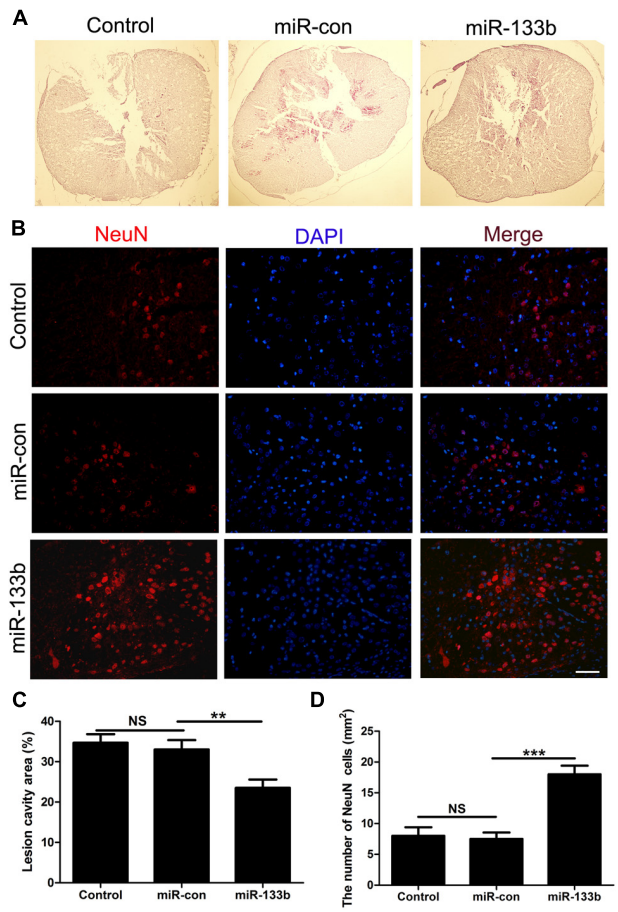

FIGURE 3 | Injection of miR-133b exosomes reduced the lesion volume and preserved NeuN+ neurons after SCI. **(A,C)** HE staining results for sections of injured spinal cord. **(B,D)** The effect of miR-133b exosomes on NeuN+ neurons was evaluated by immunofluorescence staining. Values are means ± SD. NS: $p > 0.05$, ***$p < 0.01$, ***$p < 0.00$, Scale bar = 60 μm, $n = 6$ per group.

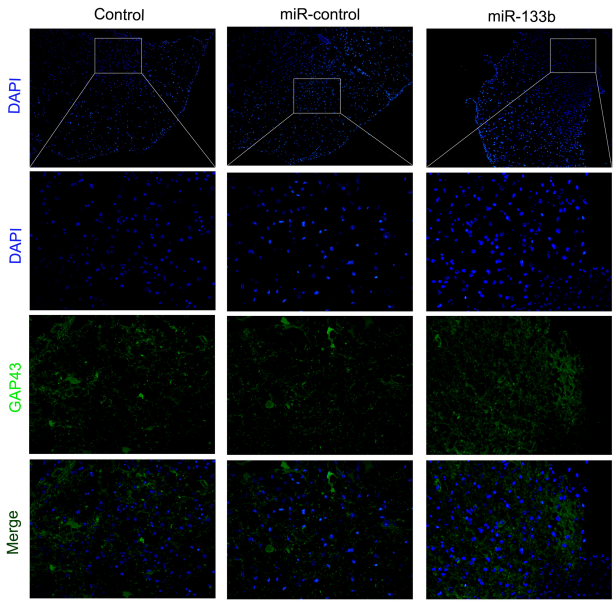

FIGURE 4 | Effect of miR-133b exosomes on GAP43 expression was measured by immunofluorescence staining. Scale bar = 60 μm, $n = 6$ per group.

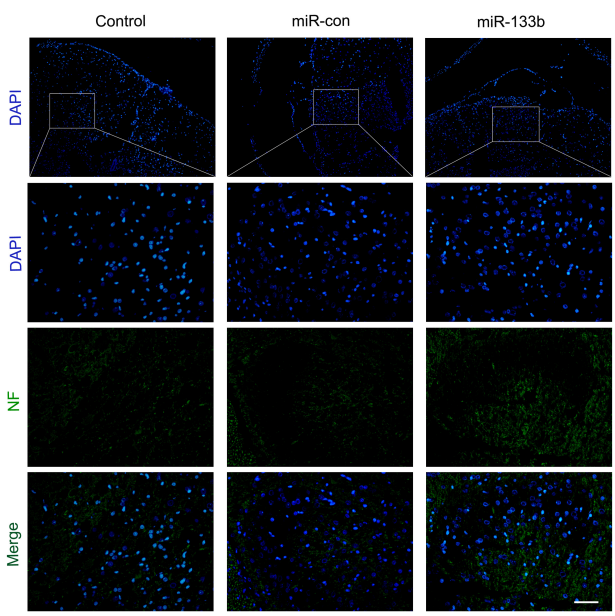

FIGURE 5 | Effect of miR-133b exosomes on NF expression was measured by immunofluorescence staining. Scale bar = 60 μm, $n = 6$ per group.

cord (Wu et al., 2016). To assess the effect of miR-133b exosomes on the expression of RhoA after SCI, we detected the levels of RhoA expression by using western blot. The results demonstrated that the expression of RhoA was significantly decreased in the injured spinal cords of rats receiving miR-133b exosome injections compared to those in miR-con exosome-treated animals ($p < 0.05$) (**Figure 6C**). These results are consistent with those of other *in vitro* and *in vivo* studies (Niu et al., 2016; Theis et al., 2016). Moreover, the phosphorylation of ERK1/2, another cell survival-related pathway protein, was significantly increased in the injured rats treated with miR-133b exosomes after SCI (**Figure 6D**).

The transcription factors CREB and STAT3 have been shown to be involved in the outgrowth of neurites (Gao et al., 2004; Qiu et al., 2005). In this study, we observed that injecting miR-133b exosomes increased the protein phosphorylation levels of STAT3 and CREB in injured spinal cords after SCI ($p < 0.05$ for p-STAT and $p < 0.05$ for p-CREB; **Figures 6E,F**).

DISCUSSION

SCI has a significant impact on both the patient and society (McDonald and Sadowsky, 2002). Following SCI, functional recovery is often poor, and to date there have been no effective therapies that have been translated to the clinic

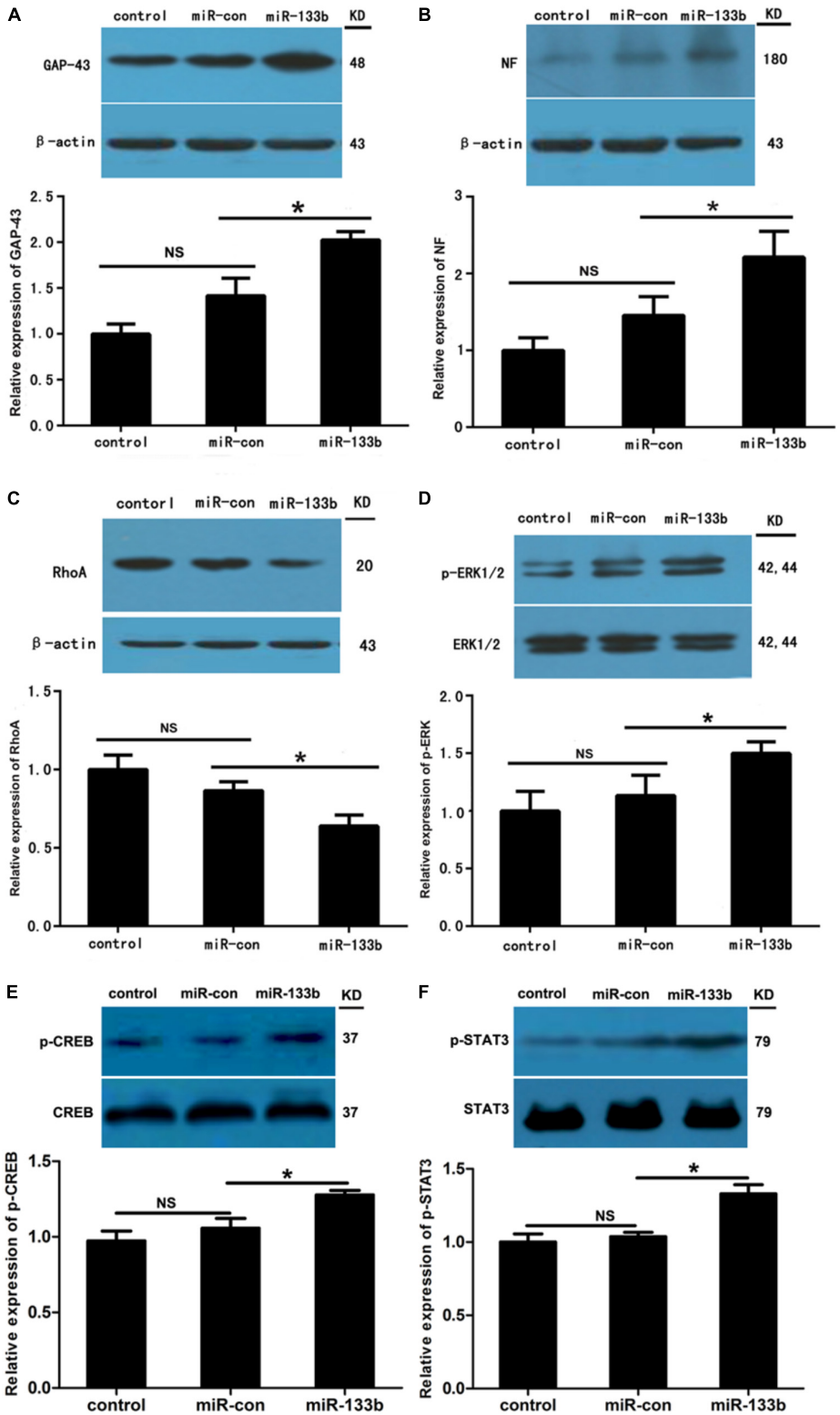

FIGURE 6 | Effect of miR-133b exosomes on expression levels of GAP43, NF, RhoA, pERK1/2, p-CREB, and p-STAT3. Western blotting showed that miR-133b exosomes increased expressions of GAP43 **(A)** and NF **(B)**, reduced the expression of RhoA **(C)**, and promoted phosphorylation of ERK1/2 **(D)**, CREB **(E)**, and STAT3 **(F)** in injured spinal cords after SCI. β-Actin was used as a control for GAP43, NF, and RhoA, and ERK1/2, CREB, and STAT3 were used as controls for pERK1/2, p-CREB, and p-STAT3, respectively. Values are presented as means ± SD. NS: $p > 0.05$, $^*p < 0.05$, $n = 4$ per group.

(Ramer et al., 2014). Increasing evidence has demonstrated that miRNAs are involved in the pathogenesis of SCI. For instance, miR-21 has been shown to decrease the death of neuronal cells and promote functional recovery after SCI (Hu et al., 2013). Recent studies have indicated that miR-133b plays important roles in neuronal differentiation, neurite outgrowth, and neuronal apoptosis in the CNS (Heyer et al., 2012; Lu et al., 2015; Niu et al., 2016; Xia et al., 2016). Moreover, further studies have shown that overexpression of miR-133b improves functional recovery after stroke in rats (Xin et al., 2013b, 2017). Exosomes, a novel intercellular communicator, have been used as biological vehicles for local or systemic delivery of miRNAs in the treatment of various diseases, such as stroke and Parkinson's disease (Xin et al., 2013a; Haney et al., 2015). In the current study, we investigated the effect of the transfer of exosome-mediated miR-133b in the treatment of SCI. After SCI, we observed significant differences in the recovery of functions between the miR-133b exosome group and the control group after SCI. Previous studies indicated that various treatments could improve the functional recovery from 3 days after SCI (Paterniti et al., 2014; Liu et al., 2015). In this study, we observed that, after 5 days, BBB scores were significantly higher in animals systemically injected with miR-133b exosomes than in the miR-con-injected rats. These findings are consistent with a recent study that demonstrated that lentiviral delivery of miR-133b improves functional recovery after SCI in mice (Theis et al., 2016).

Several mRNAs have been reported as targets of miR-133b, such as RhoA and MST2 (Care et al., 2007; Qin et al., 2012). In the present study, we found a reduction of RhoA protein levels in the injured spinal cords of rats receiving miR-133b exosomes. This finding is consistent with previous *in vitro* studies, indicating that RhoA is a direct target of miR-133b (Lu et al., 2015; Niu et al., 2016). RhoA, a member of the Rho family, has been shown to be upregulated after SCI in rats and acts on its direct downstream effector Rho-associated kinase (ROCK) (Schwab et al., 2005). Since a recent study demonstrated that the RhoA/ROCK signaling pathway plays a critical role in the death of spinal cord neurons after acute SCI (Wu et al., 2016), we next tested whether the survival of neurons was enhanced *in vivo* after miR-133b exosome injection. After SCI, neuronal death occurs at the lesion site within 24 h and is attributed to the primary mechanical force and later secondary factors such as inflammation, oxidation, and apoptosis (Liu et al., 1997; Esposito et al., 2012; Sonmez et al., 2013). In this study, at day 4 following SCI, we observed that the number of mature neurons was significantly increased in the miR-133b exosomes group. These findings are consistent with a recent study that demonstrated that the inhibition of RhoA significantly reduces the death of neuronal cells after SCI (Wu et al., 2016). In addition, we also observed that the injection of miR-133b exosomes enhanced ERK1/2 phosphorylation at the lesion site after SCI. Our previous *in vitro* study indicated that knockdown of RhoA protein by siRNA enhances the phosphorylation of ERK1/2 in PC12 cells, consistent with previous reports (Li et al., 2013; Gordon et al., 2014; Lu et al., 2015). Thus, miR-133b may promote the phosphorylation of ERK1/2 by targeting RhoA. The ERK pathway has also been shown to be crucial for the survival of neuronal cells after SCI. Previous studies have indicated that the activation of ERK1/2 protects neurons from apoptosis and improves the recovery of functions after SCI (Yune et al., 2008; Lee et al., 2010). These results suggest that the neuroprotective effect of miR-133b exosomes might involve the inhibition of RhoA and the activation of ERK1/2.

It has been established that the lack of regeneration of axons in the injured CNS is largely due to the presence of inhibitory molecules, including oligodendrocyte myelin glycoprotein, myelin-Nogo, and myelin-associated glycoprotein. To investigate the effect of miR-133b exosomes on the outgrowth of neurites, the spinal cord was analyzed by using immunohistochemical staining for NF. We observed that NF expression was elevated in the miR-133b exosomes group and this agreed with the results of western blotting. Next, we examined the expression of GAP43, a regeneration-associated gene that is upregulated in regenerating neurons (Woolf et al., 1990). A significant increase in the expression of GAP43 was observed in the injured spinal cords of rats injected with miR-133b exosomes at day 4 following SCI, suggesting that miR-133b exosomes promoted the regeneration of axons in injured spinal cords.

Growing evidence has shown that the transcription factor CREB plays important roles in the regeneration of axons (Filbin, 2003). The activation of CREB has been shown to be sufficient to overcome myelin inhibitors and to promote the regeneration of spinal axons *in vivo* (Gao et al., 2004). Here, we found that injecting miR-133b exosomes activated CREB in injured spinal cords. Moreover, the phosphorylation of STAT3, which is involved in the regeneration of axons in the spinal cord, was significantly increased in injured rats treated with miR-133b exosomes compared with those in the miR-con exosomes group (Qiu et al., 2005). These results suggested that miR-133b exosomes enhanced the regeneration of axons after SCI, at least partially, by promoting the phosphorylation of CREB and STAT3.

In conclusion, the results of this study showed that systemically injecting miR-133b exosomes upregulated miR-133b expression at the lesion site and promoted functional recovery after SCI. Moreover, we observed that miR-133b exosomes preserved neuronal cells and enhanced the regeneration of axons, which was attributed at least partially to the activation of ERK1/2, STAT3, and CREB, as well as to the inhibition of RhoA expression. These results suggest that systemic injection of exosomes generated from miRNA-modified MSCs represents a novel therapeutic approach for SCI.

AUTHOR CONTRIBUTIONS

XLu and JW designed the study. DL, PZ, XY, HL, HS, and XLi performed the experiments and analyzed the data. XLu wrote the paper. All the authors read and approved the manuscript.

FUNDING

This work was supported by the National Natural Science Foundation of China (No. 81601064) (XLu) and Jiangsu Provincial Medical Key Talent (No. ZDRCA2016040) (JW).

REFERENCES

Bartel, D. P., and Chen, C. Z. (2004). Micromanagers of gene expression: the potentially widespread influence of metazoan microRNAs. *Nat. Rev. Genet.* 5, 396–400. doi: 10.1038/nrg1328

Basso, D. M., Beattie, M. S., and Bresnahan, J. C. (1995). A sensitive and reliable locomotor rating scale for open field testing in rats. *J. Neurotrauma* 12, 1–21. doi: 10.1089/neu.1995.12.1

Care, A., Catalucci, D., Felicetti, F., Bonci, D., Addario, A., Gallo, P., et al. (2007). MicroRNA-133 controls cardiac hypertrophy. *Nat. Med.* 13, 613–618. doi: 10.1038/nm1582

Chen, L., Cui, X., Wu, Z., Jia, L., Yu, Y., Zhou, Q., et al. (2014). Transplantation of bone marrow mesenchymal stem cells pretreated with valproic acid in rats with an acute spinal cord injury. *Biosci. Trends* 8, 111–119. doi: 10.5582/bst.8.111

Datto, J. P., Bastidas, J. C., Miller, N. L., Shah, A. K., Arheart, K. L., Marcillo, A. E., et al. (2015). Female rats demonstrate improved locomotor recovery and greater preservation of white and gray matter after traumatic spinal cord injury compared to males. *J. Neurotrauma* 32, 1146–1157. doi: 10.1089/neu.2014.3702

Dietz, V., and Fouad, K. (2014). Restoration of sensorimotor functions after spinal cord injury. *Brain* 137(Pt 3), 654–667. doi: 10.1093/brain/awt262

Esposito, E., Rinaldi, B., Mazzon, E., Donniacuo, M., Impellizzeri, D., Paterniti, I., et al. (2012). Anti-inflammatory effect of simvastatin in an experimental model of spinal cord trauma: involvement of PPAR-alpha. *J. Neuroinflammation* 9:81. doi: 10.1186/1742-2094-9-81

Figley, S. A., Khosravi, R., Legasto, J. M., Tseng, Y. F., and Fehlings, M. G. (2014). Characterization of vascular disruption and blood-spinal cord barrier permeability following traumatic spinal cord injury. *J. Neurotrauma* 31, 541–552. doi: 10.1089/neu.2013.3034

Filbin, M. T. (2003). Myelin-associated inhibitors of axonal regeneration in the adult mammalian CNS. *Nat. Rev. Neurosci.* 4, 703–713. doi: 10.1038/nrn1195

Gao, Y., Deng, K., Hou, J., Bryson, J. B., Barco, A., Nikulina, E., et al. (2004). Activated CREB is sufficient to overcome inhibitors in myelin and promote spinal axon regeneration in vivo. *Neuron* 44, 609–621. doi: 10.1016/j.neuron.2004.10.030

Gordon, B. S., Kazi, A. A., Coleman, C. S., Dennis, M. D., Chau, V., Jefferson, L. S., et al. (2014). RhoA modulates signaling through the mechanistic target of rapamycin complex 1 (mTORC1) in mammalian cells. *Cell. Signal.* 26, 461–467. doi: 10.1016/j.cellsig.2013.11.035

Haney, M. J., Klyachko, N. L., Zhao, Y., Gupta, R., Plotnikova, E. G., He, Z., et al. (2015). Exosomes as drug delivery vehicles for Parkinson's disease therapy. *J. Control. Release* 207, 18–30. doi: 10.1016/j.jconrel.2015.03.033

Heyer, M. P., Pani, A. K., Smeyne, R. J., Kenny, P. J., and Feng, G. (2012). Normal midbrain dopaminergic neuron development and function in miR-133b mutant mice. *J. Neurosci.* 32, 10887–10894. doi: 10.1523/JNEUROSCI.1732-12.2012

Hu, J., Zeng, L., Huang, J., Wang, G., and Lu, H. (2015). miR-126 promotes angiogenesis and attenuates inflammation after contusion spinal cord injury in rats. *Brain Res.* 1608, 191–202. doi: 10.1016/j.brainres.2015.02.036

Hu, J. Z., Huang, J. H., Zeng, L., Wang, G., Cao, M., and Lu, H. B. (2013). Anti-apoptotic effect of microRNA-21 after contusion spinal cord injury in rats. *J. Neurotrauma* 30, 1349–1360. doi: 10.1089/neu.2012.2748

Jee, M. K., Jung, J. S., Choi, J. I., Jang, J. A., Kang, K. S., Im, Y. B., et al. (2012). MicroRNA 486 is a potentially novel target for the treatment of spinal cord injury. *Brain* 135(Pt 4), 1237–1252. doi: 10.1093/brain/aws047

Katakowski, M., Buller, B., Zheng, X., Lu, Y., Rogers, T., Osobamiro, O., et al. (2013). Exosomes from marrow stromal cells expressing miR-146b inhibit glioma growth. *Cancer Lett.* 335, 201–204. doi: 10.1016/j.canlet.2013.02.019

Lee, J. Y., Chung, H., Yoo, Y. S., Oh, Y. J., Oh, T. H., Park, S., et al. (2010). Inhibition of apoptotic cell death by ghrelin improves functional recovery after spinal cord injury. *Endocrinology* 151, 3815–3826. doi: 10.1210/en.2009-1416

Li, F., Jiang, Q., Shi, K. J., Luo, H., Yang, Y., and Xu, C. M. (2013). RhoA modulates functional and physical interaction between ROCK1 and Erk1/2 in selenite-induced apoptosis of leukaemia cells. *Cell Death Dis.* 4:e708. doi: 10.1038/cddis.2013.243

Liu, D., Huang, Y., Jia, C., Li, Y., Liang, F., and Fu, Q. (2015). Administration of antagomir-223 inhibits apoptosis, promotes angiogenesis and functional recovery in rats with spinal cord injury. *Cell Mol. Neurobiol.* 35, 483–491. doi: 10.1007/s10571-014-0142-x

Liu, X. Z., Xu, X. M., Hu, R., Du, C., Zhang, S. X., McDonald, J. W., et al. (1997). Neuronal and glial apoptosis after traumatic spinal cord injury. *J. Neurosci.* 17, 5395–5406. doi: 10.1523/JNEUROSCI.17-14-05395.1997

Long, Q., Upadhya, D., Hattiangady, B., Kim, D. K., An, S. Y., Shuai, B., et al. (2017). Intranasal MSC-derived A1-exosomes ease inflammation, and prevent abnormal neurogenesis and memory dysfunction after status epilepticus. *Proc. Natl. Acad. Sci. U.S.A.* 114, E3536–E3545. doi: 10.1073/pnas.1703920114

Lou, G., Song, X., Yang, F., Wu, S., Wang, J., Chen, Z., et al. (2015). Exosomes derived from miR-122-modified adipose tissue-derived MSCs increase chemosensitivity of hepatocellular carcinoma. *J. Hematol. Oncol.* 8:122. doi: 10.1186/s13045-015-0220-7

Lu, X. C., Zheng, J. Y., Tang, L. J., Huang, B. S., Li, K., Tao, Y., et al. (2015). MiR-133b Promotes neurite outgrowth by targeting RhoA expression. *Cell Physiol. Biochem.* 35, 246–258. doi: 10.1159/000369692

McDonald, J. W., and Sadowsky, C. (2002). Spinal-cord injury. *Lancet* 359, 417–425. doi: 10.1016/S0140-6736(02)07603-1

Niu, M., Xu, R., Wang, J., Hou, B., and Xie, A. (2016). MiR-133b ameliorates axon degeneration induced by MPP(+) via targeting RhoA. *Neuroscience* 325, 39–49. doi: 10.1016/j.neuroscience.2016.03.042

Paterniti, I., Impellizzeri, D., Di Paola, R., Esposito, E., Gladman, S., Yip, P., et al. (2014). Docosahexaenoic acid attenuates the early inflammatory response following spinal cord injury in mice: in-vivo and in-vitro studies. *J. Neuroinflammation* 11:6. doi: 10.1186/1742-2094-11-6

Phinney, D. G., Di Giuseppe, M., Njah, J., Sala, E., Shiva, S., St Croix, C. M., et al. (2015). Mesenchymal stem cells use extracellular vesicles to outsource mitophagy and shuttle microRNAs. *Nat. Commun.* 6:8472. doi: 10.1038/ncomms9472

Pinzon, A., Marcillo, A., Pabon, D., Bramlett, H. M., Bunge, M. B., and Dietrich, W. D. (2008). A re-assessment of erythropoietin as a neuroprotective agent following rat spinal cord compression or contusion injury. *Exp. Neurol.* 213, 129–136. doi: 10.1016/j.expneurol.2008.05.018

Popovich, P. G. (2014). Neuroimmunology of traumatic spinal cord injury: a brief history and overview. *Exp. Neurol.* 258, 1–4. doi: 10.1016/j.expneurol.2014.05.001

Qin, W., Dong, P., Ma, C., Mitchelson, K., Deng, T., Zhang, L., et al. (2012). MicroRNA-133b is a key promoter of cervical carcinoma development through the activation of the ERK and AKT1 pathways. *Oncogene* 31, 4067–4075. doi: 10.1038/onc.2011.561

Qiu, J., Cafferty, W. B., McMahon, S. B., and Thompson, S. W. (2005). Conditioning injury-induced spinal axon regeneration requires signal transducer and activator of transcription 3 activation. *J. Neurosci.* 25, 1645–1653. doi: 10.1523/JNEUROSCI.3269-04.2005

Ramer, L. M., Ramer, M. S., and Bradbury, E. J. (2014). Restoring function after spinal cord injury: towards clinical translation of experimental strategies. *Lancet Neurol.* 13, 1241–1256. doi: 10.1016/S1474-4422(14)70144-9

Roccaro, A. M., Sacco, A., Maiso, P., Azab, A. K., Tai, Y. T., Reagan, M., et al. (2013). BM mesenchymal stromal cell-derived exosomes facilitate multiple myeloma progression. *J. Clin. Invest.* 123, 1542–1555. doi: 10.1172/JCI66517

Schwab, J. M., Conrad, S., Monnier, P. P., Julien, S., Mueller, B. K., and Schluesener, H. J. (2005). Spinal cord injury-induced lesional expression of the repulsive guidance molecule (RGM). *Eur. J. Neurosci.* 21, 1569–1576. doi: 10.1111/j.1460-9568.2005.03962.x

Sekhon, L. H., and Fehlings, M. G. (2001). Epidemiology, demographics, and pathophysiology of acute spinal cord injury. *Spine* 24(Suppl.), S2–S12. doi: 10.1097/00007632-200112151-00002

Sonmez, E., Kabatas, S., Ozen, O., Karabay, G., Turkoglu, S., Ogus, E., et al. (2013). Minocycline treatment inhibits lipid peroxidation, preserves spinal cord ultrastructure, and improves functional outcome after traumatic spinal cord injury in the rat. *Spine* 38, 1253–1259. doi: 10.1097/BRS.0b013e3182895587

Soubeyrand, M., Badner, A., Vawda, R., Chung, Y. S., and Fehlings, M. G. (2014). Very high resolution ultrasound imaging for real-time quantitative visualization of vascular disruption after spinal cord injury. *J. Neurotrauma* 31, 1767–1775. doi: 10.1089/neu.2013.3319

Stenudd, M., Sabelstrom, H., and Frisen, J. (2015). Role of endogenous neural stem cells in spinal cord injury and repair. *JAMA Neurol.* 72, 235–237. doi: 10.1001/jamaneurol.2014.2927

Theis, T., Yoo, M., Park, C. S., Chen, J., Kugler, S., Gibbs, K. M., et al. (2016). Lentiviral delivery of miR-133b improves functional recovery after spinal cord injury in mice. *Mol. Neurobiol.* 54, 4659–4671. doi: 10.1007/s12035-016-0007-z

Thery, C., Zitvogel, L., and Amigorena, S. (2002). Exosomes: composition, biogenesis and function. *Nat. Rev. Immunol.* 2, 569–579. doi: 10.1038/nri855

Umezu, T., Tadokoro, H., Azuma, K., Yoshizawa, S., Ohyashiki, K., and Ohyashiki, J. H. (2014). Exosomal miR-135b shed from hypoxic multiple myeloma cells enhances angiogenesis by targeting factor-inhibiting HIF-1. *Blood* 124, 3748–3757. doi: 10.1182/blood-2014-05-576116

Van der Zee, C. E., Nielander, H. B., Vos, J. P., Lopes, da Silva, S., Verhaagen, J., et al. (1989). Expression of growth-associated protein B-50 (GAP43) in dorsal root ganglia and sciatic nerve during regenerative sprouting. *J. Neurosci.* 9, 3505–3512. doi: 10.1523/JNEUROSCI.09-10-03505.1989

Wang, L. J., Zhang, R. P., and Li, J. D. (2014). Transplantation of neurotrophin-3-expressing bone mesenchymal stem cells improves recovery in a rat model of spinal cord injury. *Acta Neurochir.* 156, 1409–1418. doi: 10.1007/s00701-014-2089-6

Woolf, C. J., Reynolds, M. L., Molander, C., O'Brien, C., Lindsay, R. M., and Benowitz, L. I. (1990). The growth-associated protein GAP-43 appears in dorsal root ganglion cells and in the dorsal horn of the rat spinal cord following peripheral nerve injury. *Neuroscience* 34, 465–478. doi: 10.1016/0306-4522(90)90155-W

Wu, X., Walker, C. L., Lu, Q., Wu, W., Eddelman, D. B., Parish, J. M., et al. (2016). RhoA/Rho kinase mediates neuronal death through regulating cPLA2 activation. *Mol. Neurobiol.* 54, 6885–6895. doi: 10.1007/s12035-016-0187-6

Xia, C., Cai, Y., Lin, Y., Guan, R., Xiao, G., and Yang, J. (2016). MiR-133b-5p regulates the expression of the heat shock protein 70 during rat neuronal cell apoptosis induced by the gp120 V3 loop peptide. *J. Med. Virol.* 88, 437–447. doi: 10.1002/jmv.24355

Xin, H., Katakowski, M., Wang, F., Qian, J. Y., Liu, X. S., Ali, M. M., et al. (2017). MicroRNA cluster miR-17-92 cluster in exosomes enhance neuroplasticity and functional recovery after stroke in rats. *Stroke* 48, 747–753. doi: 10.1161/STROKEAHA.116.015204

Xin, H., Li, Y., Cui, Y., Yang, J. J., Zhang, Z. G., and Chopp, M. (2013a). Systemic administration of exosomes released from mesenchymal stromal cells promote functional recovery and neurovascular plasticity after stroke in rats. *J. Cereb. Blood Flow Metab.* 33, 1711–1715. doi: 10.1038/jcbfm.2013.152

Xin, H., Li, Y., Liu, Z., Wang, X., Shang, X., Cui, Y., et al. (2013b). MiR-133b promotes neural plasticity and functional recovery after treatment of stroke with multipotent mesenchymal stromal cells in rats via transfer of exosome-enriched extracellular particles. *Stem Cells* 31, 2737–2746. doi: 10.1002/stem.1409

Yu, Y. M., Gibbs, K. M., Davila, J., Campbell, N., Sung, S., Todorova, T. I., et al. (2011). MicroRNA miR-133b is essential for functional recovery after spinal cord injury in adult zebrafish. *Eur. J. Neurosci.* 33, 1587–1597. doi: 10.1111/j.1460-9568.2011.07643.x

Yune, T. Y., Park, H. G., Lee, J. Y., and Oh, T. H. (2008). Estrogen-induced Bcl-2 expression after spinal cord injury is mediated through phosphoinositide-3-kinase/Akt-dependent CREB activation. *J. Neurotrauma* 25, 1121–1131. doi: 10.1089/neu.2008.0544

Zhang, Y., Chopp, M., Meng, Y., Katakowski, M., Xin, H., Mahmood, A., et al. (2015). Effect of exosomes derived from multipluripotent mesenchymal stromal cells on functional recovery and neurovascular plasticity in rats after traumatic brain injury. *J. Neurosurg.* 122, 856–867. doi: 10.3171/2014.11.JNS14770

Conflict of Interest Statement: The authors declare that the research was conducted in the absence of any commercial or financial relationships that could be construed as a potential conflict of interest.

frontiers in Neuroscience

ORIGINAL RESEARCH
published: 03 December 2018
doi: 10.3389/fnins.2018.00865

Rapamycin Enhances Mitophagy and Attenuates Apoptosis After Spinal Ischemia-Reperfusion Injury

Qiang Li[1†], Shane Gao[2†], Zhanrong Kang[3], Meiyan Zhang[2], Xin Zhao[4], Yu Zhai[1], Jianming Huang[3], Guo-Yuan Yang[5], Wanju Sun[6] and Jian Wang[6*]*

[1] Department of Neurology, Shanghai Ninth People's Hospital, Shanghai Jiao Tong University School of Medicine, Shanghai, China, [2] East Hospital, Tongji University School of Medicine, Shanghai, China, [3] Department of Orthopedics, Shanghai Pudong Hospital, Fudan University Pudong Medical Center, Shanghai, China, [4] Department of Orthopedics, Shanghai Ninth People's Hospital, Shanghai Jiao Tong University School of Medicine, Shanghai, China, [5] Neuroscience and Neuroengineering Research Center, Med-X Research Institute and School of Biomedical Engineering, Shanghai Jiao Tong University, Shanghai, China, [6] Department of Orthopedics, Shanghai Pudong New Area People's Hospital, Shanghai University of Medicine & Health Science, Shanghai, China

OPEN ACCESS

Edited by:
Gang Chen,
The First Affiliated Hospital of Soochow University, China

Reviewed by:
Xuping Li,
Houston Methodist Research Institute, United States
Lezi E,
Duke University, United States

***Correspondence:**
Wanju Sun
sunwanjudoctor@hotmail.com
Jian Wang
purenyiwj@163.com

[†] These authors have contributed equally to this work

Specialty section:
This article was submitted to Neurodegeneration, a section of the journal Frontiers in Neuroscience

Received: 22 July 2018
Accepted: 05 November 2018
Published: 03 December 2018

Citation:
Li Q, Gao S, Kang Z, Zhang M, Zhao X, Zhai Y, Huang J, Yang G-Y, Sun W and Wang J (2018) Rapamycin Enhances Mitophagy and Attenuates Apoptosis After Spinal Ischemia-Reperfusion Injury. Front. Neurosci. 12:865. doi: 10.3389/fnins.2018.00865

The spinal cord is extremely vulnerable to ischemia-reperfusion (I/R) injury, and the mitochondrion is the most crucial interventional target. Rapamycin can promote autophagy and exert neuroprotective effects in several diseases of the central nervous system. However, the impact of rapamycin via modulating mitophagy and apoptosis after spinal cord ischemia-reperfusion injury remains unclear. This study was undertaken to investigate the potential role of rapamycin in modulating mitophagy and mitochondria-dependent apoptosis using the spinal cord ischemia-reperfusion injury (SCIRI) mouse model. We found that rapamycin significantly ($p < 0.05$) enhanced mitophagy by increasing the translocation of p62 and Parkin to the damaged mitochondria in the mouse spinal cord injury model. At the same time, rapamycin significantly ($p < 0.05$) decreased mitochondrial apoptosis related protein (Apaf-1, Caspase-3, Caspase-9) expression by inhibiting Bax translocation to the mitochondria and the release of the cytochrome c from the mitochondria. After 24 h following SCIRI, rapamycin treatment reduced the $TUNEL^+$ cells in the spinal cord ischemic tissue and improved the locomotor function in these mice. Our results therefore demonstrate that rapamycin can improve the locomotor function by promoting mitophagy and attenuating SCIRI -induced apoptosis, indicating its potential therapeutic application in a spinal cord injury.

Keywords: apoptosis, mitophagy, ischemia-reperfusion injury, rapamycin, spinal cord

INTRODUCTION

Spinal cord ischemia-reperfusion injury is a severe clinical complication in surgical interventions of aortic diseases (Turkoz et al., 2007; Cheng et al., 2009; Dublin et al., 2010). Neurons in the spinal cord are vulnerable to ischemic injury because of a high demand for energy. Mitochondria have been proposed to be the principal subcellular target of a ischemia-reperfusion injury.

They are essential not only for generating ATP, but also involved in pathophysiological processes of cell death (Nakai et al., 1997). Functional alterations in the mitochondria resulted in an ATP level reduction, Ca^{2+} homeostasis damage, ROS stress injury and cell apoptosis(Anne Stetler et al., 2013). Therefore, mitochondria have an enormous potential causing cause severe cell damage and play an important role in the pathophysiological process of SCIRI. It is believed that pharmacological agent targeting on mitochondria is one of the most promising approaches for SCIRI therapy.

Mitophagy, the selective clearance of dysfunctional mitochondria by autophagy, is extremely important for controlling the quality and quantity of mitochondria and promoting cell survival (Yuan et al., 2015). Using the rat middle cerebral occlusion (MCAO) mode, electron microscopy has shown that the damaged mitochondria is surrounded by autophagosomes in the ischemic penumbra, suggesting that the mitochondria are degraded by autophagy. Studies also demonstrated that mitophagy activation via the Parkin translocation mitochondria pathway can inhibit cerebral ischemia-reperfusion injury (Zhang et al., 2013). Mitophagy has been implicated in the pathophysiological process of ischemia reperfusion injury and hemorrhagic stroke injury (Zhang et al., 2013; Li et al., 2017, 2018). Therefore, mitophagy may play a pivotal role in neuronal survival during SCIRI.

Rapamycin is widely used as an inducer of autophagy, acting through its inhibitory effect on a mTOR (Mizushima et al., 2008). Increasing studies reported that rapamycin reduced neuronal death by activating the autophagy process in the injured spinal cord (Sekiguchi et al., 2012; Song et al., 2015). There is cross-talk between the autophagy and apoptosis through the mitochondria. In our previous study, we found that rapamycin reduced mitochondrial dysfunction through activating mitophagy in transient MCAO model (Li et al., 2014). However, the potential neuroprotective effect of rapamycin via activating mitophagy following SCIRI, need be clarified. Furthermore, the mechanism of modulating the dynamic balance between mitophagy and apoptosis by rapamycin after SCIRI, remains to be elucidated. Thus, the present study was undertaken to investigate the neuroprotective role of rapamycin via the activation of mitophagy and the inhibition of mitochondria-dependent apoptosis in the SCIRI mice.

MATERIALS AND METHODS

Animals and Experimental Protocol

The experimental protocol was approved by the Ethical Committee of the Experimental Animal Center affiliated with the Tongji University School of Medicine and in accordance with the National Institute of Health Guide for the Care and Use of Laboratory Animals. Male C57BL/6J mice (SLAC Inc., Shanghai, China) aged between 10 and 16 weeks were used for all experiments. A total of 114 mice were randomly assigned to three groups, a schematic diagram of the experimental design is shown in **Figure 1A**. The sham group (n = 18) received the same surgical procedures, but no impact injury was sustained. The rapamycin (Sigma-Aldrich, St. Louis, MO, United States) treatment group (n = 48) received an aortic arch cross-clamping following intraperitoneal rapamycin at the onset of reperfusion (1 mg/kg, 0.5 ml aqueous solution) (Sekiguchi et al., 2012). The vehicle treatment group (n = 48) received an aortic arch cross-clamping, following an intraperitoneal equivalent volume of an aqueous solution.

Spinal Cord Ischemia-Reperfusion Injury (SCIRI)

Mice were anesthetized using 2% isoflurane and placed in the supine position. During the surgery period, the core body temperature was maintained at 37.0 ± 0.5°C using a rectal temperature probe and an automatic temperature-adjusting pad (RWD Life Science, Shenzhen, China). The aortic arch was exposed using a cervicothoracic approach as previously described (Lang-Lazdunski et al., 2000; Bell et al., 2013). A clip was placed on the aortic arch distal to the left common carotid artery and the subclavian artery for 10 min. A laser Doppler blood flow monitor (Moor Instruments, Devon, United Kingdom) was placed over the left femoral artery. Successful occlusion was defined as ≥ 90% reduction in distal flow.

Neurological Assessment

To evaluate the functional consequences of SCIRI, a locomotor rating test using the BMS was performed (Basso et al., 2006). The BMS ranges from a score of 0 for complete paraplegia to a score of 9 for normal function. An investigator blinded to the treatment group, carried out the test in the open field and the BMS scores were measured at 0, 1, 2 days pre-SCIRI and at 24 h post-SCIRI.

Mitochondria Isolation

Mice were anesthetized with sodium pentobarbital (50 mg/kg, intraperitoneal) and perfused transcardially with saline, 24 h after the SCIRI. The spinal cord tissue (T8-L4) was removed and used to isolate the mitochondria with an animal tissue active mitochondrial extraction kit (Genmed Scientifics Inc., Shanghai, China) as previosuly described (Li et al., 2014). The spinal cord tissue was briefly homogenized with a glass homogenizer (15 20 strokes) and centrifuged at 1500 g for 10 min at 4°C. The supernatant was removed and centrifuged at 10,000 g for 10 min. Next, the supernatant was separated via a cytosolic fraction, and the pelleted materials were washed three times and suspended in 10 mM Tris-HCl, pH 7.4, containing 10 mM KCl, 0.25 M sucrose and 5 mM $MgCl_2$. The protein concentration was measured using a Pierce BCA kit

Abbreviations: ATP, adenosine triphosphate; BMS, Basso Mouse Scale; DAPI, 4′-6-diamidino-2-phenylindole; IHC, immunohistochemistry; LC3, microtubule-associated protein light chain 3; MCAO, middle cerebral artery occlusion; mTOR, mammalian target of rapamycin; ROS, reactive oxygen species; SCIRI, spinal cord ischemia-reperfusion injury; TEM, transmission electron microscopy; TUNEL, Terminal deoxynucleotidyl transferase dUTP nick end labeling; VDAC, Voltage-dependent anion channel.

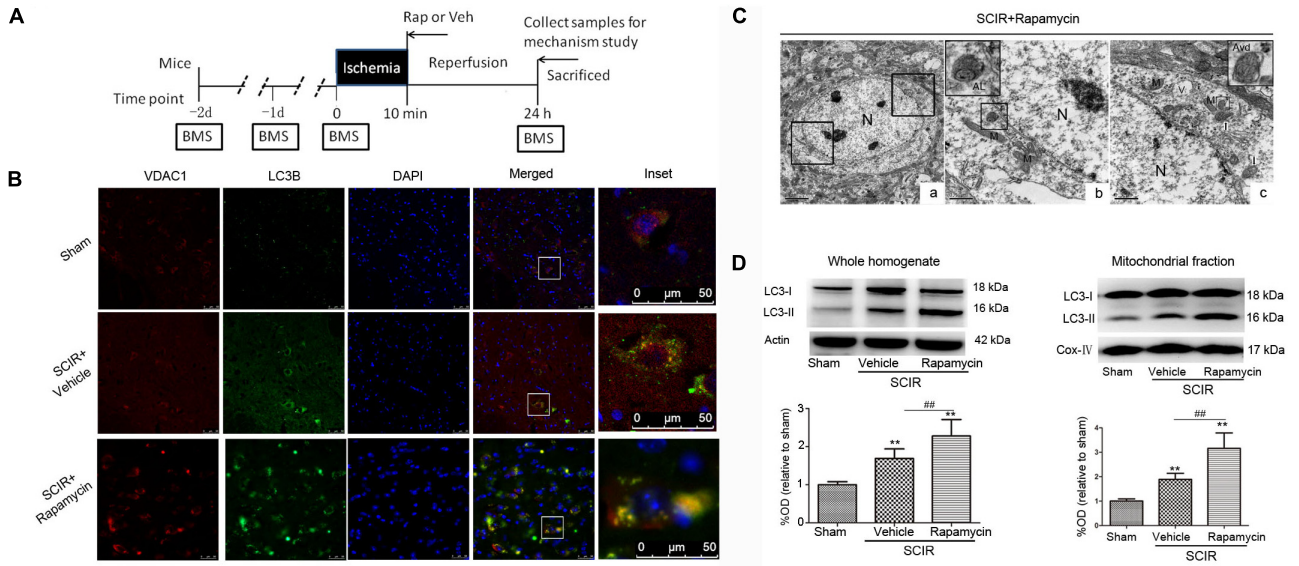

FIGURE 1 | Rapamycin treatment enhanced mitophagy after spinal cord ischemia-reperfusion injury. **(A)**. Schematic diagram of the experimental design. Experimental groups were treated with vehicle and rapamycin (intraperitoneal injection, 1mg/kg). Mice received treatmetn at reperfusion onset and were sacrificed at 24 h after SCIRI. **(B)** Immunohistochemical localization of VDAC1 (mitochondrial marker) and LC3B (autophagy marker) co-staining in spinal cord at 24 h after SCIRI. VDAC1 (red), LC3B (green). The inset images represent higher magnification of the boxed area in the corresponding merged images. **(C)**. Electron micrographs demonstrating neuron mitophagy structure in rapamycin-treated SCIRI mice. Autophagic vacuoles, autolysosomes (AL), typical mitophagy structure and swollen mitochondria (black arrow)were observed in neurons. High magnifications in **(b)** revealed a typical autolysosomes structure. High magnifications in **(c)** revealed a typical mitophagy structure, that is a degradative autophagic vacuole (Avd) including a partially degraded mitochondrial. **(b)** is the high magnification of lower-left box in the figure **C-a** and **(C)** is the high magnification of upper-right box in the figure **C-a**. M-mitochondrial, N-nuclear, V-vacuole. scale bar = 0.5 μm or 2 μm. **(C)** Representative western blots and quantitative graphs demonstrate the expression of LC3-I /LC3-II in the whole homogenates at 24 h after SCIRI. **(D)** Representative western blots and quantitative graphs demonstrate the expression of LC3-I and LC3-II in the mitochondrial fractions at 24 h after SCIRI. Data were shown as mean ± SD, $n = 6$. $^{*}p < 0.05$, $^{**}p < 0.01$ vs. Sham; $^{\#}p < 0.05$, $^{\#\#}p < 0.01$.

(Pierce, Rockford, IL, United States). The isolated mitochondrial and cytosolic fractions were collected for a western blot assay.

Western Blot Analysis

Spinal cord tissues were collected 24 h after the SCIRI, and the whole homogenate, isolated mitochondrial and cytosolic fractions were used for Western blotting. Equal amounts of protein per lane (30 μg) were briefly subjected to electrophoresis on a 4 12% SDS–PAGE gel. Proteins were electrotransferred onto a polyvinylidene difluoride membrane (Millipore, Billerica, MA, United States). The membrane was blocked with 5% non-fat dry milk/0.1% Tween-20 in Tris-buffered saline for 2 h, at room temperature. Thereafter, the membrane was incubated with different primary antibodies, including rabbit anti-LC3B (1:1000 dilution, Sigma-Aldrich), rabbit anti-p62 (1:800 dilution, Sigma-Aldrich), rabbit anti-Parkin (1:500 dilution, Santa Cruz Biotechnology Inc., Santa Cruz, CA, United States), mouse anti-Cyt C (1:1000 dilution, Santa Cruz Biotechnology Inc., Santa Cruz, CA, United States), rabbit anti-Bax (1:500 dilution, Santa Cruz Biotechnology Inc., Santa Cruz, CA, United States) and mouse anti-Cox IV (1:500 dilution, Santa Cruz Biotechnology Inc., Santa Cruz, CA, United States), β-actin (1:3000 dilution, Santa Cruz Biotechnology Inc., Santa Cruz, CA, United States), rabbit anti-cleaved caspase-3 (1:1000 dilution, Cell Signaling Technology, Danvers), rabbit anti-cleaved caspase-9 (1:1000 dilution, Cell Signaling Technology), and rabbit anti-Apaf-1 (1:1000 dilution, Cell Signaling Technology). Subsequently, the membrane was treated with horseradish peroxidase-labeled secondary antibody for 2 h at room temperature. Immunoblots were probed using an enhanced ECL substrate (Pierce). The chemiluminescence level was recorded using an imaging system (Bio-Rad, Hercules, CA, United States). The results were normalized to a loading control β–actin or Cox-IV (mitochondrial control).

Transmission Electronic Microscope

Mice were sacrificed and perfused transcardially with 4% paraformaldehyde and 0.5% glutaraldehyde in a 0.1 mol phosphate buffer,24 h post-SCIRI. The spinal cord tissue (T8-L4) was collected and coronal sections (100 μm) were cut by a vibratome, and postfixed with 4% glutaraldehyde in a 0.1 mmol cacodylate buffer (pH 7.4) for 1 h and incubated with 1% osmium tetroxide in a 0.1 mmol cacodylate buffer for 2 h. Spinal cord sections were dehydrated by an ascending series of ethanol and dry acetone and then embedded in Durcupan ACM Fluka (Sigma-Aldrich).Ultrathin sections (0.1 μm) were stained with uranyl acetate and

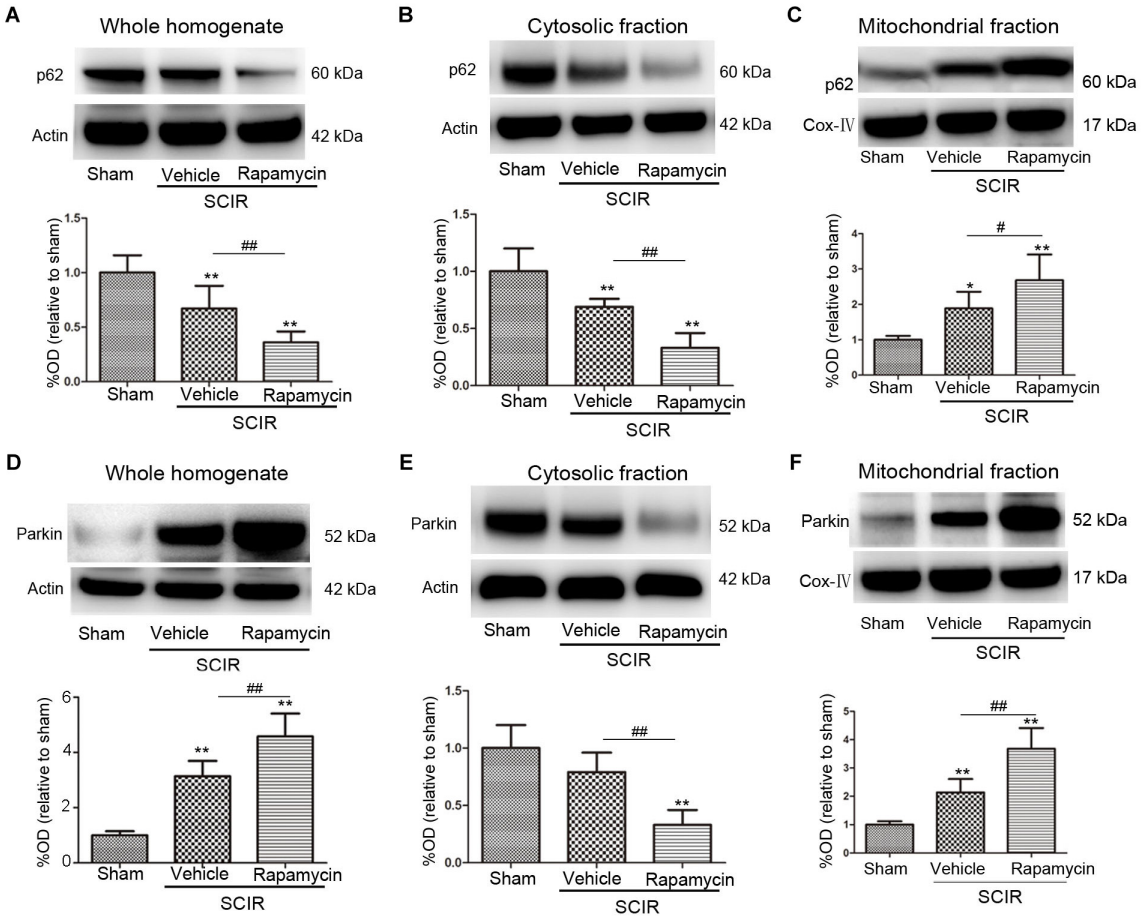

FIGURE 2 | Rapamycin enhanced mitophagy via promoting p62, Parkin translocation to the mitochondria. **(A–C)** Representative western blots and quantitative graphs demonstrate the expression of p62 in the whole homogenates, in the cytosolic fractions and in the mitochondrial fractions at 24 h after SCIRI. Data were shown as mean ± SD, $n = 6$. $^{*}p < 0.05$, $^{**}p < 0.01$ vs; Sham, $^{\#}p < 0.05$, $^{\#\#}p < 0.01$. **(D-F)** Representative western blots and quantitative graphs demonstrate the expression of Parkin in the whole homogenates, in the cytosolic fractions and in the mitochondrial fractions at 24 h after SCIRI. Cox- IV is as inner control for mitochondria protein, β-actin is as inner control for tissue homogenate protein. Data were shown as mean ± SD, $n = 6$. $^{*}p < 0.05$, $^{**}p < 0.01$ vs. Sham; $^{\#}p < 0.05$, $^{\#\#}p < 0.01$.

lead citrate and subsequently examined with a JEOL JEM-1230 transmission electron microscope (JEOL, Tokyo, Japan).

Immunohistochemistry Staining

Spinal cord tissues were collected 24 h after the SCIRI. The spinal cords (T8-L4) were fixed and sectioned into 15 μm slices using a Leica cryostat. Immunohistochemistry staining was performed as described previously (Han et al., 2016). Sections were blocked with 10% goat serum for 1 h at room temperature, followed by an incubation with primary antibodies overnight at 4°C and an incubation for 60 min at 25°C with secondary antibodies conjugated with the appropriate Alexa 594-conjugated secondary antibody (Molecular Probes, Eugene, OR, United States). The compound DAPI (Molecular Probes) was used to label cell nuclei. Primary antibodies were used in IHC as follows: rabbit anti- LC3 B (1:200 dilution, Sigma-Aldrich), mouse anti- Voltage-dependent anion channel (VDAC)1 (1:200 dilution, Millipore). Negative controls were performed without the primary antibody. The sections were examined under a fluorescence microscope (Eclipse 90i; Nikon, Tokyo, Japan).

Terminal Deoxynucleotidyl Transferase dUTP Nick End Labeling (TUNEL) Assay

A TUNEL assay is the most commonly used technique for examining apoptosis via DNA fragmentation. TUNEL staining was performed using an In Situ Cell Death Detection kit (Roche, Shanghai, China) for spinal cords 24 h after the SCIRI, according to established protocols (Zhang et al., 2018). After TUNEL labeling, cell nuclei were labeled with DAPI, and examined under a fluorescence microscope. The number of TUNEL positive cells in each section was counted. The TUNEL-positive cells were defined as cells double labeled with TUNEL and DAPI. The quantity of TUNEL-positive cells of three sections from each mouse

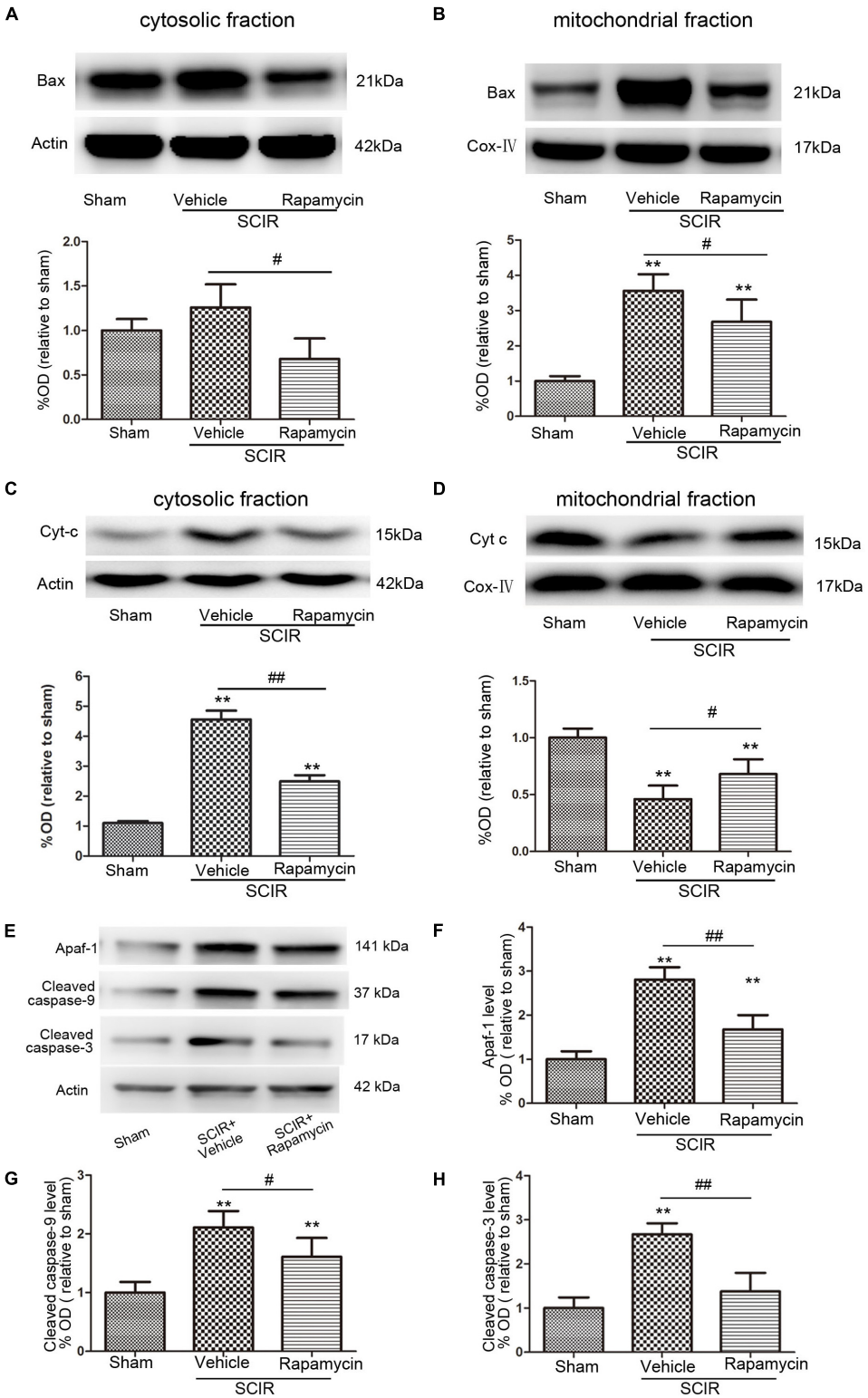

FIGURE 3 | Rapamycin treatment following spinal cord ischemic injury reduced mitochondrial release of apoptosis related proteins. **(A,B)** Representative western blots and quantitative graphs demonstrate the expression of Bax in cytosolic and mitochondrial fractions at 24 h after SCIRI. Data are presented as the mean ± SD, $n = 6$. $^{*}p < 0.05$, $^{**}p < 0.01$ vs. Sham; $^{\#}p < 0.05$, $^{\#\#}p < 0.01$. **(C,D)** Representative western blots and quantitative graphs demonstrate the expression of Cyt-c in cytosolic and mitochondrial fractions at 24 h after SCIRI. Data are presented as the mean ± SD, $n = 6$. $^{*}p < 0.05$, $^{**}p < 0.01$ vs. Sham; $^{\#}p < 0.05$, $^{\#\#}p < 0.01$. **(E–H)** Representative western blots and quantitative graphs demonstrate the expression of mitochondrial apoptosis related proteins (Apaf-1, cleaved Caspase-3, cleaved Caspase-9) at 24 h after SCIR. Data are presented as the mean ± SD, n = 6. $^{*}p < 0.05$, $^{**}p < 0.01$ vs. Sham; $^{\#}p < 0.05$, $^{\#\#}p < 0.01$.

were respectively counted at high magnification and used for analysis.

Statistical Analysis

The Mann-Whitney U test was used to compare the neurologic scores and cell numbers. A quantitative analyses of the optical density of the Western blots were analyzed by one-way ANOVA, followed by a Bonferroni *post hoc* test (GraphPad Software, San Diego, CA, United States). Parametric data were presented as mean ± SD. A p-value of less than 0.05 was considered statistically significant.

RESULTS

Rapamycin Enhanced Mitophagy After SCIRI

To determine the characteristics of the neuronal mitophagy, we performed an IHC co-staining with antibodies against the LC3B (autophagy marker) and VDAC1(mitochondrial marker) in the injured spinal cord. We found that cells expressing LC3 were increased both in the rapamycin-treated mice and in the vehicle-treated mice, compared with the sham controls. The population of cells co-staining LC3B and VDAC1 in the

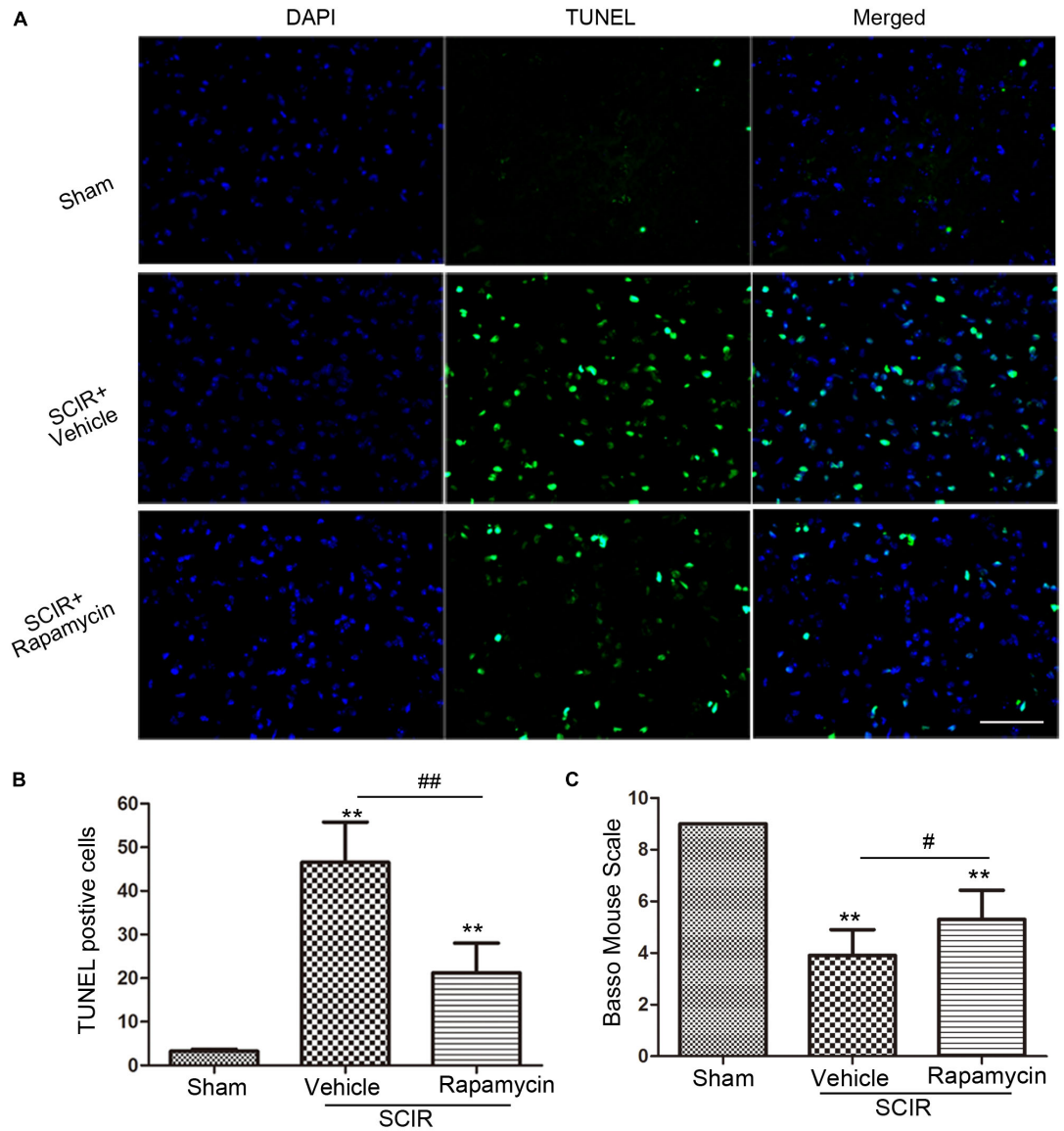

FIGURE 4 | Rapamycin attenuated spinal cord ischemia-reperfusion induced apoptosis. **(A)**. These cells were stained with TUNEL and DAPI. The merged picture shows colocolization of apoptotic and nuclear markers. Scare bar = 50 μm. **(B)**.The bar graph shows rapamycin treatment rescued neurons from apoptosis at 24 h after SCIR. Data were shown as mean ± SD, $n = 6$. The numbers of apoptotic cells were counted in three sections of ischemic spinal cord. $^{*}p < 0.05$, $^{**}p < 0.01$ vs. Sham; $^{\#}p < 0.05$, $^{\#\#}p < 0.01$. **(C)** Bar graphs show the rapamycin-treated mice have significantly higher BMS scores than the vehicle-treated mice at 24 h after injury. Data were shown as mean ± SD, $n = 16$. $^{*}p < 0.05$, $^{**}p < 0.01$ vs. Sham; $^{\#}p < 0.05$, $^{\#\#}p < 0.01$.

rapamycin-treated mice was obviously higher than that in the vehicle-treated mice (**Figure 1B**). Higher magnification revealed the accumulation of LC3B-VDAC1 positive punctate dots in the neuron (**Figure 1B**). We also examined neurons in the gray matter of spinal cord mitophagy structures, corresponding to LC3B-VDAC1 co-staining puncta used with TEM. TEM results showed that the autolysosome filled with membranous whorls and an abnormal autophagic vesicle was distributed in neurons of the gray matter (**Figures 1C-b**). Furthermore, a mitophagy structure was clearly observed, and that the partially degraded mitochondria was surrounded by double membranes (**Figure 1C-c**).

To quantitatively analyze the mitophagy level, the mitochondrial fraction was isolated from the spinal cord tissue and LC3-II expression was determined in the mitochondrial fraction of the spinal cord using Western blotting. We found that rapamycin treatment could significantly increase the level of LC3-II in the ischemic spinal cord ($p < 0.01$, **Figure 1D**). Furthermore, we found that rapamycin treatment could significantly increase LC3-II expression in the mitochondrial fraction of the spinal cord ($p < 0.01$, **Figure 1D**). The data indicated that rapamycin treatment markedly enhanced mitophagy after the SCIRI.

Rapamycin Enhanced Mitophagy via Promoting p62, Parkin Translocation to the Mitochondria

To explore the mechanism of mitophagy activated by rapamycin, we also measured the mitochondrial p62 and Parkin after the SCIRI, which are key mediators for mitophagy (Ashrafi and Schwarz, 2013). The p62 as an adapter protein, can combine with damaged mitochondrial degraded by autophagy. Our results showed that rapamycin markedly promoted p62 accumulation in the mitochondrial fraction ($p < 0.05$, **Figures 2A–C**). Interestingly, ischemia-reperfusion induced the increase of the Parkin expression in the whole homogenate ($p < 0.01$, **Figure 2D**). Compared between the cytosolic and mitochondrial fraction, the results showed that rapamycin treatment caused a significant Parkin reduction in the cytosolic fraction and an increase in the mitochondrial fraction ($p < 0.01$, **Figures 2E,F**). These data suggested that rapamycin treatment significantly increased the Parkin expression in the mitochondria fraction after SCIRI. Overall, the data revealed that rapamycin treatment significantly enhanced mitophagy by increasing the translocation of p62 and Parkin to the damaged mitochondria.

Rapamycin Inhibited the Release of Apoptosis-Related Proteins From Mitochondria

The mitochondria-dependant apoptosis is a well-accepted mechanism underlying neuronal death induced by an ischemia-reperfusion injury. The mitochondria transmit apoptotic signals through the release of cytochrome *c* to the cytoplasm during ischemia-reperfusion (Carloni et al., 2008). The release of cytochrome *c* correlates closely to the translocation of the proapoptotic proteins Bax to the mitochondria. In this present study, the results showed that SCIRI caused a significant Bax reduction in the cytosolic fraction and Bax increase in the mitochondrial fraction, indicating that SCIRI induces a robust Bax translocation from the cytosol to the mitochondria. But rapamycin treatment remarkably reduced Bax translocation after SCIRI (**Figures 3A,B**). Cytochrome *c*, an early marker of mitochondria-dependant apoptosis, was determined both in the cytosolic fraction and the mitochondrial fraction of the spinal cord. As shown in **Figures 3C,D**, cytochrome *c* expression significantly increased in the cytosolic fraction and decreased in the mitochondrial fraction after SCIRI. But rapamycin treatment significantly inhibited cytochrome *c* release from mitochondria, induced by the ischemia-reperfusion injury(**Figure 3D**), which shows that rapamycin treatment decreased the cytochrome *c* level in the cytosolic fraction and increased in the mitochondrial fraction. Moreover, western blotting results revealed that rapamycin treatment significantly decreased mitochondrial apoptosis related proteins (Apaf-1, Caspase-3, Caspase-9) released in SCIRI mice ($p < 0.01$ and $p < 0.05$, respectively, **Figures 3E–H**). Therefore, these data indicated that the activation of mitophagy by rapamycin in the reperfusion phase, attenuated mitochondria-dependent apoptosis in the ischemic spinal cord.

Rapamycin Attenuated Apoptosis and Improved Locomotor Function Following Spinal Cord Ischemia

Apoptosis underlies neuronal loss after SCIRI (Wu et al., 2014). We speculated that improved locomotor function by rapamycin treatment, may be attributed to the inhibition of cell apoptosis. To confirm this, a TUNEL assay was conducted to investigate the protective effect of rapamycin against apoptosis in SCIRI mice. We found marked TUNEL-positive cells in the spinal gray matter 24 h after SCIRI (**Figure 4A**). But rapamycin treatment significantly reduced TUNEL-positive cells after SCIRI ($p < 0.01$, **Figure 4B**). Additionally, BMS scores data, indicated the improvement of locomotor function, consistent with immunostaining results in the rapamycin-treated mice 24 h after SCIRI ($p < 0.05$, **Figure 4C**).

DISCUSSION

In the present study, we identified that autophagy and mitophagy were involved in the SCIRI process. Importantly, identified the protective roles of rapamycin on mitochondria after SCIRI: 1) rapamycin activated mitophagy by promoting p62 and Parkin translocation to the mitochondria; 2) rapamycin inhibited the release of apoptosis-related proteins from the mitochondria and attenuated mitochondria-dependent apoptosis in the ischemic spinal cord; and 3) rapamycin reduced neural tissue damage and improved locomotor function after SCIRI. The present study indicates that rapamycin treatment had a neuroprotective effect against SCIRI injury. These findings provide novel evidence that mitophagy activation can counteract apoptosis after a spinal ischemia-reperfusion injury.

Previous studies have demonstrated that the inhibition of the mTOR signaling, has a neuroprotective effect in the central nervous system (Carloni et al., 2008; Yin et al., 2012; Li et al., 2014). Some studies also demonstrate that rapamycin significantly reduces neuronal loss and cell death in the injured spinal cord (Sekiguchi et al., 2012; Wang et al., 2014). Simvastatin improves functional recovery through autophagy induction by inhibiting the mTOR signaling pathway after spinal cord injury in rats (Gao et al., 2015). Autophagy is involved in the pathophysiological process of SCIRI. Moreover, it was believed that autophagy plays opposing roles during the bimodal stage after SCIRI. Early activated autophagy alleviates spinal cord injury, but later activated autophagy excessively elevated autophagy aggravates I/R injury by inducing autophagic cell death (Fang et al., 2016). Concurrent with these findings, we found that enhancing autophagy by rapamycin treatment, immediately after reperfusion, exerts a protective role on neurons in a SCIR injury. Rapamycin treatment therefore restored neurological and motor function in SCIRI mice.

Given the benefits of autophagy activation via mTOR inhibition, the role of enhanced mitophagy of rapamycin during reperfusion, might imply a contribution to neuroprotection.

Mitophagy, the selective autophagy, is extremely crucial in maintaining mitochondrial homeostasis by removing damaged mitochondria and was implicated in the process of an ischemia-reperfusion injury (Zhang et al., 2013; Zuo et al., 2014; Yuan et al., 2015). Indeed, our results demonstrated that rapamycin could activate not only general autophagy but also mitophagy. In our study, we found marked LC3B-VDAC1 costaining puncta and a marked mitophagy structure under TEM in rapamycin-treated SCIRI mice. In addition, we found that rapamycin upregulated the LC3-II levels in a mitochondrial fraction, suggesting that mitophagosomes accumulated in spinal cord neurons. The key molecular mechanism for rapamycin-induced mitophagy activation is closely related to the p62 and Parkin pathway (Yuan et al., 2015; Tang et al., 2016). In this present study, we found that rapamycin significantly upregulated the p62 and Parkin translocation to the mitochondria after SCIRI injury. The phosphorylation of p62 has been proposed to initiate the binding of p62 to ubiquitinated proteins during autophagy and mitophagy (Ichimura et al., 2013). p62 contains a LC3 interacting domain and facilitates the recruitment of damaged mitochondria to the phagophore by binding to LC3-II (Ding et al., 2010; Geisler et al., 2010). Through polyubiquitinateion, Parkin can bind to the outer membrane of damaged mitochondria, followed by p62 binding to LC3-II, which can further result in damaged mitochondrial degradation via the autophagic machinery (Harper et al., 2018). A previous study has also demonstrated that mitophagy mediated by the Parkin protein, underlies the neuroprotection that occurrs in the process of cerebral ischemia reperfusion (Zhang et al., 2013). In addition to its role in mitophagy process, Parkin also stimulates mitochondrial biogenesis, presumably to replace damaged mitochondria with healthy and functional organelles (Shin et al., 2011). This effect of rapamycin could be examined in future studies.

Spinal cord ischemia reperfusion leads to neuronal death by inducing apoptosis (Wu et al., 2014; Foley et al., 2015). Importantly, mitochondria play a crucial role in regulating neuronal apoptosis (Zuo et al., 2014; Liu et al., 2015). Damaged mitochondria can release pro-apoptotic proteins to increase the activation of caspases and cell death (Adams and Cory, 2007; Anne Stetler et al., 2013). Removal of dysfunctional mitochondria is essential for cellular survival(Anne Stetler et al., 2013; Ashrafi and Schwarz, 2013). Therefore, mitophagy activation may subsequently attenuate apoptosis. It is supposed that the elimination of damaged mitochondria inhibits mitochondria-dependent apoptosis and subsequently promotes neuronal survival. In this study, results showed that rapamycin treatment significantly reduced Bax translocation to mitochondria and cytochrome *c* release from mitochondria in SCIRI mice. Additionally, rapamycin treatment significantly decreased the number of TUNEL-positive cells 24 h after SCIRI. Our results showed that rapamycin treatment resulted in neuroprotection and a significant functional recovery after SCIRI. We show here that these protective effects are linked to an increased mitophagic flux and inhibits mitochondria-dependent apoptosis. Our previous study reported that rapamycin could reduce brain injury after cerebral ischemia by promoting mitophagy (Li et al., 2014). The evidence in this study further demonstrated the central role of the mitochondria in neuronal survival after SCIRI. This work proves that the mitochondria is an important therapeutic target to protect against SCIRI. These findings increased our understanding of the relationship between mitophagy and neuroprotection after SCIRI.

CONCLUSION

The present work showed that rapamycin administration during the acute phase of SCIRI could significantly reduce the neural tissue damage and locomotor impairment. Enhanced mitophagy by rapamycin could inhibit apoptosis and protect against SCIRI injury. Therefore, rapamycin treatment is a promising and effective therapeutic strategy for SCIRI injury.

AUTHOR CONTRIBUTIONS

JW and WS conceived and designed the research. QL, ZK, SG, MZ, XZ, and YZ performed the experiments. QL, G-YY, and JH analyzed the data and wrote the paper. QL and JW obtained the funding. All authors read and approved the final draft.

FUNDING

This work was supported by a grant (QL, 14YZ049) from Innovation Program of Shanghai Municipal Education Commission and a grant (QL, 17ZR1416200) from Shanghai Municipal Natural Science Foundation, a grant from Shanghai Municipal Natural Science Foundation (JW, 16ZR1444600).

REFERENCES

Adams, J. M., and Cory, S. (2007). Bcl-2-regulated apoptosis: mechanism and therapeutic potential. *Curr. Opin. Immunol.* 19, 488–496. doi: 10.1016/j.coi.2007.05.004

Anne Stetler, R., Leak, R. K., Gao, Y., and Chen, J. (2013). The dynamics of the mitochondrial organelle as a potential therapeutic target. *J. Cereb. Blood Flow Metab.* 33, 22–32. doi: 10.1038/jcbfm.2012.158

Ashrafi, G., and Schwarz, T. L. (2013). The pathways of mitophagy for quality control and clearance of mitochondria. *Cell Death. Differ.* 20, 31–42. doi: 10.1038/cdd.2012.81

Basso, D. M., Fisher, L. C., Anderson, A. J., Jakeman, L. B., McTigue, D. M., and Popovich, P. G. (2006). Basso mouse scale for locomotion detects differences in recovery after spinal cord injury in five common mouse strains. *J. Neurotrauma* 23, 635–659. doi: 10.1089/neu.2006.23.635

Bell, M. T., Puskas, F., Agoston, V. A., Cleveland, J. C. Jr., Freeman, K. A., Gamboni, F., et al. (2013). Toll-like receptor 4-dependent microglial activation mediates spinal cord ischemia-reperfusion injury. *Circulation* 128(11 Suppl. 1), S152–S156. doi: 10.1161/CIRCULATIONAHA.112.000024

Carloni, S., Buonocore, G., and Balduini, W. (2008). Protective role of autophagy in neonatal hypoxia-ischemia induced brain injury. *Neurobiol. Dis.* 32, 329–339. doi: 10.1016/j.nbd.2008.07.022

Cheng, M. Y., Lyu, R. K., Chang, Y. J., Chen, C. M., Chen, S. T., Wai, Y. Y., et al. (2009). Concomitant spinal cord and vertebral body infarction is highly associated with aortic pathology: a clinical and magnetic resonance imaging study. *J. Neurol.* 256, 1418–1426. doi: 10.1007/s00415-009-5126-2

Ding, W. X., Li, M., Chen, X., Ni, H. M., Lin, C. W., Gao, W., et al. (2010). Autophagy reduces acute ethanol-induced hepatotoxicity and steatosis in mice. *Gastroenterology* 139, 1740–1752. doi: 10.1053/j.gastro.2010.07.041

Dublin, A. B., Latchaw, R. E., Herrera, D. A., and Dahlin, B. C. (2010). Delayed complication after embolotherapy of a vertebral arteriovenous fistula: spinal cord ischemia. *J. Vasc. Interv. Radiol.* 21, 392–393. doi: 10.1016/j.jvir.2009.11.008

Fang, B., Li, X. Q., Bao, N. R., Tan, W. F., Chen, F. S., Pi, X. L., et al. (2016). Role of autophagy in the bimodal stage after spinal cord ischemia reperfusion injury in rats. *Neuroscience* 328, 107–116. doi: 10.1016/j.neuroscience.2016.04.019

Foley, L. S., Fullerton, D. A., Bennett, D. T., Freeman, K. A., Mares, J., Bell, M. T., et al. (2015). Spinal cord ischemia-reperfusion injury induces erythropoietin receptor expression. *Ann. Thorac. Surg.* 100, 41–46; discussion 46. doi: 10.1016/j.athoracsur.2015.01.027

Gao, K., Wang, G., Wang, Y., Han, D., Bi, J., Yuan, Y., et al. (2015). Neuroprotective Effect of Simvastatin via Inducing the Autophagy on Spinal Cord Injury in the Rat Model. *Biomed. Res. Int.* 2015:260161. doi: 10.1155/2015/260161

Geisler, S., Holmström, K. M., Skujat, D., Fiesel, F. C., Rothfuss, O. C., Kahle, P. J., et al. (2010). PINK1/Parkin-mediated mitophagy is dependent on VDAC1 and p62/SQSTM1. *Nat. Cell Biol.* 12, 119–131. doi: 10.1038/ncb2012

Han, X., Lan, X., Li, Q., Gao, Y., Zhu, W., Cheng, T., et al. (2016). Inhibition of prostaglandin E2 receptor EP3 mitigates thrombin-induced brain injury. *J. Cereb. Blood Flow Metab.* 36, 1059–1074. doi: 10.1177/0271678X15606462

Harper, J. W., Ordureau, A., and Heo, J. M. (2018). Building and decoding ubiquitin chains for mitophagy. *Nat. Rev. Mol. Cell Biol.* 19, 93–108. doi: 10.1038/nrm.2017.129

Ichimura, Y., Waguri, S., Sou, Y. S., Kageyama, S., Hasegawa, J., Ishimura, R., et al. (2013). Phosphorylation of p62 activates the Keap1-Nrf2 pathway during selective autophagy. *Mol. Cell* 51, 618–631. doi: 10.1016/j.molcel.2013.08.003

Lang-Lazdunski, L., Matsushita, K., Hirt, L., Waeber, C., Vonsattel, J. P., Moskowitz, M. A., et al. (2000). Spinal cord ischemia. Development of a model in the mouse. *Stroke* 31, 208–213. doi: 10.1161/01.STR.31.1.208

Li, Q., Han, X., Lan, X., Gao, Y., Wan, J., Durham, F., et al. (2017). Inhibition of neuronal ferroptosis protects hemorrhagic brain. *JCI Insight* 2:e90777. doi: 10.1172/jci.insight.90777

Li, Q., Weiland, A., Chen, X., Lan, X., Han, X., Durham, F., et al. (2018). Ultrastructural characteristics of neuronal death and white matter injury in mouse brain tissues after intracerebral hemorrhage: coexistence of ferroptosis, autophagy, and necrosis. *Front. Neurol.* 9:581. doi: 10.3389/fneur.2018.00581

Li, Q., Zhang, T., Wang, J., Zhang, Z., Zhai, Y., Yang, G. Y., et al. (2014). Rapamycin attenuates mitochondrial dysfunction via activation of mitophagy in experimental ischemic stroke. *Biochem. Biophys. Res. Commun.* 444, 182–188. doi: 10.1016/j.bbrc.2014.01.032

Liu, J. M., Yi, Z., Liu, S. Z., Chang, J. H., Dang, X. B., Li, Q. Y., et al. (2015). The mitochondrial division inhibitor mdivi-1 attenuates spinal cord ischemia-reperfusion injury both in vitro and in vivo: involvement of BK channels. *Brain Res.* 1619, 155–165. doi: 10.1016/j.brainres.2015.03.033

Mizushima, N., Levine, B., Cuervo, A. M., and Klionsky, D. J. (2008). Autophagy fights disease through cellular self-digestion. *Nature* 451, 1069–1075. doi: 10.1038/nature06639

Nakai, A., Kuroda, S., Kristian, T., and Siesjo, B. K. (1997). The immunosuppressant drug FK506 ameliorates secondary mitochondrial dysfunction following transient focal cerebral ischemia in the rat. *Neurobiol. Dis.* 4, 288–300. doi: 10.1006/nbdi.1997.0146

Sekiguchi, A., Kanno, H., Ozawa, H., Yamaya, S., and Itoi, E. (2012). Rapamycin promotes autophagy and reduces neural tissue damage and locomotor impairment after spinal cord injury in mice. *J. Neurotrauma* 29, 946–956. doi: 10.1089/neu.2011.1919

Shin, J. H., Ko, H. S., Kang, H., Lee, Y., Lee, Y. I., Pletinkova, O., et al. (2011). PARIS (ZNF746) repression of PGC-1alpha contributes to neurodegeneration in Parkinson's disease. *Cell* 144, 689–702. doi: 10.1016/j.cell.2011.02.010

Song, Y., Xue, H., Liu, T. T., Liu, J. M., and Chen, D. (2015). Rapamycin plays a neuroprotective effect after spinal cord injury via anti-inflammatory effects. *J. Biochem. Mol. Toxicol.* 29, 29–34. doi: 10.1002/jbt.21603

Tang, Y. C., Tian, H. X., Yi, T., and Chen, H. B. (2016). The critical roles of mitophagy in cerebral ischemia. *Protein Cell* 7, 699–713. doi: 10.1007/s13238-016-0307-0

Turkoz, A., Gulcan, O., Kizilkilic, O., Kocum, A., and Turkoz, R. (2007). Spinal cord ischemia caused by cardiac arrest secondary to pericardial effusion. *J. Cardiothorac. Vasc. Anesth.* 21, 91–92. doi: 10.1053/j.jvca.2005.08.002

Wang, Z. Y., Liu, W. G., Muharram, A., Wu, Z. Y., and Lin, J. H. (2014). Neuroprotective effects of autophagy induced by rapamycin in rat acute spinal cord injury model. *Neuroimmunomodulation* 21, 257–267. doi: 10.1159/000357382

Wu, Y., Satkunendrarajah, K., and Fehlings, M. G. (2014). Riluzole improves outcome following ischemia-reperfusion injury to the spinal cord by preventing delayed paraplegia. *Neuroscience* 265, 302–312. doi: 10.1016/j.neuroscience.2014.01.059

Yin, L., Ye, S., Chen, Z., and Zeng, Y. (2012). Rapamycin preconditioning attenuates transient focal cerebral ischemia/reperfusion injury in mice. *Int. J. Neurosci.* 122, 748–756. doi: 10.3109/00207454.2012.721827

Yuan, Y., Zhang, X., Zheng, Y., and Chen, Z. (2015). Regulation of mitophagy in ischemic brain injury. *Neurosci Bull.* 31, 395–406. doi: 10.1007/s12264-015-1544-6

Zhang, X., Wu, Q., Lu, Y., Wan, J., Dai, H., Zhou, X., et al. (2018). Cerebroprotection by salvianolic acid B after experimental subarachnoid hemorrhage occurs via Nrf2- and SIRT1-dependent pathways. *Free Radic. Biol. Med.* 124, 504–516. doi: 10.1016/j.freeradbiomed.2018.06.035

Zhang, X., Yan, H., Yuan, Y., Gao, J., Shen, Z., Cheng, Y., et al. (2013). Cerebral ischemia-reperfusion-induced autophagy protects against neuronal injury by mitochondrial clearance. *Autophagy* 9, 1321–1333. doi: 10.4161/auto.25132

Zuo, W., Zhang, S., Xia, C. Y., Guo, X. F., He, W. B., and Chen, N. H. (2014). Mitochondria autophagy is induced after hypoxic/ischemic stress in a Drp1 dependent manner: the role of inhibition of Drp1 in ischemic brain damage. *Neuropharmacology* 86, 103–115. doi: 10.1016/j.neuropharm.2014.07.002

Conflict of Interest Statement: The authors declare that the research was conducted in the absence of any commercial or financial relationships that could be construed as a potential conflict of interest.

frontiers in Neuroscience

REVIEW
published: 14 January 2019
doi: 10.3389/fnins.2018.01022

Crosstalk Between Autophagy and Cerebral Ischemia

*Yulin Sun, Yuanhan Zhu, Xiaojun Zhong, Xinle Chen, Jun Wang and Guozheng Ying**

Department of Neurosurgery, Zhejiang Rongjun Hospital, Jiaxing, China

With the use of advanced electron microscopy and molecular biology tools, several studies have shown that autophagy is involved in the development of ischemic stroke. A series of molecular mechanisms are involved in the regulation of autophagy. In this work, the possible molecular mechanisms involved in autophagy during ischemic stroke were reviewed and new potential targets for the study and treatment of ischemic stroke were provided.

Keywords: autophagy, cerebral ischemia, mechanism, apoptosis, target

OPEN ACCESS

Edited by:
Gao Chen,
Zhejiang University, China

Reviewed by:
Yuanbo Pan,
Shanghai Jiao Tong University School of Medicine, China
Gaiqing Wang,
The Second Hospital of Shanxi Medical University, China

***Correspondence:**
Guozheng Ying
chenyongp2010@sina.com

Specialty section:
This article was submitted to Neurodegeneration, a section of the journal Frontiers in Neuroscience

Received: *30 September 2018*
Accepted: *18 December 2018*
Published: *14 January 2019*

Citation:
Sun Y, Zhu Y, Zhong X, Chen X, Wang J and Ying G (2019) Crosstalk Between Autophagy and Cerebral Ischemia. Front. Neurosci. 12:1022. doi: 10.3389/fnins.2018.01022

INTRODUCTION

The incidence of ischemic stroke has increased in recent years, accounting for 60–80% of all strokes. Generally, hypoxic ischemic encephalopathy and acute cerebrovascular accidents cause insufficient blood flow to the brain tissue, which in turn leads to brain cell metabolic disorders, leading to brain cell death, and irreversible damage to tissues. Thrombolytic therapy is a clinically effective treatment, but its limited time window and the associated high rate of recurrence limit its clinical application. Therefore, there is an extremely urgent need to find new and effective therapeutic targets and drugs for ischemic stroke.

Autophagy is a phagocytic degradation process of foreign bodies, damaged or aging organelles in the cytoplasm by autophagy lysosomal system. It belongs to non-caspase-dependent programmed death. Due to the transport and properties of active proteins after autophagy mitosis, neuronal survival is highly dependent on autophagy under physiological conditions. However, recent studies have shown that (Liu et al., 2018; Wang P. et al., 2018) after ischemic stroke, autophagy is activated and may be involved in the development of ischemic stroke. A series of molecular mechanisms are involved in the regulation of autophagy. This review focuses on the role of autophagy in ischemic stroke and its possible molecular mechanisms.

OVERVIEW OF AUTOPHAGY

Autophagy is derived from a Greek words meaning "phagy yourself." It is a highly conserved cell behavior, mainly involved in the circulation as well as reuse of macromolecular substances in cells. It is also involved in the removal of damaged organelles, and plays an important role in maintaining the homeostasis of the intracellular environment.

Autophagy can be induced by changes in the internal conditions of the cell, such as organelles and cytoplasm accumulation or damage, or the cells are stimulated by external conditions, such as hunger, high temperature, hypoxia, and hormone stimulation (Doherty and Baehrecke, 2018). Mammalian autophagy is often divided into three types: macroautophagy, microautophagy, and chaperon mediated autophagy (CMA). In general terms, "autophagy" refers to large autophagy, which is responsible for the degradation of intracellular stable and persistent proteins to produce

amino acids to maintain cell survival in the absence of nutrients. Microautophagy is a depression of the lysosomal membrane, direct phagocytosis of the cytoplasm, organelles, or nucleus to form autophagosomes, which are then degraded by lysosomal enzymes. The chaperone-mediated autophagy is selective, for instance, chaperone HSC70 recognizes a soluble cytosolic protein substrate with a KFERQ sequence and finally degrades the protein substrate with the KFERQ sequence. Its main role in the central nervous system is macrophagy and molecular chaperone-mediated autophagy (Nikoletopoulou et al., 2015).

RELATIONSHIP BETWEEN AUTOPHAGY AND ISCHEMIC STROKE

Mitochondrial dysfunction, acidosis, oxidative stress, calcium overload, excitotoxicity, and inflammatory response are involved in the development of cerebral ischemia-reperfusion injury (Halestrap, 2006), and leads to the accumulation of foreign bodies in the brain tissue to varying degrees. An increase in damaged cells may in turn induce the occurrence of autophagy. Nitatori et al. (1995) observed a significant increase in cathepsin B immunopositive lysosomes and an increase in autophagic phagocytosis using transmission of transient after cerebral ischemia in gerbils. This is the first time that autophagy was found to be activated in cerebral ischemia. Subsequently, the autophagosome structure was observed by transmission electron microscopy, and autophagy was confirmed to be involved in cerebral ischemia-reperfusion (I/R) (Kuma et al., 2004; Rami and Kogel, 2008; Li et al., 2018). Some researchers have further used pharmacological tools or autophagy-related knockout mice to study autophagy induction or inhibition, and verified the biological significance of functional autophagy in stroke (Li et al., 2018). The above evidence indicates that autophagy is involved in the development of stroke.

Recent studies have shown that (Morselli et al., 2008) acute and severe ischemia may cause "excessive autophagy," thereby promoting cell death and damage. However, chronic and mild hypoxic state trigger "moderate autophagy," thereby protecting cells by removing damaged tissues and proteins. It can be seen that during the development of cerebral ischemia, autophagy is a "double-edged sword." However, regardless of the role of autophagy in ischemic stroke, a series of signaling pathways are required to complete the process involved.

POSSIBLE MOLECULAR MECHANISMS OF AUTOPHAGY INVOLVED IN ISCHEMIC STROKE

mTOR Signaling Pathway-Mediated Autophagy

Autolysosome reproduce (ALR) is a mammalian autophagy that extends into a tubular structure and separates the original lysosome, which further matures into a new lysosome. This process requires the activation of the mammalian target of rapamycin (mTOR). mTOR is a serine/threonine protein kinase, which includes mTORC1 (rapamycin sensitive) and mTORC2 (rapamycin under sensitive), where mTORC1 is the major regulatory target. Cellular responses to hypoxia and inflammation in mammals are signaled by the mTOR pathway, including induction of autophagy and cell survival (Sciarretta et al., 2018), where mTORC1 negatively regulates autophagy. When encountering oxygen sugar deprivation or using rapamycin, the kinase activity of mTORC1 is inhibited, thereby promoting autophagy. Hei et al. (2017) found that ischemic stroke can induce autophagy by inhibiting mTOR, and can alleviate the degree of cerebral ischemia in rats with acute hyperglycemia-induced cerebral ischemic injury, which may explain the conclusion that "moderate autophagy" may have a protective effect on the "slow and mild" ischemic brain damage.

The phosphoinositide 3-kinase (PI3K) protein family is involved in the regulation of various cellular functions such as cell proliferation, differentiation, apoptosis, and glucose transport. PI3K is an intracellular phosphatidylinositol kinase. The specificity of structure and substrate is divided into three types: I, II, and III. Among them, type III PI3K (Vps34) can form a complex with becline-1 to participate in the formation of autophagy. At the same time, it catalyzes the phosphorylation of phosphatidylinositol at D3 position to produce 3-phosphophosphatidylinositol, which recruits the "-FYVE-" or "-PX-" motif in the cytoplasm of the cell. This protein is used to form autophagosome membranes. Therefore, the formation of autophagosomes depends on the action of type III PI3K (Vps34). Akt is a major downstream effector of PI3K. Akt phosphorylates TSC1/2 (tuberous sclerosis complex), preventing its negative regulation of Rab (Ras homology, enriched in brain) and further activating Rheb enrichment and mTORC1. According to previous studies, after 3 h of ischemic stroke, the expression of protein kinase PI3K/Akt was significantly reduced; after 12 h, high levels of nerve growth factor (NGF) inhibited cystylation by activating the protein kinase PI3K/Akt signaling pathway, thereby reducing damage to the ischemic brain tissue. Thus, the PI3K/Akt signaling pathway is involved in the regulation of acute neurological damage during stroke (Shioda et al., 2009; Hong et al., 2014; Xu et al., 2018).

Previous study have shown that the selective autophagy inhibitor 3-methyladenine (3-MA) can prevent cerebral ischemia through the PI3K pathway in a time-dependent manner (Yu et al., 2017). Huang et al. (2018) found that curcumin can attenuate autophagy in nerve cells by activating the PI3K/Akt-mTOR pathway, thereby attenuating cerebral ischemia-reperfusion injury in adult rats. However, in the neonatal rat hypoxia model, after treatment with the mTOR inhibitor rapamycin, phosphorylation of p70S6K downstream of mTOR can be inhibited by activating the PI3K/Akt pathway, thereby inducing autophagy and exerting neuroprotection. On the other hand, 3-MA reduces the expression of the autophagy-related protein beclin1 and abolishes the neuroprotective effect of rapamycin (Carloni et al., 2010). The above evidence suggests that the PI3K/Akt-mTOR signaling pathway may be a new target for stroke. However, based on different ischemic animal models, the regulatory effects of PI3K/Akt on mTOR signaling and its

effects on autophagy are inconsistent, and the corresponding mechanisms need to be further explored.

AMP-dependent protein kinase and autophagy play an important role in ischemic tolerance induced by cortical spreading depression (CSD), AMPK-mediated autophagy may represent a new target for stroke (Ronnett et al., 2009). The AMPK signaling pathway is an important pathway for enhancing autophagy in cell starvation. When the energy supply in the brain is reduced, the ATP/AMP ratio decreases, and AMPK is activated, which inhibits the downstream mTOR activity and activates autophagy to increase energy production (Dai et al., 2017; Wang J.F. et al., 2018; Zhang and Miao, 2018). Activated AMPK can inhibit mTORC1 in two ways: one is by regulating autophagy through TSC2 and mTOR regulation-related proteins; the other is by inducing autophagy by regulating the AMPK-mTOR pathway. AMPK-mediated autophagy contributes to the neuroprotection of ischemic preconditioning, suggesting that AMPK can be used as a target for the prevention and treatment of ischemic stroke (Liu H. et al., 2016).

In addition, Li et al. (2013) found that knocking out the p50 (NF-κB) gene during cerebral ischemia inhibited the Akt-mTOR pathway and enhanced autophagy, which in turn induced autophagic cell death. Cytoplasmic p53 can directly inhibit the formation of autophagosomes, while activated p53 translocates to the nucleus to promote AMPKβ expression, and transactivates sestrin-1, 2, and finally inhibits downstream mTOR activity to induce autophagy (Morselli et al., 2008). Brain ischemia/reperfusion can induce p53-dependent nuclear factor NF-κB expression while damage-regulated autophagy modulator (DRAM) is a positive regulator of p53-dependent autophagy. During the ischemia/reperfusion process, DRAM-mediated NF-κB/p53 signaling pathway is involved in apoptosis and autophagic cell death. Autophagy and apoptosis mechanisms can also participate in programmed cell death by regulating the p53 pathway (Cui et al., 2013). This suggests that the NF-κB-p53 signaling molecule is ultimately mediated by autophagy via mTOR, which may also serve as a potential target for stroke.

MAPK Signaling Pathway-Mediated Autophagy

Mitogen activated protein kinase (MAPK) is composed of p38, extracellular regulated protein kinases (ERK), and c-Jun N-terminal kinase (JNK). Activation of p38 MAPK signaling pathway in early ischemic stroke promotes Elk1, CHOP10, LEF2C, and protein kinase MAPKK2/3 to maintain neuronal survival and exert anti-inflammatory and anti-apoptotic effects. In the late stage, p38 MAPK is over-activated, which may promote the expression of target genes by activating transcription factors and proteins such as caspase, etc., leading to neuronal apoptosis (Ferrer et al., 2003; Li et al., 2015; Song et al., 2016). Therefore, different interventions targeted at p38 MAPK signaling molecules should be administered at different periods of ischemic stroke. Related studies have confirmed the hypothesis mentioned above, and shown that numerous drugs that enhance autophagy by activating ERK, inhibiting JNK, and p38 MAPK, are beneficial for the treatment of ischemic stroke (Jiang et al., 2014; Vercelli et al., 2015; Wang et al., 2015). The Akt/Smads signaling pathway negatively regulates autophagy in PC12 cells induced by oxygen glucose deprivation (ODD) by inhibiting JNK and p38 MAPK molecules (Xue et al., 2016). p38 inhibitors promote cell survival signaling pathways (such as ERK), attenuate mitochondrial fragmentation caused by ischemia or mitochondrial autophagy, thereby reducing the volume of cerebral infarction after ischemia and protecting nerve function (Han et al., 2015). The above evidence suggests that ERK, JNK, and p38 MAPK mediate the molecular process of autophagy in ischemic stroke, in which ERK activates as well as inhibits autophagy, whereas JNK and p38MAPK produce opposite effects.

HIF-1α Signaling Pathway-Mediated Autophagy

Molecular genetic studies have shown that the activity of hypoxia-inducible factor (HIF-1α) is closely related to ischemia-induced neuronal death. In the early stage of acute stroke, HIF-1α/HIF-2α double knockout in mice showed decreased expression of the anti-survival factors Bnip3, Bnip3L, and Pmaip1, which prevented early acute neuronal cell death and neurological damage (Barteczek et al., 2017). When HIF-1α is overexpressed, development of mitochondrial autophagy is often accompanied by inhibition of the mTOR pathway, thereby increasing neuronal survival, highlighting a novel target molecule that can be used against ischemic neuroprotection (Doeppner et al., 2012; Koh et al., 2015). When mTOR is inactivated by high expression of HIF-1α, AMPK is activated, which may explain the survival of bone marrow mesenchymal stem cells (BMSCs) induced after transplantation of HIF-1α. When BMSCs overexpressing HIF-1α are transplanted into MCAO rats, a reduction in the volume of cerebral infarction, improved neurobehavioral outcomes, inhibited production of pro-inflammatory cytokines, and enhanced secretion of neurotrophic factors occurs, suggesting that HIF-1α may promote BMSCs survival by regulating the activation of AMPK and mTOR to promote autophagy (Lv et al., 2017).

BNIP3 is one of the important target genes of HIF-1α, and BNIP3 gene expression is significantly correlated with HIF-1α gene expression (Feng et al., 2016). Increased expression of HIF-1α promotes BNIP3 gene expression which then activates autophagy. Cerebral ischemia often causes severe mitochondrial damage. By studying the mechanism of mitochondrial autophagy, new targets for ischemic brain damage may be discovered. Along this line of thought, Yuan et al. (2017) found that BNIP3L/NIX is involved in mitochondrial autophagy induced by cerebral ischemia-reperfusion, suggesting that BNIP3L may be a new therapeutic target for ischemic stroke management. In addition, other studies have shown that sirtuin family members have protective effects on neurons and attenuate cerebral ischemia (Carloni et al., 2014; Yang F. et al., 2015; Shimizu et al., 2016).

In addition, post-translational regulation of HIF-1α, SIRT1 and AMPK plays a key role in the control of glycolytic mitochondrial energy axis in response to hypoxic ischemic conditions. Under pseudo hypoxia condition, combination of

autophagy reduction, stress, and dysregulation increases the response of the impaired host to hypoxic-ischemic injury (Ham and Raju, 2017). Treatment with dexmedetomidine at the beginning of reperfusion can inhibit autophagy of neurons by up-regulating HIF-1α, thereby protecting the brain from ischemia-reperfusion injury. This finding underscores the potential of this protein as a treatment for acute ischemic injury (Zhang et al., 2016; Zhang and Zhang, 2017; Wang Y.Q. et al., 2018).

Proteins Associated With Autophagy Formation

Beclin1, LC3-II, and P62

Beclin1, LC3-phosphatidylethanolamine conjugates (LC3-II), and P62 are the three major proteins involved in autophagy process. Beclin1 plays an important role in the initiation of autophagy, primarily by forming a trimer with PI3K and Atg14, and continuously recruiting autophagy-associated proteins to mediate the initiation of autophagy (Shao et al., 2016; Qian et al., 2017). The microtubule-associated protein light chain 3 (LC3) undergoes two processing steps, one is proteolytic cleavage of pro-LC3 (LC3 precursor), and the other is delipidization of LC3-PE from autophagosomes. Both processes require the involvement of cysteine protease Atg4. Under the action of Atg4, the LC3 precursor is processed into soluble LC3-I, which is linked to phosphatidyl ethanolamine (PE) under the action of Atg7 and Atg3 to form liposoluble LC3-II-PE, which is involved in autophagocytosis, participating in the extension of the body membrane until autophagic lysosome is formed (Maejima et al., 2013; Khaminets et al., 2016; Chu, 2018). In addition, P62 located in the cytoplasm binds to ubiquitinated proteins, which in turn form a complex with LC3-II protein before it is degraded in lysosomes. During the process of autophagy, P62 is continually consumed (Moscat and Diaz-Meco, 2009; Jiang et al., 2015; Liu W.J. et al., 2016). Therefore, these three proteins are key biomarkers for detecting the level of autophagy. In the case of ischemic stroke, intracellular LC3 content and LC3-I to LC3-II transformation are significantly increased, suggesting high level of autophagy.

Interestingly, a another study showed that transformation level of lncRNA metastasis-associated lung adenocarcinoma transcripts (MALAT1) and autophagy-related proteins LC3-I, LC3-II, and beclin-1 increased after middle cerebral artery occlusion and reperfusion. They found that down-regulation of MALAT1 inhibited beclin-1-dependent autophagy by regulating the expression of miR-30a in cerebral ischemic stroke. MALAT1-miR-30a-Beclin1 was found to form lncRNA-miRNA-mRNA regulation network, thereby reducing neuronal cell death, suggesting that MALAT1 may act as a molecular chaperone of miR-30a that negatively regulates its expression (Wang P. et al., 2014; Guo et al., 2017).

Apoptosis-Related Proteins and Heat Shock Protein

Some apoptosis-related genes such as Bcl-2, Bcl-xl, Bax, and caspase can treat stroke by regulating autophagy. Since caspase and Bcl-2 can cleave autophagy-related proteins, a decrease in the level of apoptotic proteins activates autophagy. Previous studies have showed that the GABAβ receptor agonist baclofen can up-regulate the Bcl-2/Bax ratio, increase the activation of Akt, GSK-3β, and ERK, which inhibits autophagy, and significantly alleviate neuronal damage after long-term administration (Liu et al., 2015). This suggests that apoptosis-related genes may attenuate cerebral ischemia by regulating autophagy (Yang Y. et al., 2015; He et al., 2016; Xu et al., 2017).

Heat Shock Protein 27 (Hsp27) has recently become a new effective neuroprotective agent in cerebral ischemia, but the mechanism of Hsp27-mediated neuroprotection is largely unknown. Zhan et al. (2017) found that the expression of phosphorylated MK2 (MAPKAP kinase 2) and Hsp27 were reduced by p38MAPK inhibitor SB203580. Their results showed that inhibition of Hsp27 degradation following autophagy downregulation induced ischemic tolerance after hypoxia post conditioning. It has been suggested that MK2-induced Hsp27 phosphorylation may lead to neuroprotection after hypoxia treatment (Zhan et al., 2017). Blocking the cathepsin-t Bid-mitochondrial apoptosis signaling pathway by inhibiting autophagy and stabilizing the lysosomal membrane is associated with up-regulation of lysosomal Hsp70.1B in astrocytes (Zhou et al., 2017). Further, other studies have found that HSP proteins are involved in the pathophysiology of cerebral ischemia (Qi et al., 2015; Shi et al., 2017; Choi et al., 2018; Yamamoto et al., 2018). This suggests that additional studies on heat shock proteins may provide new options for clinical treatment of stroke.

OTHER RELATED PROTEINS

Recent studies have shown that α-Synuclein (α-Syn) is a potential therapeutic target for reducing brain damage after stroke. Knock-out of α-Syn significantly reduces infarction in rodent rats with focal cerebral ischemia and promotes neurological recovery. PLK2 (Polo-like kinase 2, the major kinase that mediates α-Syn S129 phosphorylation) knockout in mice during transient focal cerebral ischemia showed better functional recovery and smaller infarcts, indicating a deleterious effect of phosphorylation of the S129 site of α-Syn (Kim et al., 2016).

In the late stage of cerebral ischemia, the expression level of NGF receptor Trk A is decreased, and its endogenous neuroprotective effect is significantly down-regulated. The natural ligand of Trk A, a neurotrophic factor, may then rescue nerve cells by up-regulating the Trk A receptor signaling pathway. Some scholars used glial cell line-derived neurotrophic factor (glial cell line-derived neurotrophic factor, GDNF) and hepatocyte growth factor (HGF) to treat ischemic rats, both of which significantly reduced the infarct size, the number of LC3 and apoptosis-positive cells. These results indicate that GDNF and HGF are not only involved in anti-apoptosis, but are also associated with the inhibition of autophagy (Shang et al., 2010; Yamashita and Abe, 2016). This provides a new scientific basis for the clinical application of neurotrophic factors.

PROSPECT

In summary, autophagy and various signal transduction pathways as well as other mechanisms are involved in the

development of ischemic stroke. Continuous research and exploration are needed to establish the exact underlying mechanisms. Whether the role of autophagy in ischemic stroke is beneficial or harmful depends not only on the degree of stress in brain cells and mechanism of autophagy, but also on experimental models, detection methods, and research methods (Descloux et al., 2015; Tang et al., 2016; Wang P. et al., 2018; Wolf et al., 2018). Therefore, exploring the occurrence and development of autophagy, strengthening the role of autophagy in different stages of ischemic stroke, studying its molecular mechanisms and signal transduction pathways will help medical practitioners make full use of autophagy in clinical practice, and minimize or avoid the damage caused by autophagy to normal cells in the treatment of ischemic stroke.

AUTHOR CONTRIBUTIONS

All authors participated in designing the concept of this manuscript. YS, YZ, and XZ reviewed the literature and drafted the article. XZ, XC, and GY finalized the paper and provided suggestions to improve it.

REFERENCES

Barteczek, P., Li, L., Ernst, A. S., Bohler, L. I., Marti, H. H., and Kunze, R. (2017). Neuronal HIF-1alpha and HIF-2alpha deficiency improves neuronal survival and sensorimotor function in the early acute phase after ischemic stroke. *J. Cereb. Blood Flow Metab.* 37, 291–306. doi: 10.1177/0271678X15624933

Carloni, S., Albertini, M. C., Galluzzi, L., Buonocore, G., Proietti, F., and Balduini, W. (2014). Melatonin reduces endoplasmic reticulum stress and preserves sirtuin 1 expression in neuronal cells of newborn rats after hypoxia-ischemia. *J. Pineal Res.* 57, 192–199. doi: 10.1111/jpi.12156

Carloni, S., Girelli, S., Scopa, C., Buonocore, G., Longini, M., and Balduini, W. (2010). Activation of autophagy and Akt/CREB signaling play an equivalent role in the neuroprotective effect of rapamycin in neonatal hypoxia-ischemia. *Autophagy* 6, 366–377. doi: 10.4161/auto.6.3.11261

Choi, J. I., Ha, S. K., Lim, D. J., Kim, S. D., and Kim, S. H. (2018). S100ss, Matrix Metalloproteinase-9, D-dimer, and heat shock protein 70 are serologic biomarkers of acute cerebral infarction in a mouse model of transient MCA occlusion. *J. Korean Neurosurg. Soc.* 61, 548–558. doi: 10.3340/jkns.2017.0200

Chu, C. T. (2018). Mechanisms of selective autophagy and mitophagy: implications for neurodegenerative diseases. *Neurobiol. Dis.* doi: 10.1016/j.nbd.2018.07.015 [Epub ahead of print].

Cui, D. R., Wang, L., Jiang, W., Qi, A. H., Zhou, Q. H., and Zhang, X. L. (2013). Propofol prevents cerebral ischemia-triggered autophagy activation and cell death in the rat hippocampus through the NF-kappaB/p53 signaling pathway. *Neuroscience* 246, 117–132. doi: 10.1016/j.neuroscience.2013.04.054

Dai, S. H., Chen, T., Li, X., Yue, K. Y., Luo, P., Yang, L. K., et al. (2017). Sirt3 confers protection against neuronal ischemia by inducing autophagy: involvement of the AMPK-mTOR pathway. *Free Radic. Biol. Med.* 108, 345–353. doi: 10.1016/j.freeradbiomed.2017.04.005

Descloux, C., Ginet, V., Clarke, P. G., Puyal, J., and Truttmann, A. C. (2015). Neuronal death after perinatal cerebral hypoxia-ischemia: focus on autophagy-mediated cell death. *Int. J. Dev. Neurosci.* 45, 75–85. doi: 10.1016/j.ijdevneu.2015.06.008

Doeppner, T. R., Mlynarczuk-Bialy, I., Kuckelkorn, U., Kaltwasser, B., Herz, J., Hasan, M. R., et al. (2012). The novel proteasome inhibitor BSc2118 protects against cerebral ischaemia through HIF1A accumulation and enhanced angioneurogenesis. *Brain* 135, 3282–3297. doi: 10.1093/brain/aws269

Doherty, J., and Baehrecke, E. H. (2018). Life, death and autophagy. *Nat. Cell Biol.* 20, 1110–1117. doi: 10.1038/s41556-018-0201-5

Feng, C. C., Lin, C. C., Lai, Y. P., Chen, T. S., Marthandam Asokan, S., Lin, J. Y., et al. (2016). Hypoxia suppresses myocardial survival pathway through HIF-1alpha-IGFBP-3-dependent signaling and enhances cardiomyocyte autophagic and apoptotic effects mainly via FoxO3a-induced BNIP3 expression. *Growth Factors* 34, 73–86. doi: 10.1080/08977194.2016.1191480

Ferrer, I., Friguls, B., Dalfo, E., and Planas, A. M. (2003). Early modifications in the expression of mitogen-activated protein kinase (MAPK/ERK), stress-activated kinases SAPK/JNK and p38, and their phosphorylated substrates following focal cerebral ischemia. *Acta Neuropathol.* 105, 425–437.

Guo, D., Ma, J., Yan, L., Li, T., Li, Z., Han, X., et al. (2017). Down-regulation of lncrna MALAT1 attenuates neuronal cell death through suppressing beclin1-dependent autophagy by regulating Mir-30a in cerebral ischemic stroke. *Cell Physiol. Biochem.* 43, 182–194. doi: 10.1159/000480337

Halestrap, A. P. (2006). Calcium, mitochondria and reperfusion injury: a pore way to die. *Biochem. Soc. Trans.* 34, 232–237. doi: 10.1042/BST0340232

Ham, P. B. III, and Raju, R. (2017). Mitochondrial function in hypoxic ischemic injury and influence of aging. *Prog. Neurobiol.* 157, 92–116. doi: 10.1016/j.pneurobio.2016.06.006

Han, D., Scott, E. L., Dong, Y., Raz, L., Wang, R., and Zhang, Q. (2015). Attenuation of mitochondrial and nuclear p38alpha signaling: a novel mechanism of estrogen neuroprotection in cerebral ischemia. *Mol. Cell. Endocrinol.* 400, 21–31. doi: 10.1016/j.mce.2014.11.010

He, G., Xu, W., Tong, L., Li, S., Su, S., Tan, X., et al. (2016). Gadd45b prevents autophagy and apoptosis against rat cerebral neuron oxygen-glucose deprivation/reperfusion injury. *Apoptosis* 21, 390–403. doi: 10.1007/s10495-016-1213-x

Hei, C., Liu, P., Yang, X., Niu, J., and Li, P. A. (2017). Inhibition of mTOR signaling confers protection against cerebral ischemic injury in acute hyperglycemic rats. *Int. J. Biol. Sci.* 13, 878–887. doi: 10.7150/ijbs.18976

Hong, Y., Shao, A., Wang, J., Chen, S., Wu, H., McBride, D. W., et al. (2014). Neuroprotective effect of hydrogen-rich saline against neurologic damage and apoptosis in early brain injury following subarachnoid hemorrhage: possible role of the Akt/GSK3beta signaling pathway. *PLoS One* 9:e96212. doi: 10.1371/journal.pone.0096212

Huang, L., Chen, C., Zhang, X., Li, X., Chen, Z., Yang, C., et al. (2018). Neuroprotective effect of curcumin against cerebral ischemia-reperfusion via mediating autophagy and inflammation. *J. Mol. Neurosci.* 64, 129–139. doi: 10.1007/s12031-017-1006-x

Jiang, M., Li, J., Peng, Q., Liu, Y., Liu, W., Luo, C., et al. (2014). Neuroprotective effects of bilobalide on cerebral ischemia and reperfusion injury are associated with inhibition of pro-inflammatory mediator production and down-regulation of JNK1/2 and p38 MAPK activation. *J. Neuroinflammation* 11:167. doi: 10.1186/s12974-014-0167-6

Jiang, T., Harder, B., Rojo de la Vega, M., Wong, P. K., Chapman, E., and Zhang, D. D. (2015). p62 links autophagy and Nrf2 signaling. *Free Radic. Biol. Med.* 88, 199–204. doi: 10.1016/j.freeradbiomed.2015.06.014

Khaminets, A., Behl, C., and Dikic, I. (2016). Ubiquitin-dependent and independent signals in selective autophagy. *Trends Cell Biol.* 26, 6–16. doi: 10.1016/j.tcb.2015.08.010

Kim, T., Mehta, S. L., Kaimal, B., Lyons, K., Dempsey, R. J., and Vemuganti, R. (2016). Poststroke induction of alpha-synuclein mediates ischemic brain damage. *J. Neurosci.* 36, 7055–7065. doi: 10.1523/JNEUROSCI.1241-16.2016

Koh, H. S., Chang, C. Y., Jeon, S. B., Yoon, H. J., Ahn, Y. H., Kim, H. S., et al. (2015). The HIF-1/glial TIM-3 axis controls inflammation-associated brain damage under hypoxia. *Nat Commun.* 6:6340. doi: 10.1038/ncomms7340

Kuma, A., Hatano, M., Matsui, M., Yamamoto, A., Nakaya, H., Yoshimori, T., et al. (2004). The role of autophagy during the early neonatal starvation period. *Nature* 432, 1032–1036. doi: 10.1038/nature03029

Li, H., Wu, J., Shen, H., Yao, X., Liu, C., Pianta, S., et al. (2018). Autophagy in hemorrhagic stroke: mechanisms and clinical implications. *Prog. Neurobiol.* 16, 79–97. doi: 10.1016/j.pneurobio.2017.04.002

Li, H., Zhou, S., Wu, L., Liu, K., Zhang, Y., Ma, G., et al. (2015). The role of p38MAPK signal pathway in the neuroprotective mechanism of limb postconditioning against rat cerebral ischemia/reperfusion injury. *J. Neurol. Sci.* 357, 270–275. doi: 10.1016/j.jns.2015.08.004

Li, W. L., Yu, S. P., Chen, D., Yu, S. S., Jiang, Y. J., Genetta, T., et al. (2013). The regulatory role of NF-kappaB in autophagy-like cell death after focal cerebral ischemia in mice. *Neuroscience* 244, 16–30. doi: 10.1016/j.neuroscience.2013.03.045

Liu, H., Zhang, Y., Wu, H., D'Alessandro, A., Yegutkin, G. G., Song, A., et al. (2016). Beneficial role of erythrocyte adenosine A2B receptor-mediated AMP-activated protein kinase activation in high-altitude hypoxia. *Circulation* 134, 405–421. doi: 10.1161/CIRCULATIONAHA.116.021311

Liu, L., Li, C. J., Lu, Y., Zong, X. G., Luo, C., Sun, J., et al. (2015). Baclofen mediates neuroprotection on hippocampal CA1 pyramidal cells through the regulation of autophagy under chronic cerebral hypoperfusion. *Sci. Rep.* 5:14474. doi: 10.1038/srep14474

Liu, W. J., Ye, L., Huang, W. F., Guo, L. J., Xu, Z. G., Wu, H. L., et al. (2016). p62 links the autophagy pathway and the ubiqutin-proteasome system upon ubiquitinated protein degradation. *Cell Mol. Biol. Lett.* 21:29. doi: 10.1186/s11658-016-0031-z

Liu, Y., Xue, X., Zhang, H., Che, X., Luo, J., Wang, P., et al. (2018). Neuronal-targeted TFEB rescues dysfunction of the autophagy-lysosomal pathway and alleviates ischemic injury in permanent cerebral ischemia. *Autophagy* 2018, 1–17. doi: 10.1080/15548627.2018.1531196

Lv, B., Li, F., Han, J., Fang, J., Xu, L., Sun, C., et al. (2017). Hif-1alpha overexpression improves transplanted bone mesenchymal stem cells survival in Rat MCAO stroke model. *Front. Mol. Neurosci.* 10:80. doi: 10.3389/fnmol.2017.00080

Maejima, Y., Kyoi, S., Zhai, P., Liu, T., Li, H., Ivessa, A., et al. (2013). Mst1 inhibits autophagy by promoting the interaction between Beclin1 and Bcl-2. *Nat. Med.* 19, 1478–1488. doi: 10.1038/nm.3322

Morselli, E., Tasdemir, E., Maiuri, M. C., Galluzzi, L., Kepp, O., Criollo, A., et al. (2008). Mutant p53 protein localized in the cytoplasm inhibits autophagy. *Cell Cycle* 7, 3056–3061. doi: 10.4161/cc.7.19.6751

Moscat, J., and Diaz-Meco, M. T. (2009). p62 at the crossroads of autophagy, apoptosis, and cancer. *Cell* 137, 1001–1004. doi: 10.1016/j.cell.2009.05.023

Nikoletopoulou, V., Papandreou, M. E., and Tavernarakis, N. (2015). Autophagy in the physiology and pathology of the central nervous system. *Cell Death Differ.* 22, 398–407. doi: 10.1038/cdd.2014.204

Nitatori, T., Sato, N., Waguri, S., Karasawa, Y., Araki, H., Shibanai, K., et al. (1995). Delayed neuronal death in the CA1 pyramidal cell layer of the gerbil hippocampus following transient ischemia is apoptosis. *J. Neurosci.* 15, 1001–1011. doi: 10.1523/JNEUROSCI.15-02-01001.1995

Qi, J., Liu, Y., Yang, P., Chen, T., Liu, X. Z., Yin, Y., et al. (2015). Heat shock protein 90 inhibition by 17-Dimethylaminoethylamino-17-demethoxygeldanamycin protects blood-brain barrier integrity in cerebral ischemic stroke. *Am. J. Transl. Res.* 7, 1826–1837.

Qian, X., Li, X., Cai, Q., Zhang, C., Yu, Q., Jiang, Y., et al. (2017). Phosphoglycerate kinase 1 phosphorylates beclin1 to induce autophagy. *Mol. Cell.* 65, 917.e6–931.e6. doi: 10.1016/j.molcel.2017.01.027

Rami, A., and Kogel, D. (2008). Apoptosis meets autophagy-like cell death in the ischemic penumbra: two sides of the same coin? *Autophagy* 4, 422–426.

Ronnett, G. V., Ramamurthy, S., Kleman, A. M., Landree, L. E., and Aja, S. (2009). AMPK in the brain: its roles in energy balance and neuroprotection. *J. Neurochem.* 109(Suppl. 1), 17–23. doi: 10.1111/j.1471-4159.2009.05916.x

Sciarretta, S., Forte, M., Frati, G., and Sadoshima, J. (2018). New insights into the role of mtor signaling in the cardiovascular system. *Circ. Res.* 122, 489–505. doi: 10.1161/CIRCRESAHA.117.311147

Shang, J., Deguchi, K., Yamashita, T., Ohta, Y., Zhang, H., Morimoto, N., et al. (2010). Antiapoptotic and antiautophagic effects of glial cell line-derived neurotrophic factor and hepatocyte growth factor after transient middle cerebral artery occlusion in rats. *J. Neurosci. Res.* 88, 2197–2206. doi: 10.1002/jnr.22373

Shao, A., Wang, Z., Wu, H., Do-ng, X., Li, Y., Tu, S., et al. (2016). Enhancement of autophagy by histone deacetylase inhibitor trichostatin a ameliorates neuronal apoptosis after subarachnoid hemorrhage in rats. *Mol. Neurobiol.* 53, 18–27. doi: 10.1007/s12035-014-8986-0

Shi, Y., Jiang, X., Zhang, L., Pu, H., Hu, X., Zhang, W., et al. (2017). Endothelium-targeted overexpression of heat shock protein 27 ameliorates blood-brain barrier disruption after ischemic brain injury. *Proc. Natl. Acad. Sci. U.S.A.* 114, E1243–E1252. doi: 10.1073/pnas.1621174114

Shimizu, K., Quillinan, N., Orfila, J. E., and Herson, P. S. (2016). Sirtuin-2 mediates male specific neuronal injury following experimental cardiac arrest through activation of TRPM2 ion channels. *Exp. Neurol.* 275(Pt 1), 78–83. doi: 10.1016/j.expneurol.2015.10.014

Shioda, N., Han, F., and Fukunaga, K. (2009). Role of Akt and ERK signaling in the neurogenesis following brain ischemia. *Int. Rev. Neurobiol.* 85, 375–387. doi: 10.1016/S0074-7742(09)85026-5

Song, Y. Q., Zou, H. L., Zhao, Y. J., Yu, L. Q., Tan, Z. X., and Kong, R. (2016). Activation of p38-mitogen-activated protein kinase contributes to ischemia reperfusion in rat brain. *Genet. Mol. Res.* 15, 1–13. doi: 10.4238/gmr.15038492

Tang, Y. C., Tian, H. X., Yi, T., and Chen, H. B. (2016). The critical roles of mitophagy in cerebral ischemia. *Protein Cell* 7, 699–713. doi: 10.1007/s13238-016-0307-0

Vercelli, A., Biggi, S., Sclip, A., Repetto, I. E., Cimini, S., Falleroni, F., et al. (2015). Exploring the role of MKK7 in excitotoxicity and cerebral ischemia: a novel pharmacological strategy against brain injury. *Cell Death Dis.* 6:e1854. doi: 10.1038/cddis.2015.226

Wang, J. F., Mei, Z. G., Fu, Y., Yang, S. B., Zhang, S. Z., Huang, W. F., et al. (2018). Puerarin protects rat brain against ischemia/reperfusion injury by suppressing autophagy via the AMPK-mTOR-ULK1 signaling pathway. *Neural Regen. Res.* 13, 989–998. doi: 10.4103/1673-5374.233441

Wang, P., Liang, J., Li, Y., Li, J., Yang, X., Zhang, X., et al. (2014). Down-regulation of miRNA-30a alleviates cerebral ischemic injury through enhancing beclin 1-mediated autophagy. *Neurochem. Res.* 39, 1279–1291. doi: 10.1007/s11064-014-1310-6

Wang, P., Shao, B. Z., Deng, Z., Chen, S., Yue, Z., and Miao, C. Y. (2018). Autophagy in ischemic stroke. *Prog. Neurobiol.* 163-164, 98–117. doi: 10.1016/j.pneurobio.2018.01.001

Wang, Y., Zhen, Y., Wu, X., Jiang, Q., Li, X., Chen, Z., et al. (2015). Vitexin protects brain against ischemia/reperfusion injury via modulating mitogen-activated protein kinase and apoptosis signaling in mice. *Phytomedicine* 22, 379–384. doi: 10.1016/j.phymed.2015.01.009

Wang, Y. Q., Tang, Y. F., Yang, M. K., and Huang, X. Z. (2018). Dexmedetomidine alleviates cerebral ischemia-reperfusion injury in rats via inhibition of hypoxia-inducible factor-1α. *J. Cell Biochem.* doi: 10.1002/jcb.28058 [Epub ahead of print].

Wolf, M. S., Bayir, H., Kochanek, P. M., and Clark, R. S. B. (2018). The role of autophagy in acute brain injury: a state of flux? *Neurobiol. Dis.* doi: 10.1016/j.nbd.2018.04.018 [Epub ahead of print].

Xu, J., Huai, Y., Meng, N., Dong, Y., Liu, Z., Qi, Q., et al. (2017). L-3-n-butylphthalide activates Akt/mTOR signaling, inhibits neuronal apoptosis and autophagy and improves cognitive impairment in mice with repeated cerebral ischemia-reperfusion injury. *Neurochem. Res.* 42, 2968–2981. doi: 10.1007/s11064-017-2328-3

Xu, W., Gao, L., Li, T., Zheng, J., Shao, A., and Zhang, J. (2018). Mesencephalic astrocyte-derived neurotrophic factor (MANF) protects against neuronal apoptosis via activation of Akt/MDM2/p53 signaling pathway in a rat model of intracerebral hemorrhage. *Front. Mol. Neurosci.* 11:176. doi: 10.3389/fnmol.2018.00176

Xue, L. X., Xu, Z. H., Wang, J. Q., Cui, Y., Liu, H. Y., Liang, W. Z., et al. (2016). Activin A/Smads signaling pathway negatively regulates oxygen glucose deprivation-induced autophagy via suppression of JNK and p38 MAPK pathways in neuronal PC12 cells. *Biochem. Biophys. Res. Commun.* 480, 355–361. doi: 10.1016/j.bbrc.2016.10.050

Yamamoto, Y., Hosoda, K., Imahori, T., Tanaka, J., Matsuo, K., Nakai, T., et al. (2018). Pentose phosphate pathway activation via HSP27 phosphorylation by ATM kinase: a putative endogenous antioxidant defense mechanism during cerebral ischemia-reperfusion. *Brain Res.* 1687, 82–94. doi: 10.1016/j.brainres.2018.03.001

Yamashita, T., and Abe, K. (2016). Recent progress in therapeutic strategies for ischemic stroke. *Cell Transplant.* 25, 893–898. doi: 10.3727/096368916X690548

Yang, F., Zhou, L., Wang, D., Wang, Z., and Huang, Q. Y. (2015). Minocycline ameliorates hypoxia-induced blood-brain barrier damage by inhibition of HIF-1alpha through SIRT-3/PHD-2 degradation pathway. *Neuroscience* 304, 250–259. doi: 10.1016/j.neuroscience.2015.07.051

Yang, Y., Gao, K., Hu, Z., Li, W., Davies, H., Ling, S., et al. (2015). Autophagy upregulation and apoptosis downregulation in DAHP and triptolide treated cerebral ischemia. *Mediators Inflamm.* 2015, 120198. doi: 10.1155/2015/120198

Yu, J., Li, C., Ding, Q., Que, J., Liu, K., Wang, H., et al. (2017). Netrin-1 ameliorates blood-brain barrier impairment secondary to ischemic stroke via the activation of PI3K pathway. *Front. Neurosci.* 11:700. doi: 10.3389/fnins.2017.00700

Yuan, Y., Zheng, Y., Zhang, X., Chen, Y., Wu, X., Wu, J., et al. (2017). BNIP3L/NIX-mediated mitophagy protects against ischemic brain injury independent of PARK2. *Autophagy* 13, 1754–1766. doi: 10.1080/15548627.2017.1357792

Zhan, L., Liu, L., Li, K., Wu, B., Liu, D., Liang, D., et al. (2017). Neuroprotection of hypoxic postconditioning against global cerebral ischemia through influencing posttranslational regulations of heat shock protein 27 in adult rats. *Brain Pathol.* 27, 822–838. doi: 10.1111/bpa.12472

Zhang, W., and Zhang, J. (2017). Dexmedetomidine preconditioning protects against lung injury induced by ischemia-reperfusion through inhibition of autophagy. *Exp. Ther. Med.* 14, 973–980. doi: 10.3892/etm.2017.4623

Zhang, W., Zhang, J. Q., Meng, F. M., and Xue, F. S. (2016). Dexmedetomidine protects against lung ischemia-reperfusion injury by the PI3K/Akt/HIF-1alpha signaling pathway. *J. Anesth.* 30, 826–833. doi: 10.1007/s00540-016-2214-1

Zhang, Y., and Miao, J. M. (2018). Ginkgolide K promotes astrocyte proliferation and migration after oxygen-glucose deprivation via inducing protective autophagy through the AMPK/mTOR/ULK1 signaling pathway. *Eur. J. Pharmacol* 832, 96–103. doi: 10.1016/j.ejphar.2018.05.029

Zhou, X. Y., Luo, Y., Zhu, Y. M., Liu, Z. H., Kent, T. A., Rong, J. G., et al. (2017). Inhibition of autophagy blocks cathepsins-tBid-mitochondrial apoptotic signaling pathway via stabilization of lysosomal membrane in ischemic astrocytes. *Cell Death Dis.* 8:e2618. doi: 10.1038/cddis.2017.34

Conflict of Interest Statement: The authors declare that the research was conducted in the absence of any commercial or financial relationships that could be construed as a potential conflict of interest.

frontiers in Neuroscience

ORIGINAL RESEARCH
published: 05 March 2019
doi: 10.3389/fnins.2019.00026

Carnosic Acid Mitigates Early Brain Injury After Subarachnoid Hemorrhage: Possible Involvement of the SIRT1/p66shc Signaling Pathway

Lingfang Teng[1†], Linfeng Fan[2†], Yujiang Peng[1], Xijun He[1], Huihui Chen[1], Hongyu Duan[1], Fan Yang[1], Da Lin[1], Zheng Lin[1], Huiyong Li[1] and Bo Shao[1]*

[1] Department of Neurosurgery, The First People's Hospital of Wenling, Wenling, China, [2] Department of Pediatric Surgery, Capital Institute of Pediatrics, Beijing, China

OPEN ACCESS

Edited by:
Gang Chen,
The First Affiliated Hospital of Soochow University, China

Reviewed by:
Tatiana Rosado Rosenstock, Faculdade de Ciências Médicas da Santa Casa de São Paulo, Brazil
Xingshun Xu,
The Second Affiliated Hospital of Soochow University, China
Yuyun Xiong,
Affiliated Hospital of Jiangsu University, China

***Correspondence:**
Bo Shao
bobbyshao@yeah.net

[†] These authors have contributed equally to this work

Specialty section:
This article was submitted to Neurodegeneration, a section of the journal Frontiers in Neuroscience

Received: 02 August 2018
Accepted: 11 January 2019
Published: 05 March 2019

Citation:
Teng L, Fan L, Peng Y, He X, Chen H, Duan H, Yang F, Lin D, Lin Z, Li H and Shao B (2019) Carnosic Acid Mitigates Early Brain Injury After Subarachnoid Hemorrhage: Possible Involvement of the SIRT1/p66shc Signaling Pathway. Front. Neurosci. 13:26. doi: 10.3389/fnins.2019.00026

Carnosic acid (CA) has been reported to exhibit a variety of bioactivities including antioxidation, neuroprotection, and anti-inflammation; however, the impact of CA on subarachnoid hemorrhage (SAH) has never been elucidated. The current study was undertaken to explore the role of CA in early brain injury (EBI) secondary to SAH and the underlying mechanisms. Adult male Sprague-Dawley rats were perforated to mimic a clinical aneurysm with SAH. CA or vehicle was administered intravenously immediately after the SAH occurred. Mortality, SAH grade, neurologic function scores, brain water content, Evans blue extravasation, and the levels of reactive oxygen species (ROS) levels in the ipsilateral cortex were determined 24 h after the SAH occurred. Western blot, immunofluorescence, Fluoro-Jade C (FJC) and TUNEL staining were also performed. Our results showed that CA decreased ROS levels, alleviated brain edema and blood-brain barrier permeability, reduced neuronal cell death, and promoted neurologic function improvement. To probe into the potential mechanisms. We showed that CA increased SIRT1, MnSOD, and Bcl-2 expression, as well as decreased p66shc, Bax, and cleaved caspase-3 expression. Interestingly, sirtinol, a selective inhibitor of SIRT1, abolished the anti-apoptotic effects of CA. Taken together, these data revealed that CA has a neuroprotective role in EBI secondary to SAH. The potential mechanism may involve suppression of neuronal apoptosis through the SIRT1/p66shc signaling pathway. CA may provide a promising therapeutic regimen for management of SAH.

Keywords: subarachnoid hemorrhage, carnosic acid, p66shc, early brain injury, apoptosis

INTRODUCTION

Subarachnoid hemorrhage (SAH) is considered to be one of the most devastating cerebrovascular accidents, leading to a >50% combined morbidity and mortality rate (Chen et al., 2014b). Previous studies have attached importance to the vasospasm secondary to SAH, which is thought to mainly account for the delayed neurologic deficits that occur; however, clinical trials aimed at anti-vasospasm treatment have failed to promote the prognosis of SAH patients (Sehba et al., 2012;

Sehba and Friedrich, 2015; Fan et al., 2017). The collective evidence indicates that early brain injury (EBI) contributes to the outcome of SAH. Although the specific mechanisms underlying EBI are controversial, neuronal apoptosis is deemed to have a fatal role in the process and might explain the short and long-term severe pathology of the disease (Biller et al., 1988; Cahill et al., 2006). Thus, extra effort is needed to develop an original and drug targeting apoptosis, which may provide a therapeutic regimen for SAH management.

Apoptosis is a complicated progress and multiple factors have been reported to trigger the process. Reactive oxygen species (ROS) are major causative factors inducing apoptosis (Redza-Dutordoir and Averill-Bates, 2016; Wu et al., 2017; Xia et al., 2018). SIRT1 is a well-characterized member of the highly conserved (NAD^+)-dependent class III histone deacetylases and it could restrained ROS and apoptosis (Langley et al., 2002; Brunet et al., 2004). It has been demonstrated that overexpression of SIRT1 protects cardiomyocytes from oxidative injury (Cheng et al., 2003; McBurney et al., 2003; Xie et al., 2012). We previously reported that activated SIRT1 exhibited neuroprotection in SAH (Zhang X.S. et al., 2016); however, the underlying mechanism remains to be elucidated. P66shc, an isoform of the adapter protein ShcA, is a redox enzyme that can stimulate ROS generation and induce apoptosis (Giorgio et al., 2005; Galimov, 2010). Consistently, P66shc knockout mice have been reported to exhibit 30% longer lifespan and exert intensive resistance to oxidant stress (Berry et al., 2007; Kumar et al., 2014; Vikram et al., 2014). Recent studies suggested that p66shc may be regulated by SIRT1 (Chen et al., 2013; Shan et al., 2015). In SIRT1 transgenic diabetic mice, a decreased expression of p66shc has been observed (Zhou et al., 2011). Therefore, we hypothesize that SIRT1-mediated p66shc suppression may contributed to the prevention of SAH-induced brain injury.

Recently, more and more attentions have been paid to natural herbs in the treatment of SAH. Carnosic acid (CA), one of the dominant phenolic compounds in rosemary and sage leaves exhibits various pharmacologic properties, including antiapoptotic, antioxidant and chemopreventive activities (Shan et al., 2015). CA has been shown exhibit a protective effect against various tissue injuries by suppressing apoptosis (Xie et al., 2012; Chen et al., 2013; Shan et al., 2015). It has been reported that SIRT1 can be activated by plant polyphenols, such as resveratrol and quercetin (Chung et al., 2010). Likewise, SIRT1 may also be activated by CA. In this study, we sought to investigate the antiapoptotic effect of CA on protecting against SAH. And the regulation of SIRT1/p66shc pathway involved in CA-mediated protective activity in SAH was also explored.

MATERIALS AND METHODS

Animals and Cell Lines

Animals

Adult male Sprague-Dawley rats (Slac Laboratory Animal Company Limited, Shanghai, China) weighting between 300 and 320 g (6–8 weeks of age) were used in the current study. The animals were housed under controlled temperature and humidity conditions with a 12 h light/dark cycles. All experiments were approved by the Institutional Ethics Committee of Zhejiang Province and consistent with the Guide for the Care and Use of Laboratory Animals of the National Institutes of Health and Animal Research.

Cell Culture

PC12 cells were obtained from American Type Culture Collection (ATCC, United States). Cells were maintained in DMEM supplemented with 10% FBS, 30 μg/ml penicillin, and 100 μg/ml Streptomycin at 37°C under a 5% CO_2 atmosphere. For chemical treatment, cells were seed in 6-well plates and treated with 10 μM CA alone or together with 15 μM sirtinol for 24 h.

SAH Model

The rat model were established as previously described (Li et al., 2016). Briefly, the rats were anesthetized with 40 mg/kg of pentobarbital sodium intraperitoneally. Second, the left carotid artery and its branches were dissected. A blunted 4-0 monofilament nylon suture was stabbed into the internal carotid artery from the external carotid artery and stopped until resistance appeared. Then the bifurcation of the anterior and middle cerebral arteries was punctured. Sham rats underwent a similar procedure without the vessel puncture. Finally, the suture was withdrawn after approximately 15 s. All rats were maintained at 37.5°C on a heating pad with rectal thermometer.

Study Design

Experiment 1

To character the time course of p66shc after SAH, we detected the protein using a western blot assay in sham and SAH models for 1, 3, 6, 12, 24, 48, and 72 h (n = 6). Additionally, immunofluorescence co-staining was performed to localize p66shc in SAH rats (n = 6).

Experiment 2

One hundred twenty rates (163 rats were used and 43 rats died) were randomly allocated into four groups: sham (n = 30), SAH (n = 30/45), SAH + vehicle (n = 30/44), and SAH + CA (n = 30/44). The SAH group, the SAH + vehicle group and the SAH + CA groups were subjected to SAH. In addition, SAH + vehicle group and SAH + CA groups were treated with vehicle and CA, respectively. A similar procedure to that used in the SAH group was performed in the sham group but without perforation. All rats were evaluated 24 h after SAH was induced. SAH grade, neurologic score, brain water content, and Evans blue extravasation, and ROS assay, TUNEL staining, FJC staining, and Western blot analysis results were determined in each group.

Experiment 3

Seventy-two rats (107 rats were used and 35 rats died) were randomly assigned into 4 groups at random: SAH + vehicle group (n = 18/28), SAH + CA group (n = 18/26), SAH + sirtinol group (n = 18/27) and SAH + CA + sirtinol group (n = 18/26). Rats in the SAH + vehicle, the SAH + CA and the SAH + sirtinol group were exposed to SAH and treated with vehicle,

CA, and sirtinol, respectively. The SAH + CA + sirtinol group was exposed in SAH and dealt with CA and sirtinol. The end point was 24 h after SAH. Brain water content, and Western blot analysis, FJC staining findings and TUNEL staining were determined in each group, respectively.

Drug Administration

Carnosic acid was purchased from Tokyo Chemical Industry (Tokyo, Japan) and dissolved in dimethyl sulfoxide (DMSO). The dose and the time point of CA was chose according to a previous study (Miller et al., 2015). Vehicle (0.5% DMSO in a 10% Ethanol/90% PBS solution) or CA (3 mg/kg in a 10% Ethanol/90% PBS vehicle solution) were administrated intraperitoneally immediately after SAH. CA and its vehicle were administered 24 h prior to tissue collection. Sirtinol (Sigma-Aldrich, St. Louis, MO, United States) was administered via intracerebroventricular injection as previously described (Yan et al., 2016; Li et al., 2018). In brief, a small burr hole was drilled into the skull (1.5 mm posterior and 1.0 mm lateral relative to the bregma) after the rats were anesthetized. A 10 μl Hamilton syringe needle (Microliter 701; Hamilton Company, Reno, NV, United States) needle was inserted into the left lateral ventricle through the hole at a depth of (3.5 mm below the horizontal plane of the bregma). Sirtinol (a SIRT1 inhibitor) was dissolved in DSMO and further diluted in sterile saline to a final DSMO concentration of 0.5% [the dose of sirtinol was selected based on previous study (Zhang X.S. et al., 2016)]. Either sirtinol or vehicle was injected into the left lateral ventricle 2 h before SAH. The syringe was left *in situ* for at least 10 min before removal to prevent backfilling and then the hole was filled with bone wax.

SAH Grades and Neurologic Scores

The severity of the SAH was evaluated using the SAH grading scale as previously described (Sugawara et al., 2008). In brief, the basal cisterns were allocated into 6 segments and each segment was scored from 0 to 3 based on the amount of bleeding as follows: grade 3, blood clots covered all arteries; grade 2, mediocre blood with visible arteries; grade 1, minimal subarachnoid blood; and grade 0, no SAH. We determined the total score by summing each segment score. We evaluated neurologic function 24 h after SAH according to the modified Garcia score (Garcia et al., 1995). Evaluation of autonomic exercise, exercise coordination, physical activity, and somatic sensation was included. The score ranged from 3 to 18. Six tests including response to vibrissa touch, limb symmetry, body proprioception, climbing, spontaneous activity, and forelimb outstretching were scored and total scores were measured. An independent observer performed all evaluation.

Brain Water Content

The right and left hemispheres of the brains were removed after the rats were euthanized. Each part of the brain was weighed immediately upon removal (wet weight), then put in an oven at 105°C to dry. The brain parts were re-weighed after 72 h (dry weight). The brain water content was computed as follows: (wet weight-dry weight)/wet weight × 100%.

Evans Blue Extravasation

Evans blue could combine with plasma albumin and permeate into the brain tissues by the disruptive BBB. So the permeability of the blood-brain barrier (BBB) was assessed according to Evans blue extravasation. Evans blue extravasation was performed as previously reported (Chen et al., 2014a). The left femoral vein was injected with Evans Blue dye (2%, 5 mL/kg) under general anesthesia 24 h after surgery. After circulating for 60 min, the rats were euthanized, then perfused with 0.01 mol/L phosphate-buffered saline (PBS). The brain was immediately removed and separated into the same regions. We weighed and homogenized the samples in 3 ml of 50% trichloroacetic acid, then centrifuged the samples at 15000 × *g* for 30 min. The supernatant (1 ml) was separated and mixed with an equal volume of the mixture (1:3 trichloroacetic acid and ethanol). Then the samples were centrifuged again for 30 min after a 12 h incubation at 4°C. Then, we assessed the supernatant through spectrophotometry (620 nm for excitation and 680 nm for emission).

ROS Assay

The left basal cortical specimen in the face of the blood clot was collected at 24 h after SAH. We used a ROS assay kit (Nanjing Jiancheng Bio-engineering Institute, Nanjing, China) to detect the ROS levels of the rats' brains referring to the manufacturer protocol. Briefly, rats were perfused with 0.01 mol/L PBS after euthanasia. We subsequently obtained fresh tissues from the brains. Then, the samples were weighed and homogenized in PBS (1 g: 20 ml). The mixtures were centrifuged at 1000 × *g* for 10 min at 4°C and measured the protein content of the supernatant with a DC protein assay kit (Bio-Rad, Hercules, CA, United States). According to the protocol, the DCFH-DA (10 μl, 1 mol/L) and supernatant (190 μl) were mixed into 96-well plates and the same volume of PBS was added to the supernatant as a control. The samples were detected by spectrofluorophotometry after incubation for 30 min 3°C, 480 nm excitation wavelength and 520 nm emission wavelength. The ROS levels are presented as fluorescence intensity/gram protein (Li et al., 2016).

Immunofluorescence, TUNEL, and Fluoro-Jade C (FJC) Staining

Rats were perfused transcardially with PBS (0.1 mol/L) followed by 4% paraformaldehyde and euthanized 24 h after SAH. The brains of each group (n = 6) were gained and dipped in the 4% PFA for 24 h, and then dehydrated with sucrose solution (30%). The brains were frozen in tissue-freezing media to cut into coronary sections (7 μm). Conforming to the immunofluorescence protocol, we washed the coronal sections with 0.01 M PBS 3 times and then blocked with 10% normal goat serum (with 0.1% Triton X-100 in 0.01 M PBS) sealing solution. Subsequently the sections were incubated overnight with relevant primary antibodies including anti-p66shc (ab54518, Abcam), anti-NeuN (ab177487, Abcam). After washed with PBS several times the sections were hatched with related secondary antibodies including fluorescein isothiocyanate-labeled goat anti-mouse antibody (Jackson ImmunoResearch) and rhodamine-conjugated goat anti-rabbit

antibody (Jackson ImmunoResearch). The sections were stained with DAPI after washing again, then mounted with glycerol. We observed the sections using a fluorescent microscope (Olympus, Tokyo, Japan) and merged the photomicrographs by Image-Pro Plus 6.0 (Olympus, Melville, NY, United States). Five random files per coverslip were imaged. We used FJC staining to identify degenerating neurons according to the manufacturer's instructions for the FJC staining kit (Biosensis, NY, United States). In addition, terminal deoxynucleotidyl transferase-dUTP nick end labeling (TUNEL) staining was also applied to determine apoptotic cell according to the manufacturer's protocol (Roche Inc., Basel, Switzerland). An independent investigator counted FJC and TUNEL positive neurons in the left piriform cortex.

SIRT1 Activity

SIRT1 activity in brain was determined with a SIRT1 Fluorometric Kit (Biomol International) according to the manufacturer's instructions and as described previously (Escande et al., 2010). This assay uses a small lysine-acetylated peptide, corresponding to K382 of human p53, as a substrate. SIRT1 could deacetylate the lysine residue, and this process is dependent on the addition of exogenous NAD^+. Briefly, samples were homogenized in NETN buffer and then incubated for 10 min at 37°C. Next, 10 mM DTT was added to the medium and the mixtures were incubated for 10 min at 37°C again. The mixtures (20–30 μg protein/well) were then incubated in SIRT1 assay buffer to determine the SIRT1-independent or SIRT1-dependent activity. After 1 h incubation, the reaction was terminated by adding the solution containing Fluor de Lys Developer (Enzo Life Sciences) and 2 mM nicotinamide. And then the mixtures were incubated for 60 min at 37°C. The samples were detected with an excitation wavelength of 360 nm and an emission wavelength of 460 nm (Spectramax Gemini XPS; Molecular Devices). The SIRT1-dependent activity was assessed after subtracting fluorescence values obtained in the absence of NAD^+.

Western Blot

We performed Western blot as previously described (Zhang X.S. et al., 2016). Briefly, samples were obtained from cells or the left basal cortical, then lyzed on ice or homogenized and centrifuged (1000 × *g*) for 10 min at 4°C. A DC protein assay kit (Bio-Rad, Hercules, CA, United States) was used to detect the protein content. Equal amounts (60 μg) of proteins were added into polyacrylamide-SDS gels. The proteins were transferred to nitrocellulose membranes after separated by electrophorese. Membranes were incubated overnight at 4°C with the following primary antibodies followed by sealing with non-fat dry milk buffer: anti-p66shc (ab54518, Abcam), anti-SIRT1 (ab110304, Abcam), anti-ß-actin (ab8226, Abcam), anti-MnSOD (ab13533, Abcam), anti-Bax (ab32503, Abcam), anti-Bcl-2 (ab32124, Abcam), and anti-caspase-3 (ab13585, Abcam). Then, the membranes were incubated with the corresponding secondary antibodies at room temperature for 1h. The protein densities were detected via X-ray film and quantified with ImageJ software (NIH).

Statistical Analysis

Data were expressed as mean ± SD or median with interquartile range. The analyses were carried out using GraphPad Prism 7 (GraphPad Software Inc., San Diego, CA, United States) and SPSS (version 24.0; SPSS, Inc., Chicago, IL, United States). We used one-way analysis of variance (ANOVA) followed by Tukey's multiple comparison test to analyze differences among the groups when the data met the normal distribution and homogeneity of variance. For the non-normal distribution and unequal variance parameters, differences among the groups were analyzed using Kruskal–Wallis test. The Garcia score and SAH grading score were analyzed using the Mann–Whitney *U*-test. Statistical significance was defined as $P < 0.05$.

RESULTS

Expression of p66shc After SAH

The expression of p66shc in the sham group and in rats euthanized at 1, 3, 6, 12, 24, 48, and 72 h after SAH was detected by Western blot (**Figure 1A**). The result showed that the expression of p66shc was reduced at 1 and 3 h after SAH, but began to increase at 6 h and peaked at 24 h ($P < 0.05$, **Figures 1A,B**). Immunofluorescence co-staining of p66shc with NeuN (the marker of neurons) confirmed that p66shc was localized in neurons (**Figure 1C**).

Mortality, SAH Grade, and Neurologic Dysfunction

Representative brains from the sham, SAH, SAH + vehicle, and SAH + CA groups are presented in **Figure 2A**. More blood clots were found in the brain of the SAH group compared with the Sham group, and treatment with CA significantly reduced the blood clots. The neurological scores showed that significant neurological impairments occurred in SAH and SAH + vehicle groups when compared with the sham group. Administration of CA significantly improved neurological impairments 24 h after SAH ($P < 0.05$, **Figure 2B**). There was no significant difference among the mortality rates of the different groups. There were no significant differences in SAH grade between the SAH + vehicle and SAH + CA groups ($P > 0.05$, **Figure 2C**).

CA Ameliorated Brain Edema and Disruption of BBB

We observed great changes of the brain water content at 24 h after SAH. The brain water content of the left and right cerebral hemisphere increased in SAH and SAH + vehicle group in comparison with the sham group ($P < 0.05$, **Figure 2D**). After CA treatment, the brain water content in the left and right hemisphere was notably reduced compared with SAH + vehicle group ($P < 0.05$, **Figure 2D**). A remarkable extravasation of Evans blue dye into the left and right hemispheres was found in SAH and SAH + vehicle group in comparison with the sham group ($P < 0.05$, **Figure 2E**). CA significantly decreased Evans

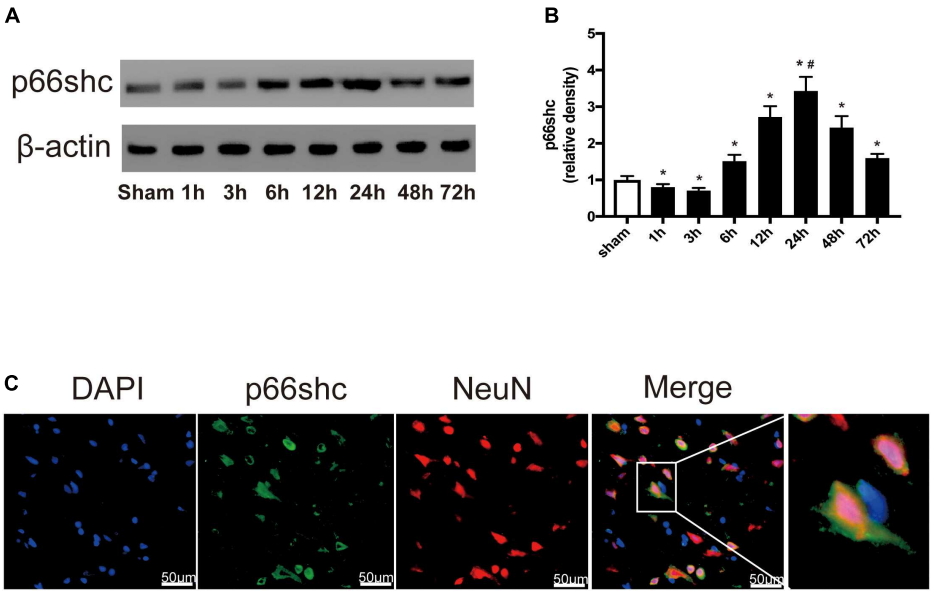

FIGURE 1 | (A) Representative Western blot bands of p66shc at different time course in ipsilateral basal cortex after subarachnoid hemorrhage (SAH) induction. **(B)** Quantitative analysis of p66shc expression. $n = 6$ for each group. The bars represent the mean ± SD. $^{*}P < 0.05$ versus sham, $^{\#}P < 0.05$ versus every other group. The densities of the protein bands were analyzed in relation to β-actin and normalized to the sham group. **(C)** Representative microphotographs of immunofluorescence staining showing localization of p66shc (green) with NeuN (red) in ipsilateral basal cortex of SAH 24 h group (scale bar = 50 μm). The rightmost image was magnified by digital zoom.

blue dye extravasation in the left and right hemispheres ($P < 0.05$, **Figure 2E**).

Administration of CA Activated the SIRT1/p66shc Pathway and Inhibited Apoptosis

Carnosic acid was administered intraperitoneally after the SAH was induced. Western blot analysis showed that administration of CA significantly upregulated the expression of SIRT1 and downregulated the expression of p66shc compared to the SAH and SAH + vehicle groups ($P < 0.05$, **Figures 3A–C**). Consistent with the result from western blot, the activity of SIRT1 was significantly increased after SAH, and this increase was further extended by administration of CA ($P < 0.05$, **Figure 3D**). To determine the direct effect of CA on SIRT1 expression, PC12 cells were treated with CA. Western blot analysis showed that treatment with CA significantly increased SIRT1 expression (**Figure 3E**). The expression of MnSOD, a mitochondria-resident enzyme that governs ROS, was significantly decreased after SAH induction and upregulated after CA administration ($P < 0.05$, **Figures 3F,G**). Apoptosis associated proteins, such as Bax, Bcl-2, and cleaved caspase-3 were dramatically altered 24 h after SAH compared with the sham group, and the changes were reversed by CA administration ($P < 0.05$, **Figures 3H–J**). In addition, levels of ROS were remarkably increased after SAH, whereas they were markedly reduced in the SAH + CA group ($P < 0.05$, **Figure 3K**).

Few TUNEL-positive neurons were detected in the sham group after SAH. The numbers of TUNEL-positive neurons in the cortex in the SAH and SAH + vehicle group were remarkably higher compared with the sham group. In comparison with the SAH and SAH + vehicle groups, CA treatment decreased the apoptosis index ($P < 0.05$, **Figures 4A,C**). FJC-positive cells representing degenerating neurons dramatically increased after SAH and CA treatment reversed this change ($P < 0.05$, **Figures 4B,D**). These results suggest that CA treatment inhibits neuron apoptosis and SIRT1/p66shc cascade might account for this inhibition.

Inhibition of SIRT1 Abolished the Neuroprotective Effect of CA

To test whether SIRT1 upregulation plays a causal role in CA-mediated neuroprotection, sirtinol, a selective inhibitor of SIRT1, was applied. The results showed that inhibition of SIRT1 by sirtinol significantly abolished the neurological improvements induced by CA, as indicated by the neurological scores ($P < 0.05$, **Figure 5A**). Additionally, the levels of ROS rebounded after sirtinol administration ($P < 0.05$, **Figure 5B**). In PC12 cells, treatment with sirtinol abolished the inhibitor effect of CA on p66shc inhibition ($P < 0.05$, **Figures 5C–E**). Moreover, Western blot showed that upregulation of SIRT1 and downregulation of p66shc caused by CA were also reversed by sirtinol ($P < 0.05$, **Figures 5F–H**).

Inhibition of SIRT1 Reversed the Anti-apoptotic Effect of CA After SAH

As shown in the Western blot analysis 24 h after SAH, administration of CA significantly increased MnSOD expression and the tendency was notably reversed in the SAH + CA

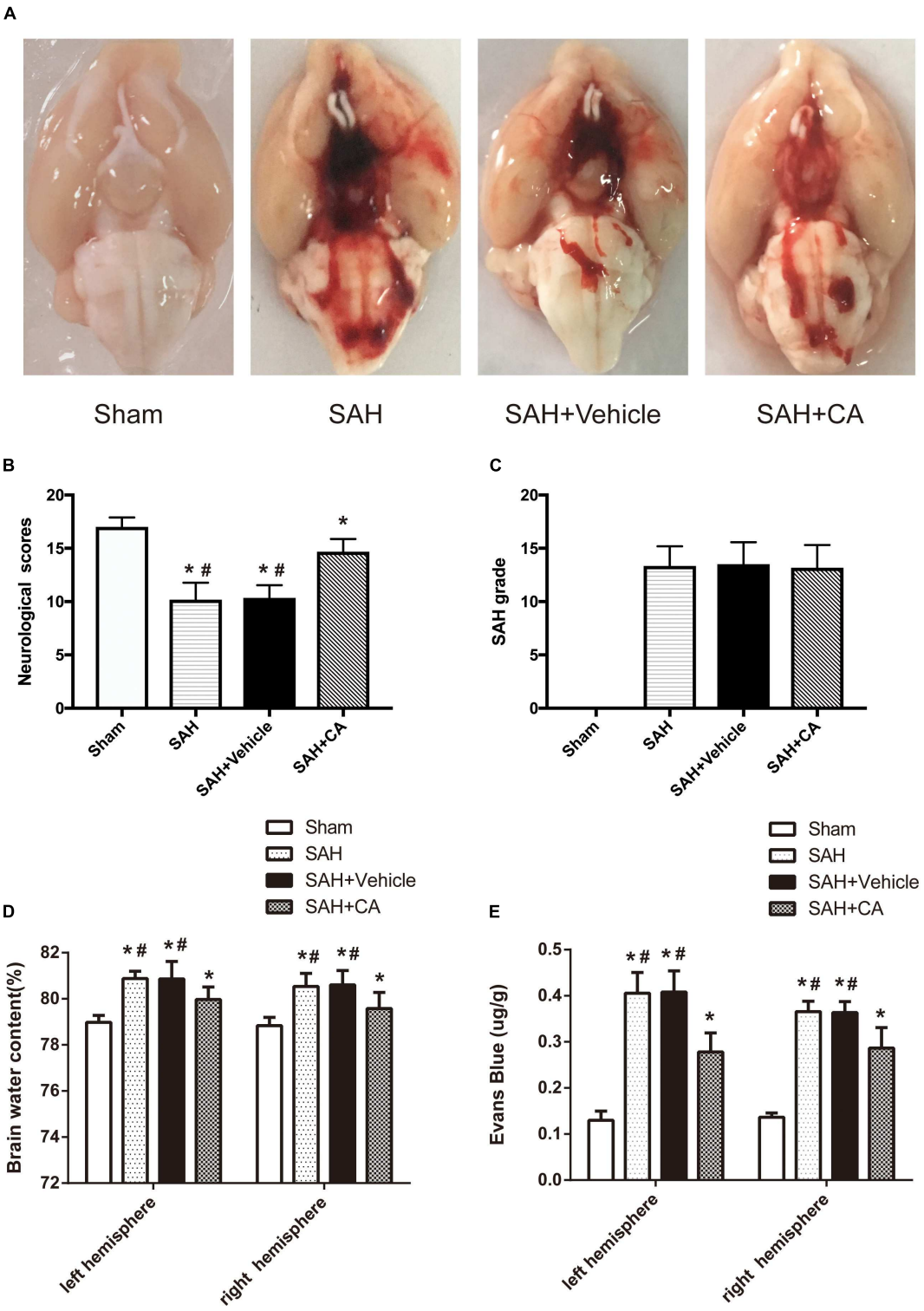

FIGURE 2 | Typical representation of brains from each group and SAH grade, neurological scores, brain water content, and Evans blue dye extravasation at 24 h after SAH. **(A)** Representative brains from the sham, SAH, SAH + vehicle, SAH + CA group. **(B)** Quantitative analyses of neurological scores. The bars represent the mean ± SD. $n = 30$. **(C)** Quantitative analyses of SAH severity. The bars represent the mean ± SD. $n = 30$. **(D)** Quantitative analyses of brain water content. The bars represent the mean ± SD. $n = 6$. **(E)** Quantitative analyses of Evans blue dye extraversion. The bars represent the mean ± SD. $n = 6$. $^{*\#}P < 0.05$ vs. Sham, $^{*}P < 0.05$ vs. SAH.

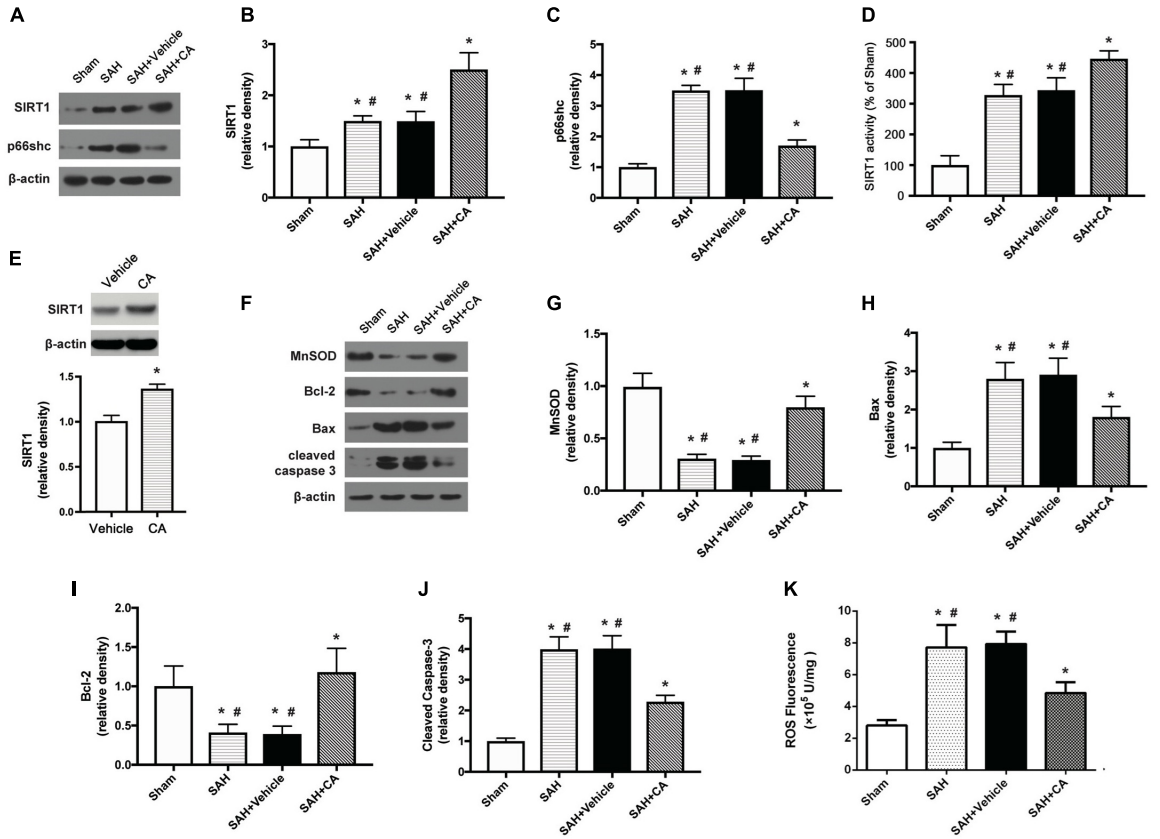

FIGURE 3 | Carnosic acid attenuated apoptosis 24 h after subarachnoid hemorrhage (SAH) via activating SIRT1/p66shc signaling pathway. **(A)** Representative Western blot bands of SIRT1, p66shc. **(B,C)** Quantitative analyses of SIRT1 **(B)**, p66shc **(C)**. **(D)** Activity of SIRT1 in the brain. **(E)** The effect of CA on SIRT1 expression. **(F)** Representative Western blot bands of MnSOD, Bax, Bcl-2, and cleaved caspase-3. **(G–J)** Quantitative analyses of, MnSOD **(G)**, Bax **(H)**, Bcl-2 **(I)**, cleaved caspase-3 **(J)**. The densities of the protein bands were analyzed in relation to β-actin and normalized to the sham group. **(K)** Quantitation of ROS. The histograms represent the median with interquartile range, $n = 6$. The statistical differences between two groups were analyzed by Kruskal–Wallis test. $^{*\#}P < 0.05$ vs. Sham, $^{*}P < 0.05$ vs. SAH.

+ sirtinol group ($P < 0.05$, **Figure 5I**). Upregulation of Bcl-2 in the SAH + CA group was also dramatically suppressed by sirtinol ($P < 0.05$, **Figure 5J**). Sirtinol also reversed the CA-induced decrease of Bax and cleaved caspase-3 expression ($P < 0.05$, **Figures 5K,L**).

Further, TUNEL and FJC staining were used to measure apoptotic cells and degenerating neurons in the ipsilateral cortex. Results showed that treatment of CA significantly decreased the apoptosis index and FJC-positive cells. However, these alterations were markedly reversed by sirtinol ($P < 0.05$, **Figures 6A–D**).

DISCUSSION

Mounting evidence implies that EBI within the first 72 h of SAH plays a central role in SAH. The treatment of EBI could be a potential therapeutic strategy for the management of patients surviving a SAH. However, the underlying molecular mechanisms has not been elucidated (Ostrowski et al., 2006). The possible mechanisms involving EBI after SAH involve disruption of the BBB, brain edema, oxidative stress, and neural apoptosis (Sehba et al., 2012). CA, one of the major phenolic compounds extracted from *Rosmarinus officinalis*, is a well-established anti-adipogenic and antioxidant agent (Jordan et al., 2012; Park and Mun, 2013). Recently, CA has been reported to have favorable efficacy in managing some diseases. For example, CA protects myocardial cells, renal cells, SH-SY5Y cells, and hepatocytes against injury by inhibiting apoptosis (Sahu et al., 2011, 2014; Chen J.H. et al., 2012). The mechanisms by which CA regulates neural apoptosis in SAH is unknown. In a recent study, we successfully established the vascular perforation model to mimic clinical aneurysm subarachnoid hemorrhage (aSAH), which is the most common cause of SAH. We observed that CA treatment alleviated neuronal cell death and improved neurological outcome, diminished levels of ROS, and dramatically alleviated BBB disruption and brain edema dramatically. We therefore suggest that the SIRT1/p66shc pathway might be involved in the protective mechanism underlying CA treatment of SAH.

Emerging evidence indicates that under pathophysiologic circumstances, acute and chronic overproduction of ROS are vitally important in the development of cardio-cerebral vascular diseases. ROS, which are highly reactive free radicals including

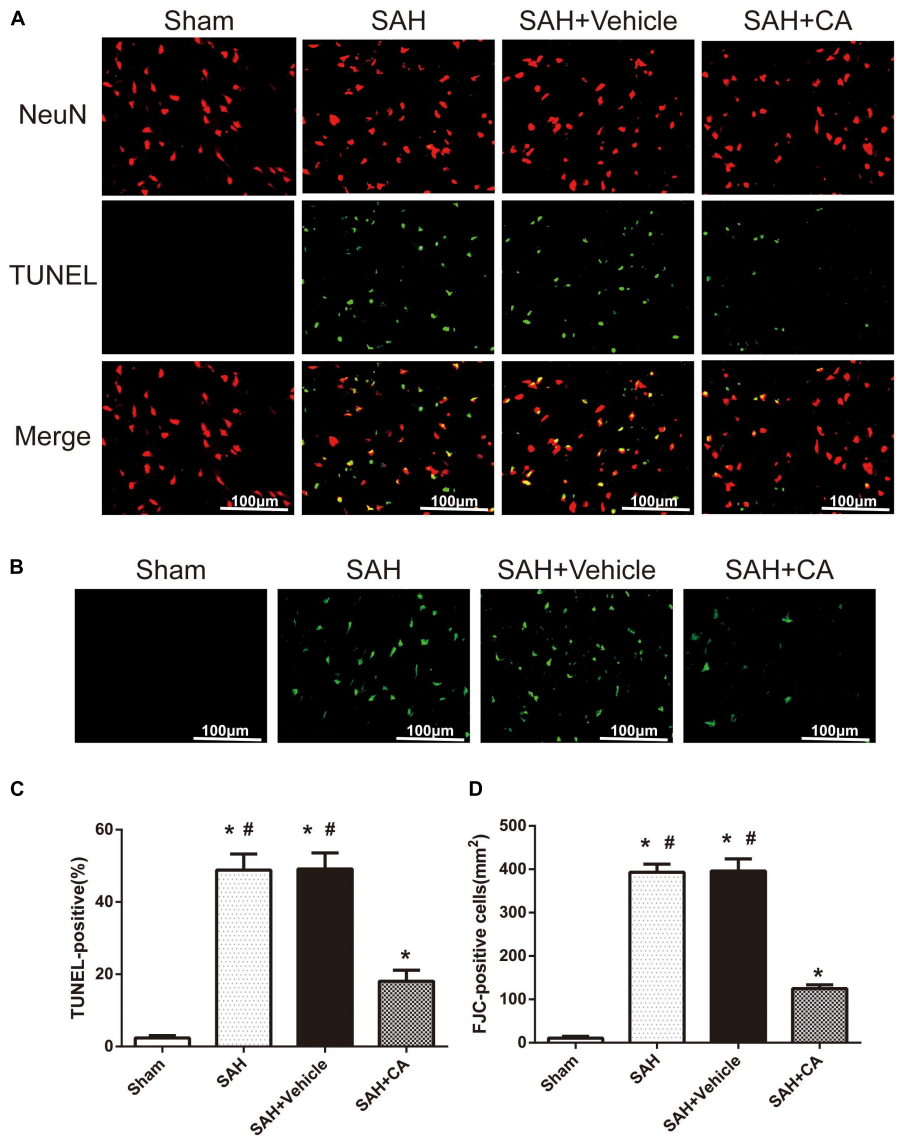

FIGURE 4 | Carnosic acid reduced degenerating neurons and neuronal cells death in the ipsilateral cortex at 24 h after SAH. **(A)** Representative co-labeling TUNEL/NeuN photomicrographs of the ipsilateral cortex in the different groups (scale bar = 100 μm). **(B)** Representative FJC photomicrographs in the different groups (scale bar = 100 μm). **(C)** Quantification of TUNEL-positive neurons, expressed as percentage of total ($NeuN^+$) cells. **(D)** Quantification of FJC-positive degenerating neurons. The bars represent the mean ± SD. $n = 6$. $^{*\#}P < 0.05$ vs. Sham, $^{*}P < 0.05$ vs. SAH.

a variety of small molecule radicals such as superoxide anion (O_2), hydroxyl radical (OH), and hydrogen peroxide (H_2O_2), which are important components of cellular signaling pathways physiologically (Venditti et al., 2013; Fan et al., 2017). ROS are also the most important cause of oxidative stress. The increased levels of ROS could incur brain injury by various means, including apoptosis, BBB disruption, and inflammation (Cahill et al., 2006; Olmez and Ozyurt, 2012; Sehba and Friedrich, 2015; Zhang L. et al., 2016). Thus, we measured the levels of ROS in recent study. The cortical ROS levels surged 24 h after SAH and were inhibited by CA. This result further verified the antioxidative activity of CA. To further explore the potential mechanism underlying antioxidative stress by CA, we focused on SIRT1, an NAD-dependent deacetylase. Recently, it has been demonstrated that activation of SIRT1 plays a critical protective role in mediating tissue injury in multiple experimental models and human diseases including cardiac, brain and kidney injuries caused by ischemia/reperfusion (Hsu et al., 2010; Wang et al., 2011; Lempiainen et al., 2012). Interestingly, SIRT1 is widely expressed in the central nervous system and SIRT1 is activated by plant polyphenols. Consistent with our hypothesis, the current study determined that CA treatment facilitated the activation of SIRT1 after SAH and the positive regulatory effect of CA on SAH was restrained by sirtinol, a SIRT1 inhibitor. These results indicate that CA might be a potential activator of SIRT1. Nevertheless, it is notable that the expression of SIRT1 increased

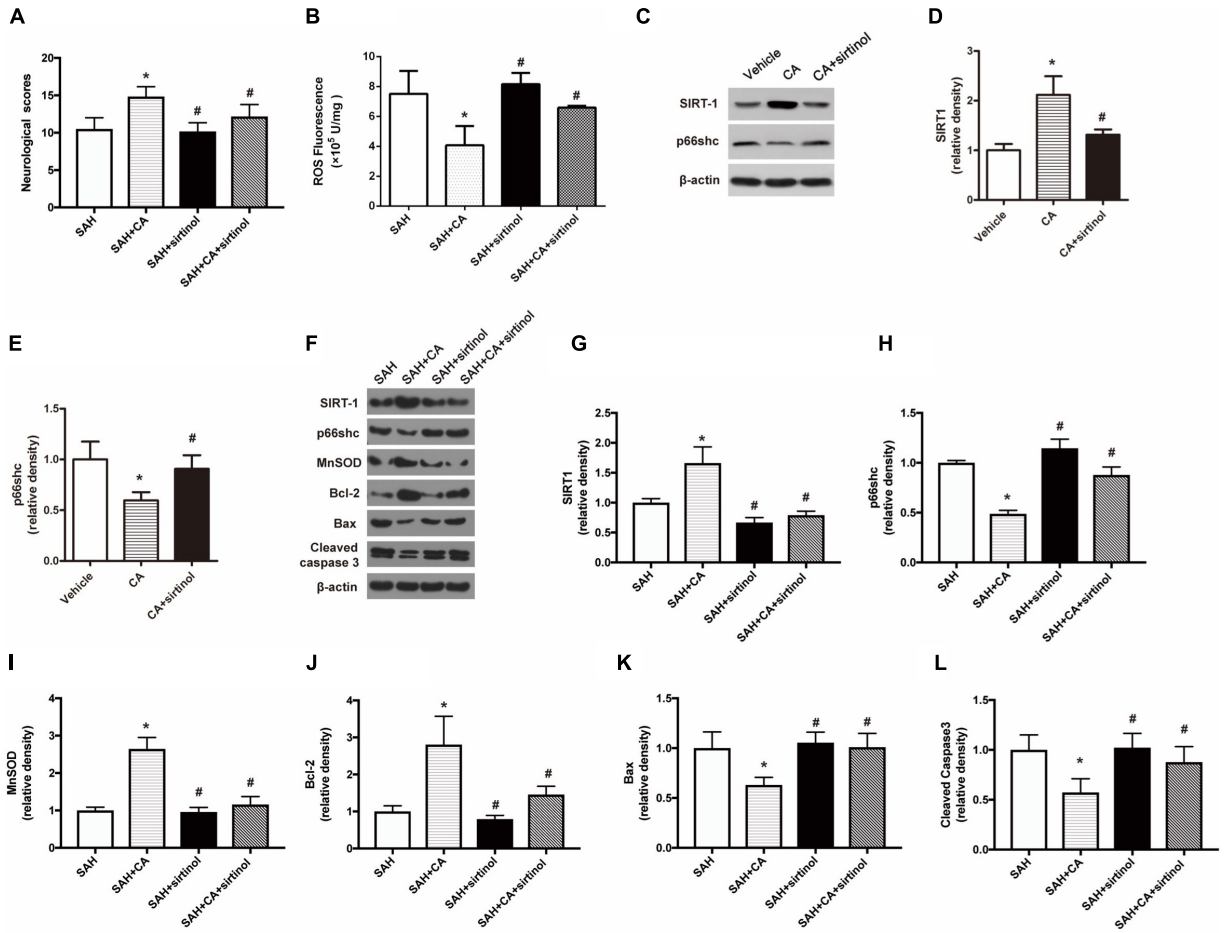

FIGURE 5 | SIRT1 inhibitor sirtinol abolished the beneficial effect of carnosic acid on apoptosis. **(A)** Quantitative analyses of neurological scores. The bars represent the mean ± SD. $n = 18$. **(B)** Quantitative analyses of ROS. The histograms represent the median with interquartile range, $n = 6$. **(C–E)** Western blot assay and quantitative analyses of SIRT1 **(D)**, p66shc **(E)** in PC12 cells after treatment with CA alone or together with sirtinol. $^{*}P < 0.05$ vs. Vehicle, $^{\#}P < 0.05$ vs. CA. **(F–L)** Western blot assay **(F)** and quantitative analyses of SIRT1 **(G)**, p66shc **(H)**, MnSOD **(I)**, Bcl-2 **(J)**, Bax **(K)**, cleaved caspase-3 **(L)** expressions in ipsilateral cortex. The densities of the protein bands were analyzed in relation to β-actin and normalized to the sham group. The bars represent the mean ± SD. $n = 6$. $^{*}P < 0.05$ vs. SAH, $^{\#}P < 0.05$ vs. SAH + CA.

slightly at 24 h after SAH. We speculate that self-protection against injury stress might be responsible for this result, which is supported by the results of a previous study (Li et al., 2018).

It has been shown that SIRT1 regulates energy metabolism, oxidative stress, and apoptosis by targeting different genes in the liver (Purushotham et al., 2009). P66shc has been reported to be targeted by SIRT1 through deacetylation of histone H3 lysine (Zhou et al., 2011). Moreover, it has been suggested that CA-promoted activation of the SIRT1/p66shc pathway protects rats against apoptosis in an ischemia/reperfusion (I/R) injury model (Yan et al., 2014). P66shc, an intracellular mediator converts oxidative signals into ROS and induces apoptosis during multiple pathologic conditions, such as diabetes and glomerulopathies (Menini et al., 2007; Zaccagnini et al., 2007). A P66shc defective mutant is unable to maintain normal oxidative stress in p66shc$^{-/-}$ cells and p66shc knockout strengthen cellular resistance to apoptosis induced by H_2O_2 and ultraviolet light (Menini et al., 2007). Furthermore, p66shc has been suggested to downregulate the expression of antioxidant enzymes and regulatory factors, such as glutathione peroxidase-1, MnSOD (the primary superoxide scavenger) and REF-1 (Miyazawa and Tsuji, 2014). Interestingly, it has been shown that the expression of p66shc is decreased and oxidative stress is reduced markedly in the SIRT1 transgenic diabetic mice (Chen H. et al., 2012). In agreement with these observations, we found that CA treatment reversed the upregulation of p66shc caused by SAH and sirtinol induced an increase in p66shc. Interestingly, CA increased the levels of MnSOD after SAH and sirtinol abolished these changes. Together, these results imply that SIRT1 suppressed p66shc expression and oxidative stress during SAH and that activation of the SIRT1/p66shc pathway might be involved in the neuroprotective effect of CA in SAH.

Current views hold that the formation of a multi-subunit protein complex, which eventually forms a pore in the mitochondrial membrane is promoted by various signals in the course of mitochondrial-dependent apoptosis.

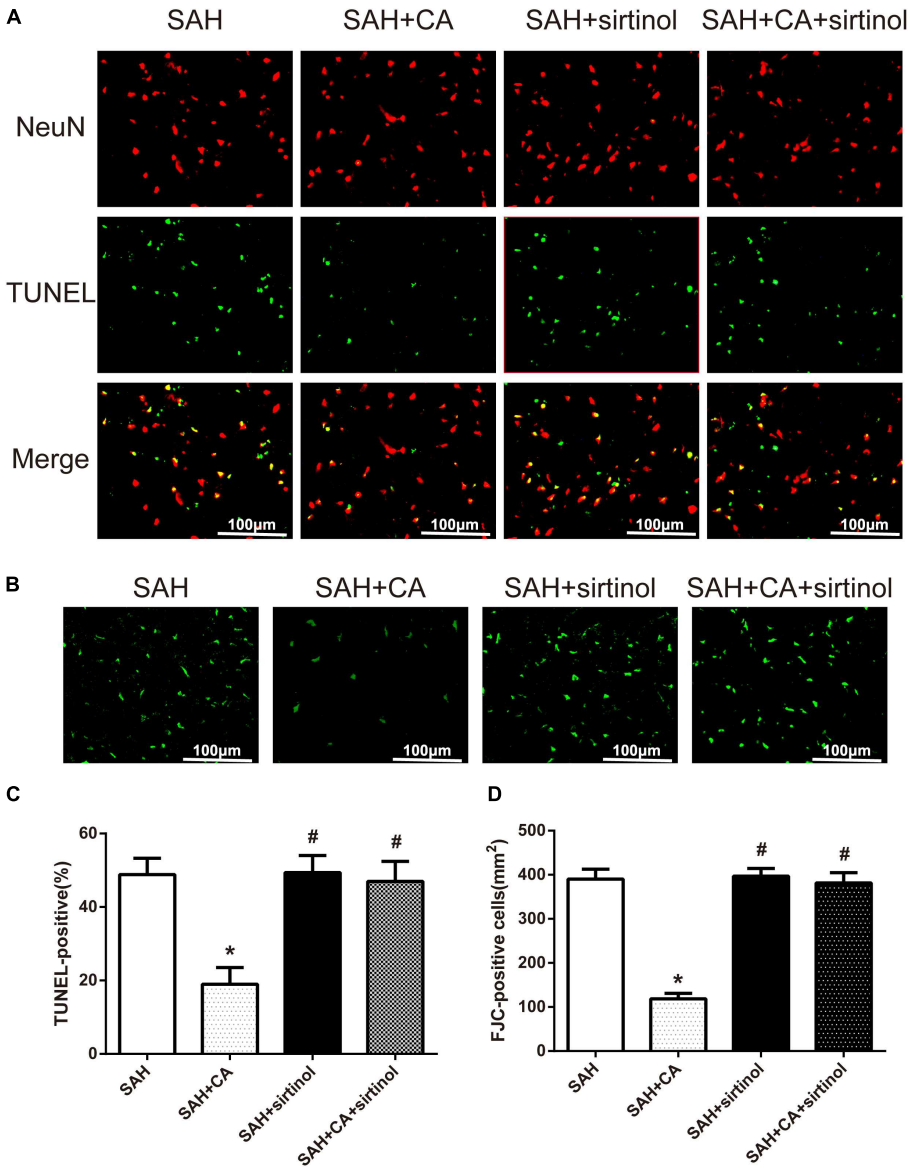

FIGURE 6 | SIRT1 inhibitor sirtinol abolished carnosic acid-reduced degenerating neurons and neuronal cells death in the ipsilateral cortex at 24 h after SAH. **(A)** Representative co-labeling TUNEL/NeuN photomicrographs of the ipsilateral cortex in the different groups (scale bar = 100 μm). **(B)** Representative FJC photomicrographs in the different groups (scale bar = 100 μm). **(C)** Quantification of TUNEL-positive neurons, expressed as percentage of total ($NeuN^+$) cells. **(D)** Quantification of FJC-positive degenerating neurons. The bars represent the mean ± SD. $n = 6$. $^*P < 0.05$ vs. SAH, $^{\#}P < 0.05$ vs. SAH + CA.

The permeabilization of mitochondrial membranes results in proapoptotic proteins activation. It has been demonstrated that p66shc is necessary for permeabilization of mitochondrial membranes (Galimov, 2010). The protective effects of SIRT1 against cardiac I/R can be explained by SIRT1 overexpression inducing up-regulation of MnSOD and Bcl-2 and down-regulation of Bax (Hsu et al., 2010). Similarly, suppression of p66shc protected against intestinal I/R induced by lung injury via the regulation of MnSOD, Bcl-2 and caspase-3 (Wang et al., 2012). In our study, FJC and TUNEL staining revealed that the neuronal degeneration and apoptosis secondary to SAH were suppressed by CA. Additionally, we also determined that the expression of Bax and cleaved caspase-3 were increased markedly after SAH, while CA treatment reserved the changes. The expression of Bcl-2 were presented on the contrary, namely, CA administration increased the expression of Bcl-2. Moreover, Sirtinol diminished the anti-apoptotic effect of CA on EBI. Based on these observations, we deduced that the activation of p66shc is strongly linked to apoptosis secondary to SAH and it is likely that CA protects neuron against apoptosis via suppression of the SIRT1/p66shc signaling pathway.

Several restrictions exist in the present study. First, we discussed the neuroprotection of CA in the early stage of SAH, the long-term effect in SAH needs to be further investigated.

Second, several studies have revealed the effect of CA regulating inflammation. In our study, we focused on the anti-apoptosis effect of CA on SAH, however, we cannot completely absolutely exclude the possibility that neuroinflammation is involved in the neuroprotection of CA in EBI after SAH. Therefore, further studies are needed to explore the role of CA in neuroinflammation after SAH. In addition, ROS-induced oxidative stress after SAH warrants further experiments.

In conclusion, this study extended our understanding of the neuroprotective effects of CA on EBI after SAH. We demonstrated that CA-induced SIRT1 upregulation plays a protective role in EBI secondary to SAH. The potential mechanisms may involve the suppression of neuronal apoptosis through the SIRT1/p66shc pathway. Indeed, CA might be a novel and potential therapeutic strategy for SAH management.

AUTHOR CONTRIBUTIONS

LT and LF contributed to the study design, data analysis, and paper writing. YP, XH, HC, HD, FY, DL, ZL, and HL contributed to the SAH model performance and data collection. BS contributed to the instruction of the total research.

REFERENCES

Berry, A., Capone, F., Giorgio, M., Pelicci, P. G., De Kloet, E. R., Alleva, E., et al. (2007). Deletion of the life span determinant p66Shc prevents age-dependent increases in emotionality and pain sensitivity in mice. *Exp. Gerontol.* 42, 37–45. doi: 10.1016/j.exger.2006.05.018

Biller, J., Godersky, J. C., and Adams, H. P. Jr. (1988). Management of aneurysmal subarachnoid hemorrhage. *Stroke* 19, 1300–1305. doi: 10.1161/01.STR.19.10.1300

Brunet, A., Sweeney, L. B., Sturgill, J. F., Chua, K. F., Greer, P. L., Lin, Y., et al. (2004). Stress-dependent regulation of FOXO transcription factors by the SIRT1 deacetylase. *Science* 303, 2011–2015. doi: 10.1126/science.1094637

Cahill, J., Calvert, J. W., and Zhang, J. H. (2006). Mechanisms of early brain injury after subarachnoid hemorrhage. *J. Cereb. Blood Flow Metab.* 26, 1341–1353. doi: 10.1038/sj.jcbfm.9600283

Chen, H., Wan, Y., Zhou, S., Lu, Y., Zhang, Z., Zhang, R., et al. (2012). Endothelium-specific SIRT1 overexpression inhibits hyperglycemia-induced upregulation of vascular cell senescence. *Sci. China Life Sci.* 55, 467–473. doi: 10.1007/s11427-012-4329-4

Chen, J. H., Ou, H. P., Lin, C. Y., Lin, F. J., Wu, C. R., Chang, S. W., et al. (2012). Carnosic acid prevents 6-hydroxydopamine-induced cell death in SH-SY5Y cells via mediation of glutathione synthesis. *Chem. Res. Toxicol.* 25, 1893–1901. doi: 10.1021/tx300171u

Chen, H. Z., Wan, Y. Z., and Liu, D. P. (2013). Cross-talk between SIRT1 and p66Shc in vascular diseases. *Trends Cardiovasc. Med.* 23, 237–241. doi: 10.1016/j.tcm.2013.01.001

Chen, J., Chen, G., Li, J., Qian, C., Mo, H., Gu, C., et al. (2014a). Melatonin attenuates inflammatory response-induced brain edema in early brain injury following a subarachnoid hemorrhage: a possible role for the regulation of pro-inflammatory cytokines. *J. Pineal Res.* 57, 340–347. doi: 10.1111/jpi.12173

Chen, J., Wang, L., Wu, C., Hu, Q., Gu, C., Yan, F., et al. (2014b). Melatonin-enhanced autophagy protects against neural apoptosis via a mitochondrial pathway in early brain injury following a subarachnoid hemorrhage. *J. Pineal Res.* 56, 12–19. doi: 10.1111/jpi.12086

Cheng, H. L., Mostoslavsky, R., Saito, S., Manis, J. P., Gu, Y., Patel, P., et al. (2003). Developmental defects and p53 hyperacetylation in Sir2 homolog (SIRT1)-deficient mice. *Proc. Natl. Acad. Sci. U.S.A.* 100, 10794–10799. doi: 10.1073/pnas.1934713100

Chung, S., Yao, H., Caito, S., Hwang, J. W., Arunachalam, G., and Rahman, I. (2010). Regulation of SIRT1 in cellular functions: role of polyphenols. *Arch. Biochem. Biophys.* 501, 79–90. doi: 10.1016/j.abb.2010.05.003

Escande, C., Chini, C. C., Nin, V., Dykhouse, K. M., Novak, C. M., Levine, J., et al. (2010). Deleted in breast cancer-1 regulates SIRT1 activity and contributes to high-fat diet-induced liver steatosis in mice. *J. Clin. Invest.* 120, 545–558. doi: 10.1172/JCI39319

Fan, L. F., He, P. Y., Peng, Y. C., Du, Q. H., Ma, Y. J., Jin, J. X., et al. (2017). Mdivi-1 ameliorates early brain injury after subarachnoid hemorrhage via the suppression of inflammation-related blood-brain barrier disruption and endoplasmic reticulum stress-based apoptosis. *Free Radic. Biol. Med.* 112, 336–349. doi: 10.1016/j.freeradbiomed.2017.08.003

Galimov, E. R. (2010). The Role of p66shc in oxidative stress and apoptosis. *Acta Nat.* 2, 44–51. doi: 10.1016/j.freeradbiomed.2017.08.003

Garcia, J. H., Wagner, S., Liu, K. F., and Hu, X. J. (1995). Neurological deficit and extent of neuronal necrosis attributable to middle cerebral artery occlusion in rats. Statistical validation. *Stroke* 26, 627–634, discussion 635. doi: 10.1161/01.STR.26.4.627

Giorgio, M., Migliaccio, E., Orsini, F., Paolucci, D., Moroni, M., Contursi, C., et al. (2005). Electron transfer between cytochrome c and p66Shc generates reactive oxygen species that trigger mitochondrial apoptosis. *Cell* 122, 221–233. doi: 10.1016/j.cell.2005.05.011

Hsu, C. P., Zhai, P., Yamamoto, T., Maejima, Y., Matsushima, S., Hariharan, N., et al. (2010). Silent information regulator 1 protects the heart from ischemia/reperfusion. *Circulation* 122, 2170–2182. doi: 10.1161/CIRCULATIONAHA.110.958033

Jordan, M. J., Lax, V., Rota, M. C., Loran, S., and Sotomayor, J. A. (2012). Relevance of carnosic acid, carnosol, and rosmarinic acid concentrations in the in vitro antioxidant and antimicrobial activities of *Rosmarinus officinalis* (L.) methanolic extracts. *J. Agric. Food Chem.* 60, 9603–9608. doi: 10.1021/jf302881t

Kumar, S., Vikram, A., Kim, Y. R., S Jacobs, J., and Irani, K. (2014). P66Shc mediates increased platelet activation and aggregation in hypercholesterolemia. *Biochem. Biophys. Res. Commun.* 449, 496–501. doi: 10.1016/j.bbrc.2014.05.029

Langley, E., Pearson, M., Faretta, M., Bauer, U. M., Frye, R. A., Minucci, S., et al. (2002). Human SIR2 deacetylates p53 and antagonizes PML/p53-induced cellular senescence. *EMBO J.* 21, 2383–2396. doi: 10.1093/emboj/21.10.2383

Lempiainen, J., Finckenberg, P., Levijoki, J., and Mervaala, E. (2012). AMPK activator AICAR ameliorates ischaemia reperfusion injury in the rat kidney. *Br. J. Pharmacol.* 166, 1905–1915. doi: 10.1111/j.1476-5381.2012.01895.x

Li, J., Chen, J., Mo, H., Chen, J., Qian, C., Yan, F., et al. (2016). Minocycline protects against NLRP3 inflammasome-induced inflammation and P53-associated apoptosis in early brain injury after subarachnoid hemorrhage. *Mol. Neurobiol.* 53, 2668–2678. doi: 10.1007/s12035-015-9318-8

Li, Q., Peng, Y., Fan, L., Xu, H., He, P., Cao, S., et al. (2018). Phosphodiesterase-4 inhibition confers a neuroprotective efficacy against early brain injury following experimental subarachnoid hemorrhage in rats by attenuating neuronal apoptosis through the SIRT1/Akt pathway. *Biomed. Pharmacother.* 99, 947–955. doi: 10.1016/j.biopha.2018.01.093

McBurney, M. W., Yang, X., Jardine, K., Hixon, M., Boekelheide, K., Webb, J. R., et al. (2003). The mammalian SIR2alpha protein has a role in embryogenesis and gametogenesis. *Mol. Cell. Biol.* 23, 38–54. doi: 10.1128/MCB.23.1.38-54.2003

Menini, S., Iacobini, C., Ricci, C., Oddi, G., Pesce, C., Pugliese, F., et al. (2007). Ablation of the gene encoding p66Shc protects mice against AGE-induced glomerulopathy by preventing oxidant-dependent tissue injury and further AGE accumulation. *Diabetologia* 50, 1997–2007. doi: 10.1007/s00125-007-0728-7

Miller, D. M., Singh, I. N., Wang, J. A., and Hall, E. D. (2015). Nrf2-ARE activator carnosic acid decreases mitochondrial dysfunction, oxidative damage and neuronal cytoskeletal degradation following traumatic brain injury in mice. *Exp. Neurol.* 264, 103–110. doi: 10.1016/j.expneurol.2014.11.008

Miyazawa, M., and Tsuji, Y. (2014). Evidence for a novel antioxidant function and isoform-specific regulation of the human p66Shc gene. *Mol. Biol. Cell* 25, 2116–2127. doi: 10.1091/mbc.E13-11-0666

Olmez, I., and Ozyurt, H. (2012). Reactive oxygen species and ischemic cerebrovascular disease. *Neurochem. Int.* 60, 208–212. doi: 10.1016/j.neuint.2011.11.009

Ostrowski, R. P., Colohan, A. R., and Zhang, J. H. (2006). Molecular mechanisms of early brain injury after subarachnoid hemorrhage. *Neurol. Res.* 28, 399–414. doi: 10.1179/016164106X115008

Park, M. Y., and Mun, S. T. (2013). Dietary carnosic acid suppresses hepatic steatosis formation via regulation of hepatic fatty acid metabolism in high-fat diet-fed mice. *Nutr. Res. Pract.* 7, 294–301. doi: 10.4162/nrp.2013.7.4.294

Purushotham, A., Schug, T. T., Xu, Q., Surapureddi, S., Guo, X., and Li, X. (2009). Hepatocyte-specific deletion of SIRT1 alters fatty acid metabolism and results in hepatic steatosis and inflammation. *Cell Metab.* 9, 327–338. doi: 10.1016/j.cmet.2009.02.006

Redza-Dutordoir, M., and Averill-Bates, D. A. (2016). Activation of apoptosis signalling pathways by reactive oxygen species. *Biochim. Biophys. Acta* 1863, 2977–2992. doi: 10.1016/j.bbamcr.2016.09.012

Sahu, B. D., Putcha, U. K., Kuncha, M., Rachamalla, S. S., and Sistla, R. (2014). Carnosic acid promotes myocardial antioxidant response and prevents isoproterenol-induced myocardial oxidative stress and apoptosis in mice. *Mol. Cell. Biochem.* 394, 163–176. doi: 10.1007/s11010-014-2092-5

Sahu, B. D., Rentam, K. K., Putcha, U. K., Kuncha, M., Vegi, G. M., and Sistla, R. (2011). Carnosic acid attenuates renal injury in an experimental model of rat cisplatin-induced nephrotoxicity. *Food Chem. Toxicol.* 49, 3090–3097. doi: 10.1016/j.fct.2011.08.018

Sehba, F. A., and Friedrich, V. (2015). Early events after aneurysmal subarachnoid hemorrhage. *Acta Neurochir. Suppl.* 120, 23–28. doi: 10.1007/978-3-319-04981-6_4

Sehba, F. A., Hou, J., Pluta, R. M., and Zhang, J. H. (2012). The importance of early brain injury after subarachnoid hemorrhage. *Prog. Neurobiol.* 97, 14–37. doi: 10.1016/j.pneurobio.2012.02.003

Shan, W., Gao, L., Zeng, W., Hu, Y., Wang, G., Li, M., et al. (2015). Activation of the SIRT1/p66shc antiapoptosis pathway via carnosic acid-induced inhibition of miR-34a protects rats against nonalcoholic fatty liver disease. *Cell Death Dis.* 6, e1833. doi: 10.1038/cddis.2015.196

Sugawara, T., Ayer, R., Jadhav, V., and Zhang, J. H. (2008). A new grading system evaluating bleeding scale in filament perforation subarachnoid hemorrhage rat model. *J. Neurosci. Methods* 167, 327–334. doi: 10.1016/j.jneumeth.2007.08.004

Venditti, P., Di Stefano, L., and Di Meo, S. (2013). Mitochondrial metabolism of reactive oxygen species. *Mitochondrion* 13, 71–82. doi: 10.1016/j.mito.2013.01.008

Vikram, A., Kim, Y. R., Kumar, S., Naqvi, A., Hoffman, T. A., Kumar, A., et al. (2014). Canonical Wnt signaling induces vascular endothelial dysfunction via p66Shc-regulated reactive oxygen species. *Arterioscler. Thromb. Vasc. Biol.* 34, 2301–2309. doi: 10.1161/ATVBAHA.114.304338

Wang, G. Z., Yao, J. H., Jing, H. R., Zhang, F., Lin, M. S., Shi, L., et al. (2012). Suppression of the p66shc adapter protein by protocatechuic acid prevents the development of lung injury induced by intestinal ischemia reperfusion in mice. *J. Trauma Acute Care Surg.* 73, 1130–1137. doi: 10.1097/TA.0b013e318265d069

Wang, P., Xu, T. Y., Guan, Y. F., Tian, W. W., Viollet, B., Rui, Y. C., et al. (2011). Nicotinamide phosphoribosyltransferase protects against ischemic stroke through SIRT1-dependent adenosine monophosphate-activated kinase pathway. *Ann. Neurol.* 69, 360–374. doi: 10.1002/ana.22236

Wu, P., Li, Y., Zhu, S., Wang, C., Dai, J., Zhang, G., et al. (2017). Mdivi-1 alleviates early brain injury after experimental subarachnoid hemorrhage in rats, possibly via inhibition of Drp1-activated mitochondrial fission and oxidative stress. *Neurochem. Res.* 42, 1449–1458. doi: 10.1007/s11064-017-2201-4

Xia, P., Pan, Y., Zhang, F., Wang, N., Wang, E., Guo, Q., et al. (2018). Pioglitazone confers neuroprotection against ischemia-induced pyroptosis due to its inhibitory effects on HMGB-1/RAGE and Rac1/ROS pathway by activating PPAR. *Cell Physiol. Biochem.* 45, 2351–2368. doi: 10.1159/000488183

Xie, Y., Zhang, J., Ye, S., He, M., Ren, R., Yuan, D., et al. (2012). SirT1 regulates radiosensitivity of hepatoma cells differently under normoxic and hypoxic conditions. *Cancer Sci.* 103, 1238–1244. doi: 10.1111/j.1349-7006.2012.02285.x

Yan, F., Cao, S., Li, J., Dixon, B., Yu, X., Chen, J., et al. (2016). Pharmacological inhibition of PERK attenuates early brain injury after subarachnoid hemorrhage in rats through the activation of Akt. *Mol. Neurobiol.* 54, 1808–1817. doi: 10.1007/s12035-016-9790-9

Yan, H., Jihong, Y., Feng, Z., Xiaomei, X., Xiaohan, Z., Guangzhi, W., et al. (2014). Sirtuin 1-mediated inhibition of p66shc expression alleviates liver ischemia/reperfusion injury. *Crit. Care Med.* 42, e373–e381. doi: 10.1097/CCM.0000000000000246

Zaccagnini, G., Martelli, F., Magenta, A., Cencioni, C., Fasanaro, P., Nicoletti, C., et al. (2007). p66(ShcA) and oxidative stress modulate myogenic differentiation and skeletal muscle regeneration after hind limb ischemia. *J. Biol. Chem.* 282, 31453–31459. doi: 10.1074/jbc.M702511200

Zhang, L., Wu, J., Duan, X., Tian, X., Shen, H., Sun, Q., et al. (2016). NADPH oxidase: a potential target for treatment of stroke. *Oxid. Med. Cell. Longev.* 2016:5026984. doi: 10.1155/2016/5026984

Zhang, X. S., Wu, Q., Wu, L. Y., Ye, Z. N., Jiang, T. W., Li, W., et al. (2016). Sirtuin 1 activation protects against early brain injury after experimental subarachnoid hemorrhage in rats. *Cell Death Dis.* 7:e2416. doi: 10.1038/cddis.2016.292

Zhou, S., Chen, H. Z., Wan, Y. Z., Zhang, Q. J., Wei, Y. S., Huang, S., et al. (2011). Repression of P66Shc expression by SIRT1 contributes to the prevention of hyperglycemia-induced endothelial dysfunction. *Circ. Res.* 109, 639–648. doi: 10.1161/CIRCRESAHA.111.243592

Conflict of Interest Statement: The authors declare that the research was conducted in the absence of any commercial or financial relationships that could be construed as a potential conflict of interest.

Advantages of publishing in Frontiers

OPEN ACCESS
Articles are free to read for greatest visibility and readership

FAST PUBLICATION
Around 90 days from submission to decision

HIGH QUALITY PEER-REVIEW
Rigorous, collaborative, and constructive peer-review

TRANSPARENT PEER-REVIEW
Editors and reviewers acknowledged by name on published articles

Frontiers
Avenue du Tribunal-Fédéral 34
1005 Lausanne | Switzerland

Visit us: www.frontiersin.org
Contact us: frontiersin.org/about/contact

REPRODUCIBILITY OF RESEARCH
Support open data and methods to enhance research reproducibility

DIGITAL PUBLISHING
Articles designed for optimal readership across devices

FOLLOW US
@frontiersin

IMPACT METRICS
Advanced article metrics track visibility across digital media

EXTENSIVE PROMOTION
Marketing and promotion of impactful research

LOOP RESEARCH NETWORK
Our network increases your article's readership